SCUOLA NORMALE SUPERIORE

Classe di Scienze

Collisional Excitation in Space: from the Interstellar Medium to Planetary Atmospheres

Author: **Francesca Tonolo**

SNS Internal Advisor:
Dott. **Zoi Salta**

Supervisor:
Prof.ssa **Cristina Puzzarini**

Co-supervisor:
Dott. **Luca Bizzocchi**

A thesis submitted in fulfillment of the requirements
for the degree of Doctor of Philosophy
in

Astrochemistry
(cycle XXXV)

Settore Scientifico Disciplinare: CHIM/02 – Chimica Fisica

List of Publications

1. M. L. Dubernet, C. Boursier, O. Denis-Alpizar, Y. A. Ba, N. Moreau, C. M. Zwölf, M. A. Amor, D. Babikov, N. Balakrishnan, C. Balança, M. Ben Khalifa, A. Bergeat, C. T. Bop, L. Cabrera-González, C. Cárdenas, A. Chefai, P. J. Dagdigian, F. Dayou, S. Demes, B. Desrousseaux, F. Dumouchel, A. Faure, R. C. Forrey, J. Franz, R. M. García-Vázquez, F. Gianturco, A. Godard Palluet, L. González-Sánchez, G. C. Groenenboom, P. Halvick, K. Hammami, F. Khadri, Y. Kalugina, I. Kleiner, J. Kłos, F. Lique, J. Loreau, B. Mandal, B. Mant, S. Marinakis, D. Ndaw, P. Pirlot Jankowiak, T. Price, E. Quintas-Sánchez, R. Ramachandran, E. Sahnoun, C. Santander, P. C. Stancil, T. Stoecklin, J. Tennyson, F. Tonolo, R. Urzúa-Leiva, B. Yang, E. Yurtsever, M. Zóltowski (2023). BASECOL2023 scientific content, *A&A*, **683**, A40.

2. F. Tonolo*, L. Bizzocchi, V. M. Rivilla, F. Lique, M. Melosso, C. Puzzarini (2024). Collisional excitation of PO^+ by *para*-H_2: potential energy surface, scattering calculations, and astrophysical applications, *MNRAS*, **527**, 2279.

3. A. Melli, M. Melosso, L. Bizzocchi, S. Alessandrini, N. Jiang, F. Tonolo, S. Boi, G. Castellan, C. Sapienza, J.-C. Guillemin, L. Dore, C. Puzzarini (2022). Rotational Spectra of Unsaturated Carbon Chains Produced by Pyrolysis: The Case of Propadienone, Cyanovinylacetylene, and Allenylacetylene, *J. Phys. Chem. A*, **126**, 6210 – 6220.

4. F. Tonolo*, F. Lique, M. Melosso, C. Puzzarini, L. Bizzocchi (2022). Hyperfine resolved rate coefficients of $HC^{17}O^+$ with H_2 ($j = 0$), *MNRAS*, **516**, 2653 – 2661.

5. V. Rivilla, L. Colzi, I. J. Serra, J. M. Pintado, A. Megías, M. Melosso, L. Bizzocchi, Á. López-Gallifa, A. Martínez-Henares, S. Massalkhi, B. Tercero,

*Articles to which I was addressed as corresponding author.

P. de Vicente, J.-C. Guillemin, J. García de la Concepción, F. Rico-Villas, S. Zeng, S. Martín, M. A. Requena-Torres, F. Tonolo, S. Alessandrini, L. Dore, V. Barone, C. Puzzarini (2022). Precursors of the RNA-world in space: Detection of (Z)-1,2-ethenediol in the interstellar medium, a key intermediate in sugar formation, *ApJL*, **929**, L11.

6. M. Melosso, L. Bizzocchi, H. Gazzeh, F. Tonolo, J.-C. Guillemin, S. Alessandrini, V. M Rivilla, L. Dore, V. Barone, C. Puzzarini (2022). Gas-phase identification of (Z)-1,2-ethenediol, a key prebiotic intermediate in the formose reaction, *Chem. Commun.*, **58**, 2750-2753.

7. F. Tonolo, L. Bizzocchi, M. Melosso, F. Lique, L. Dore, V. Barone, C. Puzzarini (2021). An improved study of HCO^+ and He system: Interaction potential, collisional relaxation, and pressure broadening, *J. Chem. Phys.*, **155**, 234306.

8. A. Melli[†], F. Tonolo[†], V. Barone, C. Puzzarini (2021). Extending the Applicability of the Semi-experimental Approach by Means of "Template Molecule" and "Linear Regression" Models on Top of DFT Computations, *J. Phys. Chem. A*, **125**, 9904-9916.

9. S. Alessandrini, F. Tonolo, C. Puzzarini (2021). In search of phosphorus in astronomical environments: The reaction between the CP radical ($X^2\Sigma^+$) and methanimine, *J. Chem. Phys.*, **154**, 054306.

10. F. Tonolo, J. Lupi, C. Puzzarini, V. Barone, (2020). The quest for a plausible formation route of formyl cyanide in the interstellar medium: a state-of-the-art quantum-chemical and kinetic approach, *ApJ*, **900**, 85.

[†]The two authors equally contributed to this work.

Abstract

In the last decades, the synergy between astronomical observations and laboratory studies (increasingly based on the interplay of experiment and theory) has led to the discovery of an ever-increasing number of molecules in many astrophysical sources, with the astronomical spectra becoming more and more detailed. This suggests that a rich chemistry is taking place in all stages of the life cycle of a star. However, in space, harsh physical conditions pose severe constraints to the chemical processes it hosts, which greatly differ from those occurring in terrestrial environments. For instance, in the interstellar medium, molecular energy level populations are rarely at the local thermodynamic equilibrium (LTE) because the density is usually so low ($\sim 10^2 - 10^6\,\mathrm{cm}^{-3}$) that collisions compete with radiative processes (Kłos and Lique, 2017). Under such conditions, deriving molecular abundances from spectral lines requires the knowledge of the collisional rate coefficients of the molecule under consideration for the most abundant perturbing species. The nature of the latter depends on the investigated astronomical environment. For instance, in interstellar clouds, the most important perturbers are molecular hydrogen (H_2), atomic hydrogen and He, the latter being also used as an approximation of H_2 (Roueff and Lique, 2013). Differently, if one aims to constrain molecular abundances in cometary comas, collisional excitation is generally dominated by H_2O (and/or electrons) and, for comets at large heliocentric distances, by CO (Bockelée-Morvan et al., 2004). In planetary atmospheres, the molecular composition is not standard and is, instead, very system-specific; in the thermosphere of Titan, for example, N_2 and CH_4 are the most abundant collisional partners (Rezac et al., 2013). Given the extreme conditions of those environments, which are difficult to be reproduced in the laboratory, the knowledge of the collisional rate coefficients strongly relies on theoretical calculations. However, pressure-broadening measurements are frequently employed to provide an experimental validation of the computational procedure (Meuwly and Hutson, 1999).

During my PhD, I have mainly focused my research on the theoretical and ex-

perimental determination of the relevant collisional parameters of molecules of astrochemical interest. The aim of this research is to support new astronomical investigations and gain more information regarding gas densities, molecular abundances and excitation temperatures *via* radiative transfer models. Going into detail, this thesis will describe the various steps required to retrieve the collisional coefficients and derive non-LTE molecular column densities. First, an accurate characterization of the interaction potential for the collisional system is needed. This is accomplished by fitting the potential to an expansion over angular functions on top of a grid of interaction energies computed by means of highly accurate *ab initio* calculations. In this respect, the good performance of explicitly correlated coupled-cluster methods for mapping the short- and long- range multi-dimensional interaction potential energy surface is pointed out. Having characterized the potential, in order to ensure the right balance between accuracy and efficiency of the scattering calculations, preliminary tests on the influence of the rotational basis of each collider on the value of the collisional cross sections are carried out. Indeed, this allows to apply proper approximations to the potential in order to decrease the computational effort while not significantly affecting the accuracy. Subsequently, a validation of the methodology employed is performed by exploiting the computational-experimental comparison for the bound state spectroscopic parameters and/or pressure broadening coefficients. The latter, moreover, may be very helpful in the determination of accurate rest transition frequencies in support of astronomical surveys. Then, the standard time-independent coupled scattering equations are solved using the MOLSCAT program (Hutson and Green, 1994), thus providing the collisional (de-) excitation rate coefficients. The last step is the solution of radiative transfer equations (RADEX code; van der Tak et al. 2007) to model astrophysical observations and derive molecular column densities.

With the purpose of contributing to each step of the collisional framework, the systems investigated in this thesis are: HCO^+/He, $HC^{17}O^+/H_2$, $HC^{18}O^+$/Ar, PO^+/H_2, HCN/N_2 and HC_3N/N_2. Each of them provides insights into one or more specific parts of the collisional procedure summarized above, with a special focus on their relevance to astrophysical applications. Moreover, these systems are intended to range over various astrophysical conditions that may be found in space, from the interstellar medium to Titan's atmosphere, thereby broadening the range of application of the outlined research protocol.

Contents

Chapter 1

Introduction

Our perception and knowledge of the universe have experienced an extensive transformation over the past decades. In contrast with the prevailing scientific thought over 50 years ago, the space revealed itself in a new guise: a chemically fertile place where molecules are ubiquitous and reach high degree of complexity, from a dimensional point of view (to date, molecules containing up to 70 atoms have been detected; Müller et al. (2005)) but also in terms of variety of atoms and functional groups. The exploration of chemical diversity through the universe led scientists to define the concept of chemical evolution, which came from the recognition that the stages over the entire life cycle of stars can be defined by the composition where they are formed (Suzuki et al., 1992; Yamamoto, 2017). This makes chemical compositions excellent tracers to diagnose the evolutionary stage and the physical properties of astronomical sources. Moreover, the detection of complex organic and potentially prebiotic molecules, such as amino acids, in meteorites and other astronomical environments, has further stimulated the debate on the origin of the building blocks of life in the universe. As a consequence, the adoption of a chemical approach in astronomy has become increasingly important, thus giving birth to a rapidly growing research field: astrochemistry, which studies the birth and evolution of our universe from a molecular point of view.

One of the major aims of astrochemistry is to understand the chemical evolution of astronomical objects, starting from an accurate census of their molecular content (Woon, 2004; McGuire, 2022). In this regard, the strong synergism between laboratory spectroscopy and radioastronomy permitted in the last years to identify a large number of molecules in space, and in particular in the interstellar medium (ISM), *i.e.*, the rarefied matter consisting of gas and dust that exists between stars within a galaxy. Most of these molecules have been detected by means of radio observations of their rotational spectral lines, which can be considered actual molecular fingerprints. Nevertheless, there are still many features that remain unassigned in ra-

dioastronomical surveys. Indeed, molecular identifications can only be accomplished if the molecular spectra are known with great accuracy, this requiring a thorough experimental laboratory work. Since the analysis of a rotational spectrum can be extremely complex and, if not adequately supported, can lead to misleading results, quantum chemistry plays a very important role in guiding experimental studies.

In space, moreover, molecular energy level populations are rarely at the local thermodynamic equilibrium (LTE) because the density is usually so low that collisions compete with radiative processes (Kłos and Lique, 2017). Under such conditions, the interpretation of observed interstellar spectra in terms of molecular abundances requires the knowledge of collisional rate coefficients of the molecules involved due to the most abundant perturbing species.

In the last decades, the application of molecular beams and laser techniques has begun to provide very detailed information about collisions (*e.g.*, van Dishoeck 1997; Yang et al. 2010, 2011; Chefdeville et al. 2012 and Brouard et al. 2014). The deflection of a molecule's trajectory due to molecular beams experiments is up to now one of the most sensitive probes of the interaction potential (the reader is referred to Bergeat et al. 2020 and Besemer et al. 2022 for some illustrative applications). However, the experimental setups able to probe collision dynamics for astrophysical applications are still scarce. To overcome this limitation, state-of-art quantum chemistry techniques are a reliable means to directly estimate collisional rate coefficients. As a matter of fact, computational approaches employing advanced treatments of both electronic and nuclear motions can support the experiments providing results with comparable accuracy (Lique et al., 2010b). Furthermore, the interplay of experiment and theory provides a means of reciprocal validation. For example, experimental measurement of the pressure broadening and pressure shift coefficients can be used to verify the computational accuracy.

Having retrieved the information related to the chemical composition and abundance of a given astronomical object, the next step is the investigation of its chemical reactivity, which means to understand how the detected molecules were formed and how can further react. This also represents an important step toward the determination of the physical conditions and evolutionary stage of the astronomical object under consideration. However, the extreme conditions of the ISM put severe constraints on the chemical reactions that can occur, thus requiring the study of possible reaction mechanisms from both thermochemical and kinetic points of view. This information together with reaction networks connecting all detected molecules then feed astrochemical models that, in principle, should be able to describe the chemical evolution of the astrochemical object under consideration.

To sum up, it all boils down to three main astrochemical questions: what molecules are present in the universe? What is their abundance? How could they be formed and how can they further evolve? The answers to these questions can only

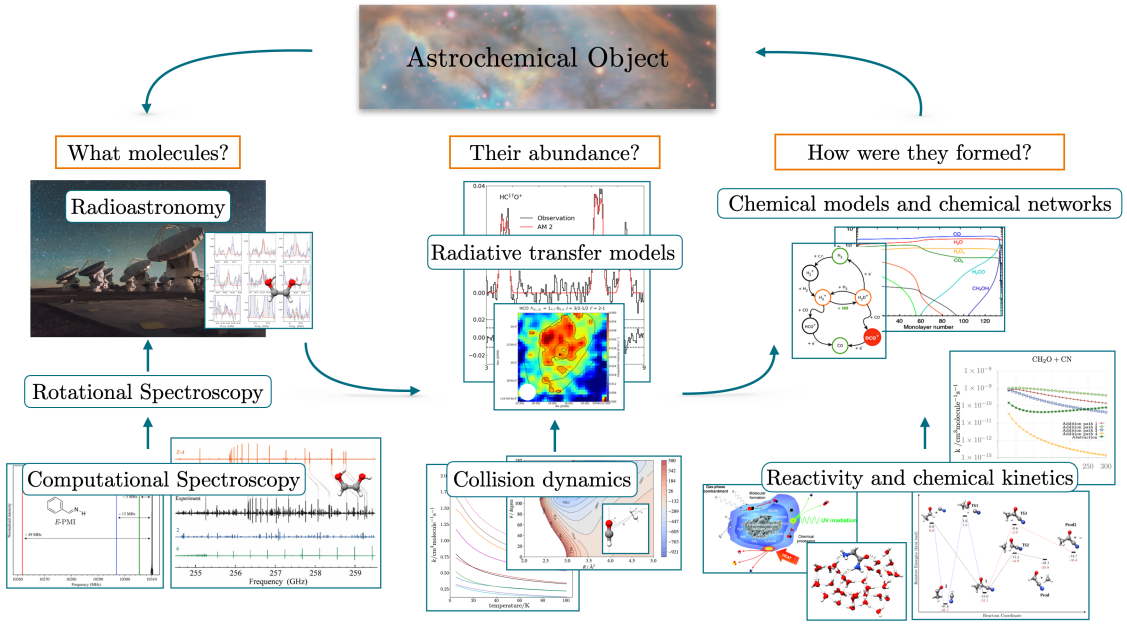

Figure 1.1: Main research lines involved in astrochemistry. The images were taken from Rivilla et al. (2022a); Melli et al. (2021); Asensio et al. (2022); Tonolo et al. (2022); Alessandrini et al. (2021); Tonolo et al. (2020); Caselli and Ceccarelli (2012).

be obtained by putting together many pieces, each bringing precise and precious information, of a giant puzzle that covers different research fields, from the macroscale of astrophysical investigations to the atomistic view of molecular spectroscopy and quantum chemistry, to proceed with chemical reactivity and its modeling, and to conclude with a flavor of biology and geology when moving towards planets. In order to provide a glimpse of this complex picture, a schematic summary of the main research lines involved in the field of astrochemistry is presented in Figure 1.1. Together with the high interdisciplinary nature they entail, such investigations require to range over extremely diverse physical conditions, from the dense environments of the hot ionized medium or in the inner midplanes of protoplanetary disks, to the cold and rarefied conditions of molecular clouds.

In this Chapter, I will present the framework of the research projects I have carried out during my Ph.D., which aim to bring a contribution to current frontiers in astrochemistry. In § 1.1 more details about the discovery of the molecular wealth in the ISM are provided, while in § 1.2 the focus is the role of chemical complexity to trace the evolutionary stages of the life cycle of stars. Finally, a glimpse into the characteristics of Titan's atmosphere, whose relevance lies on the fact that it is considered a primordial Earth, is provided in § 1.3.

1.1 Molecules in Space

Most of the baryonic mass of our galaxy, *i.e.*, the Milky Way, is located in stars. However, 10% of this matter resides in the ISM, both in the form of gas and dust particles. In these environments, the discovery of molecules is quite recent. Indeed, in the early 1900s, the ISM was considered nearly an empty space, allowing only the presence of rarefied atoms stemming from the Big Bang and stellar nucleosynthesis. Despite the discovery of the interstellar gas (Hartmann, 1979) and dust (Trumpler, 1930), the conditions of such environments were considered too hostile to allow for any kind of chemical reactivity and complexity. This belief was not undermined even by the detection of the first diatomic molecules such as CH, CN and CH^+ (McKellar, 1940; Douglas and Herzberg, 1941). For about 20 years the interest on molecules waned, and no new species other than these first few diatoms were discovered. When, in 1955, C. H. Townes proposed for the first time to use the microwave radiation to investigate the presence of molecules in the ISM, he did not receive much attention from the scientific community (Townes, 1957). Only in the late 1960s, with the onset of radioastronomy — which shed light on the Big Bang model by recording the cosmic microwave background (CMB) radiation — the identification of the first polyatomic molecules in the ISM challenged all the previous convictions. The first molecules discovered were ammonia (NH_3) in 1968 (Cheung et al., 1969a), water (H_2O) (Cheung et al., 1969b) and formaldehyde (H_2CO), the first organic molecule (Snyder et al., 1969), in 1969. In 1975, methyl formate was detected as well, thus leading to the definition of complex organic molecules (COM) (Herbst and van Dishoeck, 2009) which are molecules containing more than 5 atoms and at least one carbon. The detection of new molecules proceeded with a constant pace until 2020 (McGuire, 2022), with a steep increase in the last three years when more than 80 new molecules were discovered, *i.e.*, nearly 1/4 of the molecular species detected so far. Indeed, more than 300 molecules have been identified in the ISM and circumstellar shells (Müller et al., 2005), including molecules of interest from a prebiotic point of view such as glycolaldehyde, the basic unit for sugars formation (Hollis et al., 2000), propylene oxide, the first chiral molecule (McGuire et al., 2016), and very recently also glycolamide (Rivilla et al., 2023), an isomer of glycine, the simplest amino acid.

1.2 Chemical Evolution: Tracing the Life Cycle of Stars

As already mentioned, molecular complexity and the life cycle of a star, which evolves from a dying star to the formation of a new star and planetary systems passing through the diffuse and molecular clouds evolutionary stage, proceed hand in hand, leading to the concept of chemical evolution. At its first stage, the pres-

ence of interstellar UV radiation, which is able to deeply penetrate the cloud, forms hot/warm ionized medium where the particles are both diffuse and ionized by molecular photodissociation (McKee and Ostriker, 1977; Yamamoto, 2017). In this phase, only simple molecules are observed and the dominant form of gas-phase carbon is C^+. Triggered by a perturbation such as gravitational instability, the cloud starts to collapse and protons recombine with electrons forming diffuse clouds, where atomic and molecular hydrogen coexist. At this stage, carbon is present in its neutral form, and its hydrogenated compounds (CH, CH_2) react with oxygen to form CO. Since CO is a very stable molecule, it no longer reacts in the gas phase. However, during the C $\rightarrow$ CO conversion, various organic unsaturated molecules are produced by gas-phase reactions, such as simple carbon-chain molecules. In the late stage of the C $\rightarrow$ CO conversion, the increasing abundance of N_2 molecule produces also simple nitrogen-containing species. As the temperature decreases and the density increases, hydrogen molecules become the dominant form of hydrogen (the cloud being shielded by UV radiation) and the cloud is referred to as a molecular cloud. Here, the depletion of molecules, *i.e.*, the abundance reduction of a given molecule in the gas phase due to its adsorption on dust grains, becomes significant. This has a huge impact on molecular compositions: for example, the depletion of CO from the gas phase extends the lifetime of N_2H^+ and $H_3{}^+$ (the reaction with CO being their major destruction route). Moreover, grain-surface reactions start to impact on the chemical networks, thus supporting the release of saturated organic molecules, which are mainly formed on dust grains.

At this point, the increase in density within the cloud undergoes the influence of gravitational contraction, causing matter to accumulate toward the center of the nebula to form the so called pre-stellar cores. During this phase, hydrogenation reactions govern the molecular kinetics, leading to the formation of molecules such as water (H_2O), formaldehyde (H_2CO), or methanol (CH_3OH). From the gravitational contraction of molecular cloud cores, protostars are born, and the rise in temperature triggers violent ejections and molecular outflows, creating envelopes around the future star. These envelopes are characterized by high chemical complexity because of the energy supplied by the protostellar shocks, and tend to dissipate energy to form the so-called protoplanetary disks. Subsequently, interstellar dust begins to aggregate into planetesimals (the seeds of future planets), comets, and asteroids. In the meanwhile, the protostars evolve into main-sequence stars, which, in their late stages, show considerable mass loss and release gas and dust into the ISM. Massive stars (*i.e.*, stars with a mass higher than 8 times the solar mass, $M_\odot$), at the end of their lives, return in the ISM a considerable mass through supernova explosions. It winds up a dog chasing its own tail: interstellar matter circulates through and defines the entire life cycle of stars to be subsequently released back into space and providing the primordial elements of new stellar and planetary systems.

An immediate implication emerging from this evolutionary cycle is that, besides studying chemical complexity, molecules play a great diagnostic role. The most representative example is provided by CO and its isotopologues as chemical thermometers for the interstellar gas (the reader is referred to Yamamoto (2017) for more details and Peng et al. (2012) for a practical example). HCO^+ and CCS have often been used as tracers of molecular ionization (Wootten et al., 1979; Caselli et al., 1998) and magnetic field (see Koley (2022) and references therein), respectively, whereas the N_2H^+ and CO ratio governs the degree of depletion into dust grains (Bergin et al., 2001; Aikawa et al., 2001). In addition, major diagnostic importance is attributed to those molecules that could play a role in terms of "abiogenesis", namely, the formation of prebiotic species from abiotic systems (Pearce et al., 2017; Puzzarini, 2022). In this regard, the chemistry involving the carbon, hydrogen, oxygen, nitrogen, phosphorus, and sulfur atoms (CHONPS), *i.e.*, the elements found in all living systems (Öberg and Bergin, 2021; Bergner et al., 2022), acquires a particular relevance. Among them, P-bearing molecules deserve a special mention in the search of the constituent elements of life: while phosphorus abundance in living organisms is relatively high (Fagerbakke et al., 1996), its actual observed abundance in space is several orders of magnitude lower (Chantzos et al., 2020). This discordance, which is very high compared with that of the other elements, may be caused by an observational gap. For this reason, research activities targeting new detections of P-bearing species in the ISM, together with the investigation of their molecular abundances and chemical pathways, deserve a special attention.

1.3 Titan: an Alien, yet Familiar World

One of the current frontiers of astrochemistry, besides drawing an accurate picture of our universe and its evolutionary processes, lies in the investigation of which processes occurred in the formation of the terrestrial environments, with a special focus on the origin of life. However, despite the efforts of several experiments to simulate the terrestrial primordial stages — first of all, the well-known Miller–Urey experiment (Miller, 1953) — it is impossible to properly model in a laboratory all the processes that may have been concurred to the early Earth chemistry. In this context, the study of objects similar to the primitive Earth takes a particular relevance. This would provide important insights into the initial conditions of the terrestrial evolutionary processes and the chemical networks that occurred in the first abiogenetic phenomena. A particularly suitable environment for this type of investigations is Titan, the largest moon of Saturn. As far as we know, Titan is the only celestial body in our solar system, in addition to Earth, with a nitrogen-rich atmosphere. Moreover, it is characterized by a manifest seasonality and its pressure and temperature conditions allow for an active "methanological" cycle, with many

features reminiscent of the hydrological terrestrial one being found: methane and ethane form clouds and precipitate onto the surface to produce lakes, where an icy crust is found and forms a mosaic of surface features (from mountains peaks to sand dunes), and even possibly erupts as a slurry of ammonia in cryovolcanoes (Cable et al., 2012).

The first information about Titan's atmosphere was retrieved from the data collected by the Voyager 1 and Voyager 2 space probes, which revealed a chemically dense and reactive atmosphere, mainly composed of N_2 ($\sim$ 97%) and CH_4 ($\sim$ 2%) (Tyler et al., 1981; Smith et al., 1982). Subsequently, the Cassini-Huygens mission (Matson et al., 2002; Brown et al., 2009) further emphasized the role of Titan's atmosphere as a chemical factory: it discovered a wealth of reactive molecules that, thanks to both endogenous and exogenous energy sources (*e.g.*, the radiation from the Sun and energetic particles from Saturn's magnetosphere), promote intense ionic and radicalic reactivity leading to a high chemical complexity. The result is the formation of large organic molecules. Among their precursors, the HCN, HNC and HC_3N linear nitriles play a strong diagnostic role of the physical characteristics of Titan's atmosphere, because they show vertical gradients from their primary formation site in the upper atmosphere to condensation below 80 km of altitude (Thelen et al., 2019). However, due to the rapidly decreasing density, non-LTE effects can become important, resulting in unreliable abundance retrievals if not adequately assisted by collisional investigations (Cordiner et al., 2018). The formation of gaseous hydrocarbons and nitriles can further proceed by means of ionization and polymerization processes, thus forming aerosol particles (which are responsible for the typical Titan's haze) that can grow to form aggregates that subsequently fall on the surface (Cable et al., 2012).

1.4 Principal Aim of this Thesis

The purpose of this thesis work is to identify a general protocol for the collisional characterization of molecular systems of astrochemical interest. In particular, special attention will be paid on the derivation of reliable collisional data that would support the astrophysical modeling of ionic and neutral species in the ISM and Titan's atmosphere.

This thesis is organized as follow. In Chapter 2, the theoretical background will be presented, with a particular focus on spectroscopy and collision dynamics. An in-depth description of the computational strategies will be provided in Chapter 3. Chapter 4 will delve into the details of pressure broadening experiments, from the description of the instrument employed to the experimental procedure and the subsequent analysis. In Chapter 5, the theory behind astrophysical modeling by means of radiative transfer calculations will be outlined. Finally, in Chapter 6, the

adopted protocols and the outcomes obtained on six different collisional systems of astrophysical interest will be reported, while in Chapter 7 the final conclusions will be drawn.

During the four years of my Ph.D. I have also devoted my attention to research topics, still pertaining the astrochemical framework, which, however, fall outside the collision dynamics investigations which are the foundations of this thesis. A brief description of some of them will be provided in Appendix B.

Chapter 2

Theoretical Background

2.1 Astronomical Spectroscopy

The knowledge we have gained so far about composition, distributions and kinematics of matter throughout the astronomical sources of the universe, relies in large part on the information brought to the observer by the electromagnetic radiation collected by telescopes, with a small contribution being given by carriers such as meteorites, cosmic ray particles or material samples collected by space probes. Each region of the electromagnetic spectrum provides a different viewpoint to observe the space. Indeed, in the microwave (MW), infrared (IR), or visible (Vis) and ultraviolet (UV) regions, the (de-)excitation transitions are related to a rotational, vibrational or electronic motion, respectively. In the last decades, the vast majority of molecular detections in the gas phase has been accomplished using radioastronomy in the cm, mm and sub-mm wavelenght ranges. Nevertheless, the birth of radioastronomy is quite recent: after World War II, new receivers were instrumental in opening up the radio window in the Earth atmosphere's (roughly, from 15 MHz to a high frequency cut-off at about 1300 GHz). Indeed, the atmosphere surrounding the Earth is transparent to radio and MW radiation as long as none of its constituents is able to absorb it to a noticeable extent. Prior to radioastronomy, observations were restricted to measurements from the near UV to the near IR, in correspondence of the optical window (Fig. 2.1). To overcome this limitation, observational facilities developed new strategies involving baloons, high-flying aircrafts or satellites. Examples are provided by the Hubble Space Telescope (HST), the Far Ultraviolet Spectroscopic Explorer (FUSE), the Infrared Space Observatory (ISO) satellite, the Herschel, Spitzer and James Webb (JWST) space telescopes (Gardner et al., 2006), the latter launched in December 2021. With the dawn of radioastronomy, instead, astronomers got the opportunity to look at the universe directly from the ground. In the last decades and in particular in the very last years, observational breakthroughs

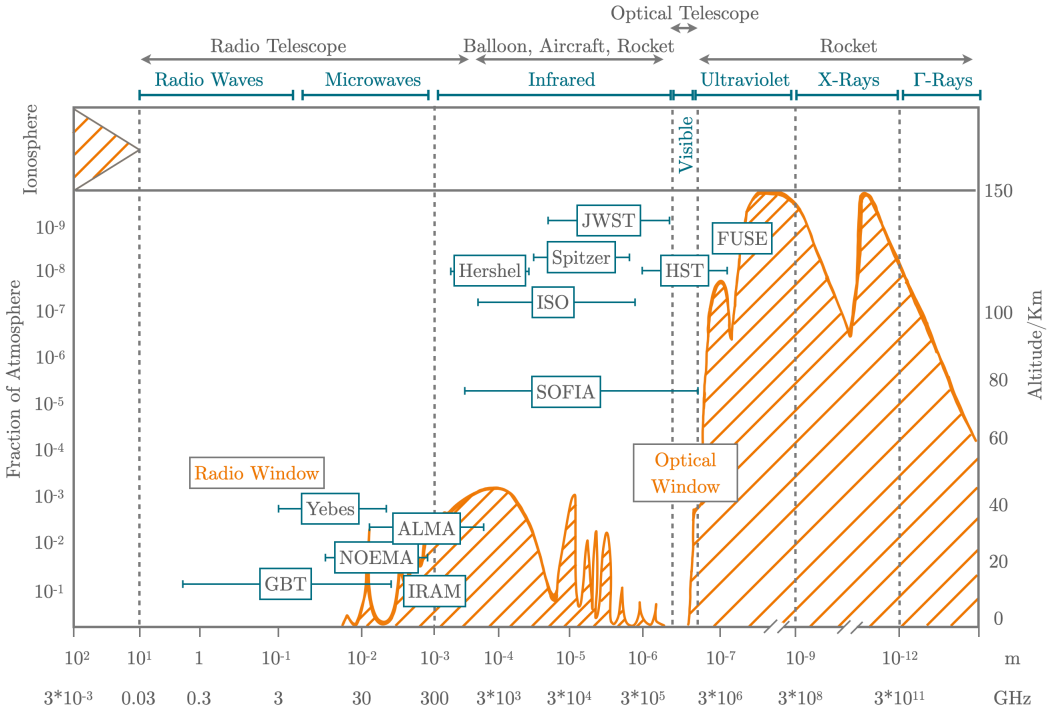

Figure 2.1: Transmission of the Earth's atmosphere for electromagnetic radiation. The orange trace indicates the altitude at which the radiation is attenuated by a factor of 1/2 (Figure adapted from Fig. 1.1 in (Rohlfs and Wilson, 2013)).

have been obtained owing to the rapid technological advances. Radiotelescopes have become very powerful tools due to unprecedented resolution and sensitivity of the Atacama Large Millimeter/submillimeter Array (ALMA), whose working frequency range is 35−950 GHz (Wootten and Thompson, 2009), the accuracy and versatility of the Green Bank Telescope (GBT) covering the $0.1 - 100$ GHz range (Prestage et al., 2009; White et al., 2022), and the high technology instruments of the radiotelescope (40 m diameter) in the Yebes Observatory, which covers the $2 - 90$ GHz frequency range (Tercero et al., 2021; López-Pérez et al., 2021). Radioastronomical facilities permit the observation of pure rotational transitions of molecules, from which the molecular abundances and excitation temperatures* can be retrieved. This information is strictly related to the environments in which rotational transitions are observed, bringing important hints on the model of the targeted astronomical object. In detail, molecules are identified by means of transitions between energy levels due to the absorption or emission of a photon. This modifies the electromagnetic spectrum in the same way as the touch of human fingers affects surfaces: they leave impressions, as fingerprints, which are detailed and unique evidences of the main character of the modification. Indeed, the rotational features are extremely sensi-

*The reader is referred to ¶ 2.1.2 for a detailed definition of the excitation temperature.

tive to the molecular structure, and even allow for discriminating among the isotopic species of the same molecule. The only constraint is that rotational transitions are observed only if the molecule has a nonzero dipole moment (the reason for this will be clear from the treatment in the next section). In radioastronomy, we usually refer to emission because this is the most common way in which radiation is collected. In fact, rotational transitions involve very low energies and can thus occur even in very cold regions of the ISM. Higher-energy transitions (vibrational and electronic), on the other hand, are generally observed in absorption. For electronic transitions, in particular, absorption is the only possible observational option. The difference between emission and absorption lies in the way the spectra are recorded. Emission spectra are collected directly from the astronomical object and represent a convolution of all the emissions due to all molecules there present, without any directional constraint. On the contrary, absorption spectra require a setup similar to the one of a spectrometer: a source of radiation, which usually is a nearby star emitting in the continuum, a sample cell, which is the astronomical object itself, and a detector which is the telescope. These three elements should be along the line of sight of the telescope.

In the following, we will outline the theoretical framework embedding the derivation of the spectroscopical and collisional data required to interpret radioastronomical spectra. Their astrophysical applications, in terms of the derivation of molecular abundances, will be instead provided in Chapter 5.

2.1.1 Interaction of Radiation with Matter

With the only exception of the blackbody radiation, which only depends on the temperature of the emitting source, matter at non-zero temperature emits an electromagnetic radiation that contains a wealth of information regarding its composition, structure and density. This kind of emission is called thermal radiation. This implies that the accuracy of information we can infer from the spectral lines of interstellar clouds is strictly related to how good we are in describing the thermal radiation from its atoms and molecules. For the sake of simplicity, let us consider a two-level system, with a fundamental level l (lower) and an excited level u (upper), separated by the energy $E = E_u - E_l$, with g_l and g_u being their degeneracies, respectively. When an electromagnetic wave and a molecule "collide", different phenomena can occur: radiative interaction, transmission or scattering (see Fig. 2.2). If the electromagnetic wave has a resonant frequency (*i.e.*, it corresponds to the energy difference E), then radiative interaction might occur. The processes belonging to this category are: the spontaneous emission, stimulated emission and absorption of a photon, whose probability per unit time are represented by A_{ul}, $B_{ul}\,J_\nu$ and $B_{lu}\,J_\nu$, respectively. A_{ij} and B_{ij} are the Einstein coefficients for the spontaneous emission and for the induced emission/absorption between the levels i and j, respectively. J_ν

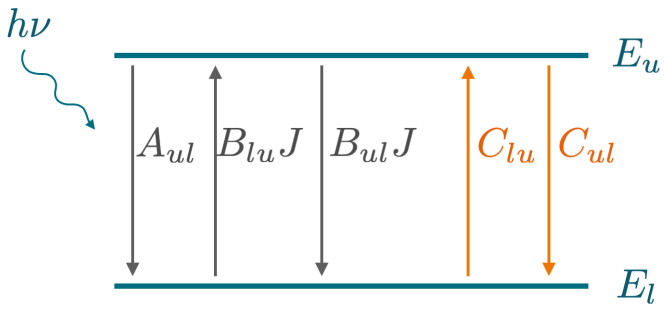

Figure 2.2: Processes involved in the distribution of population in a two-level system.

represents the mean intensity of the radiation for the solid angle of incidence:

$$J_\nu = \frac{1}{4\pi}\int I_\nu d\Omega\,. \tag{2.1}$$

If we assume that the radiation cames directly from the source without having been affected by any cloud's emission or absorption process, J_ν corresponds to the intensity of the radiation at ν frequency, which can be approximated as a blackbody B_ν with a temperature T_b:

$$J_\nu \to B_\nu(T_b) = \frac{2h\nu^3}{c^2}\frac{1}{\exp\left(h\nu/k_BT_b\right)-1}\,, \tag{2.2}$$

where h denotes the Planck constant, c the speed of light and k_B the Boltzmann constant. The units of $B_\nu(T_b)$ are $\mathrm{erg\,s^{-1}\,cm^{-2}\,Hz^{-1}\,sr^{-1}}$. For most of the cases, $B_\nu(T_b)$ corresponds to the CMB radiation, for which $T_b = 2.73\,\mathrm{K}$.

The Einstein A_{ul} coefficient governs spontaneous processes that are independent of the radiation energy, and is given by:

$$A_{u\ell} = \frac{64\pi^4\nu_{u\ell}^3 S_{u\ell}\mu^2}{3hc^3 g_u}, \tag{2.3}$$

with $S_{u\ell}$ being the line strenght (see Gordy et al. 1984 and Chapter 5 for more details) and μ the dipole moment of the molecule. The B_{ul} and B_{lu} Einstein coefficients are related to each other and are proportional to the Einstein A_{ul} coefficient *via* the following equations:

$$g_l B_{lu} = g_u B_{ul}\,, \tag{2.4}$$

$$B_{ul} = \frac{c^2}{2h\nu_{ul}^3}A_{ul}\,. \tag{2.5}$$

Moreover, collisional excitation and de-excitation of the target molecule with the perturbing gas of the surrounding environment can affect the population of the levels and depend on the composition and density of the cloud. The rate coefficients for collisional excitation and de-excitation processes are denoted as C_{lu} and C_{ul}, respectively, and are related to the density of the gas (ρ), its mean relative velocity with respect to the target molecule ($< v >$) and to the cross section for the collisional de-excitation, σ_{ul}:

$$C_{ul}(T) = \rho\,\sigma_{ul} \;< v >= \rho\, k_{ul}(T)\,, \tag{2.6}$$

where $k_{ul}(T)$ is the collisional rate coefficient for the $u \rightarrow l$ transition. From the principle of detailed balance, they also must satisfy the relation:

$$g_l C_{lu} = g_u C_{ul} \exp\left(-\frac{h\nu}{k_B T_k}\right)\,, \tag{2.7}$$

where T_k is the kinetic temperature of the perturbing gas.

The population distribution between rotational levels is defined from the balance of excitation and de-excitation by collisional and radiative processes:

$$\frac{dn_l}{dt} = -B_{lu}J_\nu n_l + B_{ul}J_\nu n_u + A_{ul}n_u - C_{lu}n_l + C_{ul}n_u\,, \tag{2.8}$$

where n_l and n_u are the number of molecules in level l and u per unit volume, respectively. Using the relations (2.4) and (2.5), Eq. (2.8) becomes:

$$\frac{dn_l}{dt} = -\frac{A_{ul}\left(\frac{g_u}{g_l}n_l - n_u\right)}{\exp\left(\frac{h\nu}{k_B T_b}\right) - 1} + A_{ul}n_u + C_{ul}\left\{n_u - \frac{g_u}{g_l}n_l \exp\left(-\frac{h\nu}{k_B T_k}\right)\right\}\,. \tag{2.9}$$

Since in the steady state $\frac{dn_l}{dt} = 0$ and $n_l + n_u$ is constant, we hence obtain:

$$\boxed{\frac{n_u g_l}{n_l g_u} = \frac{A_{ul}\left\{\exp\left(\frac{h\nu}{k_B T_b}\right) - 1\right\}^{-1} + C_{ul}\exp\left(-\frac{h\nu}{k_B T_k}\right)}{A_{ul}\exp\left(\frac{h\nu}{k_B T_b}\right)\left\{\exp\left(\frac{h\nu}{k_B T_b}\right) - 1\right\}^{-1} + C_{ul}}\,.} \tag{2.10}$$

This is the general form of the statistical equilibrium equation. Its resolution is mandatory in order to interpret the radioastronomical spectra in terms of abundances of molecules and to extract information about the physical parameters of the astronomical object (the reader is referred to Chapter 5 for more details). The same discussion can be easily extended to multilevel systems, where a set of rate equations similar to Eq. (2.10) is solved to determine level populations.

2.1.2 Beyond LTE approximation: the Role of Collisions in Space

Eq. (2.10) shows that we need information from both radiative and collisional processes in order to derive the population distribution. In detail, radiative information is governed by the radiation temperature (T_b), while collisional information is determined by the kinetic temperature of the surrounding gas (T_k). In order to derive the population distribution at one formal temperature, the excitation temperature T_{ex} is defined: it represents the balanced mean between T_b and T_k and permits to describe the population between the levels with a distribution analogue to the Boltzmann one. Its value depends on the surrounding environment, on the molecular system and on the kind of transition. We can thus adjust Eq. (2.10) as:

$$\boxed{\frac{n_u g_l}{n_l g_u} = \exp\left(-\frac{h\nu}{k_B T_{ex}}\right).} \tag{2.11}$$

When T_{ex}, T_b and T_k are greater than $\frac{h\nu}{k_B}$, we have

$$T_{ex} = T_k \frac{T_b A_{ul} + \frac{h\nu}{k_B} C_{ul}}{T_k A_{ul} + \frac{h\nu}{k_B} C_{ul}}. \tag{2.12}$$

At high densities of perturbing gas, $T_{ex} \sim T_k$. In such situations, the system is at LTE. This means that the collisions are sufficiently frequent in comparison with radiation probabilities to thermalize the system with the surrounding gas. In such conditions, $C_{ul} >> A_{ul}$ and Eq. (2.10) thus simplifies to:

$$\frac{n_u g_\ell}{n_\ell g_u} \cong \exp\left(-\frac{h\nu}{k_B T_k}\right). \tag{2.13}$$

This limiting case is always fulfilled in the conditions of the terrestrial environments, where the density of the atmosphere guarantees thermodynamic equilibrium. If the collisions are less frequent, cooling by radiation processes becomes more and more important, reaching the opposite limiting case: the level population is thermalized by the CMB radiation and $T_{ex} = 2.73\,\mathrm{K}$. In this case, Eq. (2.10) can be approximated to:

$$\frac{n_u g_\ell}{n_\ell g_u} \cong \exp\left(-\frac{h\nu}{k_B T_b}\right). \tag{2.14}$$

For intermediate densities, the level population is determined by the balance between collisional and radiative processes. In this respect, three different cases can be distinghished: the most common one is the so-called subthermal condition, where $T_b < T_{ex} < T_k$ and T_{ex} steadily increases as density increases (see left side of Fig. 2.3). In some cases, however, specific conditions may cause an inversion of the population

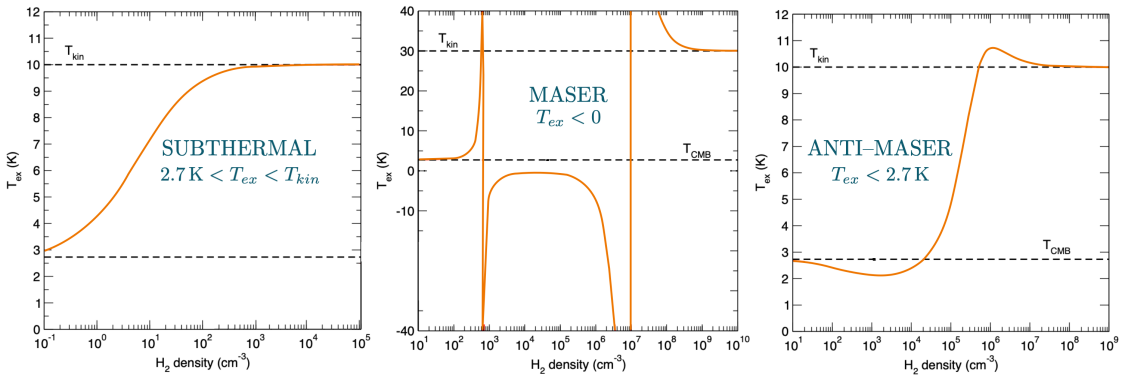

Figure 2.3: Three different phenomena that can occur from radiative equilibrium to LTE conditions by increasing the perturber density. From the left to the right side: subthermal, MASER and ANTI-MASER conditions. Figure taken from the lecture's slides of Prof. Alexandre Faure during the "Laboratory Astrophysics: Tracking the Evolution of Cosmic Matter towards Molecular Complexity" Winter School (Les Houches, 5-10 February 2023).

between levels, this occurs whenever the left-hand side of Eq. (2.10) is greater than unity. In these cases, the population of the upper energy level (n_u) is greater than the factor $(g_u/g_l)n_l$, thus leading to a negative T_{ex}. This phenomenum is known as microwave amplification of stimulated emission of radiation (MASER), and results in very bright line emission because of its exponential amplification (central image of Fig. 2.3). Finally, deviation from LTE could also enhance absorption. This is the case of ANTI-MASER, also denoted as "cosmic-refrigerators", where T_{ex} is less than 2.73 K but never reaches negative values (right side of Fig. 2.3). For an accurate description of these last peculiar situations, the reader is referred to Chapter 14 of Rohlfs and Wilson (2013).

For a line to be detectable, the gas density must be sufficiently high to permit emission between the levels. This means that collisions need to be sufficiently frequent to maintain a certain population in the upper level against de-excitation radiative phenomena. The minimum density of the perturbing gas in order to guarantee such population balance is called critical density, $n^{cr}_{u\to l}$, and is defined as:

$$n^{cr}_{u\to l} = \frac{\beta_{u\to l} * A_{u\to l}}{\sum_l k_{u\to l}(T)} \quad \text{with} \quad 0 < \beta_{u\to l} < 1\,, \tag{2.15}$$

where the $\beta_{u\to l}$ escape probability coefficient measures the optical thickness of the $u \to l$ transition, which corresponds to how easily the emitted radiation can be partially reabsorbed by the cloud, *i.e.*, the radiation trapping effect. $\beta_{u\to l}$ is an approximate correction but it represents a good descriptor for radiative transfer

applications. For an optically thin line[†], $\beta_{u\to l} = 1$.

Since the Einstein A_{ul} coefficient is proportional to the third power of the frequency and the square of the transition dipole moment (see Eq. (2.3)), different molecules and frequency ranges can be used to trace different density conditions of a cloud. For example, the emission of the lowest rotational transition of CO occurs in sparse regions and it is useful to delineate the large-scale structure of molecular clouds (Liszt and Lucas, 1998; Dame et al., 2001; Goldsmith et al., 2008; Bolatto et al., 2013).

In astrophysical media, the presence of extremely different densities avoids LTE condition to represent a reliable approximation to predict molecular abundances. In these environments, the role of collisional (de-)excitation processes to trace the different conditions is clearly crucial (for illustrative examples, the reader is referred to Lique et al. (2006); Daniel et al. (2006); Maret et al. (2009); Sarrasin et al. (2010); Daniel et al. (2012); Lanza et al. (2014)). Indeed, their efficiency relies on the composition of the medium and is strictly related to the density of the main perturbers and to the excitation temperature.

The first excitation studies of astrophysical molecules date back to 1970s, with the advent of radioastronomy (Townes and Cheung, 1969; Green and Thaddeus, 1974; Augustin and Miller, 1974). However, the limited computational resources forced to employ very approximate and scarcely accurate models. Only in the early 2000s, the progress made in terms of new theoretical methods and the availability of more powerful computational resources led to a breakthrough in terms of collisional data. In this context, the improvement of experimental techniques to benchmark theoretical approaches acquires a central importance. Although it is still difficult in laboratory to measure collisional properties in astrophysically relevant conditions, experimental results represent the best way to validate the computational procedure. For example, a stringent test for the accuracy of the potential employed in the scattering calculations is provided by pressure broadening measurements (Meuwly and Hutson, 1999). These experiments are line measurements in controlled pressure and temperature conditions and lead to the derivation of collisional line broadening and line shift coefficients, which are related to the real and imaginary parts of the collisional cross sections (see Eqs. (2.95) and (2.96) in ¶ 2.2.4). Moreover, the advances in experimental methods involving molecular beams and laser-based detection techniques permitted in the last decades to measure the relative state-to-state cross sections as a function of the collisional energy (Schewe et al., 2015) and also to observe interference effects in inelastic molecular collisions at low energy (Chefdeville et al., 2012; Bergeat et al., 2015; de Jongh et al., 2020). In concert with the advances made by molecular beam experiments, the use of the CRESU (Cinétique de Réaction en Ecoulment Supersonique Uniforme) apparatus, coupled with a tun-

[†]The reader is referred to Chapter 5 for the definition and explaination of the optical depth.

able pulsed IR pump laser to perform double resonance (DR) experiments (Rowe et al., 1984; Rowe and Marquette, 1987; Sims et al., 1994), pushed the comparison of absolute scale direct experimental measurements and theoretical calculations to the limit. With this technique, Labiad et al. (2022) directly measured the absolute state-to-state rate coefficients for rotational energy transfer of CO in collision with H_2 at very low temperatures ($5 - 20\,K$).

To summarize, significant progresses have been made in computing and measuring collisional rate coefficients down to the quantum regime. The accurate knowledge of these data is indeed crucial for modeling abundances and extracting many physical parameters of the astrophysical targets, such as the gas density, T_k, T_{ex}, the ionization rate, etc.. While experimental studies are still primarily focused on small and light species, theoretical studies are now able to deal with a larger variety of collisional systems of ever-increasing complexity. However, the comparison of theoretical results with the available experimental data contributed to benchmark the computational accuracies that could be achieved: for modern calculations, the typical deviations on the values of state-to-state rate coefficients are around 20% for biatomic and triatomic species, (Carty et al., 2004; Lique et al., 2010b; Yang et al., 2010), this ensuring high confidence on radiative transfer calculations and providing robust determinations of molecular abundances and physical properties of the astronomical environments. However, as the system size increases or stronger interactions are involved, the limited computational resources often require to use approximate methods such as time-dependent approaches (Pechukas, 1969), quasi-classical trajectories (Blais and Truhlar, 1976; Truhlar and Muckerman, 1979) or statistical approximations (Pechukas, 1976). Another way to ease the computational effort is to template the H_2 collider with He, since both of them are expected to similarly interact with the target species. Even if it is a crude approximation, it represents up-to-date the best way to obtain reliable data in a computationally undemanding manner for medium-sized molecules (Schöier et al., 2005; Lique et al., 2008). Given these premises, the need for further improvements thus emerges, aiming at reducing the computational effort without compromising the accuracy. For instance, a promising perspective in this direction can be provided by combining accurate calculations with extrapolation laws or machine learning techniques (see, *e.g.*, Meuwly 2021).

Nowadays, the available computed and experimental information is collected in collisional databases that are in constant growth: the most commonly used to interpret astrophysical spectra are the LAMDA (Schöier et al., 2010; van der Tak et al., 2020), BASECOL (Dubernet et al., 2024) and EMAA (`https://emaa.osug.fr`) databases. Nevertheless, there is still room for improvement. Indeed, only very few molecules among those observed in space have been characterized from a collisional point of view. In addition, there is a lack of collisional data for perturbers

that are not those of the ISM (which generally are H_2 and He). This prevents any reliable modeling of the molecular abundances and physical characteristics.

Finally, the detection of many molecular isotopologues sheds light on the investigation of the different evolutionary stages of our universe, thus exploiting the role of the so-called "isotopic anomalies" to link pristine small Solar System bodies and the first phases of the Sun formation (Caselli and Ceccarelli, 2012), and allows to model abundances of their thicker isotopic species (Yamamoto, 2017). However, up to a few years ago, all the abundance estimates for a given isotopologue were based on the collisional rate coefficients of the parent species. In some cases, this has been demonstated to be a unreliable approximation, in particular whenever the mass difference has an important effect (Wiesenfeld et al., 2011; Dumouchel et al., 2012; Faure et al., 2012; Bergeat et al., 2022). The same applies to hyperfine structures, which, despite their major diagnostic value for astrophysics, have been poorly resolved with respect to their collisional (de-)excitation. For these reasons, numerous efforts are currently devoted to collect highly accurate collisional data for the largest number of species.

2.2 Derivation of the Collisional Coefficients

The fundamental molecular data needed to interpret a non-LTE spectrum are: energy levels, radiative rates and collisional rate coefficients. While the first two can be inferred from spectroscopic measurements, the retrieval of collisional rate coefficients requires accurate quantum calculations. An overview of the current methodology for their derivation is outlined in this section. The starting point in this direction is a proper description of the molecular system, which is based on the best possible theoretical treatment as a result of the compromise between completeness and simplification. In this regard, the construction of the Hamiltonian and the formulation of the corresponding Schrödinger equation are presented in ¶ 2.2.1. ¶ 2.2.2 reports the solution of the ro-vibrational problem to derive the spectroscopic parameters of the target molecules as isolated entities. Then, the first step in the determination of the collisional coefficients is the calculation of the interaction potential between the molecular partners, *i.e.*, the target molecule and the colliding perturber, the procedure being described in ¶ 2.2.3. The potential obtained is then introduced in quantum scattering calculations, which solve the nuclear problem and determine the collisional cross sections, the latter providing the bases for the derivation of several collisional properties, as outlined in ¶ 2.2.4.

2.2.1 Description of the Molecular System

In a microscopic scale, the energetics and motion of a molecular system are described by the non-relativistic time-independent Schrödinger equation, which, in shorthand operator form, is written as:

$$\hat{\mathcal{H}}\psi(\mathbf{r},\mathbf{R}) = E\psi(\mathbf{r},\mathbf{R})\,. \tag{2.16}$$

$\psi(\mathbf{r},\mathbf{R})$ denotes the eigenstates of the system which depend on its electronic ($\mathbf{r}$) and nuclear ($\mathbf{R}$) coordinates. The molecular Hamiltonian operator ($\hat{\mathcal{H}}$) describes all the interactions that occur between the eigenstates of the system. Finally, E represents the corresponding eigenvalues which provide the energy levels of the system. When external fields are not present, $\hat{\mathcal{H}}$ is given by the sum of five operators representing the electronic and nuclear contributions to kinetic and potential energies:

$$\hat{\mathcal{H}} = \hat{\mathcal{T}}_n(\mathbf{R}) + \hat{\mathcal{T}}_e(\mathbf{r}) + \hat{\mathcal{V}}_{nn}(\mathbf{R}) + \hat{\mathcal{V}}_{ee}(\mathbf{r}) + \hat{\mathcal{V}}_{en}(\mathbf{r},\mathbf{R})\,. \tag{2.17}$$

In detail, these terms are defined as:

$$\begin{cases} \text{Kinetic} \begin{cases} \text{Nuclear} \rightarrow \hat{\mathcal{T}}_n(\mathbf{R}) = -\sum_k \dfrac{\hbar^2}{m_k}\nabla_k^2\,; \\ \text{Electronic} \rightarrow \hat{\mathcal{T}}_e(\mathbf{r}) = -\sum_i \dfrac{\hbar^2}{m_e}\nabla_i^2\,; \end{cases} \\ \text{Potential} \begin{cases} \text{Repulsive nucleus-nucleus} \rightarrow \hat{\mathcal{V}}_{nn}(\mathbf{R}) = +\sum_{k<l} \dfrac{e^2 Z_k Z_l}{R_{kl}}\,; \\ \text{Repulsive electron-electron} \rightarrow \hat{\mathcal{V}}_{ee}(\mathbf{r}) = +\sum_{i<j} \dfrac{e^2}{r_{ij}}\,; \\ \text{Attractive electron-nucleus} \rightarrow \hat{\mathcal{V}}_{en}(\mathbf{r},\mathbf{R}) = -\sum_i \sum_k \dfrac{e^2 Z_k}{r_{ik}}\,. \end{cases} \end{cases} \tag{2.18}$$

m_e and e are the mass and the charge of the electron, respectively, and m_k and Z_k are the mass and the charge of the k^{th} nucleus, respectively. The Laplacian operator ∇_p^2 corresponds to $\frac{\partial^2}{\partial p^2} = \frac{\partial^2}{\partial X^2} + \frac{\partial^2}{\partial Y^2} + \frac{\partial^2}{\partial Z^2}$, with $\{X, Y, Z\}$ being the coordinates of each particle p. r_{ik} represents the distance between the i^{th} electron and the k^{th} nucleus, r_{ij} that between the i^{th} and j^{th} electrons and R_{kl} that between the k^{th} and l^{th} nuclei.

In most cases, the resolution of Eq. (2.16) requires the Born–Oppenheimer (BO) approximation to be applied. This approximation is based on the very small electron-to-proton mass ratio ($\sim 5.4 \times 10^{-4}$), which permits to assume that, for any change in the nuclei configuration, the electrons are sufficiently fast to immediately adjust

their position. In mathematical terms, this means that the wave function can be factorized as:

$$\psi(\mathbf{r}, \mathbf{R}) = \psi_e(\mathbf{r}, \mathbf{R})\, \psi_n(\mathbf{R})\,, \tag{2.19}$$

where $\psi_e(\mathbf{r}, \mathbf{R})$ is the electronic wave function, which depends only parametrically on R, and $\psi_n(\mathbf{R})$ is the nuclear wave function. This allows for the separation of the problem into an electronic and a nuclear part. The first one entails the solution of the so-called electronic Schrödinger equation:

$$[\hat{\mathcal{T}}_e(\mathbf{r}) + \hat{\mathcal{V}}_{nn}(\mathbf{R}) + \hat{\mathcal{V}}_{en}(\mathbf{r},\ \mathbf{R}) + \hat{\mathcal{V}}_{ee}(\mathbf{r})]\, \psi_e(\mathbf{r},\mathbf{R}) = E_e(\mathbf{R})\, \psi_e(\mathbf{r},\mathbf{R})\,. \tag{2.20}$$

The eigenvalues $E_e(\mathbf{R})$ are parametrically dependent on the nuclei position and define the potential energy surface (PES), a hypersurface which is function of the $3N-6$ internal coordinates of the molecule ($3N-5$ in the linear case), where N is the number of atoms. Noteworthy, differences in mass of the nuclei do not affect the solution of the electronic Schrödinger equation. This means that the dynamics for different isotopologues takes places on the same PES, the only information about the isotope mass being contained in the $\hat{\mathcal{T}}_n(\mathbf{R})$ kinetic term. Having solved the electronic problem and built the PES ($E_e(\mathbf{R})$), one can proceed with solving the nuclear Schrödinger equation:

$$[\hat{\mathcal{T}}_n(\mathbf{R}) + E_e(\mathbf{R})]\, \psi_n(\mathbf{R}) = E\, \psi_n(\mathbf{R})\,. \tag{2.21}$$

At this point, we need to make a preliminary distinction. If the PES refers to the different sets of nuclear arrangements of an isolated molecule, its employment to solve the nuclear Schrödinger equation leads to retrieve the rotational and vibrational energy levels (see the discussion in ¶ 2.2.2). When studying a collisional problem, though, we are interested to the relative motions of the colliding particles and to the collisional energies. In this case, we will refer to the "collisional PES" or interaction potential. For an accurate characterization of the latter, careful considerations on the choice of internal coordinates and an appropriate grid of points to map the potential (¶ 2.2.3) are required.

For the resolution of a collisional scattering problem we therefore need the information that can be obtained from both the PES of the isolated colliders and the PES defined by their interaction. Solving the nuclear Schrödinger equation on the former allows us to obtain the vibrational and rotational states involved for each collider as an isolated entity. The solution of the nuclear problem for the collisional PES, on the other hand, provides a means to derive the transition cross sections between the different states of the target system due to collisions with the perturber molecule.

2.2.2 Elements of Rotational and Vibrational Spectroscopy

As already mentioned, the first step for describing the dynamics of a collisional system is the knowledge of the energies involved, and thus the ro-vibrational levels of the two isolated partners. This requires the solution of the nuclear Schrödinger equation on the molecular PES, for which an overview is presented in this subsection. However, for a more detailed treatment, we refer the reader to Papousek and Aliev (1982), Gordy et al. (1984), and Zare and Harter (1988).

To derive the ro-vibrational Hamiltonian operator for a polyatomic system, it is useful to adopt a body-fixed (BF) reference system that satisfies Eckart's conditions (Eckart, 1935). Within this coordinate frame, the kinetic energy can be decomposed into three independent terms: a vibrational term, depending only on the masses of the nuclei and on their displacement from their equilibrium configuration; a Coriolis energy term, describing the ro-vibrational interaction; a pure rotational energy term, defined as:

$$T_r = \frac{1}{2}\boldsymbol{\omega}^\top \boldsymbol{I}\boldsymbol{\omega}\,, \tag{2.22}$$

where $\boldsymbol{\omega}$ is the angular velocity vector and $\boldsymbol{I}$ is the instantaneous moment of inertia tensor, whose elements are:

$$I_{\alpha\beta} = \sum_k m_k \left[(R_k)^2 \delta_{\alpha\beta} - (R_k)_\alpha (R_k)_\beta \right] . \tag{2.23}$$

α and β denote the coordinates relative to the BF frame. Moreover, it is useful to introduce the dimensionless coordinates $q_s = \omega_s^{1/2} Q_s$, where Q_s is the s-th normal coordinate associated to the harmonic wavenumber ω_s and permits to move from the $3N$ space domain of the cartesian coordinates to the $3N-6$ ($3N-5$ if linear) molecular domain of independent normal coordinates. The advantage of this transformation is that the Kinetic Energy and Potential Energies expressed in such coordinates do not have mixed terms. While we report only the final result, the reader is referred to Papousek and Aliev (1982) for a detailed derivation of the ro-vibrational nuclear Hamiltonian. The latter, also denoted as Watson Hamiltonian, is given by:

$$\begin{aligned}\hat{\mathcal{H}} =& \frac{1}{2}\sum_{\alpha,\beta}\left(\hat{J}_\alpha - \hat{\pi}_\alpha\right)\mu_{\alpha\beta}\left(\hat{J}_\beta - \hat{\pi}_\beta\right) + \frac{1}{2}\sum_s \omega_s \hat{p}_s^2 + \\ &+ \hat{\mathcal{V}}(\mathbf{q}) - \frac{1}{8}\sum_\alpha \mu_{\alpha\alpha}\,.\end{aligned} \tag{2.24}$$

Here, the energetic contributions are expressed in terms of momenta. $\hat{J}_\alpha$ is the projection of the total angular momentum ($\mathbf{J}$) along the α axis, while $\hat{\pi}_\alpha$ is the

projected vibrational angular momentum on the α axis. $\mu_{\alpha\beta}$ are the components of the inverse of the effective inertia tensor $\boldsymbol{I}'$, defined as:

$$I'_{\alpha\beta} = I_{\alpha\beta} - \sum_{stu} \zeta^{\alpha}_{su}\zeta^{\beta}_{tu} Q_s Q_t \,, \tag{2.25}$$

where ζ^{α}_{st} is the Coriolis coupling constant, which couples Q_s and Q_t *via* rotation about α. The $\hat{p}_s$ operator in the second term of the right-hand side of Eq. (2.24) is the dimensionless vibrational momentum conjugate to q_s. The third term on the right-hand side represents the potential energy as a function of the dimensionless normal coordinates of the system. Finally, the last term on the right-hand side of Eq. (2.24) is denoted as the Watson term. It derives from the normal coordinate representation and is a mass-dependent contribution to the potential (Papousek and Aliev, 1982).

Expanding the Ro-Vibrational Hamiltonian

Starting from the Watson Hamiltonian, the ro-vibrational energy levels of a target molecule can be retrieved from the resolution of the associated Schrödinger equation. However, an exact formulation of the inverse inertia tensor $\boldsymbol{\mu}$ and of the potential as a function of $\mathbf{q}$ is usually unknown. Therefore, they are both expanded as Taylor series with respect to the normal coordinates q_s:

$$\mu_{\alpha\beta} = \mu^{(e)}_{\alpha\beta} + \sum_{s} \left(\frac{\partial \mu_{\alpha\beta}}{\partial q_s}\right)_e q_s + \frac{1}{2}\sum_{st} \left(\frac{\partial^2 \mu_{\alpha\beta}}{\partial q_s \partial q_t}\right)_e q_s q_t + \cdots \tag{2.26}$$

$$\hat{\mathcal{V}}(\mathbf{q}) = \frac{1}{2}\sum_{s} \omega_s q_s^2 + \frac{1}{6}\sum_{s,t,u} k'_{stu} q_s q_t q_u + \frac{1}{24}\sum_{st,uv} k'_{stuv} q_s q_t q_u q_v + \ldots \tag{2.27}$$

where $\mu^{(e)}_{\alpha\beta} = \frac{\delta_{\alpha\beta}}{I^{(e)}_{\alpha}}$ and $\omega_s = \left(\frac{\partial^2 V}{\partial q_s^2}\right)_e$, $k'_{stu} = \left(\frac{\partial^3 V}{\partial q_s \partial q_t \partial q_u}\right)_e$ and $k'_{stuv} = \left(\frac{\partial^4 V}{\partial q_s \partial q_t \partial q_u \partial q_v}\right)_e$ are, respectively, the harmonic, cubic and quartic force constants in a normal mode representation. By introducing Eqs. (2.26) and (2.27) in Eq. (2.24), the ro-vibrational Hamiltonian can be recasted as a series of terms $\hat{\mathcal{H}}_{m,n}$ based on the powers m for the vibrational operators (coordinates $\mathbf{q}$ and linear moments $\hat{\mathbf{p}}$) and n for the rotational operators ($\hat{\mathbf{J}}$):

$$\boxed{\hat{\mathcal{H}} = \sum_{m,n} \hat{\mathcal{H}}_{m,n} \,.} \tag{2.28}$$

Starting from this block-diagonal effective Hamiltonian, the terms required for the correct description of the system under consideration are selected.

Vibrational Hamiltonian

By considering only the first purely vibrational terms of the expansion in Eq. (2.28), one has:

$$\begin{aligned}\hat{\mathcal{H}}_{20} &= \frac{1}{2}\sum_{s}\omega_s\left(\hat{p}_s^2+q_s^2\right)\,,\\ \hat{\mathcal{H}}_{30} &= \frac{1}{6}\sum_{s,t,u}k'_{stu}q_sq_tq_u\,,\\ \hat{\mathcal{H}}_{40} &= \frac{1}{24}\sum_{s,t,u,v}k'_{stuv}q_sq_tq_uq_v\,,\\ &\dots\,.\end{aligned} \tag{2.29}$$

$\hat{\mathcal{H}}_{20}$ is the Hamiltonian of the harmonic oscillator, followed by the cubic and quartic potential terms, respectively, which describe the anharmonicity of molecular vibrations. The solution of the nuclear problem within the vibrational terms of the Hamiltonian leads to the vibrational levels of a molecular system and the so-called zero-point vibrational energy (ZPE) contribution, *i.e.*, the minimum energy contribution that all molecules undergo in their fundamental state. For a detailed treatment, the reader is referred, for example, to Barone (2004, 2005) and Yu and Bowman (2015).

The Principal Inertia System

Before solving the nuclear problem for the rigid rotor and semi-rigid rotor starting from the Hamiltonian in Eq. (2.28), it is convenient to define the Principal Inertia System representation in the BF frame, whose definition starts from assuming the molecular equilibrium configuration ($Q_s = 0$ for each s normal coordinate). In this case, both the inertia tensor and its inverse (μ) can be represented by diagonalizable matrices. Diagonalization "rotates" the axis of the molecule-fixed system into the axes of the Principal System of Inertia (a, b, c). In this representation, the diagonal elements of μ tensor are the inverse of the components of the inertia tensor along the a, b, c axes:

$$\mu = \begin{pmatrix} 1/I_a^{(e)} & 0 & 0 \\ 0 & 1/I_b^{(e)} & 0 \\ 0 & 0 & 1/I_c^{(e)} \end{pmatrix}\,, \tag{2.30}$$

with, by convention, $I_a \leq I_b \leq I_c$.

The values of the three principal moments of inertia allow a classification of the molecules based on the rotational symmetry:

Spherical top rotors: $I_a = I_b = I_c$.

Linear rotors: $I_a = 0, I_b = I_c$.

Symmetric top rotors: Molecules containing a $C_{n>2}$ symmetry axis.

- **Prolate** $\rightarrow I_a < I_b = I_c$.
- **Oblate** $\rightarrow I_a = I_b < I_c$.

Asymmetric top rotors: $I_a \neq I_b \neq I_c$.

Rigid Rotor Approximation

For collisional studies, the rigid rotor formulation of the molecular Hamiltonian is often employed. This means to consider only the first purely rotational term of the expansion of the ro-vibrational Hamiltonian of Eq. (2.28):

$$\hat{\mathcal{H}}_{02} = \sum_{\alpha} B_{\alpha}^{(e)} \hat{J}_{\alpha}^2 = A^{(e)} \hat{J}_a^2 + B^{(e)} \hat{J}_b^2 + C^{(e)} \hat{J}_c^2 \,, \tag{2.31}$$

where $B_{\alpha}^{(e)}$ is defined as the inverse of the corresponding α component of the moment of inertia ($\frac{1}{2I_{\alpha}^{(e)}}$ [‡]) and takes the denomination of $A^{(e)}, B^{(e)}$ and $C^{(e)}$ for $\alpha = a, b, c$, respectively.

Let us now focus on the linear rigid rotor, which is the symmetry of most of the target molecules considered in this thesis. In such a case, the Hamiltonian simplifies to:

$$\hat{\mathcal{H}} = B^{(e)} \hat{J}^2, \text{ with } \hat{J}^2 = \hat{J}_b^2 + \hat{J}_c^2 \,. \tag{2.32}$$

In the Principal System of Inertia, $\hat{\mathcal{H}}$ commutes with $\hat{J}^2$ and thus they have a common set of eigenfunctions (Zare and Harter, 1988), denoted as $|JM\rangle$[§]. J quantizes the total angular momentum and M, which assumes the values from $-J$ to J, quantizes its projection along the Z axis in the Space Fixed (SF) reference system. In such representation, $\hat{\mathcal{H}}$ is diagonal and its eigenvalues correspond to $B^{(e)}$ multiplied for the eigenvalues of $\hat{J}^2$ in the same basis. Therefore, the total energy results to be:

$$E_J = B^{(e)} J(J+1) \,. \tag{2.33}$$

Semi-Rigid Rotor Approximation

Within the rigid rotor approximation, the coupling between the vibrational and rotational motions is neglected. Therefore, this approximation does not consider any deviation of nuclei from their equilibrium position due to vibrations. If the system is instead considered non-rigid, the effects of vibration and centrifugal distortion

[‡]We use the atomic unit system, in which the electronic mass (m_e), charge (e) and the reduced Planck's constant ($\hbar$) are measuring units equal to 1.

[§]In the following, the Dirac notation will be adopted. This is a simplified way to describe a state of the system by reporting only the quantum numbers instead of expliciting the wave function.

should be taken into account. To accomplish this, one can resort to perturbation theory to solve the ro-vibrational problem. This implies a first-order contact transformation, which is a similarity transformation that converts the Hamiltonian in order to remove off-diagonal terms from the first order of its expansion (Eq. (2.28)). This transformation allows the inclusion of the "semi-rigid" contributions into the rotational Hamiltonian.

Focusing on the linear molecule, within the semi-rigid rotor approximation, the effects of centrifugal distortion reflect the deformation of the molecular structure due to the rotation itself and can be described by the $\hat{\mathcal{H}}_{\rm dist}$ Hamiltonian (Watson, 1977; Aliev and Watson, 1985):

$$\hat{\mathcal{H}}_{\rm dist} = \hat{\mathcal{H}}_{04} + \hat{\mathcal{H}}_{06} = -D(\hat{J}_\alpha^2)^2 + H(\hat{J}_\alpha^2)^3\,, \tag{2.34}$$

where D and H are the quartic and sextic centrifugal distortion constants, respectively. We hence obtain the following correction to rotational energy:

$$E_{\rm dist} = -DJ^2(J+1)^2 + HJ^3(J+1)^3\,. \tag{2.35}$$

To describe the effect of molecular vibration, the terms of the vibration-rotation Hamiltonian that need to be incorporated in the Hamiltonian are $\hat{\mathcal{H}}_{22}, \hat{\mathcal{H}}_{42}, \hat{\mathcal{H}}_{24}$, etc.. For rotational constants, second-order perturbation treatment leads to the following expression:

$$B_v^\beta = B_e^\beta - \sum_s \alpha_s^\beta \left(v_s + \frac{1}{2}\right) + \sum_{s,t} \gamma_{st}^\beta \left(v_s + \frac{1}{2}\right)\left(v_t + \frac{1}{2}\right) + \dots\,, \tag{2.36}$$

where β refers to a generic inertial axis, the sums run over the vibrational normal modes s and t, α_s^β denotes the vibration-rotation interaction constant arising from the $\hat{\mathcal{H}}_{22}$ term, while γ_{st}^β are higher order terms for the vibration-rotation interaction.

Nuclear Quadrupole Coupling

The presence of one or more nuclei with a nuclear spin ≥ 1 leads to interactions that split the rotational levels into multiple components (see, for example, Fig. 2.4). The effect on the rotational spectrum is the so-called hyperfine structure[¶]. When a nucleus has a nuclear spin $I \geq 1$, its charge distribution is not spherical and is thus characterized by a non-vanishing electric quadrupole moment. The interaction between the nuclear quadrupole moment and the electric field at the corresponding

[¶]Hyperfine splitting can be caused also by other electric and magnetic interactions such as the nuclear spin-rotation coupling. For the purposes of this thesis, only the nuclear quadrupole coupling interaction is considered because it produces by far the largest effect on the rotational spectrum.

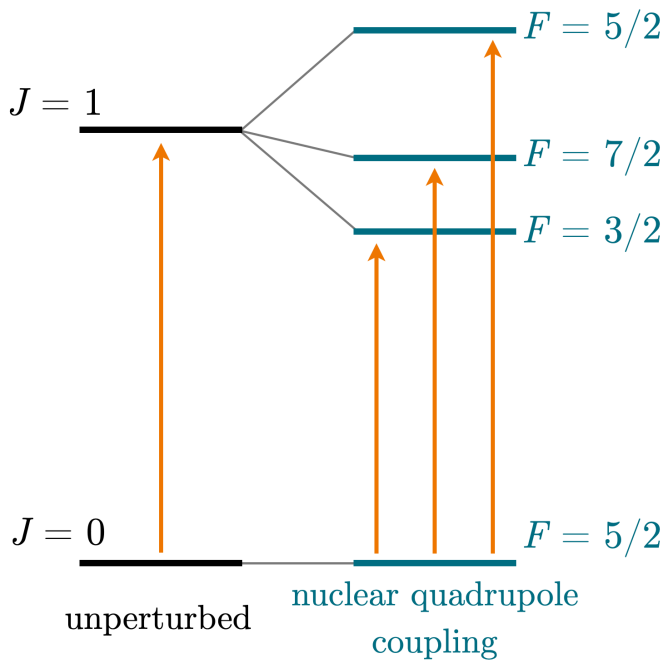

Figure 2.4: Hyperfine splitting of the first two rotational levels of $HC^{17}O^+$ induced by the nuclear quadrupole coupling of the ^{17}O nucleus ($I = 5/2$).

nucleus then occurs. In terms of momenta, this interaction determines the coupling between the nuclear spin momentum **I** and the rotational angular momentum **J**, thus leading to the total angular momentum **F**. This requires the definition of a new quantum number F, which can assume the values from $|I - J|$ to $I + J$.

To account for the nuclear quadrupole coupling, the additional contribution $\hat{\mathcal{H}}_Q$ needs to be incorporated in the Hamiltonian:

$$\hat{\mathcal{H}} = \hat{\mathcal{H}}_{rot} + \hat{\mathcal{H}}_Q \,, \tag{2.37}$$

where

$$\hat{H}_Q = \frac{eQq_J}{2J(2J-1)(2I-1)I} \left[3(\mathbf{I}\cdot\mathbf{J})^2 + \frac{3}{2}\mathbf{I}\cdot\mathbf{J} - \mathbf{I}^2\mathbf{J}^2 \right] . \tag{2.38}$$

eQ is the nuclear quadrupole moment, which is a tabulated value that depends on the distribution of the charge density over the nuclear volume. The coefficient q_J is the expectation value of the SF component of the electric-field gradient tensor q at the same nucleus averaged over the rotational motion. In the case of a linear molecule, we have:

$$q_J = -q\frac{J}{2J+3} \,, \tag{2.39}$$

In the $|IJF\rangle$ basis, the eigenvalues of $\hat{H}_Q$ are:

$$E_Q = \frac{eQq_J}{2J(2J-1)(2I-1)I}\left[\frac{3}{4}C(C+1) - J(J+1)I(I+1)\right], \tag{2.40}$$

with

$$C = F(F+1) - J(J+1) - I(I+1)\,. \tag{2.41}$$

In the linear molecule case, this expression reduces to:

$$E_Q = -eQq\frac{\frac{3}{4}C(C+1) - I(I+1)J(J+1)}{2(2J-1)(2J+3)I(2I-1)}\,. \tag{2.42}$$

Interaction of radiation with a rotating molecule

When a molecule interacts with the radiation field, this interaction is expressed by $\hat{\mathcal{H}}_{int}$:

$$\boxed{\hat{\mathcal{H}}_{int} = -\hat{\mu}\cdot\mathbf{E}\,,} \tag{2.43}$$

where $\hat{\mu}$ is the electric dipole moment which mediates the interaction between the molecule and the electric field $\mathbf{E}$ of the radiation. The transition probability of a molecule thus depends on both the radiation electric field and on the effect of the dipole moment operator on the initial state i, leading to the final state f: in bracket notation, the transition probability is expressed by $\langle i|\hat{\mu}|f\rangle$, which is denoted as transition moment (see Bauder 2011 for further details). The matrix elements of the transition moment $\langle i|\hat{\mu}|f\rangle$ determine whether a transition can take place or not: when it is null the transition is prohibited, otherwise the transition is allowed and the value of $\langle i|\hat{\mu}|f\rangle$ contributes to the intensity of the transition.

In the case of a linear molecule, in absence of electric or magnetic interactions, the $|i\rangle$ and $|f\rangle$ states are associated to the $\{J, M\}$ and $\{J', M'\}$ quantic numbers and the molecular dipole moment (μ) is always directed along the principal inertial axis coincident with the molecular one. The projection of the latter along the $\mathbf{e}$ propagation direction of the radiation gives rise to the following expression:

$$\langle JM|\mu_e|J'M'\rangle = (-1)^M\left[(2J+1)\,(2J'+1)\right]^{1/2}\begin{pmatrix} J & 1 & J' \\ -M & 0 & M'\end{pmatrix}\mu\,, \tag{2.44}$$

where $(:::)$ are the Wigner $3j$–symbols, a more symmetrical form of the Clebsch–Gordan coefficients[‖], which appear in the coupling of two angular momenta (Zare and Harter, 1988). In order to be non zero, the transition moment needs to satisfy the triangular conditions: $-M + 0 + M = 0$ and $|J+1| \geq J' \geq |J-1|$. Starting

[‖] See the next subsection for further details.

from these, the selection rules of a linear molecule are directly inferred:

$$\begin{aligned} \Delta J &= \pm 1\,; \\ \Delta M &= 0\,. \end{aligned} \tag{2.45}$$

The transition moment for the $J \rightarrow J+1$ transition thus becomes:

$$\langle JM\,|\mu_e|\,J+1M\rangle = \mu \left[\frac{(J+M+1)(J-M+1)}{(2J+1)(2J+3)}\right]^{1/2}\,. \tag{2.46}$$

When a nuclear quadrupole coupling occurs, the selection rules for the F quantum number should also be considered:

$$\Delta F = 0,\, \pm 1\,. \tag{2.47}$$

2.2.3 Interaction Potential

In order to solve the nuclear Schrödinger equation for a scattering problem, an accurate characterization of the interaction potential between the collisional partners is needed. This requirement is usually fulfilled by mapping the collisional PES and describing it with a suitable functional form.

First of all, the coordinates to describe the geometry of the collisional complex and the degrees of freedom to be varied in order to fully map the interaction PES are chosen. A first assumption in this regard is to consider the two colliders as rigid bodies. This approximation is known as the rigid-body (RB) hypothesis, which is usually well met in the non-reactive low-temperature conditions typical of the astrophysical media. Indeed, in such conditions, it can be assumed that there is not enough external energy to significantly populate vibrationally excited states of the two scatterers. This approximation, however, should always be verified, especially when molecules exhibit large amplitude vibrational motions**, which require low energies to be excited. Moreover, the coordinates used to describe the geometry of the collision complex should be appropriate for the calculation of the elements of the scattering matrix, which depend on the symmetry of the colliding rotors. Usually, BF frame Jacobi coordinates are employed. For the systems of interest to this thesis, these are the R distance between the center of mass of the target molecule and the collider, the θ angle between the molecular axis and the R vector, and, if required, other angles that describe the orientation of the collider in and out the plane defined by the target molecular axis and R. In Fig. 2.5, two examples are depicted: a linear molecule-atom system and the interaction between two linear molecules. For non-

**Molecular vibrations whose displacement vectors are of the same order of magnitude of the molecular parameters. Among them, those commonly encountered in rotational spectroscopy are the internal rotation of the methyl group -CH_3 and the inversion of the amino group -NH_2.

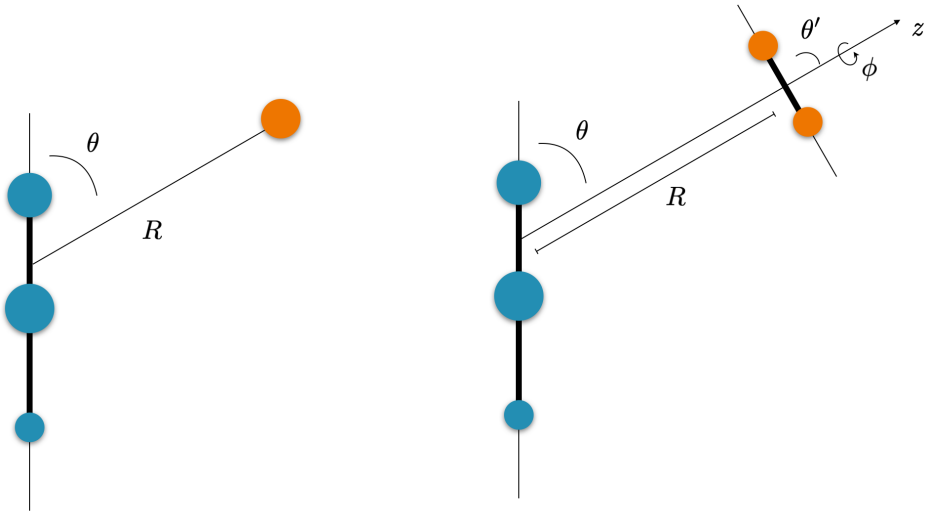

Figure 2.5: Jacobi internal coordinates defining the geometries of linear-atom and linear-linear rotors collisional systems.

reactive collisions, the interaction PES between the collision partners is usually governed by weak van der Waals interactions. In order to describe the interaction potential, the adopted procedure is to identify a grid of points that can suitably map the PES behavior and to compute the electronic energy in correspondence of them. This implies the use of *ab initio* methods to solve the electronic Schrödinger equation. For a detailed description of the computational methodologies employed to derive the electronic energies for each point of the grid, the reader is referred to Chapter 3.

For each set of Jacobi coordinates, the interaction energy (E_{int}) is determined as follows:

$$E_{\text{int}} = E_{\text{AB}} - (E_{\text{A}} + E_{\text{B}})\,, \tag{2.48}$$

where E_{AB} is the molecular complex energy, while E_{A} and E_{B} are the energies of the two fragments. Each interaction energy has also to be augmented for the counterpoise (CP) correction in order to balance out the energy overestimation given by the basis set superposition error (BSSE). The BSSE is due to the overlap of the basis sets of the isolated colliders, which results in an "artificial" improved estimate of the interaction energy. This means that the energy of the isolated colliders and that of the collisional system are no longer comparable. Once the CP correction is incorporated, the comparison of these energies becomes meaningful. The CP correction is commonly computed by means of the formula proposed by Boys and

Bernardi (1970):

$$\Delta E_{\mathrm{CP}} = (E_{\mathrm{A}}^{\mathrm{AB}} - E_{\mathrm{A}}^{\mathrm{A}}) + (E_{\mathrm{B}}^{\mathrm{AB}} - E_{\mathrm{B}}^{\mathrm{B}}), \tag{2.49}$$

where $E_{\mathrm{X}}^{\mathrm{AB}}$ is the energy of the isolated collider calculated in the same basis functions used for the entire collisional system and $E_{\mathrm{X}}^{\mathrm{X}}$ is the energy of the isolated collider computed with its own basis set (X = A,B). The selection of the grid points to map the collisional PES aims to cover with a dense mesh the portion of potential where the largest anisotropy effects are expected, *e.g.*, in proximity of the potential well. This is accomplished by chemical intuition, but also from the comparison with similar systems.

The next step is to build an analytic representation of the computed interaction energies. The functional form of the potential should be able to describe all the interaction forces that can occur in the collisional process. Accordingly, the interaction potential can be divided in three parts: the short-range region, where the Coulombic repulsion between electrons causes the potential to be strongly repulsive; a middle-range region, where attractive and repulsive forces equilibrate; the long-range region, where the potential is only attractive. Particular attention should be paid to the inner and outer ranges of the potential. In the inner range, the radial grid should sample regions where the repulsive potential energy is higher than the expected highest collision energy at which scattering calculations will be carried out. In the outer part, all the long-range interaction effects should be appropriately incorporated, which are the electrostatic, the induction and dispersion components. In order to accurately describe the potential at large R distances, a switching function that connects the fitted coefficients at small R values with an extrapolated radial R^{-n} dependence at large R values is often introduced. The resulting radial coefficients $v_\lambda(R)$[††] can be thus fitted to a functional form as:

$$\begin{aligned} v_\lambda(R) = \mathrm{e}^{-a_1^\lambda R}\left(a_2^\lambda + a_3^\lambda R + a_4^\lambda R^2 + a_5^\lambda R^3\right) + \\ - \frac{1}{2}\left[1 + \tanh R/R_{\mathrm{ref}}\right]\left(\frac{C_4^\lambda}{R^4} + \frac{C_6^\lambda}{R^6} + \frac{C_8^\lambda}{R^8} + \frac{C_{10}^\lambda}{R^{10}}\right), \end{aligned} \tag{2.50}$$

where C_n^λ denotes the coefficients of the R^{-n} terms and a_n^λ describes the short-range exponential dependence of the potential with respect to the first powers of R. The hyperbolic tangent factor provides a smooth transition between the short-range region ($0 < R < R_{\mathrm{ref}}$), where computed PES points are available, and the long-range extrapolated domain ($R > R_{\mathrm{ref}}$). This formula is particularly suited to describe charged collisional systems, where the long-range parts of the potential are characterized by a sizable electrostatic and induction contribution that scales with the interparticle distance as R^{-4} and is proportional to the square of the charge of

[††]The radial coefficients define the dependence of the potential as a function of the R distance. For each set of Jacobi angles, a proper expression for these coefficients must be then introduced.

the ion and to the static electric dipole polarizability of the collider.

Finally, the obtained radial coefficients need to be expressed as an expansion over the angular functions. This requires properly chosen expressions that depend on the symmetry of the two colliders. For the systems addressed in this thesis, the formulas that have been employed are reported in the following. For an interaction system formed by a linear rigid rotor and an atom, the potential can be defined as:

$$V\left(R,\theta\right)=\sum_{\lambda}v_{\lambda}(R)P_{\lambda}\left(\cos\theta\right)\ , \tag{2.51}$$

where $P_{\lambda}\left(\cos\theta\right)$ is a Legendre polynomial and $v_{\lambda}(R)$ are the radial coefficients of Eq. (2.50) (Lique and Faure, 2019). For an interaction between two linear rigid rotors (Green, 1975; Wernli et al., 2007), the potential is written as:

$$V\left(R,\theta,\theta',\phi\right)=\sum_{l_1l_2\mu}v_{l_1l_2\mu}(R)s_{l_1l_2\mu}\left(\theta,\theta',\phi\right)\ , \tag{2.52}$$

where $v_{\lambda}(R)=v_{l_1l_2\mu}(R)$ and the l_1, l_2 and μ indices are associated with the rotational angular moments of the target molecule (j_1), of the collider (j_2), and with their vector sum, respectively. The $s_{l_1l_2\mu}$ coefficients are defined as products of spherical harmonics ($Y_{l_im}(\theta,\phi)$) and the Clebsch-Gordan vector-coupling coefficients (see Green 1975; Brown et al. 2003; Edmonds 2016 for further details):

$$\begin{aligned}s_{l_1l_2\mu}(\theta,\theta',\phi)=\left(\frac{2l_1+1}{4\pi}\right)^{1/2}\Bigg[&\langle l_10l_20|l_1l_2\mu0\rangle P_{l_10}(\theta)P_{l_20}(\theta')\\&+\sum_{m}(-1)^m2\langle l_1ml_2-m|l_1l_2\mu0\rangle P_{l_1m}(\theta)P_{l_2m}(\theta')\cos(m\phi)\Bigg]\ ,\end{aligned} \tag{2.53}$$

where m is associated with the projection of μ along the Z axis of the SF reference system and $P_{l_im}(\theta)=Y_{l_im}(\theta,\phi)\mathrm{e}^{-\mathrm{i}\,m\phi}$. The l_2 index reflects the anisotropy of the potential with respect to the orientation of the collider. If the collider is homonuclear, *e.g.*, H_2 or N_2, l_2 is forced to be even. In this cases, the potential does not show large variations with respect to the orientation of the collider. Thus, a good approximation is to neglect the terms with $l_2>2$ in the basis expansion (Faure et al., 2005; Wernli et al., 2006). Accordingly, the only basis functions that describe the dependence of the potential on the relative orientations of H_2 are the Y_{00}, Y_{20}, Y_{21} and Y_{22} spherical harmonics. This significantly reduces the computational effort, since, at fixed R and θ values, the dependence of the potential on the orientation of the collider can be entirely described from the knowledge of only four orientations $\{\theta',\phi\}$. Hence, by choosing five sets of $\{\theta',\phi\}$ orientations it will be possible both to fully describe the dependence of the potential on them and to have an overdetermined system to test the accuracy of the l_2 truncation. Usually, the chosen

orientations are those selected by Wernli et al. (2007) for the HC_3N-H_2 system:

$$x \to \left(\theta' = \frac{\pi}{2}, \phi = 0\right) ; \tag{2.54a}$$

$$y \to \left(\theta' = \frac{\pi}{2}, \phi = \frac{\pi}{2}\right) ; \tag{2.54b}$$

$$z \to (\theta' = 0, \phi = 0) ; \tag{2.54c}$$

$$a \to \left(\theta' = \arccos\left(\frac{1}{\sqrt{3}}\right), \phi = \frac{\pi}{4}\right) ; \tag{2.54d}$$

$$b \to \left(\theta' = \pi - \arccos\left(\frac{1}{\sqrt{3}}\right), \phi = \frac{\pi}{4}\right) . \tag{2.54e}$$

In order to introduce the analytical dependence over $\{\theta', \phi\}$, Eq. (2.52) can be expressed as the product of two terms, which depend on the $\{R, \theta\}$ and $\{\theta', \phi\}$ couples of Jacobi coordinates:

$$V(R, \theta, \theta', \phi) = \sum_{l_2, \mu \geq 0} C_{l_2\mu}(R, \theta) t_{l_2\mu}(\theta', \phi) , \tag{2.55}$$

where

$$\begin{aligned} C_{l_2\mu}(R, \theta) &= \left(\sum_{l_1} v_{l_1 l_2 \mu}(R) P_{l_1}(\theta)\right) \qquad \text{and} \\ t_{l_2\mu}(\theta', \phi) &= Y_{l_2 -\mu}(\theta', \phi) + (-1)^{\mu} Y_{l_2\mu}(\theta', \phi) . \end{aligned} \tag{2.56}$$

Within the $l_2 \leq 2$ approximation of the potential, only four (l_2, μ) terms are taken in account: (0,0),(2,0),(2,1) and (2,2). By separately fitting the five orientations of Eq. (2.54), a system of five equations and four variables has to be solved. The five 2D potentials are denoted by the following coordinates, $V(R, \theta, x)$, $V(R, \theta, y)$, $V(R, \theta, z)$, $V(R, \theta, a)$, $V(R, \theta, b)$ and can be defined as:

$$V_i(R, \theta) = \sum_{j=1}^{4} T_{ij} C_j, i = 1, \ldots, 5 , \tag{2.57}$$

where T_{ij} denotes the matrix elements defined by the $t_{l_2\mu}(i)$ components, with i denoting each orientation:

$$T = \frac{1}{\sqrt{\pi}} \begin{pmatrix} 1 & -\frac{\sqrt{5}}{2} & 0 & \frac{1}{2}\sqrt{\frac{15}{2}} \\ 1 & -\frac{\sqrt{5}}{2} & 0 & -\frac{1}{2}\sqrt{\frac{15}{2}} \\ 1 & \sqrt{5} & 0 & 0 \\ 1 & 0 & -\sqrt{\frac{5}{6}} & 0 \\ 1 & 0 & \sqrt{\frac{5}{6}} & 0 \end{pmatrix} . \tag{2.58}$$

$C_{l_2\mu}(R,\theta)$ can be thus expressed as a combination of the 2D potentials:

$$\begin{aligned} C_{00} =& \frac{\sqrt{\pi}}{7}[2\,(V(R,\theta,a)+V(R,\theta,b))+ \\ & \underbrace{+\,(V(R,\theta,x)+V(R,\theta,y)+V(R,\theta,z))]}_{\sqrt{\pi}\,V_{\mathrm{av}}(R,\theta)}\,, \end{aligned} \tag{2.59}$$

$$C_{20} = \sqrt{\frac{\pi}{5}}\,[V(R,\theta,z) - V_{\mathrm{av}}(R,\theta)]\ , \tag{2.60}$$

$$C_{21} = \sqrt{\frac{3\pi}{10}}\,[V(R,\theta,a) - V(R,\theta,b)]\ , \tag{2.61}$$

$$C_{22} = \sqrt{\frac{2\pi}{15}}\,[V(R,\theta,x) - V(R,\theta,y)]\ . \tag{2.62}$$

Hence, the global 4D potential can be introduced *via* the following equation:

$$\begin{aligned} V\,(R,\theta,\theta',\phi) =& \,2\,\sqrt{\pi}\,V_{\mathrm{av}}(R,\theta)\,Y_{00}(\theta',\phi) \\ & +2\,\sqrt{\frac{\pi}{5}}\,[V(R,\theta,z) - V_{\mathrm{av}}(R,\theta)]\,Y_{20}(\theta',\phi)+ \\ & +\sqrt{\frac{3\pi}{10}}\,[V(R,\theta,a) - V(R,\theta,b)]\,[Y_{2-1}(\theta',\phi) - Y_{21}(\theta',\phi)]+ \\ & +\sqrt{\frac{2\pi}{15}}\,[V(R,\theta,x) - V(R,\theta,y)]\,[Y_{2-2}(\theta',\phi) + Y_{22}(\theta',\phi)]\,, \end{aligned} \tag{2.63}$$

which, as a function of the θ' and ϕ coordinates, assumes the following form (Wernli et al., 2006):

$$\begin{aligned} V(R,\theta,\theta',\phi) =& \,V_{\mathrm{av}}(R,\theta)+ \\ & +\frac{1}{2}\,[V(R,\theta,z) - V_{\mathrm{av}}(R,\theta)]\,\left(3\cos^2\theta' - 1\right)+ \\ & +\frac{3}{2}\,[V(R,\theta,a) - V(R,\theta,b)]\sin\theta'\cos\theta'\cos\phi+ \\ & +\frac{1}{2}\,[V(R,\theta,x) - V(R,\theta,y)]\sin^2\theta'\cos\left(2\phi\right)\ . \end{aligned} \tag{2.64}$$

2.2.4 Dynamics of the nuclei

In ¶ 2.2.2, the resolution of the nuclear Schrödinger equation for the Watson Hamiltonian to derive the energy of the ro-vibrational levels for an isolated molecule has been introduced. Moving to a colliding system, the ro-vibrational Hamiltonian is not only given by the Hamiltonian of the two isolated colliders, but instead, it also takes into account the interaction potential and kinetics of the entire collisional

system. The quantum mechanical treatment of molecular collision theory was first introduced by Arthurs and Dalgarno (1960) and has been extensively developed in the last decades. Here, a brief overview of the main theoretical aspects is provided. For a more detailed account and for the resolution of the algebraic steps, the reader is referred to Drake (2006) and Flower (2007).

As mentioned in the previous subsection, the interaction potential of a collisional system $V(R, \boldsymbol{\theta})$ can be obtained by solving the electronic Schrödinger equation for a suitable grid of points. The functional form used for describing the resulting PES has been introduced as well. Here, we recall that the gradients of the PES (*i.e.*, first derivatives of the energy with respect to the chosen nuclear coordinates) describe the forces acting on the system and that the potential vanishes at infinite distances ($\lim_{R\to\infty} V(R, \boldsymbol{\theta}) = 0$). We also recall that we work in a BF reference frame and that the $\{R, \boldsymbol{\theta}\}$ coordinates denote the Jacobi coordinates of the system, *i.e.*, the R distance and the relative orientations between the colliders, and, beyond the rigid rotor approximation, they also include their internal degrees of freedom. For a linear rigid rotor + atom system, $\boldsymbol{\theta}$ corresponds to the θ angle of Eq. (2.51), while for a linear rigid rotor + linear rigid rotor system, it is composed by the three $\{\theta, \theta', \phi\}$ coordinates (Eq. (2.52)).

The kinetic energy operator of the collisional system is expressed by the sum of the Laplacian operators of the two colliders (see Eq. (2.18)), here denoted as A and B:

$$\hat{\mathcal{T}}(\mathbf{R}_\mathrm{A}, \mathbf{R}_\mathrm{B}) = -\frac{\nabla^2_{\mathbf{R}_\mathrm{A}}}{2m_A} - \frac{\nabla^2_{\mathbf{R}_\mathrm{B}}}{2m_B}\,, \tag{2.65}$$

where $\mathbf{R}_\mathrm{A}$ and $\mathbf{R}_\mathrm{B}$ are the internal coordinates of A and B in the SF system. Resorting to the relative motion of the particles, this expression becomes (Flower, 2007; Lique and Faure, 2019):

$$\hat{\mathcal{T}}(\mathbf{R}_{c.o.m.}, \mathbf{R}) = -\frac{\nabla^2_{\mathbf{R}_{c.o.m.}}}{2M} - \frac{\nabla^2_{\mathbf{R}}}{2\mu}\,, \tag{2.66}$$

where $M = m_A + m_B$ and $\mu = (m_A m_B)/(m_A + m_B)$ are the total and reduced masses of the system, respectively. $\mathbf{R}$ describes the relative position of the two colliders and $\mathbf{R}_{c.o.m.} = (m_\mathrm{A}\mathbf{R}_\mathrm{A} + m_\mathrm{B}\mathbf{R}_\mathrm{B})/M$ the position of the center of mass of the A+B system. In this SF frame, the translational motion of the entire system is decoupled from the internal motion and can thus be neglected for the description of the collisional process. Moreover, the term describing the kinetic energy of the relative motion between A and B can be split into a radial part that depends only on the R distance, and an angular kinetic term:

$$-\frac{\nabla^2_{\mathbf{R}}}{2\mu} = -\frac{1}{2\mu}\frac{\partial^2}{\partial R^2} + \frac{\hat{\mathcal{L}}^2}{2\mu R^2}\,. \tag{2.67}$$

The operator $\hat{\mathcal{L}}$ is the angular momentum that refers to the relative motion between the two colliders and is associated to the L quantum number. Hence, the scattering Hamiltonian assumes the following form:

$$\hat{\mathcal{H}} = -\frac{1}{2\mu}\frac{\partial^2}{\partial R^2} + \frac{\hat{\mathcal{L}}^2}{2\mu R^2} + \hat{\mathcal{H}}_{\mathrm{A}} + \hat{\mathcal{H}}_{\mathrm{B}} + V(R, \boldsymbol{\theta})\,, \tag{2.68}$$

where $\hat{\mathcal{H}}_{\mathrm{A}}$ and $\hat{\mathcal{H}}_{\mathrm{B}}$ are the ro-vibrational Hamiltonian operators of the colliders A and B, seen as isolated entities.

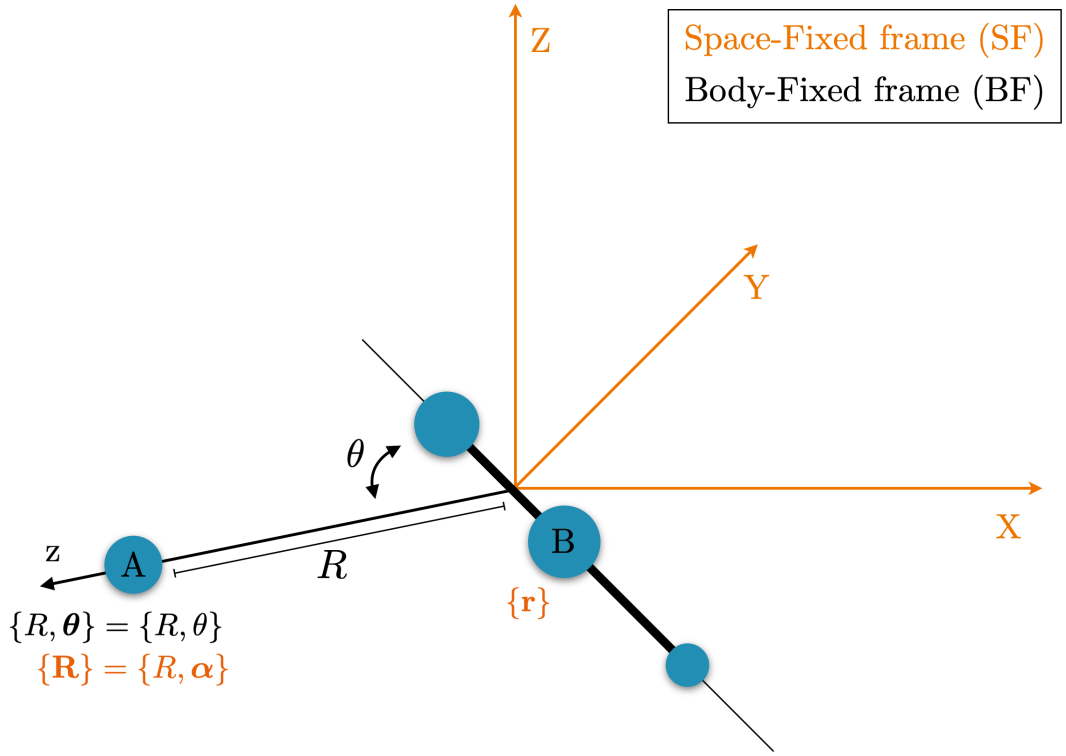

Figure 2.6: SF and BF coordinates for the collision between the A atom and the B rigid linear rotor. In the BF frame, the orientation of A with respect to B is defined by the $\{R, \boldsymbol{\theta}\}$ Jacobi coordinates, where $\boldsymbol{\theta} = \theta$. In the SF frame, the A and B scatterers are defined by the $\{\mathbf{R}\}$ and $\{\mathbf{r}\}$ coordinates, respectively. $\boldsymbol{\alpha}$ denotes the orientation of the BF z axis with respect to the SF $\{X, Y, Z\}$ frame.

In the following, the collision between a structureless atom A and a closed-shell linear rigid rotor molecule B (Fig. 2.6) is considered. This simplifies the comprehension of the physics of the system while avoiding cumbersome notation in the formulation of the quantum mechanical equations. For deviations due to the internal structure of A and/or to the open-shell character of the colliders, the reader is

referred to Alexander (1982a,b), Flower (2007) and references therein. In the system under consideration R is the distance between the A atom and the center of mass of B, $\boldsymbol{\theta} = \theta$ is the angle defining the orientation of A with respect to the molecular axis of B (see Fig. 2.6), and $\hat{\mathcal{H}}_B = B\hat{j}_{\rm B}^2$ (Eq. (2.32)). As a convention, in the following part of this Chapter, lower-case letters refer to the operators of the isolated colliders, while for the entire system upper-case letters are employed.

In absence of external fields, the nuclear Schrödinger equation for the linear rotor-atom system thus becomes:

$$\left(-\frac{1}{2\mu}\frac{\partial^2}{\partial R^2} + \frac{\hat{\mathcal{L}}^2}{2\mu R^2} + B\hat{j}_{\rm B}^2 + V(R,\theta)\right)\Psi(\mathbf{R},\mathbf{r}) = E\,\Psi(\mathbf{R},\mathbf{r})\,, \tag{2.69}$$

where $\mathbf{R} = R, \boldsymbol{\alpha}$, with $\boldsymbol{\alpha}$ denoting the orientation of the BF z axis (Fig. 2.6) with respect to the SF $\{X, Y, Z\}$ frame, and $\mathbf{r}$ denotes the coordinates of B in the SF frame. The rotational degrees of freedom of the system are represented by the total angular momentum $J = j_{\rm B} + L$ and its projection along the Z axis $M = m_{\rm B} + m_L$ quantum numbers. During the collision, the values of J and M are conserved, together with the parity (p) of the eigenfunctions representing the A+B system. The latter is related to the inversion symmetry operation of the coordinates of all the nuclei with respect to the origin of the SF frame. Indeed, $\Psi(\mathbf{r},\mathbf{R})$ is an eigenfunction not only of $\hat{J}^2$ and $\hat{J}_z$, with eigenvalues $J(J+1)$ and M, respectively, but also of the inversion operator, with eigenvalue denoted by the parity, $p = \pm 1$, of the wave function (the reader is referred to Flower 2007 for more details). The full scattering wave function $\Psi(\mathbf{R},\ \mathbf{r})$ for a given set of $\{p, J, M\}$ quantum numbers can be expanded over the remaining degrees of freedom as:

$$\Psi^{pJM}(\mathbf{r},\mathbf{R}) = \frac{1}{R}\sum_{j_B L} F_{j_B L}^{pJM}(R)\mathcal{Y}_{j_B L}^{pJM}(\mathbf{r},\boldsymbol{\alpha})\,. \tag{2.70}$$

Within this expansion, for each $(j_B L; pJM)$ channel, the total wave function is divided in a $F_{j_B L}^{pJM}(R)$ radial part, that only depends on R, and in an angular part $\mathcal{Y}_{j_B L}^{pJM}(\mathbf{r},\boldsymbol{\alpha})$, formed by a product of spherical harmonics Y:

$$\mathcal{Y}_{j_B L}^{pJM}(\mathbf{r},\boldsymbol{\alpha}) = \sum_{m_B m_L} C_{m_B m_L M}^{j_B L J} Y_{j_B m_B}(\mathbf{r}) Y_{L m_L}(\boldsymbol{\alpha})\,, \tag{2.71}$$

where $C_{m_B m_L M}^{j_B L J}$ are the Clebsch–Gordan coefficients and are related to the Wigner $3j$–symbol through:

$$C_{m_B m_L M}^{j_B L J} = (-1)^{j_B - L + M}(2J+1)^{\frac{1}{2}}\begin{pmatrix} j_B & L & J \\ m_B & m_L & -M \end{pmatrix}. \tag{2.72}$$

Consequently, it is possible to solve the Schrödinger equation on the $\mathcal{Y}_{j_B L}^{pJM}(\mathbf{r},\boldsymbol{\alpha})$ angular part, and then introduce the radial dependence by numerical propagation of R on a grid. Although the BF frame represents a more natural choice because the interaction potential is expressed within this coordinate system, the use of the SF coordinates in the definition of $\mathcal{Y}_{j_B L}^{pJM}(\mathbf{r},\boldsymbol{\alpha})$ is employed because it avoids the inclusion of the Coriolis terms in the evaluation of the centrifugal interaction embodied by the relative angular momentum $\hat{\mathcal{L}}$. Indeed, the $\mathcal{Y}_{j_B L}^{pJM}(\mathbf{r},\boldsymbol{\alpha})$ functions form a complete orthonormal basis set for the motion in these coordinates and are eigenfunctions of the $\hat{\mathcal{L}}^2$ and $\hat{j}_B^2$ operators:

$$\begin{aligned} \hat{j}_B^2\, \mathcal{Y}_{j_B L}^{pJM}(\mathbf{r},\boldsymbol{\alpha}) &= j_B(j_B+1)\, \mathcal{Y}_{j_B L}^{pJM}(\mathbf{r},\boldsymbol{\alpha})\,; \\ \hat{\mathcal{L}}^2\, \mathcal{Y}_{j_B L}^{pJM}(\mathbf{r},\boldsymbol{\alpha}) &= L(L+1)\, \mathcal{Y}_{j_B L}^{pJM}(\mathbf{r},\boldsymbol{\alpha})\,. \end{aligned} \tag{2.73}$$

The Schrödinger equation, written in the $(\hat{\mathcal{H}} - E)\Psi(\mathbf{R},\mathbf{r}) = 0$ form, thus becomes:

$$\left[B\hat{j}_B^2 - \frac{1}{2\mu R}\frac{\partial^2}{\partial R^2} R + \frac{\hat{\mathcal{L}}^2}{2\mu R^2} + V(R,\theta) - E \right] \Psi(\mathbf{R},\mathbf{r}) = 0\,. \tag{2.74}$$

By introducing the expansion of the total wave function given in Eq. (2.70) and projecting the result into a $\mathcal{Y}_{j'_B L'}^{p'J'M'}(\mathbf{r},\boldsymbol{\alpha})$ basis function, we finally obtain:

$$\begin{aligned} &\left[\frac{\mathrm{d}^2}{\mathrm{d}R^2} - \frac{L(L+1)}{R^2} + k_{j_B}^2 \right] F_{j_B L}^{pJM}(R) = 2\mu \sum_{j'_B L' p' J' M'} F_{j'_B L'}^{p'J'M'}(R) \\ &\int \mathcal{Y}_{j_B L}^{*\,pJM}(\mathbf{r},\boldsymbol{\alpha})\, V(R,\theta)\, \mathcal{Y}_{j'_B L'}^{p'J'M'}(\mathbf{r},\boldsymbol{\alpha})\, \mathrm{d}\mathbf{r}\mathrm{d}\boldsymbol{\alpha}\,, \end{aligned} \tag{2.75}$$

where

$$k_{j_B}^2 = 2\mu[E - Bj_B(j_B+1)]\,. \tag{2.76}$$

Eq. (2.75) represents a set of ordinary differential equations, also denoted as coupled equations, which involve second-order derivatives with respect to R and which are linear in the function of the radial coordinate $F_{j_B L}^{pJM}(R)$. A loop over each set of $\{pJM\}$ blocks leads to the resolution of the scattering problem. To this aim, powerful numerical techniques have been developed. In this thesis work, those incorporated in the MOLSCAT package of programs (Hutson and Green, 1994) have been employed.

In order to evaluate the matrix elements on the right-hand side of Eq. (2.75), we need to express the potential as a function of the SF coordinates. For an atom plus a linear rigid rotor system, $V(R,\theta)$ is defined as an expansion in terms of the Legendre polynomials P_λ (see Eq. (2.51)). The angular dependence of the potential

can be thus evaluated as a linear combination of spherical harmonics by exploiting the spherical harmonic addition theorem (Rose, 1995):

$$P_\lambda(\cos\theta) = \frac{4\pi}{2\lambda+1} \sum_{\nu=-\lambda}^{\lambda} Y_{\lambda\nu}(\mathbf{r}) Y^*_{\lambda\nu}(\boldsymbol{\alpha}) \,. \tag{2.77}$$

This theorem converts from the dependence of the potential on the θ BF coordinate to the dependence on the SF $\{\mathbf{r}, \boldsymbol{\alpha}\}$ ones, thus permitting the resolution of the integral of Eq. (2.75). By applying the composition relations for spherical harmonics (Rose, 1995) and employing further algebraic steps (see Flower 2007 for a detailed description), Eq. (2.75) can be written as:

$$\left[\frac{\mathrm{d}^2}{\mathrm{d}R^2} - \frac{L(L+1)}{R^2} + k^2_{j_B}\right] F^{pJ}_{j_B L}(R) = 2\mu \sum_{j'_B L' \lambda} v_\lambda(R) f^J_\lambda(j_B L j'_B L') F^{pJ}_{j'_B L'}(R) \,, \tag{2.78}$$

where $f^J_\lambda(j_B L, j'_B L')$ are the Percival–Seaton coefficients (Percival and Seaton, 1957), which depend on the $3j$– ((:::) matrices) and $6j$– ({:::} matrix) symbols of Wigner:

$$\begin{aligned} f^J_\lambda(j_B L, j'_B L') = (-1)^{j_B + j'_B - J} \frac{\left[(2j_B+1)(2L+1)\,(2j'_B+1)\,(2L'+1)\right]^{\frac{1}{2}}}{(2\lambda+1)} \\ \begin{pmatrix} j_B & j'_B & \lambda \\ 0 & 0 & 0 \end{pmatrix} \times \begin{pmatrix} L & L' & \lambda \\ 0 & 0 & 0 \end{pmatrix} \times (-1)^{j_B + L + j'_B + L'} \begin{Bmatrix} j_B & L & J \\ L' & j'_B & \lambda \end{Bmatrix} . \end{aligned} \tag{2.79}$$

At this point, the set of coupled equations can be solved by propagation of $F_l(R)$, where l represents a $|j_B, L, m_B, m_L, p, J, M\rangle$ channel. Despite only some of the channels are open, *i.e.*, energetically accessible for a given collision energy, it is required to include several closed channels in order to accurately solve the scattering problem, particularly for transitions involving states whose energies approach the limit of accessibility. The propagation can occur either directly on $F_l(R)$ or on its logarithmic derivative $F_l(R)'/F_l(R)$[‡‡], the latter being numerically more stable. It starts from the classically forbidden region at short range, where the boundary condition $\lim_{R\to 0} F_l(R) = 0$ is fulfilled, and proceeds up to a distance at long range beyond which the interaction potential may be neglected. At long distances, $F_l(R)$ is thus matched to an analytic function that shapes the asymptotic boundary conditions in the $R \to \infty$ limit:

$$\lim_{R\to\infty} F_l(R) = k^{\frac{1}{2}} R \left[j_l(kR) A_l - n_l(kR) B_l\right] \,, \tag{2.80}$$

where $j_l(kR)$ and $n_l(kR)$ are the spherical Bessel functions (Abramowitz and Stegun, 1965). For each chosen channel l, a set of A_l and B_l coefficients is retrieved.

[‡‡] $\frac{f'(x)}{f(x)} = \frac{d}{dx} \ln f(x)$ for a given $f(x)$ function.

The matrices containing these solution vectors for each l channel are the **A** and **B** matrices, from which the reactance (**K**) and the scattering (**S**) matrices are derived:

$$\mathbf{K} = \mathbf{B}\mathbf{A}^{-1}\,, \tag{2.81}$$

$$\boxed{\mathbf{S} = (\mathbf{I} + i\mathbf{K})^{-1}(\mathbf{I} - i\mathbf{K})\,,} \tag{2.82}$$

with **I** being the identity matrix. The S–matrix connects an initial state l with an outgoing scattered state l' and represents the final outcome of the quantum scattering calculations. Experimental observables that describe completed collisions (inelastic cross sections, pressure broadening cross sections, hyperfine cross sections, ...) can be written in terms of the elements of the S–matrix. This is diagonal in J, reflecting the conservation of the total angular momentum during the collision, and is independent of M.

Inelastic Cross Sections and State-to-State Rate Coefficients

From the S–matrix elements, the cross sections from an initial j_B to a final j'_B state of the B molecule at a given collision energy E_c can be computed:

$$\sigma_{j_B \to j'_B}(E_c) = \frac{\pi}{k^2_{j_B}} \sum_{p,J,M} \frac{2J+1}{2j_B+1} \sum_{l,l'} \left| \delta_{j_B j'_B}\, \delta_{ll'} - S^{\,pJM}_{ll'} \right|^2 . \tag{2.83}$$

Ideally, one should perform the sum over J up to an infinite value in order to include all possible contributions in the expansion. In practice, one needs to find the appropriate truncation limit in the J sum in order to discard only negligible contributions to the cross section value and to keep the sum finite. This truncation limit depends on the molecular system and is usually chosen in order to have the inelastic cross sections converged within $0.005\,\text{Å}^2$. This value allows for achieving a good compromise between the desired accuracy and the computational cost. Starting from the inelastic cross sections, the collisional state-to-state rate coefficients are straightforwardly derived by thermal averaging over the collision energy:

$$\boxed{\begin{aligned} k_{j_B \to j'_B}(T_k) = &\left(\frac{8}{\pi \mu k_B^3 T_k^3}\right)^{1/2} \\ &\times \int_0^\infty \sigma_{j_B \to j'_B}(E_c)\, E_c \exp\left(-E_c/k_B T_k\right) \mathrm{d}E_c\,, \end{aligned}} \tag{2.84}$$

where T_k is the kinetic temperature for which the Boltzmann distribution of particle velocities holds. These rate coefficients represent the information needed for the radiative transfer problem to model astronomical spectra and derive molecular

abundances. To solve the integral in Eq. (2.84), one should have at disposal an infinite number of cross sections for each E_c value. Due to limitations in computational resources, one needs to find the best possible approximation of the integral by choosing an energy range which is well suited for the targeted astrophysical applications and with a sufficiently fine grid to account for all the resonances that can affect cross sections values. Once the transition rate from j_B to j'_B is known, the inverse j'_B to j_B rate can be easily retrieved by means of the detailed balance principle:

$$k_{j_B \to j'_B}(T) = \frac{g_{j_B}}{g_{j'_B}} k_{j_B \to j'_B}(T) e^{-\Delta E / k_B T_k} , \tag{2.85}$$

where $\Delta E = E_{j_B} - E_{j'_B}$.

Decoupling Approximations

The exact resolution of scattering equations implies to consider all the coupled channels involved in the collision. This is known as close coupled approach (CC), and it is feasible only when collisions involve small species at low collisional energy. In fact, the required CPU time is directly proportional to the number of coupled channels, thus making calculations above a few hundred of cm^{-1} for heavy molecules computationally inaccessible. In such cases, it is necessary to resort to approximate methods like the coupled states (CS) approximation or the infinite order sudden (IOS) approximation.

The CS approximation (McGuire and Kouri, 1974) neglects the Coriolis coupling between the total angular momentum and the rotational momentum of the target molecule, which is included in the $\hat{\mathcal{L}}$ operator of Eq. (2.68). Hence, within the CS approach, fewer states are coupled, thus decreasing the computational time of a factor between 3 and 10 compared to CC. Moreover, this approximation is expected to be relatively accurate, with discrepancies with respect to the CC results of, in the worst case, 20%. The larger deviations will correspond to the resonant regime of the cross sections, at very low collisional energies.

The IOS approximation (Pack, 1974) ignores the rotation of the colliders in the assumption that the collision time among them is much faster than the rotation time. Each orientation of the colliders is hence decoupled from the others. The IOS approximation, while providing good performances for heavy molecules at high collisional energies, can lead to physically unsound results for collisions at low energy, where the rotation of the colliders can significantly affect the magnitude of the cross sections.

Quasiclassical Trajectory Method

When collisional calculations involve high temperatures ($T > 2000\,\mathrm{K}$), it becomes necessary to further reduce computational cost. In such scenarios, a commonly employed alternative is the quasiclassical trajectory (QCT) method (Mandy and Martin, 1993; Martin and Mandy, 1995; Lepp et al., 1995), which integrates classical mechanics for treating the scattering process alongside Monte Carlo sampling of the initial conditions. This substantially decreases the computational cost of scattering calculations and offers a valuable option for computing state-to-state rate coefficients at high temperatures. However, in the case of cold collisions, which constitute the main focus of this thesis, this approach fails to provide sufficiently accurate results. Hence, it was not further considered. For more details regarding this method, the reader is referred to Truhlar and Muckerman (1979); Bonnet and Rayez (1997); Aoiz et al. (2006).

Hyperfine Resolved Rate Coefficients

When the rotational levels of a molecule are split because of a hyperfine interaction, which is —in the present context— the nuclear quadrupole coupling, the dynamics of collisional (de-)excitations for hyperfine components needs to be solved as well.

In a full quantum close-coupling approach, an additional contribution (due to quadrupole coupling) to the molecular Hamiltonian needs to be added, and this introduces in the S–matrix the dependence on the F quantum number (see ¶ 2.2.2). However, this considerably increases the computational cost of the dynamic problem. A common approximation, known as the recoupling approach, ignores in a first stage the quadrupolar coupling contribution. Indeed, the hyperfine splitting energies are tipically much lower than the rotational and collisional energies. This enables a separation between the two degrees of freedom in the resolution of the scattering close-coupled equations. The spin-wave functions are subsequently incorporated in the rotational ones by means of a formula developed by Alexander and Dagdigian (1985). In detail, the inelastic cross-sections associated with a $j_B F \rightarrow j'_B F'$ transition are obtained from the rotational scattering matrix elements $S^J(j_B l; j'_B l')$ (nuclear-spin free) derived from the close-coupling calculations:

$$T^J\left(j_B l; j'_B l'\right) = 1 - S^J(j_B l; j'_B l')\,, \tag{2.86}$$

where $T^J\left(j_B l; j'_B l'\right)$ are the T-matrix elements, which are linked to the so-called tensor of opacities $P^K\left(j_B \rightarrow j'_B\right)$ (see Alexander and Davis 1983 for a detailed derivation of the latter) *via*:

$$P^K\left(j_B \rightarrow j'_B\right) = \frac{1}{2K+1} \sum_{ll'} \left| T^K\left(j_B l; j'_B l'\right) \right|^2 , \tag{2.87}$$

where

$$T^K\left(j_B l; j'_B l'\right) = (-1)^{-j_B - l'}\left(2K+1\right)\sum_J (-1)^J \left(2J+1\right) \times \left\{ \begin{array}{ccc} l' & j'_B & J \\ j_B & l & K \end{array} \right\} T^J\left(j_B l; j'_B l'\right) . \tag{2.88}$$

From the opacity tensor elements $P^K\left(j_B \rightarrow j'_B\right)$, the recoupled inelastic cross sections ($\sigma^{\mathrm{REC}}_{j_B F \rightarrow j'_B F'}$) are obtained as:

$$\sigma^{\mathrm{REC}}_{j_B F \rightarrow j'_B F'} = \frac{\pi}{k^2_{j_B F}}\left(2F'+1\right)\sum_K \left\{ \begin{array}{ccc} j_B & j'_B & K \\ F' & F & I \end{array} \right\}^2 P^K\left(j_B \rightarrow j'_B\right) . \tag{2.89}$$

Having computed the inelastic cross sections $\sigma^{\mathrm{REC}}_{j_B F \rightarrow j'_B F'}$, the corresponding rate coefficients are straightforwardly derived at a given temperature T by averaging over collision energy (E_{c}):

$$k_{j_B F \rightarrow j'_B F'}(T) = \left(\frac{8}{\pi \mu k^3_{\mathrm{B}} T^3}\right)^{1/2} \int_0^\infty \sigma^{\mathrm{REC}}_{j_B F \rightarrow j'_B F'} E_{\mathrm{c}}\, \mathrm{e}^{-E_{\mathrm{c}}/k_{\mathrm{B}}T}\, \mathrm{d}E_{\mathrm{c}} . \tag{2.90}$$

The recoupling approximation, albeit not exact, is commonly considered as the "reference" approach (Faure and Lique, 2012) because it is extremely accurate in predicting the hyperfine-resolved rate coefficients. However, it requires to store all the elements of the spin-free S–matrix and to compute the opacity tensor between the rotational levels, this implying a significant computational effort.

In order to further reduce the computational cost, the NG approximation (Neufeld and Green, 1994) is commonly applied. The latter is based on the IOS assumption, which ignores the rotational energy spacing with respect to the collision energy. The inelastic rotational rate coefficients $k^{IOS}_{j_B \rightarrow j'_B}(T)$ can be thus directly derived from the rotational excitation rate coefficients involving the fundamental $j_B = 0$ state (Corey and McCourt, 1983):

$$k^{IOS}_{j_B F \rightarrow j'_B F'}(T) = (2j_B+1)(2j'_B+1)(2F'+1)\sum_L \left(\begin{array}{ccc} j'_B & j_B & L \\ 0 & 0 & 0 \end{array} \right)^2 \times \left\{ \begin{array}{ccc} j_B & j'_B & L \\ F' & F & I \end{array} \right\}^2 k^{IOS}_{0 \rightarrow L}(T) . \tag{2.91}$$

Within this approach, propensity rules are properly included through the Wigner coefficients. In order to assure a good behavior at temperatures well below the potential well, a scaling procedure is finally employed:

$$k_{j_B F \rightarrow j'_B F'}(T) = \frac{k^{\mathrm{IOS}}_{j_B F \rightarrow j'_B F'}(T)}{k^{\mathrm{IOS}}_{j_B \rightarrow j'_B}(T)} k^{\mathrm{CC}}_{j_B \rightarrow j'_B}(T) . \tag{2.92}$$

This exploits the assumption of the following equality with the close-coupled rotational rate coefficients:

$$\sum_{F'} k_{j_B F \to j'_B F'}(T) = k^{\mathrm{CC}}_{j_B \to j'_B}(T)\,. \tag{2.93}$$

Another simple alternative approach that is widely used for astrophysical applications (see Guilloteau and Baudry 1981; Keto and Rybicki 2010) is the statistical method denoted as M_j-randomizing limit or proportional approach (RAN, Alexander and Dagdigian, 1985). This method assumes a statistical reorientation of the quantum number F' after the collision, thus neglecting any dependence on the initial conditions of the system. This allows to express the $j_B F \to j'_B F'$ hyperfine-resolved rate coefficients from the corresponding pure rotational one $j_B \to j'_B$ through

$$k_{j_B F \to j'_B F'}(T) = \frac{(2F'+1)}{(2j'_B+1)(2I+1)} k_{j_B \to j_B}(T)\,. \tag{2.94}$$

The RAN approximation performs well at low temperatures, where statistical effects have a preponderant impact on the rate coefficients. However, it does not include in its formulation the effect of the propensity rules, which becomes increasingly prominent at high temperatures.

Bound States

If all the asymptotic channels are closed for a given energy, the two colliders will form a stable bound complex having a geometry which corresponds to the bottom of the potential well. If this bound state complex is stable, then it allows for experimental spectroscopic characterization, thus providing a means to validate the accuracy of the computed potential. This is accomplished by performing bound states calculations which provide the rotational energy levels for the bound state complex. Bound state calculations are carried out using the BOUND routine (Hutson and Green, 1994) and are formulated as a set of coupled differential equations similar to those encountered in scattering theory. The difference between the two cases is in the boundary conditions that must be applied. Indeed, the bound-state $F_l(R)$ radial function approaches zero in the classically forbidden regions at both short range, $R \to 0$, and long range, $R \to \infty$. The coupled equations that satisfy this boundary condition at both ends exist only at specific energies, which are the eigenvalues of the total Hamiltonian of Eq. (2.68) and represent the energies levels of the bound complex.

Pressure Broadening and Shift Coefficients

Among the observables that reflect the collisional behavior of a molecular system, the pressure broadening and pressure shift coefficients play a crucial role. These coefficients are associated with collisional perturbations affecting transitions between the rotational levels of a molecule, and their magnitude depends on the pressure of the surrounding environment. They manifest as line broadening and shifting in frequency of the observed spectral lines. For a more detailed treatment of these effects, the reader is referred to § 4.2. By performing scattering calculations for the upper and lower states of a spectroscopic transition, line shape cross sections for its broadening and shifting effects due to collisions can be derived. Indeed, the integration of the inelastic cross sections over the entire distribution of thermal energy leads to an average value $\bar{\sigma}$, whose real and imaginary part are the pressure broadening (γ) and pressure shift (s) coefficients, respectively:

$$\bar{\sigma} = \frac{1}{(kT)^2} \int_0^\infty E \mathrm{e}^{-E/kT} \sigma(E) dE \,, \tag{2.95}$$

$$\gamma - \mathrm{i}s = n_p \bar{\nu} \bar{\sigma} = \frac{56.6915}{\sqrt{\mu T}} \bar{\sigma} \,, \tag{2.96}$$

where $\bar{\nu} = (8k_B T/\pi\mu)^{1/2}$ is the mean velocity of the colliders and n_p represents the density of the gas. In terms of units, γ and s are expressed in $\mathrm{cm}^{-3}\,\mathrm{atm}^{-1}$, $\bar{\sigma}$ in $\mathrm{Å}^2$, μ (reduced mass of the system) in amu and T in Kelvin.

Chapter 3

Computational Details

As anticipated in Chapter 2, the characterization of the collisional behavior of a molecular system starts from the resolution of the electronic Schrödinger equation of both the isolated colliders and the global colliding system, whose eigenvalues define the PES of each molecule and the interaction potential between them, respectively. However, for many-electrons systems, the electronic Schrödinger equation is not exactly solvable, and this forces us to rely on approximate approaches.

The main sources of error in quantum-chemical calculations depend on the approximations introduced in the level of theory exploited, this being defined as the combination of the method used for the description of the wave function and the basis set employed for its construction. To better detail: first, in order to build the wave function, we need to describe the molecular orbitals (MOs) as mathematical functions that adhere to the antisymmetry property of the Pauli principle (Pauli, 1925). This is often fulfilled by a linear combination of atomic orbitals (AOs), which are functions whose number and form is defined by the computational basis set. Ideally, these AOs should be infinite in order to correctly describe the MOs and their truncation introduces the first main source of error, denoted as basis-set truncation error (BSE). The MOs are then used to obtain the multi-electron wave function. In some cases, the multi-electron wave function is defined as a linear combination of Slater determinants* describing possible electronic configurations. Another way out is represented by density functional theory (DFT), where the electronic energy is no longer computed using the "wave function picture", but instead it is determined as a function of the electronic density.

The second error source is the so-called N-electron error, *i.e.*, the error due to the truncation of the electronic excitation orders incorporated in the wave function.

*A Slater determinant is a linear combination of $\psi_n(i)$ spin-orbitals, which are functions of the spatial orbital and the spin function coordinates of the i-th electron, multiplied for an antisymmetrizer factor (see Shavitt and Bartlett 2009 for further details).

The vectorial sum of the BSE and the N-electron error leads to the apparent error affecting the level of theory considered. Figure 3.1 provides a graphical representation of how the BSE and N-electron errors combine to give the apparent error. It is there noted that only when the two errors are null, then the exact solution is obtained. The choice of the computational level of theory must thus find the best compromise between accuracy and computational cost, which often depends on the size of the system under consideration and the type of application.

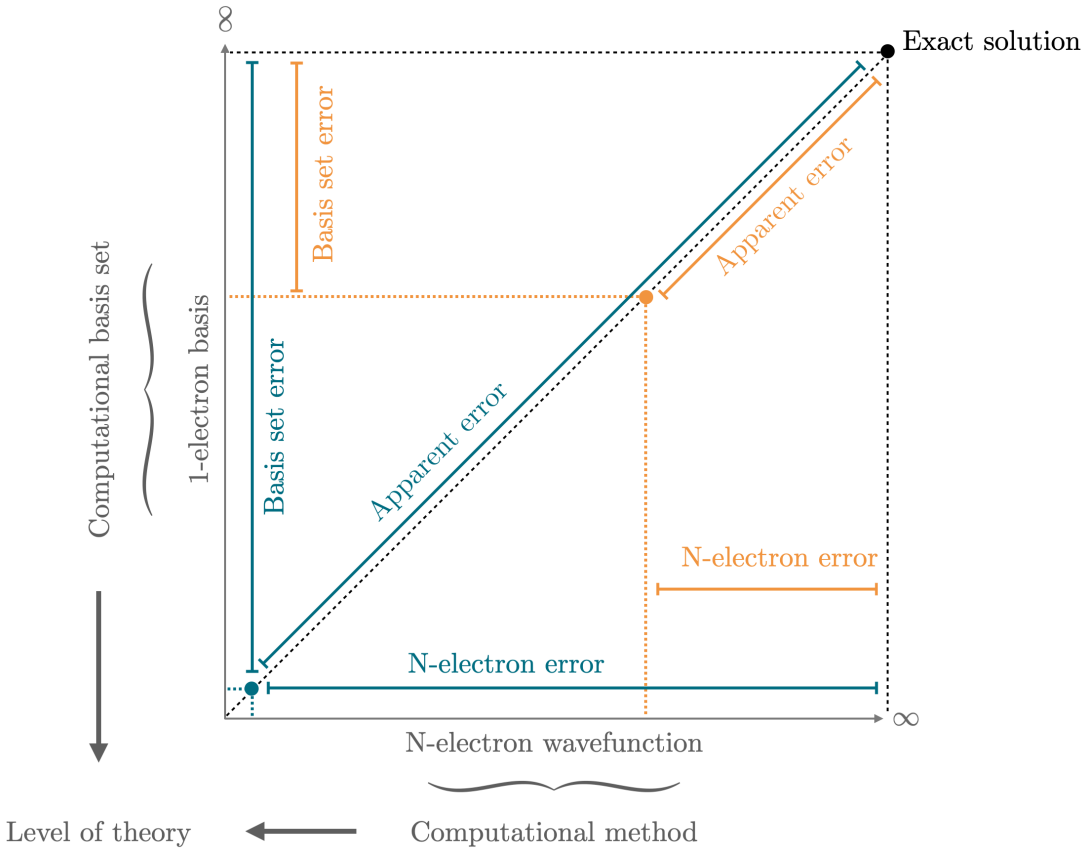

Figure 3.1: Errors in quantum-chemical calculations with respect to the exact solution of the electronic Schrödinger equation.

This Chapter is organized as follows. In § 3.1, the methods employed in this thesis for the treatment of electronic correlation term are presented, while the basis sets used to define the MOs are outlined in § 3.2.

3.1 Quantum-Chemical Methods

Over the years, a large variety of methods has been developed with the aim of obtaining approximate solutions of the electronic Schrödinger equation. The first introduced was the Hartree–Fock Self-Consistent Field (HF-SCF) method (Hartree

and Black, 1933; Hartree et al., 1939), which is an independent-electron model that considers each electron as surrounded by a mean repulsive potential due to the presence of the other electrons. In the HF-SCF theory, for each i electron, the Hamiltonian is written as the sum of mono- ($\hat{h}_i$) and pseudomono- ($\hat{\mathcal{J}}_{ij}, \hat{\mathcal{K}}_{ij}$) electronic operators:

$$\hat{\mathcal{F}}_i = \hat{h}_i + \sum_{j}^{N_{\text{elec}}} \left(\hat{\mathcal{J}}_{ij} - \hat{\mathcal{K}}_{ij} \right) , \tag{3.1}$$

where the $\hat{h}_i$ operator accounts for the kinetic energy of the i-th electron and its potential interaction with the nuclei; $\hat{\mathcal{J}}_{ij}$ and $\hat{\mathcal{K}}_{ij}$ are the Coulomb and Exchange operators, respectively, they provide the mean-field description of the electron-electron repulsion, and incorporate the MOs (ψ_i, ψ_j) in their definition through:

$$\begin{aligned} \hat{\mathcal{J}}_{ij} \left|\psi_j(2)\right\rangle &= \left\langle \psi_i(1) \left| \hat{g}_{12} \right| \psi_i(1)\psi_j(2) \right\rangle , \\ \hat{\mathcal{K}}_{ij} \left|\psi_j(2)\right\rangle &= \left\langle \psi_i(1) \left| \hat{g}_{12} \right| \psi_j(1)\psi_i(2) \right\rangle . \end{aligned} \tag{3.2}$$

Here, $\hat{g}_{ij}$ is a two-electron operator which represents the electron-electron repulsion contribution.

The operator $\hat{\mathcal{F}}_i$ of Eq. (3.1), denoted as the Fock operator, thus depends on the MOs. This means that, in order to have a proper description of $\hat{\mathcal{F}}_i$, the variational principle within the so-called self-consistent field (SCF) procedure is exploited. In detail, an initial guess of the wave function (Ψ_{HF}), represented as one Slater determinant, is iteratively refined in order to minimize the energy and the procedure is stopped once the convergence criterium is met (see Roothaan 1951 and Jensen 2017 for further details).

In the HF method, since the electron-electron interaction is described by means of an average interaction of one electron with all the other electrons, istantaneous interactions are neglected and thus correlation effects are not incorporated. Indeed, electronic correlation energy is, by definition, the difference between the total energy of the system and the HF-SCF energy in the limit of an infinite basis set. The electronic correlation term impacts only for the 1% to, at most, 10% of the total value of the energy; however, HF theory is not able to provide quantitative, or even semi-quantitative, results. In order to incorporate correlation energy in quantum-chemical calculations, many different strategies have been developed. In the following subsection, the main aspects of the correlated method employed in this thesis will be outlined.

3.1.1 Coupled Cluster Theory

Since its formulation in the late 1960s (Čížek, 1966, 1969), Coupled Cluster (CC) theory has represented a major breakthrough for the solution of the electronic Schrödinger equation and is currently one of the most reliable approaches to accurately derive the molecular properties of a system. CC methodologies aim to correct Ψ_{HF}, taken as the reference wave function Ψ_0, with the inclusion of electron excitation from single to infinite order, thus involving all the unoccupied molecular orbitals (Jensen, 2017). This is accomplished by introducing an excitation operator, the cluster operator ($\hat{T}$), that generates all the excited Slater determinants for each m^{th} excitation order, where m is the number of excited electrons:

$$|\Psi\rangle = \exp(\hat{T})\,|\Psi_0\rangle = \left(1 + \hat{T} + \frac{\hat{T}^2}{2!} + \frac{\hat{T}^3}{3!} + \dots\right)|\Psi_0\rangle\ , \tag{3.3}$$

where:

$$\hat{T} = \hat{T}_1 + \hat{T}_2 + \hat{T}_3 + \cdots + \hat{T}_{N_{el}}\ , \tag{3.4}$$

$$\hat{T}_m = \frac{1}{(m!)^2} \sum_{i,j,k,\dots a,b,c,\dots} t_{ijk\dots}^{abc\dots} a^{+} i b^{+} j \dots\ . \tag{3.5}$$

In Eq. (3.5) the second quantisation formalism[†] is adopted to account for electronic excitations: p^{+} represents the creation operator, responsible for the "creation" of an electron in a virtual orbital (indicated by $a, b, c \dots$), while p is the annihilation operator, which destroys an electron in an occupied orbital (indicated by $i, j, k \dots$). The cluster amplitudes, $t_{ijk\dots}^{abc\dots}$, are the weighting factors in the cluster operator. The CC function (Ψ) is thus obtained by incorporating Eqs. (3.4) and (3.5) into Eq. (3.3). At this point, the Schrödinger equation to obtain the CC correlation energy is solved by projecting Ψ onto Ψ_0:

$$\left\langle \Psi_0 \left| \hat{\mathcal{H}} \right| \Psi \right\rangle = \left\langle \Psi_0 \left| \hat{\mathcal{H}} \exp(\hat{T}) \right| \Psi_0 \right\rangle\ . \tag{3.6}$$

Since the Hamiltonian operator is formed by only one and two-electron terms (see Eq. (3.24) in Jensen 2017), CC correlation energy is completely determined by the singles and doubles amplitudes and two-electron integrals over MOs:

$$E_{\mathrm{CC}} = E_0 + \sum_{i<j,a<b} \left(t_{ij}^{ab} + t_i^a t_j^b - t_i^b t_j^a\right)\left(\langle \phi_i \phi_j \mid \phi_a \phi_b \rangle - \langle \phi_i \phi_j \mid \phi_b \phi_a \rangle\right) = E\,. \tag{3.7}$$

In Eq. (3.7), however, single- and double-excitation amplitudes are coupled with higher-order excitations *via* amplitude equations. To retrieve the contribution of

[†]The reader is referred to Shavitt and Bartlett (2009) for a detailed treatment of this formalism.

Table 3.1: Computational cost of CC methods.

Scaling	methods
N^4	HF-SCF
N^6	CCD, CCSD
N^7	CCSD(T)
N^8	CCSDT

higher-order excitations to the energy, the amplitude equations need to be solved. This leads in principle to the exact solution of the electronic problem, being the full CC wave function comprehensive of all the possible excited determinants for the system. However, this is unfeasible, and thus the cluster operator needs to be restricted to certain classes of excitations. Such truncation in the CC wave function has a great impact on the accuracy of the CC method. For instance, the first improvement over HF is given by the inclusion of the $\hat{T} = \hat{T}_2$ cluster operator, leading to the CCD method, while the additional inclusion of the single excitations, $\hat{T} = \hat{T}_1 + \hat{T}_2$, leads to the improved CCSD model, still mantaining a similar computational effort. The addition of higher-order excitations ($\hat{T}_3, \hat{T}_4, \hat{T}_5, ...$) further improves the accuracy of the method (CCSDT, CCSDTQ, CCSDTQ5, ..., respectively), but requires a more demanding computational effort. This results in computationally unfeasible calculations for medium-sized molecules already at the CCSDT level because of the large number of determinants incorporated in the wave function. A possible way out in this regard is offered by the CCSD(T) method, which keeps the computational cost affordable by incorporating triple excitations by means of a perturbative treatment. In detail, the CCSD amplitudes are employed to compute the contribution of the triples *via* fourth order perturbation theory and adding also a fifth order perturbation term to account for the coupling between singles and triples (Jensen, 2017).

The computational cost of quantum-chemical methods is typically identified by the so-called "N scaling" factor, which denotes how the computational effort increases as the size of the basis set (N) enlarges; the corresponding classification is provided in Table 3.1 for the CC methods. This table also reflects the accuracy order.

Given its inverse relationship with the number of excitations considered, the N-electron error is considered quite small already at the CCSD(T) level of theory, which offers the best compromise between accuracy and computational cost for the characterization of small/medium-sized systems. However, in analogy to all the others correlated methods, CCSD(T) exhibits a very slow convergence to the complete

basis limit (CBS)[‡]. To get accurate results, it is therefore frequently required to increase the number of basis functions used to describe MOs, thus leading to a considerable increase in computational cost. The slow convergence of CC methods is mainly due to the manner in which the orbitals, used for computation, describe the electronic cusp, *i.e.*, the trend of the wave function for interelectronic distances approaching to zero. To enhance the description of the electronic cusp, a bi-electronic distance dependence can be explicitly included in the electronic wave function. This contribution improves the performance of the wave function for small interelectronic separations and greatly reduces the computational cost without resorting to large basis sets. The methods that introduce this contribution are the so-called explicitly correlated methods, which differ in the functional form used to introduce the bi-electronic distance. For example, if a linear form is used ($\Psi \sim r_{12}$), the methods are denoted as R12, while, if a Slater-type form is used (see Eq. (3.8)), the methods are denoted as F12 (Adler et al., 2007; Peterson et al., 2008; Knizia et al., 2009).

$$F\left(r_{12}\right) = -\frac{1}{\gamma} e^{-\gamma r_{12}} \approx \sum c_i e^{-\alpha r_{12}^2} \,. \tag{3.8}$$

Here, the exponential correlation factor, denoted by the γ correlation coefficient, is fitted to a combination of i (typically six) Gaussian functions, defined by the α parameter.

Among CC-F12 methods, the CCSD(T)-F12 one has been widely used as a reference method for the purpose of this thesis. The latter incorporates a perturbative treatment of triple excitations (T) to initial CCSD-F12 calculation and has been demonstrated to be very suitable to map the short- and long-range multidimensional collisional PESs (see Lique et al. 2010a; Ajili et al. 2013 and references therein).

One limitation of standard CCSD(T) and explicitly-correlated CCSD(T)-F12 methods is that they are based on a single-reference wave function (thus not incorporating static electron correlation). For CC methods, it is possible to check the suitability of a single-reference wave function from the single-excitation amplitudes. A widely used tool is the T_1-diagnostics, defined as:

$$\mathbb{T}_1 = \frac{\sqrt{\left(t_i^a\right)^2 + \left(t_j^b\right)^2 + \cdots + \left(t_k^c\right)^2 + \cdots}}{\sqrt{N_{\mathrm{el}}}} \,, \tag{3.9}$$

where the numerator is the norm of the t_i^a vector and N_{el} the number of electrons. If $\mathbb{T}_1$ is larger than 0.02 for closed-shell and than 0.04 for open-shell molecules, then the reference wave function is very likely not well described by a single configuration.

[‡]The reader is referred to the § 3.2 for further details about CBS convergence.

If static correlation is non-negligible, a single-determinant description is not able to adequately describe the system under consideration. In such cases, one has to resort to multi-reference approaches such as the multi-configuration self-consistent field (MCSCF, Grein and Chang 1971; Werner and Knowles 1985; Knowles and Werner 1985) or multi-reference configuration interaction (MRCI, Whitten and Hackmeyer 1969; Kahn et al. 1974; Shavitt 1998) methods. The systems of interest to this thesis do not exhibit strong non-dynamical correlation effects, thus the use of multi-reference methods could have been avoided.

3.2 Basis Sets

As previously mentioned, the resolution of the electronic Schrödinger equation requires an initial guess of the wave function. As a first step toward its construction, it is necessary to define mathematical functions able to describe the atomic orbitals. The linear combination of these, in fact, leads to the MOs, which are the building blocks for the construction of the wave function.

There are two main types of basis functions commonly used to describe atomic orbitals: Slater Type Orbitals (STO) and Gaussian Type Orbitals (GTO). Slater type orbitals exhibit a nucleus-electron distance (r) dependence that mimics that of hydrogen-atom orbitals. Their functional form is:

$$\chi_{\zeta,n,l,m}(r,\theta,\varphi) = NY_{l,m}(\theta,\varphi)r^{n-1}\mathrm{e}^{-\zeta r}\,, \tag{3.10}$$

where ζ, n and l, m are the radial and angular coefficients, respectively, N is a normalization constant and $Y_{l,m}(\theta,\varphi)$ are spherical harmonic functions. STO functionals accurately describe the shape of atomic orbitals, but the calculation of their multi-centre two-electron integrals (which enter in the $\hat{\mathcal{J}}_{ij}$ and $\hat{\mathcal{K}}_{ij}$ terms, see Eq. (3.2)) cannot be performed analitically. One way to ease the computational effort is offered by Gaussian-type functions, which have the following form:

$$\chi_{\zeta,n,l,m}(r,\theta,\varphi) = NY_{l,m}(\theta,\varphi)r^{2n-2-l}\mathrm{e}^{-\zeta r^2}\,. \tag{3.11}$$

The advantage of the latter is the analytical resolution of the integrals mentioned above. However, Gaussian functions fail in reproducing the radial behavior with the same accuracy as Slater-type functions. This is clearly evident in Figure 3.2. Here, for a 1s-type orbital, the radial behavior of a STO function is depicted in orange, while that of a GTO function is shown in blue. The dependence on $-r^2$ in the exponential of GTO functions fails indeed in reproducing the orbital "cusp" (discontinuous derivative) for $r = 0$, which is instead well described by the dependence on

$-r$ in the exponential of STO functions. Moreover, the GTO function decreases too rapidly as the distance r increases.

To summarize, STO functions better predict the radial behavior. However, having at disposal an analytical resolution of the bi-electronic integrals with GTO functions is a tool that cannot be overlooked. For this reason, linear combinations of several GTO functions, denoted as primitive functions, whose coefficients are optimized to better simulate the Slater-type pattern, are often considered. The resulting functions are called contracted GTO (cGTO) functions. For example, the radial dependence of a 1s-type orbital can be already reasonably reproduced by means of a linear combination of three primitive GTO functions, forming the so-called STO-3G contracted function (black curve in Figure 3.2).

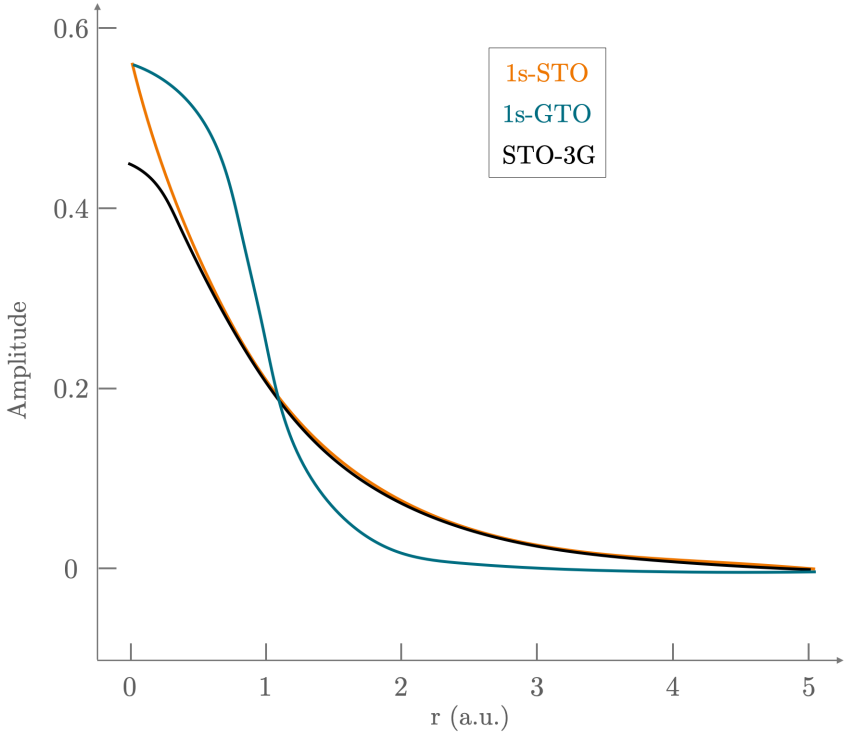

Figure 3.2: Comparison of the radial part of the STO, GTO and STO-3G basis functions for the 1s-type orbital.

The basis sets employed in this thesis belong to the series developed by Dunning and coworkers (Dunning Jr, 1989) and are denoted by the acronym: cc-pVnZ, where cc stands for "correlation-consistent", which means that the basis set has been optimized for being used with correlated methods. The size of the basis set is denoted in terms of the number of basis functions used to describe one valence orbital. This is indicated by the VnZ part of the acronym, which specifies that n basis functions describe each valence orbital. Each core orbital, instead, is represented by a sin-

gle cGTO. Finally, the term p indicates that the basis also includes polarization functions, which have a quantum number l greater than the largest value of valence orbitals. Quite often, this type of basis sets is not flexible enough to correctly describe the electron density in regions far from the maximum (Kendall et al., 1992). It is therefore necessary to add the contribution of diffuse functions, which have very small radial exponents (*i.e.*, loose functions) and are therefore more diffuse at long range. The addition of diffuse functions in the basis set is denoted by the prefix "aug-".

As already discussed, there are two main sources of error in quantum calculations: the first is caused by the incompleteness of the basis set, the second by the truncation of the wave function model. As regards the former, one can resort to extrapolation formulas to estimate the CBS limit, which is the limit of an infinite basis set.

The convergence behavior to the CBS limit is strictly dependent on the form of the basis set and on the considered property. For example, a hierarchical series shows a monotonic convergence behavior: as the size of the basis set increases, the computed generic property tends to the best obtainable value given the method chosen. At the CBS limit, the deviation from the exact solution depends solely on the N-electron error and is denoted as the intrinsic error (see Fig. 3.3). This means that, by choosing an appropriate mathematical expression, it is possible to extrapolate the value of a given property to the CBS limit starting from the results

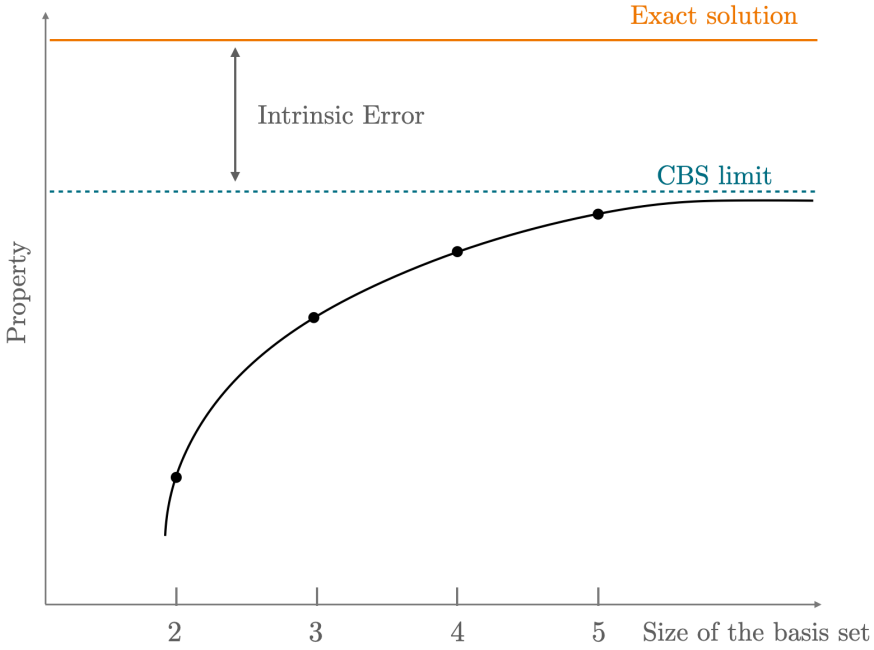

Figure 3.3: Monotonic convergence of a generic property with respect to the size of the basis set.

obtained for a set of finite basis sets. Moreover, the convergence rate also depends on the applied method. For example, methods that include electron correlation treatment are typically slower to converge than the HF-SCF method. We will focus only on the estimation of the CBS value for energy, but similar arguments can be formulated for all properties of a molecular system, such as the structural parameters or dipole moment.

A large variety of extrapolative formulas have been proposed in the literature. For the HF energy, the most commonly used approach exploits the Feller's extrapolative formula (Feller, 1993), which requires the HF energy computed with three basis sets belonging to a hierarchical series

$$E_{HF}^{\infty} = E_{HF}^{n} - Be^{-Cn}\,, \tag{3.12}$$

where B, C and E_{HF}^{∞} represent the parameters to be determined and n is the cardinal number of the basis set. For the extrapolation of the correlation energy, E_{corr}, the two-point extrapolative formula developed by Helgaker and coworkers (Helgaker et al., 1997) is often employed:

$$\Delta E_{corr}^{\infty} = \frac{n^3 E_{corr}^{n} - (n-1)^3 E_{corr}^{n-1}}{n^3 - (n-1)^3}\,. \tag{3.13}$$

The results from these two formulas are then combined to obtain the total energy extrapolated to the CBS limit:

$$E_{tot}^{\infty} = E_{HF}^{\infty} + \Delta E_{corr}^{\infty}\,. \tag{3.14}$$

There are also extrapolative formulas that are directly applied on the total energy, such as the one developed by Peterson et al. (1994). This is a three-point mixed Gaussian-exponential formula:

$$E_n = E_{tot}^{\infty} + \alpha \mathrm{e}^{-(n-1)} + \beta \mathrm{e}^{-(n-1)^2}\,, \tag{3.15}$$

with α, β and E_{tot}^{∞} being the parameters to determine.

The extrapolation of the basis set greatly improves the accuracy of a computational calculation, with the only error left over being the intrinsic error due to the choice of method employed.

Chapter 4

Experimental Measurements

Along with their *ab initio* counterpart, several experimental techniques have been devised to study the collisional behavior of molecular systems. However, the direct derivation of the collisional rate coefficients under the physical conditions of the ISM still remains a challenging task, thus being far from enabling systematic investigations (Smith, 2011).

The experimental methodologies that came the closest to satisfy these requirements are double resonance (DR) techniques. They exploit pump-probe measurements: a radiation perturbs the rotational thermal distribution of the sample population and another one measures its temporal evolution until the thermodynamic equilibrium is achieved through collisional processes (Daly and Oka, 1970; Brechignac et al., 1980; Messer and De Lucia, 1984). The breaktrough of this technique has been accomplished once coupled with a tunable pulsed IR pump laser to populate a rotational level of an otherwise unpopulated vibrational state. This approach, employed in combination with the CRESU apparatus, allows for the direct derivation of state-to-state collisional rate coefficients down to few K (Orr, 1995; James et al., 1998; Carty et al., 2004). Crossed-molecular-beam experiments, conversely, do not lead to the derivation of the absolute rate coefficients, but they can measure the relative state-to-state cross sections. This is achieved by monitoring the population distribution of a molecular beam from a single initial state and after collision with a beam composed by the perturbing gas. In detail, the sample molecular population is initially collimated to the fundamental state *via* supersonic jet cooling. This beam of molecules is then crossed with a second beam, composed of the collisional partner, and afterwards the final distribution of the population is measured by laser-induced fluorescence or resonance-enhanced multiphoton ionization (van Dishoeck, 1997; Yang et al., 2010, 2011; Chefdeville et al., 2012).

Rotational energy transfer processes can also be investigated by pressure broadening experiments (De Lucia and Green, 1988). These procedures do not provide

either direct or indirect measurements of the state-to-state rate coefficients, but they lead to estimates of average quantities (pressure broadening and pressure shift coefficients) which are related to the scattering S–matrix. In terms of astrophysical interest, the results of pressure broadening experiments play an important role to validate the theoretical results and the employed approximations. An interesting side product of this approach is the ability to provide reliable laboratory data for the stable molecules that compose planetary atmospheres. In such environments, the impact of the main perturbing gas on the molecular population of the minor atmosphere component is poorly known, and the data needed to retrieve molecular abundances are far from being complete, especially at high temperatures. Even in these conditions, the large vertical gradients in abundance through the atmosphere force non-LTE effects to be investigated as well. Moreover, laboratory measurements acquire a special importance when the target or the perturber species are difficult to treat from a computational point of view because of a complex internal energy level structure. For these reasons, the N_2-rich atmosphere of Titan represents an interesting test case for experimental validation *via* pressure broadening experiments. On one hand, both the coupling between the different rotational levels of N_2 and the influence of *para*-$N_2(j = 1)$ have a strong impact on the dynamics, thus burdening the calculations from a computational point of view; on the other hand, N_2 is a cheap and stable gas to be treated in laboratory experiments. The study of N_2 broadening behavior of molecules present in Titan can thus provide a useful support to the data retrieval from planetary atmosphere's observations.

Given its support to the computational investigation for some collisional systems of interest for this PhD thesis, the main aspects related to pressure broadening measurements are presented in this Chapter. In § 4.1, the experimental setup is described, which consists in the frequency-modulated mm-/submm-wave (FM-mmW) spectrometer of the Rotational and Computational Spectroscopy Lab at the Department of Chemistry "Giacomo Ciamician" (University of Bologna). In § 4.2, the details regarding the acquisition of the data, their analysis and their use to validate the theoretical calculation are provided.

4.1 Frequency-Modulated Millimeter-wave Spectrometer

The block diagram of the FM-mmW spectrometer is depicted in Figure 4.1. This instrument can operate in the frequency range between 75 GHz and 1.6 THz, and it is able to measure transition frequencies with an accuracy of a few tens of kHz. The microwave radiation sources are several Gunn diodes, covering the 75-134 GHz frequency range, which can be coupled with a series of active and passive frequency multipliers to reach frequencies up to 1.6 THz. In order to achieve frequency stabilization, the Gunn diode radiation is phase-locked to an external rubidium frequency

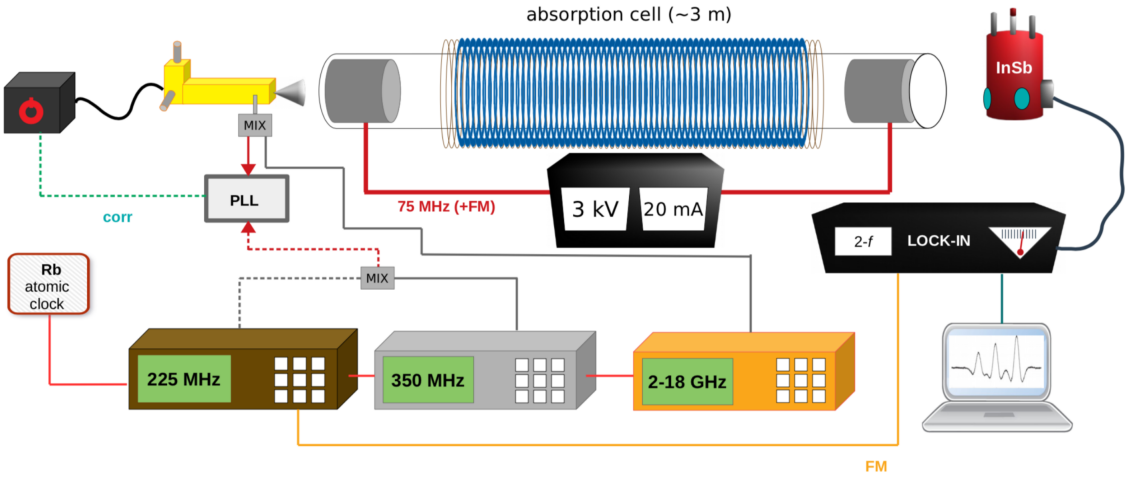

Figure 4.1: Block diagram of the FM-mmW spectrometer at the Rotational and Computational Spectroscopy Lab (University of Bologna). Image taken from the website of the Rotational and Computational Spectroscopy Lab: `https://site.unibo.it/rotational-computational-spectroscopy/en/facilities`.

standard. In detail, the Gunn output is mixed with the signal generated by a 2-18 GHz synthesizer referenced to an external rubidium frequency standard; their difference (set at 75 MHz) enters the phase-lock loop (PLL), which provides continuous stabilization to the Gunn output frequency. The absorption cell is a 3 m long Pyrex tube, 5 cm in diameter, equipped with two cylindrical hollow electrodes at both ends. To improve the signal/noise ratio, the frequency modulation technique is used. This is obtained by sine-wave modulating ($f = 16.67$ kHz) the 75 MHz reference signal. The output signal, detected by Schottky barrier diode, is subsequently demodulated by a Lock-in amplifier tuned at twice the modulation frequency ($2f$), so that the recorded spectrum is the second derivative of the natural profile. For further details regarding the instrumentation, the reader is referred to Melosso et al. (2019a,b).

4.2 Line shape and Pressure Broadening Experiments

Since the early 1900s, the investigation of spectral line shapes has received a wide experimental and theoretical interest (Birnbaum, 1967). Overall, the main aim was to minimize the factors responsible for line broadening, thus improving the spectral resolution and enabling more accurate and detailed analysis of molecular spectra. Over the years, the examination of line shapes assumed a strategic importance for either practical applications, *e.g.*, the design of gaseous molecular lasers and radiative transfer modeling of terrestrial and extra-terrestrial atmospheres, but also to study the physical relaxation phenomena responsible for the shape itself (Rabitz, 1974).

In ordinary experimental conditions, the mutual interactions between the particles of the sample and with the surrounding gas cause perturbations to molecular energy levels. The absorption is thus distributed over a range of frequencies, causing modifications on the line shape of the corresponding transition, which vary according to the type and degree of perturbation (Gordy et al., 1984).

In the following, we will describe the main contributions affecting the line shapes in a microwave experiment, and the information that can be extracted from them. To do so, the line shape function (ϕ_ν) needs to be introduced. The starting point is the Beer law (Beer, 1852), which states that the variation in intensity, from an initial I_0 value to a final I one, of electromagnetic radiation collimated at a frequency v, and transmitted through a slab of gas of length L, can be defined in terms of the so-called absorption coefficient, α_ν:

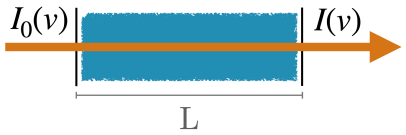

$$, \qquad I(\nu)/I_0(\nu) = \exp\left(-\alpha_\nu L\right) . \tag{4.1}$$

The line shape function is defined as:

$$\phi(\nu) = \frac{\alpha_\nu}{\int_{\text{line}} \alpha_\nu d\nu} , \tag{4.2}$$

and must satisfy the normalization condition: $\int_{-\infty}^{\infty} \phi(\nu) d\nu = 1$. In principle, the exact knowledge of the line shape of an experimental line allows for the determination of the absolute absorption coefficients of the investigated system (Rabitz, 1974; Pickett, 1980a). However, the exact form of $\phi(\nu)$ is unknown. We thus have to resort to a model that, by accounting for the main factors that affect the line shape, defines a mathematical function that provides the best approximation of $\phi(\nu)$. This procedure is also denoted as line profile analysis. Once the function that best models the experimental line is identified, two key parameters can be directly inferred from spectroscopic measurements (as depicted in Figure 4.2): the resonant frequency (ν_0) of the transition and its full width at the half maximum (FWHM), denoted as $\Delta\nu$.

In the microwave domain, line widths can vary from few kilohertz to few megahertz and depend on three factors: natural broadening, Doppler effect and pressure broadening. For a rigorous treatment, the reader is referred to Anderson (1949); Townes and Schawlow (1975); Gordy et al. (1984) and Brown et al. (2003). In the following, the main theoretical foundations are provided.

Natural line width is determined by the Heisenberg uncertainty principle leading to a finite lifetime of the upper state (u). If we assume a molecular system as completely isolated from radiation fields and colliding particles, the lifetime τ of the state u is given by the inverse of the Einstein coefficient for spontaneous emission,

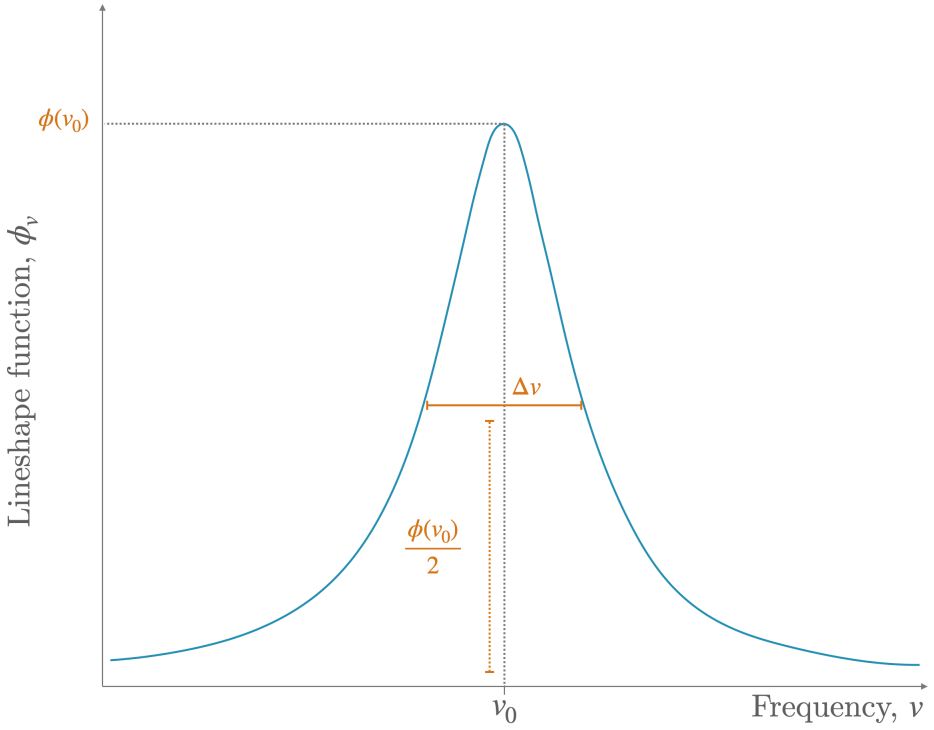

Figure 4.2: Derivation of the resonant frequency (ν_0) and line width (Δ_ν) of an experimental transition from its line shape function, $\phi(\nu)$.

A_{ui}. The line width is related to the probability of spontaneous emission to a lower state i as follows:

$$\Delta\nu_n = \frac{\Delta E}{h} \approx \frac{1}{2\pi(\tau)} \approx \frac{1}{2\pi}\sum_i A_{ui}\,. \tag{4.3}$$

Since A_{ui} depends on the third power of the transition frequency, in the mm-wave energy range, the natural line width of a rotational line is tipically of the order of tens of μHz and it has a negligible effect with respect to other broadening factors. For this reason, the natural line width is usually not taken in account when modeling the line profile in the microwave region.

A more relevant contribution to the line width is due to the Doppler effect. This is caused by the different velocities of the molecules due to thermal motions. Indeed, the frequency of the radiation absorbed by a molecule depends on its relative velocity component along the propagation direction of the radiation. Different velocities lead to slightly different absorbed frequencies, with the corresponding Doppler shifts contributing to the total line shape function. The Doppler line width ($\Delta\nu_d$) thus

depends on the temperature (T) and on the mass (m) of the system:

$$\Delta\nu_d = 2 \cdot \underbrace{\frac{\nu_0}{c}\sqrt{2\ln 2 \cdot \frac{k_B T}{m}}}_{\Gamma_d}, \tag{4.4}$$

where ν_0 is the resonant absorption frequency of the molecule at rest and Γ_d is the Doppler half-width. In thermal equilibrium conditions, the velocity distribution of the molecules follows the Maxwell–Boltzmann distribution. Hence, the line shape that defines the Doppler contribution can be modeled by a Gaussian function expressed in terms of Γ_d (orange function depicted in Figure 4.3):

$$\phi_d(\nu) = \phi_d(\nu_0) \cdot \exp\left[-2\ln 2\left(\frac{\nu - \nu_0}{\Gamma_d}\right)^2\right], \tag{4.5}$$

with

$$\phi_d(\nu_0) = \frac{\sqrt{\ln 2}}{\sqrt{\pi}}\frac{1}{\Gamma_d}. \tag{4.6}$$

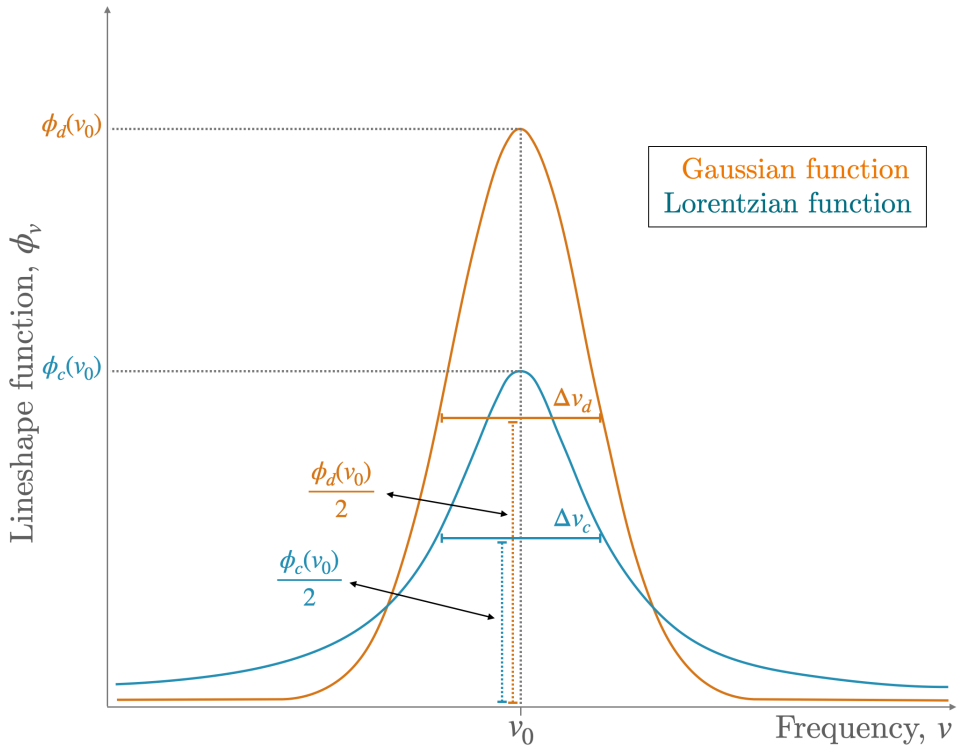

Figure 4.3: Gaussian and Lorentzian functions employed to model the line broadening due to Doppler and collisional broadening effects, respectively.

The most important source of broadening in microwave experiments is pressure broadening. Since 1930 (Margenau, 1930), it has been known that pressure in a microwave experiment can have a large impact on both the shape and the resonant frequency of the observed transition. Both these effects, *i.e.*, pressure broadening and pressure shift, respectively, arise from collisions between molecules: the pressure broadening is caused by collisional energies exchanges that shorten the lifetime of the initial and final states of the transition; the pressure shift, conversely, appears when the collisional rate is sufficiently high to perturbate both the lower and upper state energy levels of the molecular system, thus leading to an observed shift of the line-center. The first theory that accounted for the spectral distribution caused by collisions was developed by Lorentz (1905). Within this theory, collisions are assumed to be strong enough to destroy the coherence of the energy states. In the case of rotating molecules, this assumption implies that the orientation of the molecules after each collision has no relationship with their orientation before collision. Subsequently, Debye (1934) considered the case of molecules with a non-zero dipole moment, which causes the molecular orientation to be not completely random after each collision, but redistributed to minimize the interactions with the radiation electric field. About a decade later, van Vleck and Weisskopf (1945) somewhat merged the Lorentz and Debye theories by developing a general expression for the line shape function, which assumed the following form:

$$\phi_c(\nu,\nu_0) = \frac{1}{\pi}\left[\underbrace{\frac{\overbrace{\Delta\nu_c/2}^{\Gamma}}{(\nu-\nu_0)^2+\underbrace{(\Delta\nu_c/2)^2}_{\Gamma^2}} + \frac{\overbrace{\Delta\nu_c/2}^{\Gamma}}{(\nu+\nu_0)^2+\underbrace{(\Delta\nu_c/2)^2}_{\Gamma^2}}}_{\text{Lorentzian function}}\right], \tag{4.7}$$

where $\Delta\nu_c$ and Γ denote the collisional line width and the corresponding half-width, respectively. Since collisions lead to finite lifetime, the expression of the line width is given by:

$$\Delta\nu_c = \frac{1}{2\pi\,\tau_{\text{coll}}}, \tag{4.8}$$

with τ being in the present case the time between two collisions (τ_{coll}). It is worth to remark that, for a molecular sample, the time elapsing between collisions is inversely proportional to the pressure to which it is subjected. This implies a linear proportionality between the pressure and the collisional line width.

At low pressures, τ_{coll} is sufficiently low so that $\Delta\nu_c \ll \nu_0$. In this case, the first term in Eq. (4.7) dominates and can be safely considered as the only contribution to the line shape. This permits to reduce Eq. (4.7) to the one obtained by Lorentz,

which is therefore referred to as the Lorentzian function (blue curve depicted in Figure 4.3). This approximation is commonly adopted in the analysis of microwave and millimeter-wave measurements, where the sample pressure is usually in the $0.75 - 150\,\mathrm{mTorr}$ $(1 - 200\,\mu\mathrm{Bar})$ range. As pressure increases, however, the line shape analysis needs to take into account the general expression of Eq. (4.7) because the function tends to be increasingly asymmetric.

In the rotational spectroscopy domain, pressure and Doppler effects have comparable importance, with pressure broadening effect being dominant at high pressures and low frequencies. On the other hand, given the direct proportionality between $\Delta\nu_d$ and ν_0, the Doppler contribution has a greater influence at higher frequencies. Hence, in order to guarantee a reliable line shape analysis of rotational transitions, both Doppler and collisional broadening effects need to be simultaneously taken in account. A widely adopted function that is well-suited for this purpose is the Voigt function (Herbert, 1974), which is defined as the convolution of a Gaussian and a Lorentzian function:

$$\phi_V(\nu) = \phi_d(\nu) * \phi_c(\nu) = \int_{-\infty}^{\infty} \phi_d(u)\phi_c(\nu - u)du\,. \tag{4.9}$$

By making $\phi_d(u)$ and $\phi_c(\nu - u)$ explicit, the Voigt shape function assumes the following form:

$$\boxed{\phi_V(\nu) = \frac{\sqrt{\ln 2}}{\sqrt{\pi}\Gamma_d}\left[\frac{a}{\pi}\int_{-\infty}^{\infty}\frac{\exp\left(-y^2\right)}{a^2 + (w-y)^2}dy\right]\,,} \tag{4.10}$$

where

$$\begin{aligned} a &= 2\sqrt{\ln 2}\Delta\nu_c/\Gamma_d\,; \\ w &= 4\sqrt{\ln 2}\,(\nu - \nu_0)\,/\Gamma_d\,; \\ y &= 4\delta\sqrt{\ln 2}/\Gamma_d\,, \qquad \text{with}\,\delta = u - u_0\,. \end{aligned} \tag{4.11}$$

Although the integral of this profile cannot be evaluated analitically, many available computational procedures have been developed in order to make this function suitable to fit the line shape, *e.g.*, the ones proposed by Humlíček, Josef (1979) and Letchworth and Benner (2007).

Despite the good performance of the Voigt function to model line broadening effects, the mean thermal velocity approximation can lead, in some cases, to systematic errors in the derivation of the line shape parameters (see, *e.g.*, Lisak and Hodges 2008; Kochanov 2012; Hartmann et al. 2021). In such cases, a correlated model, which includes additional fitting parameters, needs to be adopted. In the past years, many efforts have been made to develop the best correlated line shape model, with several examples being available in the literature (see, for example,

Table 4.1: Summary of the described line profiles model in terms of the number of parameters (N) required to characterize the line shape.

Profile name	Parameters	
	N	
Doppler	1	Γ_d
Lorentz	1	Γ
Voigt	2	$\Gamma_d\,,\Gamma$
qSDVP	3	$\Gamma_d\,,\Gamma\,,\Gamma_2$

those presented in Dicke 1953; Berman 1972; Hess 1972; Ciuryło et al. 2002; Tran et al. 2009; Hartmann et al. 2013; May et al. 2013; Tennyson et al. 2014; Fortney et al. 2019). In the following, only the model employed in this thesis work to analyze the line shapes obtained by pressure broadening experiments will be detailed. This is the quadratic speed-dependent Voigt profile (qSDVP) (Berman, 1972; Ward et al., 1974; Pickett, 1980b; Pine, 1994; Rohart et al., 1994), which introduces a quadratic speed dependency of the relaxation rates by means of the Γ_2 additional parameter in the formulation of the line width:

$$\Gamma'\left(v_{\mathrm{a}}\right)=\Gamma+\Gamma_2\left[\left(v_{\mathrm{a}}/\overline{v}_{\mathrm{a}}\right)^2-3/2\right]\,. \tag{4.12}$$

Here, v_{a} is the relative speed between the active molecule and the perturber, and $\overline{v}_{\mathrm{a}}$ represents its mean value over the thermal distribution of all the perturber velocities (Pine, 1994; Tennyson et al., 2014).

To summarize, different models have been proposed, each of which accounts for different contributions to the line shape analysis. A comparison of their different degree of complexity in terms of the number of parameters is reported in Table 4.1.

A final remark is warranted in regards of the techniques employed to record the rotational spectra. The source frequency modulation, coupled with second harmonic detection (2f), is a technique that allows to significantly increase the signal-to-noise ratio of the absorption signals (see § 4.1), but it modifies the line profiles that are actually recorded (Karplus, 1948). The modulated line shape function, $\phi(\nu)^M$, is indeed a convolution of $\phi(\nu)$ with a periodic function which depends on twice the modulation frequency, ν_M (Puzzarini et al., 2002; Colmont et al., 2005):

$$\phi(\nu)^M=\phi(\nu)*F(2\nu_M)\,. \tag{4.13}$$

The modulated shape function $\phi(\nu)^M$ is the second derivative of the actual absorption profile. Since there is no analytical formulation of $\phi(\nu)^M$, several numerical

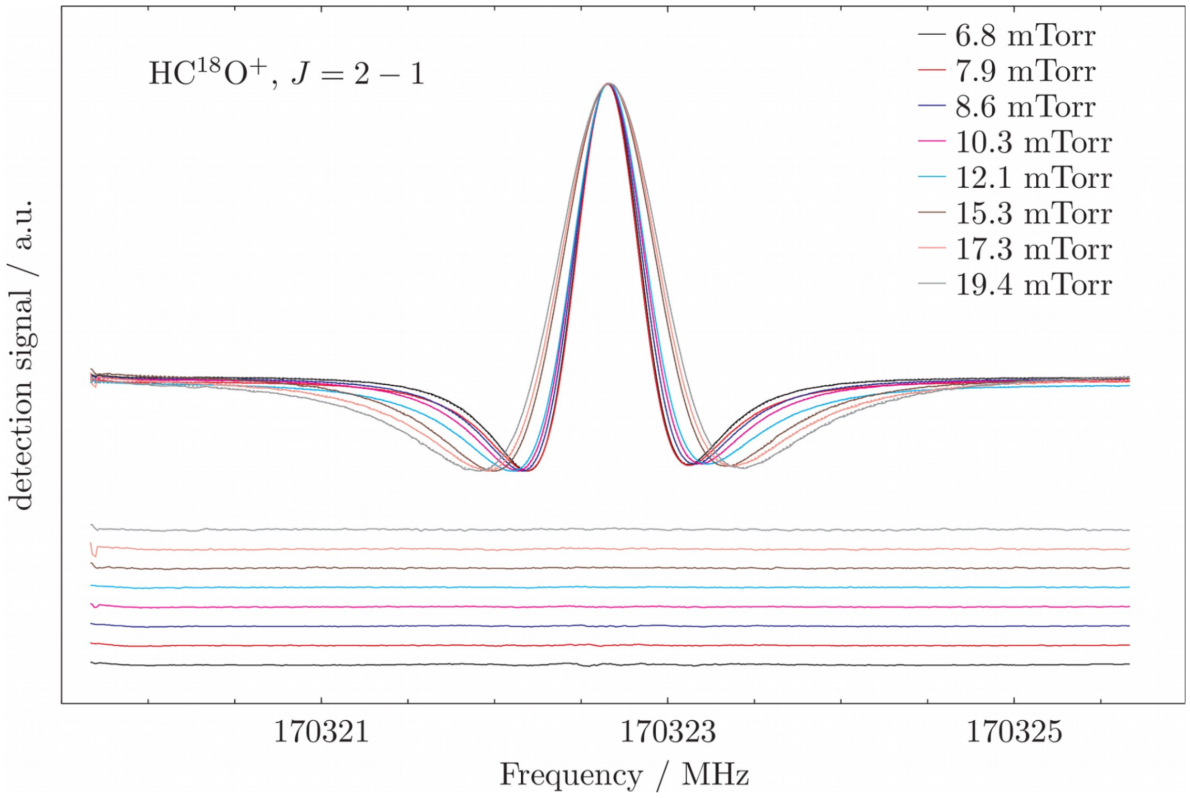

Figure 4.4: Line shape analysis, employing the qSDVP model, of the $J = 2 - 1$ transition of $HC^{18}O^+$ broadened by Ar. The transition has been recorded at 85 K by discharging 3 mTorr of $C^{18}O$, 1 mTorr of H_2 and increasing quantities (6-20 mTorr) of Ar. Anomalous glow discharge conditions were manteined: ΔV=2500 V, i=12 mA, longitudinal magnetic field $B \sim 250$ G. At the bottom of the figure, residuals (*i.e.*, the observed-calculated differences) are also reported.

methods have been developed to incorporate the modulation contribution into the line shape model (see, for example, Dore 2003).

In the context of this thesis, line profile analysis has been conducted to determine the pressure broadening and pressure shift coefficients for some rotational transitions. The retrieval of these coefficients has allowed for the validation of theoretical calculations through comparison with their computed counterparts. Furthermore, it permitted to improve the precision of the corresponding rest frequency in support of radioastronomical investigations. To evaluate pressure broadening effects, spectroscopic measurements must be conducted under controlled pressure and temperature conditions. In detail, a rotational transition of the target is recorded at increasing pressures of the perturbing gas. Then, each line profile is modeled with a function that takes into account all the contributions that affect its shape. In this thesis, the correlated qSDVP model has been consistently used, with ν_0, Γ and Γ_2 being adjusted in the line shape least square fitting. To give an example, Figure 4.4 shows the results of this analysis for the $J = 2 - 1$ transition of $HC^{18}O^+$ recorded

at different pressures of the Ar buffer gas (Bizzocchi et al., 2024). It can be seen that flat and featureless residuals (bottom part of Figure 4.4) were obtained for all pressures, thus validating the suitability of the adopted qSDVP model.

For each set of measurements, a linear regression of the collisional line width (Γ) vs pressure ($P_{\text{perturber}}$) is performed, from which the pressure broadening coefficient γ is directly retrieved:

$$\Gamma = \gamma \times P_{\text{perturber}} + \Gamma_0 \,, \tag{4.14}$$

where Γ_0 is the line width due to target itself. Analogously, the pressure shift coefficient (s) is obtained by fitting the shifts $\nu - \nu_0$ as a function of the perturbing gas pressure, according to the following expression:

$$\nu - \nu_0 = s \times P_{\text{perturber}} \,. \tag{4.15}$$

The results of the two fits obtained for the measurements on the $J = 2-1$ transition of $HC^{18}O^+$ at different pressures of Ar are shown in Figure 4.5.

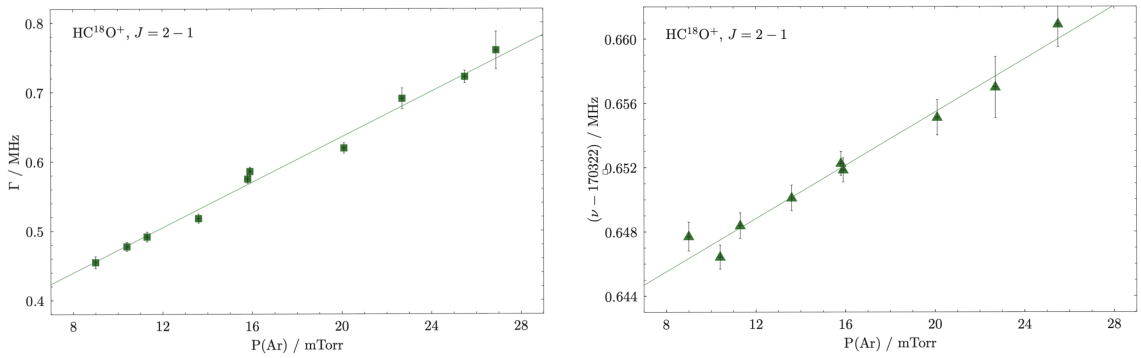

Figure 4.5: Set of measurements for the Ar-broadening of the $J = 2 - 1$ transition of $HC^{18}O^+$. Left panel: linear fit of the collisional half-width against the pressure of Ar. Right panel: linear fit of the frequency shifts against the pressure of Ar. In both panels, three times the uncertainties retrieved from line profile analysis are shown.

Chapter 5

Astrophysical Modeling

Interpreting a radioastronomical spectrum requires to deal with both the radiative transfer problem and statistical equilibrium equations. This requires the availability of fundamental molecular data, *i.e.*, the spectroscopic constants, which define the energy of the molecular levels, and the collisional state-to-state coefficients, which define the population distribution among energy levels. The derivation of these latter parameters has been described in Chapter 2. In this Chapter, the approach used to derive molecular abundances from radioastronomical observations of spectral lines is detailed.

5.1 Derivation of Molecular Abundances

All the information that can be derived from spectral line observations comes from the variation in intensity of an electromagnetic wave with a frequency ν that travels through an interstellar cloud. In this environment, the intensity of the radiation might vary due to absorption and emission processes by the surrounding atoms and molecules. The understanding of these phenomena permits to derive the molecular abundances, expressed in terms of column densities (given in units of cm^{-2}). This quantity represents the corresponding molecular volume density (cm^{-3}) integrated over the line of sight. In the following sections the formal derivation of this information is presented.

5.1.1 Radiative Transfer

If the beam of the radio telescope is sufficiently large, it is possible to assume that the radiation it collects travels in straight lines (beam diameter $\gg \lambda$). In this conditions, the infinitesimal variation in intensity dI_ν for an infinitesimal propagation of the

radiation along the direction of propagation dx is:

$$dI_\nu = -\alpha_\nu I_\nu dx + j_\nu dx \,. \tag{5.1}$$

The first term on the right-hand side of Eq. (5.1) describes the absorption process which reduces the radiation intensity, and is defined by the absorption coefficient α_ν. The second term describes the enhancement in intensity given by emission processes by means of the emissivity coefficient j_ν. The ratio between j_ν and α_ν denotes the so-called source function S_ν, whose physical meaning is to measure how many photons are removed and replaced by new photons by the surrounding environment:

$$S_\nu = \frac{j_\nu}{\alpha_\nu} = \frac{n_l A_{lu}}{n_u B_{ul} - n_l B_{lu}} \,. \tag{5.2}$$

We now introduce the optical depth, which depends on both the absorption coefficient and the physical thickness of the cloud (L). Thus, it describes the degree to which the cloud prevents light from passing through it:

$$\tau_\nu = \alpha_\nu L \,. \tag{5.3}$$

Hence, $d\tau_\nu = \alpha_\nu dx$ and the radiative transfer equation can be rewritten as:

$$\boxed{\frac{dI_\nu}{d\tau} = -I_\nu + S_\nu \,.} \tag{5.4}$$

The solution of Eq. (5.4) requires the introduction of some boundary conditions: outside the borders of the cloud, the radiation does not experience any molecular absorption or emission phenomena, and thus the source radiation is expected to coincide with the radiation of a blackbody at the temperature of the CMB radiation ($B_\nu\left(T_\mathrm{b}\right)$).

Assuming that the cloud is physically and chemically homogeneous (with constant S_ν inside its borders), the intensity of the radiation along the propagation direction is thus given by:

$$I_\nu = S_\nu + \exp\left(-\tau_\nu\right)\left[B_\nu\left(T_\mathrm{b}\right) - S_\nu\right] \,. \tag{5.5}$$

We now assume that the cloud is enclosed by a blackbody at temperature T_k. After sufficient time, this cloud will establish a thermal equilibrium with the blackbody, in which emission and absorption are balanced, *i.e.*, the Kirchhoff's law of thermal radiation applies. Hence, $S_\nu = B_\nu(T_k)$ and the radiation intensity assumes

the following form:

$$I_\nu = B_\nu(T_k) + \exp\left(-\tau_\nu\right)\left[B_\nu\left(T_b\right) - B_\nu(T_k)\right] \ . \tag{5.6}$$

Tipically, radio observations are performed through "switching", which is the comparison of the signal received from the target cloud against a reference point outside the cloud, where only the effect of CMB contributes to the radiation intensity. This allows for the cancellation of instrumental errors and measurement fluctuations due to atmospheric effects. The actual observed intensity thus results to be:

$$\Delta I_\nu = \left[B_\nu(T_k) - B_\nu\left(T_b\right)\right]\left\{1 - \exp\left(-\tau_\nu\right)\right\} \ . \tag{5.7}$$

Finally, this expression is commonly represented by a temperature scale. Indeed, by defining the intensity as a temperature at which a blackbody emits the same intensity, one obtains:

$$T_{\rm ant} = \frac{h\nu}{k_B}\left\{\frac{1}{\exp\left(h\nu/k_B T_k\right) - 1} - \frac{1}{\exp\left(h\nu/k_B T_b\right) - 1}\right\}\left\{1 - \exp\left(-\tau_\nu\right)\right\} \ . \tag{5.8}$$

The antenna temperature ($T_{\rm ant}$) is the actual quantity observed during radioastronomical observations. At radio to mm regimes, the Rayleigh–Jeans approximation can be safely adopted, since $h\nu/k_B T_k \ll 1$, hence Eq. (5.8) becomes:

$$T_{\rm ant} = \left(T_k - T_b\right)\left\{1 - \exp\left(-\tau_\nu\right)\right\} \ . \tag{5.9}$$

The equality in Eq. (5.9) provides a direct relationship between the intensity measured by radio telescope ($T_{\rm ant}$) and the optical depth, which contains all the relevant information about molecular abundances. However, it is based on a number of assumptions which are not always valid. For example, it assumes an homogeneous cloud model with a low optical depth. In many instances, one has to resort to a more complex model to describe the variation of the source function S_ν throughout the entire region of the targeted astronomical object (see, *e.g.*, Keto et al. 2004; Brinch and Hogerheijde 2010).

5.1.2 Statistical Equilibrium

Having solved the radiative transfer differential equation, which unveils the dependence of the radiation intensity on the optical depth, we need to express τ_ν as a function of the cloud physical properties we want to investigate. This is possible by exploiting the statistical equilibrium equations presented in Chapter 2, ¶ 2.1.1 (Eq. (2.10)). Hence, considering a two-level system as the one represented in Fig. 2.2,

the Einstein B coefficients play a role in the definition of the α_ν coefficient:

$$\alpha_\nu = \frac{h\nu}{4\pi}\phi(\nu)\left(n_l B_{lu} - n_u B_{ul}\right) . \tag{5.10}$$

Here, $\phi(\nu)$ is the line profile function (see Eq. (4.2) of § 4.2). Using the relations of Eqs. (2.4) and (2.5), and by exploiting the definition of T_{ex} to describe the population between the levels, the absorption coefficient takes the form:

$$\boxed{\alpha_{ul} = \frac{c^2 n_u}{8\pi\nu_{ul}^2\Delta\nu}\left\{\exp\left(\frac{h\nu_{ul}}{k_B T_{ex}}\right) - 1\right\} A_{ul} ,} \tag{5.11}$$

where the line profile function has been approximated to a square wave with a line width of $\Delta\nu$ (see Fig. 5.1), thus being $\phi(\nu) = \frac{1}{\Delta\nu}$.

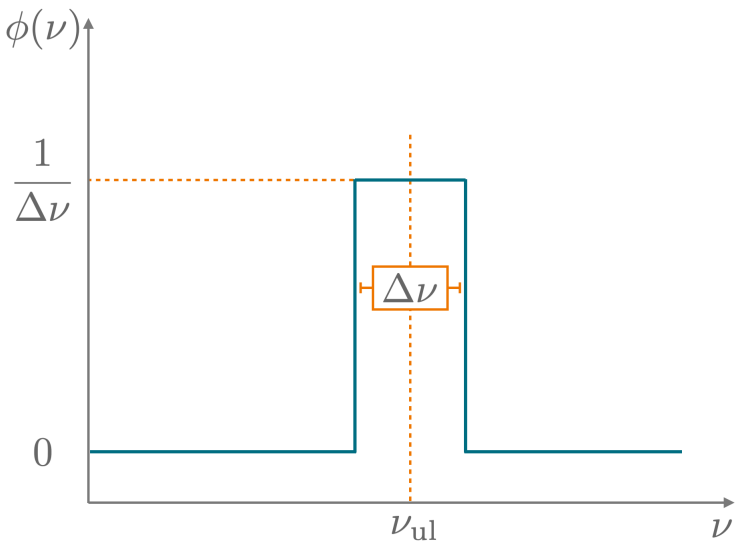

Figure 5.1: Line profile function commonly employed for astrophysical purposes in the derivation of molecular abundances.

Under LTE conditions, $T_{ex} = T_k$ and the total number of molecules n is related to n_u *via* the partition function $Q(T_k)$*. By expliciting the line width in terms of velocity rather than frequency ($\Delta v = \frac{\Delta\nu}{\nu_{ul}}c$) and by introducing the definition of the column density ($N = nL$) as the product of the total number of molecules and the physical thickness of the cloud (L), we finally obtain an expression for the optical

*In detail, $n_u = \frac{g_u}{Q(T_k)}\, n\, e^{-E_u/kT_k}$. The partition function is given by $Q(T_k) = \sum_i g_i e^{-E_i/kT_k}$, where the summation is taken over all the i energy levels, with degeneracy g_i (the reader is referred to Gordy et al. (1984); Yamamoto (2017) for more details).

depth as:

$$\tau_{ul} = \frac{8\pi^3 S_{ul}\mu^2}{3h\Delta v Q(T_k)} \left\{ \exp\left(\frac{h\nu_{ul}}{k_B T_k}\right) - 1 \right\} \exp\left(-\frac{E_u}{k_B T_k}\right) N \,. \tag{5.12}$$

Under these conditions, the observation of a single transition and the measure of its antenna temperature gives direct access to the column density of the molecule *via* Eqs. (5.9) and (5.12), if T_k is known. Conversely, the information on the number of total molecules, and thus the molecular abundance, requires the knowledge of the optical depth L.

5.1.3 Derivation of non-LTE Abundances

The approach illustrated in the previous subsection is suitable whenever the cloud under consideration can be considered as a uniform portion of homogeneous gas fulfilling LTE approximation. Such assumption implies that the energy levels of the target molecule are populated according to the Boltzmann distribution with a characteristic T_{ex}, which is considered equal to T_k. This condition is met at high densities, when collisions represent the dominant mechanism determining the de-excitation. At low densities, radiative decay competes with collisions, so that generally it results $T_{ex} < T_k$. Still, the fact that a single temperature governs the population of the entire energy level manifold, allows for the use of the usual LTE-based approaches (*e.g.*, the rotational diagram method, Goldsmith and Langer 1999).

In the general case, the assumption of a Boltzmann distribution for the molecular levels no longer holds throughout the cloud as both collisional and radiative processes contribute to the distribution of the population among the levels. Different portions of gas thus experience different radiation intensities. In this case, the radiative transfer relation, Eq. (5.4), cannot be reduced to the simple analytic equality between τ and N of Eq. (5.12), but it becomes a strongly coupled problem that can only be solved by numerical analysis.

These methods, denoted as non-LTE modelings, require molecular collision data as input, in addition to spectroscopic data. Their increasing complexity is compensated by the advantage that they not only provide the column density as output, but also the kinetic temperature (T_k), and the volume density (ρ) of the gas can be constrained, in principle, from multi-line observations. In the following, the main features of such approach are synthetically described.

From the definitions provided in ¶ 5.1.1, the emissivity and absorption coeffi-

cients can be written as:

$$j_v = \frac{h\nu_0}{4\pi} n_u A_{ul} \phi(v) \,, \tag{5.13}$$

$$\alpha_v = \frac{h\nu_0}{4\pi} \left(n_l B_{lu} - n_u B_{ul}\right) \phi(v) \,, \tag{5.14}$$

with $\phi(v)$ being the line shape function expressed in velocity units. $\phi(v)$ is usually described by a Gaussian function because of the Doppler line broadening due to the turbulent velocity field:

$$\phi(v) = \frac{2\sqrt{\ln 2}}{\sqrt{\pi}} \frac{c}{\nu_0 \Delta v} \exp\left(-4 \ln 2 \frac{c^2}{\nu_0^2} \frac{(v - v_0)^2}{\Delta v^2}\right) \,, \tag{5.15}$$

where $(v - v_0)$ is the difference between the velocity of the gas and the systemic velocity of the source[†], and Δv is the line FWHM expressed in velocity units. If an internal cloud motion is present, the line profile is angle-dependent and the projection of the local velocity vector onto the photon propagation direction enters the term $(v - v_0)$.

When α_v and j_v are known at each position in the source, the velocity-dependent distribution of the emission in the sky (the observable quantity in radioastronomy) is obtained by ray tracing, *i.e.*, by integrating the local mean radiation intensity, I_v, over all solid angles (as already discussed in ¶ 2.1.1):

$$J_v = \frac{1}{4\pi} \int I_v \, \Omega \,, \tag{5.16}$$

where I_v comes from the solution of Eq. (5.4) along the ray propagation direction under consideration, $\mathbf{s}$,

$$I_v = I_v(0) \mathrm{e}^{-\tau_v} + \int_0^{\tau_v} S_v(\tau_v') \mathrm{e}^{-(\tau_v - \tau_v')} \, \tau_v' \,, \tag{5.17}$$

where $\tau_v \equiv \alpha_v \, s$, I_v is the radiation emerging from the considered portion of gas, and $I_v(0)$ is the background radiation impinging on the medium. In practice, the integration of Eqs. (5.16) and (5.17) does not extend to infinity, but is restricted to the cloud edges where the radiation field is set equal to the CMB.

As said above, both collisions and radiation determine the level populations through the equation of statistical equilibrium:

$$n_l \left[\sum_{u<l} A_{lu} + \sum_{u \neq l} \left(B_{lu} J_v + C_{lu}\right)\right] = \sum_{u>l} n_u A_{ul} + \sum_{u \neq l} n_u \left(B_{ul} J_v + C_{ul}\right) \,, \tag{5.18}$$

[†]The systemic velocity measures the relative motion of an astronomical object with respect to the observer in the local system of rest. Usually is referred to as v_{LSR}.

where C_{ul} are the macroscopic collisional rate coeffi for the $u \to l$ transition which depend on the gas density (ρ) and the state-to-state collisional rate coefficients through:

$$C_{ul} = k_{u \to l} n_{\rm gas} \, . \tag{5.19}$$

For a given set of spectroscopic and collisional coefficients (A_{ul}, B_{ul}, C_{ul}), Eq. (5.18) can be easily solved (*e.g.*, through matrix inversion) for each position in the source in which the radiation field J_ν is known. However, since J_ν contains contributions from the CMB, and the spectral line term itself depends on the level populations through Eqs. (5.12), (5.13), and (5.14), the problem must be tackled by an iterative approach.

It is customary to start from an initial guess for the level populations of the target molecule; from these, the source function S_ν is computed *via* Eqs. (5.13) and (5.14). Then, I_ν and J_ν are derived through Eqs. (5.17) and (5.16); statistical equilibrium is solved *via* Eq. (5.18), and a new level population set is obtained. This yields, in turn, an update value for J_ν, after which the populations are again computed. The cycle is repeated until the radiation field and the populations are converged to a consistent solution. The approach is depicted in the block diagram shown in Figure 5.2.

The practical implementation of this loop requires the discretization of the source into a number of elementary cells, each characterized by homogeneous properties ($\rho(\mathrm{H_2})$, $T_{\rm ex}$, $v_{\rm turb}$, ...). It is also assumed that the material in each cell is in "quasi"-

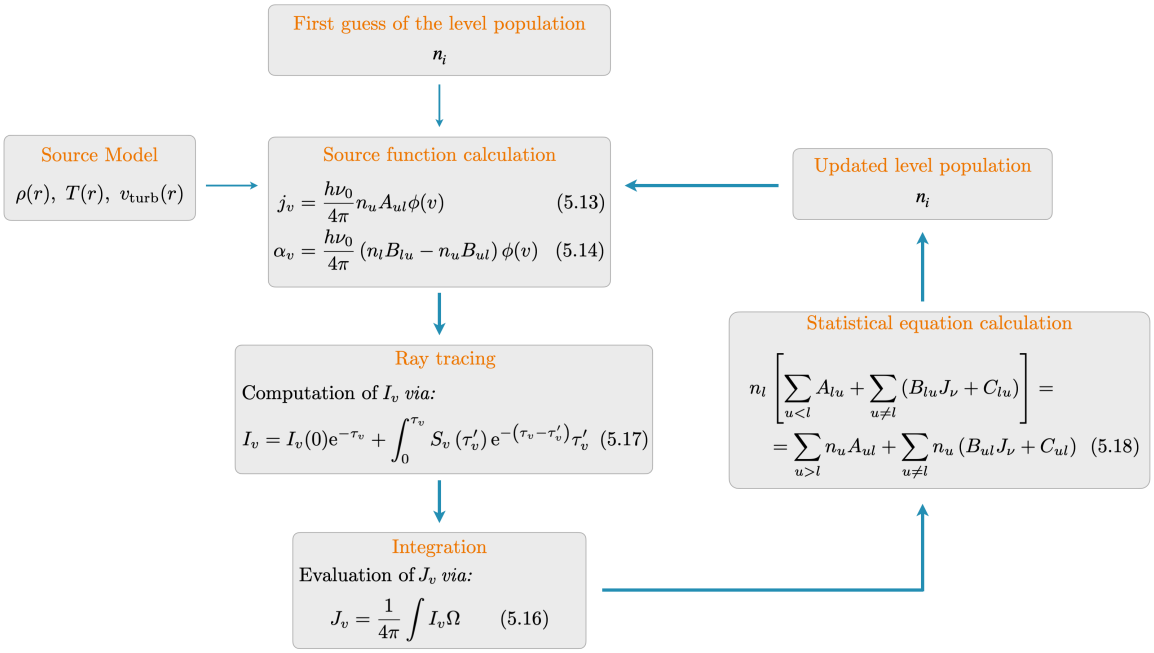

Figure 5.2: Flow diagram of the molecular radiative transfer problem.

LTE conditions, *i.e.*, the molecular excitation can be represented by a single temperature ($T_{\rm ex}$). Well defined source models are based on a grid that is sufficiently fine to consider these assumptions valid. A discrete source model also leads to transform the integral of Eq. (5.16) into a summation over a finite set of integration points to evaluate J_v. This can be obtained as the sum of the emissions received in a given cell from each of the other cells the ray propagates to, weighted with the corresponding subtended solid angle.

The combination of radiative transfer and statistical equilibrium problems can be synthetically formalized by defining the so-called Λ operator, which acts on the source function S_v, which in turn depends on the level population and then also on J_v itself:

$$\boxed{J_v = \Lambda[S_v(J_v)]\,.} \tag{5.20}$$

Given that the source model is gridded, Λ can be seen as a matrix whose elements describe the radiative coupling between any given cell pair, *i.e.*, Λ_{ij} gives information on how the radiation field in cell i depends on the excitation in the cell j. Iteratively, one has to solve:

$$J_v = \Lambda[S_v^{\dagger}(J_v)]\,, \tag{5.21}$$

in such a way that the updated value of J_v is obtained by operating Λ on the previous source function $S_v^{\dagger}$ (and thus on the previous populations).

Various numerical approaches are used to efficiently solve Eq. (5.21): some implementations involve the use of a carefully chosen fixed set of directions for rays to be summed up in Eqs. (5.16) and (5.17); these are called Λ-iteration codes (*e.g.*, MOLLIE; see Keto and Rybicki 2010). More general tools adopt Monte Carlo methods to obtain good approximations of J_v without too much fine-tuning; among these, we find RADEX (van der Tak et al., 2007) and LIME (Brinch and Hogerheijde, 2010).

In principle, non-LTE modelings can be used to constrain all the physical parameters of the investigated astronomical object. This procedure, however, requires accurate information by multi-line observations and is thus feasible only for molecules that are highly abundant and easy to observe *via* radioastronomical investigations. Moreover, as the number of parameters to be optimized increases, more complexity is added to the numerical method, which hence suffers for a slower convergence. For these reasons, it is customary to employ an *a priori* defined source model, starting from which the molecular abundances are optimized and all other parameters are kept fixed. The source model is often derived from observations of highly abundant molecules in the target astronomical object or it is built from theoretical magnetohydrodynamic modelings based on other observational constraints.

As a final remark, all non-LTE modelings require the knowledge of molecular collisional data, which indeed are mandatory to fully solve the statistical equilibrium

equation expressed in Eq. (5.11). This stresses the need of complete datasets of collisional rate coefficients in order derive the non-LTE molecular abundances of an astronomical object.

Chapter 6

Results and Discussion

During my PhD, I focused my attention on the investigation of six different collisional systems: HCO^+/He (Tonolo et al., 2021), $HC^{17}O^+/H_2$ (Tonolo et al., 2022), $HC^{18}O^+$/Ar, PO^+/H_2 (Tonolo et al., 2024), HCN/N_2 and HC_3N/N_2. As described in this Chapter, each of them provides a specific piece of information, targeting some critical steps of the non-LTE analysis framework. While the corresponding results are presented and discussed in this Chapter, the mathematical treatment of these steps has been detailed in the previous ones. First of all, the choice of the investigated molecules and their astrochemical relevance is motivated (§ 6.1). Subsequently, in § 6.2, the procedure employed to characterize the interaction potential and its validation in terms of accuracy obtainable is described. § 6.3 reports an application on the fundamental role played by the interplay between theory and experiment in minimizing the uncertainties in transition-frequency measurements. In § 6.4, the derivation of the collisional rate coefficients and the accuracy required to provide suitable datasets in support of astrophysical modeling is presented. Finally, the use of collisional coefficients for the derivation of molecular column densities and gas densities in the diverse conditions of astrophysical media is outlined in § 6.5.

6.1 The *Rationale* behind the Selection of the Collisional Systems

The selection process of the collisional systems investigated in this thesis work has followed some general guidelines. First of all, the molecular targets must be molecules that not only have been detected in space, but also play an important role as tracers of the evolutionary stage and physical characteristics of the astronomical objects where they were observed. The choice of the proper collisional partner relied on the information we were seeking. For example, the HCO^+/He system was selected as an appropriate test case to identify a general procedure to

build the interaction potential. Hence, the lack of internal degrees of freedom of He provided a simple way to benchmark and validate the performance of the computational strategy without additional constraints on the collider. Moreover, He is the second most abundant perturber in the ISM. Thus, it can represent a reasonable compromise to inspect the collisional behavior of interstellar species. In other cases, such as $HC^{18}O^+$, the goal was to provide some theoretical parameters that could be directly compared with the experimental findings. In this case, a collisional partner that would reproduce the experimental conditions (Ar) was chosen. Finally, for some systems, the main purpose was to provide the first dataset of rotational (de-)excitation collisional coefficients. Since their derivation requires high accuracies in order to meet the astrophysical needs, the most abundant perturber was consistently chosen. Therefore, concerning species of interest in the ISM ($HC^{17}O^+$ and PO^+), H_2 was selected, while for studies on the Titan atmosphere, HCN and HC_3N being the target species, N_2 was chosen as collider. In the following, the individual choice of the collisional targets and their role as tracers of astrophysical interest is discussed in more detail.

6.1.1 Why Ions?

As already outlined in Chapter 1, the degree of molecular ionization of an astrophysical object represents an astronomical fingerprint of its evolutionary stage. Indeed, it depends on the molecular density of the cloud and its exposure to UV and cosmic-ray radiation. Moreover, because of the extreme conditions of interstellar clouds, ions play a prominent role in chemical reactivity (Herbst, 2005); indeed, reactions occurring in the gas-phase need to be exothermic and without any activation energy, and these conditions require highly reactive species like ions (Herbst and Klemperer, 1973; Snow and Bierbaum, 2008).

Going into details, in diffuse clouds and/or the periphery of molecular clouds, where the interstellar UV radiation can well penetrate, the ionization degree* is as high as $\sim 10^{-4}$ (Le Petit et al., 2004). With the increase in density and the subsequent formation of dense molecular clouds, it starts to decrease until being entirely determined by the rate of cosmic-ray ionization, *i.e.*, $\sim 10^{-7}$ (Caselli et al., 1998). At this stage, the HCO^+ and H_3^+ ions are the dominant carriers of positive charge (Herbst and Klemperer, 1973); their main destruction route occurs by dissociative recombination, making their abundance closely related to the electron density of the studied region (Wootten et al., 1979). The H_3^+ and HCO^+ ions also contribute to the dissociation of molecules through proton transfer and subsequent electron recombination (Yamamoto, 2017). They thus play a major role both in the interstellar chemistry and dynamics of the interstellar gas, and provide much information on the

*We define ionization degree, $x(e) = n(e)/n(H_2)$, with $n(e)$ and $n(H_2)$ being the electron and H_2 densities, respectively (Caselli et al., 2002).

characteristics of the sources responsible for their ionization (Guélin et al., 1982b; Jørgensen et al., 2004).

HCO^+ is the most abundant ion in dense molecular clouds (Herbst, 2005). HCO^+ was detected for the first time in 1970 (Buhl and Snyder, 1970). However, its identification was confirmed only five years later, when the first characterization of its rotational spectrum was accomplished (Woods et al., 1975). Later on, it has been widespreadly observed and has been found abundant toward a large number of objects with different physical characteristics (Snyder et al., 1976; Langer et al., 1978; Welch et al., 1981): from diffuse clouds (Scappini et al., 2000; Liszt et al., 2004) to star forming regions (Purcell et al., 2006) and protoplanetary nebulae (Contreras and Sahai, 2004), passing through photodissociation and photon-dominated regions (Owl et al., 2000; Savage and Ziurys, 2004), giant molecular clouds (Snyder et al., 1977) and dense cores (see Lattanzi et al. 2007 for a more exhaustive list of recent detections).

Many investigations on the HCO^+ ion have been carried out in the last years, both from a computational and experimental point of view. In the framework of collisional studies, the first computed set of state-to-state rate coefficients dates back to 1984 and regards collisions of HCO^+ with He (Monteiro, 1985). In 2008, a refinment of the HCO^+ + He collisional PES was performed by Buffa et al. (2008), who derived the corresponding pressure broadening and pressure shift coefficients, and compared them with the experimental values. These latter were obtained for three rotational lines of HCO^+ at 88 K. In 2009, starting from the same potential, the state-to-state rate coefficients were also retrieved (Buffa et al., 2009). About ten years later, Salomon et al. (2019) measured the rotational parameters associated with the ground state of the HCO^+–He bound system by means of double resonance experiments. Recently, the theoretical investigations were also extended to collisions with *para*- (Yazidi et al., 2014) and *ortho*-H_2 (Massó and Wiesenfeld, 2014; Denis-Alpizar et al., 2020), with the rotational de-excitation rate coefficients being accurately determined.

Ion chemistry is also well suited to investigate the cosmic distribution of still poorly explored chemical elements. Moreover, this type of analysis can provide new hints on the degree of chemical depletion onto interstellar grains and on the gas-grain chemical networks through the diverse evolutionary stages of molecular clouds. In this regard, ions of elements such as S, N, P assume a prominent role. These elements typically undergo strong depletion on interstellar grains and dust particles (Herbst, 2005), which affects all the evolutionary stages of star formation and is particularly relevant in dense cloud regions (Stantcheva and Herbst, 2004). For this reason, the study of their reactivity and the degree of complexity they can reach represents a challenging and still unexplored topic. The release of these elements in the gas phase usually occurs in the presence of shocks and ionization

sources such as cosmic rays. This happens for instance in the warm regions near the center of protostars or in shocked regions in which jets of material are strongly blown out, thus developing shock waves that heat up molecules and sputter many species from the grains (Flower and Pineau des Forêts, 2003). The detection of SO^+, NO^+ and PO^+ (Turner, 1992; Cernicharo et al., 2014; Rivilla et al., 2022b) significantly contributed to the knowledge of the reactive networks involving these elements. Indeed, their formation is strictly connected to the abundance of S^+, N^+ and P^+, respectively. In fact, the $X^+ + OH \rightarrow XO^+ + H$ reaction, with X= S, N, P, is considered their main formation route (Herbst and Leung, 1989; Rivilla et al., 2022b). In a recently published paper, Rivilla et al. (2022b) compared the column densities of SO^+, NO^+ and PO^+ with respect to both the cosmic abundances of their isolated elements and their neutral counterparts toward the G+0.693-0.027 molecular cloud. These results indicated that, in the ISM, P is more efficiently ionized than N and S, probably due to a higher cosmic-ray ionization rate (Heays et al., 2017). Given the still poorly constrained chemistry of phosphorus in the ISM, this outcome stresses the predominant role that P-bearing ions such as P^+ and PO^+ can play in the chemical networks of P with respect to the chemistries of N and S.

6.1.2 Why Phosphorus?

Phosphorus, along with carbon, hydrogen, oxygen, nitrogen and sulfur, plays a crucial role in abiogenesis (Rivilla et al., 2016; Pearce et al., 2017; Öberg and Bergin, 2021; Bergner et al., 2022). Indeed, it is an ubiquitous element on Earth and is relatively abundant in living organisms (Fagerbakke et al., 1996) because it is a key component of many biomolecules, especially when combined with oxygen atoms (it represents a building block to form phosphates, PO_3^-). Out of Earth, P-bearing compounds have been found in various environments such as planetary atmospheres (Bregman et al., 1975; Ridgway et al., 1976), meteorites (Pasek and Lauretta, 2005; Schwartz, 2006), comets (Altwegg et al., 2016; Rivilla et al., 2020), circumstellar envelopes of evolved stars (Agúndez et al., 2007; Tenenbaum et al., 2007; Halfen et al., 2008; Agúndez et al., 2014; Rivilla et al., 2020), and even in Enceladus's ocean (Postberg et al., 2023), the latter offering insights into the origin of life on Jupiter's moons. However, despite extensive searches, only few P-bearing molecules have been identified in the ISM, showing limited distributions (Chantzos et al., 2020). As mentioned in the previous section, this might be related to its depletion onto interstellar grains (Lebouteiller and Ferlet, 2005). The first P-bearing species detected in the ISM were PN (Ziurys, 1987; Turner and Bally, 1987) and the CP radical (Guélin et al., 1990), followed by HCP (Agúndez et al., 2007), PO (Lefloch et al., 2016; Rivilla et al., 2016, 2018; Bergner et al., 2019), C_2P (Halfen et al., 2008), PH_3 (Agúndez et al., 2014) and, more recently, PO^+ (Rivilla et al., 2022b). Despite the lack of observational data, some studies on P-reactivity (Viana et al., 2009; de la

Concepción et al., 2021; Alessandrini et al., 2021; Baptista and De Almeida, 2023) and chemical modeling (Fontani et al., 2016; Rivilla et al., 2016; Lefloch et al., 2016; Jiménez-Serra et al., 2018; Chantzos et al., 2020; Rivilla et al., 2022b) have been carried out, but the understanding of P chemistry in the ISM still remains somewhat limited. Clearly, there is the need of further astrochemical investigations, including detections of new P-bearing species and accurate determination of their abundances. Regarding the latter issue, the extreme conditions of the ISM environments prevent from the LTE approximation to be valid, thus pointing out the need of collisional rate coefficients to properly describe the molecular excitation of P-bearing molecules. However, a list of accurate collisional data for such molecules is still far from being complete.

To sum up, the need for a comprehensive study of P chemistry in space clearly emerges; in particular, the detection of P-bearing species, the determination of their abundances and the investigation of their collisional behavior with the most abundant perturber in the ISM deserve specific efforts. In this regard, the recent detection of PO^+ in the G+0.693-0.027 molecular cloud (Rivilla et al., 2022b) triggered a collisional investigation of this ion in order to support the interpretation and modeling of the present and future observations in the ISM. The G+0.693-0.027 cloud is located in the SgrB2 region at the galactic center, where other P-bearing species have been previously identified (Rivilla et al., 2018). This molecular cloud is characterized by a relatively low H_2 gas density ($1 \times 10^4\,cm^{-3}$; Zeng et al. 2020), thus making LTE conditions far from being fulfilled. In more details, molecules are not thermalized at the kinetic temperature of the cloud ($50-120\,K$; Zeng et al. 2018), but they reach a "quasi-thermalization" at an excitation temperature (T_{ex}) that is significantly lower than T_k (see detailed explaination of this effect in Goldsmith and Langer 1999). In absence of collisional data, the LTE approach is used, giving typical T_{ex} in the range of $5-20\,K$ (see Zeng et al. 2018). Except for a recent study concerning its collisional behavior with He (Chahal and Dhilip Kumar, 2023), to the best of our knowledge, no thorough investigation of the collisional excitation of PO^+ has been carried out. Since for molecular hydrides and ions He does not represent a suitable template of collisions with H_2 (Roueff and Lique, 2013), new collisional data able to test the suitability of the LTE approximation to model the transitions detected are therefore needed.

6.1.3 Why Isotopologues?

As already mentioned in Chapter 5, the optical depth of a rotational transition is proportional to its column density, its line strength and to the square of its dipole moment. This means that for abundant species characterized by large dipole moment, such as HCN or HCO^+, the optical depth can often be much higher than unity. In these cases, the line is defined as optically thick. In such a case, the photons emit-

ted in the interior of the cloud are completely reabsorbed within the cloud, and the intensity is determined by the surface temperature. That is, within the line profile, the cloud behaves like a blackbody at the excitation temperature of the molecule. Consequently, the column density cannot be retrieved. In these cases, a common observational way out is to combine observations of the thick lines due to the main isotopic species with those of their thinner equivalents. This is usually accomplished by observing the transitions of the corresponding rare isotopologues. Hence, for the abundant interstellar molecules, several isotopologues have been detected in space and their transitions have a crucial importance for modeling purposes. In the absence of collisional data for the isotopologues of interest, a commonly employed strategy is to use the collisional rate coefficients of the parent species to estimate their abundance. However, this approximation resulted to be questionable in some cases, in particular, when the mass difference is considerable, such as in the case of H/D substitution (*e.g.*, Dumouchel et al. 2012). In order to achieve high accuracies, hence, specific dynamic calculations for each different isotopologue are thus reccomended (Wiesenfeld et al., 2011; Faure et al., 2012; Dumouchel et al., 2012).

Given the prominent role of HCO^+ as a tracer of high-density regions, this strategy is commonly employed in order to decrease the optical opacity of its transitions and obtain reliable determinations of its molecular abundance from the observed emissions. Indeed, the low-J transitions of HCO^+ are often found to be optically thick and line trapping effects from the surrounding gas could challenge the identification of the density to which these lines are sensitive. In these cases, the thinner emissions originated from the corresponding lines of the less abundant isotopologues are typically modeled. However, since $H^{13}CO^+$ ($\sim 1\%$) is still optically thick in many sources, one has often to resort to species containing heavy isotopes of oxygen such as $HC^{18}O^+$ ($\sim 0.2\%$) and $HC^{17}O^+$ ($\sim 0.04\%$). These rare variants play a major diagnostic role, thus making their accurate spectroscopic characterization a strategic requisite for astrochemical modeling (Jimenez-Donaire et al., 2017).

Given these premises, many efforts have been made to retrieve the collisional coefficients of some isotopologues of HCO^+ (see, *e.g.*, Pagani et al. 2012, Denis-Alpizar et al. 2020 and references therein). However, in spite of several spectroscopic studies and astrophysical detections (Guélin et al., 1982a; Plummer et al., 1983; Dore et al., 2001), to the best of our knowledge, a thorough study of the collision physics of the $HC^{17}O^+ - H_2$ system has not been carried out yet.

Moreover, the need of precise measurements of the rotational transitions for the rare isotopologues of HCO^+ can face some limitations in laboratory experiments. Indeed, the low-J transitions of molecular ions exhibit a large sensitivity to pressure effects inside the cell. To retrieve accurate rest frequencies, experimental investigation of the pressure-broadening and, above all, pressure-shift effects needs to be performed, with calculations playing a crucial role to support it (the reader is

referred to § 6.3 for further details).

6.1.4 Why Titan Atmosphere?

Titan hosts a dense and dynamical atmosphere, where a huge variety of hydrocarbons and nitrile species are produced from the chemical activation of N_2 and CH_4 due to UV radiation as well as energetic particles from the magnetosphere of Saturn. These species often show vertical density gradients from their formation in the upper atmosphere to their condensation below 80 km from the ground (Bézard, 2014; Vuitton et al., 2014; Hörst, 2017; Thelen et al., 2018). This causes significant departures from LTE condition starting from altitudes of a few hundreds of km (Yelle, 1991; Rezac et al., 2013; Cordiner et al., 2018). To reliably investigate the chemistry and dynamics of Titan's atomosphere, hence, the knowledge of the collisional coefficients of the leading species with the most abundant perturbing gas, *i.e.*, molecular nitrogen (N_2), is required.

Up to now, very limited collisional characterizations targeting the molecular species present in Titan's atmosphere have been carried out. In order to fill this gap, the first step is an accurate investigation of the most abundant species in this medium, such as HCN and HC_3N. These molecules result from the very first steps of the chemistry starting in the upper atmosphere from N_2 and are potential prebiotic molecules (Bézard, 2014; Vuitton et al., 2014; Thelen et al., 2018). Therefore, they might have some relevance in understanding the origin of life. As mentioned in § 1.3, Titan is a good proxy of the early Earth and provides the opportunity to test the endogeneous synthesis theory for the origin of life (Cable et al., 2012; Cordiner et al., 2014). Because of their large dipole moment (2.7 D for HCN and 3.7 D for HC_3N), they need rather high densities to be thermalized, thus demanding a thorough investigation of their collisional behavior.

HCN and HC_3N were discovered by Voyager 1 Ultraviolet Spectrometer (UVS) and Infrared Spectrometer (IRIS) observations during the spacecraft's flyby of Titan in 1980 (Broadfoot et al., 1981; Hanel et al., 1981; Kunde et al., 1981). They were subsequently observed by the Cassini-Huygens mission (Matson et al., 2002; Brown et al., 2009), by ground-based observations performed with IRAM 30 m (Marten et al., 2002) and, more recently, with ALMA (Cordiner et al., 2014). Since that time, a large number of models have been developed to derive their formation and destruction processes as well as their distribution among different regions of Titan's atmosphere (see Gurwell 2004; Coustenis et al. 2007; Molter et al. 2016 and references therein). Regarding HCN, different pressure broadening experiments have been carried out (*e.g.*, Smith et al. 1984; Pine 1993; Schmidt et al. 1993; Smith et al. 2008; Yang et al. 2008), but measurements for rotational transitions involving levels with $J < 5$ are still lacking. Moreover, to date, no dataset for the (de-)excitation collisional coefficients with N_2 has been retrieved so far. The same applies to HC_3N, for

which only few pressure broadening measurements with N_2 in the millimeter-wave range (Rohart, 1993; Colmont et al., 2007) have been performed so far.

6.2 Construction and Validation of the Interaction Potential

Generally speaking, the starting point of any collisional analysis is the investigation of the intermolecular PES of the system. For any application, the interaction potential needs to be exhaustively sampled and evaluated.

First, a suitable set of internal Jacobi coordinates has to be properly chosen in order to well describe the collisional system. In all the applications presented in this thesis, the two fragments were considered as rigid bodies. This approximation is based on the assumption that the lowest vibrational mode of each isolated collider is high enough in energy to be irrilevant under the non-reactive low-temperature conditions addressed. The HCO^+ ion was thus held fixed to its experimentally determined equilibrium geometry: $r_{C\text{-}H} = 1.0920$ Å and $r_{C\text{-}O} = 1.1056$ Å (Dore et al., 2003). The same has been applied for PO^+, by considering $r_{P\text{-}O} = 1.4250$ Å (Petrmichl et al., 1991). For HCN: $r_{C\text{-}H} = 1.0606$ Å and $r_{C\text{-}N} = 1.1533$ Å were used (Piccardo et al., 2015); for HC_3N: $r_{C1\text{-}H} = 1.0624$ Å, $r_{C1\text{-}C2} = 1.2058$ Å, $r_{C2\text{-}C3} = 1.3764$ Å and

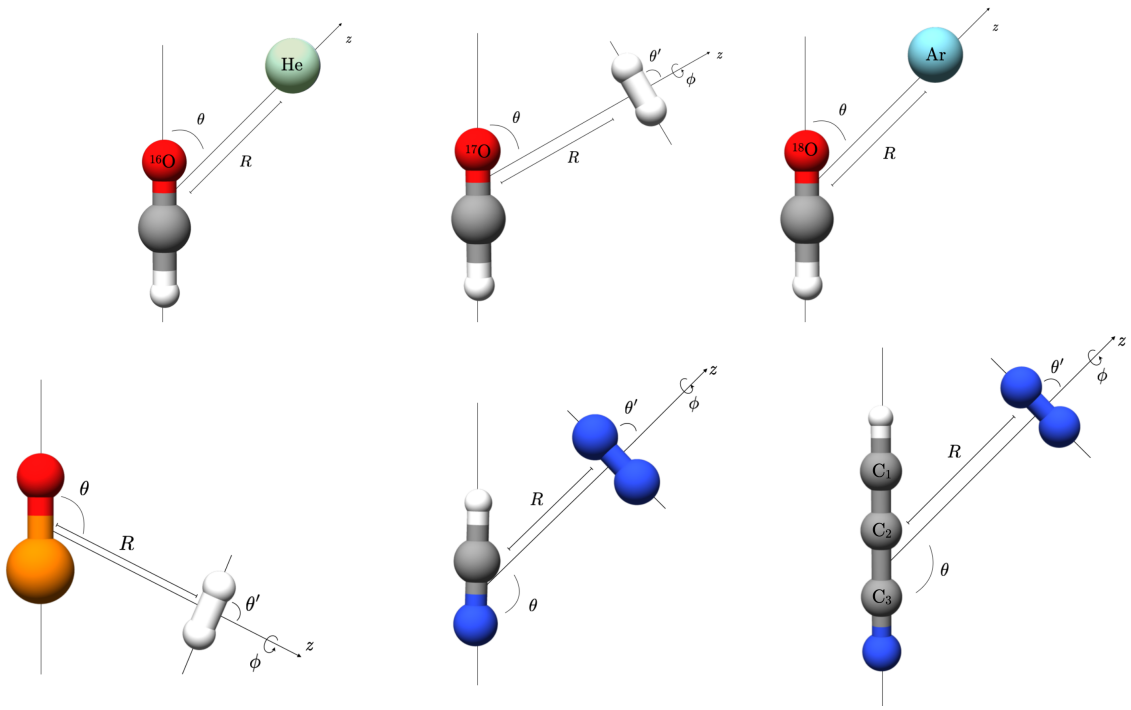

Figure 6.1: Jacobi internal coordinates of the systems targeted in this thesis. On the top, starting from the left side, the HCO^+/He, $HC^{17}O^+/H_2$ and $HC^{18}O^+/Ar$ systems are depicted. On the bottom, from the left to the right, the PO^+/H_2, HCN/N_2 and HC_3N/N_2 ones are illustrated.

$r_{\text{C3-N}} = 1.1605\,\text{Å}$. Regarding the H_2 collider, the bond length of $r_{\text{H-H}} = 0.7667\,\text{Å}$ was employed, which corresponds to the vibrationally averaged value on its vibrational ground state (Jankowski and Szalewicz, 1998). This is considered the best approximation when colliding with other species (*e.g.*, Yazidi et al. 2014). Finally, for N_2, the experimentally determined equilibrium distance, $r_{\text{N-N}} = 1.09768\,\text{Å}$, was employed (Huber, 1979). In Figure 6.1, the Jacobi coordinates considered for each investigated system are depicted, which correspond to the $\{R, \theta\}$ coordinates for the linear molecule - atom systems, and $\{R, \theta, \theta', \phi\}$ for the linear molecule - linear molecule ones.

For each set of Jacobi coordinates, the interaction energy has been evaluated as explained in ¶ 2.2.3. Worth to mention is that, within the BO approximation, the interaction energy does not depend on the chosen isotopologue for either the target or the collider species. This means that, from the PES of a parent species, those of all its isotopologues can also be easily derived, the only difference being the shift of the Jacobi coordinates for the displacement of the center of mass. To investigate the $HC^{17}O^+/H_2$ and $HC^{18}O^+/Ar$ systems, the collisional PESs of their parent species have been investigated. This permitted to test the accuracy of our methodology by comparing the results with previous studies (Massó and Wiesenfeld, 2014; Yazidi et al., 2014).

In the following subsection, a preliminary benchmark on the performance of *ab initio* calculations for the HCO^+ + He collisional system is outlined. This work allowed us to validate the level of accuracy to be used for all the other systems. Next, the construction of the potential will be discussed in detail, with special focus on the employed approximations and to the applicability of the results.

6.2.1 *Ab Initio* Calculations

The wealth of collisional data for HCO^+, already summarized in ¶ 6.1.1, makes this species suitable to benchmark the performance of different levels of theory for the description of its interaction potential. In particular, the computational-experimental comparison offered by the HCO^+ + He system is well suited for such a purpose. Hence, different computational methods and basis sets have been used for computing the interaction energy for a set of 25 geometries, with the aim of finding the best compromise between accuracy and computational cost. In particular, the latter should be such to allow the extension towards larger systems. The results are reported in Table 6.1: the method employed in all computations is CCSD(T) (Watts et al., 1993), which has been used in the standard formulation as well as in the explicitly-correlated F12 version. As already detailed in Chapter 3, F12 calculations are suitable to map the short and long-range regions of the collisional PES (Kendall et al., 1992; Adler et al., 2007; Peterson et al., 2008; Knizia et al., 2009; Lique et al., 2010a; Ajili et al., 2013). These methods have been used in conjunction with

Table 6.1: CP-corrected interaction energies (cm^{-1}) for different geometries of the HCO^+ and He collisional system.

Geometry		CCSD(T)					CCSD(T)-F12[a]	
		Peterson CBS Extrap.[a]		Feller+Helgaker CBS Extrap.[b]		aug-QZ[c]	aug-TZ[d]	jun-TZ[e]
R	θ	aug[f]	jun[g]	aug	jun			
2.0	0.0	16670.07	16674.57	17812.85	17689.38	16763.42	16717.49	16752.53
3.5	0.0	−66.41	−61.07	−8.77	−24.23	−61.02	−69.90	−60.37
5.0	0.0	−15.40	−16.70	−8.41	−8.83	−15.66	−15.64	−14.17
7.5	0.0	−0.90	−2.20	−0.73	−0.68	−2.91	−2.90	−2.36
10.0	0.0	1.30	−0.01	0.80	0.82	−0.93	−0.97	−0.78
2.0	45.0	6313.38	6315.28	7348.92	7220.16	6370.79	6340.73	6379.80
3.5	45.0	−70.39	−66.35	−26.91	−39.02	−69.54	−71.53	−61.78
5.0	45.0	−14.09	−16.70	−9.72	−10.01	−16.13	−16.03	−14.10
7.5	45.0	−0.90	−2.20	−0.96	−0.84	−3.08	−3.11	−2.52
10.0	45.0	1.30	−0.01	0.74	0.70	−0.99	−1.04	−0.83
2.0	90.0	2139.73	2139.50	2741.54	2634.35	2177.23	2152.64	2196.11
3.5	90.0	−91.50	−85.25	−59.17	−66.54	−89.72	−91.22	−81.39
5.0	90.0	−18.49	−18.90	−15.30	−14.50	−20.46	−20.26	−18.10
7.5	90.0	−4.40	−5.70	−1.87	−1.52	−3.84	−3.82	−3.19
10.0	90.0	1.30	−2.20	0.57	0.52	−1.19	−1.23	−1.00
2.0	135.0	9549.84	9543.82	10301.07	10195.37	9623.74	9578.38	9620.42
3.5	135.0	−178.60	−171.79	−123.26	−138.63	−171.77	−174.03	−158.42
5.0	135.0	−33.90	−32.09	−29.97	−28.07	−35.98	−35.93	−32.66
7.5	135.0	−3.10	−4.40	−3.60	−3.02	−5.52	−5.48	−4.72
10.0	135.0	−2.20	−2.20	0.16	0.25	−1.55	−1.58	−1.31
2.0	180.0	191024.32	191019.68	193450.01	193365.57	191419.52	191286.67	191318.90
3.5	180.0	−269.65	−271.98	−126.56	−155.74	−265.64	−268.54	−250.38
5.0	180.0	−60.70	−50.55	−49.50	−48.73	−58.24	−58.93	−53.99
7.5	180.0	−5.29	−7.90	−5.01	−4.28	−6.97	−6.84	−6.03
10.0	180.0	−2.20	−2.20	−0.17	0.00	−1.80	−1.80	−1.53
CPU time [h]		9000	7400	8500	4300	8500	2600	1700

[a]Extrapolation to the CBS limit of the fc-CCSD(T) energies performed with the Peterson three-points extrapolation formula with n =T, Q, 5.

[b]Extrapolation of the HF-SCF energy performed with the three-point formula by Feller (n =T, Q, 5), combined with extrapolation of the fc-CCSD(T) correlation energy using the two-point (n =T, Q) formula by Helgaker and coworkers.

[c]aug-cc-pVQZ basis set.

[d]aug-cc-pVTZ basis set.

[e]jun-cc-pVTZ basis set.

[f]aug-cc-pVnZ basis sets.

[g]jun-cc-pVnZ basis sets.

[h]Mean CPU time (s) needed to compute one point of the energy grid (rounded values).

two correlation-consistent basis sets (Dunning Jr, 1989): the fully augmented aug-cc-pVnZ basis sets and the partially-augmented jun-cc-pVnZ sets (Kendall et al., 1992; Woon and Dunning Jr, 1993; Papajak et al., 2011). Indeed, sufficiently flexible basis sets are needed for the correct description of the behavior in the regions far from the electronic density maximum. In combination with CCSD(T)-F12, the jun-cc-pVTZ and aug-cc-pVTZ basis sets have been tested. Instead, both basis sets, with n=T, Q and 5, have been considered in conjunction with CCSD(T) in

order to perform the extrapolation to the CBS limit. Two different schemes have been employed for such a task. In one case, the total energy was retrieved as the sum of the HF-SCF energy extrapolated to the CBS limit by means of the Feller exponential formula (Eq. (3.12), with n =T,Q,5, Feller 1993) and the CCSD(T) correlation energy extrapolated to CBS using the Helgaker and co-workers formula (Eq. (3.13), with n =T, Q, Helgaker et al. 1997). The second scheme leads to the total energy extrapolated to the CBS limit by applying the mixed exponential and Gaussian formula by Peterson *et al.* to the CCSD(T) electronic energy (Eq. (3.15), with n =T, Q, 5, Peterson et al. 1994). The latter was considered as the "reference" approach for this benchmark test, the aim being to achieve similar accuracy at a reduced computational cost. A first remark from the inspection of Table 6.1 is the poor performance of the Feller–Helgaker composite scheme, which fails to predict the energy trend with the same accuracy of the Peterson's scheme, with only a slight reduction in terms of computational cost. Nevertheless, this benchmark shows a remarkably good performance of the CCSD(T)-F12 method with respect to the results obtained *via* the computationally expensive extrapolation scheme: overall, the energy differences are always smaller than $2.5\,\mathrm{cm}^{-1}$, with a mean relative error of $\sim$ 5% in the short range. F12 methods in combination with triple-ζ quality basis set perform even better than the conventional CCSD(T) model in conjunction with the aug-cc-pVQZ basis set. Moreover, a remarkable feature is the similar behavior of partially and fully augmented basis sets in describing the energetics of the system. However, in the long range regions, where dispersive interactions are stronger, the discrepancies among them are more prominent. To sum up, the main outcome of this benchmark test is the good performances of the CCSD(T)-F12 method in combination with the aug-cc-pVTZ basis set, which indeed offered the best compromise between accuracy and computational cost. The performances of this approach were also validated by comparing the computed bound-state rotational parameters and pressure broadening and shift coefficients with their experimental counterparts (detailed in ¶ 6.2.5 and ¶ 6.2.6).

On the basis of this benchmark test, all the calculations of the systems investigated in this thesis were performed at the CCSD(T)-F12/aug-cc-pVnZ level of theory, with n=T,Q purposely chosen on the basis of the accuracy to achieve and the dimension of the system. For the calculations carried out for the PO^+ target, moreover, for the P atom, additional d functions have been incorporated in the basis set (thus, leading to the aug-cc-pV(n+d)Z set). A summary of the level of theories employed for each collisional system is outlined in Table 6.2, where further information regarding the construction of the grid of points is also reported. Each grid of *ab initio* energies was chosen in order to have a denser mesh in the R coordinate near the most anisotropic parts of the potential (*e.g.*, in proximity of the potential wells) and to be coarser in the regions where the energy slightly depends on the system

Table 6.2: Details for the computation of the interaction potential. For each collisional system, the employed level of theory (third column), total number of grid points (fourth column), range of distances in the R Jacobi coordinate (fifth column) and number of selected θ angles (sixth column) are reported.

Target	Collider	Level of Theory	n_{tot}	R range	$n(\theta)$
HCO^+	He	CCSD(T)-F12/aug-cc-pVTZ	390	$2-10$ Å	13
HCO^+	H_2	CCSD(T)-F12/aug-cc-pVQZ	3375	$2-10$ Å	25
HCO^+	Ar	CCSD(T)-F12/aug-cc-pVQZ	390	$2-12$ Å	13
PO^+	H_2	CCSD(T)-F12/aug-cc-pV(Q+d)Z	3250	$2-12$ Å	25
HCN	N_2	CCSD(T)-F12/aug-cc-pVTZ	3345	$2-12$ Å	25
HC_3N	N_2	CCSD(T)-F12/aug-cc-pVTZ	3415	$2-15$ Å	25

geometry. The θ angles were instead always chosen in order to have equally spaced values from 0 to 180 degrees. When the H_2 or N_2 colliders were considered, only 5 orientations in the $\{\theta', \phi\}$ coordinates with respect to the target molecule have been taken into account. This approximation was found to be appropriate for all the systems, since the dependence of the potential on the orientations of the collider is rather weak.

6.2.2 The Interaction Potential

For the solution of the nuclear Schrödinger equation by means of close coupling equations, the interaction potential has to be expressed as an expansion over angular functions. As already reported in Chapter 2, the potential of a linear rigid rotor + atom and linear rigid rotor + linear rigid rotor systems can be described by the expressions reported in Eq. (2.51) and Eq. (2.52), respectively. Here, the accuracy of the expansion, which is expressed in terms of Legendre polynomials or spherical harmonics, depends on the choice of the angles that better map the orientation of the collider with respect to the target molecule. The number of the terms considered for the expansion (λ) governs the magnitude of the inelastic rotational transitions because they allow for changes of the molecular angular momentum by $\Delta j = \pm\lambda$. They thus need to be carefully chosen. Moreover, in order to accurately reproduce the computed energies, the analytic potential fit should show deviations smaller than 1.5% across the entire grid.

In the cases of linear rigid rotor + atom (HCO^+/He and HCO^+/Ar) systems, 2D global potentials over the R and θ coordinates were derived and are depicted in Figure 6.2. Regarding the former (left side of Figure 6.2), the potential showed a global minimum with the He atom collinear with HCO^+ at $R = 3.6$ Å, with a resulting energy of $-279.78\,\text{cm}^{-1}$. For HCO^+ colliding with Ar (right side of Figure 6.2), instead, the global minimum was found at $R = 3.8$ Å and interaction energy of $-1620.07\,\text{cm}^{-1}$. The increasing in size of the collider, indeed, does not

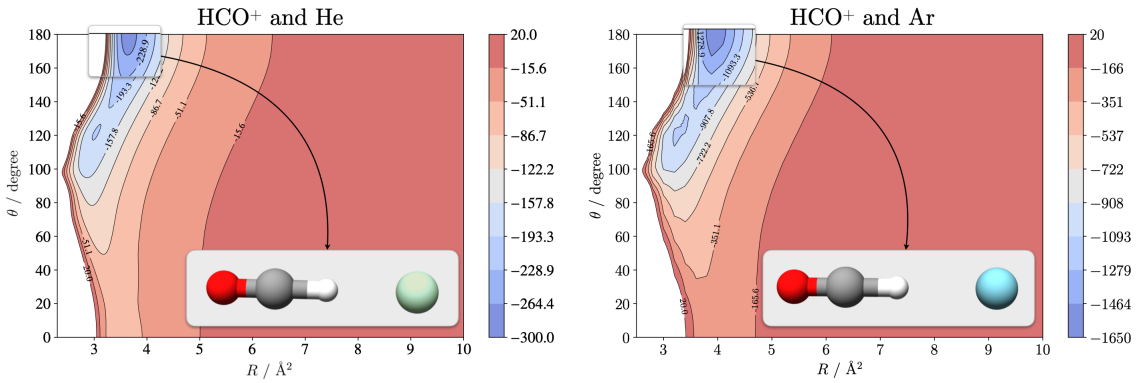

Figure 6.2: Contour plots for the HCO^+ interaction PESs with He and Ar atoms. The geometries of the global minima of the two potentials are shown. Energies are in cm^{-1}.

affect in a significant way the behavior of the potential with respect to the R and θ coordinates, but has a huge impact on the magnitude of the interaction, which is almost 6 times greater in terms of energy for HCO^+ + Ar with respect to HCO^+ + He. This difference can be explained by the larger polarizability of Ar with respect to He, which increases the interaction between the electron clouds of the target and that of the collider.

In Figures 6.3, 6.4, 6.5 and 6.6, the energy plots for each orientation of the investigated systems are depicted. As regards the HCO^+ + H_2 potential, each 2D cut revealed a minimum at $\theta = 180$ degrees, wherein the hydrogen molecule approaches the hydrogen side of HCO^+. Moreover, the potential presents a rather deep well when the H_2 fragment is perpendicularly oriented with respect to the plane containing HCO^+ and the H_2 center of mass ($\theta' = \pi/2, \phi = \pi/2$, middle panel on the left side of Figure 6.3) and $R \sim 3.44$ Å. This is in accordance with the findings of the benchmark study performed by Massó and Wiesenfeld (2014) at different levels of theory. As concerns the PO^+ and H_2 collisional system, the potential (Figure 6.4) exhibits a minimum at $R \sim 2.8$ Å and $\theta \sim 112.5$ degrees for each orientation, with the H_2 slightly leaning toward the phosphorus side of PO^+. The behavior of this potential is consistent with the topology found by Chahal and Dhilip Kumar (2023) for PO^+ interacting with He. However, the magnitude of the interaction with H_2 is almost seven times larger, this already casting some doubts on the suitability of using He to simulate the collisional behavior of H_2 in the ISM. Indeed, for the $\{\theta' = 90, \phi = 0\}$ orientation, which corresponds to the global (and unique) minimum of the potential in the case of H_2, the energy is -1234.12 cm^{-1}, while for the interaction with He the minimum is located at $-181.97\,cm^{-1}$. For these collisional systems, only minor anisotropy of the potential with respect to the orientation of the collider ($\{\theta', \phi\}$ coordinates) is apparent, thus validating the choice of excluding the basis terms with $l_2 > 2$ in the angular expansion of the PES.

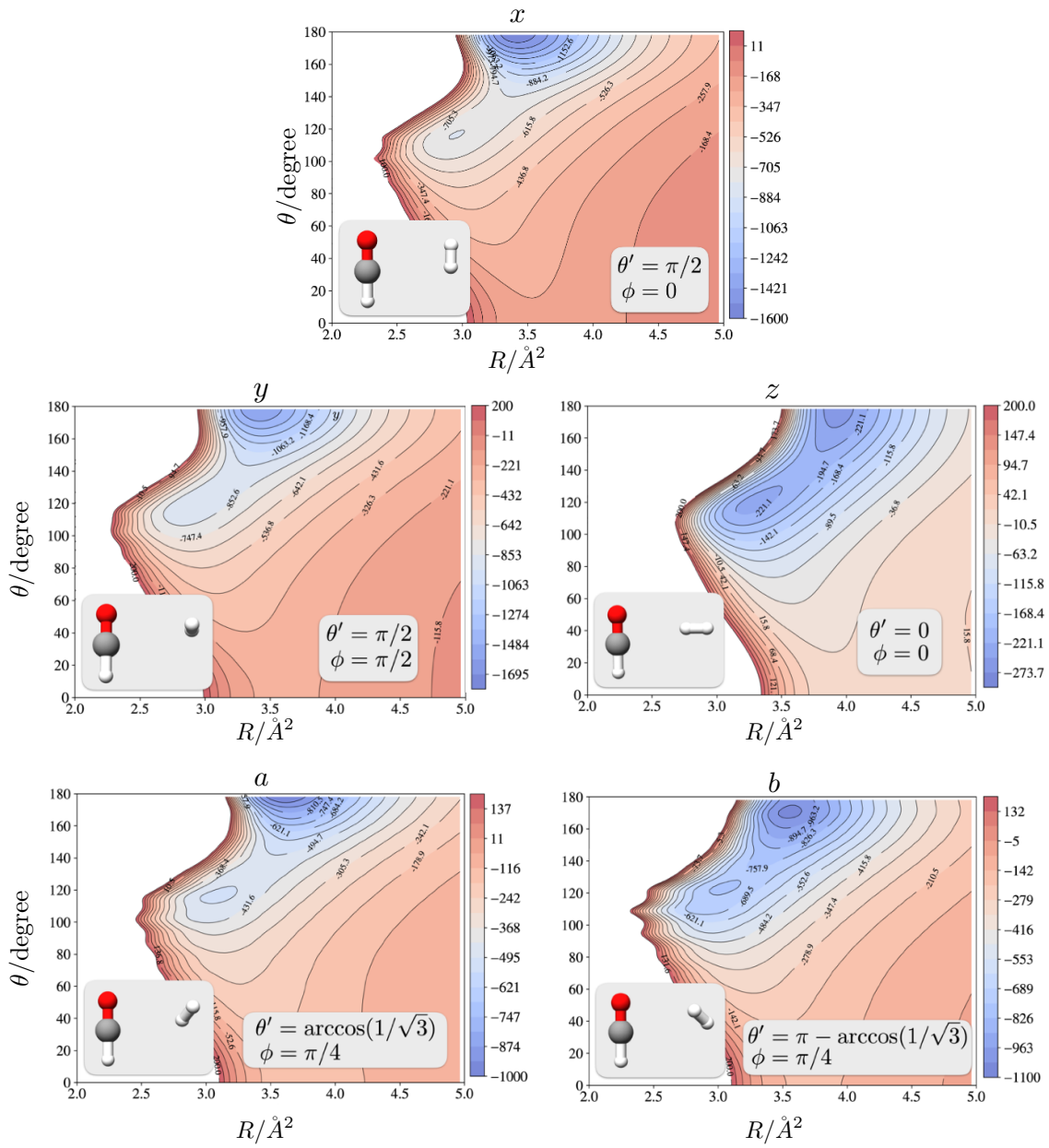

Figure 6.3: Contour plots of the HCO^+ – H_2 interaction PES for five different orientations as a function of R and θ. Energies are in cm^{-1}.

Different is the situation for HCN and HC_3N colliding with N_2 (Figures 6.5 and 6.6, respectively), which instead exhibit a marked anisotropy with respect to the $\{\theta', \phi\}$ orientations. The internal structure of N_2, in fact, significantly impacts on the interaction of the collider with the target molecule. In the case of HC_3N + N_2, this is even more evident, thus limiting to some extent the accuracy of the fit of the potential, which indeed shows several oscillations. We therefore expect that for the latter two systems the truncation of the expansion at the $l_2 < 2$ terms might lead to

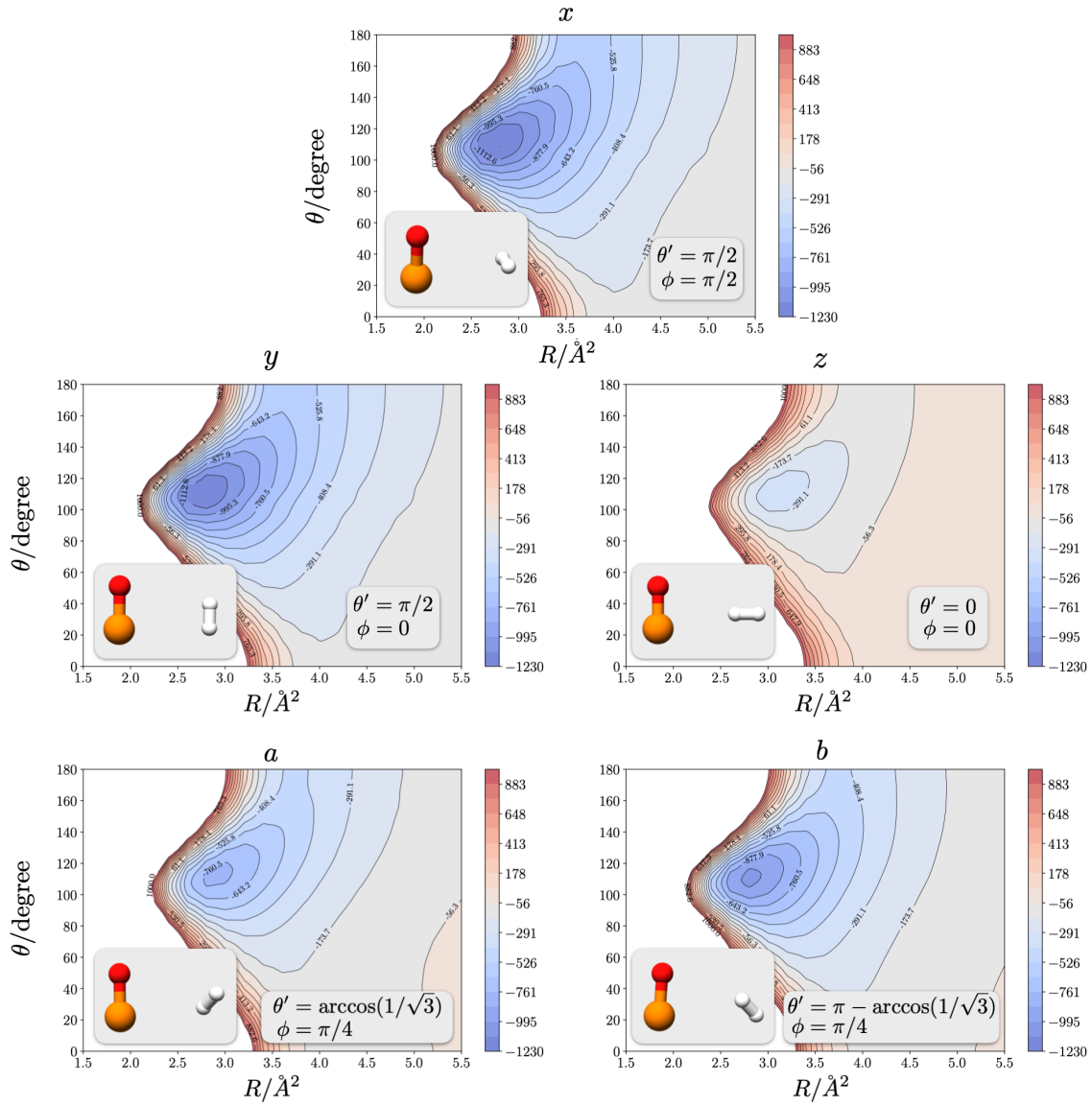

Figure 6.4: Contour plots of the PO^+ – H_2 interaction PES for five different orientations as a function of R and θ. Energies are in cm^{-1}.

the loss of some collisional information. For this reason, we tested the reliability of these potentials by comparing the associated pressure broadening coefficients with the experimental counterpart (as presented in ¶ 6.2.6). The potential of HCN with N_2 exhibits a global minimum when the nitrogen molecule is aligned with HCN on the hydrogen side. Indeed, the resulting van der Waals interaction greatly stabilizes the complex, whose energy at $R = 4.7$ Å is $-432.33\,cm^{-1}$. For the other orientations, conversely, the interaction is weaker, reaching maximum values of about $-204\,cm^{-1}$ when the nitrogen is oriented perpendicular to the HCN molecular axis and on the side of the nitrogen atom. A similar pattern is found for the $HC_3N + N_2$ potential:

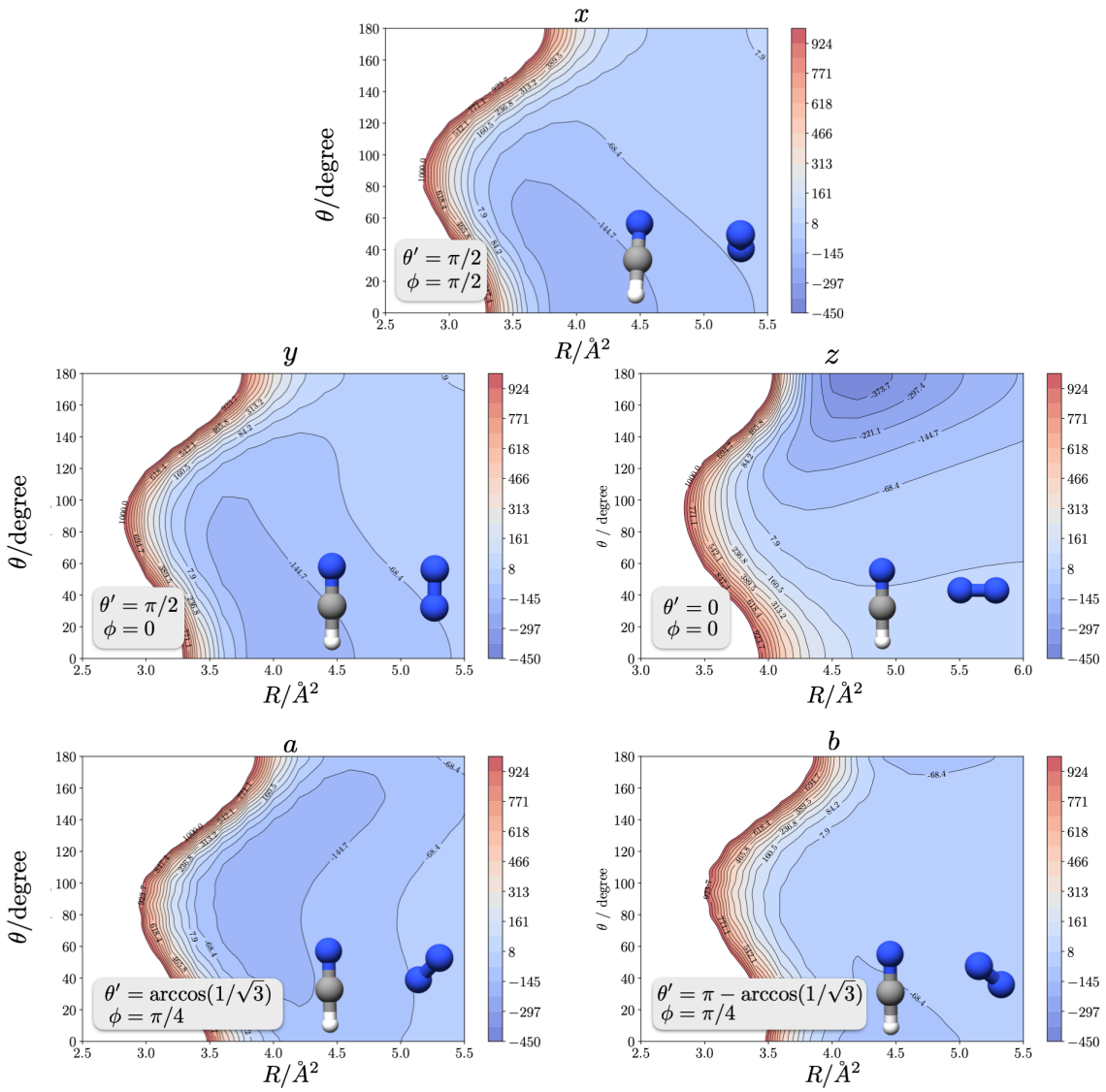

Figure 6.5: Contour plots of the HCN – N_2 interaction PES for five different orientations as a function of R and θ. Energies are in cm^{-1}.

the global minimum, with $E_{int} = -384.34\,cm^{-1}$, was found at $R = 6.0$ Å and with N_2 aligned with the HC_3N molecular axis from the hydrogen side, while the second minimum in terms of interaction strength is formed when N_2 approaches the nitrogen side of HC_3N perpendicularly with respect to its molecular axis. Finally, for all the systems here considered, starting from the information for the five orientations, the 4D potential was obtained by introducing the functional dependence on the $\{\theta', \phi\}$ angles using the expression in Eq. (2.64).

To fit the linear rotor + linear rotor potentials, the $l_2 > 2$ truncation approximation was taken in account[†]. This approximation, indeed, was already found to be

[†]The reader is referred to ¶ 2.2.3 for more details about this truncation.

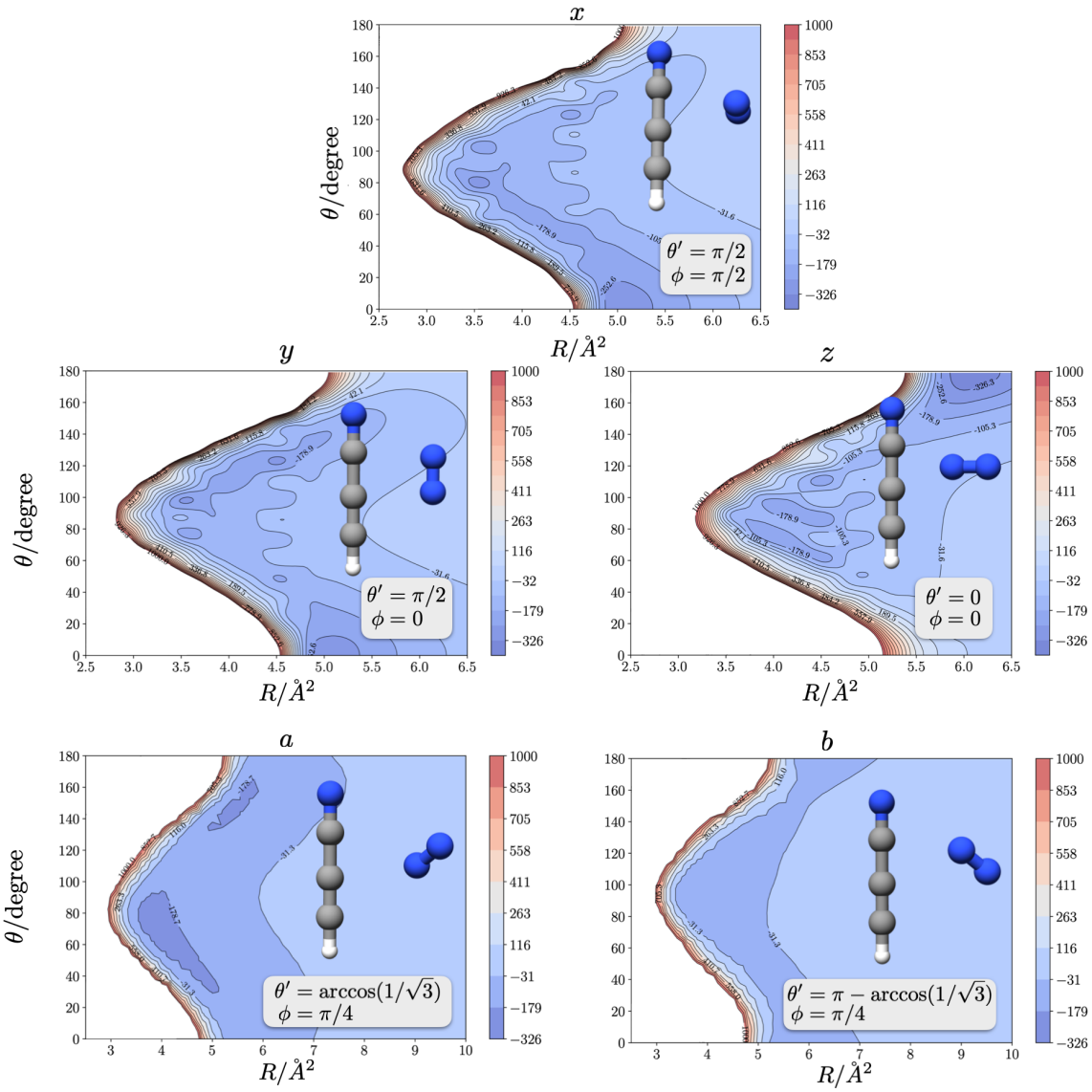

Figure 6.6: Contour plots of the HC_3N – N_2 interaction PES for five different orientations as a function of R and θ. Energies are in cm^{-1}.

appropriate for similar systems (Faure et al., 2005; Wernli et al., 2006) and noticeably simplified the construction of the potential: only five different orientations over the $\{\theta', \phi\}$ coordinates were chosen and, for each of them, the computed energies were fitted to a 2D potential over R and θ.

6.2.3 The Spherical Approximation

The 4D potentials built in the previous subsection allowed us to fully include the rotational structure of H_2 and N_2 in the scattering calculations. In order to reduce the computational effort, tests have been performed to evaluate the impact of the

coupling between $j = 0$[‡] and $j > 0$ rotational states of H_2 and N_2. These tests rely on the comparison of the cross sections computed at a fixed energy using the global 4D potential and the 2D potential, where the latter has been obtained by averaging the energies for the five different orientations considered (V_{av} of Eq. (2.59)) and subsequently fitting the results to the 2D expansion given in Eq. (2.51). The use of the 2D averaged potential, also denoted as spherical approximation, retains only the leading term $l_2 = \mu = 0$ in the expansion of the potential expressed by Eq. (2.52). This is equivalent to treat the H_2 and N_2 colliders as structureless species and simplify the potential to the interaction of a linear rigid body with a sphere (Lique et al., 2008; Dumouchel et al., 2011). This formulation significantly reduces the cost of the collision dynamics calculations and has already been found to be successful, especially with ions (*e.g.*, Spielfiedel et al. 2015; Balança et al. 2020; Cabrera-González et al. 2020). Its validity has thus been verified for all the four systems considered. As regards the $HC^{17}O^+ + H_2$ system, the values of the

Table 6.3: Computed cross sections, at $E = 50\,cm^{-1}$, for $HC^{17}O^+ - H_2(j = 0)$ collisions obtained from the 2D spherically averaged potential and the full 4D potential which includes the coupling with the $j = 2$ rotational level of H_2.

$j' \to j$	Cross sections / Å^2		% Deviation
	4D	2D	
$1 \to 0$	58.14	53.41	−8.86
$2 \to 0$	52.59	50.31	−4.54
$3 \to 0$	46.12	44.00	−4.84
$4 \to 0$	27.26	30.28	9.98
$5 \to 0$	16.81	15.74	−6.80
$2 \to 1$	59.78	60.87	1.80
$3 \to 1$	48.43	53.18	8.92
$4 \to 1$	36.70	35.19	−4.30
$5 \to 1$	17.09	18.77	8.93
$3 \to 2$	55.24	52.95	−4.32
$4 \to 2$	45.75	41.75	−9.56
$5 \to 2$	20.39	21.02	3.01
$4 \to 3$	56.79	51.02	−11.31
$5 \to 3$	24.43	23.19	−5.35
$5 \to 4$	40.04	35.63	−12.39
Average absolute % deviation			6.99

$j(H_2) = 0$ partial cross sections, computed at $50\,cm^{-1}$ and using the reduced 2D potential, were compared with those obtained using the global 4D potential and accounting for the $j(H_2) = 0, 2$ coupling effect. The results, reported in Table 6.3,

[‡]Unlike the commonly used spectroscopic notation, throughout this Chapter, we adopt the lower-case letter j to label the rotational quantum number of the isolated collider, while for the entire collisional system, the upper-case letter J is employed.

show an average relative absolute deviation of $\sim 7\,\%$ and a maximum discrepancy of $\sim 12.4\,\%$.

Table 6.4: Computed cross sections, at $E = 150\,\mathrm{cm}^{-1}$, for $PO^+ - H_2(j = 0)$ collisions obtained from the 2D spherically averaged potential and the full 4D potential which includes the coupling with the $j = 2$ rotational level of H_2.

$j' \to j$	Cross sections / Å^2		% Deviation
	2D	4D	2D/4D
$1 \to 0$	33.10	30.46	−8.68
$2 \to 0$	17.43	19.16	9.02
$3 \to 0$	9.32	8.48	−9.88
$4 \to 0$	12.64	11.89	−6.29
$5 \to 0$	11.43	11.68	2.10
$6 \to 0$	10.55	11.76	10.30
$2 \to 1$	26.61	24.55	−8.42
$3 \to 1$	16.84	15.16	−11.08
$4 \to 1$	11.75	12.82	8.38
$5 \to 1$	11.57	11.19	−3.42
$6 \to 1$	13.28	14.05	5.45
$3 \to 2$	26.06	30.57	14.73
$4 \to 2$	15.67	14.23	−10.14
$5 \to 2$	12.61	12.92	2.39
$6 \to 2$	12.77	13.55	5.76
$4 \to 3$	27.30	28.84	5.32
$5 \to 3$	14.64	14.90	1.77
$6 \to 3$	13.89	12.39	−12.11
$5 \to 4$	27.51	26.88	−2.34
$6 \to 5$	15.64	14.98	−4.44
Average absolute % deviation			7.10

The same analysis has been performed for the $PO^+ + H_2$ system, which showed a similar behavior (Table 6.4), with an average relative absolute error of $\sim 7\,\%$ and a maximum discrepancy of $\sim 14.7\,\%$. These deviations fall within the required accuracy range for astrophysical applications and thus validate the results derived using the spherical average potential approximation. The 2D formulation of the potential was thus applied to the entire energy grid.

To check the validity of the spherical approximation also for the N_2 collider, Table 6.5 compares the 4D and 2D cross sections obtained at $20\,\mathrm{cm}^{-1}$ for the HCN–N_2 collisional system. As a consequence of the greater molecular mass, which is reflected in the value of the rotational constants, the N_2 molecule is characterized by rotational levels that are much closer to each other than those of H_2, which have thus a greater influence when energy exchanges are involved. This is mirrored in the comparison of the cross sections: the incorporation of $j(N_2) = 2$ in the rotational basis leads to an average deviation of about 28% and a maximum discrepancy as

Table 6.5: Computed cross sections, at $E = 20\,\mathrm{cm}^{-1}$, for HCN$-$ $N_2(j = 0)$ collisions obtained from the 2D spherically averaged potential and the full 4D potential which includes the coupling with the $j = 2$ rotational level of N_2.

$j' \to j$	Cross sections / Å^2		% Deviation
	2D	4D	2D/4D
$1 \to 0$	69.25	90.94	31.33
$2 \to 0$	41.39	48.45	17.06
$3 \to 0$	12.83	8.29	−35.38
$0 \to 1$	27.09	35.57	31.33
$2 \to 1$	60.17	50.87	−15.46
$3 \to 1$	18.39	9.88	−46.31
$0 \to 2$	14.87	17.41	17.06
$1 \to 2$	55.28	46.74	−15.46
$3 \to 2$	24.34	18.44	−24.24
$0 \to 3$	16.21	10.47	−35.38
$1 \to 3$	59.40	31.89	−46.31
$2 \to 3$	85.55	64.81	−24.24
Average absolute % deviation			28.29

large as $\sim 46\%$. Such discrepancies, however, still fall within the limit of reliability for the spherical approximation because they lead to variations in the cross sections values within a factor of 2. We expect that this will translate into discrepancies on the state-to-state rate coefficients of about 20%. On the other hand, the computational gain provided by the spherical approximation is remarkable. For the astrophysical applications we seek — in particular if such data would provide the first collisional set of observational data for the Titan's atmosphere — the spherical approximation hence guarantees the right balance between accuracy, reproducibility and computational effort. This assumption, moreover, has been supported by the validation of the potential based on pressure broadening experiments, which will be described in ¶ 6.2.6. Given the similarity in the topology of the interaction potential, the same considerations are also expected to apply to HC_3N as molecular target. Consequently, the final calculations of all these systems were thus performed using the 2D averaged potential.

In Figure 6.7, the 2D averaged potentials for the systems are depicted. In passing we note that a spherical average of the HCO^+ and H_2 potential was also performed by Yazidi et al. (2014). This permits a comparison of the topology they obtained with ours[§], which points out a good agreement. Indeed, both potentials present a global minimum at $R = 3.6$ Å and $\theta = 180$ degrees and are highly anisotropic with respect to the θ angle. However, the potential computed by Yazidi et al. (2014)

[§]We recall the reader that, within the BO approximation, the interaction electronic energy of the fragments does not depend on the chosen isotopologue for both the target and the collider species. The potential for HCO^+ and $HC^{17}O^+$ is thus the same, the only difference being the shift of the Jacobi internal coordinates due to the variation of the center of mass.

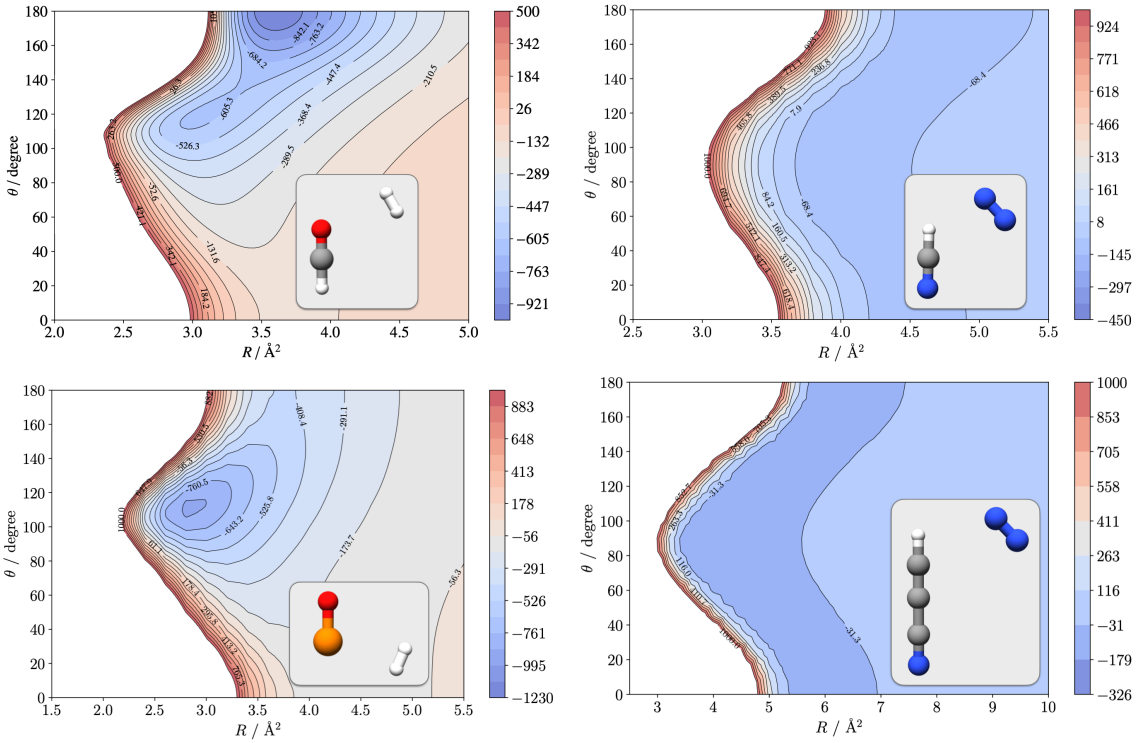

Figure 6.7: Contour plot of the averaged potential V_{av} over the five orientations for the linear rotor – linear rotor collisional systems considered in this thesis work (upper panels: on the left side the HCO^+ and H_2 system, on the right side the HCN and N_2 system; bottom panels: on the left side the PO^+ and H_2 system, on the right side the HC_3N and N_2 system).

accounted only for three orientations of H_2 and adopted a lower level of theory. Our computed PES, hence, represents the most accurate description to date of a spherical potential for the HCO^+ and H_2 system.

6.2.4 *Ortho*- and *Para*-States of the Collider

In certain circumstances, collisions with the $j = 1$ state the collider can also have an impact on scattering calculations. This is the case of the region where PO^+ was detected. Indeed, despite the low density regime, the kinetic temperature of the G+0.693-0.027 molecular cloud can reach 140 K, thus leading to *ortho*-H_2 of (which is less stable than the *para*-species by $\sim$120 cm^{-1}) to be also significantly populated[¶].

[¶]We recall the reader that the homonuclearity of H_2 and N_2 leads to the existence of two distinct molecular forms: *para* and *ortho*. This distinction arises from the nuclear spin statistics. In detail: in the case of the H_2 molecule, nuclei are fermions ($I(\mathrm{H}) = 1/2$) so that the Fermi–Dirac statistics forces the total wave function to be antisymmetric under the exchange of nuclei. In the electronic and vibrational ground states, this requirement is met by a combination of the even rotational states ($j = 0, 2, 4, \dots$) with the $(2I + 1)I = 1$ odd spin states, and of the odd rotational states ($j = 1, 3, 5, \dots$) with the $(2I + 1)(I + 1) = 3$ even spin states. Conversely, in the case of N_2, nuclei are bosons ($I(^{14}\mathrm{N}) = 1$) and the total wave function should be symmetric with

Table 6.6: Comparison of the computed cross sections of PO^+, at $E = 150\,cm^{-1}$, accounting for collisions with *para*-H_2 ($j = 0$) and *ortho*-H_2 ($j = 1$).

$j' \rightarrow j$	Cross sections / Å^2		% Deviation
	j=0	j=1	*o-*/*p-*
$1 \rightarrow 0$	33.10	33.84	−2.19
$2 \rightarrow 0$	17.43	20.46	−14.81
$3 \rightarrow 0$	9.32	10.88	−14.35
$4 \rightarrow 0$	12.64	14.39	−12.17
$5 \rightarrow 0$	11.43	12.56	−9.02
$6 \rightarrow 0$	10.55	12.26	−13.95
$2 \rightarrow 1$	26.61	29.11	−8.57
$3 \rightarrow 1$	16.84	19.70	−14.52
$4 \rightarrow 1$	11.75	13.16	−10.72
$5 \rightarrow 1$	11.57	13.92	−16.87
$6 \rightarrow 1$	13.28	17.37	−23.56
$3 \rightarrow 2$	26.06	27.96	−6.79
$4 \rightarrow 2$	15.67	18.19	−13.87
$5 \rightarrow 2$	12.61	14.26	−11.54
$6 \rightarrow 2$	12.77	17.02	−24.93
$4 \rightarrow 3$	27.30	31.06	−12.10
$5 \rightarrow 3$	14.64	16.36	−10.54
$6 \rightarrow 3$	13.89	16.93	−17.98
$5 \rightarrow 4$	27.51	29.77	−7.59
$6 \rightarrow 5$	15.64	17.08	−8.44
Average absolute % deviation			12.73

In such conditions, a proper evaluation on the impact of the $j(H_2) = 1$ state on the value of the cross sections is deserved. This was performed by comparing the cross sections of the PO^+ and H_2 system accounting for collisions with *para*-H_2 ($j = 0$) and *ortho*-H_2 ($j = 1$) at $150\,cm^{-1}$. The results, shown in Table 6.6, point out a mean average deviation of $\sim 13\%$ and a maximum discrepancy of $\sim 24.93\%$. For the astrophysical purposes of this research, we do not expect such deviations to induce large discrepancies in the rate coefficients between collisions with *ortho-* and *para*-H_2. This result, in accordance with the outcomes reported for other ions (Kłos and Lique, 2011; Walker et al., 2017; Lara-Moreno et al., 2019; Dagdigian, 2019; Desrousseaux et al., 2019), justified the approximation of considering only *para*-H_2 in the rotational basis of scattering calculations. Moving to the HCN target, the deviations for the cross sections for *ortho-* and *para*-N_2 are more pronounced.

respect to their exchange according to the Bose–Einstein statistics. Hence, even rotational states ($j = 0, 2, 4, \dots$) combine with the $(2I+1)(I+1) = 6$ even spin states and the odd rotational states ($j = 1, 3, 5, \dots$) with the $(2I + 1)I = 3$ odd spin ones. The higher multiplicity states (odd j for H_2 and even j for N_2) are referred to as the *ortho*-states; the lower multiplicity ones (even j for H_2 and odd j for N_2) are the *para*-states. The reader is referred to Gordy et al. (1984) for further details.

Nevertheless, as shown in Table 6.7, at $35\,\mathrm{cm}^{-1}$, the average relative deviation of the cross sections is about 54%. Hence, *para*-N_2 ($j = 1$) has a strong impact on the

Table 6.7: Comparison of the computed cross sections of HCN, at $E = 35\,\mathrm{cm}^{-1}$, accounting for collisions with *ortho*-N_2 ($j = 0$) and *para*-N_2 ($j = 1$).

$j' \rightarrow j$	Cross sections / Å^2		% Deviation
	j=0	j=1	*o*-/*p*-
$1 \rightarrow 0$	44.13	84.13	90.64
$2 \rightarrow 0$	50.72	95.49	88.27
$3 \rightarrow 0$	27.76	35.62	28.31
$4 \rightarrow 0$	9.17	4.30	−53.13
$2 \rightarrow 1$	40.70	83.88	106.10
$3 \rightarrow 1$	36.48	38.88	6.58
$4 \rightarrow 1$	12.44	6.95	−44.16
$3 \rightarrow 2$	36.94	53.18	43.97
$4 \rightarrow 2$	23.78	10.63	−55.29
$4 \rightarrow 3$	20.91	15.61	−25.33
Average absolute % deviation			54.18

cross sections value. However, this differently reflects in the prediction of thermally averaged quantities as the macroscopic pressure broadening coefficients, leading to much smaller discrepancies (as will be detailed in ¶ 6.2.6). This validated the use of only *ortho*-N_2 ($j = 0$) in the rotational basis of scattering calculations. By assuming a similar behavior for HC_3N, the use of only the *ortho*-state of N_2 has been supported by validation using the outcomes of pressure broadening experiments.

6.2.5 Bound State Calculations

A way to test the accuracy of the interaction potential is offered by the comparison with the available experimental data. In this respect, HCO^+ + He is the most suitable system because it has already been extensively investigated in laboratory. For example, bound state energy calculations can be exploited for validating the HCO^+ + He interaction potential because the experimental counterpart is available. Indeed, Salomon et al. (2019) measured the rotational transitions of the He−HCO^+ van der Waals complex using double resonance spectroscopy in a ion trap apparatus. In order to compare the experimental results, bound state calculations have been performed (see ¶ 2.2.4 for more details). The computed and experimental rotational transitions together with the corresponding spectroscopic parameters are gathered in Table 6.8. For bound states calculations, the reduced mass of the collisional system was set to 3.5172 amu, while the rotational energies of HCO^+ have been obtained from its experimental rotational parameters (Cazzoli et al., 2012): $B = 1.4875\,\mathrm{cm}^{-1}$, $D = 2.76 \times 10^{-6}\,\mathrm{cm}^{-1}$, and $H = 2.58 \times 10^{-12}\,\mathrm{cm}^{-1}$. The rotational basis of HCO^+ considered its first 19 j states and the coupled equations were solved with R varying

Table 6.8: Rotational transitions (MHz) and spectroscopic parameters of the He−HCO^+ van der Waals complex in the vibrational ground state.

$J' \rightarrow J$		Computed[a]	Experimental[b]	% Deviation
0	1	17381.45707	17395.1112	0.08
1	2	34755.08955	34782.5930	0.08
2	3	52104.04912	52154.8930	0.10
3	4	69454.38773	69504.5481	0.07
4	5	86754.36121	86824.3164	0.08
5	6	104023.1563	104107.0922	0.08
6	7	121235.5004	121345.9633	0.09
7	8	138402.6059	138534.1142	0.09
8	9	155532.4171	155664.8274	0.09
9	10	172563.4768	172731.3559	0.10
10	11	189540.7237	189726.8475	0.10
11	12	206444.7613	206644.3117	0.10
12	13	223231.2502	223476.4892	0.11
13	14	239966.9244	240215.7559	0.10
14	15	256559.9273	256853.9714	0.11
15	16	273065.8015	273382.4879	0.12
B[c]		8691.18(59)	8698.1947(16)	0.08
D		0.3221(79)	0.318741(46)	1.07
$H \times 10^5$		6.7(41)	10.03(6)	33.00
$L \times 10^7$		−0.92(70)	−2.681(39)	65.67

[a]Obtained from bound state calculations.
[b]From Salomon et al. (2019). Centrifugal distortion constants higher in order than L are not reported.
[c]Numbers in parentheses are 1σ errors in units of the last quoted digit.

from 2 to 6 Å and in the energy range between 0 and $-300\,\mathrm{cm}^{-1}$. The numerical propagation of the radial part of the wave function[‖] has been performed by means of the Manopoulos diabatic modified log-derivative (LDMD) propagator (Manolopoulos, 1986). The latter propagates the log-derivative matrix of the wave function with equally spaced steps of size optimized to a value of 0.05 Å. From the inspection of Table 6.8, it is noted that the experimental and computed transition frequencies on average agree well within 0.1%. By fitting these latter using a semi-rigid linear molecule Hamiltonian, we derived the B rotational constant of the HCO^+−He complex and its centrifugal corrections up to the optic term (D, H, L); they are also reported in Table 6.8 (bottom part, left column). The comparison with the corresponding experimentally derived values shows that the rotational constant B agrees within 0.1%. Moving to the centrifugal distortion constants, it is observed a worsening in the agreement: from about 1% for the quartic term to ∼66% for the

[‖]For more details, the reader is referred to ¶ 2.2.4.

octic parameter. However, it has to be noted that these, in particular H and L, are extremely small terms and that the trend is correctly reproduced. In conclusion, the computed rotational parameters of He−HCO^+ compared quite well with the corresponding experimental values. This points out the reliability of the calculations and somewhat validates the potential.

6.2.6 Pressure Broadening

Another way to validate the interaction potential is provided by pressure broadening measurements. As already discussed in ¶ 2.2.4, pressure broadening and pressure shift coefficients can be computed from the S–matrix, which is the main outcome of scattering calculations. These coefficients are not directly linked with the state-to-state inelastic rate coefficients, but they derive from the same matrix, whose accuracy, in turn, depends on the quality of the description of the collisional potential. While the optimization of the parameters required for scattering calculations will be detailed in § 6.4, we recall here that the computation of the corresponding cross sections requires S–matrix elements involving both the initial and final states of the considered transition. The coupled equations thus need to be solved in terms of the kinetic energy instead of the total energy. The real and imaginary parts of the

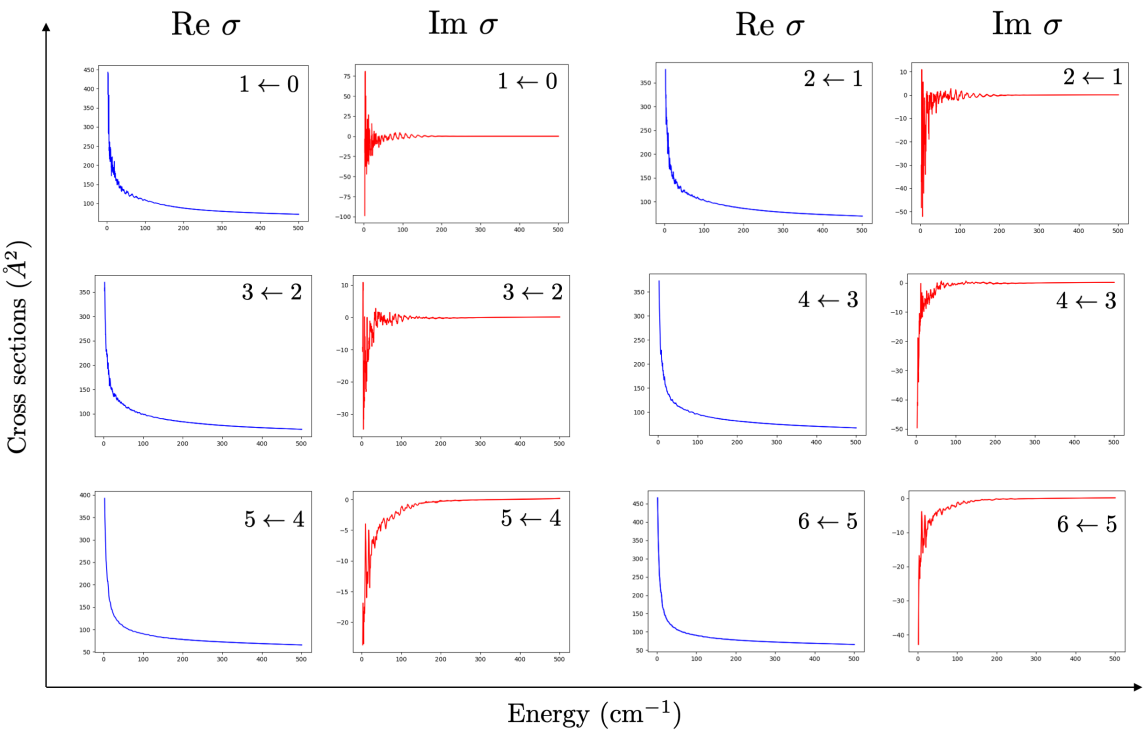

Figure 6.8: Energy dependence of the real and imaginary parts of the computed cross sections for the six-lowest rotational transitions of HCO^+ perturbed by collisions with He.

computed cross sections for a pair of upper and lower states describe the pressure broadening and pressure shift, respectively, of the corresponding transition.

Given the availability of literature data, the first system considered for such a comparison is HCO^+/He. Indeed, pressure broadening and shift coefficients were computed by Buffa et al. (2008) for the six-lowest rotational transitions, with experimental counterparts being also measured. For validation purposes, we thus computed these quantities by solving the scattering equations using the potential described above. In Figure 6.8, the trend of the real and imaginary parts of the cross sections over the energy distribution for the six lowest transitions of HCO^+ perturbed by collisions with He is reported. In these plots, irregular oscillations are clearly visible for all the studied transitions, in particular in the lower energy ranges for the transitions involving low lying states. These oscillations become particularly pronounced for the imaginary parts of the cross sections, thus highlighting the need to cover a wide range of energies in order to have reliable results for the estimate of the pressure broadening and shift coefficients. By averaging the real and imaginary parts of the cross sections over the energy range considered, the pressure broadening and pressure shift coefficients, respectively, are obtained. The resulting values are reported in Table 6.9, where a comparison with the experimental and previously computed results is also provided. First of all, a discrepancy with the coefficients derived by Buffa et al. (2008) (last column of Table 6.9) is noted: these latter appear systematically smaller than our computed values. However, both the coefficients derived in Buffa et al. (2008) and ours present a rather good agreement with the experimental values. Moreover, it can be noted that the coefficients presented by Buffa et al. (2008) and those recomputed by us from the cross sections reported in

Table 6.9: Measured and calculated pressure broadening and shift parameters for the six lowest rotational transitions of HCO^+ perturbed by He at 88 K.

$j' \leftarrow j''$	Frequency [MHz]	Parameter	Exp. Values [MHz/Torr]	This work [MHz/Torr]	Recomputed values[a] [MHz/Torr]	Buffa et al. (2008) [MHz/Torr]
1 ← 0	89188.5261	broadening		14.377	13.987	13.76
		shift		0.172	0.156	0.154
2 ← 1	178375.0642	broadening		13.580	13.225	13.01
		shift		0.153	0.169	0.168
3 ← 2	267557.6263	broadening		13.238	12.841	12.64
		shift		0.134	0.142	0.134
4 ← 3	356734.2246	broadening	12.39(29)	12.857	12.479	12.27
		shift	0.328(19)	0.206	0.233	0.229
5 ← 4	445902.8713	broadening	12.42(22)	12.520	12.158	11.95
		shift	0.427(29)	0.302	0.319	0.312
6 ← 5	535061.5791	broadening	12.13(29)	12.260	11.920	11.72
		shift	0.497(17)	0.343	0.367	0.364

[a]Recomputed values from the cross sections taken from Table 2 of Buffa et al. (2008).

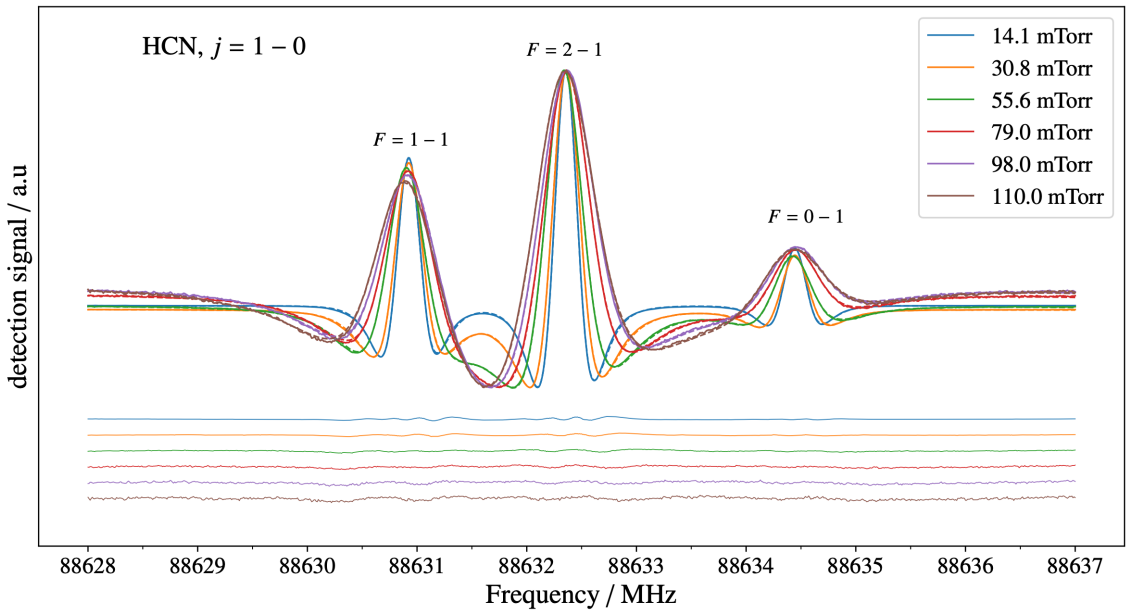

Figure 6.9: Line shape analysis of the $j = 1 - 0$ transition of HCN at different pressures of N_2. At the bottom of the figure, residuals (*i.e.*, the observed-calculated differences) are also shown.

that paper do not coincide (the last two columns on the right of Table 6.9). This discrepancy is probably attributable to a slightly different temperature considered in the thermal averaging of the cross sections. As regards pressure shift coefficients, although our computed values present a good agreement with the ones computed by Buffa et al. (2008), they show the largest deviations when compared to experiment. This was somehow expected, since pressure shift measurements are rather delicate and thus affected by significant uncertainties. Generally speaking, a good agreement between our computed data and those experimentally measured can be surely affirmed.

Other systems of interest to validate the collisional PES by means of pressure broadening experiments are those involving HCN or HC_3N colliding with N_2. Indeed, as discussed above, in order to reduce the computational cost, approximations have been introduced in the description of the rotational basis of N_2. Hence, for quantum scattering calculations, only the $j = 0$ state of N_2 was taken into account. As regards the experimental measurements, spectral recordings were conducted at a temperature of about 295 K and around 88 and 91 GHz. Here, the $j = 1-0$ rotational transition of HCN and the $j = 9 - 10$ rotational transition of HC_3N lie. These two transitions, indeed, fall in the center of the 3-mm band easily accessible to the FM-mmW spectrometer employed for the measurements, thus ensuring the optimal instrumental sensitivity. This resulted in a high signal-to-noise ratio, as shown in Figures 6.9 and 6.10. Moreover, this frequency range was not covered by previous

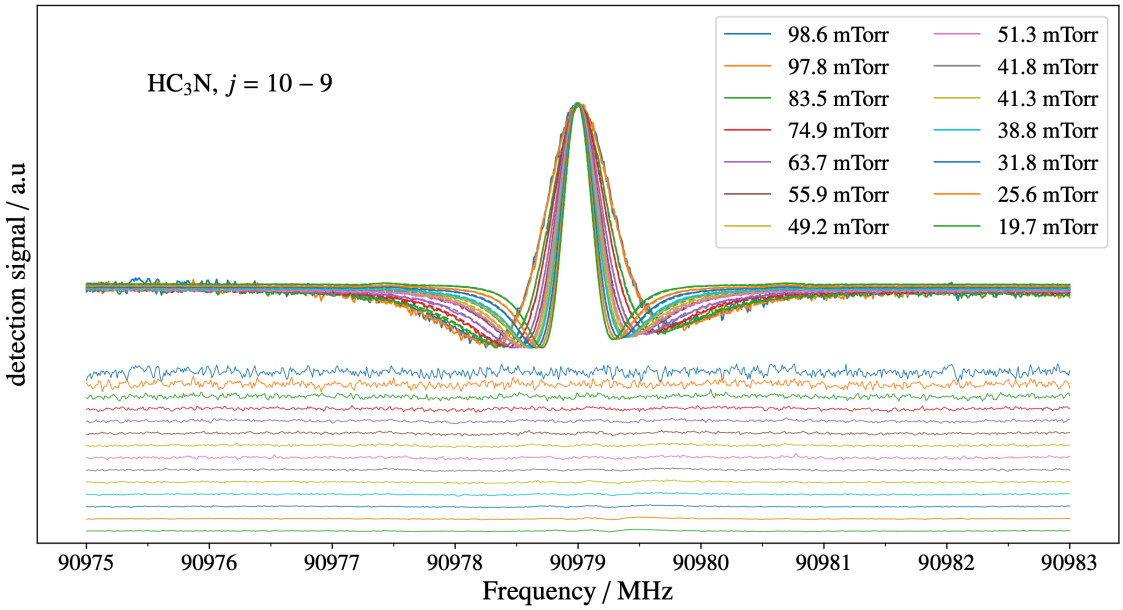

Figure 6.10: Line shape analysis of the $j = 10 - 9$ transition of HC_3N at different pressures of N_2. At the bottom of the figure, residuals (*i.e.*, the observed-calculated differences) are also displayed.

pressure broadening studies for these collisional systems. Finally, the $j = 1 - 0$ rotational transition of HCN exhibits a well-resolved hyperfine structure and this considerably simplifies its line profile analysis. The sample of HCN was prepared from mandelonitrile, which in gas phase is completely dissociated into benzaldehyde and HCN. Benzaldehyde was then condensed by flowing the mandelonitrile vapors through a 273.15 K bath. Subsequently, the purified HCN gas was collected in a trap kept at liquid nitrogen temperature. Its vapors at about 253 K were eventually used for the measurements. These were carried out as following: 0.4 mTorr of the absorber was first introduced into the cell; then, few series of measurements were carried out at increasing values of the perturber pressure. The gas pressure was found to be stable well within 0.2 mTorr. Differently, the low stability of HC_3N forced us to carry out the measurements in flow conditions to avoid the decomposition of the absorber. The HC_3N sample was prepared by the group of Professor Jean-Claude Guillemin at the Rennes Institute of Chemical Sciences, following the synthetic route described by Miller and Lemmon (1967), and thus *via* dehydratation of propiolamide with P_4O_{10} at 498 K under vacuum conditions and subsequent distillations to remove the volatile side products (mainly NH_3). For each spectral recording, the line profile was modeled using the qSDVP model, and exploiting the proFFiT line analysis code (Dore, 2003). The results of these analyses are illustrated in Figures 6.9 and 6.10 for HCN and HC_3N, respectively. Overall, both fits show very small residuals for all pressures, thereby supporting the choice of the model for the line profile. For

the $j = 1 - 0$ of HCN, the effect of the nuclear quadrupole coupling (due to ^{14}N) is such that the three hyperfine components are well separated, as clearly evident in Figure 6.9. In terms of pressure broadening, however, the cross sections for each hyperfine feature (within the recoupling approximation) are the same as that for the spin-free case. This is due to the orthogonality properties of the $6j$-symbols that causes the off-diagonal cross sections to vanish (see Green 1988 for further details). The three components of the hyperfine structure thus share the same pressure dependent parameters. Instead, for the $j = 10 - 9$ transition of HC_3N, the hyperfine structure is not resolved as this collapses at high values of j.

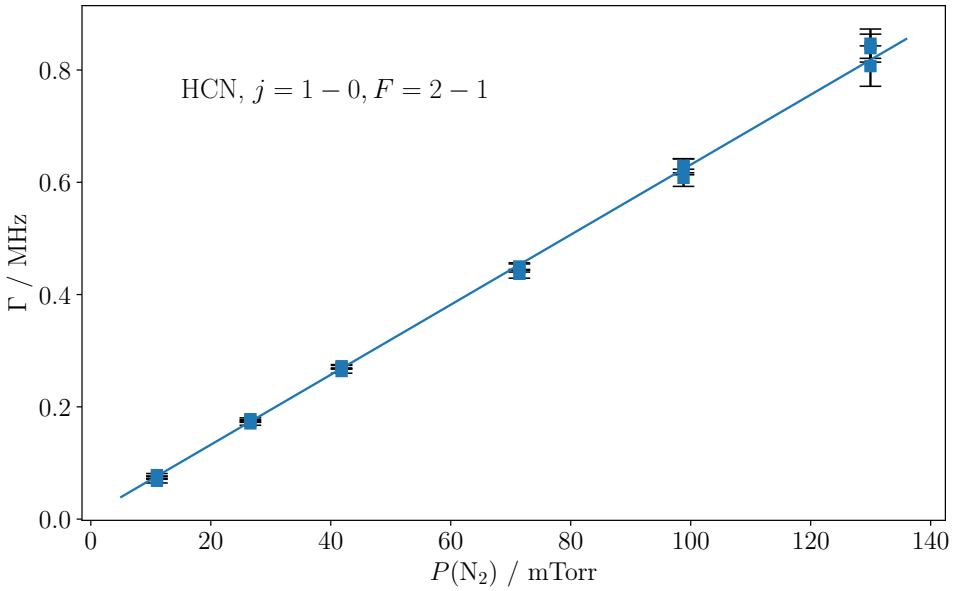

Figure 6.11: Linear fit of the Lorentzian half-width of the $F = 2 - 1$ hyperfine component of the $j = 1 - 0$ transition of HCN against the pressure of N_2. Error bars represent 3σ uncertainties.

From the line shape analysis we retrieved the center frequency ν_0, the Lorentzian half width Γ and the quadratic speed dependent parameter Γ_2**. Figures 6.11 and 6.12 show the trend of Γ vs. pressure for both the $j = 1 - 0$ transition of HCN and the $j = 10 - 9$ transition of HC_3N, respectively. Through linear regression, the experimental pressure broadening (γ) and shift (s) coefficients were obtained according to the expressions in Eqs. (4.14) and (4.15) in § 4.2. The pressure broadening coefficients of the $j = 1 - 0$ transition of HCN and the $j = 10 - 9$ transition of HC_3N compare well with their corresponding theoretical computed counterparts, with deviations of 9% and 1%, respectively (see Table 6.10). The quality of the agreement is satisfactory, considering that our calculations involve the spherical potential approximation (see ¶ 6.2.3 for more details), which holds less strictly at the experimental temperatures than for colder environments. For both HCN and HC_3N,

**The reader is referred to § 4.2 for the definition and physical meaning of these parameters.

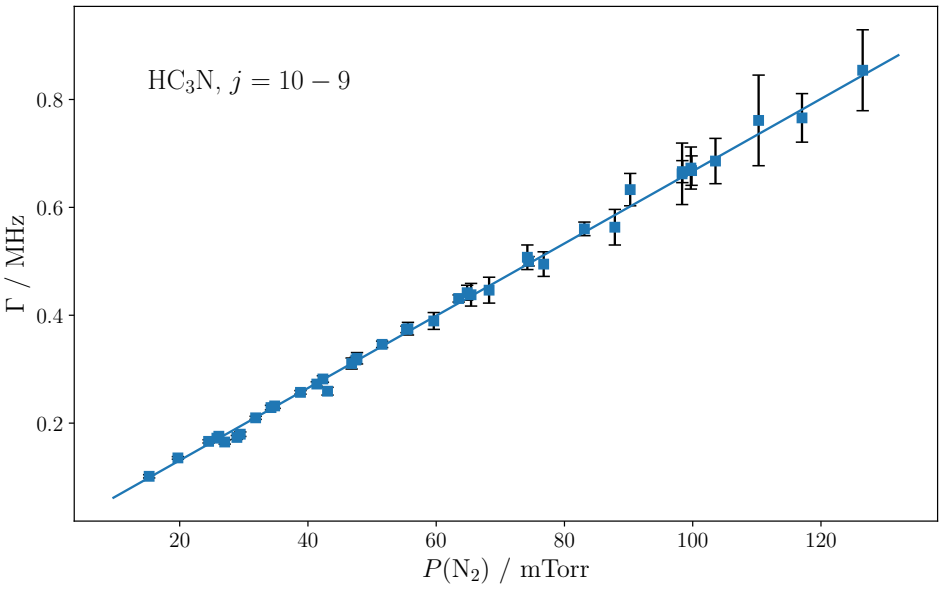

Figure 6.12: Linear fit of the Lorentzian half-width of the $j = 10 - 9$ transition of HC_3N against the pressure of N_2. Error bars represent 3σ uncertainties.

a very small pressure-dependence of the line transition frequency is observed. In detail, the pressure shift coefficient for the $j = 1 - 0$ transition of HCN turned out to be extremely small and barely determined in our experiment; a tentative fit yielded $s = -1.3(6) \times 10^{-4}\,\mathrm{MHz\,Torr^{-1}}$. The pressure shift coefficient for the $j = 10 - 9$ transition of HC_3N resulted very small too: $s = -0.15(1) \times 10^{-3}\,\mathrm{MHz\,Torr^{-1}}$. In the pressure range explored by our measurements, the collision shift is very small ($\sim$15 kHz at 100 mTorr for the $j = 10 - 9$ transition of HC_3N) and cannot be reliably inferred due to the presence of comparable if not larger systematic uncertainties. Hence, the comparison with the theoretically computed values was not deemed to be meaningful. Although they would need to be supported by comparisons for other transitions, these results provide an initial validation of the assumptions made for both systems in the construction of the potential.

Table 6.10: Comparison of computed-experimental pressure broadening coefficients for the $j = 1 - 0$ transition of HCN and the $j = 10 - 9$ transition of HC_3N at 295 K.

Target	$j' \leftarrow j$	Computed [MHz/Torr]	Experimental [MHz/Torr]	% Deviation
HCN	$1 \leftarrow 0$	5.71	6.23(19)[a]	9
HC_3N	$10 \leftarrow 9$	6.77	6.702(91)	1

[a] Constrained to be equal for all the three hyperfine components.

6.3 Accurate Rest Frequencies

The knowledge of accurate rest frequencies is of great importance for astronomical identifications and modeling of molecular lines. This implies that, from the laboratory side, very precise measurements of these transitions are carried out. One source of systematic error that should be carefully checked is the frequency shift due to collisions between the target molecule and foreign gases. This becomes particularly important when spectral measurements of ions are concerned, as their production requires a buffer gas inside the cell, whose pressure cannot be kept arbitrarily low (see *e.g.*, Buffa et al., 2006, 2008, 2010).

Here, the procedure adopted to carry out precise frequency measurements for the $HC^{18}O^+$ ion is described. In detail, pressure broadening experiments have been performed for its $j = 1 \leftarrow 0$ and $j = 2 \leftarrow 1$ transitions, for which we expect the largest collisional effects. For these two lines, the pressure broadening and shift coefficients were determined by performing several spectral recordings at increasing Ar gas buffer pressure (see below). The experiments have been perfomed using the CASAC (Center for Astrochemical Studies Absorption Cell) spectrometer located at the Max-Planck-Institut für extraterrestrische Physik in Garching. An accurate

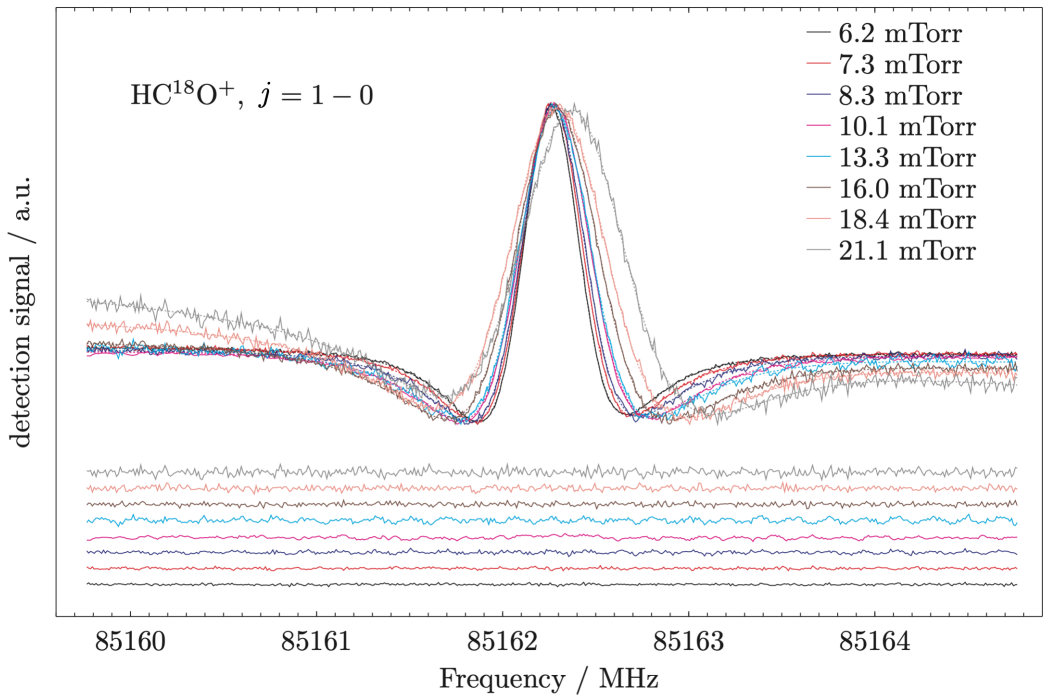

Figure 6.13: Line shape analysis of the $j = 1 - 0$ transition of $HC^{18}O^+$ broadened by Ar and employing the qSDVP model, at various pressures of the buffer gas of Ar. At the bottom of the figure, residuals (*i.e.*, the observed-calculated differences) are also reported.

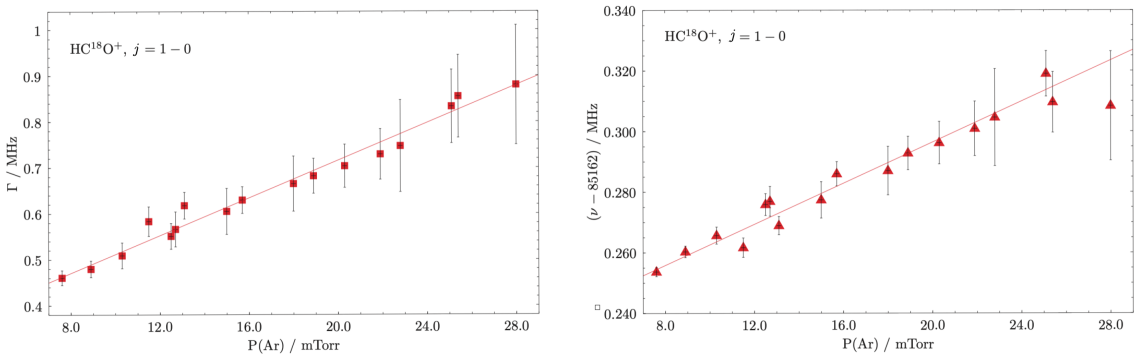

Figure 6.14: Set of measurements for the Ar-broadening of the $j = 1-0$ transition of $HC^{18}O^+$. Left panel: linear fit of the collisional half-width against the pressure of Ar. Right panel: linear fit of the frequency shifts against the pressure of Ar. In both panels, three times the uncertainties retrieved from line profile analysis are shown.

description of the apparatus is given in Bizzocchi et al. (2017). The formyl ion was produced by applying a DC glow-discharge inside the absorption cell (a 3 m long, 5 cm in diameter Pyrex tube), that hosts two stainless steel, cylindrical hollow electrodes separated by 2 m. $HC^{18}O^+$ was generated in the plasma negative column of a mixture of 3 mTorr of $C^{18}O$, 1 mTorr of H_2 and 6–20 mTorr of Ar. The plasma region is cooled at ~ 85 K by liquid nitrogen circulation. Typical discharge conditions were: current $\sim 10 - 15$ mA and voltage = 2.5 kV. A ~ 250 G magnetic field was applied coaxially to the plasma to improve the ion production in the extended negative column.

For each recorded spectrum, line width and central line frequency were retrieved by employing the qSDVP model using the `proFFiT` line analysis code (Dore, 2003). The results of this analysis are illustrated in Figures 6.13 and 4.4, which show experimental and modeled spectral traces for the $j = 1 \leftarrow 0$ and $j = 2 \leftarrow 1$ transitions, respectively. Flat and featureless residuals were obtained for all pressures. For each set of measurements, linear regression analyses of the collisional line width and the center frequency against the pressure of Ar have been performed (see Figures 6.14 and 4.5), from which the pressure broadening and shift coefficients were directly

Table 6.11: Comparison of the computed-experimental pressure broadening and pressure shift coefficients for the two lowest rotational transitions $HC^{18}O^+$ perturbed by Ar at T= 98 K.

Transition	Broadening / MHz Torr^{-1}		Shift / MHz Torr^{-1}	
	Exp.	Theor.	Exp.	Theor.
$1-0$	20.44(60)	20.513	3.38(18)	2.073
$2-1$	16.3(13)	17.643	0.826(57)	0.534

Table 6.12: Observed transition frequencies and fit residuals of the rotational transitions of $HC^{18}O^+$ up to 1.2 THz together with the corresponding spectroscopic constants.

$j+1$	j	observed [a] (MHz)	obs.-calc. (kHz)	σ (kHz)
1	0	85 162.2288	0.6	5.0
2	1	170 322.6390	−4.0	5.0
3	2	255 479.4336	2.4	10.0
4	3	340 630.7850	5.6	10.0
5	4	425 774.8705	−4.0	10.0
6	5	510 909.9110	7.4	10.0
7	6	596 034.0531	−0.8	10.0
8	7	681 145.5113	−1.4	10.0
9	8	766 242.4674	−0.6	10.0
10	9	851 323.1064	−1.1	10.0
11	10	936 385.6214	1.5	10.0
12	11	1 021 428.19251	−1.2	10.0
13	12	1 106 449.02011	1.8	20.0
14	13	1 191 446.28361	0.4	20.0

rms[b] = 3.1 kHz

Constant	Value[c]	Correlation matrix		
B / MHz	42 581.26521(26)	1.000		
D / kHz	75.5573(27)	−0.8918	1.000	
H / mHz	53.9(87)	0.7635	−0.9629	1.000

[a] Measurements from Bizzocchi et al. (2024).
[b] Root-mean-square error of the residuals.
[c] Standard errors are reported in parentheses in units of the last quoted digit.

retrieved according to Eqs. (4.14) and (4.15) of § 4.2. The results are collected in Table 6.11, where the theoretically computed values are also reported. It can be noted that the discrepancies for the pressure broadening values fall within the experimental uncertainty. The comparison of the experimental and computed pressure shift values shows larger deviations, but they still exhibit the same sign and order of magnitude, indeed agreeing within 40%. The overall good agreement between experimentally and theoretically computed parameters also provides a validation of the computational approach. The extrapolation to zero pressure of the linear regressions shown in the rightmost panels of Figures 6.14 and 4.5 provides the "unperturbed" line position, in which the contribution due to the collisional shift is removed. The corrected line center positions were then analyzed together with all the available rotational transitions for $HC^{18}O^+$, that extends up to 1.2 THz (Bizzocchi et al., 2024). The experimental frequencies were fitted using a standard semi-rigid linear rotor Hamiltonian, with the rotational constants B, the quartic centrifugal distorsion D, and the sextic distrifugal distorsion H as adjustable paramenters. Their resulting

values, together with the standard uncertainties, are reported in Table 6.12.

This investigation provided very accurate rest frequencies for the $HC^{18}O^+$ molecule up to THz regime. The observed-calculated deviations, also given in Table 6.12, are indeed remarkably small, reaching an agreement of a few parts over 10^9.

6.4 Derivation of (De-)Excitation Rate Coefficients

Moving to dynamics calculations that employ the interaction potentials described in the previous sections, collisional rate coefficients are determined by solving the standard time-independent coupled scattering equations[††] with the MOLSCAT program (Hutson and Green, 1994), as explained in ¶ 2.2.4. Full quantum calculations were performed by purposely choosing the energy range and propagation limits: the conditions are listed in Table 6.13 and have been chosen on the basis of the molecular targets and the surrounding environment. The total energy interval (second

Table 6.13: Selected energy range, propagation parameters, rotational basis and reduced mass for each targeted collisional system.

System	E_{tot} / cm^{-1}	Propagation Limits / Å	j_{max}(target)	μ
HCO^+–He	2–500	2–85	32	3.5172
$HC^{17}O^+$–H_2	2–500	2.5–50	31	1.8709
$HC^{18}O^+$–Ar	2–500	2.5–110	45	17.4598
PO^+–H_2	2–1200	1.8–50	50	1.9327
HCN–N_2	2–1000	2–70	50	13.7498
HC_3N–N_2	2–1000	2–50	50	18.5589

column of Table 6.13) was selected based on the kinetic temperature of the targeted astrophysical environment. Under the typical conditions of the ISM, where the temperatures is usually below ∼100 K, an energy range up to 500 cm^{-1} is sufficient to ensure convergence in the calculation of cross sections. However, for kinetic temperatures higher than 100 K, the upper limit of this interval has to be extended. For all systems, the total energy range was sampled with narrow steps at low energies ($0.1 - 0.2\,cm^{-1}$) which were gradually increased as energy raised. This choice stems from the irregular trends exhibited by cross sections at low kinetic energies, as depicted for instance in Figures 6.15 and 6.16, thus requiring a careful fit for this interval. On the contrary, as the kinetic energy increases, cross sections show smoother patterns and tend to converge to a constant value. For the resolution of the nuclear Schrödinger equation, the radial dependence of the wave function needs also to be

[††]The mathematical derivation and physical meaning of coupled equations are detailed in ¶ 2.2.4.

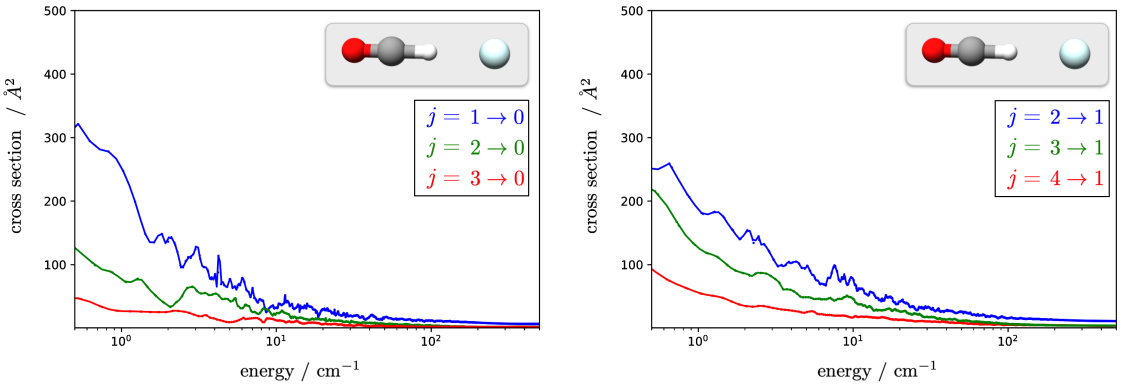

Figure 6.15: Variation of some de-excitation cross sections of the HCO^+ and He system in the $2 - 500\,cm^{-1}$ energy range.

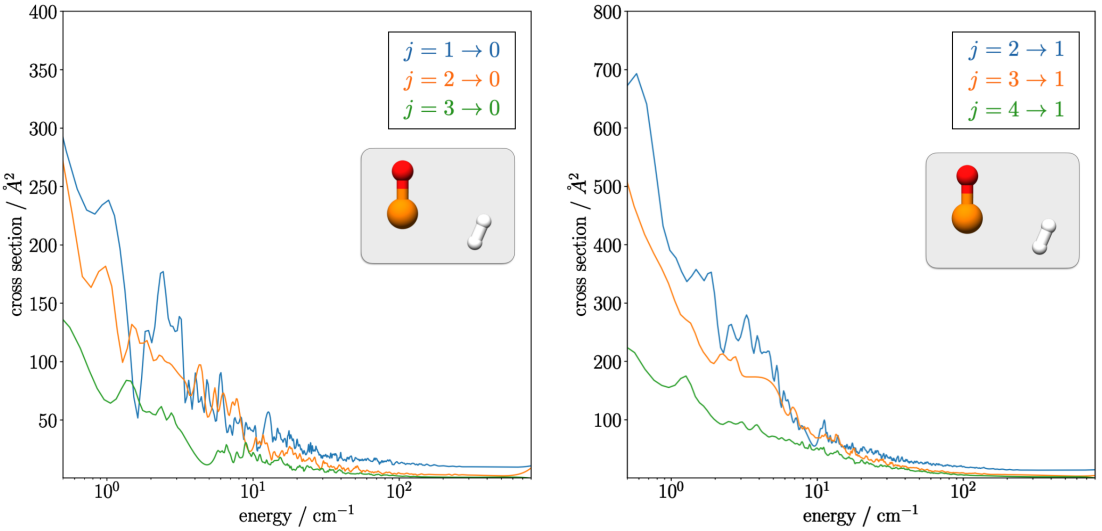

Figure 6.16: Variation of some de-excitation cross sections of the PO^+ and H_2 system in the $2 - 1200\,cm^{-1}$ energy range.

modeled by numerical propagation. In this regard, the LDMD/AIRY hybrid propagator (Alexander, 1984; Manolopoulos, 1986; Alexander and Manolopoulos, 1987) was employed, as it provides the best balance between computational efficiency and accuracy. Indeed, LDMD/AIRY allows for dealing with the short- and long-range propagation according to the potential requirements: in the short range of R, where the largest energy gradients are found, it exploits the narrowest propagation steps (provided by the LDMD propagator); for long R distances, where a broader yet smoother energy range needs to be covered, AIRY, which employs the loosest propagation steps, is adopted. The switching point between the two propagators was selected to ensure a convergence within 1.5% for the inelastic cross sections. The

same procedure has been also applied to the choice of the propagation limits (third column of Table 6.13). The cut-off of the rotational basis of the target molecule was adjusted to ensure the convergence of the inelastic cross sections. It has been optimized for different energy ranges, while the maximum extension at the highest total energy considered is reported in the fourth column of Table 6.13. The choice of the rotational basis of H_2 and N_2 instead followed the remarks outlined in ¶ 6.2.3. The maximum value of the total angular momentum was chosen as the one that allowed for the convergence of the inelastic cross sections within 0.005 Å. In the last column of Table 6.13, the reduced masses for each system are also reported, while the rotational energies have been computed from the experimental ground-state spectroscopic constants of each collider (rotational and quartic centrifugal distortion constants are collected in Table 6.14 together with the corresponding references to literature). Finally, the maximum value of the total momentum $\mathbf{J} = \mathbf{j} + \mathbf{l}$ employed

Table 6.14: Rotational parameters employed to compute the energy levels for scattering calculations.

Molecule	B_0/cm^{-1}	D_0/cm^{-1}	Reference
HCO^+	1.4875	2.76×10^{-6}	Cazzoli et al. 2012
$HC^{17}O^+$ [a]	1.4529	2.63×10^{-6}	Dore et al. 2001
$HC^{18}O^+$	1.4204	2.52×10^{-6}	Bizzocchi et al. 2024
PO^+	0.7870	9.79×10^{-6}	Petrmichl et al. 1991
HCN	1.4782	2.91×10^{-6}	Thorwirth et al. 2003
HC_3N	0.1517	2.00×10^{-8}	Tamassia et al. 2022
H_2	60.853	4.71×10^{-2}	Huber 1979
N_2	1.9982	5.76×10^{-6}	Huber 1979

[a] The energies of the hyperfine levels due to ^{17}O required for recoupling calculations have been taken from Bizzocchi et al. (2024).

in the calculations was chosen in order to allow for the convergence of the inelastic cross sections within 0.005 Å.

From the derived S–matrix elements, a full list of collisional cross sections from an initial j to a final j' state of each system was retrieved in the selected energy range. It is worth to mention that, among the systems investigated in this thesis, a comprehensive dataset of the collisional cross sections for HC_3N + N_2 is not available yet. As a future perspective, a complete collisional dataset will be obtained by exploiting the procedure adopted for the HCN and N_2 collisional system. For illustrative purposes, the energy dependence of inelastic cross sections for some transitions of the HCO^+−He and PO^+−H_2 systems are depicted in Figures 6.15 and 6.16, respectively. As expected, inelastic cross sections decrease as the collision energy increases and oscillations due to resonance effects are more prominent in the

low-energy limit range for all the transitions.

Starting from the inelastic cross sections, the (de-)excitation rate coefficients are straightforwardly derived by thermal averaging over the collision energy (see Eq. (2.84) in ¶ 2.2.4). While a complete list of the computed state-to-state rate coefficients for each system is reported in the Appendix A, in the following some considerations regarding their trends, propensity rules and comparison with previous results (when available) is outlined.

Table 6.15: Transition rate coefficients for the HCO^+ and He system at 10 K. Units are 10^{-10} cm^3 s^{-1}.

$j \rightarrow j'$	This work	Buffa et al. (2009)	Monteiro (1985)
$0 \rightarrow 1$	2.322	2.200	1.984
$0 \rightarrow 2$	0.866	0.857	0.739
$0 \rightarrow 3$	0.149	0.143	0.137
$0 \rightarrow 4$	0.022	0.021	0.014
$1 \rightarrow 2$	1.162	1.152	1.099
$1 \rightarrow 3$	0.275	0.266	0.195
$1 \rightarrow 4$	0.030	0.032	0.025
$2 \rightarrow 3$	0.643	0.657	0.566
$2 \rightarrow 4$	0.104	0.097	0.084
$3 \rightarrow 4$	0.390	0.405	0.310

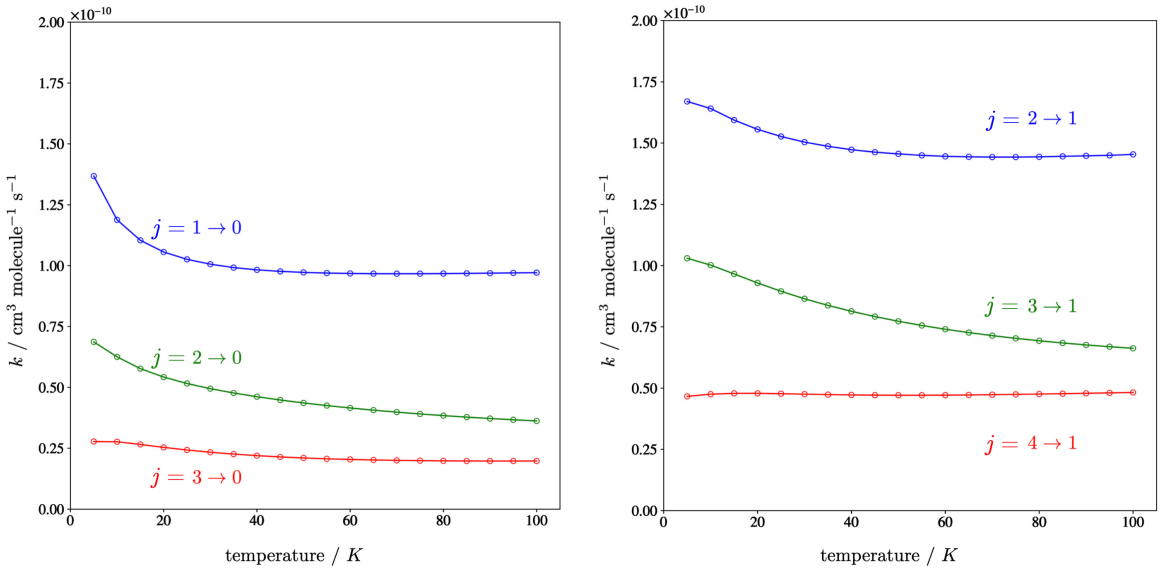

Figure 6.17: Variation of some de-excitation rate coefficients of the HCO^+ and He system in the $5 - 100$ K temperature range.

The first system addressed is HCO^+ + He, which enables the comparison with two previous works (Monteiro, 1985; Buffa et al., 2008). The results are reported in Table 6.15 and a general good agreement is noted. The absolute maximum deviation with respect to the most recent results (Buffa et al., 2008) is only 0.1×10^{-10} cm^3 s^{-1}. The rate coefficients for the $j = (1, 2, 3) \rightarrow 0$ and $j = (2, 3, 4) \rightarrow 1$ transitions up to 100 K are depicted in Figure 6.17. Here, the temperature dependence of the rate coefficients appears to follow an inversely proportional behavior. However, such a dependence reduces as Δj increases, becoming hardly discernible for $\Delta j = 3$. Moreover, in the high temperature range, all the rate coefficients become almost independent of the temperature.

Moving to the $HC^{17}O^+$ and $HC^{18}O^+$ targets, full close-coupling calculations were performed on the interaction potential shifted for the $^{16}O \rightarrow {}^{17}O/{}^{18}O$ isotopic substitution. In the case of the ^{17}O-bearing variant, the hyperfine splitting of rotational lines needs to be introduced: the ^{17}O nuclear spin ($I = 5/2$) couples with the molecular rotational angular momentum **j** through electric quadrupole interaction. Since the hyperfine structure can be a precious source of information for astrophysical purposes, hyperfine state-to-state rate coefficients were computed using recoupling techniques (which are detailed in ¶ 2.2.4). In Table 6.16, the hyperfine solved rate coefficients obtained for the first two rotational transitions at 10, 30 and 50 K are presented. Also in this case, a strong variation in the rate coefficients at very low temperature is apparent, while starting from 30 K some of them already converge to a single value. This trend is evident also in Figures 6.18 and 6.19, which depict the variation of some de-excitation rate coefficients with temperature. In detail,

Table 6.16: Hyperfine resolved (de-)excitation rate coefficients of the two lowest rotational levels of $HC^{17}O^+$ for collisions with H_2 at $T = 10, 30$ and 50 K. Units are 10^{-10} cm^3 s^{-1}.

$j, F \rightarrow j', F'$	Rate coefficients / 10^{-10} cm^3 s^{-1}		
	10 K	30 K	50 K
1, 1.5 → 0, 2.5	1.85	1.54	1.45
0, 2.5 → 1, 1.5	0.81	0.89	0.89
1, 2.5 → 0, 2.5	1.85	1.54	1.45
0, 2.5 → 1, 2.5	1.22	1.34	1.34
1, 2.5 → 1, 1.5	1.09	0.75	0.60
1, 1.5 → 1, 2.5	1.63	1.13	0.91
1, 2.5 → 1, 3.5	2.45	1.73	1.41
1, 3.5 → 1, 2.5	1.83	1.29	1.06
1, 3.5 → 0, 2.5	1.85	1.54	1.45
0, 2.5 → 1, 3.5	1.63	1.78	1.78
1, 3.5 → 1, 1.5	1.37	0.98	0.81
1, 1.5 → 1, 3.5	2.73	1.95	1.62

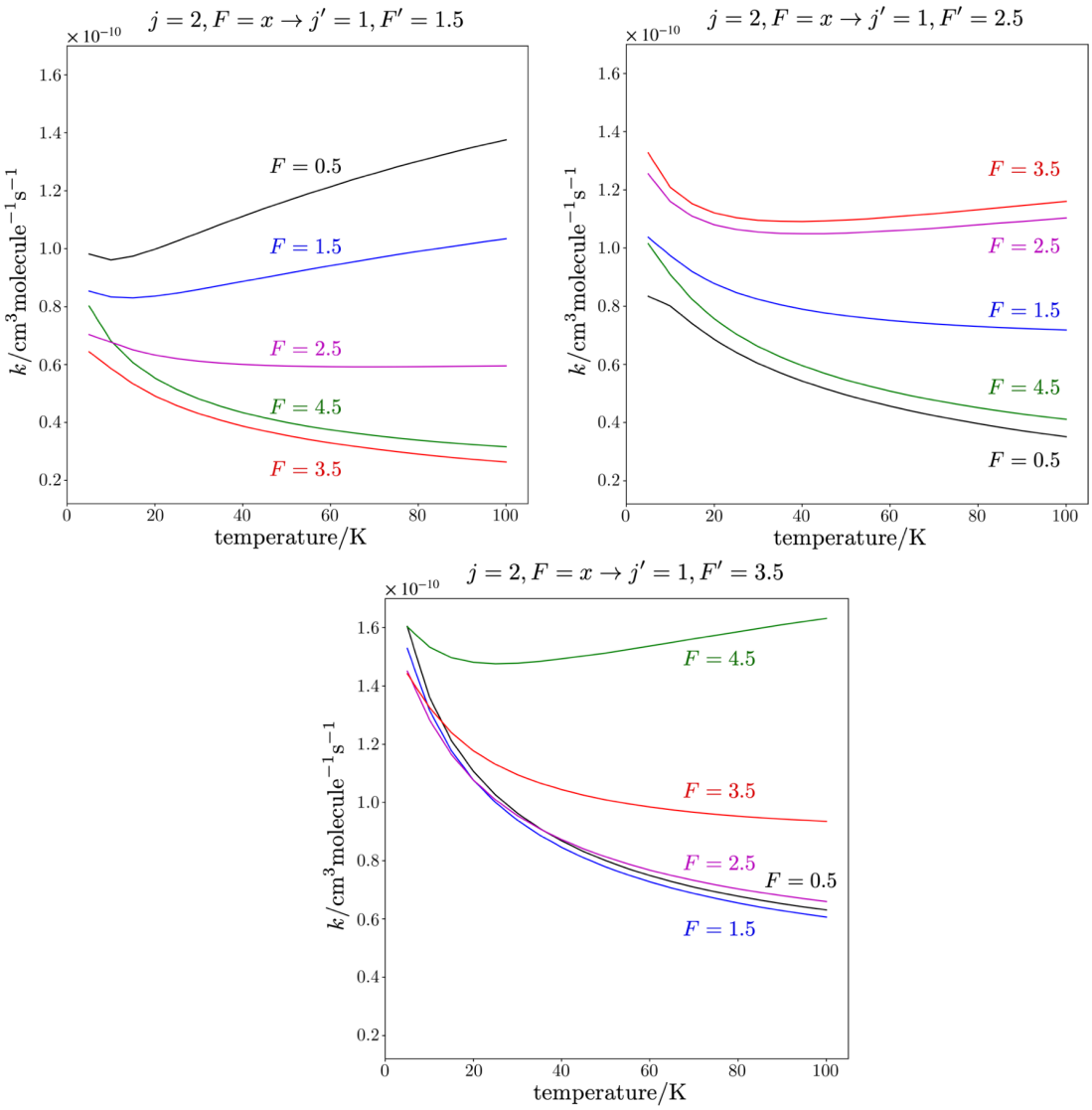

Figure 6.18: Temperature variation of the hyperfine resolved $HC^{17}O^+ - H_2$ rate coefficients for some transitions involving the same final hyperfine state.

Figure 6.18 shows the trend of the inelastic rate coefficients involving the same final hyperfine state, whereas in Figure 6.19 the quasi-elastic rate coefficients for the $j = 1$ and $j = 2$ rotational levels are reported. From both figures, a propensity for the transitions involving the final hyperfine level (F') with the highest multiplicity and for those involving $\Delta F = \Delta j$ when $F' \geq I$ and $-\Delta F = \Delta j$ when $F' < I$, is clearly evident.

The last example here considered is the PO^+ and H_2 collisional system, for which the temperature dependence of some rate coefficients is reported in Figure 6.20 ($j' \rightarrow 0, j' \rightarrow 1$ in the left panel and $\Delta j = 1$ in the right panel). Even in this case, the depicted propensity for the transitions involving $\Delta j = 1$, which decreases by

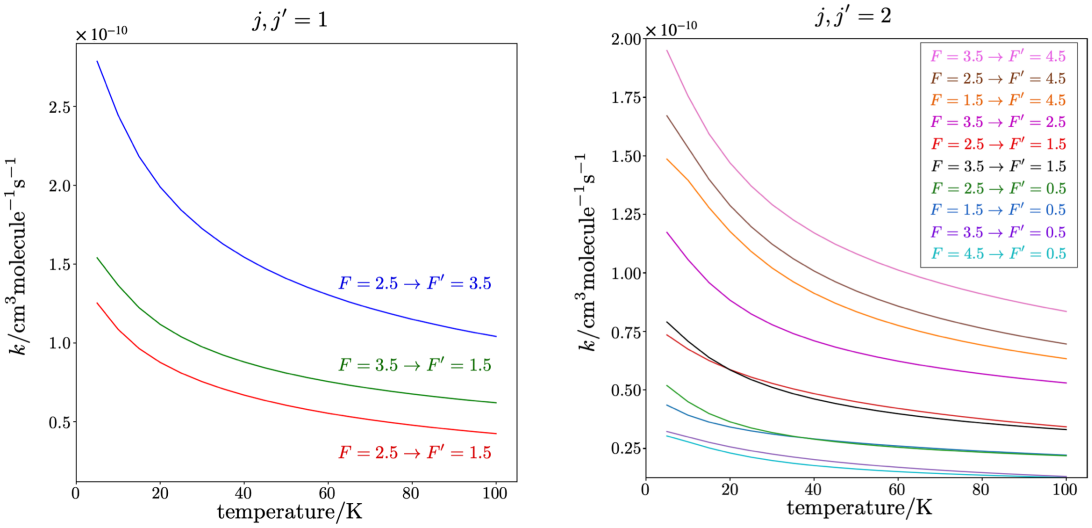

Figure 6.19: Temperature variation of the hyperfine resolved $HC^{17}O^+$ – H_2 quasi-elastic rate coefficients of the $j = 1, 2$ rotational levels.

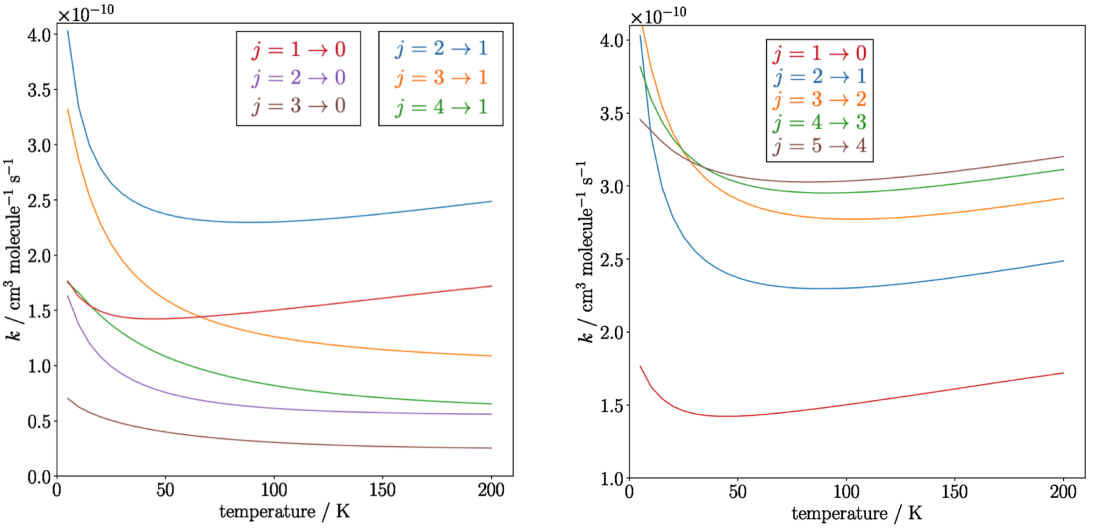

Figure 6.20: Variation of some rotational de-excitation rate coefficients as a function of temperature for the PO^+ and H_2 collisional system.

enlarging the value of Δj, is clear. Interestingly, the propensity toward transitions involving j levels with the highest multiplicity may reverse at low temperatures ($T < 50\,\mathrm{K}$). This behavior differs from those derived for the previous two systems. However, the same pattern has already been found for the isoelectronic species NO^+ perturbed by *para*-H_2 (Cabrera-González et al., 2020), which also presents a good agreement in the absolute values of the rate coefficients. The PO^+ and H_2 system also represents a good test case for verifying the suitability of using

He to simulate the behavior of *para*-H_2. Hence, the mass scaled rate coefficients previously computed for the PO^+ and He system (Chahal and Dhilip Kumar, 2023) have been compared with our results. Figure 6.21 shows the trends as function of temperature for some of them, where our computed results for the PO^+ and H_2 system are reported as solid lines, while for the mass-scaled results by Chahal and Dhilip Kumar (2023) for the PO^+ and He system, dashed lines are employed. It is noted that the two sets of rate coefficients exhibit different behaviors at all

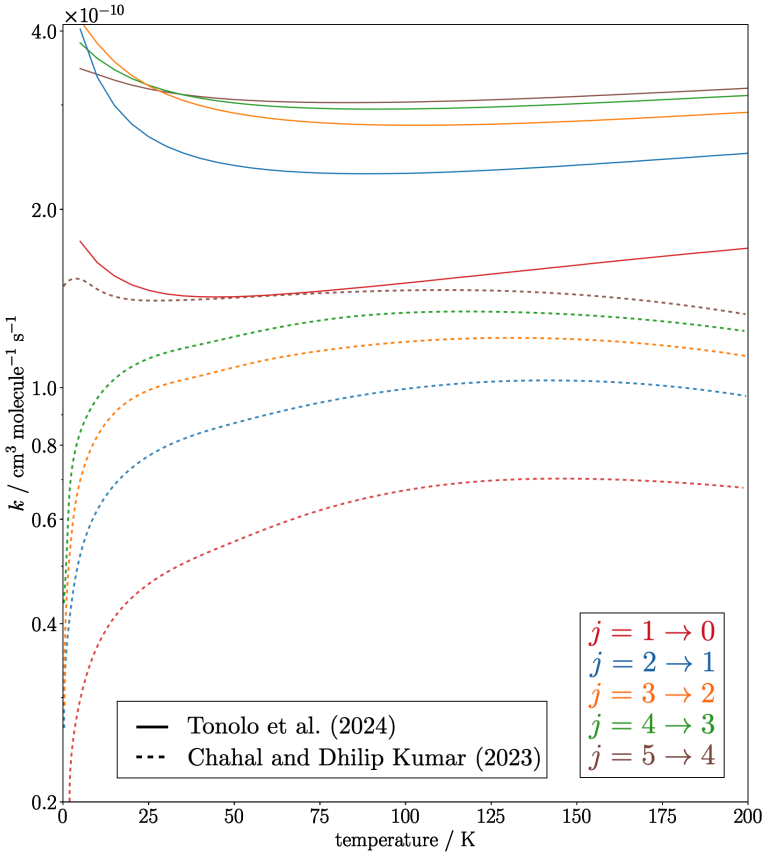

Figure 6.21: Comparison of some rotational de-excitation rate coefficients: mass-scaled results from Chahal and Dhilip Kumar (2023), dashed lines, vs this thesis (PO^++H_2), solid lines.

temperatures. Below 50 K, divergent propensity rules are noted. Moreover, the PO^+ and He rate coefficients greatly underestimate the values obtained with H_2, in several cases leading to discrepancies up to one order of magnitude. This outcome confirms what was already found for other ions (Yazidi et al., 2014; Denis-Alpizar and Rubayo-Soneira, 2019; Bop, 2019; Cabrera-González et al., 2020), that is a pronounced inaccuracy of He as a template of the H_2 perturber because of the different behaviors of the long-range part of the potential for the ion−He and ion−H_2 interactions.

6.4.1 Isotope Effect

As already mentioned in Chapter 1, a commonly employed assumption is to infer rate coefficients of an isotopic variant starting from those of its parent species. In order to test the reliability of this approximation, the impact of isotopic substitution on the values of the computed rate coefficients is here assessed. In detail, the values of the cross sections computed at $50\,\mathrm{cm}^{-1}$ for the HCO^+ and $HC^{17}O^+$ target species were compared. The results, reported in Table 6.17, show significant discrepancies, with an average deviation of about 20%. Moreover, the variation between the two

Table 6.17: Computed cross-sections, at $E = 50\,\mathrm{cm}^{-1}$, for the $HC^{17}O^+/HCO^+$ and $H_2(j = 0)$ collisions.

$j \to j'$	Cross sections / Å^2		% Deviation
	$HC^{17}O^+$	HCO^+	
$1 \to 0$	53.41	64.96	21.62
$2 \to 0$	50.31	55.34	10.00
$3 \to 0$	44.00	47.18	7.24
$4 \to 0$	30.28	41.16	35.90
$5 \to 0$	15.74	20.49	30.20
$2 \to 1$	60.87	60.25	−1.03
$3 \to 1$	53.18	49.24	−7.40
$4 \to 1$	35.19	40.20	14.22
$5 \to 1$	18.77	18.88	0.59
$3 \to 2$	52.95	64.27	21.39
$4 \to 2$	41.75	51.14	22.47
$5 \to 2$	21.02	23.86	13.47
$4 \to 3$	51.02	61.93	21.38
$5 \to 3$	23.19	37.58	62.02
$5 \to 4$	35.63	47.33	32.85
Average absolute % deviation			20.12

sets of cross sections does not present any systematic pattern. Hence, retrieving the collisional coefficients of $HC^{17}O^+$ perturbed by H_2 by simply scaling those of HCO^+ and H_2 does not represent a reliable approach and would instead lead to misleading results in radiative transfer modeling of $HC^{17}O^+$ emission lines. We also expect a similar behavior for the $HC^{18}O^+$ isotopologue, since it features an even more pronounced shift of the center of mass with respect to the parent species. This test therefore points out the need of collisional data for isotopologues for their accurate astrophysical modeling.

6.4.2 Hyperfine Structure

As already mentioned in ¶ 2.2.4, in order to avoid the computational effort required for the recoupling approach, which indeed needs to store the spin-free elements of

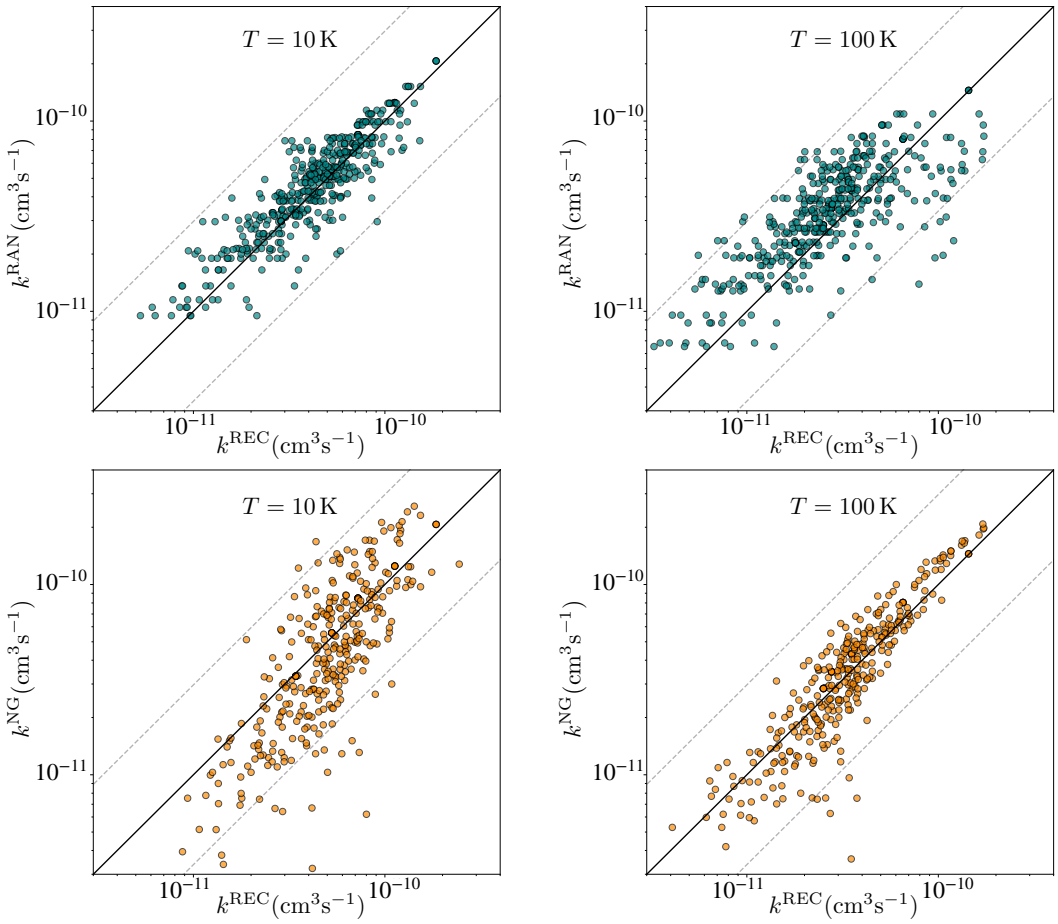

Figure 6.22: Comparison between $HC^{17}O^+-H_2$ recoupling hyperfine rate coefficients and those obtained using the RAN (top panels) and NG (bottom panels) approximations at 10 K (left panels) and 100 K (right panels). In each panel, the dashed lines delimit the region where the rate coefficients differ by less than a factor of 3.

the S–matrix and compute the opacity tensor between the rotational levels, approximations are frequently employed. Among them, the randomizing (RAN) and Neufeld & Green (NG, Neufeld and Green, 1994) strategies are the most commonly used. In order to assess the impact of these approximations on radiative transfer modeling, the outcomes of these three different methodologies are here compared for the $HC^{17}O^+$ and H_2 system. Albeit being approximate, the recoupling approach is considered almost exact (Lique and Faure, 2019) and has thus been used as the "reference" method in such comparison. The results are shown in Figure 6.22: while the RAN approximation performs better at low temperatures, the NG approach better approximates the collisional behavior at 100 K. Indeed, at 10 K, the collisions are slower and tend to stabilize a long lifetime $HC^{17}O^+-H_2$ complex in the potential well. In such conditions, the population of the energy levels evolves toward a randomized distribution according to the statistical weight of the final states (F') and

the assumption of neglecting rotational energy spacings compared to the collision energy effects (distinctive of the NG approximation) is no longer valid. Conversely, at high temperatures, the influence of the propensity rules given by the Wigner coefficients becomes increasingly prominent, thus making the NG approximation a viable alternative. Since the purpose of this work was to provide accurate results spanning a suitable temperature range to support future astrophysical modeling of $HC^{17}O^+$ in the ISM, the bias exhibited by the RAN and NG approximate methods with respect to the recoupling approach cannot be overlooked. The recoupling approach thus appears as the most reliable methodology to compute the hyperfine resolved rate coefficients for this collisional system.

6.5 Astrophysical Modeling

Once the state-to-state collisional rate coefficients are derived, it is possible to simulate the non-LTE behavior under the typical conditions of the ISM. This is achieved by means of radiative transfer calculations. Such investigations can be used either to simulate the already observed molecular transitions and refine the model of the targeted astrophysical object, or to predict the collisional behavior of the target molecule in sources where it has not yet been identified, thereby guiding future observations.

An illustrative application in this regard is provided by the investigation performed for PO^+ in collision with H_2, whose aim was to support the interpretation of recent and future observations in the ISM. Indeed, the derived dataset of collisional rate coefficients for this system enabled to simulate the low-j rotational lines of PO^+ at different astrophysical conditions, beyond the LTE approximation, including those of the molecular cloud where it has been recently observed (Rivilla et al., 2022b). From these simulations, different properties were extracted, including the relative excitation temperatures, the gas density and the molecular column density.

A spectral survey of the G+0.693-0.027 molecular cloud (Rivilla et al., 2022b) led to the observation of four different rotational transitions of PO^+, although only the $j = 1-0$ and $j = 2-1$ lines were not contaminated by other species. For this reason, some caution needs to be paid in modeling the distribution of the population among the rotational levels because of the very limited information. Radiative transfer calculations were performed using the RADEX code (van der Tak et al., 2007) for the derivation of the distribution of the population. The 19 lowest rotational states of PO^+ were considered, for which the energy levels, transition frequencies and the corresponding Einstein A coefficients[‡‡] were employed. The collisional information involved 374 transitions among the lowest 19 rotational levels and a temperature range from 5 K to 200 K. Since the structure and dynamics of the G+0.693-0.027

[‡‡]To derive the A coefficients, a PO^+ dipole moment of 3.13 D (Rivilla et al., 2022b) was used.

molecular cloud are not well constrained, the source geometry was approximated to a static sphere of uniform density. Moreover, the background temperature ($T_{\rm CMB}$) was set at 2.73 K and the line width at 18 km/s, in accordance with astronomical observations (Rivilla et al., 2022b). As a preliminary test, the variation of the ($j = 1-0$)/($j = 2-1$) intensity ratio as a function of both the kinetic temperature (T_k) and the density of hydrogen ($n(\mathrm{H_2})$) was examined. The outcome of this analysis is shown in Figure 6.23, where the isocurve corresponding to the observed intensity ratio (0.64) is marked in red. Here, the weak constraint of the T_k on $n(\mathrm{H_2})$ is

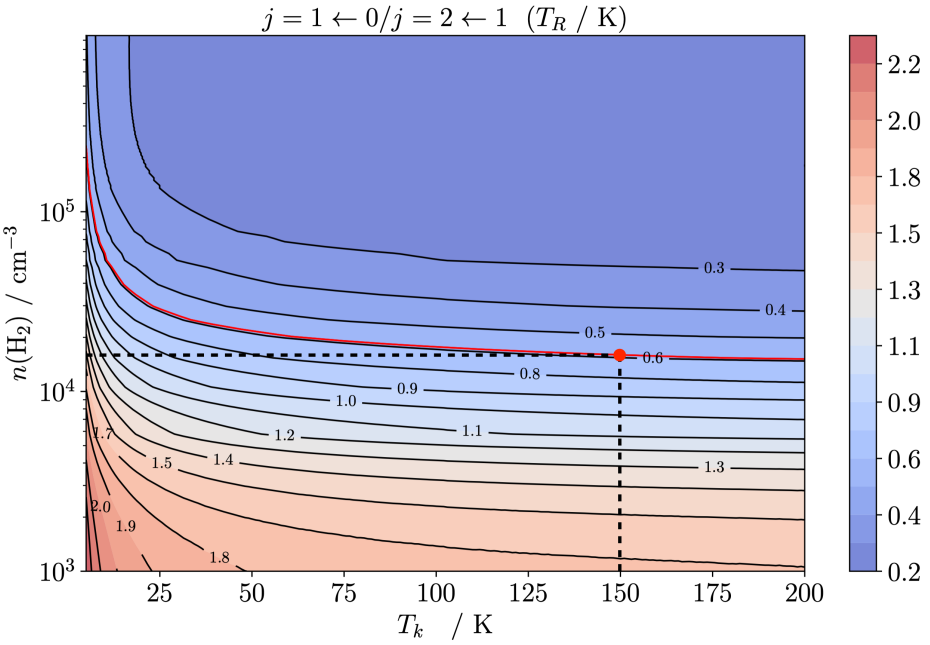

Figure 6.23: Contour plot of the variation of the $j = 1-0/j = 2-1$ intensity ratio with respect to T_k (x axis) and $n(\mathrm{H_2})$ (y axis). The isocurve of the intensity ratio observed by Rivilla et al. (2022b) is highlighted in red.

evident, in particular for $T_k > 100$ K. This small dependence of T_k on the density of hydrogen has the effect to ease the estimate of the gas density of G+0.693-0.027, irrespective of the possible inaccuracies of $T_k \sim 150$ K. The resulting density is $n(\mathrm{H_2}) \sim 1.5 \times 10^4\,\mathrm{cm^{-3}}$, a value in good agreement with the previous estimate by Zeng et al. (2020) of $\sim 1 \times 10^4\,\mathrm{cm^{-3}}$. In Figure 6.24, the line intensity trends for the two transitions, at 150 K, as a function of $n(\mathrm{H_2})$ and the column density (N) are depicted. From their analysis and the previously derived value of the gas density, the molecular column density is thus retrieved: $N \sim 3.7 \times 10^{11}\,\mathrm{cm^{-2}}$, which is $\sim 60\%$ (a factor of ~ 1.7) lower than that retrieved from LTE assumption (Rivilla et al., 2022b). In fact, the LTE model tends to underestimate the population of the higher-energy levels, therefore requiring a higher column density to reproduce the observed intensities. As a consequence, the ionization rate, governed by the

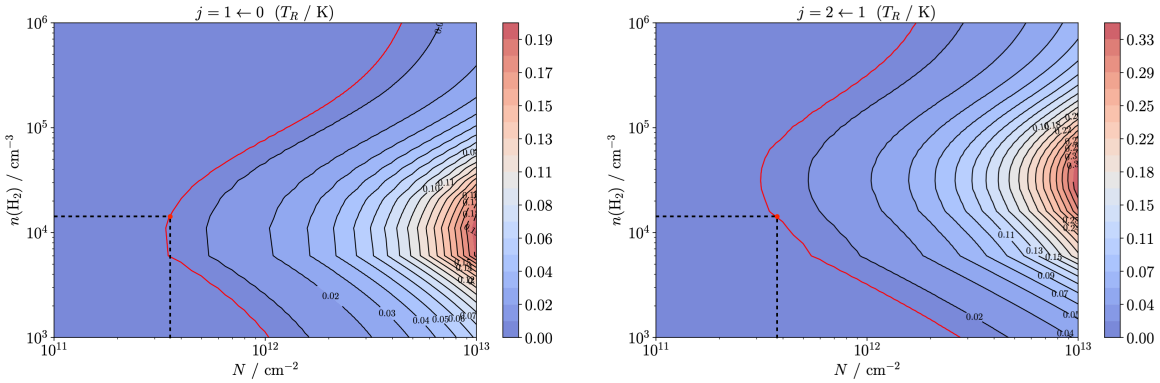

Figure 6.24: Contour plot of the variation of the $j = 1 - 0$ and $j = 2 - 1$ intensities with respect to the column density (x axis) and $n(H_2)$ (y axis). The isocurves of the two intensities observed by Rivilla et al. (2022b) are highlighted in red.

$N(PO^+)/N(PO)$ ratio, decreases with respect to the previously predicted value. The results of our analysis can be also exploited in future observations of the PO^+

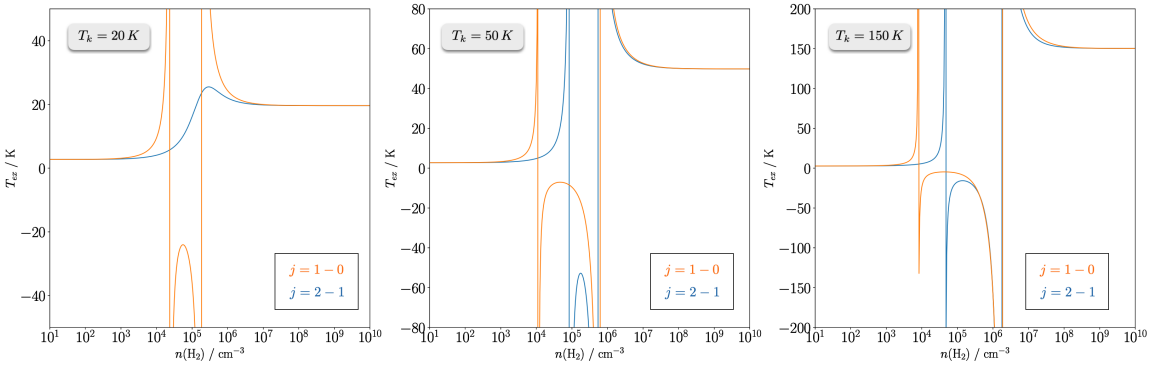

Figure 6.25: Variation of excitation temperature as a function of $n(H_2)$ for the first two transitions of PO^+ at $T_k = 20, 50$ and 150 K.

ion in different astrophysical sources. Therefore, a wider range of densities and kinetic temperatures was investigated, whose results are presented in Figure 6.25. Here, the trend of the T_{ex} of the $j = 1 - 0$ and $j = 2 - 1$ transitions as function of $n(H_2)$ for three different values of T_k is reported. It can be seen that, for densities around 10^5 cm^{-3}, maser phenomena are predicted because of an inversion of the population between the levels. Interestingly, even at $T_k = 150$ K, densities of H_2 up to 10^7 cm^{-3} are still inadequate to thermalize the first two rotational transitions of PO^+. This could have strong implications on the predictions of the line intensities of this ion for all possible types of environment (from diffuse clouds to hot cores), and points out the importance of collisional data for a reliable radiative modeling.

Chapter 7

Conclusions and Perspectives

In the last decades, the advances in the field of radioastronomy have brought a substantial amount of spectral data to the scientific community. The accurate interpretation of these data to derive the chemical and physical properties of the observed media represents a focal point for astrochemical studies. In this regard, the availability of fundamental molecular data that accurately describe the ongoing processes at the microscopic scale is essential. Specifically, understanding the collisional behavior of the observed molecules with the most abundant perturbers in their surrounding environment plays a crucial role.

This thesis work presents and validates an accurate yet affordable computational procedure for the characterization of the collisional properties of astrochemical molecules and subsequent modeling of their spectroscopic transitions in terms of abundance. Particular attention is directed to ensure the applicability and versatility of this procedure across a wide range of astrochemical environments. This has led to three publications, *i.e.*, Tonolo et al. (2021, 2022, 2024), two articles in preparation regarding the $HC^{18}O^+$/Ar and HCN/N_2 systems and one ongoing project for HC_3N perturbed by N_2.

This computational procedure consists of four main steps. The first one is the investigation of the collisional PES, which exploits the excellent performances of explicitly correlated coupled cluster methods to describe interaction energies. In this regard, the HCO^+ and He collisional system provided an excellent test case to benchmark different level of theories using previously computed results and available experimental data. The computed rotational frequencies of the corresponding lowest-lying bound state compared well with their experimental counterparts (Salomon et al., 2019), with deviations always lower than 0.12%. The computed

pressure broadening coefficients, moreover, showed a good agreement with the previously experimentally measured values for the $j = 4 \leftarrow 3$, $j = 5 \leftarrow 4$ and $j = 6 \leftarrow 5$ rotational lines (Buffa et al., 2008).

The second step consists of expressing the potential as an expansion over angular functions. This requires to resort to some approximations to reduce the computational cost of scattering calculations. This applies, in particular, to systems involving a collisional partner with a rotational structure such as H_2 and N_2. In these cases, the effects due to the coupling between the different rotational states of the collider on the inelastic cross sections need to be preliminary assessed. This brings important hints on the feasibility of neglecting the $j > 0$ rotational states of the collider (the so-called "spherical approximation"). The reduced computational cost of this approximation, if properly validated, permits to extend this procedure to larger molecular systems and to a wide range of astrochemical conditions. The impact of the $j > 0$ rotational levels of H_2 resulted to be considerably weak in interactions with $HC^{17}O^+$ and PO^+ (the inclusion of the $j = 2$ state of H_2 led to average deviations of $\sim 7\%$ in the values of the cross sections, while the cross sections of *para*-H_2 and *ortho*-H_2 agreed within $\sim 12\%$ on average). Conversely, the rotational structure of N_2 affects much more the energy involved in collisions with HCN and HC_3N. In detail, the values of the inelastic cross section showed average deviations of $\sim 30\%$ between the $j = 0$ and $j = 0, 2$ states of N_2 and of $\sim 55\%$ between its *ortho*- and *para*-states.

The third step is the solution of the close-coupling scattering equations in a range of energies that allows to derive the corresponding collisional parameters in the conditions of interest. For example, the pressure broadening and pressure shift parameters can be computed, and can be subsequently used to infer the quality of the potential (as performed for the HCO^+/He, HCN/N_2 and HC_3N/N_2 systems) and to refine the molecular rest frequencies (as in the case of the $HC^{18}O^+$ molecule). Given the considerations presented above, particular attention was paid to test the spherical potential approximation for the HCN and HC_3N molecules perturbed by N_2. Our theoretically computed values of the pressure broadening coefficients for the $j = 1 - 0$ transition of HCN and the $j = 10 - 9$ transition of HC_3N compare well with their experimental counterparts (pressure broadening experiments). They show deviations of 9% and 1%, respectively. These results validated the spherical approximation of the potential for these systems. In fact, while impacting significantly on the inelastic cross-section values, the influence of this approximation on thermally averaged quantities as the macroscopic pressure broadening coefficients are comparatively small. To enhance the feasibility of the spherical approximation, additional pressure broadening measurements for other transitions of HCN and HC_3N are currently under development. The theoretical-experimental comparison of the derived coefficients would thus support the applicability of this strategy also to other target

molecules. Indeed, in addition to a substantial reduction in terms of computational cost, this approximation provided reliable data to attempt the non-LTE modeling of molecular abundances in the Titan's atmosphere.

From the scattering calculations, the inelastic state-to-state rate coefficients are also obtained. If the rotational spectrum of the target molecular system presents a hyperfine structure due to nuclear quadruple coupling, recoupling techniques represent a viable route to decouple the effect of the nuclear spin from the angular dynamics of collisions. This approach leads to the corresponding hyperfine-resolved state-to-state rate coefficients.

The last step consists in using the collisional rate coefficients to model the rotational transitions observed in interstellar environments and planetary atmospheres, by means of radiative transfer calculations. Specifically, this thesis highlights the need of collisional parameters to model the astrophysical environments whose conditions deviate from the LTE assumption. For example, the computed collisional dataset for the PO^+/H_2 system helped to improve the derivation of the abundance of PO^+ in the G+0.693-0.027 molecular cloud, thus suggesting the need of extending this approach to a large number of molecular systems and astronomical objects.

Future perspectives of this thesis work concern the extension of collisional calculations to a wider range of molecules, including heavier ions (*e.g.*, $HCCS^+$, H_2COH^+, $H_2C_3H^+$, H_2NCO^+), longer carbon-chains such as HC_7N, or medium-sized COMs. Among the latter, a molecular system that might serve as a good candidate for the computation of collisional rate coefficients is ethanimine (CH_3CHNH). The first detection of ethanimine in space dates back to 2013 (Loomis et al., 2013), when both its isomers were identified toward the star-forming region Sagittarius B2. However, this molecule showed a clear non-LTE behavior, thus hampering the retrieval of its reliable abundance. The same issue is showed by methylamine (CH_3NH_2; Bøgelund et al. 2019) and could be a general feature for molecules with similar moieties, such as N-methyl methanimine (CH_3NCH_2). Moreover, additional studies could be directed to investigate environments different from those considered in this thesis work, such as cometary comas. In these cases, other collisional partners need to be taken in account, *e.g.*, CO or H_2O. The limited amount of collisional data for such systems highlights the need for dedicated theoretical studies. Further investigations in this direction will also help to refine our methodology, with the goal of expanding its domain of application.

Appendices

Appendix A: Full List of Computed Rate Coefficients

HCO^+ and He collisional system:

Table 1: Integrated rate coefficients $j \rightarrow j'$ from 5 to 100 K. Units are 10^{-10} cm^3 s^{-1}.

$j \rightarrow j'$	Temperature / K									
	5	10	15	20	25	30	35	40	45	50
1 → 0	1.368	1.188	1.104	1.056	1.026	1.006	0.992	0.983	0.977	0.972
2 → 0	0.687	0.625	0.577	0.542	0.516	0.495	0.477	0.462	0.448	0.436
2 → 1	1.670	1.641	1.594	1.556	1.527	1.504	1.487	1.473	1.463	1.456
3 → 0	0.278	0.277	0.266	0.254	0.243	0.234	0.226	0.220	0.215	0.210
3 → 1	1.030	1.002	0.966	0.929	0.895	0.865	0.838	0.814	0.792	0.773
3 → 2	1.683	1.659	1.635	1.618	1.606	1.598	1.593	1.591	1.592	1.594
4 → 0	0.185	0.177	0.169	0.162	0.155	0.150	0.145	0.140	0.137	0.133
4 → 1	0.466	0.475	0.479	0.479	0.477	0.475	0.474	0.472	0.471	0.471
4 → 2	1.177	1.161	1.128	1.095	1.065	1.039	1.015	0.993	0.973	0.955
4 → 3	1.711	1.680	1.648	1.628	1.616	1.610	1.609	1.609	1.612	1.617
5 → 0	0.146	0.139	0.138	0.138	0.139	0.140	0.141	0.141	0.142	0.142
5 → 1	0.412	0.388	0.373	0.364	0.356	0.350	0.344	0.338	0.333	0.328
5 → 2	0.675	0.665	0.660	0.658	0.657	0.656	0.654	0.653	0.652	0.650
5 → 3	1.122	1.143	1.139	1.125	1.109	1.091	1.073	1.055	1.039	1.023
5 → 4	1.767	1.714	1.653	1.608	1.579	1.561	1.550	1.546	1.545	1.547

$j \rightarrow j'$	Temperature / K									
	55	60	65	70	75	80	85	90	95	100
1 → 0	0.970	0.968	0.967	0.967	0.967	0.968	0.968	0.969	0.970	0.971
2 → 0	0.425	0.416	0.407	0.398	0.391	0.384	0.378	0.372	0.367	0.362
2 → 1	1.450	1.446	1.444	1.443	1.443	1.444	1.446	1.448	1.450	1.454
3 → 0	0.207	0.204	0.202	0.200	0.199	0.198	0.198	0.198	0.198	0.198
3 → 1	0.756	0.740	0.727	0.714	0.703	0.693	0.684	0.676	0.669	0.663
3 → 2	1.597	1.601	1.606	1.612	1.618	1.625	1.632	1.639	1.647	1.654
4 → 0	0.131	0.128	0.126	0.124	0.123	0.122	0.121	0.120	0.119	0.118
4 → 1	0.471	0.471	0.472	0.473	0.474	0.476	0.477	0.479	0.481	0.482
4 → 2	0.939	0.924	0.911	0.898	0.887	0.877	0.868	0.859	0.851	0.844
4 → 3	1.622	1.628	1.635	1.642	1.650	1.658	1.666	1.674	1.682	1.690
5 → 0	0.142	0.143	0.143	0.143	0.143	0.143	0.143	0.143	0.143	0.143
5 → 1	0.324	0.320	0.316	0.313	0.310	0.307	0.304	0.302	0.300	0.298
5 → 2	0.649	0.648	0.648	0.647	0.646	0.646	0.646	0.646	0.645	0.645
5 → 3	1.008	0.994	0.981	0.969	0.958	0.948	0.939	0.930	0.922	0.915
5 → 4	1.550	1.556	1.562	1.570	1.577	1.586	1.594	1.603	1.612	1.621

$HC^{17}O^+$ and H_2 collisional system:

Table 2: Integrated rate coefficients $j \rightarrow j'$ from 5 to 50 K. Units are 10^{-10} cm^3 s^{-1}.

$j \rightarrow j'$	Temperature / K									
	5	10	15	20	25	30	35	40	45	50
1 1.5 → 0 2.5	2.069	1.851	1.724	1.639	1.579	1.536	1.504	1.481	1.464	1.452
1 2.5 → 0 2.5	2.069	1.851	1.724	1.639	1.579	1.536	1.504	1.481	1.464	1.452
1 2.5 → 1 1.5	1.253	1.086	0.964	0.877	0.809	0.754	0.708	0.669	0.635	0.605
1 2.5 → 1 3.5	2.787	2.445	2.182	1.990	1.843	1.725	1.627	1.544	1.472	1.409
1 3.5 → 0 2.5	2.069	1.851	1.724	1.639	1.579	1.536	1.504	1.481	1.464	1.452
1 3.5 → 1 1.5	1.540	1.366	1.223	1.118	1.039	0.975	0.923	0.879	0.841	0.809
2 0.5 → 0 2.5	1.248	1.126	1.056	1.002	0.958	0.919	0.885	0.855	0.829	0.805
2 0.5 → 1 1.5	0.981	0.961	0.974	0.998	1.026	1.055	1.084	1.112	1.139	1.165
2 0.5 → 1 2.5	0.834	0.801	0.740	0.686	0.641	0.603	0.571	0.543	0.518	0.495
2 0.5 → 1 3.5	1.604	1.363	1.213	1.107	1.026	0.963	0.911	0.868	0.832	0.800
2 1.5 → 0 2.5	1.248	1.126	1.056	1.002	0.958	0.919	0.885	0.855	0.829	0.805
2 1.5 → 1 1.5	0.854	0.833	0.830	0.836	0.847	0.859	0.873	0.887	0.901	0.914
2 1.5 → 1 2.5	1.037	0.974	0.919	0.878	0.847	0.824	0.805	0.790	0.777	0.767
2 1.5 → 1 3.5	1.529	1.318	1.178	1.077	1.000	0.939	0.888	0.846	0.810	0.779
2 1.5 → 2 0.5	0.435	0.392	0.363	0.342	0.325	0.312	0.300	0.291	0.282	0.274
2 1.5 → 2 4.5	1.486	1.396	1.279	1.177	1.092	1.021	0.962	0.913	0.871	0.835
2 2.5 → 0 2.5	1.248	1.126	1.056	1.002	0.958	0.919	0.885	0.855	0.829	0.805
2 2.5 → 1 1.5	0.704	0.677	0.651	0.633	0.620	0.611	0.605	0.601	0.597	0.595
2 2.5 → 1 2.5	1.255	1.160	1.109	1.080	1.064	1.055	1.050	1.049	1.049	1.051
2 2.5 → 1 3.5	1.451	1.285	1.165	1.077	1.009	0.955	0.910	0.873	0.841	0.813
2 2.5 → 2 0.5	0.519	0.450	0.399	0.364	0.338	0.318	0.302	0.289	0.279	0.270
2 2.5 → 2 1.5	0.735	0.674	0.626	0.587	0.555	0.528	0.505	0.484	0.466	0.450
2 2.5 → 2 4.5	1.671	1.535	1.400	1.288	1.198	1.123	1.061	1.008	0.962	0.923
2 3.5 → 0 2.5	1.248	1.126	1.056	1.002	0.958	0.919	0.885	0.855	0.829	0.805
2 3.5 → 1 1.5	0.644	0.587	0.534	0.492	0.458	0.431	0.407	0.388	0.370	0.355
2 3.5 → 1 2.5	1.327	1.209	1.152	1.121	1.104	1.095	1.092	1.091	1.093	1.096
2 3.5 → 1 3.5	1.442	1.327	1.240	1.177	1.131	1.095	1.067	1.044	1.025	1.009
2 3.5 → 2 0.5	0.322	0.299	0.276	0.257	0.240	0.226	0.214	0.203	0.193	0.184
2 3.5 → 2 1.5	0.790	0.708	0.639	0.586	0.544	0.511	0.484	0.461	0.442	0.426
2 3.5 → 2 2.5	1.173	1.057	0.959	0.883	0.825	0.779	0.741	0.710	0.683	0.661
2 3.5 → 2 4.5	1.950	1.756	1.594	1.470	1.372	1.292	1.227	1.171	1.123	1.082
2 4.5 → 0 2.5	1.248	1.126	1.056	1.002	0.958	0.919	0.885	0.855	0.829	0.805
2 4.5 → 1 1.5	0.802	0.682	0.607	0.553	0.513	0.481	0.456	0.434	0.416	0.400
2 4.5 → 1 2.5	1.015	0.909	0.823	0.757	0.704	0.662	0.626	0.596	0.570	0.547
2 4.5 → 1 3.5	1.603	1.534	1.497	1.481	1.476	1.478	1.484	1.493	1.503	1.513
2 4.5 → 2 0.5	1.957	0.891	0.591	0.452	0.372	0.320	0.284	0.256	0.236	0.219
3 0.5 → 0 2.5	0.848	0.724	0.644	0.588	0.546	0.513	0.487	0.465	0.447	0.431
3 0.5 → 1 1.5	0.905	0.819	0.764	0.728	0.702	0.682	0.665	0.650	0.636	0.625
3 0.5 → 1 2.5	0.529	0.502	0.476	0.453	0.432	0.414	0.397	0.382	0.368	0.356
3 0.5 → 1 3.5	1.025	0.853	0.746	0.675	0.626	0.588	0.559	0.535	0.515	0.498
3 0.5 → 2 0.5	0.409	0.437	0.472	0.509	0.545	0.581	0.616	0.650	0.683	0.714
3 0.5 → 2 1.5	0.548	0.544	0.541	0.540	0.540	0.541	0.542	0.542	0.543	0.543
3 0.5 → 2 2.5	0.791	0.747	0.691	0.643	0.602	0.569	0.541	0.518	0.497	0.480
3 0.5 → 2 3.5	0.739	0.735	0.694	0.652	0.616	0.585	0.559	0.535	0.515	0.497
3 0.5 → 2 4.5	1.238	1.083	0.966	0.877	0.808	0.754	0.711	0.676	0.648	0.624
3 1.5 → 0 2.5	0.848	0.724	0.644	0.588	0.546	0.513	0.487	0.465	0.447	0.431
3 1.5 → 1 1.5	0.789	0.717	0.670	0.639	0.615	0.596	0.581	0.567	0.554	0.543
3 1.5 → 1 2.5	0.679	0.623	0.582	0.550	0.525	0.503	0.484	0.467	0.453	0.440
3 1.5 → 1 3.5	0.990	0.834	0.734	0.668	0.620	0.584	0.555	0.532	0.512	0.496
3 1.5 → 2 0.5	0.314	0.322	0.331	0.342	0.353	0.364	0.375	0.385	0.395	0.404
3 1.5 → 2 1.5	0.633	0.635	0.640	0.647	0.658	0.672	0.686	0.701	0.717	0.733
3 1.5 → 2 2.5	0.711	0.697	0.669	0.644	0.623	0.606	0.592	0.579	0.569	0.559
3 1.5 → 2 3.5	0.882	0.838	0.776	0.722	0.676	0.639	0.608	0.581	0.559	0.539
3 1.5 → 2 4.5	1.185	1.056	0.949	0.867	0.802	0.750	0.709	0.675	0.647	0.624
3 1.5 → 3 0.5	0.342	0.326	0.307	0.293	0.282	0.273	0.266	0.260	0.255	0.250
3 1.5 → 3 5.5	0.898	0.913	0.868	0.819	0.776	0.739	0.707	0.680	0.655	0.633
3 2.5 → 0 2.5	0.848	0.724	0.644	0.588	0.546	0.513	0.487	0.465	0.447	0.431
3 2.5 → 1 1.5	0.630	0.576	0.539	0.513	0.493	0.476	0.462	0.449	0.438	0.428
3 2.5 → 1 2.5	0.870	0.777	0.715	0.672	0.640	0.614	0.593	0.574	0.559	0.544
3 2.5 → 1 3.5	0.958	0.821	0.732	0.672	0.628	0.593	0.565	0.542	0.523	0.506
3 2.5 → 2 0.5	0.257	0.247	0.234	0.223	0.213	0.205	0.198	0.191	0.186	0.180
3 2.5 → 2 1.5	0.576	0.580	0.581	0.584	0.590	0.598	0.608	0.619	0.631	0.642
3 2.5 → 2 2.5	0.743	0.746	0.742	0.741	0.743	0.747	0.752	0.759	0.766	0.774
3 2.5 → 2 3.5	1.011	0.936	0.864	0.806	0.760	0.723	0.692	0.667	0.646	0.628
3 2.5 → 2 4.5	1.136	1.037	0.944	0.868	0.807	0.758	0.718	0.685	0.657	0.634
3 2.5 → 3 0.5	0.250	0.241	0.230	0.219	0.209	0.201	0.193	0.187	0.182	0.177
3 2.5 → 3 1.5	0.499	0.493	0.475	0.456	0.439	0.425	0.412	0.401	0.392	0.383
3 2.5 → 3 5.5	0.828	0.887	0.862	0.824	0.788	0.755	0.726	0.700	0.677	0.656
3 3.5 → 0 2.5	0.848	0.724	0.644	0.588	0.546	0.513	0.487	0.465	0.447	0.431
3 3.5 → 1 1.5	0.480	0.439	0.409	0.386	0.368	0.353	0.340	0.329	0.319	0.310
3 3.5 → 1 2.5	1.013	0.889	0.810	0.758	0.721	0.692	0.668	0.649	0.632	0.617
3 3.5 → 1 3.5	0.964	0.846	0.767	0.713	0.671	0.638	0.611	0.588	0.569	0.551
3 3.5 → 2 0.5	0.243	0.231	0.214	0.198	0.185	0.174	0.165	0.158	0.151	0.146

(continued)

(continued)

$j \rightarrow j'$	Temperature / K									
	5	10	15	20	25	30	35	40	45	50
3 3.5 → 2 1.5	0.429	0.418	0.398	0.380	0.364	0.350	0.338	0.327	0.316	0.307
3 3.5 → 2 2.5	0.847	0.831	0.820	0.816	0.819	0.826	0.837	0.850	0.864	0.879
3 3.5 → 2 3.5	1.077	1.010	0.959	0.922	0.897	0.878	0.865	0.856	0.850	0.846
3 3.5 → 2 4.5	1.128	1.056	0.974	0.905	0.848	0.802	0.764	0.732	0.705	0.681
3 3.5 → 3 0.5	0.171	0.178	0.176	0.171	0.165	0.158	0.153	0.147	0.142	0.138
3 3.5 → 3 1.5	0.391	0.386	0.370	0.354	0.339	0.326	0.315	0.305	0.296	0.288
3 3.5 → 3 2.5	0.659	0.644	0.613	0.584	0.561	0.541	0.524	0.510	0.497	0.486
3 3.5 → 3 4.5	1.059	1.042	0.989	0.938	0.894	0.858	0.826	0.799	0.776	0.755
3 3.5 → 3 5.5	0.956	0.972	0.940	0.900	0.861	0.827	0.796	0.768	0.744	0.721
3 4.5 → 0 2.5	0.848	0.724	0.644	0.588	0.546	0.513	0.487	0.465	0.447	0.431
3 4.5 → 1 1.5	0.414	0.365	0.332	0.308	0.289	0.274	0.261	0.250	0.241	0.232
3 4.5 → 1 2.5	0.984	0.857	0.777	0.724	0.687	0.658	0.634	0.615	0.598	0.584
3 4.5 → 1 3.5	1.061	0.952	0.878	0.825	0.785	0.752	0.725	0.701	0.681	0.663
3 4.5 → 2 0.5	0.184	0.181	0.170	0.160	0.151	0.143	0.136	0.131	0.126	0.121
3 4.5 → 2 1.5	0.477	0.441	0.403	0.371	0.345	0.324	0.307	0.293	0.281	0.270
3 4.5 → 2 2.5	0.763	0.698	0.642	0.597	0.561	0.532	0.508	0.488	0.470	0.455
3 4.5 → 2 3.5	1.100	1.075	1.062	1.059	1.064	1.075	1.089	1.106	1.125	1.144
3 4.5 → 2 4.5	1.200	1.151	1.088	1.034	0.991	0.956	0.928	0.904	0.885	0.868
3 4.5 → 3 0.5	0.142	0.143	0.139	0.134	0.129	0.124	0.121	0.117	0.114	0.111
3 4.5 → 3 1.5	0.310	0.318	0.309	0.297	0.284	0.273	0.263	0.254	0.246	0.238
3 4.5 → 3 2.5	0.540	0.545	0.524	0.500	0.477	0.456	0.438	0.422	0.407	0.394
3 4.5 → 3 5.5	1.158	1.157	1.116	1.069	1.025	0.987	0.952	0.922	0.894	0.870
3 5.5 → 0 2.5	0.848	0.724	0.644	0.588	0.546	0.513	0.487	0.465	0.447	0.431
3 5.5 → 1 1.5	0.519	0.431	0.376	0.340	0.315	0.296	0.281	0.269	0.259	0.250
3 5.5 → 1 2.5	0.623	0.550	0.499	0.462	0.434	0.411	0.392	0.376	0.362	0.349
3 5.5 → 1 3.5	1.316	1.193	1.111	1.055	1.012	0.977	0.947	0.922	0.899	0.879
3 5.5 → 2 0.5	0.252	0.219	0.195	0.177	0.162	0.151	0.143	0.136	0.130	0.125
3 5.5 → 2 1.5	0.464	0.416	0.375	0.343	0.318	0.298	0.281	0.268	0.257	0.248
3 5.5 → 2 2.5	0.665	0.617	0.565	0.521	0.486	0.457	0.433	0.413	0.397	0.382
3 5.5 → 2 3.5	0.918	0.871	0.810	0.756	0.712	0.675	0.644	0.618	0.595	0.574
3 5.5 → 2 4.5	1.424	1.424	1.420	1.424	1.434	1.449	1.467	1.487	1.507	1.528
3 5.5 → 3 0.5	0.152	0.154	0.146	0.137	0.130	0.123	0.117	0.112	0.108	0.104
4 1.5 → 0 2.5	0.557	0.528	0.494	0.462	0.434	0.411	0.391	0.374	0.360	0.348
4 1.5 → 1 1.5	0.410	0.394	0.373	0.355	0.339	0.327	0.316	0.308	0.301	0.295
4 1.5 → 1 2.5	0.377	0.390	0.379	0.363	0.347	0.332	0.318	0.306	0.295	0.285
4 1.5 → 1 3.5	0.746	0.661	0.597	0.550	0.514	0.486	0.464	0.447	0.433	0.421
4 1.5 → 2 0.5	0.404	0.386	0.375	0.365	0.357	0.350	0.344	0.338	0.334	0.330
4 1.5 → 2 1.5	0.525	0.479	0.449	0.426	0.409	0.395	0.383	0.373	0.365	0.357
4 1.5 → 2 2.5	0.586	0.541	0.505	0.475	0.449	0.427	0.408	0.392	0.378	0.366
4 1.5 → 2 3.5	0.523	0.531	0.515	0.493	0.473	0.454	0.437	0.421	0.408	0.395
4 1.5 → 2 4.5	0.817	0.733	0.672	0.625	0.588	0.558	0.532	0.510	0.490	0.472
4 1.5 → 3 0.5	0.342	0.354	0.382	0.413	0.444	0.474	0.503	0.531	0.558	0.584
4 1.5 → 3 1.5	0.505	0.519	0.527	0.535	0.541	0.548	0.555	0.561	0.568	0.575
4 1.5 → 3 2.5	0.507	0.505	0.496	0.484	0.471	0.459	0.447	0.437	0.428	0.420
4 1.5 → 3 3.5	0.587	0.554	0.527	0.503	0.481	0.462	0.445	0.430	0.417	0.406
4 1.5 → 3 4.5	0.654	0.596	0.549	0.512	0.482	0.457	0.437	0.419	0.404	0.391
4 1.5 → 3 5.5	0.874	0.799	0.740	0.694	0.657	0.627	0.601	0.578	0.558	0.539
4 1.5 → 4 6.5	0.467	0.551	0.553	0.534	0.511	0.488	0.467	0.447	0.430	0.414
4 2.5 → 0 2.5	0.557	0.528	0.494	0.462	0.434	0.411	0.391	0.374	0.360	0.348
4 2.5 → 1 1.5	0.365	0.357	0.340	0.323	0.309	0.297	0.287	0.279	0.272	0.266
4 2.5 → 1 2.5	0.456	0.448	0.426	0.404	0.384	0.368	0.353	0.341	0.330	0.320
4 2.5 → 1 3.5	0.711	0.641	0.584	0.541	0.507	0.480	0.459	0.441	0.427	0.415
4 2.5 → 2 0.5	0.272	0.249	0.234	0.223	0.215	0.208	0.202	0.197	0.192	0.189
4 2.5 → 2 1.5	0.560	0.531	0.509	0.489	0.472	0.458	0.445	0.434	0.425	0.417
4 2.5 → 2 2.5	0.583	0.553	0.524	0.500	0.479	0.462	0.447	0.434	0.422	0.412
4 2.5 → 2 3.5	0.659	0.620	0.582	0.549	0.521	0.496	0.475	0.457	0.441	0.426
4 2.5 → 2 4.5	0.781	0.718	0.665	0.623	0.589	0.560	0.535	0.513	0.494	0.477
4 2.5 → 3 0.5	0.223	0.228	0.224	0.219	0.213	0.207	0.202	0.197	0.192	0.188
4 2.5 → 3 1.5	0.443	0.448	0.473	0.500	0.527	0.553	0.579	0.604	0.628	0.652
4 2.5 → 3 2.5	0.631	0.625	0.623	0.622	0.622	0.624	0.627	0.630	0.635	0.639
4 2.5 → 3 3.5	0.605	0.583	0.559	0.537	0.517	0.499	0.484	0.471	0.458	0.448
4 2.5 → 3 4.5	0.717	0.666	0.625	0.591	0.562	0.537	0.516	0.498	0.481	0.467
4 2.5 → 3 5.5	0.850	0.776	0.718	0.672	0.636	0.606	0.580	0.558	0.538	0.520
4 2.5 → 4 1.5	0.489	0.434	0.406	0.391	0.381	0.373	0.366	0.361	0.356	0.351
4 2.5 → 4 6.5	0.501	0.574	0.574	0.555	0.533	0.511	0.491	0.472	0.455	0.439
4 3.5 → 0 2.5	0.557	0.528	0.494	0.462	0.434	0.411	0.391	0.374	0.360	0.348
4 3.5 → 1 1.5	0.321	0.317	0.303	0.289	0.276	0.264	0.255	0.246	0.239	0.233
4 3.5 → 1 2.5	0.537	0.506	0.473	0.445	0.422	0.403	0.387	0.375	0.364	0.355
4 3.5 → 1 3.5	0.675	0.622	0.574	0.534	0.503	0.477	0.457	0.439	0.425	0.413
4 3.5 → 2 0.5	0.195	0.177	0.163	0.152	0.143	0.136	0.130	0.125	0.120	0.117
4 3.5 → 2 1.5	0.457	0.438	0.420	0.403	0.388	0.376	0.365	0.355	0.347	0.339
4 3.5 → 2 2.5	0.655	0.628	0.603	0.580	0.560	0.543	0.528	0.515	0.504	0.493
4 3.5 → 2 3.5	0.780	0.708	0.655	0.614	0.582	0.554	0.531	0.512	0.494	0.479
4 3.5 → 2 4.5	0.767	0.720	0.675	0.635	0.602	0.574	0.550	0.528	0.509	0.492
4 3.5 → 3 0.5	0.146	0.143	0.139	0.135	0.130	0.126	0.122	0.118	0.115	0.112
4 3.5 → 3 1.5	0.382	0.376	0.363	0.350	0.338	0.327	0.317	0.308	0.300	0.293
4 3.5 → 3 2.5	0.588	0.580	0.597	0.619	0.642	0.666	0.691	0.715	0.740	0.764
4 3.5 → 3 3.5	0.743	0.726	0.711	0.700	0.692	0.687	0.683	0.681	0.680	0.680
4 3.5 → 3 4.5	0.773	0.734	0.700	0.669	0.642	0.618	0.598	0.579	0.563	0.548
4 3.5 → 3 5.5	0.837	0.767	0.712	0.668	0.632	0.602	0.577	0.555	0.536	0.518

(continued)

(continued)

$j \rightarrow j'$	Temperature / K									
	5	10	15	20	25	30	35	40	45	50
4 3.5 → 4 1.5	0.305	0.292	0.282	0.274	0.267	0.261	0.254	0.249	0.243	0.238
4 3.5 → 4 2.5	0.561	0.513	0.483	0.464	0.451	0.440	0.431	0.423	0.416	0.409
4 3.5 → 4 6.5	0.566	0.621	0.617	0.598	0.576	0.555	0.535	0.516	0.499	0.484
4 4.5 → 0 2.5	0.557	0.528	0.494	0.462	0.434	0.411	0.391	0.374	0.360	0.348
4 4.5 → 1 1.5	0.293	0.289	0.275	0.261	0.248	0.237	0.228	0.219	0.212	0.206
4 4.5 → 1 2.5	0.589	0.542	0.501	0.468	0.443	0.423	0.407	0.394	0.383	0.375
4 4.5 → 1 3.5	0.650	0.614	0.574	0.538	0.509	0.485	0.464	0.447	0.433	0.421
4 4.5 → 2 0.5	0.163	0.157	0.149	0.141	0.134	0.127	0.122	0.117	0.112	0.109
4 4.5 → 2 1.5	0.317	0.298	0.279	0.263	0.250	0.239	0.230	0.222	0.215	0.209
4 4.5 → 2 2.5	0.695	0.654	0.622	0.595	0.572	0.552	0.535	0.521	0.508	0.496
4 4.5 → 2 3.5	0.875	0.799	0.747	0.707	0.675	0.648	0.626	0.607	0.590	0.576
4 4.5 → 2 4.5	0.806	0.763	0.718	0.679	0.645	0.616	0.590	0.568	0.549	0.531
4 4.5 → 3 0.5	0.145	0.135	0.128	0.121	0.115	0.110	0.106	0.102	0.099	0.097
4 4.5 → 3 1.5	0.274	0.259	0.246	0.234	0.224	0.215	0.206	0.199	0.193	0.187
4 4.5 → 3 2.5	0.509	0.494	0.472	0.452	0.434	0.419	0.405	0.392	0.381	0.371
4 4.5 → 3 3.5	0.808	0.790	0.801	0.820	0.841	0.864	0.888	0.912	0.936	0.960
4 4.5 → 3 4.5	0.879	0.853	0.829	0.808	0.791	0.777	0.766	0.756	0.748	0.740
4 4.5 → 3 5.5	0.853	0.794	0.746	0.705	0.671	0.642	0.617	0.595	0.576	0.559
4 4.5 → 4 1.5	0.221	0.223	0.218	0.211	0.205	0.199	0.193	0.188	0.183	0.178
4 4.5 → 4 2.5	0.367	0.365	0.356	0.346	0.336	0.327	0.319	0.311	0.303	0.296
4 4.5 → 4 3.5	0.621	0.587	0.560	0.539	0.522	0.509	0.496	0.486	0.476	0.467
4 4.5 → 4 5.5	0.834	0.810	0.778	0.752	0.728	0.708	0.689	0.673	0.658	0.644
4 4.5 → 4 6.5	0.685	0.714	0.702	0.681	0.659	0.638	0.618	0.599	0.582	0.566
4 5.5 → 0 2.5	0.557	0.528	0.494	0.462	0.434	0.411	0.391	0.374	0.360	0.348
4 5.5 → 1 1.5	0.306	0.289	0.270	0.253	0.238	0.226	0.216	0.208	0.201	0.194
4 5.5 → 1 2.5	0.575	0.527	0.486	0.454	0.429	0.409	0.393	0.380	0.369	0.360
4 5.5 → 1 3.5	0.652	0.629	0.594	0.561	0.533	0.509	0.490	0.473	0.459	0.446
4 5.5 → 2 0.5	0.121	0.124	0.121	0.116	0.111	0.107	0.103	0.100	0.097	0.094
4 5.5 → 2 1.5	0.330	0.307	0.287	0.270	0.255	0.242	0.231	0.221	0.213	0.205
4 5.5 → 2 2.5	0.548	0.489	0.447	0.416	0.391	0.371	0.354	0.340	0.327	0.316
4 5.5 → 2 3.5	0.911	0.862	0.822	0.789	0.761	0.737	0.716	0.698	0.682	0.667
4 5.5 → 2 4.5	0.945	0.888	0.838	0.795	0.758	0.726	0.700	0.676	0.656	0.638
4 5.5 → 3 0.5	0.128	0.116	0.106	0.098	0.092	0.087	0.083	0.080	0.077	0.074
4 5.5 → 3 1.5	0.281	0.258	0.240	0.226	0.214	0.204	0.195	0.188	0.182	0.176
4 5.5 → 3 2.5	0.441	0.414	0.392	0.372	0.355	0.341	0.328	0.317	0.307	0.298
4 5.5 → 3 3.5	0.657	0.633	0.605	0.579	0.556	0.536	0.518	0.502	0.487	0.474
4 5.5 → 3 4.5	1.008	0.987	0.994	1.010	1.031	1.054	1.078	1.103	1.128	1.153
4 5.5 → 3 5.5	0.954	0.918	0.885	0.855	0.828	0.805	0.785	0.767	0.752	0.739
4 5.5 → 4 1.5	0.165	0.179	0.177	0.172	0.167	0.161	0.156	0.151	0.146	0.142
4 5.5 → 4 2.5	0.277	0.294	0.289	0.280	0.270	0.261	0.252	0.244	0.237	0.230
4 5.5 → 4 6.5	0.948	0.922	0.890	0.862	0.838	0.815	0.795	0.776	0.758	0.742
4 6.5 → 0 2.5	0.557	0.528	0.494	0.462	0.434	0.411	0.391	0.374	0.360	0.348
4 6.5 → 1 1.5	0.385	0.338	0.304	0.279	0.260	0.246	0.235	0.226	0.219	0.213
4 6.5 → 1 2.5	0.446	0.426	0.400	0.375	0.354	0.337	0.322	0.309	0.298	0.289
4 6.5 → 1 3.5	0.700	0.681	0.647	0.614	0.585	0.562	0.542	0.525	0.511	0.499
4 6.5 → 2 0.5	0.170	0.150	0.136	0.126	0.118	0.112	0.107	0.102	0.098	0.094
4 6.5 → 2 1.5	0.308	0.283	0.262	0.246	0.232	0.221	0.211	0.203	0.195	0.188
4 6.5 → 2 2.5	0.445	0.423	0.399	0.377	0.358	0.342	0.327	0.315	0.303	0.293
4 6.5 → 2 3.5	0.653	0.615	0.578	0.545	0.516	0.492	0.471	0.453	0.437	0.422
4 6.5 → 2 4.5	1.279	1.199	1.139	1.091	1.051	1.017	0.988	0.963	0.942	0.923
4 6.5 → 3 0.5	0.148	0.135	0.125	0.117	0.111	0.106	0.102	0.098	0.095	0.091
4 6.5 → 3 1.5	0.286	0.261	0.241	0.226	0.214	0.204	0.195	0.188	0.181	0.175
4 6.5 → 3 2.5	0.418	0.382	0.353	0.331	0.312	0.297	0.285	0.274	0.264	0.255
4 6.5 → 3 3.5	0.557	0.514	0.479	0.451	0.428	0.408	0.392	0.377	0.364	0.353
4 6.5 → 3 4.5	0.758	0.723	0.690	0.659	0.631	0.606	0.585	0.566	0.549	0.534
4 6.5 → 3 5.5	1.303	1.311	1.333	1.357	1.380	1.404	1.429	1.455	1.480	1.506
5 2.5 → 0 2.5	0.330	0.342	0.337	0.328	0.318	0.310	0.302	0.295	0.289	0.284
5 2.5 → 1 1.5	0.303	0.289	0.274	0.263	0.253	0.245	0.238	0.232	0.227	0.223
5 2.5 → 1 2.5	0.291	0.298	0.292	0.283	0.275	0.267	0.260	0.253	0.246	0.240
5 2.5 → 1 3.5	0.559	0.540	0.507	0.476	0.449	0.426	0.406	0.389	0.373	0.359
5 2.5 → 2 0.5	0.204	0.189	0.176	0.167	0.160	0.155	0.152	0.149	0.146	0.145
5 2.5 → 2 1.5	0.277	0.278	0.268	0.257	0.248	0.240	0.233	0.227	0.222	0.218
5 2.5 → 2 2.5	0.325	0.333	0.326	0.316	0.305	0.296	0.287	0.279	0.273	0.267
5 2.5 → 2 3.5	0.305	0.325	0.322	0.314	0.305	0.297	0.289	0.282	0.275	0.269
5 2.5 → 2 4.5	0.612	0.582	0.547	0.517	0.493	0.471	0.452	0.435	0.420	0.406
5 2.5 → 3 0.5	0.367	0.337	0.315	0.302	0.294	0.289	0.285	0.282	0.280	0.279
5 2.5 → 3 1.5	0.467	0.443	0.422	0.407	0.395	0.385	0.377	0.370	0.365	0.360
5 2.5 → 3 2.5	0.455	0.441	0.426	0.412	0.398	0.385	0.374	0.364	0.355	0.346
5 2.5 → 3 3.5	0.502	0.484	0.462	0.441	0.422	0.405	0.390	0.376	0.363	0.352
5 2.5 → 3 4.5	0.481	0.477	0.456	0.434	0.414	0.395	0.379	0.363	0.350	0.337
5 2.5 → 3 5.5	0.574	0.529	0.488	0.454	0.426	0.402	0.381	0.362	0.347	0.333
5 2.5 → 4 1.5	0.521	0.562	0.588	0.617	0.648	0.681	0.713	0.745	0.776	0.806
5 2.5 → 4 2.5	0.496	0.512	0.516	0.517	0.518	0.519	0.519	0.520	0.520	0.521
5 2.5 → 4 3.5	0.419	0.426	0.425	0.422	0.418	0.413	0.407	0.401	0.396	0.390
5 2.5 → 4 4.5	0.459	0.451	0.439	0.428	0.418	0.407	0.398	0.388	0.379	0.370
5 2.5 → 4 5.5	0.435	0.435	0.418	0.400	0.384	0.369	0.355	0.342	0.331	0.320
5 2.5 → 4 6.5	0.377	0.365	0.345	0.327	0.310	0.296	0.283	0.272	0.262	0.253
5 2.5 → 5 7.5	0.194	0.255	0.275	0.281	0.281	0.278	0.274	0.270	0.266	0.263
5 3.5 → 0 2.5	0.330	0.342	0.337	0.328	0.318	0.310	0.302	0.295	0.289	0.284
5 3.5 → 1 1.5	0.268	0.259	0.248	0.239	0.230	0.223	0.217	0.212	0.207	0.203

(continued)

(continued)

$j \rightarrow j'$	Temperature / K									
	5	10	15	20	25	30	35	40	45	50
5 3.5 → 1 2.5	0.354	0.351	0.337	0.324	0.311	0.301	0.291	0.282	0.274	0.267
5 3.5 → 1 3.5	0.531	0.517	0.487	0.460	0.436	0.415	0.396	0.380	0.366	0.352
5 3.5 → 2 0.5	0.133	0.134	0.130	0.125	0.121	0.117	0.113	0.111	0.108	0.106
5 3.5 → 2 1.5	0.297	0.286	0.272	0.260	0.251	0.243	0.236	0.231	0.227	0.223
5 3.5 → 2 2.5	0.318	0.326	0.317	0.307	0.297	0.288	0.280	0.273	0.267	0.261
5 3.5 → 2 3.5	0.422	0.424	0.410	0.395	0.380	0.367	0.355	0.344	0.335	0.326
5 3.5 → 2 4.5	0.553	0.536	0.509	0.485	0.464	0.445	0.429	0.414	0.400	0.388
5 3.5 → 3 0.5	0.159	0.157	0.153	0.148	0.144	0.139	0.135	0.131	0.128	0.125
5 3.5 → 3 1.5	0.469	0.435	0.410	0.394	0.382	0.374	0.366	0.361	0.356	0.351
5 3.5 → 3 2.5	0.583	0.550	0.520	0.498	0.480	0.465	0.453	0.443	0.434	0.426
5 3.5 → 3 3.5	0.497	0.489	0.472	0.455	0.439	0.423	0.410	0.397	0.386	0.376
5 3.5 → 3 4.5	0.564	0.536	0.507	0.480	0.456	0.436	0.417	0.401	0.386	0.373
5 3.5 → 3 5.5	0.561	0.537	0.504	0.473	0.447	0.423	0.403	0.385	0.369	0.355
5 3.5 → 4 1.5	0.299	0.304	0.303	0.300	0.295	0.290	0.285	0.280	0.275	0.270
5 3.5 → 4 2.5	0.496	0.534	0.560	0.589	0.621	0.653	0.685	0.717	0.748	0.777
5 3.5 → 4 3.5	0.586	0.592	0.588	0.584	0.581	0.578	0.575	0.573	0.571	0.570
5 3.5 → 4 4.5	0.439	0.451	0.446	0.438	0.430	0.421	0.413	0.404	0.397	0.389
5 3.5 → 4 5.5	0.463	0.453	0.437	0.423	0.410	0.398	0.387	0.376	0.366	0.357
5 3.5 → 4 6.5	0.424	0.416	0.396	0.377	0.360	0.344	0.330	0.318	0.306	0.296
5 3.5 → 5 2.5	0.461	0.466	0.453	0.440	0.430	0.421	0.414	0.407	0.402	0.397
5 3.5 → 5 7.5	0.232	0.292	0.311	0.315	0.314	0.310	0.305	0.299	0.294	0.289
5 4.5 → 0 2.5	0.330	0.342	0.337	0.328	0.318	0.310	0.302	0.295	0.289	0.284
5 4.5 → 1 1.5	0.236	0.233	0.225	0.217	0.209	0.203	0.197	0.192	0.187	0.183
5 4.5 → 1 2.5	0.413	0.399	0.378	0.360	0.344	0.330	0.318	0.308	0.299	0.291
5 4.5 → 1 3.5	0.504	0.494	0.469	0.445	0.424	0.405	0.389	0.374	0.361	0.349
5 4.5 → 2 0.5	0.102	0.107	0.106	0.103	0.100	0.096	0.093	0.091	0.089	0.087
5 4.5 → 2 1.5	0.235	0.234	0.226	0.218	0.211	0.204	0.199	0.194	0.190	0.187
5 4.5 → 2 2.5	0.374	0.366	0.350	0.335	0.323	0.312	0.304	0.296	0.290	0.284
5 4.5 → 2 3.5	0.503	0.493	0.471	0.450	0.431	0.415	0.400	0.388	0.376	0.367
5 4.5 → 2 4.5	0.509	0.506	0.486	0.466	0.448	0.432	0.417	0.404	0.392	0.381
5 4.5 → 3 0.5	0.126	0.123	0.119	0.115	0.111	0.107	0.103	0.100	0.097	0.094
5 4.5 → 3 1.5	0.285	0.278	0.267	0.255	0.245	0.236	0.227	0.220	0.213	0.207
5 4.5 → 3 2.5	0.572	0.537	0.507	0.486	0.471	0.458	0.448	0.440	0.433	0.426
5 4.5 → 3 3.5	0.644	0.611	0.579	0.553	0.532	0.515	0.500	0.487	0.476	0.466
5 4.5 → 3 4.5	0.617	0.583	0.552	0.525	0.501	0.480	0.461	0.445	0.430	0.417
5 4.5 → 3 5.5	0.603	0.578	0.546	0.516	0.489	0.466	0.445	0.426	0.410	0.395
5 4.5 → 4 1.5	0.189	0.192	0.191	0.190	0.188	0.186	0.183	0.181	0.178	0.175
5 4.5 → 4 2.5	0.406	0.404	0.396	0.386	0.376	0.367	0.358	0.349	0.341	0.333
5 4.5 → 4 3.5	0.542	0.585	0.609	0.636	0.666	0.696	0.727	0.757	0.788	0.817
5 4.5 → 4 4.5	0.600	0.609	0.603	0.597	0.591	0.586	0.581	0.577	0.574	0.571
5 4.5 → 4 5.5	0.480	0.478	0.468	0.458	0.448	0.438	0.429	0.420	0.411	0.403
5 4.5 → 4 6.5	0.489	0.482	0.464	0.445	0.427	0.411	0.397	0.383	0.371	0.360
5 4.5 → 5 2.5	0.281	0.298	0.297	0.292	0.288	0.283	0.278	0.273	0.268	0.263
5 4.5 → 5 3.5	0.462	0.479	0.471	0.459	0.448	0.438	0.430	0.422	0.416	0.410
5 4.5 → 5 6.5	0.430	0.476	0.482	0.479	0.473	0.466	0.459	0.451	0.443	0.436
5 4.5 → 5 7.5	0.306	0.367	0.383	0.385	0.382	0.376	0.369	0.362	0.355	0.348
5 5.5 → 0 2.5	0.330	0.342	0.337	0.328	0.318	0.310	0.302	0.295	0.289	0.284
5 5.5 → 1 1.5	0.221	0.221	0.213	0.205	0.197	0.190	0.184	0.178	0.173	0.168
5 5.5 → 1 2.5	0.438	0.422	0.399	0.378	0.360	0.345	0.332	0.321	0.311	0.302
5 5.5 → 1 3.5	0.488	0.481	0.459	0.438	0.419	0.402	0.388	0.374	0.363	0.352
5 5.5 → 2 0.5	0.090	0.093	0.092	0.089	0.087	0.084	0.082	0.080	0.078	0.076
5 5.5 → 2 1.5	0.176	0.187	0.184	0.179	0.173	0.167	0.162	0.158	0.153	0.149
5 5.5 → 2 2.5	0.414	0.396	0.374	0.357	0.342	0.330	0.320	0.311	0.303	0.297
5 5.5 → 2 3.5	0.543	0.525	0.497	0.474	0.454	0.437	0.422	0.409	0.398	0.388
5 5.5 → 2 4.5	0.500	0.506	0.490	0.473	0.456	0.440	0.427	0.414	0.403	0.393
5 5.5 → 3 0.5	0.121	0.116	0.110	0.104	0.099	0.094	0.090	0.087	0.084	0.081
5 5.5 → 3 1.5	0.213	0.210	0.203	0.195	0.187	0.180	0.174	0.168	0.162	0.157
5 5.5 → 3 2.5	0.365	0.357	0.343	0.328	0.315	0.302	0.291	0.281	0.272	0.264
5 5.5 → 3 3.5	0.757	0.697	0.650	0.618	0.594	0.576	0.561	0.549	0.538	0.529
5 5.5 → 3 4.5	0.723	0.685	0.649	0.620	0.595	0.574	0.556	0.540	0.526	0.514
5 5.5 → 3 5.5	0.669	0.646	0.616	0.586	0.559	0.535	0.513	0.494	0.477	0.461
5 5.5 → 4 1.5	0.181	0.178	0.172	0.167	0.162	0.158	0.154	0.150	0.146	0.142
5 5.5 → 4 2.5	0.238	0.245	0.242	0.237	0.232	0.227	0.223	0.218	0.214	0.209
5 5.5 → 4 3.5	0.442	0.443	0.433	0.422	0.411	0.400	0.389	0.379	0.370	0.362
5 5.5 → 4 4.5	0.658	0.692	0.713	0.737	0.765	0.795	0.826	0.856	0.886	0.916
5 5.5 → 4 5.5	0.616	0.627	0.622	0.614	0.607	0.600	0.593	0.587	0.582	0.578
5 5.5 → 4 6.5	0.570	0.566	0.551	0.534	0.519	0.504	0.490	0.477	0.465	0.454
5 5.5 → 5 2.5	0.184	0.207	0.211	0.210	0.207	0.203	0.199	0.195	0.191	0.187
5 5.5 → 5 3.5	0.284	0.304	0.305	0.301	0.297	0.292	0.287	0.282	0.277	0.272
5 5.5 → 5 4.5	0.475	0.499	0.493	0.482	0.471	0.462	0.454	0.446	0.440	0.434
5 5.5 → 5 6.5	0.596	0.629	0.624	0.613	0.601	0.590	0.580	0.571	0.563	0.556
5 5.5 → 5 7.5	0.439	0.497	0.508	0.506	0.500	0.492	0.482	0.473	0.463	0.454
5 6.5 → 0 2.5	0.330	0.342	0.337	0.328	0.318	0.310	0.302	0.295	0.289	0.284
5 6.5 → 1 1.5	0.232	0.231	0.221	0.211	0.201	0.193	0.185	0.178	0.172	0.166
5 6.5 → 1 2.5	0.427	0.411	0.388	0.367	0.349	0.334	0.321	0.310	0.300	0.291
5 6.5 → 1 3.5	0.492	0.484	0.463	0.444	0.427	0.411	0.398	0.386	0.375	0.365
5 6.5 → 2 0.5	0.074	0.078	0.077	0.074	0.072	0.070	0.068	0.066	0.065	0.063
5 6.5 → 2 1.5	0.218	0.214	0.206	0.197	0.189	0.182	0.176	0.171	0.166	0.161
5 6.5 → 2 2.5	0.349	0.346	0.333	0.318	0.305	0.293	0.282	0.273	0.264	0.256
5 6.5 → 2 3.5	0.535	0.514	0.486	0.463	0.445	0.429	0.416	0.405	0.395	0.387

(continued)

(continued)

$j \rightarrow j'$	Temperature / K									
	5	10	15	20	25	30	35	40	45	50
5 6.5 → 2 4.5	0.547	0.554	0.537	0.518	0.500	0.484	0.470	0.457	0.446	0.436
5 6.5 → 3 0.5	0.087	0.087	0.083	0.080	0.076	0.072	0.069	0.067	0.064	0.062
5 6.5 → 3 1.5	0.209	0.200	0.188	0.178	0.169	0.160	0.153	0.147	0.141	0.136
5 6.5 → 3 2.5	0.339	0.319	0.300	0.284	0.270	0.257	0.246	0.237	0.228	0.220
5 6.5 → 3 3.5	0.474	0.455	0.434	0.414	0.396	0.379	0.365	0.352	0.340	0.330
5 6.5 → 3 4.5	0.919	0.860	0.807	0.770	0.742	0.720	0.702	0.687	0.674	0.663
5 6.5 → 3 5.5	0.819	0.790	0.756	0.725	0.697	0.672	0.649	0.629	0.612	0.595
5 6.5 → 4 1.5	0.140	0.140	0.135	0.129	0.123	0.118	0.114	0.109	0.106	0.102
5 6.5 → 4 2.5	0.227	0.222	0.213	0.205	0.198	0.192	0.186	0.180	0.175	0.171
5 6.5 → 4 3.5	0.301	0.298	0.291	0.284	0.277	0.271	0.265	0.259	0.253	0.248
5 6.5 → 4 4.5	0.474	0.478	0.469	0.459	0.448	0.437	0.426	0.416	0.407	0.398
5 6.5 → 4 5.5	0.839	0.880	0.899	0.921	0.946	0.973	1.001	1.030	1.059	1.087
5 6.5 → 4 6.5	0.726	0.733	0.724	0.714	0.704	0.694	0.683	0.673	0.664	0.655
5 6.5 → 5 2.5	0.109	0.131	0.138	0.138	0.137	0.135	0.132	0.130	0.127	0.124
5 6.5 → 5 3.5	0.193	0.224	0.231	0.231	0.229	0.225	0.221	0.217	0.213	0.208
5 6.5 → 5 7.5	0.702	0.747	0.745	0.733	0.720	0.707	0.694	0.682	0.670	0.659
5 7.5 → 0 2.5	0.330	0.342	0.337	0.328	0.318	0.310	0.302	0.295	0.289	0.284
5 7.5 → 1 1.5	0.292	0.281	0.262	0.245	0.231	0.219	0.208	0.198	0.190	0.183
5 7.5 → 1 2.5	0.323	0.329	0.318	0.305	0.292	0.281	0.270	0.261	0.252	0.244
5 7.5 → 1 3.5	0.527	0.512	0.490	0.470	0.453	0.438	0.425	0.414	0.404	0.395
5 7.5 → 2 0.5	0.135	0.126	0.117	0.110	0.105	0.100	0.096	0.092	0.089	0.085
5 7.5 → 2 1.5	0.226	0.217	0.205	0.195	0.186	0.179	0.172	0.166	0.160	0.155
5 7.5 → 2 2.5	0.292	0.291	0.280	0.269	0.259	0.250	0.242	0.234	0.227	0.221
5 7.5 → 2 3.5	0.380	0.392	0.384	0.372	0.360	0.348	0.337	0.328	0.319	0.312
5 7.5 → 2 4.5	0.692	0.680	0.651	0.625	0.602	0.583	0.566	0.553	0.541	0.532
5 7.5 → 3 0.5	0.097	0.088	0.080	0.074	0.070	0.065	0.062	0.059	0.056	0.054
5 7.5 → 3 1.5	0.188	0.175	0.163	0.152	0.142	0.134	0.128	0.122	0.116	0.112
5 7.5 → 3 2.5	0.287	0.274	0.257	0.242	0.229	0.217	0.207	0.198	0.190	0.182
5 7.5 → 3 3.5	0.416	0.401	0.381	0.361	0.343	0.327	0.313	0.301	0.290	0.279
5 7.5 → 3 4.5	0.602	0.585	0.561	0.538	0.515	0.495	0.476	0.460	0.445	0.431
5 7.5 → 3 5.5	1.257	1.187	1.128	1.084	1.050	1.022	1.000	0.980	0.963	0.948
5 7.5 → 4 1.5	0.106	0.102	0.096	0.091	0.086	0.082	0.079	0.075	0.073	0.070
5 7.5 → 4 2.5	0.176	0.172	0.164	0.155	0.148	0.141	0.135	0.130	0.125	0.121
5 7.5 → 4 3.5	0.271	0.267	0.256	0.245	0.234	0.225	0.217	0.209	0.202	0.196
5 7.5 → 4 4.5	0.392	0.389	0.377	0.365	0.353	0.342	0.333	0.323	0.315	0.307
5 7.5 → 4 5.5	0.590	0.593	0.583	0.572	0.560	0.548	0.536	0.525	0.514	0.504
5 7.5 → 4 6.5	1.173	1.229	1.257	1.285	1.315	1.345	1.376	1.405	1.435	1.463
6 3.5 → 0 2.5	0.299	0.287	0.280	0.273	0.266	0.258	0.251	0.243	0.236	0.230
6 3.5 → 1 1.5	0.234	0.227	0.220	0.215	0.211	0.209	0.207	0.205	0.204	0.203
6 3.5 → 1 2.5	0.209	0.212	0.210	0.209	0.206	0.203	0.200	0.196	0.193	0.189
6 3.5 → 1 3.5	0.520	0.470	0.429	0.398	0.375	0.356	0.339	0.325	0.313	0.302
6 3.5 → 2 0.5	0.233	0.195	0.174	0.160	0.151	0.143	0.138	0.133	0.129	0.126
6 3.5 → 2 1.5	0.285	0.258	0.241	0.229	0.219	0.212	0.206	0.200	0.196	0.192
6 3.5 → 2 2.5	0.318	0.304	0.291	0.280	0.271	0.262	0.254	0.247	0.240	0.234
6 3.5 → 2 3.5	0.278	0.282	0.276	0.269	0.261	0.252	0.244	0.237	0.230	0.223
6 3.5 → 2 4.5	0.465	0.430	0.386	0.350	0.323	0.302	0.285	0.271	0.259	0.249
6 3.5 → 3 0.5	0.230	0.215	0.199	0.186	0.176	0.168	0.161	0.156	0.152	0.148
6 3.5 → 3 1.5	0.301	0.291	0.278	0.268	0.258	0.251	0.244	0.239	0.234	0.230
6 3.5 → 3 2.5	0.289	0.290	0.287	0.283	0.279	0.274	0.270	0.265	0.261	0.258
6 3.5 → 3 3.5	0.406	0.365	0.343	0.328	0.316	0.306	0.297	0.289	0.281	0.275
6 3.5 → 3 4.5	0.398	0.365	0.342	0.323	0.308	0.294	0.282	0.272	0.262	0.253
6 3.5 → 3 5.5	0.369	0.333	0.302	0.279	0.261	0.246	0.233	0.223	0.214	0.206
6 3.5 → 4 1.5	0.663	0.586	0.546	0.522	0.505	0.492	0.483	0.476	0.470	0.465
6 3.5 → 4 2.5	0.543	0.487	0.458	0.441	0.429	0.419	0.411	0.405	0.399	0.393
6 3.5 → 4 3.5	0.468	0.430	0.407	0.392	0.380	0.370	0.360	0.352	0.344	0.337
6 3.5 → 4 4.5	0.427	0.406	0.385	0.368	0.353	0.340	0.329	0.318	0.309	0.300
6 3.5 → 4 5.5	0.353	0.344	0.327	0.310	0.295	0.283	0.271	0.262	0.253	0.245
6 3.5 → 4 6.5	0.351	0.335	0.315	0.298	0.283	0.271	0.260	0.251	0.244	0.238
6 3.5 → 5 2.5	1.011	0.912	0.865	0.848	0.849	0.861	0.880	0.902	0.927	0.953
6 3.5 → 5 3.5	0.623	0.586	0.559	0.542	0.532	0.525	0.520	0.516	0.513	0.511
6 3.5 → 5 4.5	0.526	0.489	0.460	0.439	0.424	0.412	0.402	0.393	0.385	0.378
6 3.5 → 5 5.5	0.445	0.412	0.384	0.362	0.346	0.332	0.320	0.310	0.301	0.293
6 3.5 → 5 6.5	0.327	0.317	0.300	0.286	0.273	0.262	0.253	0.244	0.237	0.230
6 3.5 → 5 7.5	0.322	0.301	0.285	0.272	0.261	0.251	0.242	0.235	0.228	0.223
6 3.5 → 6 8.5	0.108	0.168	0.194	0.206	0.213	0.217	0.219	0.221	0.222	0.222
6 4.5 → 0 2.5	0.299	0.287	0.280	0.273	0.266	0.258	0.251	0.243	0.236	0.230
6 4.5 → 1 1.5	0.200	0.196	0.191	0.188	0.185	0.182	0.180	0.178	0.177	0.175
6 4.5 → 1 2.5	0.287	0.277	0.266	0.258	0.251	0.245	0.240	0.235	0.230	0.226
6 4.5 → 1 3.5	0.476	0.435	0.402	0.376	0.357	0.340	0.326	0.314	0.303	0.294
6 4.5 → 2 0.5	0.125	0.116	0.110	0.105	0.102	0.099	0.096	0.094	0.092	0.090
6 4.5 → 2 1.5	0.326	0.286	0.262	0.245	0.232	0.222	0.214	0.206	0.200	0.194
6 4.5 → 2 2.5	0.314	0.294	0.279	0.267	0.257	0.248	0.241	0.234	0.228	0.222
6 4.5 → 2 3.5	0.384	0.366	0.343	0.325	0.310	0.297	0.285	0.275	0.266	0.258
6 4.5 → 2 4.5	0.432	0.408	0.374	0.346	0.324	0.306	0.291	0.278	0.267	0.257
6 4.5 → 3 0.5	0.094	0.096	0.097	0.096	0.096	0.095	0.094	0.093	0.092	0.091
6 4.5 → 3 1.5	0.286	0.274	0.260	0.247	0.237	0.229	0.222	0.216	0.211	0.207
6 4.5 → 3 2.5	0.457	0.407	0.375	0.351	0.333	0.319	0.307	0.297	0.289	0.281
6 4.5 → 3 3.5	0.320	0.326	0.322	0.315	0.307	0.300	0.293	0.287	0.281	0.275
6 4.5 → 3 4.5	0.429	0.386	0.358	0.339	0.324	0.312	0.301	0.292	0.283	0.276
6 4.5 → 3 5.5	0.407	0.370	0.340	0.317	0.299	0.283	0.270	0.259	0.249	0.240

(continued)

(continued)

$j \rightarrow j'$	Temperature / K									
	5	10	15	20	25	30	35	40	45	50
6 4.5 → 4 1.5	0.277	0.250	0.237	0.229	0.223	0.219	0.215	0.211	0.207	0.204
6 4.5 → 4 2.5	0.671	0.601	0.561	0.535	0.516	0.501	0.490	0.480	0.472	0.465
6 4.5 → 4 3.5	0.581	0.530	0.499	0.478	0.462	0.449	0.438	0.429	0.422	0.415
6 4.5 → 4 4.5	0.460	0.427	0.404	0.387	0.375	0.364	0.354	0.345	0.337	0.330
6 4.5 → 4 5.5	0.442	0.419	0.396	0.378	0.362	0.349	0.337	0.326	0.317	0.308
6 4.5 → 4 6.5	0.375	0.361	0.341	0.323	0.307	0.294	0.283	0.273	0.264	0.257
6 4.5 → 5 2.5	0.412	0.391	0.374	0.362	0.353	0.346	0.340	0.335	0.330	0.326
6 4.5 → 5 3.5	0.959	0.854	0.801	0.780	0.777	0.786	0.802	0.821	0.844	0.867
6 4.5 → 5 4.5	0.607	0.570	0.543	0.526	0.514	0.506	0.501	0.497	0.494	0.491
6 4.5 → 5 5.5	0.481	0.459	0.436	0.420	0.407	0.396	0.387	0.379	0.372	0.365
6 4.5 → 5 6.5	0.451	0.416	0.388	0.367	0.350	0.337	0.325	0.315	0.306	0.298
6 4.5 → 5 7.5	0.344	0.327	0.310	0.296	0.283	0.272	0.262	0.254	0.247	0.240
6 4.5 → 6 3.5	0.410	0.433	0.433	0.430	0.425	0.421	0.417	0.413	0.409	0.406
6 4.5 → 6 8.5	0.128	0.193	0.220	0.231	0.236	0.237	0.237	0.236	0.235	0.234
6 5.5 → 0 2.5	0.299	0.287	0.280	0.273	0.266	0.258	0.251	0.243	0.236	0.230
6 5.5 → 1 1.5	0.176	0.173	0.169	0.166	0.163	0.160	0.158	0.155	0.153	0.151
6 5.5 → 1 2.5	0.353	0.331	0.313	0.299	0.288	0.279	0.272	0.266	0.260	0.255
6 5.5 → 1 3.5	0.434	0.404	0.378	0.358	0.342	0.328	0.316	0.306	0.297	0.288
6 5.5 → 2 0.5	0.093	0.092	0.089	0.087	0.084	0.082	0.080	0.078	0.076	0.074
6 5.5 → 2 1.5	0.230	0.212	0.199	0.190	0.182	0.175	0.169	0.164	0.160	0.155
6 5.5 → 2 2.5	0.383	0.343	0.315	0.295	0.280	0.268	0.257	0.248	0.241	0.234
6 5.5 → 2 3.5	0.454	0.418	0.384	0.359	0.339	0.323	0.310	0.299	0.289	0.281
6 5.5 → 2 4.5	0.422	0.405	0.379	0.357	0.339	0.323	0.309	0.297	0.287	0.278
6 5.5 → 3 0.5	0.075	0.077	0.077	0.077	0.076	0.076	0.075	0.074	0.073	0.072
6 5.5 → 3 1.5	0.231	0.205	0.192	0.183	0.177	0.171	0.166	0.162	0.158	0.154
6 5.5 → 3 2.5	0.354	0.342	0.324	0.308	0.295	0.283	0.273	0.265	0.258	0.252
6 5.5 → 3 3.5	0.469	0.432	0.403	0.380	0.362	0.347	0.334	0.324	0.314	0.307
6 5.5 → 3 4.5	0.404	0.384	0.365	0.351	0.340	0.329	0.320	0.312	0.305	0.299
6 5.5 → 3 5.5	0.461	0.419	0.389	0.367	0.348	0.333	0.319	0.307	0.297	0.287
6 5.5 → 4 1.5	0.206	0.191	0.181	0.174	0.168	0.163	0.159	0.154	0.150	0.147
6 5.5 → 4 2.5	0.327	0.303	0.287	0.276	0.267	0.260	0.254	0.248	0.243	0.238
6 5.5 → 4 3.5	0.708	0.638	0.596	0.567	0.546	0.530	0.517	0.507	0.498	0.491
6 5.5 → 4 4.5	0.614	0.561	0.527	0.505	0.487	0.474	0.462	0.453	0.445	0.438
6 5.5 → 4 5.5	0.516	0.479	0.452	0.433	0.417	0.404	0.393	0.383	0.374	0.366
6 5.5 → 4 6.5	0.434	0.418	0.396	0.376	0.359	0.344	0.331	0.320	0.310	0.301
6 5.5 → 5 2.5	0.301	0.279	0.261	0.249	0.240	0.232	0.226	0.221	0.216	0.211
6 5.5 → 5 3.5	0.416	0.397	0.379	0.366	0.355	0.347	0.339	0.333	0.327	0.322
6 5.5 → 5 4.5	0.953	0.855	0.806	0.786	0.785	0.794	0.810	0.830	0.853	0.877
6 5.5 → 5 5.5	0.630	0.592	0.564	0.546	0.534	0.525	0.519	0.515	0.511	0.508
6 5.5 → 5 6.5	0.538	0.500	0.471	0.450	0.434	0.421	0.410	0.400	0.392	0.384
6 5.5 → 5 7.5	0.416	0.394	0.371	0.352	0.337	0.323	0.312	0.302	0.293	0.285
6 5.5 → 6 3.5	0.212	0.258	0.268	0.269	0.267	0.264	0.261	0.257	0.253	0.249
6 5.5 → 6 4.5	0.389	0.408	0.409	0.407	0.404	0.401	0.397	0.394	0.391	0.388
6 5.5 → 6 7.5	0.289	0.363	0.385	0.391	0.392	0.390	0.387	0.383	0.379	0.375
6 5.5 → 6 8.5	0.174	0.248	0.275	0.285	0.288	0.287	0.285	0.282	0.278	0.275
6 6.5 → 0 2.5	0.299	0.287	0.280	0.273	0.266	0.258	0.251	0.243	0.236	0.230
6 6.5 → 1 1.5	0.173	0.168	0.161	0.156	0.152	0.148	0.145	0.141	0.138	0.135
6 6.5 → 1 2.5	0.387	0.359	0.335	0.318	0.305	0.295	0.286	0.279	0.273	0.267
6 6.5 → 1 3.5	0.403	0.382	0.362	0.347	0.335	0.325	0.315	0.307	0.300	0.293
6 6.5 → 2 0.5	0.087	0.085	0.082	0.079	0.076	0.073	0.071	0.068	0.066	0.064
6 6.5 → 2 1.5	0.142	0.144	0.142	0.138	0.134	0.131	0.127	0.124	0.120	0.118
6 6.5 → 2 2.5	0.401	0.357	0.324	0.300	0.282	0.268	0.256	0.247	0.238	0.231
6 6.5 → 2 3.5	0.504	0.452	0.411	0.382	0.359	0.342	0.327	0.315	0.305	0.296
6 6.5 → 2 4.5	0.447	0.430	0.408	0.389	0.372	0.358	0.345	0.333	0.323	0.313
6 6.5 → 3 0.5	0.117	0.097	0.087	0.081	0.076	0.072	0.069	0.067	0.064	0.062
6 6.5 → 3 1.5	0.129	0.133	0.133	0.131	0.128	0.126	0.123	0.121	0.118	0.116
6 6.5 → 3 2.5	0.254	0.241	0.231	0.223	0.215	0.209	0.203	0.198	0.194	0.190
6 6.5 → 3 3.5	0.507	0.460	0.422	0.394	0.372	0.355	0.340	0.329	0.319	0.310
6 6.5 → 3 4.5	0.472	0.453	0.430	0.411	0.395	0.381	0.369	0.359	0.351	0.343
6 6.5 → 3 5.5	0.516	0.475	0.447	0.426	0.409	0.395	0.382	0.370	0.359	0.350
6 6.5 → 4 1.5	0.156	0.150	0.142	0.135	0.130	0.125	0.120	0.116	0.112	0.109
6 6.5 → 4 2.5	0.241	0.226	0.214	0.205	0.198	0.191	0.186	0.180	0.176	0.171
6 6.5 → 4 3.5	0.378	0.349	0.330	0.317	0.307	0.299	0.291	0.285	0.279	0.273
6 6.5 → 4 4.5	0.830	0.748	0.698	0.665	0.640	0.621	0.605	0.593	0.583	0.575
6 6.5 → 4 5.5	0.658	0.601	0.565	0.542	0.524	0.509	0.497	0.487	0.478	0.470
6 6.5 → 4 6.5	0.543	0.515	0.488	0.466	0.447	0.431	0.417	0.404	0.392	0.382
6 6.5 → 5 2.5	0.212	0.197	0.183	0.172	0.164	0.157	0.152	0.147	0.142	0.138
6 6.5 → 5 3.5	0.304	0.289	0.274	0.263	0.254	0.247	0.241	0.236	0.231	0.226
6 6.5 → 5 4.5	0.455	0.433	0.414	0.400	0.389	0.379	0.371	0.364	0.358	0.352
6 6.5 → 5 5.5	1.060	0.947	0.891	0.867	0.863	0.871	0.886	0.905	0.927	0.951
6 6.5 → 5 6.5	0.670	0.633	0.605	0.586	0.572	0.563	0.555	0.549	0.544	0.540
6 6.5 → 5 7.5	0.552	0.517	0.486	0.461	0.442	0.426	0.413	0.401	0.390	0.381
6 6.5 → 6 3.5	0.121	0.160	0.172	0.175	0.175	0.173	0.171	0.168	0.165	0.163
6 6.5 → 6 4.5	0.202	0.253	0.267	0.270	0.270	0.267	0.264	0.261	0.258	0.255
6 6.5 → 6 5.5	0.396	0.421	0.425	0.425	0.423	0.421	0.418	0.416	0.413	0.411
6 6.5 → 6 7.5	0.472	0.519	0.529	0.530	0.528	0.525	0.521	0.518	0.514	0.511
6 6.5 → 6 8.5	0.275	0.359	0.386	0.393	0.393	0.389	0.385	0.379	0.374	0.368
6 7.5 → 0 2.5	0.299	0.287	0.280	0.273	0.266	0.258	0.251	0.243	0.236	0.230
6 7.5 → 1 1.5	0.203	0.189	0.177	0.168	0.160	0.154	0.148	0.143	0.138	0.134
6 7.5 → 1 2.5	0.369	0.342	0.320	0.303	0.290	0.279	0.271	0.263	0.257	0.251

(continued)

(continued)

$j \rightarrow j'$	Temperature / K									
	5	10	15	20	25	30	35	40	45	50
6 7.5 → 1 3.5	0.391	0.377	0.362	0.351	0.342	0.334	0.327	0.320	0.314	0.309
6 7.5 → 2 0.5	0.060	0.061	0.059	0.057	0.055	0.053	0.051	0.049	0.048	0.046
6 7.5 → 2 1.5	0.192	0.181	0.167	0.156	0.147	0.140	0.134	0.128	0.123	0.119
6 7.5 → 2 2.5	0.277	0.265	0.248	0.233	0.221	0.211	0.203	0.196	0.190	0.184
6 7.5 → 2 3.5	0.520	0.462	0.420	0.390	0.367	0.349	0.334	0.322	0.311	0.302
6 7.5 → 2 4.5	0.533	0.501	0.474	0.452	0.434	0.418	0.404	0.392	0.381	0.370
6 7.5 → 3 0.5	0.066	0.063	0.060	0.057	0.054	0.051	0.049	0.047	0.045	0.044
6 7.5 → 3 1.5	0.175	0.151	0.137	0.128	0.120	0.114	0.109	0.105	0.101	0.098
6 7.5 → 3 2.5	0.233	0.213	0.199	0.189	0.182	0.175	0.169	0.164	0.160	0.156
6 7.5 → 3 3.5	0.286	0.282	0.274	0.266	0.259	0.253	0.247	0.241	0.236	0.232
6 7.5 → 3 4.5	0.638	0.587	0.543	0.508	0.480	0.458	0.439	0.424	0.411	0.400
6 7.5 → 3 5.5	0.596	0.563	0.538	0.519	0.502	0.487	0.474	0.463	0.452	0.443
6 7.5 → 4 1.5	0.107	0.105	0.100	0.094	0.090	0.086	0.082	0.079	0.077	0.074
6 7.5 → 4 2.5	0.202	0.193	0.183	0.174	0.166	0.159	0.153	0.148	0.143	0.139
6 7.5 → 4 3.5	0.310	0.290	0.274	0.262	0.252	0.243	0.236	0.229	0.223	0.217
6 7.5 → 4 4.5	0.446	0.412	0.389	0.374	0.362	0.351	0.343	0.335	0.328	0.322
6 7.5 → 4 5.5	0.980	0.886	0.828	0.789	0.760	0.738	0.720	0.705	0.694	0.684
6 7.5 → 4 6.5	0.761	0.703	0.664	0.637	0.616	0.598	0.582	0.568	0.555	0.543
6 7.5 → 5 2.5	0.133	0.130	0.123	0.117	0.112	0.108	0.104	0.100	0.097	0.095
6 7.5 → 5 3.5	0.246	0.227	0.211	0.200	0.191	0.183	0.176	0.171	0.166	0.161
6 7.5 → 5 4.5	0.368	0.341	0.320	0.305	0.294	0.285	0.277	0.270	0.263	0.258
6 7.5 → 5 5.5	0.515	0.491	0.470	0.454	0.441	0.431	0.422	0.414	0.407	0.400
6 7.5 → 5 6.5	1.189	1.077	1.019	0.994	0.988	0.995	1.010	1.030	1.052	1.076
6 7.5 → 5 7.5	0.803	0.751	0.709	0.680	0.658	0.642	0.628	0.616	0.606	0.597
6 7.5 → 6 3.5	0.067	0.099	0.111	0.116	0.117	0.117	0.115	0.114	0.112	0.111
6 7.5 → 6 4.5	0.125	0.169	0.184	0.189	0.190	0.189	0.188	0.186	0.185	0.183
6 7.5 → 6 8.5	0.512	0.593	0.611	0.613	0.609	0.602	0.595	0.588	0.581	0.573
6 8.5 → 0 2.5	0.299	0.287	0.280	0.273	0.266	0.258	0.251	0.243	0.236	0.230
6 8.5 → 1 1.5	0.281	0.251	0.227	0.210	0.196	0.186	0.177	0.169	0.162	0.157
6 8.5 → 1 2.5	0.274	0.260	0.247	0.236	0.227	0.219	0.212	0.205	0.199	0.193
6 8.5 → 1 3.5	0.408	0.398	0.385	0.376	0.369	0.363	0.357	0.353	0.349	0.345
6 8.5 → 2 0.5	0.103	0.093	0.081	0.073	0.066	0.061	0.057	0.054	0.052	0.050
6 8.5 → 2 1.5	0.172	0.161	0.146	0.134	0.124	0.116	0.110	0.105	0.101	0.097
6 8.5 → 2 2.5	0.241	0.233	0.218	0.205	0.195	0.186	0.178	0.171	0.165	0.159
6 8.5 → 2 3.5	0.333	0.329	0.317	0.306	0.295	0.285	0.276	0.268	0.260	0.252
6 8.5 → 2 4.5	0.733	0.654	0.605	0.570	0.544	0.523	0.506	0.490	0.477	0.466
6 8.5 → 3 0.5	0.059	0.053	0.047	0.043	0.040	0.038	0.036	0.034	0.033	0.032
6 8.5 → 3 1.5	0.122	0.111	0.101	0.093	0.088	0.083	0.079	0.075	0.072	0.070
6 8.5 → 3 2.5	0.211	0.191	0.175	0.163	0.154	0.146	0.140	0.134	0.129	0.124
6 8.5 → 3 3.5	0.326	0.295	0.274	0.259	0.246	0.236	0.227	0.218	0.211	0.205
6 8.5 → 3 4.5	0.437	0.411	0.394	0.381	0.370	0.360	0.351	0.343	0.335	0.327
6 8.5 → 3 5.5	0.839	0.798	0.759	0.726	0.699	0.676	0.657	0.641	0.627	0.615
6 8.5 → 4 1.5	0.099	0.094	0.088	0.083	0.079	0.076	0.073	0.071	0.069	0.067
6 8.5 → 4 2.5	0.153	0.147	0.138	0.131	0.125	0.119	0.115	0.111	0.108	0.105
6 8.5 → 4 3.5	0.229	0.222	0.210	0.199	0.190	0.181	0.174	0.168	0.163	0.158
6 8.5 → 4 4.5	0.354	0.339	0.321	0.306	0.293	0.281	0.271	0.262	0.254	0.247
6 8.5 → 4 5.5	0.572	0.533	0.505	0.485	0.468	0.454	0.441	0.429	0.419	0.409
6 8.5 → 4 6.5	1.399	1.254	1.175	1.126	1.091	1.063	1.041	1.023	1.007	0.993
6 8.5 → 5 2.5	0.120	0.112	0.106	0.101	0.097	0.094	0.091	0.088	0.085	0.083
6 8.5 → 5 3.5	0.167	0.159	0.151	0.144	0.138	0.133	0.128	0.124	0.121	0.117
6 8.5 → 5 4.5	0.249	0.236	0.223	0.211	0.202	0.194	0.187	0.181	0.175	0.171
6 8.5 → 5 5.5	0.396	0.371	0.348	0.330	0.316	0.304	0.294	0.286	0.278	0.271
6 8.5 → 5 6.5	0.658	0.618	0.583	0.557	0.538	0.523	0.509	0.498	0.487	0.477
6 8.5 → 5 7.5	1.663	1.521	1.442	1.405	1.393	1.396	1.408	1.425	1.446	1.468

Table 3: Integrated rate coefficients $j \rightarrow j'$ from 55 to 100 K. Units are 10^{-10} cm^3 s^{-1}.

$j \rightarrow j'$	Temperature / K									
	55	60	65	70	75	80	85	90	95	100
1 1.5 → 0 2.5	1.444	1.438	1.435	1.433	1.434	1.436	1.441	1.447	1.455	1.464
1 2.5 → 0 2.5	1.444	1.438	1.435	1.433	1.434	1.436	1.441	1.447	1.455	1.464
1 2.5 → 1 1.5	0.578	0.554	0.532	0.513	0.495	0.478	0.463	0.449	0.437	0.425
1 2.5 → 1 3.5	1.354	1.305	1.260	1.220	1.184	1.150	1.120	1.091	1.065	1.041
1 3.5 → 0 2.5	1.444	1.438	1.435	1.433	1.434	1.436	1.441	1.447	1.455	1.464
1 3.5 → 1 1.5	0.780	0.755	0.732	0.712	0.693	0.676	0.661	0.646	0.633	0.621
2 0.5 → 0 2.5	0.783	0.763	0.745	0.729	0.714	0.700	0.687	0.675	0.664	0.654
2 0.5 → 1 1.5	1.190	1.215	1.239	1.262	1.286	1.310	1.334	1.360	1.387	1.416
2 0.5 → 1 2.5	0.475	0.456	0.439	0.424	0.409	0.396	0.384	0.372	0.361	0.351
2 0.5 → 1 3.5	0.773	0.749	0.728	0.709	0.692	0.676	0.661	0.647	0.633	0.619
2 1.5 → 0 2.5	0.783	0.763	0.745	0.729	0.714	0.700	0.687	0.675	0.664	0.654
2 1.5 → 1 1.5	0.928	0.941	0.955	0.968	0.982	0.996	1.010	1.025	1.042	1.059
2 1.5 → 1 2.5	0.758	0.751	0.745	0.739	0.735	0.731	0.727	0.725	0.722	0.720
2 1.5 → 1 3.5	0.751	0.727	0.706	0.687	0.670	0.654	0.639	0.626	0.613	0.600
2 1.5 → 2 0.5	0.267	0.260	0.254	0.249	0.244	0.239	0.234	0.230	0.226	0.222
2 1.5 → 2 4.5	0.803	0.775	0.751	0.729	0.709	0.691	0.675	0.660	0.647	0.634
2 2.5 → 0 2.5	0.783	0.763	0.745	0.729	0.714	0.700	0.687	0.675	0.664	0.654
2 2.5 → 1 1.5	0.594	0.593	0.592	0.592	0.593	0.593	0.594	0.595	0.596	0.597

(continued)

(continued)

$j \rightarrow j'$	Temperature / K									
	55	60	65	70	75	80	85	90	95	100
2 2.5 → 1 2.5	1.055	1.059	1.063	1.069	1.075	1.081	1.088	1.095	1.102	1.110
2 2.5 → 1 3.5	0.789	0.768	0.749	0.732	0.717	0.704	0.691	0.680	0.670	0.661
2 2.5 → 2 0.5	0.262	0.255	0.249	0.243	0.238	0.234	0.230	0.226	0.222	0.219
2 2.5 → 2 1.5	0.435	0.421	0.409	0.397	0.386	0.376	0.367	0.358	0.350	0.342
2 2.5 → 2 4.5	0.888	0.858	0.831	0.806	0.784	0.763	0.745	0.727	0.712	0.697
2 3.5 → 0 2.5	0.783	0.763	0.745	0.729	0.714	0.700	0.687	0.675	0.664	0.654
2 3.5 → 1 1.5	0.341	0.329	0.318	0.308	0.299	0.291	0.283	0.276	0.269	0.263
2 3.5 → 1 2.5	1.100	1.106	1.112	1.119	1.126	1.134	1.142	1.150	1.159	1.167
2 3.5 → 1 3.5	0.996	0.984	0.975	0.967	0.960	0.954	0.948	0.944	0.940	0.937
2 3.5 → 2 0.5	0.176	0.169	0.163	0.157	0.152	0.147	0.142	0.138	0.134	0.130
2 3.5 → 2 1.5	0.411	0.398	0.387	0.376	0.367	0.359	0.351	0.344	0.337	0.331
2 3.5 → 2 2.5	0.641	0.623	0.607	0.593	0.580	0.569	0.558	0.548	0.539	0.530
2 3.5 → 2 4.5	1.045	1.012	0.983	0.956	0.932	0.910	0.889	0.870	0.852	0.836
2 4.5 → 0 2.5	0.783	0.763	0.745	0.729	0.714	0.700	0.687	0.675	0.664	0.654
2 4.5 → 1 1.5	0.387	0.375	0.364	0.355	0.347	0.339	0.333	0.327	0.321	0.316
2 4.5 → 1 2.5	0.526	0.508	0.492	0.477	0.463	0.451	0.440	0.430	0.420	0.411
2 4.5 → 1 3.5	1.525	1.537	1.550	1.564	1.578	1.593	1.610	1.628	1.647	1.669
2 4.5 → 2 0.5	0.205	0.194	0.185	0.177	0.170	0.164	0.159	0.154	0.150	0.146
3 0.5 → 0 2.5	0.418	0.406	0.396	0.388	0.380	0.374	0.368	0.362	0.358	0.353
3 0.5 → 1 1.5	0.614	0.604	0.596	0.588	0.581	0.574	0.568	0.562	0.557	0.553
3 0.5 → 1 2.5	0.345	0.334	0.325	0.316	0.307	0.300	0.292	0.286	0.279	0.273
3 0.5 → 1 3.5	0.484	0.472	0.461	0.451	0.442	0.435	0.428	0.421	0.415	0.409
3 0.5 → 2 0.5	0.744	0.773	0.801	0.828	0.854	0.880	0.905	0.930	0.956	0.981
3 0.5 → 2 1.5	0.543	0.544	0.544	0.544	0.544	0.544	0.544	0.544	0.544	0.544
3 0.5 → 2 2.5	0.465	0.451	0.439	0.428	0.419	0.410	0.402	0.395	0.389	0.383
3 0.5 → 2 3.5	0.480	0.465	0.451	0.438	0.426	0.415	0.404	0.394	0.385	0.376
3 0.5 → 2 4.5	0.605	0.589	0.575	0.563	0.553	0.543	0.535	0.528	0.521	0.515
3 1.5 → 0 2.5	0.418	0.406	0.396	0.388	0.380	0.374	0.368	0.362	0.358	0.353
3 1.5 → 1 1.5	0.533	0.524	0.516	0.509	0.502	0.495	0.490	0.484	0.479	0.475
3 1.5 → 1 2.5	0.428	0.417	0.407	0.398	0.390	0.382	0.375	0.368	0.362	0.356
3 1.5 → 1 3.5	0.481	0.469	0.458	0.448	0.439	0.431	0.423	0.416	0.410	0.404
3 1.5 → 2 0.5	0.414	0.422	0.431	0.439	0.446	0.454	0.461	0.467	0.474	0.480
3 1.5 → 2 1.5	0.748	0.763	0.778	0.793	0.807	0.821	0.835	0.848	0.860	0.872
3 1.5 → 2 2.5	0.550	0.543	0.536	0.529	0.523	0.518	0.513	0.508	0.504	0.500
3 1.5 → 2 3.5	0.521	0.506	0.492	0.479	0.467	0.457	0.447	0.438	0.430	0.423
3 1.5 → 2 4.5	0.604	0.587	0.573	0.560	0.549	0.539	0.530	0.522	0.515	0.508
3 1.5 → 3 0.5	0.247	0.243	0.241	0.238	0.236	0.234	0.232	0.230	0.228	0.227
3 1.5 → 3 5.5	0.613	0.594	0.577	0.561	0.546	0.533	0.520	0.507	0.496	0.485
3 2.5 → 0 2.5	0.418	0.406	0.396	0.388	0.380	0.374	0.368	0.362	0.358	0.353
3 2.5 → 1 1.5	0.419	0.411	0.404	0.397	0.390	0.385	0.379	0.374	0.370	0.365
3 2.5 → 1 2.5	0.532	0.521	0.510	0.501	0.493	0.485	0.478	0.471	0.465	0.459
3 2.5 → 1 3.5	0.491	0.478	0.467	0.457	0.447	0.439	0.431	0.424	0.417	0.410
3 2.5 → 2 0.5	0.175	0.171	0.166	0.162	0.159	0.155	0.152	0.149	0.146	0.143
3 2.5 → 2 1.5	0.654	0.666	0.678	0.690	0.701	0.712	0.723	0.733	0.743	0.753
3 2.5 → 2 2.5	0.781	0.789	0.797	0.804	0.811	0.818	0.825	0.832	0.838	0.844
3 2.5 → 2 3.5	0.613	0.599	0.588	0.577	0.568	0.560	0.553	0.546	0.540	0.534
3 2.5 → 2 4.5	0.613	0.596	0.580	0.567	0.554	0.543	0.533	0.524	0.515	0.507
3 2.5 → 3 0.5	0.172	0.168	0.165	0.162	0.159	0.156	0.154	0.151	0.149	0.147
3 2.5 → 3 1.5	0.375	0.368	0.362	0.356	0.351	0.346	0.342	0.338	0.334	0.330
3 2.5 → 3 5.5	0.636	0.619	0.602	0.586	0.572	0.558	0.545	0.533	0.521	0.510
3 3.5 → 0 2.5	0.418	0.406	0.396	0.388	0.380	0.374	0.368	0.362	0.358	0.353
3 3.5 → 1 1.5	0.302	0.295	0.288	0.282	0.277	0.271	0.267	0.262	0.258	0.254
3 3.5 → 1 2.5	0.604	0.592	0.582	0.573	0.564	0.557	0.550	0.543	0.537	0.532
3 3.5 → 1 3.5	0.536	0.523	0.511	0.499	0.489	0.480	0.472	0.464	0.456	0.449
3 3.5 → 2 0.5	0.141	0.136	0.132	0.129	0.126	0.123	0.121	0.119	0.117	0.115
3 3.5 → 2 1.5	0.298	0.290	0.282	0.275	0.268	0.262	0.256	0.250	0.245	0.239
3 3.5 → 2 2.5	0.894	0.910	0.926	0.941	0.956	0.971	0.986	1.000	1.014	1.028
3 3.5 → 2 3.5	0.843	0.842	0.842	0.842	0.843	0.845	0.847	0.849	0.851	0.853
3 3.5 → 2 4.5	0.661	0.643	0.627	0.612	0.599	0.587	0.576	0.566	0.557	0.548
3 3.5 → 3 0.5	0.134	0.130	0.127	0.123	0.120	0.118	0.115	0.113	0.110	0.108
3 3.5 → 3 1.5	0.281	0.275	0.268	0.263	0.258	0.253	0.248	0.244	0.240	0.236
3 3.5 → 3 2.5	0.476	0.467	0.459	0.451	0.444	0.437	0.431	0.425	0.420	0.415
3 3.5 → 3 4.5	0.736	0.719	0.704	0.690	0.677	0.665	0.654	0.643	0.634	0.625
3 3.5 → 3 5.5	0.701	0.682	0.664	0.648	0.633	0.618	0.605	0.592	0.580	0.569
3 4.5 → 0 2.5	0.418	0.406	0.396	0.388	0.380	0.374	0.368	0.362	0.358	0.353
3 4.5 → 1 1.5	0.225	0.219	0.213	0.207	0.202	0.198	0.193	0.190	0.186	0.182
3 4.5 → 1 2.5	0.571	0.560	0.550	0.541	0.533	0.525	0.518	0.512	0.507	0.501
3 4.5 → 1 3.5	0.646	0.632	0.618	0.606	0.595	0.585	0.576	0.567	0.559	0.551
3 4.5 → 2 0.5	0.117	0.114	0.110	0.107	0.104	0.101	0.099	0.097	0.094	0.092
3 4.5 → 2 1.5	0.262	0.254	0.247	0.241	0.236	0.231	0.227	0.223	0.219	0.216
3 4.5 → 2 2.5	0.442	0.430	0.420	0.410	0.402	0.394	0.387	0.380	0.374	0.368
3 4.5 → 2 3.5	1.163	1.183	1.203	1.222	1.242	1.262	1.282	1.303	1.324	1.346
3 4.5 → 2 4.5	0.854	0.841	0.830	0.820	0.812	0.804	0.797	0.791	0.785	0.780
3 4.5 → 3 0.5	0.108	0.106	0.103	0.101	0.098	0.096	0.094	0.092	0.090	0.089
3 4.5 → 3 1.5	0.231	0.225	0.219	0.214	0.208	0.204	0.199	0.195	0.191	0.187
3 4.5 → 3 2.5	0.382	0.372	0.362	0.353	0.345	0.337	0.330	0.323	0.317	0.311
3 4.5 → 3 5.5	0.847	0.827	0.808	0.791	0.775	0.760	0.746	0.733	0.721	0.709
3 5.5 → 0 2.5	0.418	0.406	0.396	0.388	0.380	0.374	0.368	0.362	0.358	0.353
3 5.5 → 1 1.5	0.243	0.237	0.231	0.227	0.222	0.218	0.215	0.212	0.209	0.206
3 5.5 → 1 2.5	0.338	0.329	0.320	0.312	0.305	0.298	0.291	0.286	0.280	0.275

(continued)

(continued)

$j \rightarrow j'$	Temperature / K									
	55	60	65	70	75	80	85	90	95	100
3 5.5 → 1 3.5	0.861	0.844	0.829	0.816	0.803	0.792	0.781	0.771	0.762	0.754
3 5.5 → 2 0.5	0.121	0.118	0.115	0.113	0.111	0.109	0.108	0.106	0.105	0.104
3 5.5 → 2 1.5	0.240	0.233	0.228	0.222	0.218	0.214	0.210	0.207	0.204	0.201
3 5.5 → 2 2.5	0.370	0.359	0.349	0.341	0.333	0.326	0.320	0.314	0.308	0.303
3 5.5 → 2 3.5	0.556	0.540	0.526	0.512	0.500	0.489	0.479	0.470	0.461	0.453
3 5.5 → 2 4.5	1.549	1.570	1.591	1.612	1.633	1.654	1.675	1.696	1.718	1.741
3 5.5 → 3 0.5	0.101	0.097	0.094	0.092	0.089	0.087	0.085	0.083	0.081	0.079
4 1.5 → 0 2.5	0.337	0.327	0.319	0.311	0.304	0.298	0.292	0.287	0.282	0.277
4 1.5 → 1 1.5	0.290	0.287	0.283	0.281	0.278	0.277	0.275	0.274	0.274	0.273
4 1.5 → 1 2.5	0.276	0.267	0.260	0.253	0.246	0.240	0.235	0.229	0.224	0.220
4 1.5 → 1 3.5	0.411	0.403	0.396	0.390	0.385	0.380	0.376	0.372	0.369	0.365
4 1.5 → 2 0.5	0.326	0.323	0.320	0.318	0.316	0.315	0.313	0.312	0.311	0.310
4 1.5 → 2 1.5	0.351	0.345	0.340	0.335	0.331	0.327	0.324	0.320	0.317	0.315
4 1.5 → 2 2.5	0.355	0.345	0.337	0.329	0.321	0.315	0.308	0.303	0.297	0.293
4 1.5 → 2 3.5	0.384	0.373	0.364	0.354	0.346	0.338	0.330	0.323	0.316	0.309
4 1.5 → 2 4.5	0.456	0.441	0.428	0.416	0.404	0.394	0.384	0.374	0.366	0.358
4 1.5 → 3 0.5	0.609	0.633	0.656	0.679	0.700	0.721	0.740	0.759	0.778	0.795
4 1.5 → 3 1.5	0.581	0.588	0.594	0.600	0.607	0.612	0.618	0.624	0.629	0.635
4 1.5 → 3 2.5	0.412	0.406	0.399	0.394	0.389	0.384	0.380	0.376	0.372	0.368
4 1.5 → 3 3.5	0.396	0.387	0.379	0.372	0.365	0.359	0.354	0.348	0.344	0.339
4 1.5 → 3 4.5	0.379	0.369	0.359	0.351	0.342	0.335	0.328	0.321	0.315	0.309
4 1.5 → 3 5.5	0.522	0.506	0.491	0.477	0.464	0.452	0.441	0.430	0.420	0.410
4 1.5 → 4 6.5	0.400	0.388	0.376	0.366	0.357	0.348	0.341	0.334	0.328	0.322
4 2.5 → 0 2.5	0.337	0.327	0.319	0.311	0.304	0.298	0.292	0.287	0.282	0.277
4 2.5 → 1 1.5	0.261	0.256	0.253	0.249	0.247	0.244	0.242	0.240	0.239	0.238
4 2.5 → 1 2.5	0.312	0.304	0.298	0.292	0.286	0.281	0.277	0.273	0.269	0.265
4 2.5 → 1 3.5	0.405	0.396	0.389	0.382	0.377	0.372	0.367	0.363	0.359	0.355
4 2.5 → 2 0.5	0.185	0.182	0.180	0.177	0.175	0.173	0.172	0.170	0.168	0.167
4 2.5 → 2 1.5	0.409	0.403	0.397	0.392	0.388	0.384	0.380	0.377	0.374	0.371
4 2.5 → 2 2.5	0.403	0.395	0.387	0.380	0.374	0.368	0.362	0.357	0.352	0.348
4 2.5 → 2 3.5	0.413	0.401	0.391	0.381	0.372	0.363	0.355	0.348	0.341	0.334
4 2.5 → 2 4.5	0.461	0.447	0.434	0.421	0.410	0.400	0.390	0.381	0.372	0.364
4 2.5 → 3 0.5	0.184	0.180	0.177	0.174	0.171	0.168	0.165	0.162	0.160	0.158
4 2.5 → 3 1.5	0.675	0.697	0.719	0.740	0.760	0.780	0.799	0.817	0.835	0.852
4 2.5 → 3 2.5	0.644	0.649	0.655	0.660	0.665	0.671	0.676	0.681	0.686	0.691
4 2.5 → 3 3.5	0.438	0.429	0.421	0.414	0.408	0.401	0.396	0.390	0.385	0.380
4 2.5 → 3 4.5	0.454	0.442	0.432	0.422	0.413	0.404	0.396	0.389	0.382	0.376
4 2.5 → 3 5.5	0.504	0.489	0.475	0.462	0.450	0.438	0.428	0.418	0.408	0.399
4 2.5 → 4 1.5	0.347	0.344	0.340	0.337	0.334	0.332	0.329	0.327	0.325	0.323
4 2.5 → 4 6.5	0.425	0.412	0.400	0.389	0.379	0.370	0.362	0.354	0.347	0.340
4 3.5 → 0 2.5	0.337	0.327	0.319	0.311	0.304	0.298	0.292	0.287	0.282	0.277
4 3.5 → 1 1.5	0.228	0.223	0.218	0.215	0.211	0.208	0.206	0.203	0.201	0.199
4 3.5 → 1 2.5	0.347	0.341	0.335	0.330	0.326	0.322	0.319	0.316	0.313	0.311
4 3.5 → 1 3.5	0.403	0.394	0.386	0.379	0.372	0.367	0.362	0.357	0.352	0.348
4 3.5 → 2 0.5	0.113	0.110	0.107	0.105	0.102	0.100	0.098	0.096	0.094	0.093
4 3.5 → 2 1.5	0.333	0.327	0.321	0.316	0.312	0.308	0.304	0.301	0.298	0.295
4 3.5 → 2 2.5	0.484	0.476	0.468	0.462	0.455	0.450	0.444	0.439	0.435	0.431
4 3.5 → 2 3.5	0.466	0.453	0.442	0.432	0.423	0.414	0.406	0.399	0.392	0.386
4 3.5 → 2 4.5	0.476	0.462	0.449	0.437	0.426	0.415	0.405	0.396	0.387	0.379
4 3.5 → 3 0.5	0.109	0.107	0.104	0.102	0.101	0.099	0.097	0.096	0.095	0.093
4 3.5 → 3 1.5	0.286	0.280	0.275	0.270	0.265	0.261	0.256	0.252	0.249	0.245
4 3.5 → 3 2.5	0.787	0.810	0.832	0.853	0.874	0.894	0.913	0.932	0.950	0.968
4 3.5 → 3 3.5	0.680	0.680	0.681	0.683	0.684	0.685	0.687	0.689	0.691	0.692
4 3.5 → 3 4.5	0.534	0.522	0.511	0.500	0.491	0.482	0.473	0.465	0.458	0.451
4 3.5 → 3 5.5	0.503	0.489	0.476	0.463	0.452	0.442	0.432	0.423	0.414	0.406
4 3.5 → 4 1.5	0.233	0.229	0.224	0.220	0.216	0.213	0.209	0.206	0.203	0.200
4 3.5 → 4 2.5	0.404	0.398	0.393	0.389	0.384	0.380	0.377	0.373	0.370	0.367
4 3.5 → 4 6.5	0.469	0.456	0.444	0.432	0.421	0.411	0.402	0.393	0.385	0.377
4 4.5 → 0 2.5	0.337	0.327	0.319	0.311	0.304	0.298	0.292	0.287	0.282	0.277
4 4.5 → 1 1.5	0.200	0.195	0.190	0.186	0.182	0.179	0.176	0.173	0.170	0.168
4 4.5 → 1 2.5	0.368	0.362	0.357	0.352	0.349	0.346	0.343	0.341	0.339	0.338
4 4.5 → 1 3.5	0.410	0.401	0.392	0.385	0.378	0.372	0.367	0.362	0.357	0.353
4 4.5 → 2 0.5	0.105	0.102	0.099	0.097	0.094	0.092	0.090	0.088	0.086	0.085
4 4.5 → 2 1.5	0.203	0.198	0.193	0.188	0.184	0.180	0.176	0.173	0.169	0.166
4 4.5 → 2 2.5	0.486	0.477	0.469	0.461	0.455	0.449	0.443	0.438	0.433	0.429
4 4.5 → 2 3.5	0.562	0.551	0.540	0.530	0.521	0.513	0.506	0.499	0.492	0.486
4 4.5 → 2 4.5	0.516	0.501	0.488	0.476	0.465	0.454	0.444	0.435	0.426	0.418
4 4.5 → 3 0.5	0.094	0.092	0.090	0.088	0.087	0.086	0.084	0.083	0.082	0.081
4 4.5 → 3 1.5	0.182	0.178	0.174	0.170	0.166	0.163	0.160	0.158	0.155	0.152
4 4.5 → 3 2.5	0.362	0.353	0.345	0.338	0.331	0.325	0.319	0.313	0.308	0.302
4 4.5 → 3 3.5	0.983	1.006	1.028	1.050	1.071	1.092	1.111	1.131	1.149	1.167
4 4.5 → 3 4.5	0.734	0.728	0.724	0.719	0.715	0.712	0.709	0.706	0.703	0.701
4 4.5 → 3 5.5	0.544	0.530	0.518	0.506	0.496	0.486	0.477	0.468	0.460	0.453
4 4.5 → 4 1.5	0.174	0.169	0.165	0.162	0.158	0.155	0.152	0.149	0.146	0.143
4 4.5 → 4 2.5	0.289	0.283	0.277	0.271	0.266	0.261	0.256	0.251	0.247	0.243
4 4.5 → 4 3.5	0.460	0.452	0.446	0.440	0.434	0.429	0.424	0.419	0.415	0.411
4 4.5 → 4 5.5	0.632	0.620	0.610	0.600	0.591	0.583	0.576	0.569	0.562	0.556
4 4.5 → 4 6.5	0.551	0.537	0.524	0.511	0.500	0.489	0.478	0.469	0.460	0.451
4 5.5 → 0 2.5	0.337	0.327	0.319	0.311	0.304	0.298	0.292	0.287	0.282	0.277
4 5.5 → 1 1.5	0.189	0.184	0.180	0.176	0.172	0.169	0.166	0.163	0.160	0.158

(continued)

(continued)

$j \rightarrow j'$	Temperature / K									
	55	60	65	70	75	80	85	90	95	100
4 5.5 → 1 2.5	0.353	0.347	0.342	0.338	0.334	0.331	0.328	0.325	0.323	0.321
4 5.5 → 1 3.5	0.435	0.426	0.418	0.410	0.404	0.398	0.392	0.387	0.383	0.379
4 5.5 → 2 0.5	0.091	0.089	0.086	0.084	0.082	0.080	0.078	0.076	0.075	0.073
4 5.5 → 2 1.5	0.199	0.193	0.187	0.182	0.177	0.173	0.169	0.165	0.161	0.158
4 5.5 → 2 2.5	0.306	0.297	0.289	0.282	0.275	0.268	0.262	0.257	0.251	0.247
4 5.5 → 2 3.5	0.655	0.643	0.633	0.624	0.615	0.607	0.600	0.594	0.588	0.582
4 5.5 → 2 4.5	0.621	0.607	0.593	0.581	0.570	0.560	0.550	0.541	0.533	0.525
4 5.5 → 3 0.5	0.072	0.070	0.068	0.066	0.064	0.063	0.062	0.060	0.059	0.058
4 5.5 → 3 1.5	0.171	0.167	0.162	0.159	0.155	0.152	0.149	0.146	0.143	0.141
4 5.5 → 3 2.5	0.290	0.282	0.275	0.269	0.263	0.258	0.253	0.248	0.243	0.239
4 5.5 → 3 3.5	0.461	0.450	0.439	0.430	0.420	0.412	0.404	0.396	0.389	0.382
4 5.5 → 3 4.5	1.178	1.202	1.226	1.248	1.271	1.293	1.314	1.334	1.354	1.373
4 5.5 → 3 5.5	0.728	0.718	0.709	0.700	0.693	0.686	0.680	0.674	0.669	0.664
4 5.5 → 4 1.5	0.138	0.134	0.130	0.127	0.123	0.120	0.117	0.114	0.112	0.109
4 5.5 → 4 2.5	0.224	0.218	0.212	0.207	0.202	0.198	0.193	0.189	0.186	0.182
4 5.5 → 4 6.5	0.726	0.712	0.698	0.685	0.674	0.662	0.652	0.642	0.632	0.623
4 6.5 → 0 2.5	0.337	0.327	0.319	0.311	0.304	0.298	0.292	0.287	0.282	0.277
4 6.5 → 1 1.5	0.208	0.205	0.201	0.199	0.196	0.194	0.192	0.190	0.189	0.187
4 6.5 → 1 2.5	0.280	0.273	0.266	0.260	0.255	0.250	0.245	0.241	0.236	0.233
4 6.5 → 1 3.5	0.488	0.479	0.471	0.465	0.459	0.453	0.449	0.445	0.441	0.438
4 6.5 → 2 0.5	0.091	0.088	0.085	0.083	0.080	0.078	0.076	0.074	0.072	0.071
4 6.5 → 2 1.5	0.182	0.176	0.171	0.166	0.162	0.158	0.154	0.150	0.147	0.143
4 6.5 → 2 2.5	0.284	0.276	0.268	0.261	0.254	0.248	0.242	0.236	0.231	0.226
4 6.5 → 2 3.5	0.410	0.398	0.387	0.377	0.368	0.360	0.352	0.345	0.338	0.331
4 6.5 → 2 4.5	0.906	0.891	0.878	0.866	0.855	0.845	0.836	0.828	0.821	0.814
4 6.5 → 3 0.5	0.088	0.086	0.083	0.081	0.078	0.076	0.074	0.072	0.070	0.068
4 6.5 → 3 1.5	0.169	0.164	0.159	0.155	0.151	0.147	0.143	0.139	0.136	0.133
4 6.5 → 3 2.5	0.247	0.240	0.234	0.227	0.222	0.216	0.211	0.207	0.202	0.198
4 6.5 → 3 3.5	0.343	0.334	0.326	0.318	0.311	0.305	0.298	0.293	0.287	0.282
4 6.5 → 3 4.5	0.520	0.508	0.497	0.487	0.477	0.469	0.460	0.453	0.446	0.439
4 6.5 → 3 5.5	1.531	1.556	1.580	1.604	1.628	1.650	1.673	1.694	1.715	1.735
5 2.5 → 0 2.5	0.280	0.275	0.272	0.268	0.265	0.262	0.259	0.256	0.254	0.251
5 2.5 → 1 1.5	0.219	0.216	0.213	0.210	0.208	0.205	0.203	0.201	0.200	0.198
5 2.5 → 1 2.5	0.234	0.228	0.223	0.218	0.213	0.208	0.204	0.199	0.195	0.191
5 2.5 → 1 3.5	0.346	0.335	0.324	0.314	0.306	0.297	0.289	0.282	0.275	0.269
5 2.5 → 2 0.5	0.143	0.142	0.142	0.141	0.141	0.141	0.142	0.142	0.143	0.143
5 2.5 → 2 1.5	0.214	0.211	0.208	0.206	0.204	0.202	0.201	0.199	0.198	0.197
5 2.5 → 2 2.5	0.262	0.257	0.254	0.250	0.247	0.244	0.241	0.239	0.236	0.234
5 2.5 → 2 3.5	0.263	0.258	0.253	0.248	0.243	0.239	0.235	0.231	0.227	0.224
5 2.5 → 2 4.5	0.393	0.380	0.369	0.359	0.349	0.340	0.331	0.323	0.315	0.308
5 2.5 → 3 0.5	0.277	0.276	0.276	0.275	0.275	0.275	0.275	0.275	0.275	0.275
5 2.5 → 3 1.5	0.355	0.351	0.348	0.345	0.342	0.340	0.337	0.335	0.334	0.332
5 2.5 → 3 2.5	0.339	0.332	0.325	0.320	0.314	0.309	0.304	0.300	0.296	0.292
5 2.5 → 3 3.5	0.341	0.332	0.323	0.315	0.307	0.300	0.293	0.287	0.281	0.275
5 2.5 → 3 4.5	0.326	0.315	0.305	0.296	0.288	0.280	0.273	0.266	0.260	0.254
5 2.5 → 3 5.5	0.321	0.310	0.300	0.292	0.284	0.277	0.271	0.265	0.260	0.256
5 2.5 → 4 1.5	0.836	0.864	0.892	0.919	0.945	0.970	0.995	1.018	1.041	1.063
5 2.5 → 4 2.5	0.521	0.522	0.523	0.524	0.525	0.526	0.527	0.529	0.530	0.531
5 2.5 → 4 3.5	0.385	0.380	0.375	0.370	0.366	0.362	0.358	0.354	0.350	0.346
5 2.5 → 4 4.5	0.362	0.354	0.346	0.339	0.333	0.326	0.320	0.314	0.309	0.303
5 2.5 → 4 5.5	0.311	0.302	0.294	0.286	0.279	0.272	0.266	0.260	0.255	0.249
5 2.5 → 4 6.5	0.245	0.238	0.232	0.226	0.221	0.216	0.212	0.208	0.204	0.201
5 2.5 → 5 7.5	0.260	0.257	0.255	0.253	0.251	0.250	0.249	0.248	0.248	0.248
5 3.5 → 0 2.5	0.280	0.275	0.272	0.268	0.265	0.262	0.259	0.256	0.254	0.251
5 3.5 → 1 1.5	0.199	0.195	0.192	0.189	0.187	0.184	0.182	0.179	0.177	0.175
5 3.5 → 1 2.5	0.261	0.254	0.249	0.243	0.238	0.233	0.229	0.225	0.220	0.217
5 3.5 → 1 3.5	0.341	0.330	0.320	0.311	0.302	0.294	0.287	0.280	0.273	0.267
5 3.5 → 2 0.5	0.104	0.103	0.101	0.100	0.099	0.098	0.097	0.096	0.095	0.095
5 3.5 → 2 1.5	0.220	0.218	0.216	0.215	0.214	0.213	0.212	0.212	0.211	0.211
5 3.5 → 2 2.5	0.257	0.252	0.248	0.245	0.242	0.239	0.236	0.233	0.231	0.229
5 3.5 → 2 3.5	0.319	0.312	0.306	0.300	0.294	0.289	0.284	0.280	0.275	0.271
5 3.5 → 2 4.5	0.376	0.365	0.355	0.346	0.337	0.329	0.321	0.314	0.307	0.301
5 3.5 → 3 0.5	0.122	0.120	0.118	0.116	0.114	0.112	0.110	0.108	0.107	0.106
5 3.5 → 3 1.5	0.348	0.344	0.342	0.339	0.337	0.335	0.333	0.332	0.330	0.329
5 3.5 → 3 2.5	0.419	0.412	0.407	0.401	0.397	0.392	0.389	0.385	0.382	0.379
5 3.5 → 3 3.5	0.367	0.358	0.351	0.343	0.337	0.331	0.325	0.320	0.315	0.310
5 3.5 → 3 4.5	0.361	0.351	0.341	0.332	0.324	0.316	0.309	0.302	0.296	0.290
5 3.5 → 3 5.5	0.343	0.331	0.321	0.312	0.304	0.296	0.289	0.283	0.277	0.271
5 3.5 → 4 1.5	0.266	0.262	0.258	0.254	0.251	0.247	0.244	0.241	0.239	0.236
5 3.5 → 4 2.5	0.806	0.834	0.861	0.887	0.913	0.937	0.960	0.983	1.005	1.026
5 3.5 → 4 3.5	0.569	0.568	0.568	0.567	0.567	0.568	0.568	0.568	0.569	0.569
5 3.5 → 4 4.5	0.383	0.376	0.370	0.365	0.360	0.355	0.350	0.346	0.342	0.338
5 3.5 → 4 5.5	0.348	0.340	0.333	0.326	0.319	0.313	0.307	0.301	0.296	0.291
5 3.5 → 4 6.5	0.287	0.279	0.272	0.265	0.258	0.253	0.247	0.242	0.238	0.233
5 3.5 → 5 2.5	0.392	0.388	0.384	0.381	0.378	0.375	0.372	0.369	0.367	0.364
5 3.5 → 5 7.5	0.285	0.280	0.276	0.273	0.270	0.267	0.264	0.262	0.260	0.258
5 4.5 → 0 2.5	0.280	0.275	0.272	0.268	0.265	0.262	0.259	0.256	0.254	0.251
5 4.5 → 1 1.5	0.178	0.175	0.171	0.168	0.165	0.162	0.159	0.157	0.154	0.152
5 4.5 → 1 2.5	0.283	0.277	0.270	0.265	0.260	0.255	0.250	0.246	0.242	0.238
5 4.5 → 1 3.5	0.338	0.328	0.319	0.310	0.302	0.294	0.287	0.281	0.274	0.268

(continued)

(continued)

$j \rightarrow j'$	Temperature / K									
	55	60	65	70	75	80	85	90	95	100
5 4.5 → 2 0.5	0.085	0.083	0.082	0.080	0.079	0.078	0.077	0.076	0.075	0.074
5 4.5 → 2 1.5	0.184	0.181	0.179	0.177	0.175	0.174	0.172	0.171	0.170	0.169
5 4.5 → 2 2.5	0.279	0.275	0.271	0.268	0.265	0.262	0.260	0.258	0.256	0.254
5 4.5 → 2 3.5	0.358	0.350	0.342	0.336	0.330	0.324	0.319	0.314	0.309	0.305
5 4.5 → 2 4.5	0.370	0.361	0.352	0.344	0.336	0.329	0.322	0.316	0.310	0.304
5 4.5 → 3 0.5	0.092	0.090	0.087	0.085	0.083	0.082	0.080	0.078	0.077	0.075
5 4.5 → 3 1.5	0.202	0.197	0.192	0.188	0.184	0.180	0.177	0.174	0.170	0.168
5 4.5 → 3 2.5	0.421	0.416	0.411	0.407	0.404	0.401	0.398	0.396	0.393	0.391
5 4.5 → 3 3.5	0.457	0.450	0.443	0.436	0.431	0.425	0.421	0.416	0.412	0.409
5 4.5 → 3 4.5	0.406	0.395	0.386	0.377	0.369	0.362	0.356	0.350	0.344	0.339
5 4.5 → 3 5.5	0.381	0.369	0.358	0.348	0.338	0.330	0.322	0.315	0.308	0.301
5 4.5 → 4 1.5	0.173	0.170	0.168	0.166	0.164	0.162	0.160	0.158	0.156	0.154
5 4.5 → 4 2.5	0.326	0.319	0.312	0.306	0.301	0.295	0.290	0.286	0.281	0.277
5 4.5 → 4 3.5	0.845	0.873	0.900	0.926	0.951	0.976	0.999	1.022	1.044	1.065
5 4.5 → 4 4.5	0.569	0.567	0.566	0.565	0.564	0.564	0.563	0.563	0.563	0.564
5 4.5 → 4 5.5	0.396	0.389	0.383	0.377	0.371	0.366	0.361	0.356	0.352	0.348
5 4.5 → 4 6.5	0.350	0.341	0.332	0.324	0.317	0.310	0.303	0.297	0.291	0.286
5 4.5 → 5 2.5	0.259	0.254	0.249	0.245	0.241	0.237	0.233	0.229	0.226	0.222
5 4.5 → 5 3.5	0.405	0.400	0.396	0.393	0.389	0.386	0.383	0.381	0.378	0.376
5 4.5 → 5 6.5	0.429	0.422	0.415	0.409	0.403	0.398	0.393	0.388	0.384	0.380
5 4.5 → 5 7.5	0.341	0.335	0.329	0.323	0.318	0.313	0.308	0.304	0.300	0.296
5 5.5 → 0 2.5	0.280	0.275	0.272	0.268	0.265	0.262	0.259	0.256	0.254	0.251
5 5.5 → 1 1.5	0.164	0.160	0.156	0.152	0.149	0.145	0.142	0.139	0.136	0.133
5 5.5 → 1 2.5	0.294	0.287	0.280	0.274	0.269	0.264	0.259	0.255	0.251	0.247
5 5.5 → 1 3.5	0.342	0.333	0.324	0.316	0.309	0.302	0.295	0.289	0.283	0.278
5 5.5 → 2 0.5	0.075	0.074	0.072	0.071	0.070	0.069	0.068	0.067	0.066	0.065
5 5.5 → 2 1.5	0.146	0.142	0.139	0.136	0.133	0.130	0.128	0.125	0.123	0.121
5 5.5 → 2 2.5	0.291	0.286	0.281	0.277	0.274	0.271	0.268	0.266	0.264	0.262
5 5.5 → 2 3.5	0.380	0.372	0.365	0.358	0.353	0.347	0.343	0.338	0.334	0.331
5 5.5 → 2 4.5	0.384	0.375	0.368	0.360	0.354	0.348	0.342	0.336	0.331	0.326
5 5.5 → 3 0.5	0.078	0.076	0.074	0.071	0.069	0.068	0.066	0.064	0.063	0.061
5 5.5 → 3 1.5	0.153	0.148	0.145	0.141	0.137	0.134	0.131	0.128	0.126	0.123
5 5.5 → 3 2.5	0.257	0.251	0.245	0.239	0.234	0.229	0.225	0.221	0.217	0.213
5 5.5 → 3 3.5	0.522	0.515	0.509	0.504	0.499	0.495	0.492	0.489	0.486	0.484
5 5.5 → 3 4.5	0.503	0.493	0.484	0.477	0.470	0.463	0.457	0.452	0.447	0.443
5 5.5 → 3 5.5	0.447	0.434	0.422	0.411	0.401	0.391	0.383	0.374	0.367	0.360
5 5.5 → 4 1.5	0.139	0.136	0.133	0.130	0.127	0.124	0.122	0.119	0.117	0.115
5 5.5 → 4 2.5	0.206	0.202	0.198	0.195	0.192	0.189	0.187	0.184	0.182	0.179
5 5.5 → 4 3.5	0.354	0.346	0.340	0.333	0.327	0.322	0.317	0.312	0.307	0.303
5 5.5 → 4 4.5	0.944	0.972	0.999	1.026	1.052	1.077	1.101	1.124	1.147	1.169
5 5.5 → 4 5.5	0.574	0.570	0.567	0.565	0.563	0.561	0.559	0.558	0.557	0.556
5 5.5 → 4 6.5	0.443	0.433	0.424	0.415	0.407	0.399	0.392	0.385	0.379	0.373
5 5.5 → 5 2.5	0.183	0.179	0.175	0.172	0.168	0.165	0.162	0.159	0.156	0.153
5 5.5 → 5 3.5	0.268	0.263	0.259	0.255	0.251	0.247	0.243	0.239	0.236	0.233
5 5.5 → 5 4.5	0.429	0.425	0.421	0.417	0.414	0.411	0.408	0.406	0.404	0.402
5 5.5 → 5 6.5	0.549	0.543	0.537	0.532	0.528	0.523	0.520	0.516	0.513	0.510
5 5.5 → 5 7.5	0.445	0.436	0.428	0.420	0.413	0.405	0.399	0.392	0.386	0.380
5 6.5 → 0 2.5	0.280	0.275	0.272	0.268	0.265	0.262	0.259	0.256	0.254	0.251
5 6.5 → 1 1.5	0.161	0.156	0.151	0.147	0.143	0.139	0.136	0.132	0.129	0.126
5 6.5 → 1 2.5	0.283	0.275	0.269	0.263	0.257	0.252	0.247	0.242	0.238	0.234
5 6.5 → 1 3.5	0.356	0.348	0.340	0.333	0.326	0.320	0.314	0.308	0.303	0.298
5 6.5 → 2 0.5	0.061	0.060	0.058	0.057	0.055	0.054	0.053	0.051	0.050	0.049
5 6.5 → 2 1.5	0.157	0.154	0.150	0.147	0.144	0.142	0.139	0.137	0.134	0.132
5 6.5 → 2 2.5	0.249	0.243	0.237	0.231	0.226	0.221	0.216	0.212	0.208	0.204
5 6.5 → 2 3.5	0.379	0.373	0.367	0.362	0.357	0.353	0.349	0.346	0.343	0.341
5 6.5 → 2 4.5	0.428	0.420	0.413	0.407	0.401	0.396	0.391	0.386	0.382	0.378
5 6.5 → 3 0.5	0.059	0.057	0.055	0.054	0.052	0.050	0.049	0.048	0.046	0.045
5 6.5 → 3 1.5	0.131	0.127	0.123	0.120	0.116	0.113	0.111	0.108	0.106	0.103
5 6.5 → 3 2.5	0.213	0.207	0.201	0.196	0.191	0.187	0.183	0.179	0.176	0.172
5 6.5 → 3 3.5	0.321	0.312	0.305	0.298	0.292	0.286	0.280	0.276	0.271	0.267
5 6.5 → 3 4.5	0.653	0.645	0.638	0.631	0.625	0.620	0.615	0.611	0.608	0.604
5 6.5 → 3 5.5	0.581	0.567	0.555	0.544	0.533	0.524	0.515	0.506	0.499	0.491
5 6.5 → 4 1.5	0.099	0.096	0.093	0.090	0.088	0.085	0.083	0.081	0.079	0.077
5 6.5 → 4 2.5	0.166	0.162	0.158	0.155	0.151	0.148	0.145	0.142	0.139	0.137
5 6.5 → 4 3.5	0.243	0.238	0.234	0.230	0.226	0.223	0.220	0.216	0.213	0.210
5 6.5 → 4 4.5	0.390	0.383	0.376	0.370	0.364	0.359	0.353	0.349	0.344	0.340
5 6.5 → 4 5.5	1.115	1.142	1.169	1.195	1.220	1.245	1.269	1.293	1.316	1.338
5 6.5 → 4 6.5	0.646	0.639	0.631	0.624	0.618	0.612	0.606	0.601	0.596	0.591
5 6.5 → 5 2.5	0.122	0.119	0.117	0.114	0.112	0.110	0.108	0.106	0.105	0.103
5 6.5 → 5 3.5	0.205	0.201	0.197	0.194	0.191	0.188	0.185	0.182	0.180	0.177
5 6.5 → 5 7.5	0.648	0.637	0.627	0.618	0.609	0.600	0.592	0.584	0.577	0.570
5 7.5 → 0 2.5	0.280	0.275	0.272	0.268	0.265	0.262	0.259	0.256	0.254	0.251
5 7.5 → 1 1.5	0.176	0.170	0.165	0.160	0.155	0.151	0.147	0.143	0.140	0.136
5 7.5 → 1 2.5	0.236	0.229	0.223	0.217	0.211	0.205	0.200	0.195	0.191	0.186
5 7.5 → 1 3.5	0.386	0.379	0.372	0.366	0.360	0.354	0.349	0.344	0.340	0.336
5 7.5 → 2 0.5	0.082	0.080	0.077	0.075	0.073	0.071	0.069	0.067	0.066	0.064
5 7.5 → 2 1.5	0.150	0.145	0.141	0.137	0.134	0.130	0.127	0.124	0.121	0.118
5 7.5 → 2 2.5	0.215	0.210	0.205	0.200	0.196	0.192	0.188	0.184	0.180	0.177
5 7.5 → 2 3.5	0.305	0.298	0.292	0.287	0.282	0.277	0.272	0.268	0.264	0.260
5 7.5 → 2 4.5	0.523	0.517	0.511	0.506	0.501	0.498	0.495	0.492	0.490	0.488

(continued)

(continued)

$j \rightarrow j'$	Temperature / K									
	55	60	65	70	75	80	85	90	95	100
5 7.5 → 3 0.5	0.052	0.050	0.048	0.047	0.046	0.044	0.043	0.042	0.041	0.041
5 7.5 → 3 1.5	0.108	0.104	0.101	0.098	0.095	0.093	0.091	0.089	0.087	0.086
5 7.5 → 3 2.5	0.176	0.170	0.165	0.160	0.156	0.152	0.148	0.145	0.141	0.138
5 7.5 → 3 3.5	0.270	0.262	0.254	0.247	0.240	0.234	0.228	0.223	0.218	0.213
5 7.5 → 3 4.5	0.419	0.407	0.397	0.387	0.378	0.369	0.361	0.354	0.347	0.341
5 7.5 → 3 5.5	0.935	0.924	0.913	0.904	0.896	0.888	0.881	0.875	0.870	0.865
5 7.5 → 4 1.5	0.068	0.066	0.064	0.063	0.061	0.060	0.059	0.058	0.057	0.056
5 7.5 → 4 2.5	0.117	0.114	0.111	0.108	0.105	0.103	0.101	0.099	0.097	0.095
5 7.5 → 4 3.5	0.190	0.185	0.180	0.176	0.171	0.167	0.164	0.160	0.157	0.154
5 7.5 → 4 4.5	0.299	0.292	0.285	0.279	0.274	0.268	0.263	0.258	0.253	0.249
5 7.5 → 4 5.5	0.494	0.484	0.476	0.468	0.460	0.452	0.445	0.439	0.432	0.426
5 7.5 → 4 6.5	1.491	1.519	1.546	1.572	1.597	1.622	1.646	1.670	1.692	1.714
6 3.5 → 0 2.5	0.223	0.217	0.212	0.206	0.201	0.196	0.192	0.187	0.183	0.179
6 3.5 → 1 1.5	0.202	0.201	0.201	0.200	0.200	0.199	0.199	0.198	0.198	0.197
6 3.5 → 1 2.5	0.186	0.182	0.179	0.175	0.172	0.169	0.166	0.163	0.160	0.158
6 3.5 → 1 3.5	0.292	0.282	0.274	0.266	0.258	0.251	0.245	0.239	0.233	0.228
6 3.5 → 2 0.5	0.123	0.121	0.119	0.117	0.116	0.114	0.113	0.112	0.111	0.110
6 3.5 → 2 1.5	0.188	0.185	0.181	0.179	0.176	0.173	0.171	0.169	0.167	0.165
6 3.5 → 2 2.5	0.228	0.222	0.217	0.212	0.207	0.203	0.199	0.195	0.191	0.187
6 3.5 → 2 3.5	0.217	0.211	0.205	0.200	0.195	0.190	0.186	0.181	0.177	0.174
6 3.5 → 2 4.5	0.240	0.232	0.226	0.220	0.215	0.210	0.206	0.202	0.199	0.196
6 3.5 → 3 0.5	0.146	0.143	0.142	0.141	0.140	0.139	0.139	0.139	0.139	0.139
6 3.5 → 3 1.5	0.227	0.224	0.222	0.220	0.218	0.217	0.216	0.215	0.214	0.213
6 3.5 → 3 2.5	0.254	0.251	0.248	0.246	0.243	0.241	0.238	0.236	0.234	0.232
6 3.5 → 3 3.5	0.268	0.262	0.257	0.252	0.247	0.242	0.238	0.234	0.230	0.226
6 3.5 → 3 4.5	0.245	0.238	0.231	0.225	0.220	0.214	0.209	0.205	0.200	0.196
6 3.5 → 3 5.5	0.199	0.193	0.188	0.183	0.178	0.175	0.171	0.168	0.165	0.163
6 3.5 → 4 1.5	0.462	0.459	0.457	0.455	0.454	0.453	0.452	0.452	0.452	0.452
6 3.5 → 4 2.5	0.388	0.384	0.380	0.376	0.372	0.369	0.366	0.363	0.361	0.358
6 3.5 → 4 3.5	0.330	0.323	0.317	0.312	0.306	0.301	0.296	0.291	0.287	0.282
6 3.5 → 4 4.5	0.292	0.285	0.278	0.271	0.265	0.260	0.254	0.249	0.244	0.240
6 3.5 → 4 5.5	0.238	0.231	0.225	0.220	0.215	0.210	0.206	0.202	0.199	0.195
6 3.5 → 4 6.5	0.233	0.229	0.226	0.223	0.221	0.219	0.218	0.217	0.216	0.215
6 3.5 → 5 2.5	0.979	1.006	1.033	1.059	1.085	1.111	1.136	1.161	1.185	1.208
6 3.5 → 5 3.5	0.509	0.507	0.506	0.504	0.503	0.502	0.501	0.500	0.499	0.498
6 3.5 → 5 4.5	0.371	0.365	0.359	0.353	0.347	0.342	0.337	0.332	0.327	0.323
6 3.5 → 5 5.5	0.285	0.278	0.272	0.266	0.260	0.255	0.249	0.245	0.240	0.236
6 3.5 → 5 6.5	0.224	0.218	0.213	0.208	0.204	0.200	0.196	0.192	0.189	0.186
6 3.5 → 5 7.5	0.218	0.213	0.209	0.206	0.203	0.200	0.197	0.195	0.193	0.191
6 3.5 → 6 8.5	0.223	0.223	0.224	0.224	0.224	0.224	0.224	0.224	0.225	0.225
6 4.5 → 0 2.5	0.223	0.217	0.212	0.206	0.201	0.196	0.192	0.187	0.183	0.179
6 4.5 → 1 1.5	0.174	0.173	0.172	0.171	0.170	0.168	0.167	0.166	0.165	0.164
6 4.5 → 1 2.5	0.222	0.219	0.215	0.212	0.209	0.206	0.203	0.200	0.197	0.195
6 4.5 → 1 3.5	0.285	0.276	0.269	0.261	0.254	0.248	0.242	0.236	0.231	0.225
6 4.5 → 2 0.5	0.088	0.086	0.085	0.083	0.082	0.081	0.080	0.079	0.078	0.077
6 4.5 → 2 1.5	0.189	0.185	0.181	0.177	0.174	0.171	0.168	0.165	0.163	0.161
6 4.5 → 2 2.5	0.217	0.213	0.209	0.205	0.201	0.198	0.195	0.192	0.189	0.186
6 4.5 → 2 3.5	0.251	0.244	0.238	0.232	0.227	0.222	0.218	0.213	0.209	0.205
6 4.5 → 2 4.5	0.249	0.241	0.234	0.228	0.223	0.218	0.213	0.209	0.205	0.202
6 4.5 → 3 0.5	0.090	0.089	0.088	0.088	0.087	0.086	0.085	0.084	0.083	0.081
6 4.5 → 3 1.5	0.203	0.200	0.197	0.195	0.193	0.192	0.191	0.190	0.189	0.188
6 4.5 → 3 2.5	0.275	0.270	0.265	0.261	0.257	0.254	0.251	0.248	0.246	0.244
6 4.5 → 3 3.5	0.270	0.266	0.262	0.258	0.255	0.252	0.249	0.246	0.243	0.241
6 4.5 → 3 4.5	0.269	0.262	0.256	0.251	0.246	0.241	0.237	0.232	0.229	0.225
6 4.5 → 3 5.5	0.232	0.225	0.219	0.213	0.208	0.204	0.199	0.195	0.192	0.188
6 4.5 → 4 1.5	0.201	0.198	0.195	0.192	0.189	0.187	0.184	0.182	0.180	0.177
6 4.5 → 4 2.5	0.460	0.455	0.451	0.447	0.445	0.442	0.440	0.438	0.437	0.436
6 4.5 → 4 3.5	0.409	0.404	0.399	0.395	0.391	0.388	0.384	0.381	0.378	0.376
6 4.5 → 4 4.5	0.323	0.317	0.311	0.306	0.301	0.296	0.291	0.287	0.283	0.279
6 4.5 → 4 5.5	0.300	0.294	0.287	0.282	0.276	0.272	0.267	0.263	0.260	0.256
6 4.5 → 4 6.5	0.250	0.245	0.240	0.236	0.233	0.229	0.227	0.224	0.222	0.220
6 4.5 → 5 2.5	0.321	0.317	0.314	0.310	0.306	0.303	0.299	0.296	0.293	0.290
6 4.5 → 5 3.5	0.891	0.916	0.941	0.965	0.990	1.013	1.037	1.060	1.083	1.105
6 4.5 → 5 4.5	0.490	0.489	0.488	0.487	0.487	0.487	0.487	0.487	0.487	0.487
6 4.5 → 5 5.5	0.359	0.353	0.347	0.342	0.337	0.333	0.328	0.324	0.320	0.316
6 4.5 → 5 6.5	0.291	0.284	0.278	0.272	0.267	0.262	0.257	0.253	0.249	0.245
6 4.5 → 5 7.5	0.234	0.229	0.224	0.220	0.216	0.212	0.209	0.206	0.203	0.200
6 4.5 → 6 3.5	0.402	0.399	0.396	0.393	0.390	0.387	0.384	0.382	0.379	0.377
6 4.5 → 6 8.5	0.232	0.231	0.229	0.228	0.227	0.226	0.225	0.224	0.223	0.222
6 5.5 → 0 2.5	0.223	0.217	0.212	0.206	0.201	0.196	0.192	0.187	0.183	0.179
6 5.5 → 1 1.5	0.149	0.147	0.145	0.143	0.142	0.140	0.138	0.137	0.135	0.133
6 5.5 → 1 2.5	0.251	0.247	0.243	0.240	0.237	0.234	0.231	0.228	0.225	0.223
6 5.5 → 1 3.5	0.280	0.273	0.266	0.259	0.253	0.247	0.242	0.237	0.232	0.227
6 5.5 → 2 0.5	0.072	0.070	0.069	0.067	0.065	0.064	0.062	0.061	0.059	0.058
6 5.5 → 2 1.5	0.152	0.148	0.145	0.142	0.139	0.137	0.134	0.132	0.130	0.128
6 5.5 → 2 2.5	0.228	0.223	0.219	0.214	0.210	0.207	0.204	0.201	0.198	0.196
6 5.5 → 2 3.5	0.273	0.267	0.261	0.255	0.250	0.245	0.241	0.237	0.233	0.230
6 5.5 → 2 4.5	0.269	0.261	0.254	0.248	0.242	0.236	0.231	0.227	0.222	0.218
6 5.5 → 3 0.5	0.071	0.070	0.068	0.067	0.066	0.065	0.064	0.063	0.062	0.061
6 5.5 → 3 1.5	0.151	0.148	0.145	0.143	0.140	0.138	0.136	0.134	0.132	0.130

(continued)

(continued)

$j \rightarrow j'$	Temperature / K									
	55	60	65	70	75	80	85	90	95	100
6 5.5 → 3 2.5	0.247	0.242	0.238	0.235	0.232	0.230	0.228	0.227	0.225	0.224
6 5.5 → 3 3.5	0.300	0.294	0.289	0.285	0.281	0.278	0.275	0.272	0.270	0.267
6 5.5 → 3 4.5	0.293	0.288	0.283	0.279	0.275	0.271	0.268	0.264	0.261	0.258
6 5.5 → 3 5.5	0.279	0.271	0.264	0.257	0.251	0.246	0.241	0.236	0.231	0.227
6 5.5 → 4 1.5	0.143	0.140	0.137	0.134	0.131	0.128	0.126	0.123	0.121	0.119
6 5.5 → 4 2.5	0.234	0.230	0.226	0.222	0.219	0.216	0.213	0.210	0.208	0.205
6 5.5 → 4 3.5	0.484	0.479	0.475	0.471	0.468	0.466	0.463	0.462	0.460	0.459
6 5.5 → 4 4.5	0.431	0.426	0.421	0.417	0.413	0.410	0.407	0.404	0.401	0.399
6 5.5 → 4 5.5	0.358	0.352	0.345	0.340	0.335	0.330	0.326	0.321	0.318	0.314
6 5.5 → 4 6.5	0.293	0.286	0.279	0.274	0.268	0.263	0.259	0.255	0.251	0.248
6 5.5 → 5 2.5	0.207	0.203	0.200	0.196	0.193	0.190	0.186	0.183	0.181	0.178
6 5.5 → 5 3.5	0.317	0.312	0.308	0.303	0.299	0.296	0.292	0.289	0.285	0.282
6 5.5 → 5 4.5	0.902	0.927	0.952	0.977	1.002	1.026	1.050	1.074	1.097	1.120
6 5.5 → 5 5.5	0.506	0.505	0.504	0.503	0.502	0.502	0.501	0.501	0.501	0.501
6 5.5 → 5 6.5	0.377	0.370	0.364	0.358	0.353	0.348	0.343	0.338	0.334	0.330
6 5.5 → 5 7.5	0.277	0.271	0.265	0.259	0.254	0.249	0.245	0.240	0.236	0.233
6 5.5 → 6 3.5	0.245	0.242	0.238	0.234	0.231	0.228	0.224	0.221	0.218	0.215
6 5.5 → 6 4.5	0.386	0.383	0.381	0.379	0.377	0.375	0.374	0.372	0.371	0.369
6 5.5 → 6 7.5	0.371	0.368	0.364	0.360	0.356	0.353	0.349	0.346	0.343	0.339
6 5.5 → 6 8.5	0.272	0.268	0.265	0.262	0.259	0.256	0.254	0.251	0.249	0.247
6 6.5 → 0 2.5	0.223	0.217	0.212	0.206	0.201	0.196	0.192	0.187	0.183	0.179
6 6.5 → 1 1.5	0.132	0.129	0.126	0.123	0.121	0.119	0.116	0.114	0.112	0.110
6 6.5 → 1 2.5	0.263	0.258	0.254	0.250	0.247	0.244	0.241	0.238	0.235	0.232
6 6.5 → 1 3.5	0.286	0.280	0.274	0.269	0.264	0.259	0.254	0.250	0.245	0.241
6 6.5 → 2 0.5	0.062	0.060	0.058	0.056	0.055	0.053	0.052	0.050	0.049	0.048
6 6.5 → 2 1.5	0.115	0.112	0.110	0.107	0.105	0.103	0.101	0.099	0.098	0.096
6 6.5 → 2 2.5	0.224	0.219	0.214	0.209	0.205	0.201	0.198	0.195	0.192	0.189
6 6.5 → 2 3.5	0.289	0.282	0.276	0.271	0.266	0.262	0.258	0.254	0.251	0.248
6 6.5 → 2 4.5	0.305	0.297	0.289	0.282	0.276	0.270	0.264	0.259	0.254	0.249
6 6.5 → 3 0.5	0.060	0.058	0.057	0.055	0.054	0.052	0.051	0.050	0.048	0.047
6 6.5 → 3 1.5	0.113	0.111	0.109	0.107	0.105	0.103	0.101	0.099	0.098	0.096
6 6.5 → 3 2.5	0.186	0.182	0.179	0.176	0.173	0.171	0.168	0.166	0.164	0.162
6 6.5 → 3 3.5	0.303	0.298	0.293	0.288	0.285	0.282	0.279	0.277	0.275	0.273
6 6.5 → 3 4.5	0.336	0.331	0.326	0.321	0.318	0.314	0.311	0.308	0.306	0.304
6 6.5 → 3 5.5	0.341	0.333	0.326	0.319	0.312	0.306	0.301	0.296	0.291	0.286
6 6.5 → 4 1.5	0.106	0.103	0.100	0.097	0.095	0.093	0.090	0.088	0.086	0.084
6 6.5 → 4 2.5	0.167	0.163	0.159	0.156	0.153	0.150	0.147	0.144	0.141	0.139
6 6.5 → 4 3.5	0.269	0.264	0.260	0.256	0.253	0.250	0.247	0.244	0.241	0.239
6 6.5 → 4 4.5	0.568	0.562	0.558	0.554	0.551	0.549	0.547	0.545	0.544	0.544
6 6.5 → 4 5.5	0.463	0.457	0.451	0.446	0.442	0.437	0.434	0.430	0.427	0.424
6 6.5 → 4 6.5	0.372	0.363	0.355	0.348	0.341	0.334	0.328	0.322	0.317	0.312
6 6.5 → 5 2.5	0.134	0.131	0.128	0.125	0.122	0.120	0.117	0.115	0.113	0.110
6 6.5 → 5 3.5	0.222	0.218	0.214	0.211	0.207	0.204	0.201	0.198	0.195	0.192
6 6.5 → 5 4.5	0.346	0.341	0.336	0.332	0.328	0.324	0.320	0.317	0.313	0.310
6 6.5 → 5 5.5	0.976	1.002	1.027	1.052	1.078	1.103	1.127	1.151	1.175	1.198
6 6.5 → 5 6.5	0.536	0.533	0.530	0.528	0.525	0.523	0.522	0.520	0.518	0.517
6 6.5 → 5 7.5	0.372	0.364	0.357	0.349	0.343	0.337	0.331	0.325	0.320	0.315
6 6.5 → 6 3.5	0.160	0.157	0.155	0.152	0.150	0.148	0.146	0.144	0.142	0.140
6 6.5 → 6 4.5	0.251	0.248	0.245	0.241	0.238	0.235	0.232	0.229	0.226	0.223
6 6.5 → 6 5.5	0.409	0.407	0.405	0.403	0.402	0.400	0.399	0.397	0.396	0.395
6 6.5 → 6 7.5	0.507	0.504	0.501	0.498	0.495	0.492	0.490	0.487	0.484	0.482
6 6.5 → 6 8.5	0.363	0.357	0.352	0.347	0.342	0.338	0.333	0.329	0.325	0.321
6 7.5 → 0 2.5	0.223	0.217	0.212	0.206	0.201	0.196	0.192	0.187	0.183	0.179
6 7.5 → 1 1.5	0.130	0.126	0.123	0.119	0.116	0.113	0.110	0.107	0.104	0.101
6 7.5 → 1 2.5	0.246	0.241	0.236	0.232	0.228	0.225	0.221	0.218	0.215	0.212
6 7.5 → 1 3.5	0.304	0.299	0.294	0.290	0.286	0.282	0.279	0.275	0.272	0.268
6 7.5 → 2 0.5	0.045	0.043	0.042	0.041	0.040	0.039	0.038	0.037	0.036	0.035
6 7.5 → 2 1.5	0.115	0.111	0.108	0.105	0.102	0.099	0.097	0.095	0.092	0.090
6 7.5 → 2 2.5	0.179	0.175	0.171	0.167	0.163	0.160	0.157	0.154	0.152	0.149
6 7.5 → 2 3.5	0.294	0.287	0.281	0.275	0.270	0.266	0.262	0.258	0.255	0.251
6 7.5 → 2 4.5	0.361	0.353	0.345	0.337	0.331	0.324	0.318	0.313	0.307	0.302
6 7.5 → 3 0.5	0.042	0.041	0.040	0.038	0.037	0.036	0.035	0.034	0.033	0.032
6 7.5 → 3 1.5	0.094	0.091	0.089	0.086	0.084	0.082	0.079	0.077	0.076	0.074
6 7.5 → 3 2.5	0.152	0.149	0.145	0.143	0.140	0.137	0.135	0.133	0.131	0.129
6 7.5 → 3 3.5	0.227	0.224	0.220	0.217	0.214	0.211	0.208	0.206	0.204	0.201
6 7.5 → 3 4.5	0.391	0.383	0.376	0.371	0.366	0.362	0.358	0.355	0.353	0.351
6 7.5 → 3 5.5	0.434	0.426	0.419	0.412	0.406	0.401	0.395	0.390	0.386	0.381
6 7.5 → 4 1.5	0.072	0.070	0.068	0.066	0.065	0.063	0.062	0.061	0.059	0.058
6 7.5 → 4 2.5	0.136	0.132	0.129	0.127	0.124	0.122	0.120	0.118	0.117	0.115
6 7.5 → 4 3.5	0.212	0.208	0.203	0.200	0.196	0.193	0.190	0.187	0.185	0.183
6 7.5 → 4 4.5	0.316	0.311	0.306	0.301	0.297	0.293	0.290	0.287	0.283	0.280
6 7.5 → 4 5.5	0.676	0.669	0.663	0.659	0.655	0.652	0.649	0.647	0.645	0.644
6 7.5 → 4 6.5	0.532	0.522	0.513	0.504	0.496	0.489	0.482	0.475	0.469	0.463
6 7.5 → 5 2.5	0.092	0.090	0.088	0.086	0.084	0.082	0.080	0.079	0.077	0.076
6 7.5 → 5 3.5	0.157	0.153	0.150	0.147	0.144	0.141	0.139	0.136	0.134	0.132
6 7.5 → 5 4.5	0.253	0.248	0.243	0.239	0.235	0.232	0.228	0.225	0.222	0.219
6 7.5 → 5 5.5	0.394	0.388	0.383	0.378	0.374	0.369	0.365	0.361	0.357	0.353
6 7.5 → 5 6.5	1.102	1.127	1.153	1.179	1.205	1.231	1.256	1.281	1.305	1.329
6 7.5 → 5 7.5	0.588	0.581	0.573	0.567	0.560	0.554	0.549	0.543	0.538	0.533
6 7.5 → 6 3.5	0.109	0.108	0.106	0.105	0.103	0.102	0.101	0.100	0.099	0.098

(continued)

(continued)

$j \rightarrow j'$	Temperature / K									
	55	60	65	70	75	80	85	90	95	100
6 7.5 → 6 4.5	0.181	0.179	0.177	0.175	0.173	0.172	0.170	0.169	0.167	0.166
6 7.5 → 6 8.5	0.566	0.559	0.553	0.547	0.540	0.534	0.529	0.523	0.518	0.513
6 8.5 → 0 2.5	0.223	0.217	0.212	0.206	0.201	0.196	0.192	0.187	0.183	0.179
6 8.5 → 1 1.5	0.151	0.146	0.142	0.137	0.134	0.130	0.126	0.123	0.120	0.117
6 8.5 → 1 2.5	0.187	0.182	0.177	0.172	0.168	0.164	0.160	0.156	0.152	0.148
6 8.5 → 1 3.5	0.341	0.338	0.335	0.333	0.330	0.327	0.325	0.322	0.320	0.318
6 8.5 → 2 0.5	0.048	0.046	0.045	0.044	0.043	0.042	0.041	0.041	0.040	0.039
6 8.5 → 2 1.5	0.093	0.090	0.088	0.085	0.083	0.081	0.080	0.078	0.077	0.075
6 8.5 → 2 2.5	0.154	0.149	0.145	0.141	0.137	0.133	0.130	0.127	0.124	0.121
6 8.5 → 2 3.5	0.246	0.239	0.233	0.228	0.222	0.217	0.213	0.208	0.204	0.200
6 8.5 → 2 4.5	0.455	0.446	0.438	0.430	0.423	0.416	0.410	0.405	0.399	0.395
6 8.5 → 3 0.5	0.030	0.029	0.029	0.028	0.027	0.027	0.026	0.025	0.025	0.024
6 8.5 → 3 1.5	0.067	0.065	0.063	0.061	0.060	0.058	0.057	0.055	0.054	0.053
6 8.5 → 3 2.5	0.120	0.116	0.112	0.109	0.106	0.103	0.101	0.098	0.096	0.094
6 8.5 → 3 3.5	0.199	0.193	0.188	0.184	0.179	0.175	0.171	0.168	0.165	0.161
6 8.5 → 3 4.5	0.321	0.314	0.308	0.303	0.298	0.293	0.288	0.283	0.279	0.275
6 8.5 → 3 5.5	0.605	0.597	0.589	0.583	0.578	0.573	0.569	0.565	0.562	0.560
6 8.5 → 4 1.5	0.066	0.065	0.064	0.063	0.062	0.062	0.061	0.061	0.061	0.060
6 8.5 → 4 2.5	0.102	0.100	0.098	0.096	0.095	0.093	0.092	0.091	0.090	0.089
6 8.5 → 4 3.5	0.154	0.150	0.147	0.144	0.141	0.139	0.136	0.135	0.133	0.131
6 8.5 → 4 4.5	0.240	0.234	0.229	0.224	0.219	0.214	0.210	0.207	0.203	0.200
6 8.5 → 4 5.5	0.400	0.391	0.383	0.376	0.368	0.362	0.355	0.349	0.344	0.338
6 8.5 → 4 6.5	0.981	0.971	0.962	0.954	0.947	0.941	0.935	0.930	0.925	0.921
6 8.5 → 5 2.5	0.081	0.080	0.078	0.077	0.075	0.074	0.073	0.072	0.071	0.070
6 8.5 → 5 3.5	0.114	0.112	0.109	0.107	0.105	0.103	0.102	0.100	0.098	0.097
6 8.5 → 5 4.5	0.166	0.162	0.159	0.155	0.152	0.149	0.147	0.144	0.142	0.139
6 8.5 → 5 5.5	0.264	0.258	0.253	0.247	0.243	0.238	0.234	0.230	0.226	0.222
6 8.5 → 5 6.5	0.468	0.460	0.452	0.445	0.438	0.431	0.424	0.418	0.412	0.407
6 8.5 → 5 7.5	1.492	1.516	1.540	1.565	1.589	1.613	1.637	1.660	1.683	1.705

$HC^{18}O^+$ and Ar collisional system:

Table 4: Integrated rate coefficients $j \rightarrow j'$ from 5 to 100 K. Units are 10^{-10} cm^3 s^{-1}.

$j \rightarrow j'$	Temperature / K									
	5	10	15	20	25	30	35	40	45	50
1 → 0	2.117	2.699	2.857	3.028	3.227	3.437	3.647	3.849	4.040	4.217
2 → 0	1.329	1.236	1.153	1.099	1.070	1.061	1.065	1.079	1.099	1.123
2 → 1	5.560	5.240	4.887	4.651	4.512	4.442	4.421	4.434	4.470	4.523
3 → 0	0.750	0.793	0.792	0.785	0.778	0.772	0.768	0.766	0.765	0.766
3 → 1	3.611	3.543	3.349	3.172	3.026	2.910	2.818	2.747	2.691	2.648
3 → 2	5.755	5.719	5.462	5.220	5.025	4.878	4.770	4.696	4.648	4.622
4 → 0	0.542	0.543	0.529	0.515	0.502	0.491	0.482	0.475	0.469	0.464
4 → 1	2.594	2.529	2.399	2.275	2.167	2.076	1.999	1.936	1.892	1.883
4 → 2	4.088	4.041	3.870	3.696	3.541	3.408	3.295	3.201	3.122	3.057
4 → 3	5.435	5.503	5.346	5.162	4.993	4.848	4.730	4.636	4.562	4.507
5 → 0	0.298	0.304	0.302	0.298	0.293	0.288	0.284	0.280	0.276	0.273
5 → 1	1.649	1.651	1.601	1.544	1.489	1.440	1.395	1.356	1.321	1.290
5 → 2	3.010	2.991	2.903	2.804	2.707	2.619	2.539	2.468	2.404	2.348
5 → 3	3.685	3.723	3.655	3.565	3.475	3.391	3.313	3.243	3.181	3.125
5 → 4	5.450	5.428	5.295	5.140	4.989	4.852	4.731	4.627	4.538	4.465

$j \rightarrow j'$	Temperature / K									
	55	60	65	70	75	80	85	90	95	100
1 → 0	4.382	4.534	4.674	4.803	4.922	5.032	5.133	5.225	5.310	5.387
2 → 0	1.149	1.177	1.204	1.232	1.259	1.286	1.311	1.335	1.358	1.380
2 → 1	4.588	4.660	4.738	4.820	4.904	4.989	5.074	5.157	5.239	5.319
3 → 0	0.768	0.770	0.773	0.777	0.781	0.786	0.790	0.795	0.799	0.803
3 → 1	2.616	2.592	2.576	2.566	2.564	2.567	2.576	2.591	2.611	2.637
3 → 2	4.613	4.618	4.633	4.658	4.689	4.725	4.765	4.808	4.853	4.898
4 → 0	0.460	0.457	0.454	0.452	0.451	0.450	0.449	0.449	0.449	0.449
4 → 1	1.947	2.149	2.580	3.349	4.577	6.383	8.875	12.140	16.250	21.230
4 → 2	3.002	2.956	2.919	2.887	2.861	2.840	2.822	2.807	2.794	2.784
4 → 3	4.465	4.435	4.412	4.393	4.375	4.354	4.328	4.295	4.251	4.196
5 → 0	0.270	0.268	0.265	0.264	0.262	0.261	0.259	0.258	0.258	0.257
5 → 1	1.262	1.237	1.215	1.196	1.178	1.162	1.148	1.135	1.123	1.112
5 → 2	2.298	2.253	2.214	2.178	2.147	2.118	2.093	2.070	2.048	2.029
5 → 3	3.077	3.033	2.996	2.962	2.933	2.908	2.885	2.865	2.847	2.831
5 → 4	4.405	4.357	4.319	4.291	4.270	4.256	4.247	4.244	4.244	4.246

PO^+ and H_2 collisional system:

Table 5: Integrated rate coefficients $j \rightarrow j'$ from 5 to 50 K. Units are 10^{-10} cm^3 s^{-1}.

$j \rightarrow j'$	Temperature / K									
	5	10	15	20	25	30	35	40	45	50
1 → 0	1.766	1.626	1.544	1.492	1.460	1.440	1.429	1.424	1.423	1.424
2 → 0	1.631	1.375	1.203	1.082	0.993	0.924	0.870	0.825	0.788	0.758
2 → 1	4.029	3.343	2.994	2.788	2.652	2.558	2.490	2.439	2.401	2.372
3 → 0	0.704	0.627	0.577	0.537	0.505	0.478	0.454	0.434	0.416	0.400
3 → 1	3.318	2.868	2.532	2.287	2.101	1.956	1.839	1.744	1.665	1.598
3 → 2	4.165	3.811	3.550	3.366	3.232	3.132	3.054	2.994	2.945	2.907
4 → 0	0.713	0.641	0.578	0.528	0.489	0.457	0.431	0.409	0.391	0.374
4 → 1	1.752	1.660	1.552	1.454	1.370	1.297	1.233	1.177	1.127	1.083
4 → 2	3.436	3.097	2.844	2.645	2.484	2.351	2.239	2.144	2.062	1.991
4 → 3	3.818	3.595	3.441	3.326	3.239	3.173	3.121	3.081	3.049	3.024
5 → 0	0.457	0.436	0.411	0.390	0.370	0.353	0.338	0.324	0.312	0.301
5 → 1	1.357	1.276	1.199	1.131	1.071	1.019	0.973	0.933	0.898	0.866
5 → 2	2.167	2.049	1.918	1.806	1.712	1.632	1.564	1.504	1.451	1.404
5 → 3	3.422	3.167	2.952	2.777	2.633	2.511	2.408	2.318	2.241	2.173
5 → 4	3.455	3.379	3.304	3.242	3.193	3.155	3.124	3.099	3.080	3.064
6 → 0	0.311	0.313	0.302	0.288	0.273	0.260	0.248	0.238	0.229	0.220
6 → 1	0.954	0.952	0.922	0.885	0.849	0.816	0.787	0.760	0.737	0.715
6 → 2	1.719	1.644	1.563	1.485	1.415	1.353	1.298	1.248	1.204	1.165
6 → 3	2.248	2.149	2.052	1.967	1.893	1.828	1.769	1.715	1.666	1.621
6 → 4	3.280	3.103	2.942	2.802	2.681	2.577	2.486	2.407	2.337	2.276
6 → 5	3.110	3.044	2.990	2.955	2.933	2.920	2.911	2.907	2.905	2.905
7 → 0	0.232	0.222	0.218	0.214	0.211	0.207	0.204	0.201	0.198	0.195
7 → 1	0.752	0.738	0.709	0.679	0.649	0.622	0.597	0.574	0.554	0.535
7 → 2	1.363	1.343	1.303	1.260	1.218	1.179	1.142	1.109	1.078	1.049
7 → 3	1.912	1.808	1.715	1.634	1.564	1.503	1.449	1.400	1.357	1.318
7 → 4	2.370	2.242	2.140	2.057	1.985	1.921	1.864	1.811	1.763	1.718
7 → 5	3.077	2.942	2.815	2.705	2.611	2.530	2.461	2.400	2.346	2.299
7 → 6	2.630	2.637	2.631	2.626	2.625	2.628	2.634	2.643	2.653	2.664
8 → 0	0.196	0.189	0.181	0.172	0.164	0.157	0.151	0.145	0.141	0.136
8 → 1	0.714	0.704	0.682	0.660	0.641	0.624	0.608	0.594	0.580	0.567
8 → 2	1.019	0.970	0.926	0.887	0.852	0.821	0.793	0.768	0.745	0.725
8 → 3	1.598	1.559	1.512	1.465	1.419	1.376	1.336	1.298	1.263	1.230
8 → 4	1.935	1.845	1.773	1.714	1.661	1.614	1.571	1.531	1.495	1.461
8 → 5	2.066	2.033	1.968	1.906	1.851	1.800	1.754	1.712	1.673	1.637
8 → 6	2.704	2.712	2.676	2.625	2.573	2.522	2.475	2.431	2.391	2.354
8 → 7	2.331	2.314	2.307	2.312	2.326	2.344	2.366	2.390	2.414	2.439
9 → 0	0.213	0.210	0.206	0.202	0.197	0.193	0.189	0.184	0.179	0.175
9 → 1	0.467	0.460	0.445	0.429	0.413	0.399	0.386	0.374	0.364	0.355
9 → 2	0.974	0.951	0.924	0.899	0.876	0.854	0.834	0.814	0.794	0.776
9 → 3	1.112	1.072	1.041	1.014	0.989	0.966	0.944	0.924	0.905	0.888
9 → 4	1.634	1.572	1.512	1.458	1.410	1.368	1.330	1.296	1.264	1.235
9 → 5	1.919	1.923	1.887	1.843	1.800	1.758	1.719	1.682	1.647	1.615
9 → 6	1.833	1.814	1.788	1.758	1.727	1.696	1.666	1.637	1.609	1.583
9 → 7	2.606	2.613	2.592	2.556	2.516	2.475	2.436	2.398	2.363	2.331
9 → 8	2.107	2.106	2.112	2.127	2.149	2.176	2.204	2.234	2.265	2.296
10 → 0	0.125	0.123	0.118	0.113	0.109	0.106	0.104	0.102	0.100	0.099
10 → 1	0.612	0.576	0.549	0.527	0.508	0.491	0.474	0.459	0.444	0.431
10 → 2	0.630	0.625	0.610	0.594	0.580	0.567	0.555	0.544	0.535	0.527
10 → 3	1.003	0.986	0.964	0.945	0.927	0.909	0.892	0.876	0.859	0.843
10 → 4	1.272	1.278	1.258	1.233	1.207	1.182	1.159	1.136	1.115	1.094
10 → 5	1.469	1.458	1.428	1.395	1.363	1.333	1.306	1.280	1.256	1.234
10 → 6	1.968	1.995	1.967	1.926	1.883	1.840	1.798	1.759	1.722	1.688
10 → 7	1.634	1.654	1.647	1.634	1.617	1.599	1.580	1.561	1.543	1.524
10 → 8	2.379	2.419	2.408	2.382	2.351	2.318	2.286	2.255	2.227	2.200
10 → 9	1.771	1.829	1.866	1.904	1.944	1.984	2.024	2.063	2.102	2.139
11 → 0	0.185	0.167	0.155	0.146	0.138	0.132	0.126	0.121	0.116	0.112
11 → 1	0.330	0.321	0.314	0.308	0.303	0.298	0.295	0.292	0.289	0.287
11 → 2	0.791	0.748	0.711	0.680	0.653	0.629	0.607	0.587	0.569	0.552
11 → 3	0.889	0.882	0.865	0.845	0.825	0.806	0.789	0.773	0.759	0.746
11 → 4	1.079	1.056	1.032	1.009	0.989	0.970	0.952	0.935	0.919	0.903
11 → 5	1.451	1.420	1.384	1.347	1.313	1.280	1.251	1.223	1.198	1.174
11 → 6	1.429	1.397	1.371	1.347	1.326	1.307	1.288	1.271	1.254	1.238
11 → 7	1.886	1.901	1.882	1.851	1.816	1.780	1.746	1.712	1.680	1.650
11 → 8	1.562	1.534	1.531	1.527	1.521	1.512	1.502	1.490	1.478	1.466
11 → 9	2.237	2.236	2.232	2.219	2.202	2.183	2.163	2.143	2.124	2.106
11 → 10	1.606	1.616	1.652	1.696	1.744	1.792	1.839	1.885	1.929	1.973
12 → 0	0.085	0.090	0.094	0.096	0.097	0.098	0.098	0.098	0.098	0.098
12 → 1	0.385	0.353	0.332	0.315	0.300	0.287	0.275	0.264	0.255	0.246
12 → 2	0.556	0.560	0.557	0.551	0.543	0.536	0.528	0.521	0.514	0.508
12 → 3	0.736	0.755	0.748	0.734	0.717	0.700	0.683	0.667	0.651	0.636
12 → 4	0.994	0.992	0.977	0.957	0.935	0.913	0.892	0.873	0.855	0.839
12 → 5	1.050	1.033	1.022	1.012	1.001	0.990	0.979	0.967	0.956	0.944
12 → 6	1.396	1.382	1.356	1.325	1.293	1.262	1.234	1.207	1.182	1.160

(continued)

(continued)

$j \rightarrow j'$	Temperature / K									
	5	10	15	20	25	30	35	40	45	50
12 → 7	1.354	1.334	1.319	1.303	1.287	1.271	1.255	1.241	1.227	1.213
12 → 8	1.787	1.806	1.794	1.771	1.744	1.716	1.688	1.661	1.635	1.610
12 → 9	1.475	1.453	1.444	1.440	1.438	1.435	1.431	1.425	1.419	1.412
12 → 10	2.099	2.128	2.132	2.126	2.114	2.101	2.087	2.073	2.059	2.046
12 → 11	1.462	1.491	1.529	1.575	1.623	1.672	1.720	1.767	1.813	1.858
13 → 0	0.067	0.065	0.064	0.063	0.061	0.060	0.059	0.058	0.057	0.055
13 → 1	0.321	0.331	0.336	0.339	0.340	0.338	0.336	0.333	0.329	0.326
13 → 2	0.418	0.417	0.405	0.392	0.379	0.368	0.357	0.348	0.339	0.330
13 → 3	0.662	0.679	0.674	0.665	0.654	0.644	0.633	0.624	0.615	0.606
13 → 4	0.738	0.781	0.782	0.772	0.759	0.744	0.729	0.714	0.700	0.686
13 → 5	0.889	0.953	0.960	0.951	0.935	0.917	0.900	0.884	0.868	0.854
13 → 6	0.945	1.010	1.024	1.025	1.020	1.013	1.004	0.994	0.984	0.973
13 → 7	1.257	1.323	1.330	1.318	1.298	1.275	1.252	1.229	1.207	1.186
13 → 8	1.244	1.269	1.264	1.255	1.244	1.233	1.223	1.212	1.202	1.191
13 → 9	1.678	1.738	1.735	1.719	1.699	1.678	1.655	1.633	1.611	1.590
13 → 10	1.288	1.357	1.381	1.392	1.396	1.397	1.396	1.393	1.389	1.384
13 → 11	1.859	1.953	1.980	1.988	1.988	1.985	1.979	1.973	1.966	1.958
13 → 12	1.254	1.345	1.392	1.437	1.483	1.531	1.579	1.628	1.676	1.723
14 → 0	0.056	0.099	0.116	0.123	0.125	0.124	0.123	0.121	0.118	0.116
14 → 1	0.069	0.119	0.139	0.146	0.148	0.148	0.147	0.145	0.143	0.141
14 → 2	0.233	0.369	0.416	0.436	0.445	0.447	0.447	0.444	0.441	0.437
14 → 3	0.220	0.350	0.390	0.404	0.407	0.406	0.403	0.398	0.393	0.387
14 → 4	0.327	0.517	0.579	0.604	0.615	0.619	0.619	0.617	0.615	0.612
14 → 5	0.355	0.590	0.680	0.719	0.735	0.739	0.737	0.732	0.724	0.715
14 → 6	0.421	0.693	0.793	0.835	0.852	0.858	0.857	0.853	0.847	0.841
14 → 7	0.438	0.728	0.848	0.908	0.939	0.957	0.965	0.968	0.967	0.964
14 → 8	0.604	0.972	1.099	1.151	1.171	1.176	1.173	1.166	1.156	1.145
14 → 9	0.575	0.922	1.042	1.094	1.120	1.133	1.140	1.142	1.142	1.140
14 → 10	0.762	1.245	1.418	1.490	1.521	1.533	1.533	1.528	1.519	1.509
14 → 11	0.553	0.917	1.071	1.152	1.201	1.233	1.254	1.269	1.278	1.285
14 → 12	0.868	1.415	1.619	1.713	1.763	1.792	1.809	1.820	1.827	1.831
14 → 13	0.545	0.921	1.089	1.193	1.272	1.340	1.402	1.461	1.517	1.570
15 → 0	0.061	0.063	0.059	0.054	0.051	0.048	0.046	0.045	0.044	0.043
15 → 1	0.365	0.351	0.337	0.326	0.315	0.305	0.296	0.288	0.280	0.274
15 → 2	0.262	0.258	0.250	0.244	0.239	0.234	0.230	0.226	0.222	0.218
15 → 3	0.576	0.577	0.569	0.562	0.554	0.546	0.538	0.531	0.523	0.517
15 → 4	0.509	0.519	0.515	0.509	0.501	0.493	0.484	0.476	0.467	0.459
15 → 5	0.746	0.747	0.735	0.724	0.716	0.708	0.700	0.694	0.687	0.681
15 → 6	0.791	0.824	0.833	0.832	0.827	0.818	0.807	0.796	0.784	0.772
15 → 7	0.964	0.992	0.988	0.979	0.968	0.956	0.944	0.932	0.920	0.910
15 → 8	1.016	1.052	1.057	1.058	1.057	1.053	1.048	1.042	1.034	1.026
15 → 9	1.209	1.279	1.283	1.275	1.261	1.245	1.229	1.212	1.196	1.180
15 → 10	1.103	1.181	1.195	1.196	1.192	1.188	1.183	1.177	1.172	1.167
15 → 11	1.443	1.565	1.595	1.599	1.592	1.579	1.564	1.547	1.531	1.514
15 → 12	1.094	1.166	1.193	1.211	1.225	1.235	1.244	1.250	1.255	1.258
15 → 13	1.621	1.772	1.818	1.835	1.840	1.840	1.838	1.835	1.832	1.828
15 → 14	0.961	1.080	1.147	1.201	1.252	1.302	1.353	1.404	1.454	1.504
16 → 0	0.114	0.103	0.093	0.086	0.082	0.078	0.075	0.072	0.070	0.068
16 → 1	0.152	0.145	0.138	0.133	0.130	0.127	0.125	0.122	0.120	0.118
16 → 2	0.474	0.458	0.439	0.424	0.410	0.397	0.386	0.376	0.366	0.358
16 → 3	0.322	0.320	0.314	0.308	0.302	0.296	0.291	0.286	0.282	0.277
16 → 4	0.688	0.688	0.674	0.660	0.648	0.637	0.626	0.616	0.607	0.599
16 → 5	0.570	0.562	0.551	0.542	0.534	0.526	0.518	0.509	0.501	0.494
16 → 6	0.866	0.851	0.828	0.810	0.796	0.783	0.773	0.763	0.755	0.747
16 → 7	0.877	0.884	0.879	0.872	0.863	0.852	0.841	0.830	0.818	0.806
16 → 8	1.034	1.036	1.018	1.001	0.985	0.971	0.957	0.945	0.933	0.922
16 → 9	0.953	1.008	1.028	1.038	1.043	1.044	1.042	1.039	1.034	1.028
16 → 10	1.120	1.186	1.206	1.210	1.206	1.198	1.187	1.175	1.162	1.150
16 → 11	1.032	1.089	1.106	1.116	1.122	1.126	1.128	1.129	1.129	1.128
16 → 12	1.421	1.515	1.539	1.543	1.538	1.528	1.516	1.502	1.487	1.472
16 → 13	0.994	1.065	1.100	1.124	1.142	1.157	1.169	1.180	1.188	1.195
16 → 14	1.619	1.734	1.776	1.792	1.798	1.797	1.795	1.791	1.788	1.784
16 → 15	0.906	0.997	1.059	1.111	1.162	1.212	1.262	1.312	1.362	1.412
17 → 0	0.015	0.026	0.032	0.035	0.038	0.039	0.040	0.040	0.040	0.040
17 → 1	0.092	0.144	0.159	0.162	0.161	0.159	0.156	0.152	0.149	0.146
17 → 2	0.096	0.154	0.174	0.181	0.183	0.182	0.181	0.179	0.176	0.174
17 → 3	0.290	0.427	0.462	0.470	0.468	0.463	0.456	0.448	0.441	0.434
17 → 4	0.197	0.295	0.322	0.329	0.330	0.328	0.325	0.322	0.318	0.314
17 → 5	0.404	0.599	0.656	0.675	0.680	0.679	0.675	0.669	0.662	0.655
17 → 6	0.313	0.461	0.503	0.518	0.522	0.522	0.520	0.516	0.511	0.505
17 → 7	0.457	0.682	0.748	0.771	0.778	0.778	0.775	0.771	0.766	0.761
17 → 8	0.433	0.653	0.729	0.762	0.777	0.784	0.785	0.784	0.780	0.775
17 → 9	0.506	0.770	0.857	0.891	0.904	0.907	0.906	0.902	0.896	0.890
17 → 10	0.484	0.755	0.859	0.911	0.942	0.960	0.972	0.978	0.981	0.982
17 → 11	0.554	0.856	0.972	1.028	1.058	1.074	1.081	1.083	1.081	1.078
17 → 12	0.523	0.812	0.922	0.979	1.013	1.036	1.052	1.064	1.072	1.078
17 → 13	0.721	1.121	1.274	1.346	1.382	1.399	1.405	1.406	1.402	1.397
17 → 14	0.487	0.784	0.913	0.985	1.031	1.064	1.088	1.107	1.123	1.135
17 → 15	0.811	1.262	1.445	1.538	1.590	1.621	1.640	1.652	1.661	1.666
17 → 16	0.465	0.750	0.880	0.964	1.032	1.092	1.149	1.204	1.257	1.309

(continued)

(continued)

$j \rightarrow j'$	Temperature / K									
	5	10	15	20	25	30	35	40	45	50
18 → 0	0.041	0.046	0.046	0.044	0.042	0.040	0.038	0.037	0.036	0.035
18 → 1	0.112	0.109	0.106	0.104	0.103	0.102	0.101	0.101	0.100	0.099
18 → 2	0.291	0.277	0.266	0.258	0.252	0.247	0.242	0.237	0.233	0.229
18 → 3	0.242	0.243	0.241	0.239	0.238	0.235	0.233	0.230	0.228	0.225
18 → 4	0.665	0.655	0.633	0.614	0.597	0.580	0.566	0.552	0.540	0.528
18 → 5	0.399	0.408	0.403	0.396	0.388	0.381	0.374	0.367	0.361	0.356
18 → 6	0.825	0.841	0.831	0.816	0.800	0.784	0.769	0.755	0.742	0.730
18 → 7	0.607	0.607	0.595	0.583	0.573	0.564	0.555	0.547	0.539	0.531
18 → 8	0.911	0.916	0.898	0.879	0.861	0.846	0.832	0.819	0.808	0.799
18 → 9	0.794	0.817	0.818	0.816	0.811	0.806	0.800	0.793	0.785	0.777
18 → 10	0.978	0.998	0.992	0.981	0.968	0.955	0.942	0.930	0.919	0.908
18 → 11	0.877	0.934	0.956	0.968	0.976	0.980	0.983	0.984	0.983	0.981
18 → 12	1.051	1.080	1.089	1.094	1.095	1.094	1.090	1.086	1.080	1.073
18 → 13	0.920	0.974	0.999	1.017	1.031	1.042	1.050	1.057	1.062	1.065
18 → 14	1.336	1.403	1.428	1.440	1.445	1.444	1.439	1.433	1.424	1.415
18 → 15	0.882	0.941	0.984	1.020	1.048	1.071	1.089	1.104	1.116	1.126
18 → 16	1.642	1.683	1.693	1.699	1.702	1.703	1.702	1.700	1.697	1.695
18 → 17	0.863	0.934	0.980	1.019	1.059	1.100	1.143	1.188	1.233	1.279
19 → 0	0.025	0.034	0.038	0.041	0.042	0.042	0.042	0.042	0.041	0.040
19 → 1	0.122	0.125	0.118	0.113	0.109	0.107	0.105	0.104	0.103	0.102
19 → 2	0.179	0.175	0.165	0.159	0.156	0.154	0.153	0.152	0.150	0.149
19 → 3	0.423	0.399	0.370	0.350	0.336	0.325	0.317	0.310	0.304	0.298
19 → 4	0.308	0.309	0.297	0.288	0.282	0.277	0.273	0.269	0.266	0.263
19 → 5	0.791	0.769	0.728	0.695	0.669	0.646	0.627	0.611	0.596	0.582
19 → 6	0.435	0.443	0.432	0.422	0.413	0.405	0.398	0.392	0.385	0.380
19 → 7	0.882	0.897	0.876	0.855	0.835	0.817	0.801	0.785	0.771	0.757
19 → 8	0.628	0.630	0.610	0.593	0.580	0.570	0.560	0.551	0.542	0.535
19 → 9	1.011	0.999	0.960	0.929	0.904	0.883	0.865	0.850	0.836	0.824
19 → 10	0.835	0.847	0.832	0.820	0.812	0.804	0.797	0.790	0.783	0.775
19 → 11	1.080	1.074	1.038	1.010	0.987	0.968	0.952	0.937	0.924	0.913
19 → 12	0.944	0.976	0.976	0.978	0.982	0.985	0.986	0.987	0.986	0.983
19 → 13	1.114	1.111	1.090	1.079	1.073	1.068	1.063	1.058	1.053	1.047
19 → 14	1.028	1.046	1.036	1.032	1.032	1.035	1.038	1.040	1.043	1.045
19 → 15	1.436	1.467	1.446	1.431	1.420	1.410	1.402	1.393	1.384	1.375
19 → 16	0.996	1.023	1.026	1.034	1.045	1.057	1.068	1.079	1.088	1.097
19 → 17	1.799	1.805	1.773	1.752	1.737	1.725	1.716	1.708	1.701	1.695
19 → 18	0.939	0.986	1.005	1.029	1.058	1.092	1.128	1.167	1.208	1.249

Table 6: Integrated rate coefficients $j \rightarrow j'$ from 55 to 100 K. Units are 10^{-10} cm^3 s^{-1}.

$j \rightarrow j'$	Temperature / K									
	55	60	65	70	75	80	85	90	95	100
1 → 0	1.428	1.433	1.440	1.447	1.455	1.464	1.473	1.482	1.492	1.502
2 → 0	0.732	0.710	0.691	0.675	0.661	0.649	0.638	0.629	0.621	0.614
2 → 1	2.349	2.332	2.319	2.310	2.303	2.299	2.297	2.297	2.298	2.300
3 → 0	0.386	0.373	0.361	0.351	0.342	0.333	0.325	0.318	0.312	0.306
3 → 1	1.541	1.492	1.449	1.412	1.379	1.351	1.325	1.302	1.281	1.262
3 → 2	2.876	2.850	2.830	2.814	2.801	2.791	2.783	2.778	2.775	2.773
4 → 0	0.360	0.348	0.337	0.327	0.318	0.310	0.303	0.296	0.290	0.284
4 → 1	1.044	1.009	0.977	0.948	0.922	0.898	0.876	0.856	0.837	0.820
4 → 2	1.929	1.874	1.826	1.782	1.744	1.709	1.677	1.649	1.623	1.599
4 → 3	3.004	2.988	2.976	2.967	2.961	2.956	2.953	2.952	2.953	2.954
5 → 0	0.291	0.282	0.274	0.266	0.260	0.253	0.248	0.242	0.237	0.233
5 → 1	0.837	0.811	0.788	0.766	0.746	0.728	0.711	0.696	0.681	0.667
5 → 2	1.361	1.323	1.288	1.257	1.227	1.200	1.176	1.153	1.132	1.112
5 → 3	2.112	2.059	2.011	1.969	1.930	1.896	1.864	1.835	1.809	1.785
5 → 4	3.053	3.043	3.037	3.032	3.029	3.028	3.028	3.029	3.031	3.034
6 → 0	0.213	0.206	0.199	0.193	0.188	0.183	0.179	0.175	0.171	0.167
6 → 1	0.696	0.678	0.662	0.647	0.633	0.620	0.608	0.597	0.586	0.576
6 → 2	1.129	1.096	1.066	1.039	1.014	0.991	0.970	0.950	0.931	0.914
6 → 3	1.579	1.541	1.505	1.472	1.441	1.412	1.385	1.360	1.336	1.314
6 → 4	2.221	2.172	2.129	2.089	2.054	2.022	1.993	1.967	1.943	1.921
6 → 5	2.907	2.909	2.913	2.918	2.923	2.930	2.936	2.944	2.951	2.960
7 → 0	0.192	0.189	0.186	0.183	0.180	0.178	0.175	0.172	0.170	0.167
7 → 1	0.519	0.503	0.489	0.477	0.465	0.454	0.444	0.435	0.426	0.418
7 → 2	1.023	0.998	0.975	0.953	0.933	0.913	0.895	0.878	0.862	0.847
7 → 3	1.283	1.251	1.222	1.195	1.170	1.147	1.126	1.107	1.089	1.072
7 → 4	1.677	1.638	1.602	1.568	1.536	1.506	1.478	1.452	1.427	1.404
7 → 5	2.256	2.218	2.184	2.153	2.124	2.099	2.075	2.053	2.033	2.015
7 → 6	2.676	2.689	2.702	2.716	2.730	2.745	2.759	2.774	2.789	2.804
8 → 0	0.132	0.129	0.126	0.123	0.121	0.119	0.117	0.115	0.113	0.111
8 → 1	0.554	0.542	0.531	0.520	0.509	0.499	0.489	0.480	0.471	0.462
8 → 2	0.706	0.690	0.674	0.661	0.648	0.636	0.625	0.615	0.606	0.597
8 → 3	1.200	1.171	1.144	1.119	1.095	1.072	1.051	1.031	1.012	0.994
8 → 4	1.431	1.402	1.376	1.351	1.328	1.307	1.287	1.268	1.251	1.234
8 → 5	1.603	1.571	1.542	1.514	1.487	1.463	1.440	1.418	1.397	1.378
8 → 6	2.321	2.290	2.261	2.235	2.210	2.188	2.167	2.147	2.129	2.112

(continued)

(continued)

$j \rightarrow j'$	Temperature / K									
	55	60	65	70	75	80	85	90	95	100
8 → 7	2.464	2.489	2.514	2.538	2.562	2.586	2.609	2.632	2.654	2.676
9 → 0	0.171	0.166	0.162	0.158	0.155	0.151	0.147	0.144	0.141	0.138
9 → 1	0.347	0.340	0.334	0.328	0.323	0.318	0.314	0.310	0.307	0.304
9 → 2	0.758	0.741	0.725	0.709	0.694	0.680	0.666	0.653	0.640	0.628
9 → 3	0.872	0.856	0.842	0.829	0.817	0.806	0.795	0.785	0.775	0.766
9 → 4	1.208	1.183	1.159	1.136	1.115	1.095	1.076	1.058	1.041	1.025
9 → 5	1.585	1.557	1.530	1.506	1.482	1.460	1.440	1.420	1.402	1.384
9 → 6	1.557	1.534	1.511	1.489	1.469	1.449	1.431	1.413	1.397	1.381
9 → 7	2.300	2.272	2.245	2.220	2.198	2.176	2.156	2.138	2.120	2.104
9 → 8	2.326	2.356	2.385	2.414	2.443	2.470	2.498	2.524	2.551	2.576
10 → 0	0.098	0.097	0.096	0.095	0.095	0.094	0.093	0.093	0.092	0.092
10 → 1	0.418	0.406	0.395	0.384	0.374	0.364	0.355	0.346	0.338	0.330
10 → 2	0.519	0.513	0.506	0.501	0.496	0.491	0.486	0.482	0.478	0.475
10 → 3	0.827	0.811	0.796	0.781	0.767	0.753	0.740	0.727	0.715	0.703
10 → 4	1.076	1.058	1.041	1.025	1.010	0.996	0.983	0.970	0.958	0.946
10 → 5	1.212	1.192	1.173	1.155	1.138	1.121	1.105	1.090	1.075	1.061
10 → 6	1.655	1.625	1.596	1.569	1.544	1.520	1.497	1.476	1.456	1.437
10 → 7	1.506	1.489	1.472	1.456	1.440	1.425	1.411	1.397	1.384	1.371
10 → 8	2.175	2.152	2.130	2.110	2.091	2.074	2.058	2.043	2.029	2.016
10 → 9	2.176	2.212	2.247	2.280	2.313	2.345	2.377	2.407	2.437	2.466
11 → 0	0.109	0.105	0.102	0.099	0.096	0.093	0.091	0.088	0.086	0.084
11 → 1	0.285	0.283	0.281	0.279	0.278	0.276	0.275	0.274	0.272	0.271
11 → 2	0.536	0.522	0.508	0.495	0.482	0.471	0.460	0.449	0.439	0.430
11 → 3	0.734	0.723	0.713	0.704	0.695	0.687	0.680	0.673	0.666	0.659
11 → 4	0.888	0.874	0.860	0.846	0.833	0.820	0.807	0.795	0.783	0.772
11 → 5	1.152	1.131	1.112	1.095	1.078	1.062	1.047	1.033	1.020	1.008
11 → 6	1.222	1.207	1.192	1.177	1.163	1.149	1.136	1.123	1.110	1.098
11 → 7	1.621	1.594	1.569	1.544	1.522	1.500	1.480	1.461	1.443	1.425
11 → 8	1.453	1.441	1.428	1.416	1.404	1.393	1.382	1.371	1.360	1.350
11 → 9	2.088	2.072	2.056	2.042	2.028	2.015	2.003	1.992	1.982	1.972
11 → 10	2.014	2.055	2.094	2.132	2.169	2.205	2.240	2.274	2.307	2.339
12 → 0	0.098	0.097	0.097	0.096	0.096	0.095	0.095	0.094	0.094	0.093
12 → 1	0.238	0.230	0.224	0.217	0.211	0.206	0.201	0.196	0.191	0.187
12 → 2	0.502	0.497	0.491	0.486	0.481	0.477	0.472	0.468	0.464	0.460
12 → 3	0.621	0.607	0.594	0.581	0.568	0.557	0.545	0.535	0.524	0.515
12 → 4	0.824	0.810	0.798	0.786	0.776	0.766	0.757	0.748	0.740	0.733
12 → 5	0.932	0.920	0.908	0.896	0.884	0.872	0.861	0.850	0.839	0.828
12 → 6	1.139	1.119	1.101	1.085	1.069	1.054	1.040	1.028	1.015	1.004
12 → 7	1.200	1.187	1.175	1.163	1.151	1.139	1.128	1.117	1.106	1.095
12 → 8	1.586	1.563	1.541	1.521	1.501	1.482	1.465	1.448	1.432	1.416
12 → 9	1.405	1.397	1.388	1.380	1.372	1.363	1.355	1.347	1.338	1.331
12 → 10	2.032	2.020	2.008	1.997	1.986	1.976	1.966	1.957	1.949	1.940
12 → 11	1.902	1.944	1.986	2.026	2.066	2.104	2.141	2.177	2.213	2.247
13 → 0	0.054	0.053	0.052	0.051	0.050	0.049	0.048	0.047	0.046	0.045
13 → 1	0.322	0.318	0.314	0.310	0.307	0.303	0.299	0.296	0.293	0.290
13 → 2	0.322	0.315	0.308	0.301	0.295	0.289	0.283	0.278	0.273	0.268
13 → 3	0.599	0.591	0.584	0.578	0.572	0.566	0.561	0.556	0.551	0.546
13 → 4	0.672	0.659	0.646	0.634	0.623	0.612	0.601	0.591	0.581	0.571
13 → 5	0.841	0.829	0.818	0.807	0.798	0.789	0.781	0.773	0.766	0.759
13 → 6	0.962	0.951	0.940	0.928	0.917	0.906	0.895	0.884	0.873	0.863
13 → 7	1.167	1.148	1.131	1.115	1.100	1.086	1.073	1.061	1.049	1.038
13 → 8	1.181	1.171	1.161	1.152	1.142	1.132	1.123	1.114	1.105	1.096
13 → 9	1.570	1.550	1.531	1.513	1.495	1.479	1.463	1.447	1.433	1.419
13 → 10	1.379	1.373	1.367	1.360	1.354	1.347	1.341	1.334	1.328	1.322
13 → 11	1.951	1.943	1.936	1.929	1.921	1.915	1.908	1.902	1.896	1.890
13 → 12	1.769	1.814	1.858	1.901	1.943	1.984	2.023	2.062	2.099	2.136
14 → 0	0.114	0.111	0.109	0.107	0.105	0.103	0.102	0.100	0.098	0.097
14 → 1	0.139	0.137	0.135	0.133	0.131	0.129	0.127	0.126	0.124	0.123
14 → 2	0.433	0.428	0.424	0.419	0.415	0.410	0.406	0.402	0.398	0.394
14 → 3	0.381	0.375	0.369	0.363	0.357	0.352	0.346	0.341	0.336	0.331
14 → 4	0.608	0.604	0.601	0.597	0.593	0.589	0.586	0.582	0.579	0.575
14 → 5	0.705	0.695	0.684	0.674	0.664	0.653	0.643	0.634	0.624	0.615
14 → 6	0.834	0.827	0.820	0.813	0.807	0.800	0.794	0.789	0.783	0.778
14 → 7	0.959	0.953	0.945	0.937	0.929	0.920	0.911	0.902	0.893	0.883
14 → 8	1.134	1.122	1.111	1.099	1.088	1.078	1.067	1.057	1.048	1.039
14 → 9	1.136	1.132	1.127	1.122	1.116	1.110	1.104	1.098	1.091	1.085
14 → 10	1.497	1.485	1.472	1.459	1.446	1.434	1.421	1.409	1.397	1.386
14 → 11	1.289	1.291	1.292	1.292	1.291	1.290	1.288	1.285	1.282	1.280
14 → 12	1.833	1.834	1.833	1.832	1.831	1.829	1.826	1.824	1.821	1.819
14 → 13	1.622	1.672	1.720	1.767	1.812	1.856	1.898	1.940	1.980	2.019
15 → 0	0.042	0.041	0.041	0.040	0.040	0.039	0.039	0.039	0.038	0.038
15 → 1	0.267	0.262	0.256	0.251	0.247	0.243	0.239	0.235	0.231	0.228
15 → 2	0.215	0.212	0.209	0.206	0.203	0.200	0.198	0.195	0.193	0.191
15 → 3	0.510	0.503	0.497	0.492	0.486	0.481	0.476	0.471	0.466	0.461
15 → 4	0.451	0.443	0.436	0.428	0.421	0.415	0.408	0.402	0.396	0.390
15 → 5	0.676	0.671	0.666	0.661	0.657	0.652	0.648	0.644	0.640	0.636
15 → 6	0.760	0.748	0.736	0.724	0.713	0.701	0.690	0.680	0.670	0.659
15 → 7	0.899	0.890	0.881	0.872	0.864	0.856	0.849	0.842	0.836	0.830
15 → 8	1.018	1.008	0.999	0.989	0.979	0.969	0.959	0.949	0.939	0.929
15 → 9	1.165	1.150	1.137	1.123	1.111	1.099	1.087	1.076	1.066	1.056

(continued)

(continued)

$j \rightarrow j'$	Temperature / K									
	55	60	65	70	75	80	85	90	95	100
15 → 10	1.161	1.155	1.149	1.143	1.137	1.131	1.124	1.118	1.112	1.105
15 → 11	1.497	1.481	1.466	1.451	1.436	1.422	1.409	1.396	1.383	1.371
15 → 12	1.261	1.263	1.263	1.264	1.263	1.263	1.261	1.260	1.258	1.256
15 → 13	1.825	1.821	1.817	1.813	1.809	1.805	1.802	1.798	1.795	1.791
15 → 14	1.552	1.600	1.647	1.693	1.737	1.781	1.823	1.864	1.904	1.944
16 → 0	0.066	0.064	0.063	0.061	0.060	0.059	0.058	0.057	0.056	0.055
16 → 1	0.116	0.115	0.113	0.112	0.110	0.109	0.108	0.107	0.105	0.104
16 → 2	0.350	0.343	0.337	0.331	0.325	0.320	0.316	0.311	0.307	0.303
16 → 3	0.273	0.269	0.265	0.262	0.258	0.255	0.251	0.248	0.245	0.242
16 → 4	0.590	0.583	0.575	0.569	0.562	0.556	0.550	0.544	0.539	0.534
16 → 5	0.486	0.478	0.471	0.463	0.456	0.449	0.443	0.436	0.430	0.424
16 → 6	0.740	0.733	0.727	0.721	0.716	0.710	0.705	0.700	0.695	0.691
16 → 7	0.793	0.781	0.770	0.758	0.747	0.736	0.725	0.714	0.704	0.694
16 → 8	0.912	0.902	0.893	0.884	0.876	0.869	0.861	0.854	0.848	0.842
16 → 9	1.021	1.014	1.005	0.997	0.988	0.979	0.970	0.961	0.952	0.942
16 → 10	1.137	1.125	1.113	1.101	1.090	1.079	1.069	1.059	1.050	1.040
16 → 11	1.127	1.124	1.122	1.118	1.115	1.111	1.106	1.102	1.097	1.092
16 → 12	1.458	1.443	1.429	1.416	1.403	1.390	1.378	1.366	1.354	1.343
16 → 13	1.201	1.206	1.210	1.212	1.215	1.216	1.217	1.218	1.218	1.218
16 → 14	1.780	1.776	1.773	1.769	1.766	1.763	1.759	1.756	1.754	1.751
16 → 15	1.461	1.509	1.556	1.602	1.647	1.690	1.733	1.775	1.816	1.855
17 → 0	0.040	0.039	0.039	0.038	0.038	0.037	0.037	0.036	0.036	0.035
17 → 1	0.143	0.141	0.139	0.137	0.135	0.133	0.131	0.130	0.129	0.128
17 → 2	0.172	0.170	0.167	0.165	0.164	0.162	0.160	0.158	0.157	0.155
17 → 3	0.427	0.420	0.414	0.408	0.402	0.397	0.392	0.387	0.382	0.378
17 → 4	0.311	0.307	0.303	0.300	0.296	0.292	0.289	0.286	0.282	0.279
17 → 5	0.648	0.641	0.634	0.627	0.620	0.614	0.608	0.602	0.596	0.590
17 → 6	0.500	0.494	0.488	0.482	0.476	0.470	0.464	0.458	0.452	0.447
17 → 7	0.756	0.750	0.745	0.740	0.735	0.730	0.725	0.720	0.716	0.711
17 → 8	0.768	0.761	0.754	0.746	0.737	0.729	0.721	0.712	0.704	0.695
17 → 9	0.884	0.877	0.871	0.865	0.859	0.853	0.847	0.841	0.836	0.831
17 → 10	0.980	0.977	0.973	0.968	0.962	0.956	0.949	0.942	0.935	0.927
17 → 11	1.073	1.067	1.060	1.053	1.046	1.038	1.031	1.023	1.016	1.009
17 → 12	1.082	1.084	1.085	1.085	1.084	1.083	1.081	1.078	1.075	1.072
17 → 13	1.389	1.381	1.372	1.363	1.354	1.344	1.335	1.326	1.316	1.307
17 → 14	1.145	1.153	1.160	1.166	1.170	1.174	1.177	1.180	1.182	1.183
17 → 15	1.670	1.672	1.674	1.675	1.676	1.676	1.677	1.677	1.677	1.676
17 → 16	1.360	1.409	1.457	1.504	1.550	1.595	1.639	1.682	1.723	1.764
18 → 0	0.034	0.033	0.033	0.032	0.032	0.032	0.031	0.031	0.031	0.031
18 → 1	0.098	0.097	0.097	0.096	0.095	0.094	0.093	0.092	0.091	0.090
18 → 2	0.225	0.222	0.219	0.216	0.213	0.211	0.208	0.206	0.204	0.202
18 → 3	0.222	0.220	0.217	0.215	0.212	0.210	0.207	0.205	0.203	0.201
18 → 4	0.518	0.508	0.499	0.491	0.483	0.475	0.469	0.462	0.456	0.450
18 → 5	0.350	0.345	0.340	0.336	0.331	0.327	0.323	0.319	0.316	0.312
18 → 6	0.718	0.707	0.697	0.687	0.678	0.669	0.661	0.653	0.646	0.638
18 → 7	0.524	0.517	0.510	0.503	0.497	0.491	0.485	0.479	0.473	0.467
18 → 8	0.789	0.781	0.773	0.766	0.760	0.753	0.747	0.741	0.736	0.731
18 → 9	0.769	0.761	0.753	0.745	0.736	0.728	0.719	0.711	0.703	0.695
18 → 10	0.898	0.889	0.880	0.872	0.864	0.857	0.850	0.844	0.838	0.832
18 → 11	0.978	0.973	0.969	0.963	0.957	0.951	0.944	0.937	0.930	0.922
18 → 12	1.066	1.059	1.052	1.044	1.037	1.029	1.021	1.014	1.006	0.999
18 → 13	1.068	1.069	1.070	1.070	1.069	1.068	1.066	1.064	1.062	1.059
18 → 14	1.405	1.395	1.384	1.373	1.363	1.352	1.342	1.332	1.322	1.312
18 → 15	1.135	1.142	1.148	1.153	1.158	1.161	1.164	1.167	1.169	1.171
18 → 16	1.692	1.689	1.687	1.684	1.682	1.679	1.677	1.675	1.673	1.672
18 → 17	1.324	1.370	1.414	1.458	1.502	1.545	1.587	1.628	1.668	1.708
19 → 0	0.039	0.038	0.037	0.036	0.035	0.034	0.034	0.033	0.032	0.031
19 → 1	0.102	0.101	0.100	0.100	0.099	0.098	0.098	0.097	0.097	0.096
19 → 2	0.148	0.146	0.145	0.143	0.142	0.140	0.139	0.137	0.136	0.134
19 → 3	0.293	0.289	0.285	0.281	0.277	0.274	0.271	0.268	0.265	0.263
19 → 4	0.260	0.257	0.254	0.251	0.248	0.246	0.243	0.241	0.238	0.236
19 → 5	0.570	0.559	0.548	0.539	0.530	0.521	0.513	0.506	0.499	0.492
19 → 6	0.374	0.369	0.365	0.360	0.356	0.352	0.348	0.344	0.340	0.337
19 → 7	0.745	0.733	0.722	0.712	0.702	0.693	0.684	0.676	0.668	0.660
19 → 8	0.527	0.520	0.513	0.507	0.500	0.494	0.488	0.482	0.477	0.472
19 → 9	0.813	0.803	0.794	0.786	0.778	0.770	0.763	0.757	0.750	0.744
19 → 10	0.767	0.759	0.751	0.742	0.734	0.726	0.718	0.710	0.702	0.694
19 → 11	0.902	0.892	0.883	0.875	0.867	0.860	0.853	0.846	0.840	0.834
19 → 12	0.980	0.976	0.971	0.966	0.960	0.954	0.947	0.941	0.934	0.926
19 → 13	1.041	1.034	1.028	1.021	1.014	1.008	1.001	0.994	0.987	0.980
19 → 14	1.046	1.047	1.047	1.047	1.047	1.046	1.045	1.043	1.041	1.039
19 → 15	1.366	1.357	1.347	1.338	1.329	1.320	1.310	1.301	1.292	1.283
19 → 16	1.104	1.111	1.117	1.122	1.127	1.131	1.134	1.138	1.140	1.143
19 → 17	1.689	1.685	1.680	1.677	1.673	1.670	1.668	1.665	1.663	1.661
19 → 18	1.292	1.334	1.376	1.418	1.460	1.501	1.541	1.582	1.621	1.660

Table 7: Integrated rate coefficients $j \to j'$ from 105 to 150 K. Units are 10^{-10} cm^3 s^{-1}.

$j \to j'$	Temperature / K									
	105	110	115	120	125	130	135	140	145	150
1 → 0	1.512	1.523	1.534	1.544	1.555	1.566	1.577	1.588	1.599	1.610
2 → 0	0.607	0.602	0.597	0.592	0.588	0.585	0.582	0.579	0.576	0.574
2 → 1	2.304	2.309	2.315	2.322	2.329	2.337	2.346	2.355	2.364	2.375
3 → 0	0.300	0.295	0.291	0.287	0.283	0.280	0.277	0.274	0.271	0.269
3 → 1	1.246	1.230	1.216	1.204	1.192	1.181	1.171	1.162	1.153	1.145
3 → 2	2.773	2.774	2.777	2.780	2.784	2.790	2.796	2.803	2.810	2.818
4 → 0	0.278	0.273	0.269	0.264	0.260	0.256	0.253	0.249	0.246	0.243
4 → 1	0.805	0.790	0.777	0.765	0.754	0.743	0.734	0.725	0.716	0.708
4 → 2	1.577	1.557	1.538	1.521	1.505	1.491	1.477	1.464	1.452	1.441
4 → 3	2.957	2.960	2.965	2.970	2.976	2.983	2.990	2.998	3.006	3.015
5 → 0	0.229	0.225	0.221	0.217	0.214	0.211	0.208	0.206	0.203	0.201
5 → 1	0.655	0.643	0.632	0.621	0.611	0.602	0.593	0.584	0.576	0.568
5 → 2	1.093	1.076	1.060	1.046	1.032	1.019	1.006	0.995	0.984	0.974
5 → 3	1.763	1.743	1.724	1.707	1.691	1.676	1.662	1.649	1.637	1.626
5 → 4	3.038	3.043	3.048	3.054	3.061	3.068	3.076	3.084	3.092	3.101
6 → 0	0.164	0.160	0.157	0.155	0.152	0.150	0.147	0.145	0.143	0.141
6 → 1	0.567	0.558	0.550	0.542	0.535	0.528	0.521	0.515	0.509	0.503
6 → 2	0.898	0.883	0.869	0.856	0.843	0.831	0.820	0.809	0.799	0.790
6 → 3	1.293	1.273	1.255	1.237	1.221	1.205	1.191	1.177	1.164	1.151
6 → 4	1.900	1.882	1.864	1.848	1.833	1.820	1.807	1.795	1.783	1.773
6 → 5	2.968	2.977	2.987	2.997	3.007	3.017	3.028	3.039	3.050	3.061
7 → 0	0.165	0.163	0.160	0.158	0.156	0.154	0.152	0.150	0.148	0.146
7 → 1	0.411	0.404	0.398	0.392	0.386	0.381	0.376	0.371	0.366	0.362
7 → 2	0.832	0.819	0.805	0.793	0.781	0.770	0.759	0.749	0.739	0.729
7 → 3	1.056	1.041	1.027	1.014	1.002	0.990	0.979	0.968	0.958	0.948
7 → 4	1.382	1.361	1.342	1.323	1.306	1.289	1.274	1.259	1.245	1.231
7 → 5	1.997	1.982	1.967	1.953	1.940	1.928	1.916	1.905	1.895	1.886
7 → 6	2.819	2.834	2.850	2.865	2.881	2.896	2.912	2.927	2.943	2.959
8 → 0	0.110	0.109	0.107	0.106	0.105	0.104	0.103	0.102	0.101	0.100
8 → 1	0.454	0.446	0.438	0.431	0.424	0.417	0.410	0.404	0.398	0.392
8 → 2	0.589	0.582	0.575	0.568	0.562	0.556	0.550	0.545	0.540	0.535
8 → 3	0.976	0.960	0.944	0.929	0.915	0.901	0.888	0.876	0.864	0.853
8 → 4	1.219	1.204	1.190	1.176	1.164	1.152	1.140	1.129	1.118	1.108
8 → 5	1.359	1.342	1.325	1.310	1.295	1.281	1.268	1.256	1.244	1.232
8 → 6	2.096	2.081	2.067	2.054	2.041	2.029	2.018	2.007	1.997	1.988
8 → 7	2.698	2.720	2.741	2.762	2.783	2.803	2.824	2.844	2.864	2.883
9 → 0	0.135	0.132	0.129	0.127	0.124	0.122	0.119	0.117	0.115	0.113
9 → 1	0.301	0.298	0.295	0.293	0.291	0.289	0.287	0.285	0.283	0.281
9 → 2	0.616	0.605	0.594	0.584	0.574	0.564	0.555	0.546	0.538	0.530
9 → 3	0.758	0.750	0.742	0.735	0.728	0.721	0.715	0.709	0.703	0.697
9 → 4	1.009	0.995	0.981	0.967	0.954	0.942	0.930	0.919	0.908	0.897
9 → 5	1.367	1.351	1.336	1.322	1.308	1.295	1.282	1.270	1.258	1.247
9 → 6	1.366	1.352	1.338	1.325	1.313	1.301	1.290	1.280	1.270	1.260
9 → 7	2.089	2.074	2.061	2.048	2.036	2.025	2.015	2.005	1.995	1.986
9 → 8	2.602	2.627	2.651	2.675	2.699	2.722	2.745	2.767	2.790	2.812
10 → 0	0.091	0.091	0.091	0.090	0.090	0.089	0.089	0.088	0.088	0.088
10 → 1	0.323	0.315	0.309	0.302	0.296	0.290	0.284	0.278	0.273	0.268
10 → 2	0.471	0.468	0.465	0.462	0.459	0.456	0.453	0.451	0.448	0.446
10 → 3	0.691	0.680	0.669	0.659	0.649	0.639	0.630	0.620	0.612	0.603
10 → 4	0.936	0.925	0.915	0.906	0.897	0.888	0.880	0.872	0.864	0.857
10 → 5	1.048	1.035	1.023	1.011	0.999	0.988	0.978	0.967	0.957	0.948
10 → 6	1.419	1.402	1.386	1.371	1.356	1.342	1.329	1.316	1.303	1.292
10 → 7	1.359	1.348	1.337	1.326	1.316	1.307	1.297	1.288	1.280	1.272
10 → 8	2.004	1.992	1.982	1.972	1.962	1.954	1.945	1.937	1.930	1.923
10 → 9	2.494	2.522	2.550	2.576	2.603	2.628	2.654	2.678	2.703	2.727
11 → 0	0.082	0.080	0.078	0.076	0.074	0.072	0.071	0.069	0.068	0.066
11 → 1	0.269	0.268	0.267	0.266	0.264	0.263	0.262	0.260	0.259	0.258
11 → 2	0.421	0.412	0.404	0.396	0.389	0.382	0.375	0.369	0.362	0.356
11 → 3	0.653	0.648	0.642	0.637	0.632	0.627	0.622	0.618	0.613	0.609
11 → 4	0.761	0.750	0.740	0.730	0.720	0.710	0.701	0.692	0.684	0.675
11 → 5	0.996	0.985	0.974	0.964	0.954	0.945	0.936	0.927	0.919	0.911
11 → 6	1.086	1.075	1.064	1.053	1.043	1.033	1.023	1.013	1.004	0.995
11 → 7	1.409	1.393	1.378	1.364	1.350	1.337	1.325	1.313	1.301	1.290
11 → 8	1.340	1.331	1.322	1.313	1.305	1.297	1.289	1.281	1.274	1.267
11 → 9	1.963	1.954	1.946	1.938	1.931	1.924	1.917	1.911	1.905	1.900
11 → 10	2.371	2.402	2.432	2.461	2.490	2.518	2.546	2.573	2.599	2.625
12 → 0	0.092	0.092	0.091	0.090	0.090	0.089	0.089	0.088	0.087	0.086
12 → 1	0.183	0.179	0.176	0.172	0.169	0.166	0.162	0.160	0.157	0.154
12 → 2	0.456	0.452	0.449	0.445	0.442	0.438	0.435	0.431	0.428	0.424
12 → 3	0.505	0.496	0.488	0.479	0.472	0.464	0.457	0.450	0.443	0.437
12 → 4	0.726	0.719	0.713	0.707	0.701	0.695	0.690	0.685	0.680	0.676
12 → 5	0.818	0.808	0.798	0.788	0.779	0.770	0.761	0.752	0.743	0.735
12 → 6	0.993	0.983	0.973	0.964	0.955	0.946	0.938	0.930	0.923	0.916
12 → 7	1.085	1.075	1.065	1.056	1.047	1.038	1.029	1.020	1.012	1.003
12 → 8	1.402	1.388	1.375	1.362	1.350	1.338	1.327	1.316	1.305	1.295
12 → 9	1.323	1.315	1.308	1.301	1.294	1.288	1.281	1.275	1.269	1.264
12 → 10	1.933	1.926	1.919	1.913	1.907	1.901	1.896	1.890	1.885	1.881

(continued)

(continued)

$j \rightarrow j'$	Temperature / K									
	105	110	115	120	125	130	135	140	145	150
12 → 11	2.281	2.313	2.346	2.377	2.408	2.438	2.467	2.496	2.524	2.552
13 → 0	0.045	0.044	0.043	0.043	0.042	0.041	0.041	0.040	0.040	0.039
13 → 1	0.287	0.283	0.281	0.278	0.275	0.272	0.269	0.267	0.264	0.262
13 → 2	0.263	0.259	0.255	0.250	0.246	0.243	0.239	0.235	0.232	0.228
13 → 3	0.541	0.537	0.533	0.529	0.525	0.521	0.517	0.513	0.509	0.505
13 → 4	0.562	0.553	0.545	0.536	0.528	0.520	0.513	0.505	0.498	0.491
13 → 5	0.752	0.746	0.740	0.735	0.729	0.724	0.719	0.714	0.709	0.704
13 → 6	0.853	0.843	0.833	0.823	0.814	0.805	0.796	0.788	0.779	0.771
13 → 7	1.027	1.017	1.008	0.999	0.990	0.981	0.973	0.965	0.957	0.949
13 → 8	1.087	1.078	1.070	1.061	1.053	1.045	1.037	1.029	1.021	1.013
13 → 9	1.405	1.392	1.380	1.368	1.356	1.345	1.335	1.324	1.314	1.305
13 → 10	1.316	1.310	1.304	1.298	1.293	1.288	1.282	1.278	1.273	1.268
13 → 11	1.884	1.879	1.874	1.869	1.865	1.860	1.856	1.853	1.849	1.846
13 → 12	2.172	2.207	2.241	2.274	2.307	2.339	2.370	2.401	2.431	2.460
14 → 0	0.096	0.094	0.093	0.092	0.091	0.090	0.089	0.088	0.087	0.087
14 → 1	0.121	0.120	0.119	0.117	0.116	0.115	0.114	0.113	0.112	0.111
14 → 2	0.390	0.386	0.383	0.379	0.376	0.372	0.369	0.365	0.362	0.358
14 → 3	0.327	0.322	0.317	0.313	0.309	0.305	0.301	0.297	0.293	0.289
14 → 4	0.572	0.568	0.565	0.562	0.559	0.556	0.552	0.549	0.546	0.543
14 → 5	0.606	0.597	0.588	0.580	0.571	0.563	0.555	0.547	0.539	0.532
14 → 6	0.773	0.768	0.763	0.759	0.754	0.750	0.746	0.741	0.737	0.733
14 → 7	0.874	0.865	0.856	0.847	0.837	0.828	0.819	0.810	0.801	0.791
14 → 8	1.030	1.021	1.013	1.005	0.997	0.989	0.981	0.974	0.966	0.959
14 → 9	1.078	1.071	1.065	1.058	1.051	1.044	1.038	1.031	1.024	1.017
14 → 10	1.374	1.363	1.352	1.341	1.331	1.320	1.309	1.299	1.288	1.277
14 → 11	1.277	1.274	1.271	1.267	1.264	1.261	1.258	1.255	1.252	1.249
14 → 12	1.816	1.813	1.811	1.808	1.805	1.803	1.800	1.798	1.795	1.792
14 → 13	2.057	2.094	2.130	2.165	2.200	2.233	2.266	2.298	2.329	2.360
15 → 0	0.037	0.037	0.037	0.036	0.036	0.035	0.035	0.035	0.034	0.034
15 → 1	0.225	0.222	0.219	0.216	0.213	0.211	0.208	0.206	0.203	0.201
15 → 2	0.188	0.186	0.184	0.182	0.181	0.179	0.177	0.175	0.173	0.172
15 → 3	0.457	0.453	0.449	0.445	0.441	0.437	0.433	0.429	0.425	0.421
15 → 4	0.384	0.378	0.373	0.368	0.362	0.357	0.352	0.347	0.342	0.338
15 → 5	0.633	0.629	0.626	0.622	0.619	0.615	0.611	0.608	0.604	0.600
15 → 6	0.650	0.640	0.631	0.622	0.613	0.604	0.595	0.586	0.577	0.568
15 → 7	0.824	0.818	0.812	0.807	0.802	0.796	0.791	0.786	0.781	0.776
15 → 8	0.919	0.909	0.899	0.889	0.880	0.870	0.860	0.850	0.840	0.829
15 → 9	1.046	1.037	1.028	1.019	1.010	1.002	0.993	0.985	0.976	0.968
15 → 10	1.098	1.092	1.085	1.079	1.072	1.065	1.058	1.051	1.044	1.037
15 → 11	1.359	1.348	1.336	1.325	1.314	1.304	1.293	1.282	1.271	1.260
15 → 12	1.254	1.252	1.250	1.247	1.244	1.242	1.238	1.235	1.232	1.228
15 → 13	1.788	1.785	1.782	1.779	1.776	1.773	1.770	1.767	1.764	1.761
15 → 14	1.982	2.019	2.056	2.092	2.127	2.161	2.194	2.227	2.259	2.291
16 → 0	0.054	0.054	0.053	0.053	0.052	0.052	0.051	0.051	0.051	0.051
16 → 1	0.103	0.102	0.102	0.101	0.100	0.099	0.098	0.098	0.097	0.097
16 → 2	0.299	0.296	0.292	0.289	0.286	0.283	0.280	0.277	0.274	0.271
16 → 3	0.239	0.237	0.234	0.231	0.229	0.226	0.224	0.221	0.219	0.216
16 → 4	0.529	0.524	0.519	0.514	0.510	0.506	0.501	0.497	0.493	0.488
16 → 5	0.418	0.412	0.406	0.401	0.395	0.390	0.384	0.379	0.373	0.368
16 → 6	0.686	0.682	0.678	0.674	0.670	0.665	0.661	0.657	0.653	0.649
16 → 7	0.684	0.674	0.665	0.655	0.646	0.637	0.628	0.618	0.609	0.599
16 → 8	0.835	0.830	0.824	0.818	0.813	0.807	0.801	0.796	0.790	0.785
16 → 9	0.933	0.924	0.914	0.905	0.895	0.886	0.876	0.866	0.856	0.845
16 → 10	1.031	1.022	1.014	1.005	0.997	0.989	0.981	0.973	0.964	0.956
16 → 11	1.087	1.081	1.076	1.070	1.065	1.059	1.053	1.047	1.040	1.034
16 → 12	1.332	1.322	1.311	1.301	1.291	1.281	1.271	1.261	1.251	1.241
16 → 13	1.218	1.217	1.217	1.216	1.214	1.213	1.211	1.209	1.207	1.205
16 → 14	1.748	1.745	1.742	1.739	1.736	1.732	1.729	1.725	1.721	1.716
16 → 15	1.894	1.932	1.970	2.006	2.042	2.077	2.111	2.145	2.178	2.211
17 → 0	0.035	0.034	0.033	0.033	0.032	0.031	0.030	0.029	0.027	0.026
17 → 1	0.126	0.125	0.124	0.124	0.123	0.122	0.122	0.121	0.121	0.120
17 → 2	0.154	0.153	0.151	0.150	0.149	0.148	0.147	0.146	0.146	0.145
17 → 3	0.374	0.370	0.366	0.362	0.359	0.355	0.352	0.348	0.345	0.342
17 → 4	0.276	0.273	0.270	0.267	0.264	0.261	0.257	0.254	0.251	0.248
17 → 5	0.585	0.579	0.574	0.569	0.564	0.559	0.554	0.550	0.545	0.540
17 → 6	0.441	0.435	0.430	0.425	0.419	0.414	0.408	0.403	0.397	0.391
17 → 7	0.707	0.702	0.698	0.694	0.689	0.685	0.681	0.676	0.672	0.667
17 → 8	0.687	0.679	0.670	0.662	0.653	0.645	0.636	0.627	0.617	0.608
17 → 9	0.825	0.820	0.815	0.811	0.806	0.801	0.796	0.792	0.787	0.782
17 → 10	0.919	0.911	0.903	0.895	0.886	0.878	0.869	0.859	0.849	0.839
17 → 11	1.001	0.994	0.987	0.980	0.972	0.965	0.957	0.949	0.941	0.933
17 → 12	1.068	1.065	1.060	1.056	1.051	1.047	1.042	1.036	1.031	1.025
17 → 13	1.298	1.289	1.280	1.271	1.262	1.253	1.244	1.235	1.225	1.215
17 → 14	1.184	1.185	1.186	1.186	1.186	1.185	1.184	1.183	1.182	1.180
17 → 15	1.676	1.675	1.675	1.674	1.672	1.671	1.669	1.667	1.664	1.661
17 → 16	1.804	1.843	1.882	1.920	1.957	1.993	2.029	2.065	2.100	2.135
18 → 0	0.031	0.031	0.031	0.031	0.031	0.031	0.032	0.032	0.033	0.033
18 → 1	0.089	0.088	0.087	0.085	0.084	0.083	0.082	0.081	0.079	0.078
18 → 2	0.200	0.199	0.197	0.196	0.194	0.193	0.192	0.191	0.190	0.189
18 → 3	0.199	0.196	0.195	0.193	0.191	0.189	0.187	0.185	0.184	0.182

(continued)

(continued)

$j \rightarrow j'$	Temperature / K									
	105	110	115	120	125	130	135	140	145	150
18 → 4	0.445	0.440	0.435	0.430	0.425	0.421	0.416	0.412	0.407	0.403
18 → 5	0.309	0.305	0.302	0.299	0.296	0.293	0.290	0.287	0.284	0.281
18 → 6	0.631	0.625	0.618	0.612	0.605	0.599	0.593	0.587	0.580	0.574
18 → 7	0.461	0.456	0.451	0.445	0.440	0.434	0.429	0.423	0.418	0.412
18 → 8	0.725	0.721	0.716	0.711	0.706	0.702	0.697	0.692	0.688	0.683
18 → 9	0.687	0.678	0.670	0.662	0.654	0.645	0.636	0.627	0.618	0.608
18 → 10	0.826	0.821	0.815	0.810	0.805	0.799	0.794	0.789	0.783	0.778
18 → 11	0.914	0.907	0.898	0.890	0.881	0.872	0.863	0.853	0.842	0.831
18 → 12	0.992	0.984	0.976	0.969	0.961	0.952	0.943	0.934	0.924	0.914
18 → 13	1.056	1.053	1.049	1.046	1.042	1.038	1.033	1.029	1.024	1.019
18 → 14	1.302	1.292	1.282	1.272	1.262	1.251	1.240	1.229	1.217	1.205
18 → 15	1.172	1.173	1.174	1.175	1.175	1.175	1.175	1.174	1.173	1.172
18 → 16	1.670	1.668	1.666	1.664	1.661	1.659	1.656	1.653	1.649	1.645
18 → 17	1.746	1.784	1.821	1.858	1.893	1.928	1.962	1.995	2.028	2.059
19 → 0	0.030	0.029	0.027	0.026	0.024	0.022	0.020	0.018	0.015	0.011
19 → 1	0.095	0.095	0.094	0.093	0.092	0.091	0.090	0.089	0.087	0.086
19 → 2	0.133	0.132	0.130	0.129	0.127	0.126	0.125	0.124	0.122	0.121
19 → 3	0.260	0.258	0.255	0.253	0.251	0.249	0.246	0.244	0.242	0.240
19 → 4	0.233	0.231	0.229	0.227	0.225	0.222	0.220	0.218	0.216	0.214
19 → 5	0.486	0.480	0.474	0.468	0.462	0.456	0.451	0.445	0.439	0.433
19 → 6	0.333	0.330	0.327	0.324	0.321	0.319	0.316	0.314	0.311	0.309
19 → 7	0.653	0.646	0.639	0.632	0.625	0.619	0.612	0.606	0.599	0.592
19 → 8	0.466	0.461	0.456	0.451	0.447	0.442	0.437	0.433	0.428	0.423
19 → 9	0.738	0.732	0.727	0.721	0.715	0.709	0.703	0.697	0.691	0.684
19 → 10	0.686	0.678	0.670	0.662	0.654	0.646	0.637	0.628	0.619	0.610
19 → 11	0.828	0.822	0.816	0.810	0.804	0.798	0.791	0.785	0.778	0.770
19 → 12	0.919	0.911	0.903	0.895	0.887	0.878	0.869	0.859	0.849	0.838
19 → 13	0.973	0.966	0.959	0.951	0.943	0.935	0.926	0.916	0.905	0.894
19 → 14	1.037	1.034	1.032	1.029	1.026	1.022	1.019	1.015	1.011	1.007
19 → 15	1.274	1.264	1.254	1.244	1.234	1.223	1.211	1.199	1.185	1.171
19 → 16	1.144	1.146	1.147	1.148	1.148	1.148	1.147	1.146	1.144	1.141
19 → 17	1.659	1.656	1.654	1.651	1.648	1.645	1.641	1.637	1.632	1.627
19 → 18	1.699	1.737	1.775	1.813	1.850	1.887	1.924	1.961	1.998	2.035

Table 8: Integrated rate coefficients $j \rightarrow j'$ from 155 to 200 K. Units are 10^{-10} cm^3 s^{-1}.

$j \rightarrow j'$	Temperature / K									
	155	160	165	170	175	180	185	190	195	200
1 → 0	1.622	1.633	1.644	1.655	1.666	1.677	1.688	1.698	1.709	1.720
2 → 0	0.572	0.570	0.569	0.567	0.566	0.564	0.563	0.562	0.561	0.561
2 → 1	2.385	2.396	2.406	2.418	2.429	2.440	2.452	2.464	2.475	2.487
3 → 0	0.267	0.265	0.263	0.261	0.260	0.258	0.257	0.256	0.255	0.254
3 → 1	1.138	1.131	1.125	1.118	1.113	1.107	1.102	1.098	1.093	1.089
3 → 2	2.826	2.835	2.844	2.854	2.864	2.874	2.884	2.895	2.906	2.916
4 → 0	0.240	0.237	0.234	0.232	0.229	0.227	0.224	0.222	0.220	0.218
4 → 1	0.701	0.695	0.688	0.682	0.677	0.672	0.667	0.663	0.658	0.654
4 → 2	1.430	1.420	1.411	1.402	1.394	1.386	1.379	1.372	1.365	1.358
4 → 3	3.024	3.033	3.042	3.052	3.062	3.072	3.083	3.093	3.103	3.113
5 → 0	0.198	0.196	0.194	0.192	0.190	0.189	0.187	0.185	0.184	0.182
5 → 1	0.561	0.554	0.547	0.541	0.534	0.528	0.523	0.517	0.512	0.507
5 → 2	0.965	0.956	0.947	0.939	0.932	0.925	0.918	0.912	0.905	0.900
5 → 3	1.615	1.605	1.595	1.587	1.578	1.570	1.563	1.555	1.549	1.542
5 → 4	3.111	3.120	3.130	3.140	3.150	3.160	3.170	3.181	3.191	3.202
6 → 0	0.139	0.137	0.135	0.134	0.132	0.130	0.129	0.127	0.126	0.125
6 → 1	0.497	0.492	0.487	0.482	0.477	0.472	0.468	0.463	0.459	0.455
6 → 2	0.781	0.772	0.763	0.755	0.748	0.740	0.733	0.726	0.719	0.713
6 → 3	1.140	1.129	1.118	1.108	1.098	1.089	1.081	1.072	1.064	1.057
6 → 4	1.763	1.753	1.744	1.736	1.728	1.721	1.713	1.706	1.700	1.694
6 → 5	3.073	3.085	3.096	3.108	3.120	3.132	3.144	3.156	3.168	3.180
7 → 0	0.145	0.143	0.141	0.139	0.138	0.136	0.134	0.132	0.131	0.129
7 → 1	0.358	0.354	0.350	0.347	0.343	0.340	0.337	0.334	0.332	0.329
7 → 2	0.720	0.711	0.703	0.695	0.687	0.680	0.672	0.665	0.658	0.652
7 → 3	0.939	0.930	0.922	0.914	0.906	0.899	0.892	0.885	0.878	0.871
7 → 4	1.219	1.207	1.195	1.184	1.174	1.164	1.154	1.145	1.136	1.127
7 → 5	1.877	1.868	1.860	1.852	1.845	1.838	1.831	1.824	1.818	1.812
7 → 6	2.974	2.990	3.005	3.021	3.036	3.051	3.067	3.082	3.096	3.111
8 → 0	0.100	0.099	0.098	0.097	0.096	0.096	0.095	0.094	0.093	0.093
8 → 1	0.387	0.381	0.376	0.371	0.366	0.362	0.357	0.353	0.349	0.345
8 → 2	0.531	0.526	0.522	0.518	0.514	0.510	0.507	0.504	0.500	0.497
8 → 3	0.842	0.831	0.821	0.811	0.802	0.793	0.784	0.776	0.767	0.759
8 → 4	1.098	1.089	1.080	1.071	1.062	1.054	1.046	1.039	1.031	1.024
8 → 5	1.222	1.211	1.201	1.192	1.183	1.174	1.166	1.158	1.150	1.143
8 → 6	1.979	1.970	1.962	1.954	1.946	1.939	1.932	1.926	1.919	1.913
8 → 7	2.903	2.922	2.941	2.960	2.979	2.997	3.015	3.033	3.050	3.067
9 → 0	0.111	0.109	0.107	0.105	0.103	0.101	0.100	0.098	0.096	0.094
9 → 1	0.279	0.278	0.276	0.275	0.273	0.272	0.271	0.269	0.268	0.267
9 → 2	0.522	0.515	0.507	0.500	0.493	0.487	0.480	0.474	0.468	0.463

(continued)

(continued)

$j \rightarrow j'$	Temperature / K									
	155	160	165	170	175	180	185	190	195	200
9 → 3	0.692	0.687	0.682	0.677	0.672	0.668	0.663	0.659	0.655	0.651
9 → 4	0.887	0.877	0.868	0.859	0.850	0.842	0.834	0.826	0.818	0.810
9 → 5	1.236	1.225	1.215	1.205	1.195	1.186	1.177	1.168	1.159	1.151
9 → 6	1.251	1.243	1.234	1.226	1.219	1.211	1.204	1.197	1.191	1.184
9 → 7	1.978	1.969	1.962	1.954	1.947	1.941	1.934	1.928	1.923	1.917
9 → 8	2.833	2.854	2.875	2.896	2.916	2.935	2.955	2.974	2.992	3.010
10 → 0	0.087	0.087	0.086	0.086	0.085	0.084	0.084	0.083	0.082	0.081
10 → 1	0.263	0.258	0.253	0.249	0.244	0.240	0.235	0.231	0.227	0.222
10 → 2	0.443	0.441	0.438	0.436	0.434	0.431	0.429	0.427	0.425	0.422
10 → 3	0.595	0.587	0.579	0.571	0.563	0.556	0.549	0.541	0.534	0.527
10 → 4	0.850	0.843	0.836	0.830	0.824	0.818	0.812	0.806	0.801	0.795
10 → 5	0.938	0.929	0.920	0.911	0.902	0.894	0.885	0.877	0.869	0.861
10 → 6	1.280	1.269	1.259	1.249	1.239	1.229	1.220	1.211	1.203	1.194
10 → 7	1.264	1.256	1.248	1.241	1.234	1.227	1.220	1.213	1.206	1.199
10 → 8	1.917	1.910	1.904	1.899	1.893	1.888	1.883	1.879	1.874	1.870
10 → 9	2.750	2.773	2.796	2.818	2.840	2.862	2.883	2.903	2.923	2.943
11 → 0	0.064	0.063	0.061	0.059	0.058	0.056	0.054	0.053	0.051	0.049
11 → 1	0.256	0.255	0.253	0.251	0.250	0.248	0.246	0.244	0.242	0.240
11 → 2	0.350	0.345	0.339	0.334	0.328	0.323	0.318	0.313	0.309	0.304
11 → 3	0.605	0.600	0.596	0.592	0.588	0.584	0.581	0.577	0.573	0.569
11 → 4	0.667	0.659	0.651	0.643	0.635	0.628	0.620	0.613	0.605	0.598
11 → 5	0.903	0.896	0.888	0.881	0.874	0.867	0.860	0.853	0.847	0.840
11 → 6	0.986	0.977	0.969	0.960	0.952	0.944	0.936	0.928	0.921	0.913
11 → 7	1.279	1.268	1.257	1.247	1.237	1.227	1.218	1.208	1.198	1.189
11 → 8	1.260	1.254	1.247	1.241	1.234	1.228	1.222	1.216	1.209	1.203
11 → 9	1.894	1.889	1.884	1.879	1.874	1.869	1.864	1.859	1.855	1.850
11 → 10	2.651	2.676	2.700	2.724	2.748	2.771	2.793	2.815	2.836	2.857
12 → 0	0.086	0.085	0.084	0.083	0.083	0.082	0.081	0.080	0.079	0.078
12 → 1	0.151	0.148	0.146	0.143	0.141	0.138	0.135	0.133	0.130	0.127
12 → 2	0.421	0.417	0.413	0.409	0.405	0.401	0.396	0.392	0.387	0.382
12 → 3	0.430	0.425	0.419	0.413	0.408	0.403	0.398	0.393	0.388	0.383
12 → 4	0.671	0.667	0.662	0.658	0.654	0.650	0.646	0.643	0.639	0.635
12 → 5	0.727	0.719	0.711	0.703	0.696	0.688	0.681	0.673	0.666	0.659
12 → 6	0.909	0.902	0.895	0.889	0.882	0.876	0.870	0.864	0.858	0.852
12 → 7	0.995	0.987	0.980	0.972	0.964	0.957	0.949	0.942	0.935	0.927
12 → 8	1.285	1.276	1.267	1.257	1.249	1.240	1.232	1.223	1.215	1.207
12 → 9	1.258	1.253	1.247	1.242	1.237	1.232	1.227	1.222	1.218	1.213
12 → 10	1.876	1.872	1.867	1.863	1.859	1.855	1.851	1.847	1.843	1.839
12 → 11	2.579	2.605	2.631	2.657	2.682	2.706	2.730	2.753	2.775	2.797
13 → 0	0.039	0.038	0.038	0.037	0.037	0.037	0.036	0.036	0.035	0.035
13 → 1	0.259	0.256	0.254	0.251	0.248	0.246	0.243	0.240	0.237	0.235
13 → 2	0.224	0.221	0.217	0.214	0.210	0.206	0.203	0.199	0.195	0.191
13 → 3	0.501	0.497	0.493	0.489	0.485	0.481	0.476	0.472	0.467	0.462
13 → 4	0.484	0.477	0.470	0.462	0.455	0.448	0.441	0.434	0.427	0.419
13 → 5	0.699	0.694	0.689	0.684	0.678	0.673	0.668	0.662	0.656	0.651
13 → 6	0.763	0.755	0.748	0.740	0.733	0.726	0.719	0.712	0.705	0.698
13 → 7	0.941	0.933	0.925	0.918	0.910	0.902	0.893	0.885	0.876	0.868
13 → 8	1.005	0.997	0.989	0.980	0.972	0.964	0.955	0.947	0.938	0.929
13 → 9	1.295	1.286	1.277	1.268	1.260	1.251	1.243	1.235	1.227	1.219
13 → 10	1.264	1.259	1.255	1.251	1.247	1.243	1.239	1.236	1.232	1.229
13 → 11	1.842	1.839	1.836	1.834	1.831	1.829	1.827	1.825	1.823	1.821
13 → 12	2.489	2.518	2.545	2.572	2.599	2.625	2.650	2.675	2.700	2.724
14 → 0	0.086	0.086	0.085	0.085	0.084	0.084	0.084	0.084	0.084	0.084
14 → 1	0.110	0.109	0.109	0.108	0.107	0.107	0.106	0.105	0.105	0.105
14 → 2	0.355	0.352	0.348	0.345	0.341	0.338	0.334	0.330	0.326	0.322
14 → 3	0.285	0.282	0.278	0.274	0.270	0.266	0.263	0.259	0.255	0.251
14 → 4	0.540	0.536	0.533	0.529	0.525	0.521	0.518	0.513	0.509	0.505
14 → 5	0.524	0.516	0.508	0.500	0.491	0.483	0.474	0.466	0.457	0.448
14 → 6	0.728	0.724	0.719	0.715	0.710	0.705	0.700	0.694	0.689	0.683
14 → 7	0.782	0.772	0.762	0.752	0.741	0.730	0.719	0.708	0.696	0.684
14 → 8	0.951	0.943	0.935	0.927	0.919	0.911	0.902	0.893	0.884	0.874
14 → 9	1.010	1.003	0.996	0.988	0.981	0.973	0.965	0.957	0.949	0.940
14 → 10	1.266	1.255	1.243	1.231	1.219	1.206	1.193	1.179	1.164	1.150
14 → 11	1.246	1.244	1.241	1.238	1.236	1.233	1.231	1.228	1.226	1.223
14 → 12	1.790	1.787	1.785	1.782	1.780	1.777	1.775	1.772	1.769	1.766
14 → 13	2.389	2.418	2.446	2.474	2.501	2.527	2.552	2.577	2.601	2.624
15 → 0	0.033	0.032	0.032	0.031	0.030	0.029	0.028	0.027	0.026	0.025
15 → 1	0.198	0.196	0.193	0.191	0.188	0.186	0.183	0.180	0.177	0.174
15 → 2	0.170	0.168	0.166	0.165	0.163	0.161	0.160	0.158	0.156	0.154
15 → 3	0.417	0.413	0.409	0.405	0.400	0.396	0.391	0.387	0.382	0.377
15 → 4	0.333	0.328	0.322	0.317	0.312	0.307	0.301	0.295	0.289	0.283
15 → 5	0.596	0.592	0.588	0.584	0.579	0.574	0.569	0.564	0.559	0.553
15 → 6	0.559	0.549	0.540	0.530	0.520	0.509	0.499	0.488	0.476	0.464
15 → 7	0.770	0.765	0.759	0.754	0.748	0.742	0.735	0.729	0.722	0.715
15 → 8	0.819	0.808	0.796	0.785	0.773	0.760	0.747	0.733	0.719	0.705
15 → 9	0.959	0.950	0.941	0.932	0.922	0.912	0.902	0.891	0.880	0.869
15 → 10	1.030	1.022	1.014	1.006	0.998	0.989	0.980	0.971	0.961	0.951
15 → 11	1.249	1.238	1.226	1.214	1.202	1.189	1.175	1.162	1.147	1.132
15 → 12	1.224	1.220	1.215	1.210	1.205	1.199	1.193	1.187	1.180	1.172
15 → 13	1.758	1.755	1.752	1.749	1.746	1.742	1.739	1.735	1.731	1.727

(continued)

(continued)

$j \rightarrow j'$	Temperature / K									
	155	160	165	170	175	180	185	190	195	200
15 → 14	2.321	2.352	2.381	2.410	2.439	2.467	2.494	2.521	2.548	2.573
16 → 0	0.051	0.051	0.051	0.051	0.051	0.051	0.052	0.052	0.052	0.053
16 → 1	0.096	0.096	0.095	0.095	0.095	0.094	0.094	0.094	0.094	0.094
16 → 2	0.269	0.266	0.263	0.260	0.257	0.254	0.251	0.248	0.245	0.242
16 → 3	0.214	0.211	0.209	0.206	0.203	0.201	0.198	0.195	0.192	0.189
16 → 4	0.484	0.479	0.475	0.470	0.465	0.461	0.456	0.450	0.445	0.440
16 → 5	0.362	0.357	0.351	0.345	0.339	0.332	0.326	0.319	0.312	0.304
16 → 6	0.644	0.640	0.635	0.630	0.625	0.620	0.615	0.609	0.603	0.597
16 → 7	0.590	0.579	0.569	0.559	0.547	0.536	0.524	0.512	0.499	0.486
16 → 8	0.779	0.773	0.766	0.760	0.753	0.746	0.739	0.731	0.724	0.715
16 → 9	0.834	0.823	0.811	0.799	0.786	0.773	0.759	0.745	0.730	0.714
16 → 10	0.947	0.938	0.929	0.919	0.910	0.899	0.889	0.878	0.866	0.855
16 → 11	1.027	1.020	1.012	1.005	0.997	0.989	0.980	0.971	0.962	0.952
16 → 12	1.231	1.220	1.209	1.198	1.186	1.175	1.162	1.149	1.136	1.122
16 → 13	1.202	1.199	1.196	1.192	1.188	1.184	1.179	1.174	1.169	1.163
16 → 14	1.711	1.705	1.698	1.692	1.684	1.676	1.666	1.657	1.646	1.634
16 → 15	2.243	2.275	2.306	2.337	2.367	2.397	2.427	2.456	2.485	2.513
17 → 1	0.120	0.120	0.120	0.120	0.120	0.120	0.121	0.121	0.121	0.122
17 → 2	0.145	0.144	0.144	0.144	0.144	0.145	0.145	0.146	0.147	0.148
17 → 3	0.338	0.335	0.332	0.328	0.325	0.321	0.318	0.314	0.310	0.306
17 → 4	0.244	0.240	0.237	0.233	0.229	0.224	0.220	0.215	0.210	0.205
17 → 5	0.535	0.530	0.525	0.520	0.514	0.509	0.503	0.498	0.492	0.486
17 → 6	0.385	0.379	0.372	0.365	0.358	0.351	0.343	0.335	0.327	0.318
17 → 7	0.663	0.658	0.653	0.648	0.643	0.637	0.632	0.626	0.620	0.613
17 → 8	0.598	0.587	0.576	0.565	0.553	0.540	0.527	0.513	0.499	0.484
17 → 9	0.777	0.772	0.767	0.762	0.757	0.751	0.745	0.740	0.734	0.727
17 → 10	0.829	0.817	0.805	0.793	0.780	0.766	0.752	0.737	0.721	0.704
17 → 11	0.924	0.915	0.905	0.895	0.885	0.874	0.862	0.850	0.837	0.824
17 → 12	1.019	1.013	1.006	0.999	0.992	0.984	0.976	0.968	0.959	0.950
17 → 13	1.205	1.194	1.183	1.172	1.160	1.147	1.134	1.121	1.107	1.092
17 → 14	1.178	1.176	1.173	1.170	1.167	1.163	1.159	1.154	1.149	1.143
17 → 15	1.657	1.653	1.648	1.643	1.637	1.630	1.622	1.614	1.604	1.594
17 → 16	2.169	2.203	2.237	2.271	2.304	2.338	2.371	2.404	2.437	2.470
18 → 0	0.034	0.035	0.036	0.037	0.038	0.040	0.041	0.043	0.045	0.047
18 → 1	0.076	0.075	0.073	0.071	0.069	0.067	0.065	0.062	0.060	0.057
18 → 2	0.188	0.187	0.186	0.185	0.184	0.183	0.183	0.182	0.181	0.181
18 → 3	0.180	0.179	0.177	0.176	0.174	0.173	0.171	0.170	0.168	0.167
18 → 4	0.399	0.394	0.390	0.386	0.381	0.376	0.372	0.367	0.362	0.357
18 → 5	0.278	0.275	0.272	0.269	0.267	0.264	0.261	0.258	0.254	0.251
18 → 6	0.567	0.561	0.554	0.547	0.540	0.532	0.524	0.516	0.508	0.499
18 → 7	0.406	0.400	0.394	0.387	0.380	0.373	0.366	0.358	0.350	0.341
18 → 8	0.678	0.673	0.668	0.663	0.658	0.653	0.647	0.642	0.636	0.630
18 → 9	0.598	0.588	0.577	0.565	0.552	0.539	0.526	0.511	0.496	0.480
18 → 10	0.772	0.766	0.760	0.753	0.746	0.739	0.732	0.725	0.717	0.708
18 → 11	0.819	0.806	0.793	0.778	0.763	0.747	0.730	0.712	0.693	0.673
18 → 12	0.903	0.891	0.878	0.864	0.849	0.834	0.817	0.799	0.780	0.760
18 → 13	1.014	1.009	1.004	0.998	0.992	0.985	0.979	0.972	0.965	0.958
18 → 14	1.192	1.178	1.163	1.147	1.131	1.113	1.095	1.075	1.054	1.032
18 → 15	1.171	1.169	1.167	1.165	1.162	1.159	1.156	1.153	1.149	1.144
18 → 16	1.640	1.634	1.628	1.621	1.614	1.605	1.596	1.586	1.575	1.563
18 → 17	2.090	2.121	2.150	2.179	2.207	2.234	2.260	2.286	2.311	2.335
19 → 1	0.084	0.082	0.080	0.077	0.074	0.071	0.068	0.064	0.061	0.056
19 → 2	0.120	0.119	0.118	0.117	0.115	0.114	0.113	0.112	0.111	0.110
19 → 3	0.238	0.235	0.233	0.230	0.228	0.225	0.222	0.219	0.216	0.213
19 → 4	0.212	0.210	0.208	0.206	0.204	0.202	0.200	0.198	0.196	0.194
19 → 5	0.427	0.421	0.415	0.408	0.401	0.394	0.387	0.379	0.371	0.362
19 → 6	0.307	0.305	0.303	0.301	0.299	0.297	0.296	0.294	0.292	0.291
19 → 7	0.585	0.578	0.571	0.564	0.557	0.549	0.541	0.532	0.524	0.515
19 → 8	0.419	0.414	0.409	0.405	0.400	0.395	0.390	0.384	0.379	0.374
19 → 9	0.677	0.670	0.662	0.655	0.646	0.637	0.628	0.618	0.608	0.597
19 → 10	0.600	0.589	0.578	0.567	0.555	0.542	0.528	0.514	0.499	0.484
19 → 11	0.762	0.754	0.745	0.736	0.725	0.715	0.703	0.691	0.678	0.665
19 → 12	0.827	0.815	0.803	0.789	0.775	0.760	0.744	0.727	0.710	0.691
19 → 13	0.882	0.868	0.854	0.838	0.821	0.803	0.784	0.763	0.741	0.718
19 → 14	1.003	0.999	0.994	0.989	0.984	0.979	0.974	0.968	0.962	0.956
19 → 15	1.156	1.139	1.121	1.102	1.081	1.059	1.035	1.010	0.983	0.954
19 → 16	1.138	1.135	1.131	1.126	1.120	1.113	1.106	1.098	1.089	1.080
19 → 17	1.620	1.613	1.605	1.596	1.586	1.575	1.563	1.549	1.535	1.519
19 → 18	2.072	2.110	2.147	2.185	2.224	2.263	2.302	2.341	2.382	2.422

HCN and N_2 collisional system:

Table 9: Integrated rate coefficients $j \rightarrow j'$ from 5 to 50 K. Units are 10^{-10} cm^3 s^{-1}.

$j \rightarrow j'$	Temperature / K									
	5	10	15	20	25	30	35	40	45	50
1 0.0 → 0 1.0	0.579	0.773	0.851	0.889	0.909	0.921	0.929	0.935	0.941	0.948
1 0.0 → 1 1.0	0.530	0.617	0.650	0.675	0.694	0.709	0.718	0.725	0.730	0.733
1 0.0 → 1 2.0	1.272	1.543	1.604	1.623	1.634	1.645	1.658	1.677	1.701	1.731
1 1.0 → 0 1.0	0.579	0.773	0.851	0.889	0.909	0.921	0.929	0.935	0.941	0.948
1 2.0 → 0 1.0	0.579	0.773	0.851	0.889	0.909	0.921	0.929	0.935	0.941	0.948
1 2.0 → 1 1.0	0.705	0.849	0.884	0.899	0.909	0.917	0.926	0.936	0.948	0.962
2 1.0 → 0 1.0	0.227	0.332	0.413	0.477	0.527	0.568	0.604	0.634	0.662	0.688
2 1.0 → 1 0.0	0.248	0.254	0.254	0.257	0.265	0.274	0.286	0.299	0.314	0.331
2 1.0 → 1 1.0	0.353	0.411	0.430	0.441	0.451	0.461	0.473	0.487	0.503	0.521
2 1.0 → 1 2.0	0.535	0.635	0.657	0.656	0.648	0.639	0.633	0.629	0.630	0.633
2 1.0 → 2 2.0	0.672	0.856	0.950	1.012	1.061	1.103	1.139	1.173	1.206	1.237
2 1.0 → 2 3.0	0.670	0.800	0.836	0.847	0.850	0.852	0.853	0.856	0.860	0.867
2 2.0 → 0 1.0	0.227	0.332	0.413	0.477	0.527	0.568	0.604	0.634	0.662	0.688
2 2.0 → 1 0.0	0.074	0.098	0.107	0.110	0.112	0.114	0.115	0.117	0.119	0.121
2 2.0 → 1 1.0	0.509	0.550	0.557	0.562	0.569	0.579	0.592	0.609	0.629	0.652
2 2.0 → 1 2.0	0.553	0.651	0.677	0.683	0.682	0.682	0.685	0.690	0.699	0.711
2 3.0 → 0 1.0	0.227	0.332	0.413	0.477	0.527	0.568	0.604	0.634	0.662	0.688
2 3.0 → 1 0.0	0.111	0.131	0.134	0.133	0.131	0.129	0.127	0.125	0.125	0.125
2 3.0 → 1 1.0	0.297	0.359	0.376	0.377	0.374	0.371	0.368	0.368	0.369	0.372
2 3.0 → 1 2.0	0.728	0.810	0.831	0.844	0.858	0.875	0.897	0.923	0.953	0.988
2 3.0 → 2 2.0	0.564	0.698	0.754	0.786	0.809	0.828	0.845	0.861	0.877	0.894
3 2.0 → 0 1.0	0.159	0.210	0.233	0.243	0.249	0.255	0.261	0.269	0.278	0.289
3 2.0 → 1 0.0	0.092	0.138	0.169	0.192	0.212	0.229	0.247	0.265	0.285	0.305
3 2.0 → 1 1.0	0.170	0.243	0.291	0.327	0.358	0.385	0.413	0.442	0.474	0.509
3 2.0 → 1 2.0	0.289	0.371	0.419	0.451	0.476	0.498	0.521	0.548	0.580	0.618
3 2.0 → 2 1.0	0.232	0.295	0.332	0.359	0.383	0.407	0.433	0.462	0.494	0.529
3 2.0 → 2 2.0	0.270	0.353	0.389	0.404	0.411	0.417	0.423	0.434	0.450	0.472
3 2.0 → 2 3.0	0.336	0.423	0.449	0.452	0.445	0.437	0.431	0.431	0.439	0.456
3 2.0 → 3 3.0	0.701	0.896	1.013	1.087	1.138	1.182	1.245	1.353	1.529	1.787
3 2.0 → 3 4.0	0.457	0.586	0.628	0.640	0.641	0.645	0.672	0.738	0.861	1.047
3 3.0 → 0 1.0	0.159	0.210	0.233	0.243	0.249	0.255	0.261	0.269	0.278	0.289
3 3.0 → 1 0.0	0.039	0.052	0.061	0.067	0.073	0.078	0.083	0.088	0.095	0.102
3 3.0 → 1 1.0	0.226	0.316	0.375	0.417	0.451	0.483	0.514	0.548	0.585	0.626
3 3.0 → 1 2.0	0.287	0.384	0.444	0.487	0.521	0.552	0.584	0.619	0.659	0.704
3 3.0 → 2 1.0	0.153	0.202	0.221	0.228	0.230	0.230	0.232	0.235	0.242	0.253
3 3.0 → 2 2.0	0.328	0.411	0.453	0.478	0.499	0.520	0.544	0.572	0.606	0.646
3 3.0 → 2 3.0	0.357	0.459	0.497	0.509	0.511	0.510	0.512	0.519	0.535	0.559
3 4.0 → 0 1.0	0.159	0.210	0.233	0.243	0.249	0.255	0.261	0.269	0.278	0.289
3 4.0 → 1 0.0	0.062	0.078	0.087	0.092	0.097	0.100	0.104	0.109	0.115	0.123
3 4.0 → 1 1.0	0.159	0.204	0.231	0.249	0.263	0.276	0.289	0.304	0.323	0.344
3 4.0 → 1 2.0	0.331	0.470	0.562	0.630	0.685	0.736	0.787	0.842	0.901	0.965
3 4.0 → 2 1.0	0.143	0.179	0.190	0.190	0.187	0.183	0.180	0.180	0.183	0.190
3 4.0 → 2 2.0	0.247	0.317	0.342	0.348	0.347	0.344	0.343	0.346	0.354	0.369
3 4.0 → 2 3.0	0.448	0.575	0.638	0.676	0.705	0.733	0.765	0.802	0.846	0.899
3 4.0 → 3 3.0	0.550	0.703	0.784	0.829	0.858	0.885	0.929	1.012	1.153	1.361
4 3.0 → 0 1.0	0.091	0.163	0.208	0.239	0.262	0.281	0.298	0.316	0.336	0.358
4 3.0 → 1 0.0	0.056	0.079	0.091	0.099	0.104	0.109	0.115	0.123	0.134	0.147
4 3.0 → 1 1.0	0.119	0.164	0.181	0.188	0.192	0.197	0.203	0.214	0.229	0.249
4 3.0 → 1 2.0	0.149	0.194	0.215	0.225	0.231	0.237	0.250	0.272	0.304	0.347
4 3.0 → 2 1.0	0.337	0.511	0.625	0.704	0.761	0.806	0.843	0.876	0.908	0.940
4 3.0 → 2 2.0	0.275	0.419	0.509	0.565	0.601	0.627	0.648	0.669	0.693	0.720
4 3.0 → 2 3.0	0.203	0.296	0.346	0.375	0.393	0.407	0.423	0.443	0.470	0.505
4 3.0 → 3 2.0	0.232	0.311	0.355	0.391	0.426	0.466	0.516	0.581	0.663	0.761
4 3.0 → 3 3.0	0.214	0.280	0.312	0.328	0.339	0.353	0.378	0.421	0.484	0.568
4 3.0 → 3 4.0	0.287	0.343	0.361	0.364	0.361	0.364	0.383	0.428	0.502	0.605
4 3.0 → 4 4.0	0.523	0.687	0.779	0.835	0.874	0.907	0.948	1.005	1.084	1.186
4 3.0 → 4 5.0	0.239	0.306	0.332	0.343	0.350	0.367	0.407	0.484	0.604	0.767
4 4.0 → 0 1.0	0.091	0.163	0.208	0.239	0.262	0.281	0.298	0.316	0.336	0.358
4 4.0 → 1 0.0	0.030	0.040	0.042	0.041	0.040	0.040	0.040	0.040	0.042	0.045
4 4.0 → 1 1.0	0.125	0.172	0.196	0.210	0.220	0.230	0.243	0.262	0.290	0.324
4 4.0 → 1 2.0	0.169	0.226	0.250	0.260	0.267	0.273	0.285	0.306	0.335	0.374
4 4.0 → 2 1.0	0.130	0.199	0.241	0.266	0.280	0.290	0.298	0.307	0.317	0.330
4 4.0 → 2 2.0	0.384	0.575	0.698	0.781	0.843	0.891	0.934	0.975	1.017	1.061
4 4.0 → 2 3.0	0.300	0.450	0.541	0.597	0.632	0.658	0.681	0.706	0.737	0.773
4 4.0 → 3 2.0	0.147	0.193	0.214	0.224	0.230	0.238	0.254	0.282	0.325	0.382
4 4.0 → 3 3.0	0.306	0.388	0.429	0.460	0.490	0.527	0.579	0.652	0.750	0.871
4 4.0 → 3 4.0	0.280	0.354	0.385	0.398	0.406	0.418	0.445	0.496	0.574	0.680
4 5.0 → 0 1.0	0.091	0.163	0.208	0.239	0.262	0.281	0.298	0.316	0.336	0.358
4 5.0 → 1 0.0	0.028	0.036	0.041	0.043	0.045	0.046	0.049	0.055	0.062	0.073
4 5.0 → 1 1.0	0.087	0.113	0.123	0.127	0.129	0.131	0.137	0.147	0.163	0.184
4 5.0 → 1 2.0	0.209	0.288	0.323	0.342	0.353	0.365	0.382	0.407	0.442	0.486
4 5.0 → 2 1.0	0.079	0.113	0.132	0.142	0.148	0.153	0.159	0.168	0.179	0.194
4 5.0 → 2 2.0	0.177	0.265	0.317	0.346	0.364	0.377	0.389	0.403	0.422	0.445

(continued)

(continued)

$j \rightarrow j'$	Temperature / K									
	5	10	15	20	25	30	35	40	45	50
4 5.0 → 2 3.0	0.559	0.846	1.032	1.156	1.243	1.310	1.365	1.417	1.470	1.525
4 5.0 → 3 2.0	0.160	0.190	0.200	0.201	0.199	0.200	0.211	0.235	0.276	0.333
4 5.0 → 3 3.0	0.213	0.269	0.291	0.300	0.305	0.312	0.331	0.368	0.427	0.508
4 5.0 → 3 4.0	0.360	0.475	0.537	0.581	0.622	0.670	0.735	0.826	0.945	1.092
4 5.0 → 4 4.0	0.405	0.530	0.596	0.636	0.662	0.688	0.726	0.786	0.872	0.985
5 4.0 → 0 1.0	0.055	0.095	0.120	0.136	0.146	0.153	0.158	0.165	0.173	0.183
5 4.0 → 1 0.0	0.056	0.103	0.137	0.161	0.179	0.192	0.203	0.212	0.220	0.227
5 4.0 → 1 1.0	0.094	0.170	0.222	0.257	0.282	0.301	0.316	0.329	0.342	0.354
5 4.0 → 1 2.0	0.101	0.172	0.215	0.242	0.260	0.275	0.289	0.304	0.320	0.337
5 4.0 → 2 1.0	0.129	0.163	0.189	0.209	0.223	0.235	0.245	0.256	0.269	0.284
5 4.0 → 2 2.0	0.114	0.155	0.179	0.193	0.202	0.208	0.214	0.222	0.233	0.246
5 4.0 → 2 3.0	0.113	0.165	0.195	0.211	0.219	0.224	0.230	0.238	0.249	0.264
5 4.0 → 3 2.0	0.653	0.889	1.047	1.158	1.241	1.309	1.376	1.452	1.545	1.657
5 4.0 → 3 3.0	0.257	0.374	0.450	0.501	0.536	0.568	0.612	0.681	0.782	0.918
5 4.0 → 3 4.0	0.109	0.170	0.207	0.230	0.247	0.272	0.319	0.405	0.539	0.723
5 4.0 → 4 3.0	0.183	0.266	0.326	0.375	0.419	0.463	0.511	0.568	0.634	0.711
5 4.0 → 4 4.0	0.160	0.215	0.246	0.264	0.276	0.288	0.307	0.340	0.390	0.455
5 4.0 → 4 5.0	0.170	0.235	0.267	0.282	0.290	0.298	0.314	0.344	0.390	0.453
5 4.0 → 5 5.0	0.356	0.442	0.497	0.538	0.571	0.602	0.640	0.693	0.766	0.861
5 4.0 → 5 6.0	0.111	0.143	0.160	0.170	0.179	0.190	0.214	0.257	0.325	0.419
5 5.0 → 0 1.0	0.055	0.095	0.120	0.136	0.146	0.153	0.158	0.165	0.173	0.183
5 5.0 → 1 0.0	0.015	0.026	0.032	0.035	0.038	0.039	0.040	0.042	0.043	0.045
5 5.0 → 1 1.0	0.111	0.201	0.263	0.305	0.336	0.360	0.380	0.397	0.414	0.431
5 5.0 → 1 2.0	0.124	0.218	0.279	0.320	0.348	0.370	0.388	0.406	0.424	0.443
5 5.0 → 2 1.0	0.053	0.076	0.087	0.093	0.096	0.098	0.100	0.103	0.107	0.114
5 5.0 → 2 2.0	0.164	0.214	0.250	0.276	0.294	0.308	0.321	0.335	0.352	0.372
5 5.0 → 2 3.0	0.139	0.194	0.226	0.244	0.254	0.262	0.269	0.279	0.292	0.309
5 5.0 → 3 2.0	0.131	0.198	0.241	0.269	0.287	0.306	0.333	0.380	0.450	0.545
5 5.0 → 3 3.0	0.641	0.871	1.023	1.131	1.213	1.285	1.362	1.460	1.586	1.744
5 5.0 → 3 4.0	0.247	0.364	0.440	0.488	0.523	0.559	0.612	0.699	0.831	1.009
5 5.0 → 4 3.0	0.122	0.164	0.186	0.198	0.206	0.214	0.228	0.252	0.289	0.339
5 5.0 → 4 4.0	0.204	0.298	0.364	0.414	0.458	0.501	0.549	0.608	0.678	0.758
5 5.0 → 4 5.0	0.187	0.254	0.290	0.309	0.321	0.334	0.355	0.392	0.447	0.522
5 6.0 → 0 1.0	0.055	0.095	0.120	0.136	0.146	0.153	0.158	0.165	0.173	0.183
5 6.0 → 1 0.0	0.019	0.032	0.040	0.045	0.048	0.051	0.053	0.056	0.060	0.063
5 6.0 → 1 1.0	0.053	0.089	0.110	0.122	0.131	0.138	0.144	0.151	0.159	0.168
5 6.0 → 1 2.0	0.179	0.324	0.424	0.493	0.543	0.580	0.611	0.638	0.663	0.687
5 6.0 → 2 1.0	0.046	0.068	0.081	0.088	0.092	0.094	0.096	0.099	0.104	0.111
5 6.0 → 2 2.0	0.084	0.121	0.141	0.151	0.156	0.160	0.163	0.169	0.177	0.187
5 6.0 → 2 3.0	0.226	0.294	0.341	0.374	0.396	0.413	0.430	0.448	0.470	0.497
5 6.0 → 3 2.0	0.053	0.083	0.101	0.112	0.121	0.134	0.160	0.208	0.283	0.385
5 6.0 → 3 3.0	0.142	0.217	0.264	0.294	0.315	0.338	0.376	0.441	0.542	0.679
5 6.0 → 3 4.0	0.824	1.133	1.339	1.482	1.588	1.677	1.771	1.889	2.042	2.234
5 6.0 → 4 3.0	0.107	0.149	0.169	0.179	0.184	0.189	0.199	0.218	0.247	0.287
5 6.0 → 4 4.0	0.150	0.204	0.232	0.247	0.255	0.264	0.280	0.309	0.354	0.414
5 6.0 → 4 5.0	0.254	0.363	0.438	0.496	0.546	0.595	0.653	0.725	0.814	0.919
5 6.0 → 5 5.0	0.276	0.344	0.387	0.418	0.443	0.467	0.500	0.548	0.616	0.706
6 5.0 → 0 1.0	0.058	0.102	0.130	0.149	0.163	0.174	0.183	0.192	0.201	0.211
6 5.0 → 1 0.0	0.021	0.046	0.063	0.075	0.083	0.089	0.095	0.100	0.105	0.111
6 5.0 → 1 1.0	0.040	0.076	0.101	0.117	0.128	0.137	0.147	0.159	0.172	0.187
6 5.0 → 1 2.0	0.081	0.131	0.161	0.178	0.190	0.200	0.215	0.234	0.257	0.284
6 5.0 → 2 1.0	0.202	0.304	0.385	0.447	0.494	0.531	0.562	0.590	0.615	0.638
6 5.0 → 2 2.0	0.145	0.217	0.266	0.302	0.327	0.348	0.367	0.386	0.405	0.426
6 5.0 → 2 3.0	0.087	0.133	0.162	0.181	0.195	0.208	0.222	0.239	0.260	0.283
6 5.0 → 3 2.0	0.153	0.198	0.236	0.266	0.291	0.319	0.356	0.407	0.473	0.551
6 5.0 → 3 3.0	0.091	0.136	0.165	0.185	0.201	0.222	0.258	0.312	0.384	0.473
6 5.0 → 3 4.0	0.119	0.172	0.205	0.224	0.239	0.260	0.297	0.355	0.433	0.529
6 5.0 → 4 3.0	0.767	1.049	1.257	1.410	1.527	1.624	1.714	1.803	1.894	1.987
6 5.0 → 4 4.0	0.238	0.316	0.372	0.412	0.443	0.476	0.519	0.575	0.644	0.723
6 5.0 → 4 5.0	0.079	0.113	0.132	0.146	0.162	0.191	0.242	0.318	0.417	0.534
6 5.0 → 5 4.0	0.185	0.266	0.331	0.383	0.428	0.472	0.519	0.575	0.639	0.711
6 5.0 → 5 5.0	0.131	0.185	0.217	0.236	0.250	0.264	0.286	0.320	0.367	0.427
6 5.0 → 5 6.0	0.146	0.196	0.226	0.244	0.256	0.271	0.293	0.329	0.379	0.442
6 5.0 → 6 6.0	0.205	0.277	0.324	0.360	0.391	0.424	0.464	0.515	0.577	0.648
6 5.0 → 6 7.0	0.048	0.070	0.083	0.092	0.100	0.114	0.138	0.174	0.223	0.283
6 6.0 → 0 1.0	0.058	0.102	0.130	0.149	0.163	0.174	0.183	0.192	0.201	0.211
6 6.0 → 1 0.0	0.008	0.011	0.013	0.013	0.014	0.015	0.017	0.020	0.023	0.028
6 6.0 → 1 1.0	0.060	0.112	0.149	0.172	0.187	0.200	0.212	0.226	0.241	0.258
6 6.0 → 1 2.0	0.075	0.129	0.164	0.186	0.200	0.213	0.228	0.247	0.270	0.296
6 6.0 → 2 1.0	0.054	0.080	0.095	0.105	0.112	0.117	0.122	0.129	0.137	0.147
6 6.0 → 2 2.0	0.227	0.344	0.435	0.505	0.559	0.603	0.640	0.674	0.707	0.739
6 6.0 → 2 3.0	0.154	0.230	0.282	0.319	0.345	0.367	0.389	0.411	0.436	0.462
6 6.0 → 3 2.0	0.053	0.082	0.101	0.113	0.122	0.136	0.160	0.196	0.246	0.307
6 6.0 → 3 3.0	0.193	0.250	0.295	0.329	0.357	0.388	0.432	0.493	0.572	0.665
6 6.0 → 3 4.0	0.118	0.174	0.210	0.232	0.251	0.277	0.319	0.384	0.472	0.580
6 6.0 → 4 3.0	0.143	0.189	0.220	0.242	0.260	0.281	0.310	0.351	0.402	0.461
6 6.0 → 4 4.0	0.716	0.989	1.188	1.334	1.450	1.552	1.654	1.763	1.882	2.009
6 6.0 → 4 5.0	0.224	0.300	0.354	0.391	0.422	0.459	0.511	0.582	0.671	0.774
6 6.0 → 5 4.0	0.105	0.148	0.173	0.188	0.198	0.209	0.226	0.253	0.291	0.339
6 6.0 → 5 5.0	0.205	0.287	0.353	0.406	0.452	0.497	0.547	0.606	0.676	0.755

(continued)

(continued)

$j \rightarrow j'$	Temperature / K									
	5	10	15	20	25	30	35	40	45	50
6 6.0 → 5 6.0	0.152	0.212	0.247	0.269	0.284	0.300	0.325	0.364	0.418	0.487
6 7.0 → 0 1.0	0.058	0.102	0.130	0.149	0.163	0.174	0.183	0.192	0.201	0.211
6 7.0 → 1 0.0	0.019	0.030	0.037	0.041	0.043	0.045	0.048	0.052	0.057	0.063
6 7.0 → 1 1.0	0.043	0.066	0.079	0.086	0.091	0.096	0.104	0.115	0.128	0.143
6 7.0 → 1 2.0	0.081	0.157	0.210	0.244	0.267	0.286	0.304	0.326	0.350	0.376
6 7.0 → 2 1.0	0.031	0.047	0.058	0.065	0.070	0.074	0.080	0.087	0.096	0.106
6 7.0 → 2 2.0	0.074	0.110	0.132	0.146	0.156	0.164	0.174	0.185	0.199	0.215
6 7.0 → 2 3.0	0.330	0.496	0.623	0.718	0.790	0.848	0.897	0.942	0.985	1.026
6 7.0 → 3 2.0	0.067	0.097	0.114	0.125	0.133	0.144	0.165	0.196	0.239	0.291
6 7.0 → 3 3.0	0.081	0.122	0.148	0.164	0.176	0.195	0.226	0.275	0.341	0.422
6 7.0 → 3 4.0	0.216	0.287	0.343	0.385	0.421	0.462	0.521	0.603	0.710	0.839
6 7.0 → 4 3.0	0.044	0.064	0.075	0.083	0.092	0.110	0.143	0.191	0.255	0.330
6 7.0 → 4 4.0	0.144	0.192	0.224	0.247	0.267	0.292	0.331	0.386	0.457	0.540
6 7.0 → 4 5.0	0.895	1.223	1.462	1.638	1.774	1.889	2.001	2.118	2.243	2.374
6 7.0 → 5 4.0	0.101	0.135	0.156	0.168	0.177	0.187	0.202	0.227	0.261	0.305
6 7.0 → 5 5.0	0.127	0.176	0.205	0.223	0.235	0.248	0.268	0.300	0.345	0.402
6 7.0 → 5 6.0	0.234	0.335	0.412	0.472	0.523	0.572	0.628	0.696	0.778	0.873
6 7.0 → 6 6.0	0.161	0.219	0.257	0.285	0.310	0.338	0.373	0.419	0.475	0.541

Table 10: Integrated rate coefficients $j \rightarrow j'$ from 55 to 100 K. Units are 10^{-10} cm^3 s^{-1}.

$j \rightarrow j'$	Temperature / K									
	55	60	65	70	75	80	85	90	95	100
1 0.0 → 0 1.0	0.954	0.961	0.969	0.976	0.984	0.992	1.000	1.008	1.016	1.024
1 0.0 → 1 1.0	0.736	0.739	0.742	0.744	0.747	0.750	0.753	0.756	0.759	0.761
1 0.0 → 1 2.0	1.766	1.807	1.851	1.898	1.947	1.996	2.046	2.095	2.143	2.190
1 1.0 → 0 1.0	0.954	0.961	0.969	0.976	0.984	0.992	1.000	1.008	1.016	1.024
1 2.0 → 0 1.0	0.954	0.961	0.969	0.976	0.984	0.992	1.000	1.008	1.016	1.024
1 2.0 → 1 1.0	0.979	0.998	1.018	1.040	1.063	1.086	1.109	1.132	1.154	1.176
2 1.0 → 0 1.0	0.713	0.736	0.759	0.782	0.804	0.826	0.847	0.867	0.887	0.906
2 1.0 → 1 0.0	0.348	0.366	0.384	0.403	0.422	0.440	0.459	0.476	0.493	0.510
2 1.0 → 1 1.0	0.539	0.559	0.579	0.599	0.619	0.638	0.657	0.675	0.693	0.709
2 1.0 → 1 2.0	0.641	0.650	0.662	0.676	0.690	0.705	0.719	0.734	0.748	0.762
2 1.0 → 2 2.0	1.269	1.300	1.331	1.361	1.391	1.420	1.448	1.475	1.500	1.524
2 1.0 → 2 3.0	0.875	0.884	0.895	0.907	0.919	0.931	0.943	0.955	0.967	0.978
2 2.0 → 0 1.0	0.713	0.736	0.759	0.782	0.804	0.826	0.847	0.867	0.887	0.906
2 2.0 → 1 0.0	0.124	0.126	0.129	0.132	0.134	0.137	0.139	0.142	0.144	0.145
2 2.0 → 1 1.0	0.677	0.704	0.733	0.763	0.792	0.822	0.851	0.880	0.907	0.933
2 2.0 → 1 2.0	0.726	0.744	0.763	0.783	0.804	0.824	0.845	0.864	0.884	0.902
2 3.0 → 0 1.0	0.713	0.736	0.759	0.782	0.804	0.826	0.847	0.867	0.887	0.906
2 3.0 → 1 0.0	0.126	0.128	0.130	0.133	0.135	0.138	0.141	0.144	0.147	0.149
2 3.0 → 1 1.0	0.376	0.382	0.389	0.397	0.405	0.413	0.421	0.429	0.437	0.444
2 3.0 → 1 2.0	1.025	1.065	1.106	1.148	1.190	1.232	1.273	1.313	1.351	1.387
2 3.0 → 2 2.0	0.911	0.929	0.947	0.965	0.983	1.001	1.018	1.035	1.050	1.066
3 2.0 → 0 1.0	0.302	0.317	0.334	0.351	0.370	0.388	0.407	0.425	0.443	0.460
3 2.0 → 1 0.0	0.327	0.349	0.372	0.395	0.418	0.440	0.461	0.482	0.502	0.521
3 2.0 → 1 1.0	0.546	0.585	0.625	0.666	0.706	0.744	0.782	0.818	0.851	0.883
3 2.0 → 1 2.0	0.661	0.707	0.756	0.807	0.857	0.906	0.954	0.999	1.042	1.082
3 2.0 → 2 1.0	0.566	0.606	0.647	0.689	0.732	0.774	0.815	0.856	0.895	0.932
3 2.0 → 2 2.0	0.500	0.533	0.570	0.610	0.652	0.694	0.737	0.779	0.819	0.858
3 2.0 → 2 3.0	0.482	0.515	0.554	0.598	0.645	0.693	0.742	0.790	0.837	0.882
3 2.0 → 3 3.0	2.129	2.549	3.035	3.573	4.147	4.742	5.345	5.945	6.533	7.103
3 2.0 → 3 4.0	1.298	1.607	1.965	2.360	2.779	3.213	3.652	4.087	4.513	4.924
3 3.0 → 0 1.0	0.302	0.317	0.334	0.351	0.370	0.388	0.407	0.425	0.443	0.460
3 3.0 → 1 0.0	0.110	0.118	0.127	0.135	0.144	0.152	0.160	0.168	0.175	0.181
3 3.0 → 1 1.0	0.670	0.716	0.764	0.812	0.860	0.907	0.952	0.996	1.037	1.076
3 3.0 → 1 2.0	0.754	0.808	0.863	0.920	0.977	1.032	1.085	1.135	1.183	1.228
3 3.0 → 2 1.0	0.267	0.284	0.304	0.326	0.349	0.372	0.396	0.419	0.441	0.463
3 3.0 → 2 2.0	0.690	0.739	0.791	0.846	0.901	0.957	1.012	1.066	1.118	1.168
3 3.0 → 2 3.0	0.591	0.631	0.676	0.726	0.779	0.833	0.887	0.940	0.992	1.042
3 4.0 → 0 1.0	0.302	0.317	0.334	0.351	0.370	0.388	0.407	0.425	0.443	0.460
3 4.0 → 1 0.0	0.131	0.140	0.150	0.159	0.169	0.179	0.189	0.198	0.206	0.214
3 4.0 → 1 1.0	0.368	0.395	0.423	0.451	0.479	0.507	0.534	0.559	0.583	0.605
3 4.0 → 1 2.0	1.035	1.107	1.182	1.257	1.332	1.404	1.475	1.542	1.606	1.666
3 4.0 → 2 1.0	0.200	0.214	0.231	0.249	0.269	0.289	0.310	0.330	0.350	0.369
3 4.0 → 2 2.0	0.389	0.415	0.446	0.479	0.515	0.551	0.588	0.624	0.659	0.693
3 4.0 → 2 3.0	0.958	1.024	1.095	1.169	1.245	1.321	1.396	1.470	1.541	1.610
3 4.0 → 3 3.0	1.639	1.981	2.376	2.813	3.278	3.761	4.249	4.735	5.211	5.671
4 3.0 → 0 1.0	0.383	0.411	0.440	0.472	0.504	0.536	0.567	0.598	0.628	0.656
4 3.0 → 1 0.0	0.162	0.179	0.197	0.215	0.233	0.250	0.267	0.283	0.298	0.312
4 3.0 → 1 1.0	0.272	0.298	0.326	0.355	0.384	0.412	0.439	0.465	0.490	0.512
4 3.0 → 1 2.0	0.399	0.457	0.518	0.582	0.645	0.707	0.767	0.823	0.875	0.924
4 3.0 → 2 1.0	0.972	1.004	1.037	1.070	1.103	1.134	1.165	1.194	1.222	1.249
4 3.0 → 2 2.0	0.750	0.783	0.819	0.856	0.893	0.930	0.966	1.001	1.034	1.065
4 3.0 → 2 3.0	0.546	0.592	0.642	0.694	0.746	0.798	0.848	0.896	0.942	0.984
4 3.0 → 3 2.0	0.872	0.995	1.124	1.256	1.390	1.521	1.648	1.770	1.886	1.995
4 3.0 → 3 3.0	0.669	0.784	0.908	1.037	1.166	1.295	1.419	1.537	1.649	1.754

(continued)

(continued)

$j \rightarrow j'$	Temperature / K									
	55	60	65	70	75	80	85	90	95	100
4 3.0 → 3 4.0	0.732	0.880	1.040	1.208	1.379	1.548	1.712	1.869	2.017	2.156
4 3.0 → 4 4.0	1.306	1.441	1.586	1.736	1.887	2.036	2.181	2.318	2.448	2.569
4 3.0 → 4 5.0	0.968	1.200	1.452	1.717	1.987	2.255	2.517	2.769	3.008	3.232
4 4.0 → 0 1.0	0.383	0.411	0.440	0.472	0.504	0.536	0.567	0.598	0.628	0.656
4 4.0 → 1 0.0	0.048	0.052	0.056	0.060	0.065	0.070	0.074	0.078	0.082	0.086
4 4.0 → 1 1.0	0.365	0.409	0.457	0.505	0.554	0.601	0.646	0.689	0.729	0.766
4 4.0 → 1 2.0	0.421	0.473	0.528	0.586	0.643	0.699	0.753	0.804	0.852	0.896
4 4.0 → 2 1.0	0.346	0.363	0.382	0.402	0.422	0.442	0.462	0.481	0.500	0.517
4 4.0 → 2 2.0	1.108	1.156	1.205	1.255	1.304	1.353	1.399	1.444	1.487	1.527
4 4.0 → 2 3.0	0.815	0.861	0.911	0.963	1.015	1.067	1.117	1.165	1.211	1.254
4 4.0 → 3 2.0	0.452	0.531	0.617	0.706	0.796	0.885	0.971	1.053	1.131	1.203
4 4.0 → 3 3.0	1.013	1.170	1.339	1.512	1.687	1.860	2.028	2.189	2.342	2.486
4 4.0 → 3 4.0	0.809	0.957	1.116	1.283	1.451	1.618	1.779	1.933	2.079	2.215
4 5.0 → 0 1.0	0.383	0.411	0.440	0.472	0.504	0.536	0.567	0.598	0.628	0.656
4 5.0 → 1 0.0	0.085	0.098	0.113	0.128	0.143	0.157	0.171	0.184	0.197	0.208
4 5.0 → 1 1.0	0.210	0.239	0.271	0.303	0.335	0.367	0.397	0.426	0.453	0.478
4 5.0 → 1 2.0	0.538	0.596	0.658	0.721	0.784	0.845	0.905	0.961	1.014	1.062
4 5.0 → 2 1.0	0.212	0.232	0.254	0.276	0.299	0.321	0.343	0.363	0.383	0.401
4 5.0 → 2 2.0	0.472	0.503	0.537	0.572	0.608	0.643	0.678	0.711	0.742	0.772
4 5.0 → 2 3.0	1.584	1.645	1.708	1.772	1.835	1.898	1.958	2.017	2.072	2.125
4 5.0 → 3 2.0	0.404	0.486	0.575	0.669	0.764	0.858	0.949	1.037	1.119	1.197
4 5.0 → 3 3.0	0.606	0.718	0.840	0.968	1.096	1.224	1.347	1.465	1.577	1.681
4 5.0 → 3 4.0	1.264	1.454	1.656	1.865	2.074	2.281	2.482	2.674	2.856	3.027
4 5.0 → 4 4.0	1.121	1.276	1.443	1.617	1.793	1.968	2.137	2.299	2.453	2.596
5 4.0 → 0 1.0	0.194	0.208	0.223	0.239	0.255	0.271	0.287	0.302	0.317	0.330
5 4.0 → 1 0.0	0.234	0.240	0.245	0.251	0.255	0.260	0.263	0.267	0.270	0.273
5 4.0 → 1 1.0	0.366	0.378	0.390	0.401	0.411	0.421	0.429	0.438	0.445	0.451
5 4.0 → 1 2.0	0.356	0.376	0.396	0.416	0.435	0.454	0.471	0.488	0.503	0.517
5 4.0 → 2 1.0	0.301	0.320	0.341	0.362	0.383	0.404	0.425	0.445	0.464	0.481
5 4.0 → 2 2.0	0.263	0.281	0.302	0.323	0.344	0.366	0.387	0.407	0.426	0.444
5 4.0 → 2 3.0	0.283	0.305	0.328	0.353	0.378	0.403	0.427	0.451	0.473	0.493
5 4.0 → 3 2.0	1.787	1.932	2.087	2.250	2.414	2.577	2.737	2.890	3.036	3.173
5 4.0 → 3 3.0	1.086	1.280	1.492	1.717	1.947	2.176	2.401	2.618	2.824	3.018
5 4.0 → 3 4.0	0.951	1.217	1.509	1.817	2.133	2.449	2.759	3.058	3.343	3.611
5 4.0 → 4 3.0	0.796	0.887	0.982	1.078	1.175	1.270	1.361	1.449	1.533	1.612
5 4.0 → 4 4.0	0.536	0.628	0.729	0.834	0.941	1.047	1.150	1.249	1.343	1.431
5 4.0 → 4 5.0	0.531	0.621	0.718	0.819	0.922	1.024	1.123	1.217	1.306	1.389
5 4.0 → 5 5.0	0.977	1.108	1.252	1.403	1.558	1.712	1.862	2.008	2.146	2.276
5 4.0 → 5 6.0	0.535	0.671	0.820	0.979	1.141	1.304	1.464	1.618	1.765	1.904
5 5.0 → 0 1.0	0.194	0.208	0.223	0.239	0.255	0.271	0.287	0.302	0.317	0.330
5 5.0 → 1 0.0	0.048	0.050	0.053	0.055	0.058	0.061	0.063	0.065	0.067	0.069
5 5.0 → 1 1.0	0.446	0.462	0.477	0.491	0.504	0.517	0.528	0.539	0.548	0.557
5 5.0 → 1 2.0	0.462	0.482	0.502	0.521	0.539	0.557	0.573	0.588	0.602	0.615
5 5.0 → 2 1.0	0.122	0.131	0.141	0.152	0.163	0.173	0.184	0.194	0.204	0.213
5 5.0 → 2 2.0	0.395	0.421	0.449	0.478	0.507	0.536	0.564	0.591	0.617	0.641
5 5.0 → 2 3.0	0.330	0.354	0.380	0.408	0.436	0.464	0.491	0.517	0.541	0.565
5 5.0 → 3 2.0	0.664	0.801	0.953	1.113	1.277	1.441	1.602	1.757	1.905	2.043
5 5.0 → 3 3.0	1.931	2.142	2.371	2.610	2.853	3.095	3.331	3.559	3.776	3.980
5 5.0 → 3 4.0	1.229	1.485	1.765	2.061	2.364	2.667	2.964	3.250	3.523	3.780
5 5.0 → 4 3.0	0.401	0.472	0.550	0.631	0.713	0.795	0.875	0.952	1.024	1.092
5 5.0 → 4 4.0	0.848	0.945	1.046	1.148	1.251	1.351	1.448	1.540	1.628	1.710
5 5.0 → 4 5.0	0.614	0.719	0.833	0.952	1.074	1.194	1.311	1.423	1.529	1.629
5 6.0 → 0 1.0	0.194	0.208	0.223	0.239	0.255	0.271	0.287	0.302	0.317	0.330
5 6.0 → 1 0.0	0.068	0.072	0.076	0.081	0.085	0.089	0.093	0.096	0.100	0.103
5 6.0 → 1 1.0	0.178	0.189	0.199	0.210	0.221	0.231	0.241	0.250	0.259	0.266
5 6.0 → 1 2.0	0.710	0.733	0.755	0.776	0.795	0.813	0.830	0.845	0.859	0.871
5 6.0 → 2 1.0	0.119	0.128	0.138	0.148	0.159	0.169	0.179	0.189	0.198	0.207
5 6.0 → 2 2.0	0.201	0.216	0.233	0.250	0.268	0.286	0.303	0.320	0.336	0.350
5 6.0 → 2 3.0	0.528	0.563	0.600	0.639	0.678	0.718	0.756	0.793	0.828	0.861
5 6.0 → 3 2.0	0.513	0.661	0.824	0.997	1.173	1.350	1.523	1.690	1.849	1.999
5 6.0 → 3 3.0	0.850	1.048	1.267	1.497	1.734	1.970	2.201	2.425	2.637	2.838
5 6.0 → 3 4.0	2.461	2.719	2.998	3.290	3.587	3.883	4.173	4.452	4.717	4.966
5 6.0 → 4 3.0	0.336	0.392	0.454	0.518	0.583	0.647	0.709	0.768	0.824	0.877
5 6.0 → 4 4.0	0.488	0.573	0.665	0.762	0.861	0.959	1.054	1.145	1.231	1.312
5 6.0 → 4 5.0	1.039	1.171	1.309	1.452	1.594	1.735	1.871	2.002	2.126	2.243
5 6.0 → 5 5.0	0.816	0.943	1.081	1.227	1.377	1.526	1.672	1.812	1.947	2.073
6 5.0 → 0 1.0	0.222	0.234	0.246	0.258	0.269	0.280	0.291	0.301	0.310	0.319
6 5.0 → 1 0.0	0.116	0.122	0.127	0.132	0.136	0.140	0.144	0.147	0.150	0.152
6 5.0 → 1 1.0	0.203	0.218	0.234	0.248	0.262	0.274	0.285	0.295	0.304	0.312
6 5.0 → 1 2.0	0.313	0.343	0.372	0.401	0.427	0.452	0.474	0.494	0.512	0.528
6 5.0 → 2 1.0	0.660	0.680	0.699	0.716	0.732	0.746	0.759	0.770	0.780	0.788
6 5.0 → 2 2.0	0.448	0.469	0.490	0.511	0.530	0.548	0.565	0.580	0.594	0.606
6 5.0 → 2 3.0	0.309	0.336	0.363	0.390	0.416	0.440	0.463	0.485	0.504	0.522
6 5.0 → 3 2.0	0.638	0.732	0.828	0.923	1.017	1.106	1.189	1.267	1.338	1.403
6 5.0 → 3 3.0	0.573	0.681	0.792	0.903	1.011	1.114	1.211	1.300	1.382	1.456
6 5.0 → 3 4.0	0.637	0.752	0.871	0.988	1.102	1.210	1.311	1.405	1.490	1.567
6 5.0 → 4 3.0	2.081	2.175	2.266	2.353	2.435	2.512	2.582	2.647	2.705	2.758
6 5.0 → 4 4.0	0.810	0.899	0.989	1.076	1.160	1.238	1.310	1.376	1.435	1.488
6 5.0 → 4 5.0	0.663	0.798	0.935	1.068	1.195	1.315	1.426	1.528	1.619	1.702
6 5.0 → 5 4.0	0.791	0.875	0.961	1.048	1.134	1.218	1.298	1.374	1.445	1.512

(continued)

(continued)

$j \rightarrow j'$	Temperature / K									
	55	60	65	70	75	80	85	90	95	100
6 5.0 → 5 5.0	0.497	0.574	0.655	0.737	0.818	0.897	0.972	1.043	1.108	1.168
6 5.0 → 5 6.0	0.516	0.597	0.682	0.769	0.854	0.936	1.015	1.088	1.156	1.218
6 5.0 → 6 6.0	0.727	0.809	0.893	0.976	1.056	1.133	1.205	1.272	1.334	1.390
6 5.0 → 6 7.0	0.352	0.427	0.504	0.581	0.657	0.730	0.799	0.864	0.923	0.978
6 6.0 → 0 1.0	0.222	0.234	0.246	0.258	0.269	0.280	0.291	0.301	0.310	0.319
6 6.0 → 1 0.0	0.033	0.038	0.043	0.048	0.052	0.056	0.060	0.064	0.067	0.070
6 6.0 → 1 1.0	0.275	0.293	0.310	0.327	0.342	0.356	0.368	0.380	0.389	0.398
6 6.0 → 1 2.0	0.324	0.352	0.379	0.406	0.431	0.454	0.475	0.494	0.510	0.525
6 6.0 → 2 1.0	0.157	0.168	0.179	0.189	0.200	0.210	0.219	0.228	0.235	0.242
6 6.0 → 2 2.0	0.769	0.798	0.826	0.852	0.876	0.898	0.918	0.936	0.952	0.966
6 6.0 → 2 3.0	0.490	0.519	0.548	0.576	0.602	0.627	0.650	0.672	0.691	0.708
6 6.0 → 3 2.0	0.377	0.452	0.529	0.605	0.680	0.751	0.818	0.880	0.937	0.988
6 6.0 → 3 3.0	0.770	0.882	0.996	1.110	1.220	1.325	1.424	1.515	1.598	1.674
6 6.0 → 3 4.0	0.701	0.832	0.966	1.099	1.229	1.353	1.469	1.576	1.674	1.763
6 6.0 → 4 3.0	0.526	0.594	0.662	0.729	0.793	0.852	0.907	0.958	1.003	1.043
6 6.0 → 4 4.0	2.141	2.273	2.404	2.530	2.650	2.762	2.865	2.959	3.045	3.122
6 6.0 → 4 5.0	0.887	1.004	1.122	1.238	1.348	1.451	1.546	1.633	1.712	1.782
6 6.0 → 5 4.0	0.395	0.458	0.524	0.590	0.656	0.720	0.781	0.838	0.891	0.939
6 6.0 → 5 5.0	0.841	0.933	1.027	1.122	1.215	1.306	1.393	1.475	1.553	1.625
6 6.0 → 5 6.0	0.567	0.655	0.748	0.842	0.935	1.025	1.111	1.191	1.265	1.334
6 7.0 → 0 1.0	0.222	0.234	0.246	0.258	0.269	0.280	0.291	0.301	0.310	0.319
6 7.0 → 1 0.0	0.069	0.075	0.082	0.088	0.093	0.099	0.103	0.108	0.111	0.115
6 7.0 → 1 1.0	0.160	0.178	0.195	0.211	0.227	0.242	0.255	0.267	0.277	0.286
6 7.0 → 1 2.0	0.403	0.430	0.456	0.482	0.505	0.526	0.546	0.563	0.578	0.591
6 7.0 → 2 1.0	0.117	0.128	0.140	0.151	0.162	0.173	0.183	0.192	0.201	0.208
6 7.0 → 2 2.0	0.233	0.251	0.270	0.289	0.306	0.323	0.339	0.354	0.367	0.380
6 7.0 → 2 3.0	1.067	1.106	1.143	1.177	1.209	1.239	1.265	1.289	1.310	1.328
6 7.0 → 3 2.0	0.350	0.412	0.477	0.541	0.602	0.661	0.716	0.766	0.813	0.854
6 7.0 → 3 3.0	0.514	0.613	0.714	0.815	0.913	1.007	1.094	1.175	1.250	1.317
6 7.0 → 3 4.0	0.985	1.140	1.300	1.459	1.614	1.762	1.900	2.029	2.148	2.255
6 7.0 → 4 3.0	0.413	0.501	0.588	0.674	0.757	0.834	0.905	0.971	1.030	1.083
6 7.0 → 4 4.0	0.631	0.726	0.822	0.915	1.004	1.088	1.166	1.236	1.300	1.357
6 7.0 → 4 5.0	2.510	2.646	2.779	2.908	3.030	3.143	3.248	3.344	3.430	3.508
6 7.0 → 5 4.0	0.356	0.412	0.471	0.531	0.590	0.646	0.701	0.751	0.798	0.841
6 7.0 → 5 5.0	0.470	0.544	0.621	0.701	0.779	0.855	0.927	0.994	1.057	1.114
6 7.0 → 5 6.0	0.978	1.090	1.206	1.323	1.438	1.550	1.658	1.759	1.855	1.944
6 7.0 → 6 6.0	0.615	0.692	0.772	0.850	0.927	1.000	1.069	1.133	1.192	1.246

Appendix B: Side Projects

During my Ph.D. I was involved in parallel projects that fall outside the main focus of this thesis. These covered additional aspects of the astrochemical picture presented in Figure 1.1 of Chapter 1. More specifically, two different fields have been considered, both showcasing the role of quantum chemistry for astrochemical investigations: (i) the computational characterization of the rotational spectra for molecules of astrochemical interest, from the accurate determination of their equilibrium geometries to the prediction of their rotational frequencies; (ii) the characterization of reactive potential energy surfaces for gas-phase processes occurring in the interstellar medium. A brief description of these investigations is given in the following, along with the publications they have resulted with.

Determination of molecular structures

As already mentioned in Chapter 1, quantum chemistry plays a fundamental role in the search of new molecules in space, the starting point being the accurate determination of their rotational parameters. Hence, given the direct link of the molecular structure with rotational constants, the computational characterization of rotational spectra needs to start with an accurate structural determination. The accurate knowledge of the molecular rotational parameters, moreover, has a crucial role to support the laboratory assignment of rotational spectra. This, in turn, represents a key ingredient for most of the astronomical investigations, since rotational spectral lines can be considered as actual fingerprints of a molecule. However, molecular identifications can only be accomplished if the molecular spectra are known with great accuracy. This implies in many cases very accurate structures determinations. The latter require a very high-level quantum chemical treatment, *e.g.*, exploiting composite schemes rooted in the coupled cluster theory. However, for large-sized molecules, the computational cost might be unaffordable. In these cases, cheaper yet accurate approaches need to be defined.

In order to bring a contribution in this direction, we tested and validated a new approach (Melli et al., 2021), denoted as the "LEGO bricks" model. This approach is rooted in the idea that a molecular system can be seen as formed by different fragments (*i.e.*, the "LEGO bricks"), whose accurate semi-experimental (SE) equilibrium geometries are available (Piccardo et al., 2015; Penocchio et al., 2015). To join together the different "LEGO bricks", this approach relied on: (i) the template molecule approach (TM) (Piccardo et al., 2015) in order to account, at the rev-DSD-PBEP86-D3/jun-cc-pVTZ level, for the changes occurring when moving from the smaller fragment to the larger molecular system; (ii) the linear regression model (LR) to correct the inter-fragment parameters (Penocchio et al., 2015, 2016). The molecular systems considered for benchmarking the resulting structure,

denoted as TM-SE_ LR, are those obtained from addition/elimination reactions of nucleophilic unsaturated radicals (*e.g.*, CN, C_2H, and phenyl) to alkenes, imines, and aldehydes. The TM-SE_ LR scheme has thus been validated by comparison with their semi-experimental equilibrium structures (when available) and rotational constants. All DFT calculations were performed with the Gaussian software (Frisch et al., 2016). The main outcome of this study is the reliability, robustness and accuracy of this novel approach, showing an accuracy of about 0.001 Å for bond lengths and 0.1° for angles and an average relative deviation with respect to the accurate semi-experimental equilibrium rotational constants of $\sim 0.2\%$.

THE JOURNAL OF PHYSICAL CHEMISTRY A
A JOURNAL OF THE AMERICAN CHEMICAL SOCIETY

pubs.acs.org/JPCA Article

Extending the Applicability of the Semi-experimental Approach by Means of "Template Molecule" and "Linear Regression" Models on Top of DFT Computations

Alessio Melli,[§] Francesca Tonolo,[§] Vincenzo Barone,* and Cristina Puzzarini*

Cite This: *J. Phys. Chem. A* 2021, 125, 9904−9916 Read Online

ACCESS | Metrics & More | Article Recommendations | Supporting Information

ABSTRACT: The accurate determination of equilibrium structures for isolated molecules plays a central role in the evaluation and interpretation of stereoelectronic, thermodynamic, and spectroscopic properties. For small semi-rigid systems, state-of-the-art quantum-chemical computations can rival the most sophisticated experimental results. For larger molecules, cheaper yet accurate approaches need to be defined. The double-hybrid rev-DSD-PBEP86 functional already delivers remarkable results that can be further improved by means of a "Lego brick" model. This is based on the idea that a molecular system can be seen as formed by different fragments (the "Lego bricks"), whose accurate semi-experimental (SE) equilibrium geometries are available. The template molecule (TM) approach can be used to account for the modifications occurring when going from the isolated fragment to the molecular system under investigation, with the linear regression (LR) model employed to correct the linkage between the different fragments. The resulting TM-SE_LR approach has been tested with respect to available SE equilibrium structures and rotational constants. Indeed, the latter parameters straightforwardly depend on the equilibrium geometry of the system under consideration. The main outcome of our study is the reliability, robustness, and accuracy of this novel approach. The molecular systems considered for benchmarking the TM-SE_LR scheme are those formally issued from addition/elimination reactions of nucleophilic unsaturated radicals (e.g., CN, C_2H, and phenyl) to alkenes, imines, and aldehydes, whose rotational spectra have been investigated, but accurate structural determinations are not yet available.

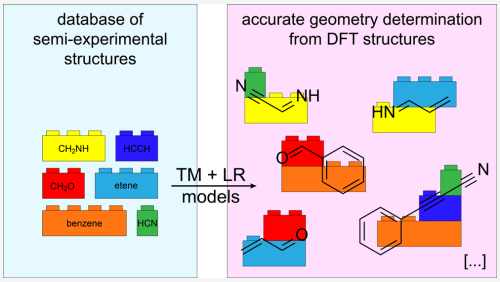

INTRODUCTION

The accurate determination of molecular structures is one of the main aims in many areas of chemistry. In physical chemistry, the prediction and interpretation of structural properties and dynamic behavior of molecules are a prerequisite for a deeper understanding of their stability and chemical reactivity.[1−10] In the field of molecular spectroscopy, there is a strong relationship between the experimental outcomes and the structure of the molecular system.[11−14] Therefore, computational spectroscopy investigations often start from structural determinations. In particular, in rotational spectroscopy, the equilibrium geometry provides the major contribution to the leading terms of this technique, the rotational constants.[2,6,11] While it is seldom straightforward to derive the molecular structure from experimental information, with quantum chemistry being often required to either support or complement such determinations, state-of-the-art computational methodologies are able to provide very accurate equilibrium structures.[6,7,15,16] Indeed, in the absence of strong non-dynamical correlation effects, composite schemes rooted in the coupled-cluster model are currently able to evaluate structural parameters with an accuracy of 0.001 Å and 0.1° for bond lengths and angles, respectively.[6,17−23] However, despite the improvement in hardware and software technologies[24,25] and the increasing availability of composite schemes at reduced computational costs (e.g., the so-called "cheap" scheme and its variants),[22,26] accurate geometry optimizations are still out of range for large molecular systems due to the extremely unfavorable scaling of accurate quantum-chemical methods with the number of degrees of freedom.

A viable route is offered by the interplay of the experiment and theory in the field of rotational spectroscopy (see, e.g., refs 6,27−32). Within the so-called semi-experimental (SE) approach,[6,33] equilibrium structural parameters are derived from a least-squares fit of the SE equilibrium rotational

Received: September 3, 2021
Revised: October 20, 2021
Published: November 9, 2021

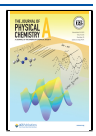

https://doi.org/10.1021/acs.jpca.1c07828
J. Phys. Chem. A 2021, 125, 9904−9916

constants (B_e^{SE}) for different isotopologues. The B_e^{SE} values are obtained by correcting the experimental vibrational ground-state rotational constants[a] (B_0^{exp}) for computed vibrational contributions (ΔB_{vib}^{calc})[33]

$$B_e^{SE} = B_0^{exp} - \Delta B_{vib}^{calc} \quad (1)$$

The accuracy of this approach is well established,[27] and its application led to the definition of a database of SE equilibrium structures of small- to medium-sized semi-rigid molecules (hereafter denoted as the SE database).[29,30]

The main drawback of the SE approach is the number of experimental data required for a complete structural characterization. The greater the molecule is, the larger the number of isotopologues to be investigated becomes. Furthermore, even if the number of available B_0^{exp} constants exceeds that of the geometrical parameters to be determined, a balanced fit requires data for the isotopic substitutions involving all nuclei.[14] This becomes exceedingly difficult when the molecular size and topological complexity increase. If the number of available isotopically substituted species is not sufficient to allow a robust evaluation of all structural parameters, the lack of information can affect both the quality of the fit and their accuracy and reliability. In these cases, to avoid biased results, some geometrical parameters (i.e., those whose "experimental information" is missing) are kept fixed in the fitting procedure, usually relying on computational determinations. However, if the level of theory employed is not sufficiently high, the results of the fit and their accuracy might be unsatisfactory.[6] In this respect, powerful way-outs are offered by the template molecule (TM)[30] and/or linear regression (LR) approaches.[29]

The TM approach has been introduced to extend the size of molecular systems amenable to accurate molecular structure determinations. It is based on the idea that, if an accurate equilibrium geometry is available (either experimentally or computationally) for a smaller molecule identical to one of the system's moieties, it can be used to provide the corresponding geometrical parameters of the system under study, corrected by the differences between predictions calculated for the moieties and the system. Alternatively, the LR approach can be employed to improve the computed geometries. Indeed, within this approach, a given structural parameter is corrected by a term previously obtained from the linear regression of the fit of semi-experimental values versus the computed counterparts (at the level of theory considered) for a large set of molecules. The LR corrections are available for the most common bond distances and angles and have been collected in a database (hereafter denoted as the LR database) for several combinations of density functionals and basis sets.[29,30,34]

The idea presented in this work is to combine the TM and SE approaches, also relying on the contribution of LR corrections, with the aim of obtaining highly accurate equilibrium structures at a very reduced computational cost. The so-called TM-SE approach is based on identifying, in the molecule under study, fragments whose structures are available in the SE database mentioned above and using them to accurately determine its equilibrium geometry, possibly employing the LR approach for inter-fragment parameters (thus leading to the TM-SE_LR approach).

Among the different classes of molecular systems whose accurate structures are not yet available, one cannot overlook those issued from addition/elimination reactions of nucleophilic unsaturated radicals (e.g., CN, C_2H, and phenyl) to alkenes, imines, and aldehydes. As a matter of fact, addition of free radicals to double bonds has been studied at length because of its interest in several fields ranging from organic synthesis to atmospheric chemistry and astrochemistry (see refs 35−38 and references therein). In particular, the products of addition/elimination of free radicals to alkenes and aldehydes are well known, but accurate structures of some of them are not yet available. The situation is even more involved for imines, which—despite their low-stability under normal terrestrial conditions—play a central role in several processes, leading to the formation of the so-called complex organic molecules in the inter- and circumstellar medium (see refs 38−41 and references therein). Overall, all products of the reactions mentioned above can be seen as formed by two well-defined moieties formally linked by a single bond between two sp^2 and/or sp carbon atoms. Among the possible products, we have chosen the systems forming a suitable playground for testing the proposed TM-SE and TM-SE_LR approaches.

In the next section, the methodology is described with all details. Then, once the set of molecular systems has been introduced, the results are reported, and the validation of our approach is discussed. Examples of applications demonstrating the approach's possible extension to larger systems are also provided. Finally, concluding remarks summarize the main outcomes of this work.

METHODOLOGY

The TM-SE(_LR) approach where, for a given molecule, suitable molecular fragments are seen as "Lego bricks" is set up as follows:

- For the "Lego bricks", we resort to the TM approach, which—as mentioned in the Introduction—is based on identifying, within the molecule, "known" fragments that belong to a smaller system for which a highly accurate equilibrium geometry is available. These fragments are the TMs and are used to determine accurately the corresponding structural parameters of the larger molecular systems (r_e(lms))

$$r_e(\text{lms}) = r_e^{\text{low-cost}}(\text{lms}) + \Delta r_e(\text{TM}) \quad (2)$$

where Δr_e(TM) is defined as

$$\Delta r_e(\text{TM}) = r_e^{\text{accu}}(\text{TM}) - r_e^{\text{low-cost}}(\text{TM}) \quad (3)$$

$r_e^{\text{low-cost}}$ is the geometrical parameter of interest calculated at the same level of theory for both the molecule under consideration (lms) and the TM, the level depending on the size of the molecule to be characterized (usually a method rooted in density functional theory, DFT). A recent benchmark study[42] showed that the double-hybrid rev-DSD-PBEP86 functional[43] in conjunction with the jun-cc-pVTZ basis set[44,45] already provides rather accurate structures. Hereafter, this level of theory, shortly denoted as revDSD, will be employed for the $r_e^{\text{low-cost}}$(lms) and $r_e^{\text{low-cost}}$(TM) of eqs 2 and 3, respectively.

- Once we have the "Lego bricks", we need to put them together, the arising question being how to connect them. For this task, whenever possible, we resort to the LR approach for improving the accuracy of DFT determinations of the inter-fragment parameters. For them, the LR approach replaces the Δr_e(TM) correction

https://doi.org/10.1021/acs.jpca.1c07828
J. Phys. Chem. A 2021, 125, 9904−9916

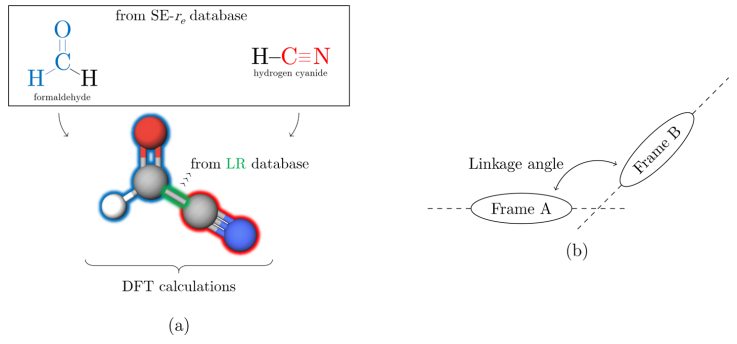

Figure 1. (a) Graphical description of the TM-SE_LR approach. (b) Definition of the linkage angle.

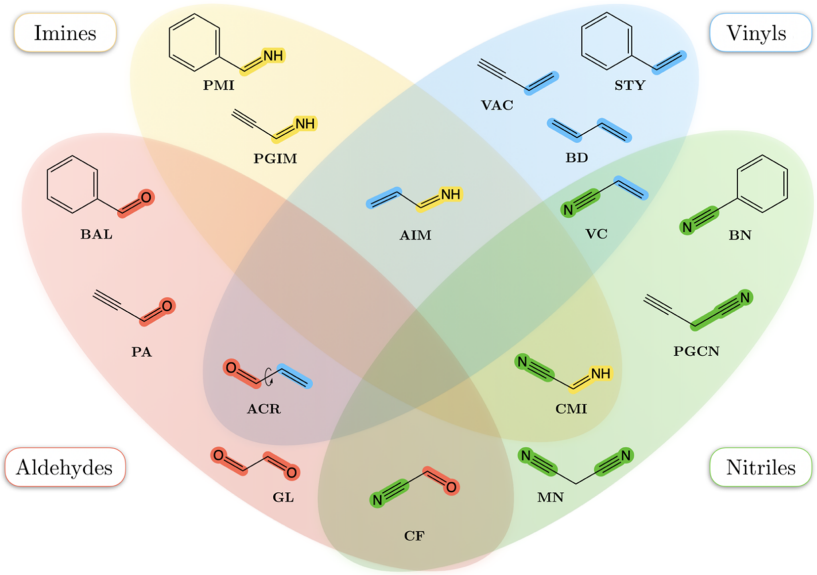

Figure 2. Dataset: molecules grouped according to their moieties, "Lego" bricks.

in eq 2 with an estimate (Δr_e(LR)) based on a linear regression model

$$\Delta r_e(\mathrm{LR}) = A r_e^{\text{low-cost}} + B \tag{4}$$

Therefore, the corrected parameter is given by

$$r_e(\mathrm{lms}) = (1 + A) r_e^{\text{low-cost}} + B \tag{5}$$

The A and B coefficients only depend on the atomic numbers of the involved atoms and were obtained by a statistical analysis of a large number of molecules. In the present context, we employ the corrective factor for the C−C (A = −0.0067 and B = 0.0069) bond length evaluated using the revDSD model and obtained from a study employing nearly 100 semi-experimental values.

If only step 1 is retained, with the linkage parameters thus kept fixed at the revDSD level, the TM-SE model is defined. The TM-SE approach is so denoted because the TMs are taken from the SE database mentioned in the Introduction. The combination of the steps 1 and 2 leads instead to the so-called TM-SE_LR approach. While in the following, we demonstrate the accuracy of the equilibrium structures "built" using the TM-SE and TM-SE_LR models, here, we note that if this approach is used to support a rotational spectroscopy study, once the latter is completed, the SE approach can be employed to refine the revDSD or LR linkage parameters, which are usually the most sensitive structural parameters.

A graphical representation of the TM-SE_LR approach is provided in Figure 1a. The example considered in this figure is formyl cyanide. In this molecule, two molecular fragments can be envisaged: the CN and HCO moieties. DFT geometry optimizations are carried out for formyl cyanide and for the TMs, namely, HCN and formaldehyde. The data available in the SE database are then used to correct the structural

https://doi.org/10.1021/acs.jpca.1c07828
J. Phys. Chem. A 2021, 125, 9904−9916

Table 1. Reference Studies Reporting the Experimental Ground-State Rotational Constants (B_0^{exp}) and Available SE Equilibrium Structures (r_e^{SE}) for the Dataset Molecules

Molecule		Ref.	Molecule		Ref.
Z-propargylimine	$\xrightarrow{B_{exp}}$	Bizzocchi et al.[54]	*trans*-acrolein	$\xrightarrow{B_{exp}}$	Jaman and Bhattacharya[55]
	$\xrightarrow{r_e^{SE}}$	This work		$\xrightarrow{r_e^{SE}}$	Puzzarini et al.[56]
E-propargylimine	$\xrightarrow{B_{exp}}$	Bizzocchi et al.[54]	*cis*-acrolein	$\xrightarrow{B_{exp}}$	Blom and Bauder[57]
Z-phenylmethanimine	$\xrightarrow{B_{exp}}$	Melli et al.[58]		$\xrightarrow{r_e^{SE}}$	Puzzarini et al.[56]
E-phenylmethanimine	$\xrightarrow{B_{exp}}$	Melli et al.[58]	cyanoformaldehyde	$\xrightarrow{B_{exp}}$	Bogey et al.[59]
Z-cyanomethanimine	$\xrightarrow{B_{exp}}$	Melosso et al.[40]	styrene	$\xrightarrow{B_{exp}}$	Caminati et al.[60]
E-cyanomethanimine	$\xrightarrow{B_{exp}}$	Melosso et al.[40]	vinylacetilene	$\xrightarrow{B_{exp}}$	Thorwirth and Lichau[61]
Z-allylimine	$\xrightarrow{B_{exp}}$	Brown et al.[62]		$\xrightarrow{r_e^{SE}}$	Thorwirth et al.[31]
E-allylimine	$\xrightarrow{B_{exp}}$	Brown et al.[62]	vinylcyanide	$\xrightarrow{B_{exp}}$	Müller et al.[63]
benzaldehyde	$\xrightarrow{B_{exp}}$	Desyatnyk et al.[64]		$\xrightarrow{r_e^{SE}}$	Thorwirth et al.[31]
propriolaldehyde	$\xrightarrow{B_{exp}}$	Jabri et al.[65]	benzonitrile	$\xrightarrow{B_{exp}}$	McGuire et al.[66]
trans-1,3-butadiene	$\xrightarrow{B_{exp}}$	Craig et al.[67]	malononitrile	$\xrightarrow{B_{exp}}$	Motiyenko et al.[68]
	$\xrightarrow{r_e^{SE}}$	Penocchio et al.[29]	propargylcyanide	$\xrightarrow{B_{exp}}$	McGuire et al.[69]
trans-glyoxal	$\xrightarrow{B_{exp}}$	Larsen et al.[70]			
	$\xrightarrow{r_e^{SE}}$	Larsen et al.[70]			

parameters of the CN and HCO moieties of formyl cyanide (see eqs 2 and 3). Finally, the DFT C−C bond distance connecting the two "Lego bricks" is corrected using the scaling factors available in the LR database.

To test the accuracy of the equilibrium structures derived using the TM-SE(_LR) approach, one can compare them with SE equilibrium geometries already available in the literature. However, this is not the best option, the TM-SE approach being designed for those cases in which the standard SE approach cannot be applied. Since rotational constants are strongly connected to molecular structures and they are experimentally determined with great accuracy,[2,6,11,27] they are the perfect means for our test. According to eq 1, to move from the ground-state to the equilibrium rotational constants and vice versa, we need the vibrational corrections, ΔB_{vib}. In the framework of vibrational perturbation theory to the second order (VPT2),[46] these are expressed as

$$\Delta B_{vib}^{i} = -\frac{1}{2}\sum_{r} \alpha_r^i \tag{6}$$

where the α_r^i constants are the vibration−rotation interaction constants, i denotes the inertial axis, and the sum runs over all r vibrational modes. The evaluation of the α_r^i values requires anharmonic force field calculations,[14,23,27,28,32] which—in the present work—have been carried out using the global-hybrid B3LYP functional[47,48] in conjunction with the partially augmented double-ζ jun-cc-pVDZ basis set. Hereafter, this level of theory is shortly referred to as B3. Although revDSD spectroscopic parameters are usually more accurate than the B3 counterparts,[42] the ΔB_{vib} contributions benefit from a fortuitous but quite general error compensation, which allows the use of cheaper B3 computations.

All DFT calculations incorporate the D3 scheme[49] for the treatment of dispersion effects combined with the Becke-Johnson (BJ) damping function.[50] Throughout this work, all computations have been performed using the Gaussian16 suite of programs.[51]

Dataset. Before reporting and discussing the results, we need to introduce and describe the dataset employed in our study. The targeted molecules are listed in Figure 2 and have been selected following two main criteria: (1) the rotational constants of the main isotopic species are available and (2) each molecule can be envisaged as formed by two fragments, whose SE equilibrium structures are available. Going into detail, the dataset is composed of 16 species (21 molecules if isomers are considered) that result from the combination of seven fragments, namely, methanimine (CH_2NH), formaldehyde (H_2CO), hydrogen cyanide (HCN), acetylene (C_2H_2), ethene (C_2H_4), acetonitrile (CH_3CN), and benzene (C_6H_6). The SE equilibrium structures of all these fragments are available in the SE database,[29,30] the only exception being methanimine and acetonitrile, whose SE equilibrium geometries are taken from refs 52 and 53, respectively. The SE equilibrium geometries employed in this work are collected in Table S1.

The structural patterns of the chosen molecules allow their classification into four distinct and partially overlapping ensembles, depicted in Figure 2, which shows (also highlighted by different colors) the "Lego bricks" within the selected molecules. The ensemble of imines, that is, species containing the −C=NH terminal group (in yellow in Figure 2), consists of four molecules: propargylimine (PGIM), phenylmethanimine (PMI), cyanomethanimine (CMI), and allylimine (AIM). The orientation of the H atom of the −CNH moiety with respect to the other fragments of the molecule leads to the *Z* (*cis*) and *E* (*trans*) isomers. In this study, all the eight structures have been considered, the experimental rotational constants being retrieved from the reference list provided in Table 1. By replacing the imine moiety with the aldehydic −HC=O group,

https://doi.org/10.1021/acs.jpca.1c07828
J. Phys. Chem. A 2021, 125, 9904−9916

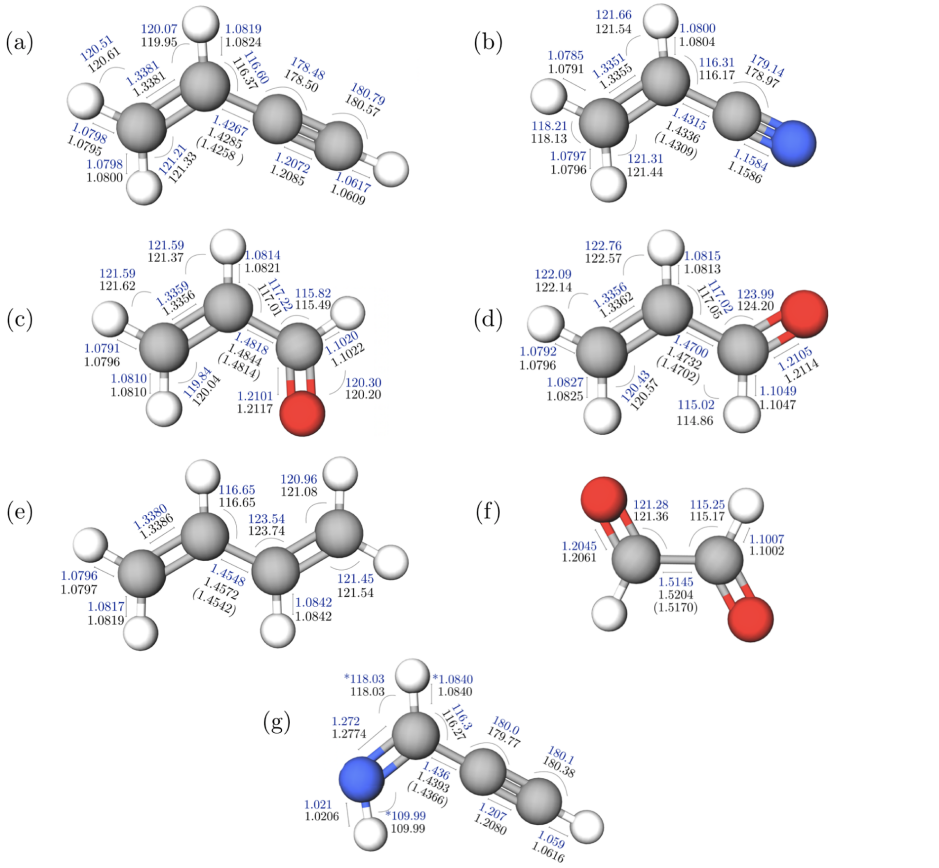

Figure 3. Molecular structures (bond lengths in angstrom and angles in degrees) of vinylacetylene (a), vinyl cyanide (b), *trans*-acrolein (c), *cis*-acrolein (d), *trans*-1,3-butadiene (e), *trans*-glyoxal (f), and *Z*-propargylimine (g). The TM-SE values are in black (for the C−C linkage bond, the TM-SE_LR value is also reported); SE parameters (errors are available in the Supporting Information, Table S2) are in blue (the asterisk denotes parameters kept fixed at the TM-SE value; the number of decimal places depends on the accuracy; see Table S2).

we obtain four molecules characterized well from an experimental point of view (see Table 1), namely, benzaldehyde (BAL), propriolaldehyde (PA), acrolein (ACR; both the *cis* and *trans* isomers), and cyanoformaldehyde (CF). The connection of two aldehydic fragments also leads to the formation of glyoxal (GL; only *trans*). They all have been collected in the red ensemble in Figure 2. Four molecules, namely, styrene (STY), vinylacetylene (VAC), 1,3-butadiene (BD; only the *trans* form), and vinyl cyanide (VC), have been selected to incorporate the vinyl $-CHCH_2$ group in the studied set of molecules, this being the light-blue set. Finally, three molecules containing the cyano −CN group, namely, benzonitrile (BN), malononitrile (MN), and propalgylcyanide (PGCN), have also been considered. The nitrile color code is green.

With the exception of MN and PGCN, all molecules present, as a linkage bond, a single CC bond connecting two unsaturated systems, and thus, non-negligible conjugation effects are expected. Therefore, the selected molecules provide a challenging test suite to validate the TM-SE model and, especially, the TM-SE_LR approach. Some molecular species present a certain degree of flexibility, which is another challenging aspect for our strategy. In particular, the two non-conjugated molecules, that is, MN and PGCN, should be good test cases with their C−C−C frame.

In Table 1, together with the list of the reference studies for the selected molecules, the references for the available SE equilibrium structures are also reported.

RESULTS AND DISCUSSION

Let us start our discussion by comparing the molecular structures issued from the TM-SE and TM-SE_LR approaches with the SE equilibrium geometries (r_e^{SE}) available in the literature for VAC, VC, *trans*-acrolein (*t*-ACR), *cis*-acrolein (*c*-ACR), *trans*-1,3-butadiene (*t*-BD), *trans*-glyoxal (*t*-GL), and *Z*-propargylimine (*Z*-PGIM). The r_e^{SE} structures of *t*-ACR and *c*-ACR have been taken from ref S6 and those of *t*-GL have been taken from ref 70; they are also available in the SE database[29]

https://doi.org/10.1021/acs.jpca.1c07828
J. Phys. Chem. A 2021, 125, 9904−9916

Table 2. Comparison of Computed Equilibrium Rotational Constants (in MHz) with the SE Counterparts for Vinylacetylene, Vinyl Cyanide, *trans*-Acrolein, *cis*-Acrolein, *trans*-1,3-Butadiene, *trans*-Glyoxal, and *Z*-Propargylimine[a]

	revDSD	TM-SE	TM-SE_LR	TM-SE_LR + corr[b]	SE(r_e^{SE})	SE(B_e^{SE})-B3[c]	SE(B_e^{SE})-CC[d]
vinylacetylene							
A_e	50611.7 (+0.39%)	50741.1 (+0.65%)	50751.6 (+0.67%)	50552.9 (+0.28%)	50413.9	50602.3 (+188.4)	50425.4 (+11.5)
B_e	4730.2 (−0.59%)	4738.2 (−0.42%)	4745.9 (−0.26%)	4752.6 (−0.12%)	4758.2	4759.4 (+1.2)	4758.0 (−0.2)
C_e	4325.9 (−0.50%)	4333.5 (−0.33%)	4340.1 (−0.18%)	4344.2 (−0.08%)	4347.8	4350.1 (+2.3)	4347.6 (−0.2)
vinyl cyanide							
A_e	50115.1 (+0.35%)	50250.1 (+0.62%)	50262.7 (+0.64%)	50071.7 (+0.27%)	49939.0	49893.3 (−45.6)	49943.9 (+4.9)
B_e	4955.5 (−0.64%)	4967.0 (−0.41%)	4975.5 (−0.24%)	4982.8 (−0.09%)	4987.3	4986.5 (−0.8)	4987.3 (+0.0)
C_e	4509.6 (−0.55%)	4520.2 (−0.31%)	4527.4 (−0.15%)	4531.9 (−0.06%)	4534.4	4533.3 (−1.1)	4534.5 (+0.1)
trans-acrolein							
A_e	47786.8 (−0.15%)	47934.4 (+0.15%)	47996.9 (+0.28%)	47899.1 (+0.08%)	47860.9	47857.9 (−2.1)	47836.7 (−23.3)
B_e	4660.4 (−0.58%)	4667.9 (−0.42%)	4675.5 (−0.26%)	4680.3 (−0.16%)	4687.8	4685.0 (−2.8)	4688.2 (+0.4)
C_e	4246.3 (−0.55%)	4253.7 (−0.37%)	4260.5 (−0.21%)	4263.7 (−0.14%)	4269.6	4267.9 (−1.7)	4270.2 (+0.6)
cis-acrolein							
A_e	22938.3 (+0.19%)	23009.8 (+0.50%)	23010.0 (+0.50%)	22971.9 (−0.10%)	22895.7	22896.4 (+0.7)	22892.8 (−2.9)
B_e	6228.5 (−1.12%)	6235.5 (−1.01%)	6250.2 (−0.78%)	6263.0 (−0.57%)	6299.1	6295.8 (−3.2)	6303.3 (+4.2)
C_e	4898.4 (−0.83%)	4906.0 (−0.69%)	4915.1 (−0.50%)	4921.3 (−0.38%)	4940.0	4939.4 (−0.6)	4943.4 (+3.4)
trans-1,3-butadiene							
A_e	42069.0 (−0.10%)	42190.6 (+0.19%)	42239.2 (+0.30%)	42123.9 (+0.03%)	42111.2	42127.1 (+16.0)	
B_e	4441.7 (−0.46%)	4445.0 (−0.38%)	4451.8 (−0.23%)	4459.7 (−0.05%)	4462.1	4460.6 (−1.4)	
C_e	4017.5 (−0.42%)	4021.3 (−0.33%)	4027.3 (−0.18%)	4032.7 (−0.05%)	4034.6	4034.3 (−0.3)	
trans-glyoxal							
A_e	55888.5 (−0.51%)	56092.7 (−0.15%)	56183.9 (+0.01%)	55973.2 (−0.36%)	56177.3	55955.7 (−221.6)	56007.1 (−170.2)
B_e	4781.5 (−0.80%)	4792.6 (−0.57%)	4802.1 (−0.37%)	4811.6 (−0.17%)	4819.9	4821.0 (+1.1)	4819.9 (0.0)
C_e	4404.7 (−0.68%)	4415.4 (−0.53%)	4423.9 (−0.34%)	4430.7 (−0.19%)	4439.1	4439.0 (−0.1)	4439.0 (−0.1)
Z-propargylimine							
A_e	54707.3 (−0.57%)	54894.9 (−0.23%)	54904.5 (−0.21%)	54690.0 (−0.61%)	55022.9	55040.7 (+17.8)	
B_e	4850.0 (−0.68%)	4858.9 (−0.50%)	4867.2 (−0.33%)	4873.9 (−0.19%)	4883.4	4883.2 (−0.2)	
C_e	4455.1 (−0.68%)	4463.8 (−0.48%)	4470.8 (−0.33%)	4475.1 (−0.23%)	4485.5	4484.2 (−1.3)	

[a]The relative differences with respect to SE(r_e^{SE}) are reported within parentheses. [b]Correction of −0.2° on the linkage angle. Referring to Figure 1b, the minus sign denotes a lowering of the linkage angle. [c]SE(B_e^{SE}) using vibrational corrections at the B3 level. The difference SE(B_e^{SE}) − SE(r_e^{SE}) is reported within parentheses. [d]SE(B_e^{SE}) using vibrational corrections at the fc-CCSD(T)/cc-pVTZ level [from ref 31 for VAC and VC, from ref 56 for ACR (*trans* and *cis*), and from ref 70 for *t*-GL]. The difference SE(B_e^{SE}) − SE(r_e^{SE}) is reported within parentheses.

together with the r_e^{SE} of *t*-BD. Those of VC and VAC were evaluated in ref 31 and that of *Z*-PGIM has been purposely determined in this work using the data from refs 54 and 71. For *Z*-PGIM, the availability, in addition to the rotational constants of the parent isotopologues, of the data for the three ^{13}C isotopic species and two deuterated variants (at the −NH and −CCH sites) has enabled a reliable, even if partial, determination of the SE equilibrium structure.

Figure 3 shows the molecular structures of the seven test cases, also providing the comparison between the TM-SE_LR and SE equilibrium geometries. These are also collected in Table S2 of the Supporting Information together with the uncertainties affecting the r_e^{SE} structures and the revDSD structural parameters. The fragments employed in the TM-SE are evident: ethylene and acetylene for VAC, ethylene and hydrogen cyanide for VC, ethylene and formaldehyde for *t*-ACR and *c*-ACR, ethylene for *t*-BD, formaldehyde for *t*-GL, and methanimine and acetylene for *Z*-PGIM. Their revDSD and SE structural parameters are collected in Table S1 of the Supporting Information. From Figure 3, a very good agreement between the TM-SE(_LR) and r_e^{SE} geometries is apparent. It is noted that the deviations are in the order of 0.001 Å for bond lengths and 0.1° for angles. There are only a very few exceptions showing discrepancies larger than 0.001 Å (but always within 2 mÅ), and these can be ascribed to conjugative effects. While the revDSD level already provides good results (deviations in the order of +0.003 Å for bond lengths and |0.2|° for angles; see Table S2 of the Supporting Information), the improvement provided by the TM-SE approach is apparent. The only somewhat uncertain comparison concerns *Z*-PGIM, for which the experimental data are not sufficient for a complete structural determination. At this point, it is interesting to check how the small discrepancies observed in the structural parameters reflect on the rotational constants, the results being reported in Table 2. Indeed, rotational constants are extremely sensitive to the molecular structure. In fact, variations of 0.001 Å in the bond distances and 0.1° in valence angles can lead to changes up to ±50 MHz for the *A* constant and ±15 MHz for *B* and *C*. This issue is very important because the first application we have in mind is the prediction of the rotational spectra of "unknown" molecules with a very good accuracy at a limited computational cost.

In Table 2, the equilibrium rotational constants straightforwardly derived from the r_e^{SE} structures are denoted as SE(r_e^{SE}). For comparison purposes, those derived from the experimental ground-state rotational constants corrected for the vibrational contributions at the B3 level are also reported, these being denoted as SE(B_e^{SE})-B3. For VAC, VC, *t*-ACR, *c*-ACR, and *t*-GL, the SE(B_e^{SE}) values obtained using vibrational corrections at the fc-CCSD(T)/cc-pVTZ[44] level available in the literature[30,31] are also given (SE(B_e^{SE})-CC). CCSD(T)[72] denotes the coupled-cluster single and double approximation augmented by a perturbative treatment of triples, and fc stands

https://doi.org/10.1021/acs.jpca.1c07828
J. Phys. Chem. A 2021, 125, 9904−9916

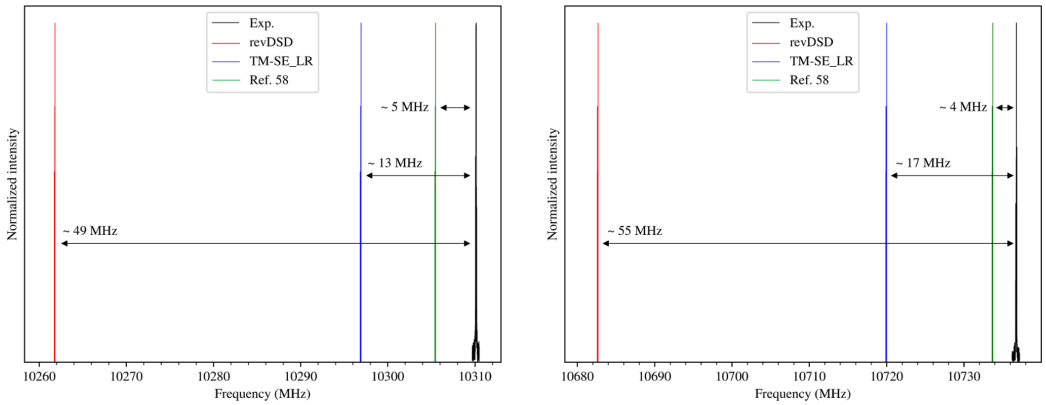

Figure 4. Comparison between the experimental spectrum (Exp.) and different simulations (revDSD, TM-SE_LR, and "cheap" scheme from ref 58) for both isomers of PMI. The $4_{1,4} \leftarrow 3_{1,3}$ transition of *E*-PMI (left panel) and the $4_{0,4} \leftarrow 3_{0,3}$ transition of *Z*-PMI (right panel) have been chosen as examples ($J_{K_a,K_c} \leftarrow J'_{K'_a,K'_c}$).

for the frozen-core approximation. The comparison between these two sets of SE B_e constants is crucial because for the other molecules of the dataset, the performance of the TM-SE(_LR) approach will be based on the latter type of SE B_e values. In principle, the two routes should lead to equivalent results. However, we note that vibrational corrections at the CCSD(T) level tend to provide a better agreement, with the average discrepancy being, in relative terms, ∼0.04%. When B3 vibrational corrections are considered, the differences are a bit larger, but the mean deviation is still as low as 0.06%. We note a few large discrepancies from the SE(r_e^{SE}) values, all for the *A* constant. When considering the B3 vibrational corrections, the largest deviations are 0.37% for VAC and 0.40% for *t*-GL. In the case of CCSD(T) vibrational corrections, the only outlier is observed for *t*-GL, the deviation being 0.30%. If we exclude these data, the relative averaged discrepancies from SE(r_e^{SE}) reduce to 0.02% for CCSD(T) and 0.03% for B3. This comparison provides a quantification of the systematic error affecting our analysis. Conservatively, we consider that the SE equilibrium rotational constants employed in the analysis of the dataset (i.e., those obtained with B3 vibrational corrections) are affected by a systematic uncertainty well within 0.1%. At this point, the accuracy of the SE equilibrium structure deserves a note. While the limited accuracy of the B3 vibrational corrections affects, even if marginally, the derived SE equilibrium rotational constants, the effects are entirely negligible on the structural determination, as demonstrated well by the literature on this topic; for example, see refs 27 and 30.

Before discussing the results of Table 2, it should be pointed out that the accuracy reached by the TM-SE and TM-SE_LR models can only be approached by applying expensive accurate composite schemes based on coupled-cluster theory.[2,5,73,74] An example is provided by the experimental investigation on the rotational spectrum of propargylimine, which also led to its detection in the interstellar medium.[54] In that work, the spectroscopic study was supported by quantum-chemical calculations, with equilibrium rotational constants obtained by means of the so-called "CCSD(T)/CBS + CV" composite scheme,[19,20] whose accuracy has been tested in refs 2 and 73. This composite scheme exploits the CCSD(T) method extrapolated to the complete basis set (CBS) limit (within the fc approximation) and incorporates the core-valence (CV) correlation correction. The CCSD(T)/CBS + CV B_e constants are 54525.7, 4876.6, and 4476.3 MHz, which deviate from the SE counterparts by 0.90, 0.14, and 0.21%, respectively, to be compared with those issuing from the TM-SE_LR model, which differ instead by 0.21, 0.33, and 0.33% (see Table 2). Another example is provided by ACR, which points out how accurate the CCSD(T)/CBS + CV composite scheme can be. In ref 56, this approach was employed in the geometry optimization of *t*- and *c*-ACR. The corresponding equilibrium rotational constants (22915.2, 6301.4, and 4942.3 MHz for *c*-ACR and 47870.0, 4689.3, and 4270.9 MHz for *t*-ACR) were found to deviate, on average, by only 0.04% from the SE(r_e^{SE}) values.

From the comparisons of Table 2, we note that—for all test cases—the deviations are small at all the levels considered, with an overall improvement when moving from revDSD to TM-SE. A further improvement is noted by resorting to the TM-SE_LR approach. In more detail, the absolute mean deviations from the SE(r_e^{SE}) values are 0.5% at the revDSD level, 0.4% for TM-SE, and 0.3% for TM-SE_LR. In several cases, as already noted in the comparison between SE(r_e^{SE}) and SE(B_e^{SE}) and well-known in the literature (see, e.g., ref 74), the agreement for the *A* constant is the most critical among the three rotational constants. Indeed, it worsens when moving from the revDSD level to the TM-SE approach, with the LR corrections being unable to improve this discrepancy. An inspection of the revDSD, SE, and TM-SE structures revealed that this is caused by very small structural modifications, and in detail, it seems to be due to missing LR corrections for linkage angles (see Figure 1b for the definition). Actually, the LR terms are available for angles, but the inter-fragment angles tend to behave differently. They somewhat resemble the inter-molecular angles in non-covalent complexes. While this might be a sort of limitation in predicting the rotational constants and the corresponding spectrum of an "unknown" molecule with high accuracy, once the latter is assigned and analyzed, the experimental rotational constants of just one isotopic species are sufficient to effectively correct the linkage parameters and lead to an equilibrium structure of great accuracy. For example,

https://doi.org/10.1021/acs.jpca.1c07828
J. Phys. Chem. A 2021, 125, 9904−9916

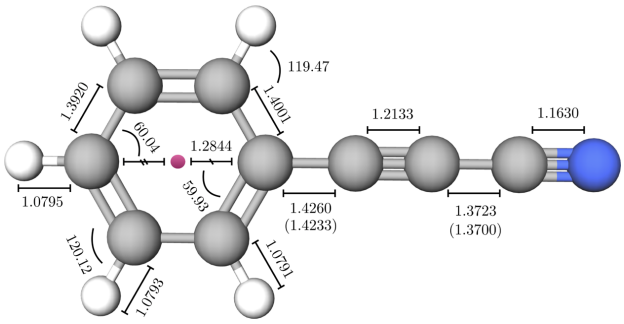

Figure 5. Structural parameters of 3-phenyl-2-propynenitrile obtained with the TM-SE and TM-SR_LR approaches. The two values in parentheses refer to LR-corrected C−C bond distances. All bond lengths are in Å, and angles are in degrees.

if we consider *Z*-CMI and refine the revDSD linkage parameters (the C−C distance and the corresponding angle) using the experimental rotational constants of the main isotopic species (the only ones investigated so far), the discrepancies with respect to the SE B_e^{SE} values reduce to −0.02, 0.001, and 0.002% for *A*, *B*, and *C*, respectively, with these being −0.21, −0.49, and −0.47%, respectively, at the TM-SE level (see Table S3). Even if we only fit the C−C linkage bond, the resulting discrepancies are extremely good: −0.15, 0.006, and 0.004%, respectively.

For the seven molecules under consideration, tests have been carried out in order to understand if a systematic corrective term can be applied to the linkage angle (see Figure 1b). The outcome of these tests (see the fourth column of Table 2) suggests that indeed, a lowering of 0.2° improves the agreement of the TM-SE_LR rotational constants with respect to the SE ones, with the only exception of the A rotational constant of *t*-GL and *Z*-PGIM. Such an improvement leads to a reduction in the absolute mean deviation to 0.2%. Interestingly, for *Z*-PGIM, an additional correction (−0.002 Å) to the C−C LR corrective term leads to an improvement for all rotational constants: 54911.6 MHz (−0.20%), 4873.3 MHz (−0.21%), and 4476.1 MHz (−0.21%). These results seem to suggest that the LR correction is not entirely able to recover conjugative effects due to double and triple bonds connected to the C−C single linkage. Such a limitation is also expected for *c*-ACR, for which the deviations on *B* and *C* are rather significant for all levels of theory, for example, from −1.12% for B at the revDSD level to −0.78% for TM-SE_LR. While the additional corrective term works well for all imines, we anticipate that the "−0.2° correction" extended to the entire dataset works fine only for the molecules containing the vinyl frame (see Table S3).

As mentioned in the Methodology section, the TM-SE and TM-SE_LR approaches have been extended to the dataset introduced above. The results are collected in Table S3 of the Supporting Information, where the revDSD, TM-SE, and TM-SE_LR equilibrium rotational constants are compared with the SE(B_e^{SE}) constants obtained from the experimental ground-state rotational constants (B_0^{exp}) and the B3 vibrational corrections. The B_0^{exp} constants and the corresponding ΔB_{vib}^{B3} corrections are reported in Table S3, which also collects the TM-SE_LR + corr results, evaluated as explained and addressed above.

From the inspection of Table S3, results in line with those of Table 2 are noted. In almost all cases, the revDSD level provides relative deviations with respect to the B_e^{SE} values within 1%. The use of the TM-SE approach improves the agreement in almost all cases, with an average relative deviation of 0.3%. A further improvement is noted once the LR corrections are considered (TM-SE_LR approach), the average relative deviation reducing to 0.2%. Based on the accuracy of the SE equilibrium rotational constants discussed above, the relative error of the TM-SE_LR rotational constants can be—on average—as low as 0.1%. Such a good agreement on the SE B_e constants implies that the TM-SE_LR structures are highly accurate, which means average deviations smaller than 0.001 Å for bond lengths and 0.1° for angles. Finally, we note that the more rigid the molecule is, the better the TM-SE approach works, as demonstrated—for example—by phenylmethanimine and benzonitrile.

Rotational Spectrum of Phenylmethanimine. As mentioned above, the TM-SE approach is particularly accurate for rigid molecular systems. To demonstrate this outcome, we applied it to the simulation of the rotational spectrum of *E*- and *Z*-PMI. For this purpose, the ground-state rotational constants have been predicted by adding the B3 vibrational corrections to the revDSD and TM-SE_LR equilibrium values (according to eq 1). To complete the set of the required spectroscopic parameters, namely, the quartic centrifugal-distortion and nitrogen quadrupole-coupling constants, we refer to the computational results reported in ref 58.

The comparison is shown in Figure 4 by means of two selected rotational transitions, one for *E*-PGIM and one for *Z*-PGIM. It is apparent that the TM-SE_LR approach leads to a significant improvement with respect to the starting revDSD level; indeed, the error associated to the transition frequency decreases by about three times. For the sake of completeness, the prediction based on the "cheap" composite scheme (from ref 58: "best theo" column of Table 1) has also been considered. It is noted that the latter (green stick spectra in Figure 4) is the most accurate; however, such a good agreement comes at the price of a much greater computational cost. In fact, the "cheap" composite scheme[22] is based on the CCSD(T) method. Furthermore, for the specific case of PGIM, the latter approach showed an extraordinarily good agreement. Therefore, this example confirms that the TM-SE_LR approach is able to provide a remarkable accuracy in rotational spectral predictions, without increasing the compu-

https://doi.org/10.1021/acs.jpca.1c07828
J. Phys. Chem. A 2021, 125, 9904−9916

Table 3. Comparison between Computed Equilibrium Rotational Constants (in MHz) and the SE Counterparts for 3-Phenyl-2-propynenitrile[a]

	B_e				
	revDSD	TM-SE	TM-SE_LR	SE[b]	B_0^{exp} [ΔB_{vib}^{B3}]
A	5681.4 (−0.35%)	5703.0 (+0.01%)	5702.0 (+0.01%)	5701.4	5659.722(15) [41.6]
B	568.5 (−0.41%)	569.9 (−0.16%)	570.7 (−0.02%)	570.8	569.582206(39) [1.2]
C	516.8 (−0.41%)	518.1 (−0.15%)	518.8 (−0.01%)	518.9	517.404488(37) [1.5]

[a]The relative differences with respect to SE(B_e^{SE}) are reported in parentheses. [b]Ground-state rotational constants from ref 75 corrected for vibrational corrections at the B3 level.

Table 4. Prediction of Rotational Constants (in MHz) of *o*-, *m*-, and *p*-cyanoethynylbenzene

	B_e (revDSD)	B_e (TM-SE)	B_e (TM-SE_LR)	ΔB_{vib}	B_0 (TM-SE_LR)[a]
o-CEB					
A	2025.1	2031.0	2033.00	4.66	2028.34
B	1330.2	1334.0	1335.48	6.11	1329.37
C	802.9	805.1	806.01	3.23	802.78
m-CEB					
A	2707.1	2715.4	2717.55	10.44	2707.11
B	906.6	909.0	910.16	3.47	906.69
C	679.1	681.0	681.81	2.80	679.01
p-CEB					
A	5673.0	5693.2	5693.19	45.85	5647.34
B	708.5	710.3	711.29	2.19	709.10
C	629.9	631.5	632.29	2.31	629.98

[a]B_e(TM-SE_LR) constants augmented by B3 vibrational corrections.

tational effort with respect to revDSD. It is thus more than suitable for guiding and supporting experimental studies.

Structure of 3-Phenyl-2-propynenitrile and Its Isomers. During the preparation of this manuscript, we became aware of the spectroscopic characterization of 3-phenyl-2-propynenitrile (PPN).[75] Since—as noted above—the TM-SE approach works extremely well for rather rigid molecules, we decided to apply it to the structural determination of PPN and its isomers, thus providing an example of extension of the TM-SE approach to a larger system. For PPN, the resulting structure is shown in Figure 5, with the corresponding rotational constants being collected in Table 3. To build the PPN molecule, three fragments have been actually employed in the TM-SE approach: the phenyl moiety from benzene, the −C≡C− group from acetylene, and the −CN frame from HCN. Within the TM-SE_LR approach, the LR correction has been applied to the two C−C linkage bonds. All details can be found in Table S4 of the Supporting Information.

From the inspection of Table 3, it is evident that—as expected—the TM-SE approach is able to predict accurate equilibrium rotational constants, which in turn means an accurate equilibrium structure. In particular, the results for the TM-SE_LR model are really impressive. Indeed, we note that going from revDSD to TM-SE leads to a reduction in the average relative error from 0.4 to 0.1%. Then, incorporation of the LR corrections further decreases the average relative deviation to 0.01%. In view of such a good performance, the TM-SE approach can be used to predict with great accuracy the rotational constants of different isomers of PPN: *o*-, *m*-, and *p*-cyanoethynylbenzene (CEB; see Table 4). Based on the analysis carried out in this manuscript and—in particular—for PPN, we expect that the equilibrium rotational constants issued from the TM-SE_LR approach have a relative accuracy well within 0.05%. Using the ground-state rotational constants of Table 4, the rotational spectra of *o*-, *m*-, and *p*-CEB have been simulated and are shown in Figure 6. For all the three molecules, the *a*-type transitions are the most intense and reach the maximum intensity in the millimeter-wave region, between 170 and 220 GHz. In this frequency region, the accuracy of the predicted rotational transitions is expected to range between 200 and 400 MHz, also accounting for the uncertainties affecting the computed centrifugal distortion constants (which are required for spectral predictions).

CONCLUSIONS

A benchmark study based on the availability of accurate semi-experimental equilibrium rotational constants for 21 molecular species allowed us to demonstrate the reliability, robustness, and accuracy of a "Lego brick" approach, the so-called TM-SE approach. For the selected molecules, each species has been seen as formed by two fragments, the "Lego bricks", for which accurate semi-experimental structures are available. Accounting, at the rev-DSD-PBEP86-D3/jun-cc-pVTZ level, for the modifications taking place when moving from the isolated fragments to the molecular species of interest leads to the definition of the TM-SE equilibrium structure. A further improvement has been obtained by correcting the inter-fragment parameters with the linear regression corrective terms available for rev-DSD-PBEP86-D3/jun-cc-pVTZ. The resulting structure has been denoted as TM-SE_LR. For the TM-SE and TM-SE_LR equilibrium rotational constants, the average relative deviation with respect to accurate semi-experimental equilibrium rotational constants has been found to be ∼0.3 and ∼0.2%, respectively. According to the thorough investigation of the equilibrium geometries of 7 from the 21 molecules, these discrepancies reflect structural differences of about 0.001 Å for bond lengths and 0.1° for angles.

In conclusion, since the only quantum-chemical calculations required by the TM-SE and TM-SE_LR models are geometry optimizations at the rev-DSD-PBEP86-D3/jun-cc-pVTZ level,

https://doi.org/10.1021/acs.jpca.1c07828
J. Phys. Chem. A 2021, 125, 9904−9916

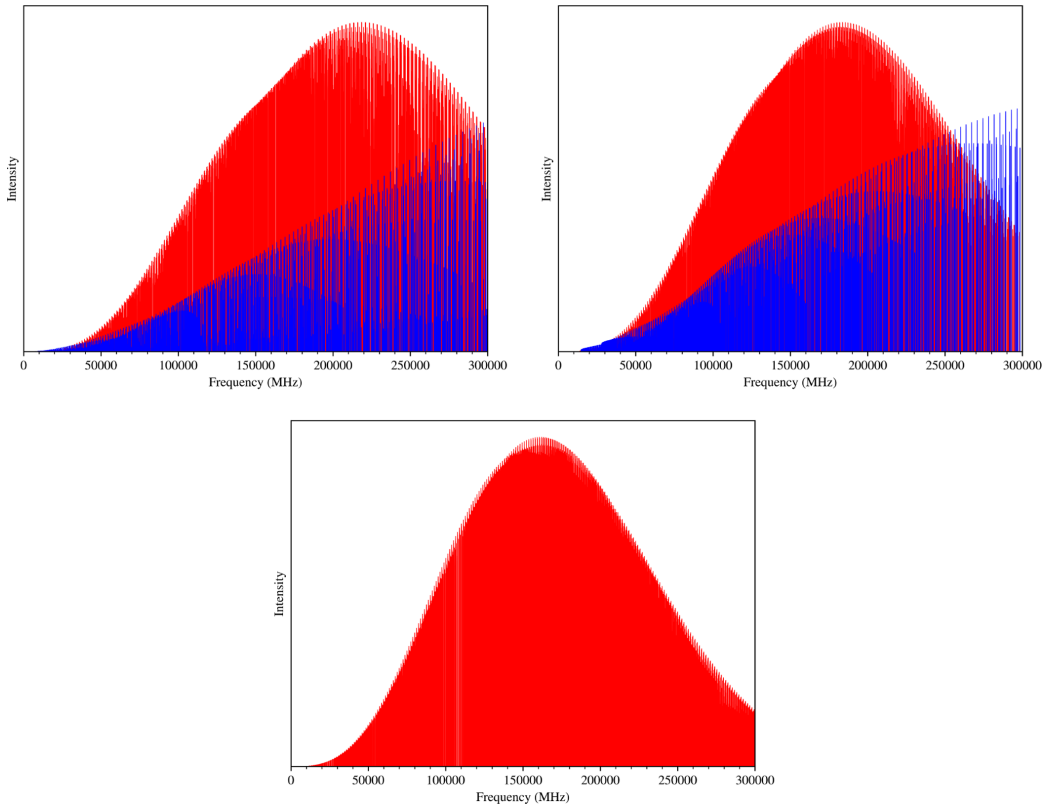

Figure 6. Simulation of the rotational spectrum of *o*- (top-left panel), *m*- (top-right panel), and *p*-CEB (bottom panel). The red and blue sticks represent the *a*- and *b*-type transitions, respectively.

they are low-cost approaches able to provide an accuracy close to that of the most sophisticated composite approaches based on the coupled-cluster ansatz. Therefore, they are very promising tools for the accurate structural characterizations of medium- to large-sized molecular systems, such as the building blocks of biological molecules. Interestingly, test computations on a reduced dataset showed that the application of the TM-SE approach to B3-optimized geometries nearly doubles the relative deviations from the semi-experimental equilibrium rotational constants, thus implying a limited worsening in the structural parameters with respect to the models discussed above.

Finally, the TM-SE(_LR) approach is also suited well for unstable species of medium to large dimensions, which are of current interest in many different fields, ranging from astrochemistry to biochemistry, and whose structures can be hardly determined by experiments. Furthermore, our test on 3-phenyl-2-propynenitrile points out that the TM-SE(_LR) approach can be reliably extended to more than two "Lego bricks", while the availability of LR corrections for bond lengths other than the C−C bond ones opens to its application to a wider range of molecular species.

■ ASSOCIATED CONTENT

Supporting Information

The Supporting Information is available free of charge at

https://pubs.acs.org/doi/10.1021/acs.jpca.1c07828.

Table S1. Template molecules: revDSD and semi-experimental equilibrium structures. Table S2: comparison between the semi-experimental and computed (revDSD, TM-SE, and TM-SE_LR) values of the structural parameters of vinylacetylene, vinyl cyanide, (*cis*, *trans*)-acrolein, *trans*-1,3-butadiene, *trans*-glyoxal, and *Z*-propargylimine. Table S3: computed equilibrium rotational constants and the SE counterparts together with the ground-state rotational constants and the corresponding vibrational corrections for the molecules of the dataset. Table S4: computed and template values of the structural parameters of 3-phenyl-2-propynenitrile and its isomers (*o*-, *m*-, and *p*-cyanoethynylbenzene) (PDF)

https://doi.org/10.1021/acs.jpca.1c07828
J. Phys. Chem. A 2021, 125, 9904−9916

AUTHOR INFORMATION

Corresponding Authors

Vincenzo Barone − *Scuola Normale Superiore, 56126 Pisa, Italy;* orcid.org/0000-0001-6420-4107; Email: vincenzo.barone@sns.it

Cristina Puzzarini − *Dipartimento di Chimica "Giacomo Ciamician", Università di Bologna, 40126 Bologna, Italy;* orcid.org/0000-0002-2395-8532; Email: cristina.puzzarini@unibo.it

Authors

Alessio Melli − *Scuola Normale Superiore, 56126 Pisa, Italy; Dipartimento di Chimica "Giacomo Ciamician", Università di Bologna, 40126 Bologna, Italy;* orcid.org/0000-0002-8469-1624

Francesca Tonolo − *Scuola Normale Superiore, 56126 Pisa, Italy; Dipartimento di Chimica "Giacomo Ciamician", Università di Bologna, 40126 Bologna, Italy*

Complete contact information is available at: https://pubs.acs.org/10.1021/acs.jpca.1c07828

Author Contributions

[§]A.M. and F.T. contributed equally to this paper.

Notes

The authors declare no competing financial interest.

ACKNOWLEDGMENTS

This work has been supported by the MIUR (grant number 2017A4XRCA) and by the University of Bologna (RFO funds). The SMART@SNS Laboratory (http://smart.sns.it) is acknowledged for providing high-performance computing facilities.

ADDITIONAL NOTE

[a]Note that for a given isotopic species, the number of rotational constants depends on the rotational symmetry. At most, there are three of them in the case of asymmetric rotors.

REFERENCES

(1) Domenicano, A.; Hargittai, I.. *Accurate Molecular Structures: Their Determination and Importance*; Oxford University Press, 1992; Vol. *1*.

(2) Puzzarini, C.; Heckert, M.; Gauss, J. The accuracy of rotational constants predicted by high-level quantum-chemical calculations. I. Molecules containing first-row atoms. *J. Chem. Phys.* **2008**, *128*, 194108.

(3) Caminati, W.; Grabow, J.-U. Microwave Spectroscopy. In *Frontiers of Molecular Spectroscopy*; Laane, J., Ed.; Elsevier: Amsterdam, 2009; Chapter 15, pp 455−552.

(4) Puzzarini, C. Rotational spectroscopy meets theory. *Phys. Chem. Chem. Phys.* **2013**, *15*, 6595−6607.

(5) Puzzarini, C. Accurate molecular structures of small- and medium-sized molecules. *Int. J. Quantum Chem.* **2016**, *116*, 1513−1519.

(6) Demaison, J.; Boggs, J. E.; Császár, A. G.. *Equilibrium Molecular Structures: From Spectroscopy to Quantum Chemistry*; CRC Press, 2016.

(7) Puzzarini, C.; Barone, V. Diving for accurate structures in the ocean of molecular systems with the help of spectroscopy and quantum chemistry. *Acc. Chem. Res.* **2018**, *51*, 548−556.

(8) Pate, B. H.; Evangelisti, L.; Caminati, W.; Xu, Y.; Thomas, J.; Patterson, D.; Perez, C.; Schnell, M. Quantitative Chiral Analysis by Molecular Rotational Spectroscopy. In *Chiral Analysis*, 2nd ed.; Polavarapu, P. L., Ed.; Elsevier, 2018; Chapter 17, pp 679−729.

(9) Graziano, G. Fingerprints of molecular reactivity. *Nat. Rev. Chem.* **2020**, *4*, 227.

(10) Arnaut, L. Relationships between structure and reactivity. In *Chemical Kinetics*, 2nd ed.; Arnaut, L., Ed.; Elsevier, 2021; Chapter 7, pp 225−245.

(11) Gordy, W.; Cook, R. L. *Microwave Molecular Spectra*; Wiley, 1984.

(12) Jensen, P.; Bunker, P. R. *Computational Molecular Spectroscopy*; John Wiley & Sons: U.K., 2000.

(13) *Computational Strategies for Spectroscopy: from Small Molecules to Nano Systems*; Barone, V., Ed.; John Wiley & Sons, Inc., 2011.

(14) Puzzarini, C.; Stanton, J. F.; Gauss, J. Quantum-chemical calculation of spectroscopic parameters for rotational spectroscopy. *Int. Rev. Phys. Chem.* **2010**, *29*, 273−367.

(15) Puzzarini, C.; Barone, V. Toward spectroscopic accuracy for organic free radicals: Molecular structure, vibrational spectrum, and magnetic properties of F2NO. *J. Chem. Phys.* **2008**, *129*, 084306.

(16) Heim, Z. N.; Amberger, B. K.; Esselman, B. J.; Stanton, J. F.; Woods, R. C.; McMahon, R. J. Molecular structure determination: Equilibrium structure of pyrimidine (m-C4H4N2) from rotational spectroscopy (reSE) and high-level ab initio calculation (re) agree within the uncertainty of experimental measurement. *J. Chem. Phys.* **2020**, *152*, 104303.

(17) Martin, J. M. L.; Taylor, P. R. The geometry, vibrational frequencies, and total atomization energy of ethylene. A calibration study. *Chem. Phys. Lett.* **1996**, *248*, 336−344.

(18) Schuurman, M. S.; Allen, W. D.; von Ragué Schleyer, P.; Schaefer, H. F., III The highly anharmonic BH5 potential energy surface characterized in the ab initio limit. *J. Chem. Phys.* **2005**, *122*, 104302.

(19) Heckert, M.; KÁllay, M.; Gauss, J. Molecular Equilibrium Geometries Based on Coupled-Cluster Calculations Including Quadruple Excitations. *Mol. Phys.* **2005**, *103*, 2109.

(20) Heckert, M.; Kállay, M.; Tew, D. P.; Klopper, W.; Gauss, J. Basis-Set Extrapolation Techniques for the Accurate Calculation of Molecular Equilibrium Geometries Using Coupled-Cluster Theory. *J. Chem. Phys.* **2006**, *125*, 044108.

(21) Puzzarini, C. Extrapolation to the complete basis set limit of structural parameters: Comparison of different approaches. *J. Phys. Chem. A* **2009**, *113*, 14530−14535.

(22) Puzzarini, C.; Barone, V. Extending the molecular size in accurate quantum-chemical calculations: The equilibrium structure and spectroscopic properties of uracil. *Phys. Chem. Chem. Phys.* **2011**, *13*, 7189−7197.

(23) Puzzarini, C.; Bloino, J.; Tasinato, N.; Barone, V. Accuracy and interpretability: The devil and the holy grail. New routes across old boundaries in computational spectroscopy. *Chem. Rev.* **2019**, *119*, 8131−8191.

(24) Cao, Y.; Romero, J.; Olson, J. P.; Degroote, M.; Johnson, P. D.; Kieferová, M.; Kivlichan, I. D.; Menke, T.; Peropadre, B.; Sawaya, N. P. D.; et al. Quantum Chemistry in the Age of Quantum Computing. *Chem. Rev.* **2019**, *119*, 10856−10915.

(25) Barone, V.; Puzzarini, C.; Mancini, G. Integration of theory, simulation, artificial intelligence and virtual reality: a four-pillar approach for reconciling accuracy and interpretability in computational spectroscopy. *Phys. Chem. Chem. Phys.* **2021**, *23*, 17079−17096.

(26) Alessandrini, S.; Barone, V.; Puzzarini, C. Extension of the "cheap" composite approach to noncovalent interactions: The jun-ChS scheme. *J. Chem. Theory Comput.* **2019**, *16*, 988−1006.

(27) Pawłowski, F.; Jørgensen, P.; Olsen, J.; Hegelund, F.; Helgaker, T.; Gauss, J.; Bak, K. L.; Stanton, J. F. Molecular equilibrium structures from experimental rotational constants and calculated vibration−rotation interaction constants. *J. Chem. Phys.* **2002**, *116*, 6482−6496.

(28) Liévin, J.; Demaison, J.; Herman, M.; Fayt, A.; Puzzarini, C. Comparison of the experimental, semi-experimental and ab initio equilibrium structures of acetylene: Influence of relativisitic effects and of the diagonal Born-Oppenheimer corrections. *J. Chem. Phys.* **2011**, *134*, 064119.

https://doi.org/10.1021/acs.jpca.1c07828
J. Phys. Chem. A 2021, 125, 9904−9916

(29) Penocchio, E.; Piccardo, M.; Barone, V. Semiexperimental equilibrium structures for building blocks of organic and biological molecules: The B2PLYP route. *J. Chem. Theory Comput.* **2015**, *11*, 4689−4707.
(30) Piccardo, M.; Penocchio, E.; Puzzarini, C.; Biczysko, M.; Barone, V. Semi-experimental equilibrium structure determinations by employing B3LYP/SNSD anharmonic force fields: Validation and application to semirigid organic molecules. *J. Phys. Chem. A* **2015**, *119*, 2058−2082.
(31) Thorwirth, S.; Harding, M. E.; Dudek, J. B.; McCarthy, M. C. Equilibrium molecular structures of vinyl carbon chains: Vinyl acetylene, vinyl diacetylene, and vinyl cyanide. *J. Mol. Spectrosc.* **2018**, *350*, 10−17.
(32) Orr, V. L.; Ichikawa, Y.; Patel, A. R.; Kougias, S. M.; Kobayashi, K.; Stanton, J. F.; Esselman, B. J.; Woods, R. C.; McMahon, R. J. Precise equilibrium structure determination of thiophene (c-C4H4S) by rotational spectroscopy-Structure of a five-membered heterocycle containing a third-row atom. *J. Chem. Phys.* **2021**, *154*, 244310.
(33) Pulay, P.; Meyer, W.; Boggs, J. E. Cubic force constants and equilibrium geometry of methane from Hartree-Fock and correlated wavefunctions. *J. Chem. Phys.* **1978**, *68*, 5077−5085.
(34) Penocchio, E.; Mendolicchio, M.; Tasinato, N.; Barone, V. Structural features of the carbon-sulfur chemical bond: a semi-experimental perspective. *Can. J. Chem.* **2016**, *94*, 1065−1076.
(35) Vereecken, L.; Groof, P. D.; Peeters, J. Temperature and pressure dependent product distribution of the addition of CN radicals to C2H4. *Phys. Chem. Chem. Phys.* **2003**, *5*, 5070−5076.
(36) Tonolo, F.; Lupi, J.; Puzzarini, C.; Barone, V. The Quest for a Plausible Formation Route of Formyl Cyanide in the Interstellar Medium: a State-of-the-art Quantum-chemical and Kinetic Approach. *Astrophys. J.* **2020**, *900*, 85.
(37) Dash, M. R.; Rajakumar, B. Abstraction and addition kinetics of C2H radicals with CH4, C2H6, C3H8, C2H4, and C3H6: CVT/SCT/ISPE and hybrid meta-DFT methods. *Phys. Chem. Chem. Phys.* **2015**, *17*, 3142−3156.
(38) Lupi, J.; Puzzarini, C.; Barone, V. Methanimine as a Key Precursor of Imines in the Interstellar Medium: The Case of Propargylimine. *Astrophys. J. Lett.* **2020**, *903*, L35.
(39) Vazart, F.; Calderini, D.; Puzzarini, C.; Skouteris, D.; Barone, V. State-of-the-Art Thermochemical and Kinetic Computations for Astrochemical Complex Organic Molecules: Formamide Formation in Cold Interstellar Clouds as a Case Study. *J. Chem. Theory Comput.* **2016**, *12*, 5385−5397.
(40) Melosso, M.; Melli, A.; Puzzarini, C.; Codella, C.; Spada, L.; Dore, L.; Degli Esposti, C.; Lefloch, B.; Bachiller, R.; Ceccarelli, C.; et al. Laboratory measurements and astronomical search for cyanomethanimine. *Astron. Astrophys.* **2018**, *609*, A121.
(41) Alessandrini, S.; Tonolo, F.; Puzzarini, C. In search of phosphorus in astronomical environments: The reaction between the CP radical (X2Σ+) and methanimine. *J. Chem. Phys.* **2021**, *154*, 054306.
(42) Barone, V.; Ceselin, G.; Fusè, M.; Tasinato, N. Accuracy meets interpretability for computational spectroscopy by means of hybrid and double-hybrid functionals. *Front. Chem.* **2020**, *8*, 584203.
(43) Santra, G.; Sylvetsky, N.; Martin, J. M. L. Minimally empirical double-hybrid functionals trained against the GMTKN55 database: revDSD-PBEP86-D4, revDOD-PBE-D4, and DOD-SCAN-D4. *J. Phys. Chem. A* **2019**, *123*, 5129−5143.
(44) Dunning, T. H. Gaussian basis sets for use in correlated molecular calculations. I. The atoms boron through neon and hydrogen. *J. Chem. Phys.* **1989**, *90*, 1007−1023.
(45) Papajak, E.; Truhlar, D. G. Convergent Partially Augmented Basis Sets for Post-Hartree−Fock Calculations of Molecular Properties and Reaction Barrier Heights. *J. Chem. Theory Comput.* **2011**, *7*, 10−18.
(46) Mills, I. M. Vibration-Rotation Structure in Asymmetric- and Symmetric-Top Molecules. In *Molecular Spectroscopy: Modern Research*; Rao, K. N., Matthews, C. W., Eds.; Academic Press, 1972; Vol. *1*, pp 115−140.
(47) Becke, A. D. Density-functional exchange-energy approximation with correct asymptotic behavior. *Phys. Rev. A: At., Mol., Opt. Phys.* **1988**, *38*, 3098.
(48) Lee, C.; Yang, W.; Parr, R. G. Development of the Colle-Salvetti correlation-energy formula into a functional of the electron density. *Phys. Rev. B: Condens. Matter Mater. Phys.* **1988**, *37*, 785.
(49) Grimme, S.; Antony, J.; Ehrlich, S.; Krieg, H. A consistent and accurate ab initio parametrization of density functional dispersion correction (DFT-D) for the 94 elements H-Pu. *J. Chem. Phys.* **2010**, *132*, 154104.
(50) Grimme, S.; Ehrlich, S.; Goerigk, L. Effect of the damping function in dispersion corrected density functional theory. *J. Comput. Chem.* **2011**, *32*, 1456−1465.
(51) Frisch, M. J.; Trucks, G. W.; Schlegel, H. B.; Scuseria, G. E.; Robb, M. A.; Cheeseman, J. R.; Scalmani, G.; Barone, V.; Petersson, G. A.; Nakatsuji, H.; et al. *Gaussian16*, Revision C.01. Gaussian Inc.: Wallingford, CT, 2019; see http://gaussian.com.
(52) Mendolicchio, M.; Penocchio, E.; Licari, D.; Tasinato, N.; Barone, V. Development and implementation of advanced fitting methods for the calculation of accurate molecular structures. *J. Chem. Theory Comput.* **2017**, *13*, 3060−3075.
(53) Puzzarini, C.; Cazzoli, G. Equilibrium structure of methylcyanide. *J. Mol. Spectrosc.* **2006**, *240*, 260−264.
(54) Bizzocchi, L.; Prudenzano, D.; Rivilla, V. M.; Pietropolli-Charmet, A.; Giuliano, B. M.; Caselli, P.; Martín-Pintado, J.; Jiménez-Serra, I.; Martín, S.; Requena-Torres, M. A.; et al. Propargylimine in the laboratory and in space: millimetre-wave spectroscopy and its first detection in the ISM. *Astron. Astrophys.* **2020**, *640*, A98.
(55) Jaman, A. I.; Bhattacharya, R. Millimeter-wave rotational spectra of trans-acrolein (propenal)(CH_2CHCOH): a DC discharge product of allyl alcohol (CH_2CHCH_2OH) vapor and DFT calculation. *J. At. Mol. Phys.* **2012**, *2012*, 363247.
(56) Puzzarini, C.; Penocchio, E.; Biczysko, M.; Barone, V. Molecular Structure and Spectroscopic Signatures of Acrolein: Theory Meets Experiment. *J. Phys. Chem. A* **2014**, *118*, 6648−6656.
(57) Blom, C. E.; Bauder, A. Microwave spectrum, rotational constants and dipole moment of s-cis acrolein. *Chem. Phys. Lett.* **1982**, *88*, 55−58.
(58) Melli, A.; Potenti, S.; Melosso, M.; Herbers, S.; Spada, L.; Gualandi, A.; Lengsfeld, K. G.; Dore, L.; Buschmann, P.; Cozzi, P. G.; et al. A Journey from Thermally Tunable Synthesis to Spectroscopy of Phenylmethanimine in Gas Phase and Solution. *Chem.—Eur. J.* **2020**, *26*, 15016−15022.
(59) Bogey, M.; Demuynck, C.; Destombes, J. L.; Vallee, Y. Millimeter-Wave Spectrum of Formyl Cyanide, HCOCN: Centrifugal Distortion and Hyperfine Structure Analysis. *J. Mol. Spectrosc.* **1995**, *172*, 344−351.
(60) Caminati, W.; Vogelsanger, B.; Bauder, A. Rotational spectrum of styrene observed by microwave Fourier transform spectroscopy. *J. Mol. Spectrosc.* **1988**, *128*, 384−398.
(61) Thorwirth, S.; Lichau, H. The millimeter-wave spectrum and the dipole moment of vinylacetylene. *Astron. Astrophys.* **2003**, *398*, L11−L13.
(62) Brown, R. D.; Godfrey, P. D.; Winkler, D. A. Hyperfine interactions in the microwave spectrum of 2-propen-1-Imine (vinylimine). *Chem. Phys.* **1981**, *59*, 243−247.
(63) Müller, H. S. P.; Belloche, A.; Menten, K. M.; Comito, C.; Schilke, P. Rotational spectroscopy of isotopic vinyl cyanide, H2CCHCN, in the laboratory and in space. *J. Mol. Spectrosc.* **2008**, *251*, 319−325.
(64) Desyatnyk, O.; Pszczółkowski, L.; Thorwirth, S.; Krygowski, T. M.; Kisiel, Z. The rotational spectra, electric dipole moments and molecular structures of anisole and benzaldehyde. *Phys. Chem. Chem. Phys.* **2005**, *7*, 1708−1715.
(65) Jabri, A.; Kolesniková, L.; Alonso, E. R.; León, I.; Mata, S.; Alonso, J. L. A laboratory rotational study of the interstellar propynal. *J. Mol. Spectrosc.* **2020**, *372*, 111333.
(66) McGuire, B. A.; Burkhardt, A. M.; Kalenskii, S.; Shingledecker, C. N.; Remijan, A. J.; Herbst, E.; McCarthy, M. C. Detection of the

https://doi.org/10.1021/acs.jpca.1c07828
J. Phys. Chem. A 2021, 125, 9904−9916

aromatic molecule benzonitrile (c -C 6 H 5 CN) in the interstellar medium. *Science* **2018**, *359*, 202−205.
(67) Craig, N. C.; Groner, P.; McKean, D. C. Equilibrium Structures for Butadiene and Ethylene: Compelling Evidence for Π-Electron Delocalization in Butadiene. *J. Phys. Chem. A* **2006**, *110*, 7461−7469.
(68) Motiyenko, R. A.; Armieieva, I. A.; Margulès, L.; Alekseev, E. A.; Guillemin, J.-C. Rotational spectroscopy of malononitrile and its corresponding monoisocyanide isomer, isocyanoacetonitrile. *Astron. Astrophys.* **2019**, *623*, A162.
(69) McGuire, B. A.; Burkhardt, A. M.; Loomis, R. A.; Shingledecker, C. N.; Kelvin Lee, K. L.; Charnley, S. B.; Cordiner, M. A.; Herbst, E.; Kalenskii, S.; Momjian, E.; et al. Early science from GOTHAM: project overview, methods, and the detection of interstellar propargyl cyanide (HCCCH2CN) in TMC-1. *Astrophys. J. Lett.* **2020**, *900*, L10.
(70) Larsen, R. W.; Pawłowski, F.; Hegelund, F.; Jørgensen, P.; Gauss, J.; Nelander, B. The equilibrium structure of trans-glyoxal from experimental rotational constants and calculated vibration-rotation interaction constants. *Phys. Chem. Chem. Phys.* **2003**, *5*, 5031−5037.
(71) McNaughton, D.; Osman, O. I.; Kroto, H. W. The microwave spectrum and structure of Z-prop-2-ynylideneamine, HC-C-CH-NH. *J. Mol. Struct.* **1988**, *190*, 195−204.
(72) Raghavachari, K.; Trucks, G. W.; Pople, J. A.; Head-Gordon, M. A fifth-order perturbation comparison of electron correlation theories. *Chem. Phys. Lett.* **1989**, *157*, 479−483.
(73) Alessandrini, S.; Gauss, J.; Puzzarini, C. Accuracy of rotational parameters predicted by high-level quantum-chemical calculations: case study of sulfur-containing molecules of astrochemical interest. *J. Chem. Theory Comput.* **2018**, *14*, 5360−5371.
(74) Gardner, M. B.; Westbrook, B. R.; Fortenberry, R. C.; Lee, T. J. Highly-accurate quartic force fields for the prediction of anharmonic rotational constants and fundamental vibrational frequencies. *Spectrochim. Acta, Part A* **2021**, *248*, 119184.
(75) Buchanan, Z.; Lee, K. L. K.; Chitarra, O.; McCarthy, M. C.; Pirali, O.; Martin-Drumel, M.-A. A rotational and vibrational investigation of phenylpropiolonitrile (C6H5C3N). *J. Mol. Spectrosc.* **2021**, *377*, 111425.

https://doi.org/10.1021/acs.jpca.1c07828
J. Phys. Chem. A 2021, 125, 9904−9916

Computational Spectroscopy

Despite the great increase in the last few years of new molecular detections in the ISM, a significant number of features in radioastronomical spectra still remains unassigned. To fill this gap, a huge laboratory effort is required, which is increasingly based on integrated experimental and computational strategies. To support the spectral assignments, computed spectra play a crucial role, especially when the species of interest is unstable and produced inside the spectrometer cell *via*, *e.g.*, electric discharge or pyrolysis (see as an example Melli et al., 2022).

In this respect, a significant example is provided by the recent characterization of (*Z*)-1,2-ethenediol. This compound is the enol form of glycolaldehyde and thus represents a key intermediate in the formose reaction. Since no rotational characterization of its spectrum was available, we decided to fill this gap, the first step being the accurate computational investigation of its rotational parameters.

A preliminary investigation of the conformational PES of (*Z*)-1,2-ethenediol was carried out by means of the double-hybrid B2PLYP (Grimme, 2006) density functional (also including the D3 correction for empirical dispersions by Grimme, Grimme et al. 2010, employing the Becke- Johnson damping function, Grimme et al. 2011) in conjunction with the aug-cc-pVTZ basis set (Kendall et al., 1992). For the energetics, zero-point energy (ZPE) corrections have also been taken into account at the same level of theory within the harmonic approximation. This analysis provided an energetic characterization of the possible conformers of (*Z*)-1,2-ethenediol, among which the most stable one was identified. The latter turned out to be the only possible observable species under the experimental conditions and was hence the only one considered for accurate spectroscopic investigation. The geometry of (*Z*)-1,2-ethenediol has been optimized by means of the so-called CCSD(T)/CBS+CV "gradient" composite scheme (Heckert et al., 2005, 2006; Barone et al., 2013), with the following energy gradient being minimized:

$$\frac{dE_{\mathrm{CBS+CV}}}{dx} = \frac{dE_{\mathrm{HF}}^{\mathrm{CBS}}}{dx} + \frac{d\Delta E_{\mathrm{CCSD(T)}}^{\mathrm{CBS}}}{dx} + \frac{d\Delta E_{CV}}{dx}\,. \tag{1}$$

Here, the first term on the right-hand side is the extrapolation of the HF-SCF energy to the CBS limit using the three-point expression by Feller (Feller, 1993), in combination with the cc-pVnZ basis sets, with n =T,Q,5. The second term is the extrapolation to the CBS limit of the CCSD(T) correlation energy obtained with the 2-point n^{-3} formula by Helgaker *et al.* (Helgaker et al., 1997) and employing the cc-pVTZ and cc-pVQZ basis sets. The last term is the core-valence contribution which is obtained as the difference between frozen-core and all-electron energies computed at the CCSD(T)/cc-pCVTZ level. From CCSD(T)/CBS+CV equilibrium structure, the equilibrium rotational constants were straightforwardly derived. Then, the vi-

brational corrections to these latter, as well as the quartic and sextic centrifugal distortion constants, have been obtained from anharmonic force field calculations at the fc-MP2/cc-pVTZ level of theory. All calculations were performed by employing the CFOUR package (Stanton et al.).

Supported by the theoretical simulation relying on the computed rotational parameters, the first experimental characterization of the rotational spectrum of (*Z*)-1,2-ethenediol was then performed (Melosso et al., 2022). It is worthwhile noting that the experimental findings resulted in excellent agreement with the outcomes of high-level quantum-chemical calculations. Shortly after, thanks to the spectroscopic catalog obtained from the experimental characterization, the first detection of (*Z*)-1,2-ethenediol in the G+0.693-0.027 molecular cloud was carried out (Rivilla et al., 2022a).

ChemComm

COMMUNICATION

View Article Online
View Journal | View Issue

Cite this: *Chem. Commun.*, 2022, **58**, 2750

Received 8th December 2021,
Accepted 26th January 2022

DOI: 10.1039/d1cc06919e

rsc.li/chemcomm

Gas-phase identification of (*Z*)-1,2-ethenediol, a key prebiotic intermediate in the formose reaction†

Mattia Melosso, *[ab] Luca Bizzocchi,[ac] Houda Gazzeh,[de] Francesca Tonolo, [ac] Jean-Claude Guillemin, [d] Silvia Alessandrini, [ac] Víctor M. Rivilla,[fg] Luca Dore, [a] Vincenzo Barone [c] and Cristina Puzzarini *[a]

Prebiotic sugars are thought to be formed on primitive Earth by the formose reaction. However, their formation is not fully understood and it is plausible that key intermediates could have formed in extraterrestrial environments and subsequently delivered on early Earth by cometary bodies. 1,2-Ethenediol, the enol form of glycolaldehyde, represents a highly reactive intermediate of the formose reaction and is likely detectable in the interstellar medium. Here, we report the identification and first characterization of (*Z*)-1,2-ethenediol by means of rotational spectroscopy. The title compound has been produced in the gas phase by flash vacuum pyrolysis of bis-*exo*-5-norbornene-2,3-diol at 750 °C, through a retro-Diels–Alder reaction. The spectral analysis was guided by high-level quantum-chemical calculations, which predicted spectroscopic parameters in very good agreement with the experiment. Our study provides accurate spectral data to be used for searches of (*Z*)-1,2-ethenediol in the interstellar space.

The origin of life from simple raw materials, *i.e.* abiogenesis, is still a hot, highly debated topic involving many research fields. While a general and robust solution to this problem is still sought, it is nowadays widely accepted that abiogenesis was not a smooth process, but more likely a dynamic scenario involving a number of successive steps and occurring across different geological eras and environments.[1] Indeed, none of the main accredited theories for the origin of life, *i.e.* primordial soup, hydrothermal vents, and extraterrestrial origin of biological building blocks, is able to fully explain how bio-relevant molecules could have formed and survived in hostile conditions, although each of them provides unique pieces to complete the overall puzzle. In this context, the extraterrestrial formation (and the subsequent delivery on Earth) of the main building blocks of life, such as amino acids and sugars, is increasingly recognized as an important pathway.[2]

One of the most important routes towards the synthesis of prebiotic species starting from simple organic material is the formose reaction, which is thought to be responsible for the formation of simple carbohydrates, such as ribose, on early Earth environments.[3] The formose reaction uses formaldehyde (H_2CO, **1**) as starting material and proceeds through aldol, reverse-aldol, and isomerization reactions, eventually forming glycolaldehyde ($HOCH_2CHO$, **2**), glyceraldehyde, and a number of four, five, and six-carbon atoms sugars.[4–6] This process, firstly discovered by Butlerov in 1861,[6] leads to the formation of fundamental biological units found in RNA and cofactors (*e.g.*, ATP and NADH). However, the formose reaction exhibits some limits in aqueous solution,[1] thereby reducing its possible role for the sugar formation on early Earth conditions.

Conversely, it is conceivable that formose-like reactions might have played an important role in the gas-phase and dust-grain surface chemistry occurring in the interstellar medium (ISM).[7] The discovery of an enantiomeric excess of L-amino acids in the Murchison meteorite[8] and then in many carbonaceous chondrites further supports this hypothesis, as L-amino acids are found to act as catalyst in the formose reaction, thus promoting the formation of sugars belonging to the D-series.[9] These findings seem to suggest that an enantiomeric imbalance has possibly emerged elsewhere and could have then been transferred to Earth by meteoritic and cometary bombardment. Therefore, it is not unrealistic to think that prebiotic molecules formed in the ISM could have played a role in setting the stage of life on early Earth. This hypothesis is also supported by the detection of interstellar glycolaldehyde[10] and many other

[a] *Dipartimento di Chimica "Giacomo Ciamician", Università di Bologna, Via F. Selmi 2, 40126 Bologna, Italy. E-mail: mattia.melosso2@unibo.it, cristina.puzzarini@unibo.it*
[b] *Scuola Superiore Meridionale, Università di Napoli Federico II, Largo San Marcellino 10, 80138 Naples, Italy*
[c] *Scuola Normale Superiore, Piazza dei Cavalieri 7, 56126 Pisa, Italy*
[d] *Univ Rennes, Ecole Nationale Supérieure de Chimie de Rennes, CNRS, ISCR – UMR6226, F-35000 Rennes, France*
[e] *Université de Monastir, Avenue Taher Hadded B. P 56, Monastir 5000, Tunisia*
[f] *Centro de Astrobiología (CSIC-INTA), Ctra. de Ajalvir Km. 4, Torrejón de Ardoz, 28850 Madrid, Spain*
[g] *INAF – Osservatorio Astrofisico di Arcetri, Largo E. Fermi 5, 50125 Florence, Italy*

† Electronic supplementary information (ESI) available. See DOI: 10.1039/d1cc06919e

complex, bio-relevant species in molecular clouds, star-forming regions, and Solar-type protostars.[11–15] Such observations demonstrate the existence of formation mechanisms of organic molecules compatible with the harsh conditions of the ISM (T = 10–100 K, number densities $\approx 10^4$ cm^{-3}), whose detailed comprehension still requires a huge effort and, in particular, the identification of key intermediate species linking small organic species to bio-relevant molecules. Hydroxymethylene (HCOH, **3**) is a prototypical short-lived species involved in sugar formation in non-aqueous conditions that escaped detection for a long time.[16] It is thought to be responsible for an efficient initiation of formose-like reactions,[17] especially at low temperatures such as those found in the ISM. In a similar manner, 1,2-ethenediol (HO–CH=CH–OH, **4**) has been suggested being deeply involved in the process of sugar formation in the ISM, *e.g.* by producing glyceraldehyde through its reaction with formaldehyde.[18]

Diol **4**, the higher energy and highly reactive enol of **2**, has been recently identified in an experiment simulating methanol-bearing interstellar ice-analogues exposed to ionizing radiation.[18] Similarly to other prebiotic species,[19–21] **4** can be formed on the icy mantles of interstellar dust grains before being released into the gas phase through thermal desorption or energetic processes, such as strong UV irradiation. This suggests that **4** is likely present in the interstellar medium. However, its detection is currently not possible, because its rotational spectrum is unknown to date. Indeed, it should be noted that the 90% of our astrochemical inventory has been discovered through the observation of rotational transitions.[22]

Compared to other techniques, *e.g.*, electronic or vibrational spectroscopy, which are more suitable for the identification of functional groups, rotational spectroscopy allows for distinguishing among different isotopologues, structural isomers, and even conformers. In this context, it is noteworthy that both **1** and **2**, as well as two additional $C_2H_4O_2$ isomers (acetic acid and methyl formate), have been identified in space thanks to the observation of their spectroscopic signatures,[10,23,24] as it has been the case for halogenated,[25] aromatic,[26,27] or chiral molecules.[28]

Here, in order to enable a step forward in the understanding of sugar formation in the ISM, we report the gas-phase synthesis of the *Z* isomer of **4** *via* flash vacuum pyrolysis (FVP) of bis-*exo*-5-norbornene-2,3-diol ($C_7H_{10}O_2$, **5**, see Scheme 1) and its spectroscopic characterization. The synthesis is based on the general retro-Diels–Alder reaction proposed by Turecek.[29] The *Z* isomer of **4** (hereafter *Z*-**4**) has been characterized *via* measurements of its spectrum using a frequency-modulation submillimeter-spectrometer and its comparison with simulations based on high-level quantum-chemical calculations (see ESI† for details).

The spectrum, recorded between 80–125 GHz and 240–375 GHz during the FVP of **5** at 750 °C, revealed absorptions due to the by-product cyclopentadiene (*c*-C_5H_6, **6**) and the more stable tautomeric form **2**.[30] However, the most intense features detected in the spectrum (Fig. 1) do not belong to any of these or other known molecules, while they match very well the spectral patterns predicted for the *Z*-(*syn*,*anti*) form of **4**.‡

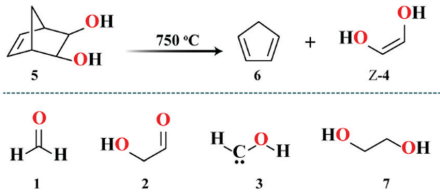

Scheme 1 (*Z*)-1,2-Ethenediol (*Z*-**4**) and cyclopentadiene (**6**) generated in the flash vacuum pyrolysis of bis-*exo*-5-norbornene-1,2-diol (**5**). Other molecules of interest are reported for the sake of clarity: formaldehyde (**1**), glycolaldehyde (**2**), hydroxymethylene (**3**), and ethylene glycol (**7**).

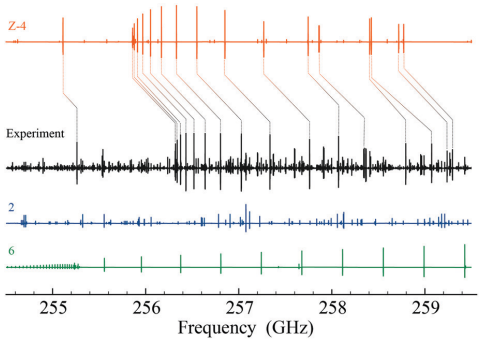

Fig. 1 Portion of the millimeter-wave spectrum around 257 GHz. The experimental spectrum (black trace) is compared with the spectral simulation of glycolaldehyde (**2**, blue trace), cyclopentadiene (**6**, green trace), and the computational guess obtained for 1,2-ethenediol (*Z*-**4**, orange trace). The intensities of the simulated spectra have been adjusted in order to match roughly the experimental spectrum.

With the help of theoretical predictions (based on coupled-cluster theory§) and using the SPCAT[31] subroutine of the CALPGM suite, the signals around 257 GHz could be unambiguously assigned to the strongest μ_a-allowed transitions of *Z*-**4** (μ_a = 1.96 D), shifted with respect to predictions by only 0.1%. This first assignment has been used to refine the spectral predictions, in order to reduce the discrepancy between the computed and observed spectra and to facilitate the interpretation of the subsequent measurements. In addition, we found that a mild heating of **5** decreases the intensity of the interfering lines produced by **2**. Under the best conditions, the *Z*-**4** to **2** abundance ratio is about 6 : 1.

The identification of *Z*-**4** was further confirmed by the presence of a tiny splitting in most of the absorption features. These splittings are a clear evidence of a tunneling motion occurring within the molecular frame, as expected in view of the similarity of *Z*-**4** with ethylene glycol (HO–$(CH_2)_2$–OH, **7**).[32] In particular, the –OH moieties undergo a concerted large amplitude tunneling motion between two equivalent positions of *Z*-(*syn*,*anti*)-**4**, thus splitting each rotational energy level into two. As a consequence, the transitions allowed by the dipole

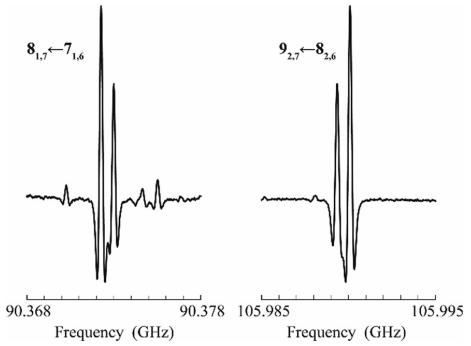

Fig. 2 Tunneling splittings recorded for two low-frequency transitions of *Z*-**4**. The observed ratio is 10 : 6 in accordance with spin-statistics.

moment component oriented along the exchange axis must occur between the two inversion states and show a 10 : 6 intensity ratio obeying to spin-statistics (Fig. 2, see also Section 2 in the ESI†). On the other hand, moderately intense *b*-type transitions (μ_b = 0.62 D) take place within the inversion states.

In agreement with the results of Kleimeier *et al.*,[18] our computed equilibrium geometry of *Z*-**4** indicates a non-planar structure (the C=C–O–H dihedral angle being about 25°), which should result in a moderate dipole moment component along the *c*-axis of the molecule (μ_c = 0.97 D). However, no μ_c-allowed transitions could be observed in the spectrum. While this fact may appear puzzling at first, the experimental evidence is explained by the very low barrier to planarity ($\approx$ 0.2 kJ mol^{-1} at the B2PLYP-D3/aug-cc-pVTZ level of theory; see ESI† for details), ruled by the motion of a single H atom. Hence, in the ground vibrational state the molecule is effectively planar, as confirmed by its inertia defect, whose value is close to zero and slightly negative (see Table 1), a clear sign of near planarity together with the low frequency out-of-plane motion.[33]

From the analysis of the spectrum, more than 1100 transitions have been assigned to *Z*-**4** and analysed with an effective Hamiltonian that accounts for centrifugal distortion as well as tunneling effects. The optimized spectroscopic constants are in excellent agreement with the corresponding computed values (Table 1). This, together with the observed tunneling splittings, provides strong evidence for the correct identification of *Z*-**4** and for its structure and internal dynamics. The small energy difference between the two inversion substates is a clear hint of a high-barrier separating the two identical conformations of *Z*-(*syn*,*anti*)-**4**. In the *aGg′* form of **7**, this energy difference is four orders of magnitude larger,[34] because the single C–C bond lowers the barrier height considerably.

The accurate spectroscopic characterization of *Z*-**4** now permits its search in the ISM. The observation of **4** would shed light on how formose-like reactions can proceed under interstellar conditions, whether following the mechanism proposed by Ricardo *et al.*[35] or a different pathway,[5] and can provide additional insights on sugar formation in extraterrestrial environments.

Table 1 Comparison of experimental and quantum-chemical spectroscopic parameters of (*Z*)-1,2-ethenediol

Constant	Unit	Value[a]	Theory[b]	Constant	Unit	Value[a]
A	MHz	19507.2(2)	19 597.9	E^*	MHz	0.361(3)
B	MHz	6312.1(2)	6298.6	E^*_J	kHz	0.12(1)
C	MHz	4772.4533(2)	4766.8	E^*_K	kHz	0.75(5)
D_J	kHz	6.9479(4)	7.21	E^*_{JJ}	Hz	0.10(1)
D_{JK}	kHz	−36.977(6)	−39.15	E^*_{JK}	Hz	0.7(1)
D_K	kHz	103.10(1)	107.88	E^*_{KK}	Hz	1.6(2)
d_1	kHz	−2.2929(2)	−2.35	F_{ab}	MHz	−218(6)
d_2	kHz	−0.15145(4)	−0.15	Δ	u Å^2	−0.078
H_J	mHz	3.1(1)	−0.26			
H_{JK}	mHz	112.7(5)	171			
H_{KJ}	mHz	−1378.(5)	−1660			
H_K	mHz	3490	3490			
h_1	mHz	2.9(1)	1.74			
h_2	mHz	1.080	1.080			
h_3	mHz	0.243	0.243			
L_{KKJ}	mHz	0.074(6)				

[a] Numbers in parentheses represent the error in the unit of the last quoted digit. When the error is not reported, the parameter is kept fixed to the corresponding computed value. [b] See ESI for details about the level of theory employed.

Being the highly energetic tautomeric form of **2**, the diol **4** can promote chemical reactions when no external energetic sources are available, as it is the case at very low temperatures. This opens up reaction channels that otherwise would be closed and expands the horizon of sugars formation in the ISM. With both **1** and **2** already detected in different astronomical environments,[10,23,36,37] the presence of **4** in the interstellar medium appears more than plausible. The interest in **4** is, however, not limited to prebiotic and interstellar chemistry; enols are also key intermediates of tropospheric acids *via* keto-enol photo-tautomerization mechanisms[38] and of hydrocarbon oxidation processes,[39] thus widening the number of applications for which our gas-phase spectroscopic identification is invaluable.

From another point of view, this work demonstrates the feasibility of producing **4** directly in the gas phase through the retro-Diels–Alder reaction of **5**, thereby allowing its spectroscopic characterization. Although the coupling of FVP with high-resolution spectroscopic techniques has been widely employed in the past for the study of enols,[40,41] carbenes,[42,43] and other unstable species,[44–46] this is the first time that an enediol is observed directly in the gas phase by rotational spectroscopy. The analysis of the spectrum, supported by quantum-chemical calculations, has revealed a vibrationally-averaged planar structure of *Z*-(*syn*,*anti*)-**4**, which undergoes a large amplitude tunneling motion that exchanges the position of the two hydroxyl groups. The experimental findings are in excellent agreement with results issuing from high-level quantum-chemical calculations. In view of the important information that can be retrieved from the spectroscopic characterization in an isolated environment, and the concrete possibility to search for the title molecule in the ISM, we are currently extending the approach presented here to a number of highly reactive species not yet observed in the gas phase.

This study was supported by Bologna University (RFO funds) and the Italian Space Agency (ASI; 'Life in Space' project, N. 2019-3-U.0).

The SMART@SNS Laboratory (http://smart.sns.it) is acknowledged for providing high-performance computing facilities. J.-C. G. thanks the Centre National d'Etudes Spatiales (CNES) and the "Programme National Physique et Chimie du Milieu Interstellaire" (PCMI) of CNRS/INSU with INC/INP co-funded by CEA and CNES for a grant. V. M. R. acknowledges support from the Comunidad de Madrid through the Atracción de Talento Investigador Modalidad 1 (Doctores con experiencia) Grant (COOL: Cosmic Origins Of Life; 2019-T1/TIC-15379).

Conflicts of interest

There are no conflicts to declare.

Notes and references

‡ Diol **4** can exist in two different stereoisomeric forms, namely *E* and *Z*, with the latter being more stable by about 20 kJ mol^{-1}.[47] The *Z* isomer possesses two configurations, the preferred (*syn*, *anti*) form and the higher energetic (*anti*, *anti*) conformer.
§ Equilibrium rotational constants obtained using the CCSD(T)/CBS+CV composite scheme (see ESI†) and augmented by vibrational corrections computed at the fc-MP2/cc-pVTZ level of theory; quartic and sextic centrifugal distortion constants obtained from anharmonic force field calculations at the fc-MP2/cc-pVTZ level.

1 N. Kitadai and S. Maruyama, *Geosci. Front.*, 2018, **9**, 1117–1153.
2 K. Ruiz-Mirazo, C. Briones and A. de la Escosura, *Chem. Rev.*, 2014, **114**, 285–366.
3 R. Shapiro, *Origins Life Evol. Biospheres*, 1988, **18**, 71–85.
4 R. Breslow, *Tetrahedron Lett.*, 1959, **1**, 22–26.
5 C. Appayee and R. Breslow, *J. Am. Chem. Soc.*, 2014, **136**, 3720–3723.
6 A. Butlerow, *Justus Liebigs Ann. Chem.*, 1861, **120**, 295–298.
7 A. F. Jalbout, L. Abrell, L. Adamowicz, R. Polt, A. J. Apponi and L. M. Ziurys, *Astrobiology*, 2007, **7**, 433–442.
8 J. R. Cronin and S. Pizzarello, *Science*, 1997, **275**, 951–955.
9 S. Pizzarello and A. L. Weber, *Origins Life Evol. Biospheres*, 2010, **40**, 3–10.
10 J. M. Hollis, F. J. Lovas and P. R. Jewell, *Astrophys. J.*, 2000, **540**, L107–L110.
11 V. M. Rivilla, I. Jimenez-Serra, J. Martin-Pintado, C. Briones, L. F. Rodriguez-Almeida, F. Rico-Villas, B. Tercero, S. S. Zeng, L. Colzi, P. de Vicente, S. Martin and M. A. Requena-Torres, *Proc. Natl. Acad. Sci. U. S. A.*, 2021, **118**(22), e2101314118.
12 S. Manigand, J. K. Jorgensen, H. Calcutt, H. S. P. Muller, N. F. W. Ligterink, A. Coutens, M. N. Drozdovskaya, E. F. van Dishoeck and S. F. Wampfler, *Astron. Astrophys.*, 2020, **635**, A48.
13 A. Belloche, R. T. Garrod, H. S. P. Muller, K. M. Menten, I. Medvedev, J. Thomas and Z. Kisiel, *Astron. Astrophys.*, 2019, **628**, A10.
14 S. Zeng, D. Quenard, I. Jimenez-Serra, J. Martin-Pintado, V. M. Rivilla, L. Testi and R. Martin-Domenech, *Mon. Not. R. Astron. Soc.*, 2019, **484**, L43–L48.
15 A. Belloche, K. M. Menten, C. Comito, H. S. P. Muller, P. Schilke, J. Ott, S. Thorwirth and C. Hieret, *Astron. Astrophys.*, 2008, **482**, 179–U137.
16 P. R. Schreiner, H. P. Reisenauer, F. C. Pickard, A. C. Simmonett, W. D. Allen, E. Matyus and A. G. Csaszar, *Nature*, 2008, **453**, 906–U942.
17 A. K. Eckhardt, M. M. Linden, R. C. Wende, B. Bernhardt and P. R. Schreiner, *Nat. Chem.*, 2018, **10**, 1141–1147.
18 N. F. Kleimeier, A. K. Eckhardt and R. I. Kaiser, *J. Am. Chem. Soc.*, 2021, **143**, 14009–14018.
19 F. Dulieu, T. Nguyen, E. Congiu, S. Baouche and V. Taquet, *Mon. Not. R. Astron. Soc.*, 2019, **484**, L119–L123.
20 M. Melosso, A. Belloche, M. A. Martin-Drumel, O. Pirali, F. Tamassia, L. Bizzocchi, R. T. Garrod, H. S. P. Muller, K. M. Menten, L. Dore and C. Puzzarini, *Astron. Astrophys.*, 2020, **641**, L160.
21 V. M. Rivilla, J. Martin-Pintado, I. Jimenez-Serra, S. Martin, L. F. Rodriguez-Almeida, M. A. Requena-Torres, F. Rico-Villas, S. S. Zeng and C. Briones, *Astrophys. J., Lett.*, 2020, **899**, L28.
22 B. A. McGuire, *Astrophys. J., Suppl. Ser.*, 2018, **239**, 17.
23 L. E. Snyder, D. Buhl, B. Zuckerman and P. Palmer, *Phys. Rev. Lett.*, 1969, **22**, 679–681.
24 S. J. El-Abd, C. L. Brogan, T. R. Hunter, E. R. Willis, R. T. Garrod and B. A. McGuire, *Astrophys. J.*, 2019, **883**, 129.
25 E. C. Fayolle, K. I. Oberg, J. K. Jorgensen, K. Altwegg, H. Calcutt, H. S. P. Muller, M. Rubin, M. H. D. van der Wiel, P. Bjerkeli, T. L. Bourke, A. Coutens, E. F. van Dishoeck, M. N. Drozdovskaya, R. T. Garrod, N. F. W. Ligterink, M. V. Persson, S. F. Wampfler and R. Team, *Nat. Astron.*, 2017, **1**, 703–708.
26 B. A. McGuire, A. M. Burkhardt, S. Kalenskii, C. N. Shingledecker, A. J. Remijan, E. Herbst and M. C. McCarthy, *Science*, 2018, **359**, 202–205.
27 B. A. McGuire, R. A. Loomis, A. M. Burkhardt, K. L. K. Lee, C. N. Shingledecker, S. B. Charnley, I. R. Cooke, M. A. Cordiner, E. Herbst, S. Kalenskii, M. A. Siebert, E. R. Willis, C. Xue, A. J. Remijan and M. C. McCarthy, *Science*, 2021, **371**, 1265–1269.
28 B. A. McGuire, P. B. Carroll, R. A. Loomis, I. A. Finneran, P. R. Jewell, A. J. Remijan and G. A. Blake, *Science*, 2016, **352**, 1449–1452.
29 F. Tureček and V. Hanuš, *Mass Spectrom. Rev.*, 1984, **3**, 85–152.
30 H. S. P. Muller, F. Schloder, J. Stutzki and G. Winnewisser, *J. Mol. Struct.*, 2005, **742**, 215–227.
31 H. M. Pickett, *J. Mol. Spectrosc.*, 1991, **148**, 371–377.
32 D. Christen, L. H. Coudert, R. D. Suenram and F. J. Lovas, *J. Mol. Spectrosc.*, 1995, **172**, 57–77.
33 T. Oka, *J. Mol. Struct.*, 1995, **352-353**, 225–233.
34 M. Melosso, L. Dore, F. Tarnassia, C. L. Brogan, T. R. Hunter and B. A. McGuire, *J. Phys. Chem. A*, 2020, **124**, 240–246.
35 A. Ricardo, F. Frye, M. A. Carrigan, J. D. Tipton, D. H. Powell and S. A. Benner, *J. Org. Chem.*, 2006, **71**, 9503–9505.
36 J. K. Jørgensen, A. Belloche and R. T. Garrod, *Annu. Rev. Astron. Astrophys.*, 2020, **58**, 727–778.
37 S. K. Blair, L. Magnani, J. Brand and J. G. A. Wouterloot, *Astrobiology*, 2008, **8**, 59–73.
38 D. U. Andrews, B. R. Heazlewood, A. T. Maccarone, T. Conroy, R. J. Payne, M. J. T. Jordan and S. H. Kable, *Science*, 2012, **337**, 1203–1206.
39 C. A. Taatjes, N. Hansen, A. McIlroy, J. A. Miller, J. P. Senosiain, S. J. Klippenstein, F. Qi, L. S. Sheng, Y. W. Zhang, T. A. Cool, J. Wang, P. R. Westmoreland, M. E. Law, T. Kasper and K. Kohse-Hoinghaus, *Science*, 2005, **308**, 1887–1889.
40 A. Mardyukov, A. K. Eckhardt and P. R. Schreiner, *Angew. Chem., Int. Ed.*, 2020, **59**, 5577–5580.
41 A. Mardyukov, F. Keul and P. R. Schreiner, *Angew. Chem., Int. Ed.*, 2021, **60**, 15313–15316.
42 C. C. Womack, K. N. Crabtree, L. McCaslin, O. Martinez, R. W. Field, J. F. Stanton and M. C. McCarthy, *Angew. Chem., Int. Ed.*, 2014, **53**, 4089–4092.
43 A. K. Eckhardt and P. R. Schreiner, *Angew. Chem., Int. Ed.*, 2018, **57**, 5248–5252.
44 P. Neuhaus and W. Sander, *Angew. Chem., Int. Ed.*, 2010, **49**, 7277–7280.
45 K. Edel, S. A. Brough, A. N. Lamm, S. Y. Liu and H. F. Bettinger, *Angew. Chem., Int. Ed.*, 2015, **54**, 7819–7822.
46 N. M. Kidwell, V. Vaquero-Vara, T. K. Ormond, G. T. Buckingham, D. Zhang, D. N. Mehta-Hurt, L. McCaslin, M. R. Nimlos, J. W. Daily, B. C. Dian, J. F. Stanton, G. B. Ellison and T. S. Zwier, *J. Phys. Chem. Lett.*, 2014, **5**, 2201–2207.
47 A. Karton and D. Talbi, *Chem. Phys.*, 2014, **436**, 22–28.

Reactive PESs

Quantum chemistry represents nowadays a very accurate and reliable means to study the reactivity of the ISM, and therefore the formation routes of the molecules there present. The discovery of various molecules, also showing some degrees of complexity, in interstellar clouds has raised many questions about how they could be formed and the chemical processes that can occur despite the harsh conditions of the ISM, which are difficult to be reproduced in experimental laboratories. The starting point for the study of the reactivity of the species present in the ISM is the analysis of the reactive PES of interest and therefore the characterization of the stationary points both from a structural and energetic point of view. This type of studies requires the application of an integrated approach, employing different levels of theory, that combines accuracy and efficiency (Vazart et al., 2016). A preliminary evaluation of the full reactive PES is performed at an affordable computational cost. The characterization of the most favored paths is then improved by employing a double hybrid functional in conjunction with a triple-ζ quality basis set to obtain molecular geometries, at which accurate energies are evaluated by means of a CCSD(T)-based composite scheme, accounting for extrapolation to the complete basis set limit and core-valence correlation (the jun-Cheap model; Alessandrini et al. 2019). The obtained energies are then combined with anharmonic zero–point energy corrections evaluated at the same level of theory as molecular geometries (Mills, 1972; Hoy et al., 1972; Barone, 2005). DFT calculations are carried out with the Gaussian software (Frisch et al., 2016), while for those based on CCSD(T) the CFOUR program (Stanton et al.) is employed.

A representative example of the application of this general strategy is provided by the investigation of the reactivity of methanimine (CH_2NH) with the CP radical ($X^2\Sigma^+$) in the ISM (Alessandrini et al., 2021). Both molecules were detected in the carbon-rich circumstellar shell IRC+10216 and thus represent two good candidates to unveil more details regarding possible chemical networks of this region. Moreover, the CH_2NH + CP reaction is particularly promising because it fits into a general mechanism involving CH_2NH with small radicals, among which we find the isoelectronic CCH and CN radicals (Vazart et al., 2015; Lupi et al., 2020).

An accurate investigation of the reactive CH_2NH + CP PES revealed the presence of submerged formation pathways for three main reaction products, namely *E*- and *Z*-2-phosphanylidyneethan-1-imine (HNCHCP) and N-(phosphaneylidynemethyl)methanimine (CH_2NCP). Despite the proof of concept of their feasible formation in the gas phase from an energetic point of view, the laboratory synthesis of species like HNCHCP and CH_2NCP is particularly complex. In order to provide a useful support to future experimental measurements and astrophysical investigation, the accurate computational characterization of their rotational spectra was also carried out.

The Journal of Chemical Physics ARTICLE scitation.org/journal/jcp

In search of phosphorus in astronomical environments: The reaction between the CP radical ($X^2\Sigma^+$) and methanimine

Cite as: J. Chem. Phys. 154, 054306 (2021); doi: 10.1063/5.0038072
Submitted: 18 November 2020 • Accepted: 29 December 2020 •
Published Online: 3 February 2021

S. Alessandrini,[1,2,a] F. Tonolo,[1,2] and C. Puzzarini[1]

AFFILIATIONS

[1]Dipartimento di Chimica "Giacomo Ciamician", Università di Bologna, Via F. Selmi 2, I-40126 Bologna, Italy
[2]Scuola Normale Superiore, Piazza dei Cavalieri 7, I-56126 Pisa, Italy

Note: This paper is part of the JCP Special Collection in Honor of Women in Chemical Physics and Physical Chemistry.
[a]**Author to whom correspondence should be addressed:** silvia.alessandrini@sns.it

ABSTRACT

Phosphorus is of particular interest in astrochemistry because it is a biogenic element together with hydrogen, carbon, nitrogen, oxygen, and sulfur. However, the chemical evolution of such element in the interstellar medium (ISM) is still far from an accurate characterization, with the chemistry of P-bearing molecules being poorly understood. To provide a contribution in this direction, we have carried out an accurate investigation of the potential energy surface for the reaction between the CP radical and methanimine (CH_2NH), two species already detected in the ISM. In analogy to similar systems, i.e., CH_2NH + X, with X = OH, CN, and CCH, this reaction can occur—from an energetic point of view—under the harsh conditions of the ISM. Furthermore, since the major products of the aforementioned reaction, namely, *E*- and *Z*-2-phosphanylidyneethan-1-imine (HN=CHCP) and N-(phosphaneylidynemethyl)methanimine (H_2C=NCP), have not been spectroscopically characterized yet, some effort has been made for filling this gap by means of accurate computational approaches.

I. INTRODUCTION

Phosphorus is an essential constituent of life on Earth due to the important roles played by its compounds in living systems. Therefore, it is considered a biogenic element together with hydrogen, carbon, nitrogen, oxygen, and sulfur.[1] While phosphorus is ubiquitous on our planet, the elemental abundance of gaseous P in the interstellar medium (ISM), i.e., due to P-bearing molecules, is still unclear, the reasons being its low cosmic abundance ($\sim 2.8 \times 10^{-7}$ with respect to hydrogen[1–3]) and the poor comprehension of its chemistry.[1,4,5] Concerning the former issue, phosphorus can only be formed by stars having a mass 15 times greater than the solar mass, thus a small subgroup of astronomical objects.[1] Furthermore, the nuclear processes involved in the production of atomic phosphorus lead to a yield of only 2.5%.[1,3] Another important consideration is related to the high condensation temperature of atomic phosphorus, which results in what is, probably, a high depletion of such an element onto dust grains, thus reducing the possibility of gas-phase reactions involving atomic phosphorus to form P-containing species.[4]

Nonetheless, some small P-bearing molecules have been detected in the ISM, and this apparent lack might be due to phosphorus molecules not yet discovered.[6] In chronological order, the first molecule observed in molecular clouds was PN,[7,8] followed a few years later by the CP radical ($X^2\Sigma^+$).[9] The latter is probably formed from photodissociation processes of the HCP molecule, also detected in the ISM, in 2007.[10] Indeed, the latter species is considered the "ferry" carrying phosphorus from the condensed state to the gas phase, via photodesorption. More recently, searches for PH_3, CCP, and the PO molecules have been proven successful,[11–13] with the latter being also the only species identified in space containing the P–O bond, whose relevance is

The Journal of Chemical Physics ARTICLE scitation.org/journal/jcp

correlated with its role in biochemistry. Tentative detections of other P-bearing species, such as, e.g., PH_2CN and CH_3PH_2, turned out to be unsuccessful.[14]

The CP and CCP radicals have been detected, up to date, only in the carbon-rich circumstellar shell IRC+10216.[9,12] Circumstellar envelopes of evolved stars are among the most remarkable chemical laboratories in the universe. Therefore, they are excellent bench tests to understand chemical synthesis in space. Among the molecules that might react with these radicals, a plausible and interesting species is methanimine (CH_2NH) whose presence in IRC+10216 was confirmed by Tenenbaum *et al.*[15] In this respect, this work aims at investigating the reaction between the CP radical and methanimine, which is particularly promising in view of the fact that the reaction involving the isoelectronic CN radical is the only formation route available so far for the production of *E*- and *Z*-cyanomethanimine (HNCHCN) in the gas phase.[16,17] Furthermore, it has been recently demonstrated that the reaction between methanimine and the CCH radical leads to the formation of propargylimine,[18] a newly detected species in the ISM,[19] and it has been suggested that the reaction of CH_2NH with small radicals is a general mechanism for the production of complex imines.[18] Among the successful reaction of methanimine, that with the OH radical[20] should also be mentioned.

In analogy with the works previously cited, the expected products of the CP+CH_2NH reaction are *E*- and *Z*-2-phosphanylidyneethan-1-imine (HN = CHCP) and N-(phosphaneylidynemethyl) methanimine (H_2C = NCP). In the present study, an accurate rotational spectroscopic characterization of these species has also been carried out, with our spectral simulations providing a useful support to experimental measurements. The accurate knowledge of the experimental rotational spectra is, indeed, the mandatory requirement for astronomical searches.[3,21]

This paper is organized as follows. In Sec. II, the computational methodologies employed for the accurate investigation of the potential energy surface (PES) of the reactive system as well as those used for the computational spectroscopic investigations are outlined. In Sec. III, the reactive PES is discussed in view of drawing the most important energetic considerations. Subsequently, the results of the spectroscopic characterization for the products will be reported, together with the corresponding spectral simulations. In the last section, the conclusions are drawn.

II. COMPUTATIONAL METHODS

The reactive PES of the CP + CH_2NH system has been explored employing the double-hybrid B2PLYP functional,[22] including the D3 dispersion correction,[23,24] and using the partially augmented jun-cc-pVTZ basis set with an additional *d* function on second-row atoms, namely, the jun-cc-pV(T+*d*)Z basis set[25–28] (available on the basis set exchange website[29–31]). The nature of the stationary points located on the reactive PES has been confirmed by Hessian evaluations at the same level of theory, which also provide the corresponding harmonic zero-point vibrational energy (ZPE) corrections. To ensure the correct linking of the reaction pathways, each transition state (TS) has been connected to the corresponding minima by means of the intrinsic reaction coordinate (IRC) analysis.[32]

To improve the quality of the CP+CH_2NH reactive PES, the next step was the refinement of the electronic energies, which have been computed using the junChS composite scheme.[33] This approach starts from a single-point energy calculation employing the CCSD(T) method (coupled cluster singles and doubles with a perturbative treatment of triples)[34] in conjunction with the jun-cc-pV(T+*d*)Z basis set and within the frozen-core approximation (fc). This leading term [*E*(CC/junTZ)] is then corrected by incorporating two terms, thus relying on the additivity approximation:

1. The extrapolation to the complete basis set (CBS) limit. This contribution (ΔE^{∞}_{MP2}) is obtained as described in Eq. (1), with second-order Møller–Plesset perturbation theory[35] (MP2) being used in fc energy calculations in conjunction with the jun-cc-pV(T+*d*)Z and jun-cc-pV(Q+*d*)Z basis sets. The total fc-MP2 energies are then extrapolated to the CBS limit by employing the n^{-3} formula by Helgaker *et al.*[36] The effective contribution is obtained by subtracting the fc-MP2/jun-cc-pV(T+*d*)Z energy from the extrapolated value,

$$\Delta E^{\infty}_{MP2} = \frac{4^3 E^{\text{jun}(Q+d)Z}_{MP2} - 3^3 E^{\text{jun}(T+d)Z}_{MP2}}{4^3 - 3^3} - E^{\text{jun}(T+d)Z}_{MP2}. \quad (1)$$

2. The core-valence (CV) correlation contribution. This term, denoted as ΔE^{CV}_{MP2}, accounts for the correlation of core electrons. It is computed as the energy difference between all-electron (ae) and fc-MP2 computations, both performed with the polarized-weighted core valence triple-ζ basis set (cc-pwCVTZ).[37]

Overall, the total junChS electronic energy is given by:

$$E(\text{junChS}) = E(\text{CC/junTZ}) + \Delta E^{\infty}_{MP2} + \Delta E^{CV}_{MP2}. \quad (2)$$

To avoid spin-contamination of higher electronic spin-states, the junChS approach was evaluated using the restricted open-shell Hartree–Fock wave function (ROHF) for both the CCSD(T)[38,39] and MP2[40,41] methods, as pointed out in Ref. 42. In contrast, B2PLYP-D3 energies have been computed using the unrestricted version of the reference wave function (UHF) in view of the fact that density functional theory (DFT) is less affected by spin-contamination.[43] While the accuracy of the junChS model has been demonstrated for the interaction energy of noncovalent complexes, this is its first application to reaction energies. For this reason, its accuracy has been checked by evaluating a small portion of the PES using an HEAT-like protocol, which is described in detail in Refs. 42 and 44–48. According to Ref. 42, the cc-pV*n*Z basis sets[25,27] have been employed to compute the extrapolation to the CBS limit of the Hartree–Fock self-consistent field (HF-SCF; with *n* = T, Q, and 5) and fc-CCSD(T) correlation (*n* = T and Q) energies. The contribution due to the correlation of inner electrons has been included at the CCSD(T)/cc-pCVTZ[37,49] level. However, to reach the "sub-kJ accuracy," other additive terms have also been considered: (i) the full account of triple excitations at the CCSDT/cc-pVTZ level of theory;[50,51] (ii) the contribution of quadruple excitations by means of the CCSDT(Q)

The Journal of Chemical Physics ARTICLE scitation.org/journal/jcp

method[52–54] in conjunction with the cc-pVDZ basis set; (iii) the scalar relativistic correction (the mass–velocity and Darwin terms) using perturbative techniques,[55,56] computed at the CCSD(T)/aug-cc-pCVDZ level; (iv) the diagonal Born–Oppenheimer correction (DBOC) computed at the HF-SCF level[57] in conjunction with the aug-cc-pVDZ basis set.[27,58]

The energetic investigation of the CP+CH_2NH reactive PES has been complemented by the spectroscopic characterization of the three major products, namely, *E*- and *Z*-HN=CHCP and H_2C=NCP. To accurately simulate their rotational spectra, the rotational and centrifugal distortion constants should be computed at the highest possible level of theory.[59] Since equilibrium rotational constants (B_e) are straightforwardly derived from the equilibrium structure, an accurate geometry optimization has been carried out. In detail, the fc-CCSD(T)/CBS(Q,5)+CV/(wCVTZ) "gradient" composite scheme[60,61] has been exploited, with the following energy gradient thus being minimized:

$$\frac{dE_{\mathrm{CBS+CV}}}{dx} = \frac{dE_{\mathrm{HF}}^{\mathrm{CBS}}}{dx} + \frac{d\Delta E_{\mathrm{CCSD(T)}}^{\mathrm{CBS}}}{dx} + \frac{d\Delta E_{CV}}{dx}, \tag{3}$$

where the first term on the right-hand side is the extrapolation of the HF-SCF energy to the CBS limit using the three-point expression by Feller[62] in combination with the cc-pV(n+d)Z basis sets, with n = T, Q, and 5. The second term is the extrapolation to the CBS limit of the CCSD(T) correlation energy obtained with the n^{-3} formula, previously introduced for the junChS model, and employing the cc-pV(Q+*d*)Z and cc-pV(5+*d*)Z sets. The last term is the CV contribution, which is computed at the CCSD(T)/cc-pwCVTZ level. Further details can be found in Refs. 60, 61, and 63. To move from equilibrium to the vibrational ground state, vibrational corrections to the equilibrium rotational constants have to be included.[59,64] Within second-order vibrational perturbation theory (VPT2),[65,66] these corrections require the knowledge of the vibration–rotation interaction constants, which, in turn, involve anharmonic force field computations (full cubic and semi-diagonal quartic force constants). These have been carried out at the B2PLYP-D3/jun-cc-pV(T+*d*)Z level.

The other parameters needed for a reliable simulation of the rotational spectrum are as follows:

1. the quartic centrifugal-distortion constants, which have been obtained from a harmonic force field computed at the ae-CCSD(T)/cc-pwCVQZ level of theory.
2. the electric dipole moment components, which have been obtained by combining the equilibrium values at the ae-CCSD(T)/pwCVQZ level with the vibrational corrections at the B2PLYP-D3/jun-cc-pV(T+*d*)Z level.

All DFT computations together with the single-point energy calculations within the junChS scheme have been carried out using the Gaussian suite of program,[67] while geometry optimizations and force-field evaluations involving the CCSD(T) method have

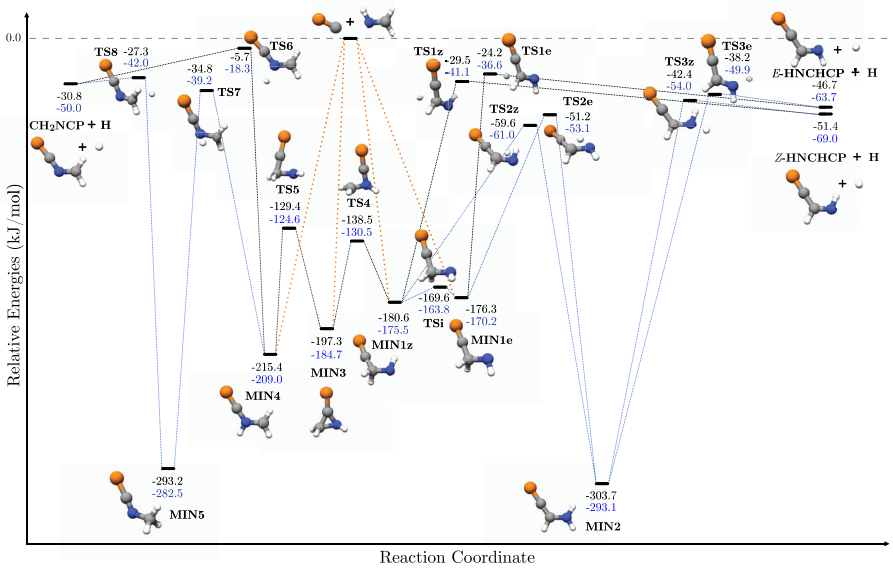

FIG. 1. CP + CH_2NH reaction pathways: junChS relative energies (black) and their harmonic ZPE-corrected (blue) counterparts.

The Journal of Chemical Physics ARTICLE scitation.org/journal/jcp

been performed employing the CFOUR quantum chemical program package.[68,69]

III. RESULTS

A. The reactive PES of the CP + CH_2NH system

The severe conditions of the interstellar clouds, namely, low temperatures (10 K–100 K) and low number density (10 cm^{-3}–10^7 cm^{-3}), pose tight constraints on reactivity, thus allowing only reactions that can occur without overcoming activation barriers, with the only exception due to tunneling effects. For this reason, we focused on reaction pathways presenting only submerged barriers. Based on previous studies,[17,18] the nucleophilic attacks of the C-end of the CP radical on both the carbon and nitrogen sides of methanimine have been considered. The resulting reaction paths are depicted in Fig. 1, which also shows the structures of all the stationary points identified.

The strong nucleophilicity of the CP radical leads to three barrierless entrance channels:

1. The CP attack to the methanimine C-end. This forms two isomers of pre-reactive complexes **MIN1**, **MIN1e**, and **MIN1z**, which can be easily interconverted through **TSi** because of the low isomerization barrier (~10 kJ mol^{-1}).
2. The CP attack to the methanimine N-end. This leads to the formation of a planar pre-reactive complex, **MIN4**.
3. The CP attack to the π-system of the imine double bond. This leads to the formation of a stable cyclic adduct (**MIN3**), which links the left (N-end) and right (C-end) portions of the reactive PES through barriers of the order of 50 kJ mol^{-1} –60 kJ mol^{-1}.

Despite the weaker electrophilic character of nitrogen compared to the carbon atom of methanimine, the **MIN4** intermediate is the most stable pre-reactive complex from an energetic point of view, analogously to what occurs in the reactions of methanimine with CN or CCH.[17,18] This might be attributed to the stabilizing effect of electronic delocalization. However, the crucial interconversion barriers between the first intermediates, i.e., **MIN4**, **MIN3**, and **MIN1e/z**, are slightly different from those obtained for the CCH radical.[18] The intermediates **MIN4** and **MIN1** (both the *E* and *Z* isomers) evolve into the products CH_2NCP and HNCHCP (both the *E* and *Z* isomers), respectively, by elimination of a hydrogen atom. The elimination mechanism can occur in two different ways: either through a path (depicted in black in Fig. 1), involving only one transition state at high energy (**TS6**, **TS1e**, and **TS1z**), but still submerged with respect to reactants, or through a two-step path (depicted in blue in Fig. 1), which involves the formation of the most stable intermediates (**MIN5** and **MIN2**) of the entire PES.

Table I shows the B2PLYP-D3/jun-cc-pV(T+*d*)Z and junChS relative energies, together with the ZPE-corrected counterparts, for

TABLE I. Relative electronic energies (kJ mol^{-1}) of the stationary points for the CP + CH_2NH reaction.

	B2PLYP-D3/jun-cc-pV(T+*d*)Z		junChS	
	Energy	ZPE corrected[a]	Energy	ZPE corrected[a]
Reactants	0.00	0.00	0.00	0.00
MIN1z	−201.48	−196.38	−180.59	−175.49
TSi	−189.85	−184.06	−169.57	−163.79
MIN1e	−196.65	−190.57	−176.29	−170.22
TS1e	−42.40	−54.73	−24.24	−36.58
TS1z	−47.15	−58.82	−29.46	−41.12
TS2z	−79.03	−80.38	−59.62	−60.98
TS2e	−69.92	−71.80	−51.19	−53.08
MIN2	−326.45	−315.89	−303.66	−293.10
TS3e	−60.41	−72.16	−38.18	−49.92
TS3z	−64.43	−75.96	−42.45	−54.00
E-HNCHCP + H	−73.10	−90.17	−46.67	−63.74
Z-HNCHCP + H	−68.14	−85.71	−51.41	−68.97
TS5	−147.84	−143.05	−129.44	−124.62
MIN3	−214.53	−201.92	−197.30	−184.75
TS4	−152.28	−144.29	−138.47	−130.48
MIN4	−241.05	−234.78	−215.36	−209.02
TS6	−36.00	−48.47	−5.68	−18.26
TS7	−58.84	−63.19	−34.76	−39.19
MIN5	−321.65	−311.06	−293.22	−282.53
TS8	−50.70	−65.57	−27.29	−42.04
CH_2NCP + H	−58.87	−78.08	−30.77	−49.96

[a]Harmonic ZPE corrections at the B2PLYP-D3/jun-cc-pV(T+*d*)Z level.

The Journal of Chemical Physics ARTICLE scitation.org/journal/jcp

all stationary points of the reactive PES. While the junChS model does not change the trends resulting from DFT calculations, it reduces the relative energies by about 14 kJ mol^{-1}– 30 kJ mol^{-1}. In particular, the largest change occurs for **TS6**, which increases the relative energy by about 30 kJ mol^{-1}, thus approaching the energy of the reactants (albeit being still submerged). Overall, we can note that the reaction barriers are approximately left unchanged.

As mentioned in Sec. II, to validate the accuracy of the junChS approach, the path Reactants → **MIN1** (both the *E* and *Z* isomers) → **TS1** (both the *E* and *Z* isomers) → HNCHCP (both the *E* and *Z* isomers) has been re-investigated employing the HEAT-like protocol[42,44–48] on top of B2PLYP-D3/jun-cc-pV(T+*d*)Z geometries. The comparison between junChS and HEAT-like energies is reported in Table II and shows a maximum absolute deviation of ~0.8 kJ mol^{-1} and an average absolute deviation of ~0.6 kJ mol^{-1}. Therefore, it has been confirmed that the approach adopted for this investigation has the required accuracy for reactive PES investigation.

B. Spectroscopic characterization of *E/Z*-HNCHCP and CH_2NCP

As mentioned in the Introduction, the identification of new molecules in astronomical environments is driven by the observation of their rotational transitions,[70] which are unambiguous fingerprints. With only few exceptions,[71–73] experimental rotational transition frequencies are required for the assignment of the spectra collected by using radio-telescopes and/or interferometers. However, whenever there is a complete lack of information, computed spectra are the mandatory starting point for experiment in the laboratory, especially if the species of interest is unstable and produced inside the spectrometer cell via, e.g., electric discharge or pyrolysis.

The laboratory synthesis of species-like HNCHCP and CH_2NCP is not feasible, and their production *in situ* is challenging. Indeed, a suitable precursor for pyrolysis needs to be envisaged, which, according to the works on propargylimine[19] and cyanomethanimine,[74] should be a substituted N-containing phosphine or a P-bearing amine. In view of the complexity of the experimental investigation, the accurate computational characterization of rotational spectra of HNCHCP and CH_2NCP is particularly important.

TABLE II. Relative electronic energies (kJ mol^{-1}) for the CH_2NH + CP → **MIN1e/z** → **TS1e/z** → E/Z-HNCHCP + H path.

	junChS	HEAT-like	$\lvert\Delta E\rvert$[a]
MIN1z	−180.59	−179.86	0.73
MIN1e	−176.29	−175.50	0.79
TS1e	−24.24	−24.67	0.43
TS1z	−29.46	−29.90	0.44
Z-HNCHCP + H	−51.41	−51.12	0.29
E-HNCHCP + H	−46.67	−45.86	0.81

[a]Absolute junChS-HEAT-like energy difference.

Table III collects the spectroscopic parameters computed with the protocol described in Sec. II. According to Ref. 63, the expected accuracy of the vibrational ground-state rotational constants is ~0.06%, while the uncertainty affecting the quartic centrifugal-distortion constants is about one order of magnitude greater.[75,76] Figure 2 depicts the simulation of the rotational spectra of the *Z* and *E* isomers of HNCHCP, at a temperature of 100 K, based on the spectroscopic parameters of Table III. Figure 2 shows that, while the maximum of intensity is around 180 GHz for both species, the larger dipole moment components of the *E* isomer result in a more intense spectrum. Since the uncertainties on the computed parameters propagate by increasing the rotational quantum number *J* (denoting the lowest rotational level involved in the transition), the most accurate estimates are obtained for rotational transitions with low *J* values, which usually lie at low frequencies. For this reason, Fig. 2 also shows a zoomed-in view of the rotational spectra in the 30 GHz–100 GHz frequency range, with the different K_a-components of each transition being evident. It has to be noted that, for both isomers, *a*- and *b*-type transitions are observable; however, the μ_b component of the dipole moment is rather small, in particular for the *Z*-HNCHCP species. As a consequence, the *b*-type spectrum of *Z*-HNCHCP is not discernible in Fig. 2; for the *E* isomer, instead, this type of transitions becomes well visible at frequencies greater than 250 GHz (darker red lines). In Fig. 3, the rotational spectrum for CH_2NCP, simulated at T = 100 K, is shown in the 0 GHz–500 GHz frequency range. Both *a*- and *b*-type transitions are evident, and the maximum of intensity is above 500 GHz. However, at such frequencies, the predictions are less accurate, and higher frequencies have thus not been considered.

TABLE III. Rotational spectroscopic parameters (MHz, if not otherwise stated) of *E*-/*Z*-HNCHCP and CH_2NCP (Watson's *S* reduction and I^r representation).

Parameter[a]	*Z*-HNCHCP	*E*-HNCHCP	CH_2NCP
A_e	50 319.38	58 098.90	61 454.73
B_e	2 846.04	2 796.71	2 997.13
C_e	2 693.69	2 668.27	2 857.76
ΔA_{vib}	272.77	52.49	1 372.17
ΔB_{vib}	−11.55	−6.82	−17.25
ΔC_{vib}	−12.34	−8.66	−16.54
A_0	50 592.15	58 151.39	62 826.90
B_0	2 834.49	2 789.89	2 979.88
C_0	2 681.35	2 659.61	2 841.22
D_J	0.65×10^{-3}	0.54×10^{-3}	0.63×10^{-3}
D_{JK}	−0.056	−0.066	−0.080
D_K	3.9	6.2	7.7
d_1	-0.90×10^{-4}	-0.70×10^{-4}	-0.88×10^{-4}
d_2	-0.47×10^{-5}	-0.32×10^{-5}	-0.45×10^{-5}
$\lvert\mu_a\rvert$/D	1.58	1.90	1.68
$\lvert\mu_b\rvert$/D	0.06	0.37	1.39
$\lvert\mu_c\rvert$/D	0.00	0.00	0.00

[a]Equilibrium rotational constants at the fc-CCSD(T)/CBS(Q,5)+CV/(wCVTZ) level. Anharmonic corrections (ΔB_{vib}'s) at the B2PLYP-D3/jun-cc-pV(T+*d*)Z level. Quartic centrifugal distortion constants at the ae-CCSD(T)/cc-pwCVQZ level. Equilibrium dipole moment components (in debye) at the ae-CCSD(T)/cc-pwCVQZ level corrected for vibrational contributions at the B2PLYP-D3/jun-cc-pV(T+*d*)Z level.

The Journal of Chemical Physics ARTICLE scitation.org/journal/jcp

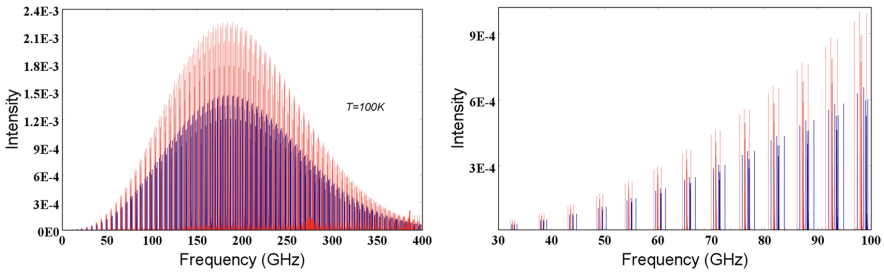

FIG. 2. Left panel: Simulated rotational spectra of *Z*- and *E*-HNCHCP, blue and red lines, respectively, up to 400 GHz. Right panel: A zoomed-in view of the rotational spectra between 30 GHz and 100 GHz. Intensity in nm^2 MHz.

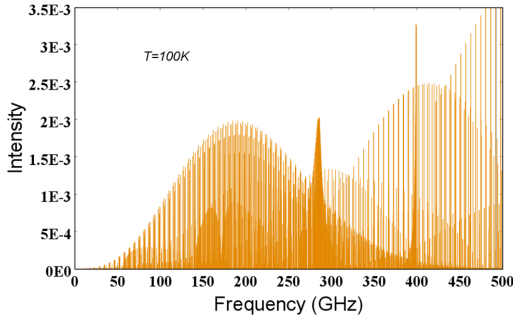

FIG. 3. Simulated rotational spectrum of CH_2NCP in the 0 GHz–500 GHz frequency range. Intensity in nm^2 MHz.

A good candidate for the observation in the case of CH_2NCP is the transition $J_{K_a,K_c} = 2_{1,2} \leftarrow 1_{1,1}$, which is predicted at 11 503.8 MHz with an error, according to estimates addressed above, of only 5.4 MHz.

IV. CONCLUSIONS

In analogy to the addition of the CN and CCH radicals to methanimine, the CP radical is expected to lead to reaction paths that are "open" (i.e., energetically accessible) under the harsh conditions of the ISM. Interestingly, the reactive CP + CH_2NH PES is, in any detail, analogous to that of the CN + CH_2NH and CCH + CH_2NH systems, thus supporting the idea of a general mechanism for the formation of complex imines in interstellar clouds. Furthermore, the present work is the first application of the new junChS model for energetic studies of reactive PESs. The comparison with the results issuing from an extremely accurate HEAT-like approach pointed out to a great accuracy and suitability for energy evaluations of reactive systems, despite its limited computational cost. Finally, this work has been complemented by the spectroscopic characterization of the major reaction products, namely, *E*-/*Z*-HNCHCP and CH_2NCP, with a methodology at the state of the art, able to predict rotational transitions with accuracy better than 0.2%.

DEDICATION

This work is dedicated to Laura Bassi-Veratti (Bologna, 1711-1778) as the symbol of all women who pursued or are pursuing a scientific academic career. She was the second woman to achieve a university degree, the very first to obtain a Ph.D. in a scientific subject, and a teaching position at the University of Bologna. She fought for equal rights for women and men in academics.

ACKNOWLEDGMENTS

This work was supported by the University of Bologna (RFO funds). SMART@SNS Laboratory (http://smart.sns.it) is acknowledged for providing high-performance computing facilities. Support by the Italian Space Agency [ASI; "Life in Space" (Project No. 2019-3-U.0)] is also acknowledged.

DATA AVAILABILITY

The data that support the findings of this study are available from the corresponding author upon reasonable request.

REFERENCES

[1] E. Maciá, "The role of phosphorus in chemical evolution," Chem. Soc. Rev. **34**, 691–701 (2005).
[2] N. Grevesse and A. J. Sauval, "Standard solar composition," Space Sci. Rev. **85**, 161–174 (1998).
[3] S. Yamamoto, *Introduction to Astrochemistry: Chemical Evolution From Interstellar Clouds to Star and Planet Formation* (Springer, Japan, 2017).
[4] V. Lebouteiller, Kuassivi, and R. Ferlet, "Phosphorus in the diffuse interstellar medium," Astron. Astrophys. **443**, 509–517 (2005).
[5] J. Chantzos, V. M. Rivilla, A. Vasyunin, E. Redaelli, L. Bizzocchi, F. Fontani, and P. Caselli, "The first steps of interstellar phosphorus chemistry," Astron. Astrophys. **633**, A54 (2020).
[6] S. N. Milam, D. T. Halfen, E. D. Tenenbaum, A. J. Apponi, N. J. Woolf, and L. M. Ziurys, "Constraining phosphorus chemistry in carbon- and oxygen-rich

The Journal of Chemical Physics ARTICLE scitation.org/journal/jcp

circumstellar envelopes: Observations of PN, HCP, and CP," Astrophys. J. **684**, 618–625 (2008).
[7]L. M. Ziurys, "Detection of interstellar PN: The first phosphorus-bearing species observed in molecular clouds," Astrophys. J. **321**, L81–L85 (1987).
[8]B. E. Turner and J. Bally, "Detection of interstellar PN: The first identified phosphorus compound in the interstellar medium," Astrophys. J. **321**, L75–L79 (1987).
[9]M. Guélin, J. Cernicharo, G. Paubert, and B. E. Turner, "Free CP in IRC+10216," Astron. Astrophys. **230**, L9–L11 (1990).
[10]M. Agúndez, J. Cernicharo, and M. Guélin, "Discovery of phosphaethyne (HCP) in space: Phosphorus chemistry in circumstellar envelopes," Astrophys. J. **662**, L91–L94 (2007).
[11]M. Agúndez, J. Cernicharo, L. Decin, P. Encrenaz, and D. Teyssier, "Confirmation of circumstellar phosphine," Astrophys. J. **790**, L27 (2014).
[12]D. T. Halfen, D. J. Clouthier, and L. M. Ziurys, "Detection of the CCP radical ($X^2\Pi_r$) in IRC+10216: A new interstellar phosphorus-containing species," Astrophys. J. **677**, L101–L104 (2008).
[13]E. D. Tenenbaum, N. J. Woolf, and L. M. Ziurys, "Identification of phosphorus monoxide ($X^2\Pi_r$) in VY Canis Majoris: Detection of the first P–O bond in space," Astrophys. J. **666**, L29–L32 (2007).
[14]D. T. Halfen, D. J. Clouthier, and L. M. Ziurys, "Millimeter/submillimeter spectroscopy of PH_2CN ($\tilde{X}^1A'$) and CH_3PH_2 ($\tilde{X}^1A'$): Probing the complexity of interstellar phosphorus in chemistry," Astrophys. J. **796**, 36 (2014).
[15]E. D. Tenenbaum, J. L. Dodd, S. N. Milam, N. J. Woolf, and L. M. Ziurys, "Comparatice spectra of oxygen-rich vs carbon-rich circumstellar shells: VY Canis Majoris and IRC+10216 at 215-285 GHz," Astrophys. J. **720**, L102–L107 (2010).
[16]V. A. Basiuk and V. I. Bogillo, "Theoretical study of amino acid precursor formation in the interstellar medium. 2. Reaction of methylenimine with CN radical," Adv. Space Res. **30**, 1445–1450 (2002).
[17]F. Vazart, C. Latouche, D. Skouteris, N. Balucani, and V. Barone, "Cyanomethanimine isomers in cold insterstellar clouds: Insights from electronic structure and kinetic calculations," Astrophys. J. **810**, 111 (2015).
[18]J. Lupi, C. Puzzarini, and V. Barone, "Methanimine as a key precursor of imines in the interstellar medium: The case of propargylimine," Astrophys. J. Lett. **903**, L35 (2020).
[19]L. Bizzocchi, D. Prudenzano, V. M. Rivilla, A. Pietropolli-Charmet, B. M. Giuliano, P. Caselli, J. Martín-Pintado, I. Jiménez-Serra, S. Martín, M. A. Requena-Torres, F. Rico-Villas, S. Zeng, and J.-C. Guillemin, "Propargylimine in the laboratory and in space: Millimetre-wave spectroscopy and its first detection in the ISM," Astron. Astrophys. **640**, A98 (2020).
[20]F. Vazart, D. Calderini, C. Puzzarini, D. Skouteris, and V. Barone, "State-of-the-art thermochemical and kinetic computations for astrochemical complex organic molecules: Formamide formation in cold interstellar clouds as a case study," J. Chem. Theory Comput. **12**, 5385–5397 (2016).
[21]M. Melosso, L. Dore, F. Tamassia, C. L. Brogan, T. R. Hunter, and B. A. McGuire., "The submillimeter rotational spectrum of ethylene glycol up to 890 GHz and application to ALMA band 10 spectral line data of NGC 6334I," J. Phys. Chem. A **124**, 240–246 (2020).
[22]S. Grimme, "Semiempirical hybrid density functional with perturbative second-order correlation," J. Phys. Chem. **124**, 034108 (2006).
[23]S. Grimme, S. Ehrlich, and L. Goerigk, "Effect of the damping function in dispersion corrected density functional theory," J. Comput. Chem. **32**, 1456–1465 (2011).
[24]S. Grimme, J. Antony, S. Ehrlich, and H. Krieg, "A consistent and accurate *ab initio* parametrization of density functional dispersion correction (DFT-D) for the 94 elements H-Pu," J. Chem. Phys. **132**, 154104 (2010).
[25]T. H. Dunning, Jr., "Gaussian basis sets for use in correlated molecular calculations. I. The atoms boron through neon and hydrogen," J. Chem. Phys. **90**, 1007–1023 (1989).
[26]T. H. Dunning, K. A. Peterson, and A. K. Wilson, "Gaussian basis sets for use in correlated molecular calculations. X. The atoms aluminum through argon revisited," J. Chem. Phys. **114**, 9244–9253 (2001).
[27]D. E. Woon and T. H. Dunning, Jr., "Gaussian basis sets for use in correlated molecular calculations. III. The atoms aluminum through argon," J. Chem. Phys. **98**, 1358–1371 (1993).
[28]E. Papajak and D. G. Truhlar, "Convergent partially augmented basis sets for post-Hartree-Fock calculations of molecular properties and reaction barrier heights," J. Chem. Theory Comput. **7**, 10–18 (2011).
[29]B. P. Pritchard, D. Altarawy, B. Didier, T. D. Gibson, and T. L. Windus, "A new basis set exchange: An open, up-to-date resource for the molecular sciences community," J. Chem. Inf. Model. **59**, 4814–4820 (2019).
[30]K. L. Schuchardt, B. T. Didier, T. Elsethagen, L. Sun, V. Gurumoorthi, J. Chase, J. Li, and T. L. Windus, "Basis set exchange: A community database for computational sciences," J. Chem. Inf. Model. **47**, 1045–1052 (2007).
[31]D. Feller, "The role of databases in support of computational chemistry calculations," J. Comput. Chem. **17**, 1571–1586 (1996).
[32]K. Fukui, "The path of chemical reactions—The IRC approach," Acc. Chem. Res. **14**, 363–368 (1981).
[33]S. Alessandrini, V. Barone, and C. Puzzarini, "Extension of the "Cheap" composite approach to noncovalent interactions: The jun-ChS scheme," J. Chem. Theory Comput. **16**, 988–1006 (2019).
[34]K. Raghavachari, G. W. Trucks, J. A. Pople, and M. Head-Gordon, "A fifth-order perturbation comparison of electron correlation theories," Chem. Phys. Lett. **157**, 479–483 (1989).
[35]C. Møller and M. S. Plesset, "Note on an approximation treatment for many-electron systems," Phys. Rev. **46**, 618–622 (1934).
[36]T. Helgaker, W. Klopper, H. Koch, and J. Noga, "Basis-set convergence of correlated calculations on water," J. Chem. Phys. **106**, 9639 (1997).
[37]K. A. Peterson and T. H. Dunning, Jr., "Accurate correlation consistent basis sets for molecular core-valence correlation effects: The second row atoms Al-Ar, and the first row atoms B-Ne revisited," J. Chem. Phys. **117**, 10548–10560 (2002).
[38]J. Gauss, W. J. Lauderdale, J. F. Stanton, J. D. Watts, and R. J. Bartlett, "Analytic energy gradients for open-shell coupled-cluster singles and doubles (CCSD) calculations using restricted open-shell Hartree—Fock (ROHF) reference functions," Chem. Phys. Lett. **182**, 207–215 (1991).
[39]J. D. Watts, J. Gauss, and R. J. Bartlett, "Coupled-cluster methods with noniterative triple excitations for restricted open-shell Hartree–Fock and other general single determinant reference functions. Energies and analytical gradients," J. Chem. Phys. **98**, 8718–8733 (1993).
[40]W. J. Lauderdale, J. F. Stanton, J. Gauss, J. D. Watts, and R. J. Bartlett, "Many-body perturbation theory with a restricted open-shell Hartree–Fock reference," Chem. Phys. Lett. **187**, 21–28 (1991).
[41]W. J. Lauderdale, J. F. Stanton, J. Gauss, J. D. Watts, and R. J. Bartlett, "Restricted open-shell Hartree–Fock-based many-body perturbation theory: Theory and application of energy and gradient calculations," J. Chem. Phys. **97**, 6606–6620 (1992).
[42]C. Puzzarini and V. Barone, "The challenging playground of astrochemistry: An integrated rotational spectroscopy—Quantum chemistry strategy," Phys. Chem. Chem. Phys. **22**, 6507–6523 (2020).
[43]A. S. Menon and L. Radom, "Consequences of spin contamination in unrestricted calculations on open-shell species: Effect of Hartree–Fock and Møller–Plesset contributions in hybrid and double-hybrid density functional theory approaches," J. Phys. Chem. A **112**, 13225–13230 (2008).
[44]A. Tajti, P. G. Szalay, A. G. Császár, M. Kállay, J. Gauss, E. F. Valeev, B. A. Flowers, J. Vázquez, and J. F. Stanton, "HEAT: High accuracy extrapolated *ab initio* thermochemistry," J. Comput. Phys. **121**, 11599–11613 (2004).
[45]Y. J. Bomble, J. Vázquez, M. Kállay, C. Michauk, P. G. Szalay, A. G. Császár, J. Gauss, and J. F. Stanton, "High-accuracy extrapolated *ab initio* thermochemistry. II. Minor improvements to the protocol and a vital simplification," J. Chem. Phys. **125**, 064108 (2006).
[46]M. E. Harding, J. Vázquez, B. Ruscic, A. K. Wilson, J. Gauss, and J. F. Stanton, "High-accuracy extrapolated *ab initio* thermochemistry. III. Additional improvements and overview," J. Chem. Phys. **128**, 114111 (2008).
[47]C. Puzzarini, Z. Salta, N. Tasinato, J. Lupi, C. Cavallotti, and V. Barone, "A twist on the reaction of the CN radical with methylamine in the interstellar medium:

The Journal of Chemical Physics ARTICLE scitation.org/journal/jcp

New hints from a state-of-the-art quantum-chemical study," Mon. Not. R. Astron. Soc. **496**, 4298–4310 (2020).
[48]J. Lupi, C. Puzzarini, C. Cavallotti, and V. Barone, "State-of-the-art quantum chemistry meets variable reaction coordinate transition state theory to solve the puzzling case of the H_2S + Cl system," J. Chem. Theory Comput. **16**, 5090–5104 (2020).
[49]D. E. Woon and T. H. Dunning, Jr., "Gaussian basis sets for use in correlated molecular calculations. V. Core-valence basis sets for boron through neon," J. Chem. Phys. **103**, 4572–4585 (1995).
[50]J. Noga and R. J. Bartlett, "The full CCSDT model for molecular electronic structure," J. Chem. Phys. **86**, 7041–7050 (1987).
[51]G. E. Scuseria and H. F. Schaefer III, "A new implementation of the full CCSDT model for molecular electronic structure," Chem. Phys. Lett. **152**, 382–386 (1988).
[52]Y. J. Bomble, J. F. Stanton, M. Kállay, and J. Gauss, "Coupled-cluster methods including noniterative corrections for quadruple excitations," J. Chem. Phys. **123**, 054101 (2005).
[53]M. Kállay and J. Gauss, "Approximate treatment of higher excitations in coupled-cluster theory," J. Chem. Phys. **123**, 214105 (2005).
[54]M. Kállay and J. Gauss, "Approximate treatment of higher excitations in coupled-cluster theory. II. Extension to general single-determinant reference functions and improved approaches for the canonical Hartree–Fock case," J. Chem. Phys. **129**, 144101 (2008).
[55]R. D. Cowan and D. C. Griffin, "Approximate relativistic corrections to atomic radial wave functions," J. Opt. Soc. Am. **66**, 1010–1014 (1976).
[56]W. Klopper, "Simple recipe for implementing computation of first-order relativistic corrections to electron correlation energies in framework of direct perturbation theory," J. Comput. Chem. **18**, 20–27 (1997).
[57]N. C. Handy, Y. Yamaguchi, and H. F. Schaefer III, "The diagonal correction to the Born–Oppenheimer approximation: Its effect on the singlet–triplet splitting of CH_2 and other molecular effects," J. Chem. Phys. **84**, 4481–4484 (1986).
[58]R. A. Kendall, T. H. Dunning, Jr., and R. J. Harrison, "Electron affinities of the first-row atoms revisited. Systematic basis sets and wave functions," J. Chem. Phys. **96**, 6796–6806 (1992).
[59]C. Puzzarini, J. F. Stanton, and J. Gauss, "Quantum-chemical calculation of spectroscopic parameters for rotational spectroscopy," Int. Rev. Phys. Chem. **29**, 273–367 (2010).
[60]M. Heckert, M. Kállay, and J. Gauss, "Molecular equilibrium geometries based on coupled-cluster calculations including quadruple excitations," Mol. Phys. **103**, 2109–2115 (2005).
[61]M. Heckert, M. Kállay, D. P. Tew, W. Klopper, and J. Gauss, "Basis-set extrapolation techniques for the accurate calculation of molecular equilibrium geometries using coupled-cluster theory," J. Chem. Phys. **125**, 044108 (2006).
[62]D. Feller, "The use of systematic sequences of wave functions for estimating the complete basis set, full configuration interaction limit in water," J. Phys. Chem. **98**, 7059–7071 (1993).
[63]S. Alessandrini, J. Gauss, and C. Puzzarini, "Accuracy of rotational parameters predicted by high-level quantum-chemical calculations: Case study of sulfur-containing molecules of astrochemical interest," J. Chem. Theory Comput. **14**, 5360–5371 (2018).
[64]C. Puzzarini, M. Heckert, and J. Gauss, "The accuracy of rotational constants predicted by high-level quantum-chemical calculations. I. Molecules containing first-row atoms," J. Chem. Phys. **128**, 194108 (2008).
[65]I. M. Mills, "Vibration-rotation structure in asymmetric-and symmetric-top molecules," Mol. Spectrosc. **1**, 115 (1972).
[66]V. Barone, "Anharmonic vibrational properties by a fully automated second-order perturbative approach," J. Chem. Phys. **122**, 014108 (2005).
[67]M. J. Frisch, G. W. Trucks, H. B. Schlegel, G. E. Scuseria, M. A. Robb, J. R. Cheeseman, G. Scalmani, V. Barone, G. A. Petersson, H. Nakatsuji, X. Li, M. Caricato, A. V. Marenich, J. Bloino, B. G. Janesko, R. Gomperts, B. Mennucci, H. P. Hratchian, J. V. Ortiz, A. F. Izmaylov, J. L. Sonnenberg, D. Williams-Young, F. Ding, F. Lipparini, F. Egidi, J. Goings, B. Peng, A. Petrone, T. Henderson, D. Ranasinghe, V. G. Zakrzewski, J. Gao, N. Rega, G. Zheng, W. Liang, M. Hada, M. Ehara, K. Toyota, R. Fukuda, J. Hasegawa, M. Ishida, T. Nakajima, Y. Honda, O. Kitao, H. Nakai, T. Vreven, K. Throssell, J. A. Montgomery, Jr., J. E. Peralta, F. Ogliaro, M. J. Bearpark, J. J. Heyd, E. N. Brothers, K. N. Kudin, V. N. Staroverov, T. A. Keith, R. Kobayashi, J. Normand, K. Raghavachari, A. P. Rendell, J. C. Burant, S. S. Iyengar, J. Tomasi, M. Cossi, J. M. Millam, M. Klene, C. Adamo, R. Cammi, J. W. Ochterski, R. L. Martin, K. Morokuma, O. Farkas, J. B. Foresman, and D. J. Fox, Gaussian16 Revision C.01, Gaussian, Inc., Wallingford, CT, 2016.
[68]J. F. Stanton, J. Gauss, L. Cheng, M. E. Harding, D. A. Matthews, and P. G. Szalay, "CFOUR, coupled-cluster techniques for computational chemistry, a quantum-chemical program package," with contributions from A. A. Auer, R. J. Bartlett, U. Benedikt, C. Berger, D. E. Bernholdt, Y. J. Bomble, O. Christiansen, F. Engel, R. Faber, M. Heckert, O. Heun, M. Hilgenberg, C. Huber, T.-C. Jagau, D. Jonsson, J. Jusélius, T. Kirsch, K. Klein, W. J. Lauderdale, F. Lipparini, T. Metzroth, L. A. Mück, D. P. O'Neill, D. R. Price, E. Prochnow, C. Puzzarini, K. Ruud, F. Schiffmann, W. Schwalbach, C. Simmons, S. Stopkowicz, A. Tajti, J. Vázquez, F. Wang, and J. D. Watts, and the integral packages MOLECULE (J. Almlöf and P. R. Taylor), PROPS (P. R. Taylor), ABACUS (T. Helgaker, H. J. Aa. Jensen, P. Jørgensen, and J. Olsen), and ECP routines by A. V. Mitin and C. van Wüllen. For the current version see http://www.cfour.de.
[69]D. A. Matthews, L. Cheng, M. E. Harding, F. Lipparini, S. Stopkowicz, T.-C. Jagau, P. G. Szalay, J. Gauss, and J. F. Stanton, "Coupled-cluster techniques for computational chemistry: The CFOUR program package," J. Chem. Phys. **152**, 214108 (2020).
[70]B. A. McGuire, "2018 census of interstellar, circumstellar, extragalactic, protoplanetary disk, and exoplanetary molecules," Astrophys. J., Suppl. Ser. **239**, 17 (2018).
[71]A. H. Saleck, R. Simon, N. Schneider, and G. Winnewisser, "Detection of interstellar $^{12}C^{15}N$," Astrophys. J. Lett. **414**, L133 (1993).
[72]J. Cernicharo, M. Guélin, M. Agúndez, M. C. McCarthy, and P. Thaddeus, "Detection of C_5N^- and vibrationally excited C_6H in IRC+10216," Astrophys. J. Lett. **688**, L83 (2008).
[73]N. Marcelino, M. Agúndez, B. Tercero, C. Cabezas, C. Bermúdez, J. D. Gallego, P. deVicente, and J. Cernicharo, "Tentative detection of HC_5NH^+ in TMC-1," Astron. Astrophys. **643**, L6 (2020).
[74]M. Melosso, A. Melli, C. Puzzarini, C. Codella, L. Spada, L. Dore, C. Degli Esposti, B. Lefloch, R. Bachiller, C. Ceccarelli, J. Cernicharo, and V. Barone, "Laboratory measurements and astronomical search for cyanomethanimine," Astron. Astrophys. **609**, A121 (2018).
[75]C. Puzzarini, G. Cazzoli, and J. Gauss, "The rotational spectra of $HD^{17}O$ and $D_2^{17}O$: Experiment and quantum-chemical calculations," J. Chem. Phys. **137**, 154311 (2012).
[76]C. Puzzarini, J. Bloino, N. Tasinato, and V. Barone, "Accuracy and interpretability: The devil and the holy grail. New routes across old boundaries in computational spectroscopy," Chem. Rev. **119**, 8131–8191 (2019).

Bibliography

M. Abramowitz and I. A. Stegun. Handbook of mathematical functions, Dover Publications. *New York*, 361, 1965.

T. B. Adler, G. Knizia, and H.-J. Werner. A simple and efficient CCSD(T)-F12 approximation. *The Journal of Chemical Physics*, 127:221106, 2007.

M. Agúndez, J. Cernicharo, and M. Guélin. Discovery of phosphaethyne (HCP) in space: Phosphorus chemistry in circumstellar envelopes. *The Astrophysical Journal*, 662:L91, 2007.

M. Agúndez, J. Cernicharo, L. Decin, P. Encrenaz, and D. Teyssier. Confirmation of circumstellar phosphine. *The Astrophysical Journal Letters*, 790:L27, 2014.

Y. Aikawa, N. Ohashi, S.-I. Inutsuka, E. Herbst, and S. Takakuwa. Molecular evolution in collapsing prestellar cores. *The Astrophysical Journal*, 552:639, 2001.

Y. Ajili, K. Hammami, N. E. Jaidane, M. Lanza, Y. N. Kalugina, F. Lique, and M. Hochlaf. On the accuracy of explicitly correlated methods to generate potential energy surfaces for scattering calculations and clustering: application to the HCl–He complex. *Physical Chemistry Chemical Physics*, 15:10062–10070, 2013.

S. Alessandrini, V. Barone, and C. Puzzarini. Extension of the "cheap" composite approach to noncovalent interactions: The jun-ChS scheme. *Journal of Chemical Theory and Computation*, 16:988–1006, 2019.

S. Alessandrini, F. Tonolo, and C. Puzzarini. In search of phosphorus in astronomical environments: The reaction between the CP radical ($X^2\Sigma^+$) and methanimine. *The Journal of Chemical Physics*, 154:054306, 2021.

M. H. Alexander. Dipolar model for collisional energy transfer between dark and radiating excited electronic states. *The Journal of Chemical Physics*, 76:429–444, 1982a.

M. H. Alexander. Rotationally inelastic collisions between a diatomic molecule in a $^2\Sigma^+$ electronic state and a structureless target. *The Journal of Chemical Physics*, 76:3637–3645, 1982b.

M. H. Alexander. Hybrid quantum scattering algorithms for long-range potentials. *The Journal of Chemical Physics*, 81:4510–4516, 1984.

M. H. Alexander and P. J. Dagdigian. Collision-induced transitions between molecular hyperfine levels: Quantum formalism, propensity rules, and experimental study of CaBr $(X^2\Sigma^+)$+ Ar. *The Journal of Chemical Physics*, 83:2191–2200, 1985.

M. H. Alexander and S. L. Davis. M dependence in rotationally inelastic collisions in cell experiments: Implications of an irreducible tensor expansion for molecules in $^1\Sigma$ electronic states. *The Journal of Chemical Physics*, 78:6754–6762, 1983.

M. H. Alexander and D. E. Manolopoulos. A stable linear reference potential algorithm for solution of the quantum close-coupled equations in molecular scattering theory. *The Journal of Chemical Physics*, 86:2044–2050, 1987.

M. Aliev and J. Watson. Molecular spectroscopy: modern research. *New-York*, 1985.

K. Altwegg, H. Balsiger, A. Bar-Nun, J.-J. Berthelier, A. Bieler, P. Bochsler, C. Briois, U. Calmonte, M. R. Combi, H. Cottin, et al. Prebiotic chemicals—amino acid and phosphorus—in the coma of comet 67P/Churyumov-Gerasimenko. *Science Advances*, 2:e1600285, 2016.

Anderson. Pressure broadening in the microwave and infra-red regions. *Physical Review*, 76:647, 1949.

F. Aoiz, M. Brouard, C. Eyles, J. Castillo, and V. Sáez Rábanos. Cumulative reaction probabilities: A comparison between quasi classical and quantum mechanical results. *The Journal of Chemical Physics*, 125, 2006.

A. Arthurs and A. Dalgarno. The theory of scattering by a rigid rotator. *Proceedings of the Royal Society of London. Series A. Mathematical and Physical Sciences*, 256:540–551, 1960.

J. F. Asensio, S. Spezzano, P. Caselli, F. Alves, O. Sipilä, E. Redaelli, L. Bizzocchi, F. Lique, and A. Mullins. Tracing the Contraction of the Pre-stellar Core L1544 with $HC^{17}O^+$ $J = 1 - 0$ Emission. *Astronomy & Astrophysics*, 667:A119, 2022.

S. D. Augustin and W. H. Miller. Semiclassical treatment of atom-asymmetric rotor collisions; rotational excitation of formaldehyde at low energies. *The Journal of Chemical Physics*, 61:3155–3163, 1974.

C. Balança, Y. Scribano, J. Loreau, F. Lique, and N. Feautrier. Inelastic rate coefficients for collisions of N_2H^+ with H_2. *Monthly Notices of the Royal Astronomical Society*, 495:2524–2530, 2020.

L. Baptista and A. A. De Almeida. Phosphine reactivity and its implications for pyrolysis experiments and astrochemistry. *The Journal of Physical Chemistry A*, 127:1000–1012, 2023.

V. Barone. Vibrational zero-point energies and thermodynamic functions beyond the harmonic approximation. *The Journal of Chemical Physics*, 120:3059–3065, 2004.

V. Barone. Anharmonic vibrational properties by a fully automated second-order perturbative approach. *The Journal of Chemical Physics*, 122:014108, 2005.

V. Barone, M. Biczysko, J. Bloino, and C. Puzzarini. The performance of composite schemes and hybrid CC/DFT model in predicting structure, thermodynamic and spectroscopic parameters: the challenge of the conformational equilibrium in glycine. *Physical Chemistry Chemical Physics*, 15:10094, 2013.

A. Bauder. Fundamentals of Rotational Spectroscopy. *Handbook of High-resolution Spectroscopy*, 2011.

Beer. Bestimmung der Absorption des rothen Lichts in farbigen Flüssigkeiten. *Annalen der Physik*, 162:78–88, 1852.

A. Bergeat, J. Onvlee, C. Naulin, A. Van Der Avoird, and M. Costes. Quantum dynamical resonances in low-energy CO ($j = 0$)+ He inelastic collisions. *Nature chemistry*, 7:349–353, 2015.

A. Bergeat, S. B. Morales, C. Naulin, L. Wiesenfeld, and A. Faure. Probing low-energy resonances in water-hydrogen inelastic collisions. *Physical Review Letters*, 125:143402, 2020.

A. Bergeat, A. Faure, L. Wiesenfeld, C. Miossec, S. B. Morales, and C. Naulin. Near-Threshold and Resonance Effects in Rotationally Inelastic Scattering of D_2O with Normal-H_2. *Molecules*, 27:7535, 2022.

E. A. Bergin, D. R. Ciardi, C. J. Lada, J. Alves, and E. A. Lada. Molecular excitation and differential gas-phase depletions in the IC 5146 dark cloud. *The Astrophysical Journal*, 557:209, 2001.

J. B. Bergner, K. I. Öberg, S. Walker, V. V. Guzmán, T. S. Rice, and E. A. Bergin. Detection of Phosphorus-bearing Molecules toward a Solar-type Protostar. *The Astrophysical Journal Letters*, 884:L36, 2019.

J. B. Bergner, Y. L. Shirley, J. K. Jørgensen, B. McGuire, S. Aalto, C. M. Anderson, G. Chin, M. Gerin, P. Hartogh, D. Kim, et al. Astrochemistry With the Orbiting Astronomical Satellite for Investigating Stellar Systems. *Frontiers in Astronomy and Space Sciences*, 8:246, 2022.

P. R. Berman. Speed-dependent collisional width and shift parameters in spectral profiles. *Journal of Quantitative Spectroscopy and Radiative Transfer*, 12:1331–1342, 1972.

M. Besemer, G. Tang, Z. Gao, A. van der Avoird, G. C. Groenenboom, S. Y. van de Meerakker, and T. Karman. Glory scattering in deeply inelastic molecular collisions. *Nature Chemistry*, 14:664–669, 2022.

B. Bézard. The methane mole fraction in Titan's stratosphere from DISR measurements during the Huygens probe's descent. *Icarus*, 242:64–73, 2014.

G. Birnbaum. Microwave pressure broadening and its application to intermolecular

forces. *Advances in Chemical Physics: Intermolecular Forces*, pages 487–548, 1967.

L. Bizzocchi, V. Lattanzi, J. Laas, S. Spezzano, B. M. Giuliano, D. Prudenzano, C. Endres, O. Sipilä, and P. Caselli. Accurate sub-millimetre rest frequencies for HOCO+ and DOCO+ ions. *Astronomy & Astrophysics*, 602:A34, 2017.

L. Bizzocchi et al. Millimetre to THz spectroscopy of $HC^{18}O^+$ and $HC17O^+$: accurate rest-frequencies for astrophysical studies. *article in prep.*, 2024.

N. C. Blais and D. G. Truhlar. Monte Carlo trajectory study of Ar+H_2 collisions. I. Potential energy surface and cross sections for dissociation, recombination, and inelastic scattering. *The Journal of Chemical Physics*, 65:5335–5356, 1976.

D. Bockelée-Morvan, J. Crovisier, M. Mumma, and H. Weaver. The composition of cometary volatiles. *Comets*, 1:391–423, 2004.

E. G. Bøgelund, B. A. McGuire, M. R. Hogerheijde, E. F. van Dishoeck, and N. F. Ligterink. Methylamine and other simple N-bearing species in the hot cores NGC 6334I MM1–3. *Astronomy & Astrophysics*, 624:A82, 2019.

A. D. Bolatto, M. Wolfire, and A. K. Leroy. The CO-to-H_2 conversion factor. *Annual Review of Astronomy and Astrophysics*, 51:207–268, 2013.

L. Bonnet and J. Rayez. Quasiclassical trajectory method for molecular scattering processes: necessity of a weighted binning approach. *Chemical Physics Letters*, 277:183–190, 1997.

C. T. Bop. Hyperfine excitation of NS^+ due to *para*-H_2 ($j = 0$) impact. *Monthly Notices of the Royal Astronomical Society*, 487:5685–5691, 2019.

S. F. Boys and F. Bernardi. The calculation of small molecular interactions by the differences of separate total energies. Some procedures with reduced errors. *Molecular Physics*, 19:553–566, 1970.

P. Brechignac, A. Picard-Bersellini, R. Charneau, and J.-M. Launay. Rotational relaxation of CO by collisions with H_2 molecules: A comparison between theory and experiment. *Chemical Physics*, 53:165–183, 1980.

J. Bregman, D. Lester, and D. Rank. Observation of the nu-squared band of PH_3 in the atmosphere of Saturn. *The Astrophysical Journal*, 202:L55, 1975.

C. Brinch and M. Hogerheijde. LIME–a flexible, non-LTE line excitation and radiation transfer method for millimeter and far-infrared wavelengths. *Astronomy & Astrophysics*, 523:A25, 2010.

A. Broadfoot, B. Sandel, D. Shemansky, J. Holberg, G. Smith, D. Strobel, J. McConnell, S. Kumar, D. Hunten, S. Atreya, et al. Extreme ultraviolet observations from Voyager 1 encounter with Saturn. *Science*, 212:206–211, 1981.

M. Brouard, D. H. Parker, and S. Y. van de Meerakker. Taming molecular collisions using electric and magnetic fields. *Chemical Society Reviews*, 43:7279–7294, 2014.

J. M. Brown, J. M. Brown, and A. Carrington. *Rotational Spectroscopy of Diatomic Molecules*. Cambridge University Press, 2003.

R. H. Brown, J.-P. Lebreton, and J. H. Waite. *Titan from Cassini-Huygens*. Springer, 2009.

G. Buffa, L. Dore, F. Tinti, and M. Meuwly. New experimental and theoretical results for argon broadening and shift of HCO^+ rotational lines. *ChemPhysChem*, 7:1764–1769, 2006.

G. Buffa, L. Dore, F. Tinti, and M. Meuwly. Experimental and theoretical study of helium broadening and shift of HCO^+ rotational lines. *ChemPhysChem*, 9: 2237–2244, 2008.

G. Buffa, L. Dore, and M. Meuwly. State-to-state rotational transition rates of the HCO^+ ion by collisions with helium. *Monthly Notices of the Royal Astronomical Society*, 397:1909–1914, 2009.

G. Buffa, O. Tarrini, L. Dore, and M. Meuwly. Experimental and theoretical study of the broadening and shifting of N_2H^+ rotational lines by helium. *ChemPhysChem*, 11:3141–3145, 2010.

D. Buhl and L. Snyder. Unidentified interstellar microwave line. *Nature*, 228:267–269, 1970.

M. L. Cable, S. M. Hörst, R. Hodyss, P. M. Beauchamp, M. A. Smith, and P. A. Willis. Titan tholins: simulating Titan organic chemistry in the Cassini-Huygens era. *Chemical Reviews*, 112:1882–1909, 2012.

L. Cabrera-González, D. Páez-Hernández, and O. Denis-Alpizar. Relaxation of NO^+ by collision with *para*-H_2 ($j = 0$). *Monthly Notices of the Royal Astronomical Society*, 494:129–134, 2020.

D. Carty, A. Goddard, I. R. Sims, and I. W. Smith. Rotational energy transfer in collisions between CO ($X^1\Sigma^+$, $\nu = 2$, $J = 0, 1, 4$, and 6) and He at temperatures from 294 to 15 K. *The Journal of Chemical Physics*, 121:4671–4683, 2004.

P. Caselli and C. Ceccarelli. Our Astrochemical Heritage. *The Astronomy and Astrophysics Review*, 20:1–68, 2012.

P. Caselli, C. Walmsley, R. Terzieva, and E. Herbst. The ionization fraction in dense cloud cores. *The Astrophysical Journal*, 499:234, 1998.

P. Caselli, C. Walmsley, A. Zucconi, M. Tafalla, L. Dore, and P. Myers. Molecular ions in L1544. II. The ionization degree. *The Astrophysical Journal*, 565:344, 2002.

G. Cazzoli, L. Cludi, G. Buffa, and C. Puzzarini. Precise THz measurements of HCO^+, N_2H^+, and CF^+ for astrophysical observations. *The Astrophysical Journal Supplement Series*, 203:11, 2012.

J. Cernicharo, S. Bailleux, E. Alekseev, A. Fuente, E. Roueff, M. Gerin, B. Tercero, S. Treviño-Morales, N. Marcelino, R. Bachiller, et al. Tentative detection of the

nitrosylium ion in space. *The Astrophysical Journal*, 795:40, 2014.

P. Chahal and T. Dhilip Kumar. PO^+-He collision: ab initio potential energy surface and inelastic rotational rate coefficients. *Monthly Notices of the Royal Astronomical Society*, 523:5869–5875, 2023.

J. Chantzos, V. M. Rivilla, A. Vasyunin, E. Redaelli, L. Bizzocchi, F. Fontani, and P. Caselli. The first steps of interstellar phosphorus chemistry. *Astronomy & Astrophysics*, 633:A54, 2020.

S. Chefdeville, T. Stoecklin, A. Bergeat, K. M. Hickson, C. Naulin, and M. Costes. Appearance of low energy resonances in CO–para-H_2 inelastic collisions. *Physical Review Letters*, 109:023201, 2012.

A. Cheung, D. Rank, C. Townes, and W. Welch. Further Microwave Emission Lines and Clouds of Ammonia in our Galaxy. *Nature*, 221, 1969a.

A. Cheung, D. M. Rank, C. Townes, D. D. Thornton, and W. Welch. Detection of water in interstellar regions by its microwave radiation. *Nature*, 221:626–628, 1969b.

R. Ciuryło, A. Bielski, J. Drummond, D. Lisak, A. May, A. Pine, D. Shapiro, J. Szudy, and R. Trawiński. High-resolution studies on the influence of velocity-changing collisions on atomic and molecular line shapes. In *AIP Conference Proceedings*, volume 645, pages 151–160. American Institute of Physics, 2002.

J. Čížek. On the correlation problem in atomic and molecular systems. Calculation of wavefunction components in Ursell-type expansion using quantum-field theoretical methods. *The Journal of Chemical Physics*, 45:4256–4266, 1966.

J. Čížek. On the use of the cluster expansion and the technique of diagrams in calculations of correlation effects in atoms and molecules. *Advances in Chemical Physics*, pages 35–89, 1969.

J.-M. Colmont, B. Bakri, F. Rohart, G. Wlodarczak, J. Demaison, G. Cazzoli, L. Dore, , and C. Puzzarini. Intercomparison between ozone-broadening parameters retrieved from millimetre-wave measurements by using different techniques. *Journal of Molecular Spectroscopy*, 231:171–187, 2005.

J.-M. Colmont, F. Rohart, and G. Wlodarczak. N_2-, H_2-, and He-induced collisional broadening of the $J = 24 \rightarrow 23$ transition of HC_3N located near 218.3 GHz at different temperatures. *Journal of Molecular Spectroscopy*, 241:119–123, 2007.

C. S. Contreras and R. Sahai. Physical structure of the protoplanetary nebula CRL 618. ii. interferometric mapping of millimeter-wavelength HCN $J = 1 - 0$, HCO^+ $J = 1 - 0$, and continuum emission. *The Astrophysical Journal*, 602:960, 2004.

M. Cordiner, C. Nixon, N. Teanby, P. Irwin, J. Serigano, S. B. Charnley, S. N. Milam, M. J. Mumma, D. Lis, G. Villanueva, et al. ALMA Measurements of the HNC and HC_3N Distributions in Titan's Atmosphere. *The Astrophysical Journal*

Letters, 795:L30, 2014.

M. Cordiner, C. Nixon, S. Charnley, N. Teanby, E. Molter, Z. Kisiel, and V. Vuitton. Interferometric Imaging of Titan's HC_3N, $H^{13}CCCN$, and $HCCC^{15}N$. *The Astrophysical Journal Letters*, 859:L15, 2018.

G. Corey and F. R. McCourt. Inelastic differential and integral cross sections for ${}^{2S+1}\Sigma$ linear molecule-${}^1S$ atom scattering: the use of Hund's case (b) representation. *The Journal of Physical Chemistry*, 87:2723–2730, 1983.

A. Coustenis, R. K. Achterberg, B. J. Conrath, D. E. Jennings, A. Marten, D. Gautier, C. A. Nixon, F. M. Flasar, N. A. Teanby, B. Bézard, et al. The composition of Titan's stratosphere from Cassini/CIRS mid-infrared spectra. *Icarus*, 189:35–62, 2007.

P. J. Dagdigian. Interaction of the SH^+ ion with molecular hydrogen: Ab initio potential energy surface and scattering calculations. *The Journal of Chemical Physics*, 150, 2019.

P. Daly and T. Oka. Microwave Studies of Collision-Induced Transitions between Rotational Levels. VII Collisions between NH_3 and Nonpolar Molecules. *The Journal of Chemical Physics*, 53:3272–3278, 1970.

T. M. Dame, D. Hartmann, and P. Thaddeus. The Milky Way in molecular clouds: a new complete CO survey. *The Astrophysical Journal*, 547:792, 2001.

F. Daniel, J. Cernicharo, and M.-L. Dubernet. The excitation of N_2H^+ in interstellar molecular clouds. I. Models. *The Astrophysical Journal*, 648:461, 2006.

F. Daniel, J. Goicoechea, J. Cernicharo, M.-L. Dubernet, and A. Faure. Influence of collisional rate coefficients on water vapour excitation. *Astronomy & Astrophysics*, 547:A81, 2012.

T. de Jongh, M. Besemer, Q. Shuai, T. Karman, A. van der Avoird, G. C. Groenenboom, and S. Y. van de Meerakker. Imaging the onset of the resonance regime in low-energy NO-He collisions. *Science*, 368:626–630, 2020.

J. G. de la Concepción, C. Puzzarini, V. Barone, I. Jiménez-Serra, and O. Roncero. Formation of phosphorus monoxide (PO) in the interstellar medium: Insights from quantum-chemical and kinetic calculations. *The Astrophysical Journal*, 922: 169, 2021.

F. C. De Lucia and S. Green. Recent advances in pressure broadening: Experiment and theory. *Journal of Molecular Structure*, 190:435–446, 1988.

P. Debye. Part I. Dielectric constant. Energy absorption in dielectrics with polar molecules. *Transactions of the Faraday Society*, 30:679–684, 1934.

O. Denis-Alpizar and J. Rubayo-Soneira. Rotational relaxation of CF^+ by collision with *para*-H_2. *Monthly Notices of the Royal Astronomical Society*, 486:1255–1259, 2019.

O. Denis-Alpizar, T. Stoecklin, A. Dutrey, and S. Guilloteau. Rotational relaxation of HCO^+ and DCO^+ by collision with H_2. *Monthly Notices of the Royal Astronomical Society*, 497:4276–4281, 2020.

B. Desrousseaux, E. Quintas-Sánchez, R. Dawes, and F. Lique. Collisional excitation of CF^+ by H_2: Potential energy surface and rotational cross sections. *The Journal of Physical Chemistry A*, 123:9637–9643, 2019.

R. Dicke. The effect of collisions upon the Doppler width of spectral lines. *Physical Review*, 89:472, 1953.

L. Dore. Using Fast Fourier Transform to compute the line shape of frequency-modulated spectral profiles. *Journal of Molecular Spectroscopy*, 221:93–98, 2003.

L. Dore, G. Cazzoli, and P. Caselli. Laboratory and astrophysical detection of the hyperfine structure of the $J = 1 - 0$ rotational transition of HCO^+. *Astronomy & Astrophysics*, 368:712–715, 2001.

L. Dore, S. Beninati, C. Puzzarini, and G. Cazzoli. Study of vibrational interactions in DCO^+ by millimeter-wave spectroscopy and determination of the equilibrium structure of the formyl ion. *The Journal of Chemical Physics*, 118:7857–7862, 2003.

A. Douglas and G. Herzberg. Note on CH^+ in Interstellar Space and in the Laboratory. *The Astrophysical Journal*, 94:381, 1941.

G. W. Drake. *Springer Handbook of Atomic, Molecular, and Optical Physics*. Springer Science & Business Media, 2006.

M.-L. Dubernet, C. Boursier, O. Denis-Alpizar, Y. A. Ba, N. Moreau, C. M. Zwölf, M. A. Amor, D. Babikov, N. Balakrishnan, C. Balança, M. Ben Khalifa, A. Bergeat, C. T. Bop, L. Cabrera-González, C. Cárdenas, A. Chefai, P. J. Dagdigian, F. Dayou, S. Demes, B. Desrousseaux, F. Dumouchel, A. Faure, R. C. Forrey, J. Franz, R. M. García-Vázquez, F. Gianturco, A. Godard Palluet, L. González-Sánchez, G. C. Groenenboom, P. Halvick, K. Hammami, F. Khadri, Y. Kalugina, I. Kleiner, J. Kłos, F. Lique, J. Loreau, B. Mandal, B. Mant, S. Marinakis, D. Ndaw, P. Pirlot Jankowiak, T. Price, E. Quintas-Sánchez, R. Ramachandran, E. Sahnoun, C. Santander, P. C. Stancil, T. Stoecklin, J. Tennyson, F. Tonolo, R. Urzúa-Leiva, B. Yang, E. Yurtsever, and M. Zóltowski. BASECOL2023 scientific content. *Astronomy & Astrophysics*, 683:A40, 2024.

F. Dumouchel, J. Kłos, and F. Lique. The rotational excitation of the interstellar HNC by *para*-and *ortho*-H_2. *Physical Chemistry Chemical Physics*, 13:8204–8212, 2011.

F. Dumouchel, J. Kłos, R. Toboła, A. Bacmann, S. Maret, P. Hily-Blant, A. Faure, and F. Lique. Fine and hyperfine excitation of NH and ND by He: On the importance of calculating rate coefficients of isotopologues. *The Journal of Chemical Physics*, 137:114306, 2012.

T. H. Dunning Jr. Gaussian basis sets for use in correlated molecular calculations. I. The atoms boron through neon and hydrogen. *The Journal of Chemical Physics*, 90:1007–1023, 1989.

C. Eckart. Some studies concerning rotating axes and polyatomic molecules. *Physical Review*, 47:552, 1935.

A. R. Edmonds. *Angular Momentum in Quantum Mechanics*. Princeton University Press, 2016.

K. M. Fagerbakke, M. Heldal, and S. Norland. Content of carbon, nitrogen, oxygen, sulfur and phosphorus in native aquatic and cultured bacteria. *Aquatic Microbial Ecology*, 10:15–27, 1996.

A. Faure and F. Lique. The impact of collisional rate coefficients on molecular hyperfine selective excitation. *Monthly Notices of the Royal Astronomical Society*, 425:740–748, 2012.

A. Faure, L. Wiesenfeld, M. Wernli, and P. Valiron. The role of rotation in the vibrational relaxation of water by hydrogen molecules. *The Journal of Chemical Physics*, 123:104309, 2005.

A. Faure, L. Wiesenfeld, Y. Scribano, and C. Ceccarelli. Rotational excitation of mono-and doubly-deuterated water by hydrogen molecules. *Monthly Notices of the Royal Astronomical Society*, 420:699–704, 2012.

D. Feller. The use of systematic sequences of wave functions for estimating the complete basis set, full configuration interaction limit in water. *The Journal of Chemical Physics*, 98:7059–7071, 1993.

D. Flower. *Molecular Collisions in the Interstellar Medium*, volume 42. Cambridge University Press, 2007.

D. R. Flower and G. Pineau des Forêts. The influence of grains on the propagation and structure of C-type shock waves in interstellar molecular clouds. *Monthly Notices of the Royal Astronomical Society*, 343:390–400, 2003.

F. Fontani, V. Rivilla, P. Caselli, A. Vasyunin, and A. Palau. Phosphorus-bearing molecules in massive dense cores. *The Astrophysical Journal Letters*, 822:L30, 2016.

J. J. Fortney, T. D. Robinson, S. Domagal-Goldman, A. D. Del Genio, I. E. Gordon, E. Gharib-Nezhad, N. Lewis, C. Sousa-Silva, V. Airapetian, B. Drouin, et al. The need for laboratory measurements and ab initio studies to aid understanding of exoplanetary atmospheres. *arXiv preprint arXiv:1905.07064*, 2019.

M. J. Frisch, G. W. Trucks, H. B. Schlegel, G. E. Scuseria, M. A. Robb, J. R. Cheeseman, G. Scalmani, V. Barone, G. A. Petersson, H. Nakatsuji, X. Li, M. Caricato, A. V. Marenich, J. Bloino, B. G. Janesko, R. Gomperts, B. Mennucci, H. P. Hratchian, J. V. Ortiz, A. F. Izmaylov, J. L. Sonnenberg, D. Williams-Young,

F. Ding, F. Lipparini, F. Egidi, J. Goings, B. Peng, A. Petrone, T. Henderson, D. Ranasinghe, V. G. Zakrzewski, J. Gao, N. Rega, G. Zheng, W. Liang, M. Hada, M. Ehara, K. Toyota, R. Fukuda, J. Hasegawa, M. Ishida, T. Nakajima, Y. Honda, O. Kitao, H. Nakai, T. Vreven, K. Throssell, J. A. Montgomery, Jr., J. E. Peralta, F. Ogliaro, M. J. Bearpark, J. J. Heyd, E. N. Brothers, K. N. Kudin, V. N. Staroverov, T. A. Keith, R. Kobayashi, J. Normand, K. Raghavachari, A. P. Rendell, J. C. Burant, S. S. Iyengar, J. Tomasi, M. Cossi, J. M. Millam, M. Klene, C. Adamo, R. Cammi, J. W. Ochterski, R. L. Martin, K. Morokuma, O. Farkas, J. B. Foresman, and D. J. Fox. Gaussian 16 Revision C.01, 2016. Gaussian Inc. Wallingford CT.

J. P. Gardner, J. C. Mather, M. Clampin, R. Doyon, M. A. Greenhouse, H. B. Hammel, J. B. Hutchings, P. Jakobsen, S. J. Lilly, K. S. Long, et al. The James Webb Space Telescope. *Space Science Reviews*, 123:485–606, 2006.

P. F. Goldsmith and W. D. Langer. Population diagram analysis of molecular line emission. *The Astrophysical Journal*, 517:209, 1999.

P. F. Goldsmith, M. Heyer, G. Narayanan, R. Snell, D. Li, and C. Brunt. Large-scale structure of the molecular gas in Taurus revealed by high linear dynamic range spectral line mapping. *The Astrophysical Journal*, 680:428, 2008.

W. Gordy, R. L. Cook, and A. Weissberger. *Microwave Molecular Spectra*, volume 18. Wiley New York, 1984.

S. Green. Rotational excitation in H_2–H_2 collisions: Close-coupling calculations. *The Journal of Chemical Physics*, 62:2271–2277, 1975.

S. Green. Effect of nuclear hyperfine structure on microwave spectral pressure broadening. *The Journal of Chemical Physics*, 88:7331–7336, 1988.

S. Green and P. Thaddeus. Rotational excitation of HCN by collisions. *The Astrophysical Journal*, 191:653–658, 1974.

F. Grein and T. Chang. Multiconfiguration wavefunctions obtained by application of the generalized Brillouin theorem. *Chemical Physics Letters*, 12:44–48, 1971.

S. Grimme. Semiempirical GGA-type density functional constructed with a long-range dispersion correction. *Journal of Computational Chemistry*, 27:1787–1799, 2006.

S. Grimme, J. Antony, S. Ehrlich, and H. Krieg. A consistent and accurate ab initio parametrization of density functional dispersion correction (DFT-D) for the 94 elements H-Pu. *The Journal of Chemical Physics*, 132, 2010.

S. Grimme, S. Ehrlich, and L. Goerigk. Effect of the damping function in dispersion corrected density functional theory. *Journal of Computational Chemistry*, 32: 1456–1465, 2011.

M. Guélin, J. Cernicharo, and R. Linke. Detection of $HC^{17}O^+$ in Sagittarius B2.

The Astrophysical Journal, 263:L89–L93, 1982a.

M. Guélin, W. Langer, and R. Wilson. The state of ionization in dense molecular clouds. *Astronomy & Astrophysics*, 107:107–127, 1982b.

M. Guélin, J. Cernicharo, G. Paubert, and B. Turner. Free CP in IRC+10216. *Astronomy & Astrophysics*, 230:L9–L11, 1990.

S. Guilloteau and A. Baudry. Thermal overlap effects and collision models-HCN. *Astronomy & Astrophysics*, 97:213–217, 1981.

M. A. Gurwell. Submillimeter observations of Titan: Global measures of stratospheric temperature, CO, HCN, HC_3N, and the isotopic ratios 12C/13C and 14N/15N. *The Astrophysical Journal*, 616:L7, 2004.

D. Halfen, D. Clouthier, and L. M. Ziurys. Detection of the CCP Radical ($X^2\Pi_r$) in IRC+10216: a new interstellar phosphorus-containing species. *The Astrophysical Journal*, 677:L101, 2008.

R. Hanel, B. Conrath, F. Flasar, V. Kunde, W. Maguire, J. Pearl, J. Pirraglia, R. Samuelson, L. Herath, M. Allison, et al. Infrared observations of the Saturnian system from Voyager 1. *Science*, 212:192–200, 1981.

J. F. Hartmann. Investigations of the spectrum and orbit of delta orionis. In *A Source Book in Astronomy and Astrophysics, 1900–1975*, pages 510–513. Harvard University Press, 1979.

J.-M. Hartmann, H. Tran, N. Ngo, X. Landsheere, P. Chelin, Y. Lu, A.-W. Liu, S.-M. Hu, L. Gianfrani, G. Casa, et al. *Ab initio* calculations of the spectral shapes of CO_2 isolated lines including non-Voigt effects and comparisons with experiments. *Physical Review A*, 87:013403, 2013.

J.-M. Hartmann, C. Boulet, and D. Robert. *Collisional effects on molecular spectra: laboratory experiments and models, consequences for applications*. Elsevier, 2021.

D. R. Hartree and M. Black. A theoretical investigation of the oxygen atom in various states of ionisation. *Proceedings of the Royal Society of London. Series A, Containing Papers of a Mathematical and Physical Character*, 139:311–335, 1933.

D. R. Hartree, W. Hartree, and B. Swirles. Self-consistent field, including exchange and superposition of configurations, with some results for oxygen. *Philosophical Transactions of the Royal Society of London. Series A, Mathematical and Physical Sciences*, 238:229–247, 1939.

A. Heays, v. Bosman, AD, and E. van Dishoeck. Photodissociation and photoionisation of atoms and molecules of astrophysical interest. *Astronomy & Astrophysics*, 602:A105, 2017.

M. Heckert, M. KÁllay, and J. Gauss. Molecular equilibrium geometries based on coupled-cluster calculations including quadruple excitations. *Molecular Physics*, 103:2109–2115, 2005.

M. Heckert, M. Kàllay, D. P. Tew, W. Klopper, and J. Gauss. Basis-set extrapolation techniques for the accurate calculation of molecular equilibrium geometries using coupled-cluster theory. *The Journal of Chemical Physics*, 125:044108, 2006.

T. Helgaker, W. Klopper, H. Koch, and J. Noga. Basis-set convergence of correlated calculations on water. *The Journal of Chemical Physics*, 106:9639–9646, 1997.

F. Herbert. Spectrum line profiles: a generalized Voigt function including collisional narrowing. *Journal of Quantitative Spectroscopy and Radiative Transfer*, 14:943–951, 1974.

E. Herbst. Molecular ions in interstellar reaction networks. In *Journal of Physics: Conference Series*, volume 4/1, page 17. IOP Publishing, 2005.

E. Herbst and W. Klemperer. The formation and depletion of molecules in dense interstellar clouds. *The Astrophysical Journal*, 185:505–534, 1973.

E. Herbst and C. M. Leung. Gas-phase production of complex hydrocarbons, cyanopolyynes, and related compounds in dense interstellar clouds. *Astrophysical Journal Supplement Series*, 69:271–300, 1989.

E. Herbst and E. F. van Dishoeck. Complex organic interstellar molecules. *Annual Review of Astronomy and Astrophysics*, 47:427–480, 2009.

S. Hess. Kinetic theory of spectral line shapes. The transition between Doppler broadening and collisional broadening. *Physica*, 61:80–94, 1972.

J. M. Hollis, F. J. Lovas, and P. R. Jewell. Interstellar glycolaldehyde: The first sugar. *The Astrophysical Journal*, 540:L107, 2000.

S. M. Hörst. Titan's atmosphere and climate. *Journal of Geophysical Research: Planets*, 122:432–482, 2017.

A. Hoy, I. Mills, and G. Strey. Anharmonic force constant calculations. *Molecular Physics*, 24:1265–1290, 1972.

K. Huber. Molecular Structure Constants of Diatomic molecules. *Molecular Spectra and Molecular Structure Constants of Diatomic Molecules*, 1979.

Humlíček, Josef. An efficient method for evaluation of the complex probability function: the Voigt function and its derivatives. *Journal of Quantitative Spectroscopy and Radiative Transfer*, 21:309–313, 1979.

J. Hutson and S. Green. MOLSCAT computer code, version 14. *Collaborative Computational Project*, 6, 1994.

P. L. James, I. R. Sims, I. W. Smith, M. H. Alexander, and M. Yang. A combined experimental and theoretical study of rotational energy transfer in collisions between NO ($X\ ^2\Pi_{1/2}$, $\nu = 3, J$) and He, Ar and N_2 at temperatures down to 7 K. *The Journal of Chemical Physics*, 109:3882–3897, 1998.

P. Jankowski and K. Szalewicz. Ab initio potential energy surface and infrared spectra of H_2CO and D_2CO van der Waals complexes. *The Journal of Chemical*

Physics, 108:3554–3565, 1998.

F. Jensen. *Introduction to computational chemistry*. John wiley & sons, 2017.

M. J. Jimenez-Donaire, F. Bigiel, A. K. Leroy, D. Cormier, M. Gallagher, A. Usero, A. Bolatto, D. Colombo, S. García-Burillo, A. Hughes, et al. Optical depth estimates and effective critical densities of dense gas tracers in the inner parts of nearby galaxy discs. *Monthly Notices of the Royal Astronomical Society*, 466: 49–62, 2017.

I. Jiménez-Serra, S. Viti, D. Quénard, and J. Holdship. The chemistry of phosphorus-bearing molecules under energetic phenomena. *The Astrophysical Journal*, 862: 128, 2018.

J. Jørgensen, F. Schöier, and E. van Dishoeck. Molecular inventories and chemical evolution of low-mass protostellar envelopes. *Astronomy & Astrophysics*, 416: 603–622, 2004.

L. R. Kahn, P. J. Hay, and I. Shavitt. Theoretical study of curve crossing: ab initio calculations on the four lowest $1\Sigma+$ states of LiF. *The Journal of Chemical Physics*, 61:3530–3546, 1974.

R. Karplus. Frequency modulation in microwave spectroscopy. *Physical Review*, 73: 1027, 1948.

R. A. Kendall, T. H. Dunning Jr, and R. J. Harrison. Electron affinities of the first-row atoms revisited. Systematic basis sets and wave functions. *The Journal of Chemical Physics*, 96:6796–6806, 1992.

E. Keto and G. Rybicki. Modeling molecular hyperfine line emission. *The Astrophysical Journal*, 716:1315, 2010.

E. Keto, G. B. Rybicki, E. A. Bergin, and R. Plume. Radiative transfer and starless cores. *The Astrophysical Journal*, 613:355, 2004.

J. Kłos and F. Lique. First rate coefficients for an interstellar anion: application to the CN—H_2 collisional system. *Monthly Notices of the Royal Astronomical Society*, 418:271–275, 2011.

G. Knizia, T. B. Adler, and H.-J. Werner. Simplified CCSD(T)-F12 methods: Theory and benchmarks. *The Journal of Chemical Physics*, 130:054104, 2009.

P. J. Knowles and H.-J. Werner. An efficient second-order MC SCF method for long configuration expansions. *Chemical Physics Letters*, 115:259–267, 1985.

V. P. Kochanov. On systematic errors in spectral line parameters retrieved with the Voigt line profile. *Journal of Quantitative Spectroscopy and Radiative Transfer*, 113:1635–1641, 2012.

A. Koley. Studying the chemical and kinematical structures of dense cores TMC-1C, L1544, and TMC-1 in the Taurus molecular cloud using CCS and NH_3 observations. *Monthly Notices of the Royal Astronomical Society*, 516:185–196, 2022.

V. Kunde, A. Aikin, R. Hanel, D. Jennings, W. Maguire, and R. Samuelson. C_4H_2, HC_3N and C_2N_2 in Titan's atmosphere. *Nature*, 292:686–688, 1981.

J. Kłos and F. Lique. Cold Molecular Collisions: Quantum Scattering Calculations and Their Relevance in Astrophysical Applications. In *Cold Chemistry*, pages 46–91. Royal Society of Chemistry, 2017.

H. Labiad, M. Fournier, L. A. Mertens, A. Faure, D. Carty, T. Stoecklin, P. Jankowski, K. Szalewicz, S. D. Le Picard, and I. R. Sims. Absolute measurements of state-to-state rotational energy transfer between CO and H_2 at interstellar temperatures. *Physical Review A*, 105:L020802, 2022.

W. D. Langer, R. W. Wilson, P. S. Henry, and M. Guelin. Observations of anomalous intensities in the lines of the HCO/plus/isotopes. *The Astrophysical Journal*, 225: L139–L142, 1978.

M. Lanza, Y. Kalugina, L. Wiesenfeld, A. Faure, and F. Lique. New insights on the HCl abundance in the interstellar medium. *Monthly Notices of the Royal Astronomical Society*, 443:3351–3358, 2014.

M. Lara-Moreno, T. Stoecklin, and P. Halvick. Rotational transitions of C_3N^- induced by collision with H_2. *Monthly Notices of the Royal Astronomical Society*, 486:414–421, 2019.

V. Lattanzi, A. Walters, B. J. Drouin, and J. C. Pearson. Rotational spectrum of the formyl cation, HCO^+, to 1.2 THz. *The Astrophysical Journal*, 662:771, 2007.

F. Le Petit, E. Roueff, and E. Herbst. H and other species in the diffuse cloud towards Persei: A new detailed model. *Astronomy & Astrophysics*, 417:993–1002, 2004.

V. Lebouteiller and R. Ferlet. Phosphorus in the diffuse interstellar medium. *Astronomy & Astrophysics*, 443:509–517, 2005.

B. Lefloch, C. Vastel, S. Viti, I. Jiménez-Serra, C. Codella, L. Podio, C. Ceccarelli, E. Mendoza, J. R. D. Lépine, and R. Bachiller. Phosphorus-bearing molecules in solar-type star-forming regions: First PO detection. *Monthly Notices of the Royal Astronomical Society*, 462:3937–3944, 2016.

S. Lepp, V. Buch, and A. Dalgarno. Collisional Excitation of H 2 Molecules by H Atoms. *The Astrophysical Journal Supplement Series*, 98:345, 1995.

K. L. Letchworth and D. C. Benner. Rapid and accurate calculation of the Voigt function. *Journal of Quantitative Spectroscopy and Radiative Transfer*, 107:173–192, 2007.

F. Lique and A. Faure. *Gas-Phase Chemistry in Space: From Elementary Particles to Complex Organic Molecules*. AAS-IOP Astronomy, 2019.

F. Lique, J. Cernicharo, and P. Cox. The excitation of SO in cold molecular clouds: TMC-1. *The Astrophysical Journal*, 653:1342, 2006.

F. Lique, R. Toboła, J. Kłos, N. Feautrier, A. Spielfiedel, L. Vincent, G. Chałasiński, and M. Alexander. Can we estimate H ($j = 0$) rate coefficients from He rate coefficients? Application to the SiS molecule. *Astronomy & Astrophysics*, 478: 567–574, 2008.

F. Lique, J. Kłos, and M. Hochlaf. Benchmarks for the generation of interaction potentials for scattering calculations: applications to rotationally inelastic collisions of C_4 ($X^3\Sigma_g^-$) with He. *Physical Chemistry Chemical Physics*, 12:15672–15680, 2010a.

F. Lique, A. Spielfiedel, N. Feautrier, I. Schneider, J. Klos, and M. Alexander. Rotational excitation of CN (X) by He: theory and comparison with experiments. *The Journal of Chemical Physics*, 132:024303, 2010b.

D. Lisak and J. T. Hodges. Low-uncertainty H_2O line intensities for the 930-nm region. *Journal of Molecular Spectroscopy*, 249:6–13, 2008.

H. Liszt and R. Lucas. CO in absorption and emission toward compact extragalactic radio continuum sources. *Astronomy & Astrophysics*, 339:561–574, 1998.

H. Liszt, R. Lucas, and J. H. Black. The abundance of HCO^+ in diffuse clouds. *Astronomy & Astrophysics*, 428:117–120, 2004.

R. A. Loomis, D. P. Zaleski, A. L. Steber, J. L. Neill, M. T. Muckle, B. J. Harris, J. M. Hollis, P. R. Jewell, V. Lattanzi, F. J. Lovas, et al. The detection of interstellar ethanimine (CH3CHNH) from observations taken during the GBT PRIMOS survey. *The Astrophysical Journal Letters*, 765:L9, 2013.

J. López-Pérez, P. de Vicente, F. Tercero-Martınez, C. Albo-Castano, J. Serna-Puente, M. Patino-Esteban, P. Garcıa-Carreno, J. González-Garcıa, I. López-Fernández, M. Dıez-González, et al. IGN Yebes Observatory Technology Development Center 2019–2020 Report. 2021.

H. Lorentz. The motion of electrons in metallic bodies I. In *KNAW, Proceedings*, volume 7, pages 438–453, 1905.

J. Lupi, C. Puzzarini, and V. Barone. Methanimine as a key precursor of imines in the interstellar medium: The case of propargylimine. *The Astrophysical Journal Letters*, 903:L35, 2020.

M. Mandy and P. Martin. Collisional excitation of H2 molecules by H atoms. *Astrophysical Journal Supplement Series*, 86:199–210, 1993.

D. Manolopoulos. An improved log derivative method for inelastic scattering. *The Journal of Chemical Physics*, 85:6425–6429, 1986.

S. Maret, A. Faure, E. Scifoni, and L. Wiesenfeld. On the robustness of the ammonia thermometer. *Monthly Notices of the Royal Astronomical Society*, 399:425–431, 2009.

H. Margenau. The second virial coefficient for gases: a critical comparison between

theoretical and experimental results. *Physical Review*, 36:1782, 1930.

A. Marten, T. Hidayat, Y. Biraud, and R. Moreno. New millimeter heterodyne observations of Titan: Vertical distributions of nitriles HCN, HC_3N, CH_3CN, and the isotopic ratio 15N/14N in its atmosphere. *Icarus*, 158:532–544, 2002.

P. Martin and M. Mandy. Analytic Temperature Dependences for a Complete Set of Rate Coefficients for Collisional Excitation and Dissociation of H2 Molecules by H Atoms. *The Astrophysical Journal*, 455:L89, 1995.

H. Massó and L. Wiesenfeld. The HCO^+–H_2 van der Waals interaction: Potential energy and scattering. *The Journal of Chemical Physics*, 141, 2014.

D. L. Matson, L. J. Spilker, and J.-P. Lebreton. The Cassini/Huygens mission to the Saturnian system. *Space Science Reviews*, 104:1–58, 2002.

A. May, W.-K. Liu, F. McCourt, R. Ciuryło, J. Sanchez-Fortún Stoker, D. Shapiro, and R. Wehr. The impact theory of spectral line shapes: a paradigm shift. *Canadian Journal of Physics*, 91:879–895, 2013.

B. A. McGuire. 2021 Census of Interstellar, Circumstellar, Extragalactic, Protoplanetary Disk, and Exoplanetary Molecules. *The Astrophysical Journal Supplement Series*, 259:30, 2022.

B. A. McGuire, P. B. Carroll, R. A. Loomis, I. A. Finneran, P. R. Jewell, A. J. Remijan, and G. A. Blake. Discovery of the interstellar chiral molecule propylene oxide (CH_3CHCH_2O). *Science*, 352:1449–1452, 2016.

P. McGuire and D. J. Kouri. Quantum mechanical close coupling approach to molecular collisions. jz-conserving coupled states approximation. *The Journal of Chemical Physics*, 60:2488–2499, 1974.

C. F. McKee and J. P. Ostriker. A theory of the interstellar medium-Three components regulated by supernova explosions in an inhomogeneous substrate. *The Astrophysical Journal*, 218:148–169, 1977.

A. McKellar. Evidence for the molecular origin of some hitherto unidentified interstellar lines. *Publications of the Astronomical Society of the Pacific*, 52:187–192, 1940.

A. Melli, F. Tonolo, V. Barone, and C. Puzzarini. Extending the Applicability of the Semi-experimental Approach by Means of "Template Molecule" and "Linear Regression" Models on Top of DFT Computations. *The Journal of Physical Chemistry A*, 125:9904–9916, 2021.

A. Melli, M. Melosso, L. Bizzocchi, S. Alessandrini, N. Jiang, F. Tonolo, S. Boi, G. Castellan, C. Sapienza, J.-C. Guillemin, et al. Rotational spectra of unsaturated carbon chains produced by pyrolysis: The case of propadienone, cyanovinylacetylene, and allenylacetylene. *The Journal of Physical Chemistry A*, 126:6210–6220, 2022.

M. Melosso, L. Bizzocchi, F. Tamassia, C. Degli Esposti, E. Canè, and L. Dore. The rotational spectrum of 15ND. Isotopic-independent Dunham-type analysis of the imidogen radical. *Physical Chemistry Chemical Physics*, 21:3564–3573, 2019a.

M. Melosso, B. Conversazioni, C. Degli Esposti, L. Dore, E. Cané, F. Tamassia, and L. Bizzocchi. The pure rotational spectrum of 15ND2 observed by millimetre and submillimetre-wave spectroscopy. *Journal of Quantitative Spectroscopy and Radiative Transfer*, 222:186–189, 2019b.

M. Melosso, L. Bizzocchi, H. Gazzeh, F. Tonolo, J.-C. Guillemin, S. Alessandrini, V. M. Rivilla, L. Dore, V. Barone, and C. Puzzarini. Gas-phase identification of (Z)-1, 2-ethenediol, a key prebiotic intermediate in the formose reaction. *Chemical Communications*, 58:2750–2753, 2022.

J. Messer and F. C. De Lucia. Measurement of pressure-broadening parameters for the CO-He system at 4 K. *Physical Review Letters*, 53:2555, 1984.

M. Meuwly. Machine learning for chemical reactions. *Chemical Reviews*, 121:10218–10239, 2021.

M. Meuwly and J. M. Hutson. Morphing ab initio potentials: A systematic study of Ne–HF. *The Journal of Chemical Physics*, 110:8338–8347, 1999.

F. A. Miller and D. H. Lemmon. The infrared and Raman spectra of dicyanodiacetylene, NCCCCCCN. *Spectrochimica Acta Part A: Molecular Spectroscopy*, 23: 1415–1423, 1967.

S. L. Miller. A production of amino acids under possible primitive earth conditions. *Science*, 117:528–529, 1953.

I. M. Mills. Vibration-Rotation Structure in Asymmetric-and Symmetric-Top Molecules. *Molecular Spectroscopy: Modern Research*, 1:115, 1972.

E. M. Molter, C. A. Nixon, M. A. Cordiner, J. Serigano, P. G. Irwin, N. A. Teanby, S. B. Charnley, and J. E. Lindberg. ALMA observations of HCN and its isotopologues on Titan. *The Astronomical Journal*, 152:42, 2016.

T. Monteiro. Rotational excitation of HCO^+ by collisions with H_2. *Monthly Notices of the Royal Astronomical Society*, 214:419–427, 1985.

H. S. Müller, F. Schlöder, J. Stutzki, and G. Winnewisser. The Cologne Database for Molecular Spectroscopy, CDMS: A Useful Tool for Astronomers and Spectroscopists. *Journal of Molecular Structure*, 742:215–227, 2005.

D. A. Neufeld and S. Green. Excitation of interstellar hydrogen chloride. *The Astrophysical Journal*, 432:158–166, 1994.

K. I. Öberg and E. A. Bergin. Astrochemistry and compositions of planetary systems. *Physics Reports*, 893:1–48, 2021.

B. J. Orr. Collision-induced state-to-state energy transfer in perturbed rovibrational manifolds of small polyatomic molecules: mechanistic insights and observations.

Chemical Physics, 190:261–278, 1995.

R. C. Y. Owl, M. M. Meixner, M. Wolfire, A. Tielens, and J. Tauber. HCN and HCO^+ images of the orion bar photodissociation region. *The Astrophysical Journal*, 540:886, 2000.

R. T. Pack. Space-fixed vs body-fixed axes in atom-diatomic molecule scattering. Sudden approximations. *The Journal of Chemical Physics*, 60:633–639, 1974.

L. Pagani, A. Bourgoin, and F. Lique. A method to measure CO and N_2 depletion profiles inside prestellar cores. *Astronomy & Astrophysics*, 548:L4, 2012.

E. Papajak, J. Zheng, X. Xu, H. R. Leverentz, and D. G. Truhlar. Perspectives on basis sets beautiful: Seasonal plantings of diffuse basis functions. *Journal of Chemical Theory and Computation*, 7:3027–3034, 2011.

D. Papousek and M. R. Aliev. *Molecular vibrational-rotational spectra*. Elsevier Scientific Publishing Company, 1982.

M. A. Pasek and D. S. Lauretta. Aqueous corrosion of phosphide minerals from iron meteorites: a highly reactive source of prebiotic phosphorus on the surface of the early Earth. *Astrobiology*, 5:515–535, 2005.

W. Pauli. On the connexion between the completion of electron groups in an atom with the complex structure of spectra. *Zeitschrift für Physik*, 31:765, 1925.

B. K. Pearce, R. E. Pudritz, D. A. Semenov, and T. K. Henning. Origin of the RNA world: The fate of nucleobases in warm little ponds. *Proceedings of the National Academy of Sciences*, 114:11327–11332, 2017.

P. Pechukas. Time-dependent semiclassical scattering theory. II. Atomic collisions. *Physical Review*, 181:174, 1969.

P. Pechukas. Statistical approximations in collision theory. In *Dynamics of Molecular Collisions: Part B*, pages 269–322. Springer, 1976.

T.-C. Peng, F. Wyrowski, L. Zapata, R. Güsten, and K. Menten. The APEX-CHAMP+ view of the Orion Molecular Cloud 1 core-Constraining the excitation with submillimeter CO multi-line observations. *Astronomy & Astrophysics*, 538: A12, 2012.

E. Penocchio, M. Piccardo, and V. Barone. Semiexperimental equilibrium structures for building blocks of organic and biological molecules: the B2PLYP route. *Journal of Chemical Theory and Computation*, 11:4689–4707, 2015.

E. Penocchio, M. Mendolicchio, N. Tasinato, and V. Barone. Structural features of the carbon–sulfur chemical bond: a semi-experimental perspective. *Canadian Journal of Chemistry*, 94:1065–1076, 2016.

I. Percival and M. Seaton. The partial wave theory of electron-hydrogen atom collisions. In *Mathematical Proceedings of the Cambridge Philosophical Society*, volume 53/3, pages 654–662. Cambridge University Press, 1957.

K. A. Peterson, D. E. Woon, and T. H. Dunning Jr. Benchmark calculations with correlated molecular wave functions. IV. The classical barrier height of the H + H_2 → H_2 + H reaction. *The Journal of Chemical Physics*, 100:7410–7415, 1994.

K. A. Peterson, T. B. Adler, and H.-J. Werner. Systematically convergent basis sets for explicitly correlated wavefunctions: The atoms H, He, B–Ne, and Al–Ar. *The Journal of Chemical Physics*, 128:084102, 2008.

R. H. Petrmichl, K. A. Peterson, and R. C. Woods. The microwave spectrum of PO^+: Comparison to SiF^+. *The Journal of Chemical Physics*, 94:3504–3510, 1991.

M. Piccardo, E. Penocchio, C. Puzzarini, M. Biczysko, and V. Barone. Semi-experimental equilibrium structure determinations by employing B3LYP/SNSD anharmonic force fields: Validation and application to semirigid organic molecules. *The Journal of Physical Chemistry A*, 119:2058–2082, 2015.

H. M. Pickett. Determination of collisional linewidths and shifts by a convolution method. *Applied Optics*, 19:2745–2749, 1980a.

H. M. Pickett. Effects of velocity averaging on the shapes of absorption lines. *The Journal of Chemical Physics*, 73:6090–6094, 1980b.

A. Pine. Self-, N_2-and Ar-broadening and line mixing in HCN and C_2H_2. *Journal of Quantitative Spectroscopy and Radiative Transfer*, 50:149–166, 1993.

A. Pine. Line shape asymmetries in Ar-broadened HF ($\nu = 1 - 0$) in the Dicke-narrowing regime. *The Journal of Chemical Physics*, 101:3444–3452, 1994.

G. Plummer, E. Herbst, and F. De Lucia. Laboratory measurement of the $J = 2$ goes to 3 rotational transition frequency of $HC^{17}O^+$. *The Astrophysical Journal*, 270:L99, 1983.

F. Postberg, Y. Sekine, F. Klenner, C. R. Glein, Z. Zou, B. Abel, K. Furuya, J. K. Hillier, N. Khawaja, S. Kempf, et al. Detection of phosphates originating from Enceladus's ocean. *Nature*, 618:489–493, 2023.

R. M. Prestage, K. T. Constantikes, T. R. Hunter, L. J. King, R. J. Lacasse, F. J. Lockman, and R. D. Norrod. The Green Bank Telescope. *Proceedings of the IEEE*, 97:1382–1390, 2009.

C. R. Purcell, R. Balasubramanyam, M. G. Burton, A. J. Walsh, V. Minier, M. R. Hunt-Cunningham, L. L. Kedziora-Chudczer, S. N. Longmore, T. Hill, I. Bains, et al. A CH_3CN and HCO^+ survey towards southern methanol masers associated with star formation. *Monthly Notices of the Royal Astronomical Society*, 367: 553–576, 2006.

C. Puzzarini. Gas-phase Chemistry in the Interstellar Medium: The Role of Laboratory Astrochemistry. *Frontiers in Astronomy and Space Sciences*, 8:252, 2022.

C. Puzzarini, L. Dore, and G. Cazzoli. A comparison of lineshape models in the analysis of modulated and natural rotational line profiles: application to the pres-

sure broadening of OCS and CO. *Journal of Molecular Spectroscopy*, 216:428–436, 2002.

H. Rabitz. Rotation and rotation-vibration pressure-broadened spectral lineshapes. *Annual Review of Physical Chemistry*, 25:155–177, 1974.

L. Rezac, A. Kutepov, A. Faure, P. Hartogh, and A. Feofilov. Rotational non-LTE in HCN in the thermosphere of Titan: Implications for the radiative cooling. *Astronomy & Astrophysics*, 555:A122, 2013.

S. T. Ridgway, L. Wallace, and G. R. Smith. The 800-1200 inverse centimeter absorption spectrum of Jupiter. *The Astrophysical Journal*, 207:1002–1006, 1976.

V. Rivilla, F. Fontani, M. Beltrán, A. Vasyunin, P. Caselli, J. Martín-Pintado, and R. Cesaroni. The first detections of the key prebiotic molecule PO in star-forming regions. *The Astrophysical Journal*, 826:161, 2016.

V. Rivilla, I. Jiménez-Serra, S. Zeng, S. Martín, J. Martín-Pintado, J. Armijos-Abendaño, S. Viti, R. Aladro, D. Riquelme, M. Requena-Torres, et al. Phosphorus-bearing molecules in the Galactic Center. *Monthly Notices of the Royal Astronomical Society: Letters*, 475:L30–L34, 2018.

V. M. Rivilla, M. N. Drozdovskaya, K. Altwegg, P. Caselli, M. Beltrán, F. Fontani, F. van Der Tak, R. Cesaroni, A. Vasyunin, M. Rubin, et al. ALMA and ROSINA detections of phosphorus-bearing molecules: The interstellar thread between star-forming regions and comets. *Monthly Notices of the Royal Astronomical Society*, 492:1180–1198, 2020.

V. M. Rivilla, L. Colzi, I. Jiménez-Serra, M.-P. Jesús, A. Megías, M. Melosso, L. Bizzocchi, A. Lopez-Gallifa, A. Martínez-Henares, S. Massalkhi, et al. Precursors of the RNA World in Space: Detection of (*Z*)-1,2-ethenediol in the Interstellar Medium, a Key Intermediate in Sugar Formation. *The Astrophysical Journal Letters*, 929:L11, 2022a.

V. M. Rivilla, J. García De La Concepción, I. Jiménez-Serra, J. Martín-Pintado, L. Colzi, B. Tercero, A. Megías, Á. López-Gallifa, A. Martínez-Henares, S. Massalkhi, et al. Ionize hard: Interstellar PO^+ detection. *Frontiers in Astronomy and Space Sciences*, 9:829288, 2022b.

V. M. Rivilla, M. Sanz-Novo, I. Jiménez-Serra, J. Martín-Pintado, L. Colzi, S. Zeng, A. Megías, Álvaro López-Gallifa, A. Martínez-Henares, S. Massalkhi, B. Tercero, P. de Vicente, S. Martín, D. S. Andrés, M. A. Requena-Torres, and J. L. Alonso. First Glycine Isomer Detected in the Interstellar Medium: Glycolamide ($NH_2C(O)CH_2OH$). *The Astrophysical Journal Letters*, 953:L20, 2023.

F. Rohart. Low-temperature dependence of the foreign gas relaxation of HC_3N with microwave coherent transients induced by frequency switching. *Journal of Molecular Spectroscopy*, 158:287–297, 1993.

F. Rohart, H. Mäder, and H.-W. Nicolaisen. Speed dependence of rotational re-

laxation induced by foreign gas collisions: Studies on CH_3F by millimeter wave coherent transients. *The Journal of Chemical Physics*, 101:6475–6486, 1994.

K. Rohlfs and T. L. Wilson. *Tools of Radio Astronomy*. Springer Science & Business Media, 2013.

C. C. J. Roothaan. New developments in molecular orbital theory. *Reviews of Modern Physics*, 23:69, 1951.

M. E. Rose. *Elementary theory of angular momentum*. Courier Corporation, 1995.

E. Roueff and F. Lique. Molecular excitation in the interstellar medium: Recent advances in collisional, radiative, and chemical processes. *Chemical Reviews*, 113: 8906–8938, 2013.

B. Rowe and J. Marquette. CRESU studies of ion/molecule reactions. *International Journal of Mass Spectrometry and Ion Processes*, 80:239–254, 1987.

B. Rowe, G. Dupeyrat, J. Marquette, and P. Gaucherel. Study of the reactions $N_2^+ + 2N_2 \rightarrow N_4^+ + N_2$ and $O_2^+ + 2O_2 \rightarrow O_4^+ + O_2$ from 20 to 160 K by the CRESU technique. *The Journal of Chemical Physics*, 80:4915–4921, 1984.

T. Salomon, M. Töpfer, P. Schreier, S. Schlemmer, H. Kohguchi, L. Surin, and O. Asvany. Double resonance rotational spectroscopy of He–HCO^+. *Physical Chemistry Chemical Physics*, 21:3440–3445, 2019.

E. Sarrasin, D. B. Abdallah, M. Wernli, A. Faure, J. Cernicharo, and F. Lique. The rotational excitation of HCN and HNC by He: new insights on the HCN/HNC abundance ratio in molecular clouds. *Monthly Notices of the Royal Astronomical Society*, 404:518–526, 2010.

C. Savage and L. Ziurys. Ion chemistry in photon-dominated regions: Examining the $[HCO^+]/[HOC^+]/[CO^+]$ chemical network. *The Astrophysical Journal*, 616: 966, 2004.

F. Scappini, C. Cecchi-Pestellini, C. Codella, and A. Dalgarno. Detection of HCO^+ towards Cygnus OB2 No. 12. *Monthly Notices of the Royal Astronomical Society*, 317:L6–L10, 2000.

H. C. Schewe, Q. Ma, N. Vanhaecke, X. Wang, J. Kłos, M. H. Alexander, S. Y. van de Meerakker, G. Meijer, A. van der Avoird, and P. J. Dagdigian. Rotationally inelastic scattering of OH by molecular hydrogen: Theory and experiment. *The Journal of Chemical Physics*, 142:204310, 2015.

C. Schmidt, J. Populaire, J. Walrand, G. Blanquet, and J. Bouanich. Diode-laser measurements of N_2-broadening coefficients in the ν_2 band of HCN at low temperature. *Journal of molecular spectroscopy*, 158:423–432, 1993.

F. Schöier, F. van der Tak, E. van Dishoeck, and J. Black. LAMDA: Leiden Atomic and Molecular Database. *Astrophysics Source Code Library*, pages ascl–1010, 2010.

F. L. Schöier, F. F. van der Tak, E. F. van Dishoeck, and J. H. Black. An atomic and molecular database for analysis of submillimetre line observations. *Astronomy & Astrophysics*, 432:369–379, 2005.

A. W. Schwartz. Phosphorus in prebiotic chemistry. *Philosophical Transactions of the Royal Society B: Biological Sciences*, 361:1743–1749, 2006.

I. Shavitt. The history and evolution of configuration interaction. *Molecular Physics*, 94:3–17, 1998.

I. Shavitt and R. J. Bartlett. *Many-body methods in chemistry and physics: MBPT and coupled-cluster theory*. Cambridge university press, 2009.

I. Sims, J.-L. Queffelec, A. Defrance, C. Rebrion-Rowe, D. Travers, P. Bocherel, B. Rowe, and I. W. Smith. Ultralow temperature kinetics of neutral–neutral reactions. The technique and results for the reactions CN+ O_2 down to 13 K and CN+ NH_3 down to 25 K. *The Journal of Chemical Physics*, 100:4229–4241, 1994.

B. A. Smith, L. Soderblom, R. Batson, P. Bridges, J. Inge, H. Masursky, E. Shoemaker, R. Beebe, J. Boyce, G. Briggs, et al. A new look at the Saturn system: The Voyager 2 images. *Science*, 215:504–537, 1982.

I. W. Smith. Laboratory astrochemistry: gas-phase processes. *Annual Review of Astronomy & Astrophysics*, 49:29–66, 2011.

M. Smith, G. Harvey, G. Pellett, A. Goldman, and D. Richardson. Measurements of the HCN ν_3 band broadened by N_2. *Journal of Molecular Spectroscopy*, 105: 105–112, 1984.

M. Smith, C. P. Rinsland, T. Blake, R. Sams, D. C. Benner, and V. M. Devi. Low-temperature measurements of HCN broadened by N_2 in the 14-μm spectral region. *Journal of Quantitative Spectroscopy and Radiative Transfer*, 109:922–951, 2008.

T. P. Snow and V. M. Bierbaum. Ion chemistry in the interstellar medium. *Annu. Rev. Anal. Chem.*, 1:229–259, 2008.

L. Snyder, W. Watson, and J. Hollis. An interpretation of the anomalous variation of $N_2H^+/HCO^+/SO_2$ in Orion-Support for ion-molecule reactions. *The Astrophysical Journal*, 212:79–83, 1977.

L. E. Snyder, D. Buhl, B. Zuckerman, and P. Palmer. Microwave detection of interstellar formaldehyde. *Physical Review Letters*, 22:679, 1969.

L. E. Snyder, J. Hollis, F. Lovas, and B. Ulich. Detection, identification, and observations of interstellar $H^{13}CO^+$. *The Astrophysical Journal*, 209:67–74, 1976.

A. Spielfiedel, M. L. Senent, Y. Kalugina, Y. Scribano, C. Balança, F. Lique, and N. Feautrier. A new ab initio potential energy surface for the collisional excitation of N_2H^+ by H_2. *The Journal of Chemical Physics*, 143, 2015.

T. Stantcheva and E. Herbst. Models of gas-grain chemistry in interstellar cloud cores with a stochastic approach to surface chemistry. *Astronomy & Astrophysics*,

423:241–251, 2004.

J. F. Stanton, J. Gauss, L. Cheng, M. E. Harding, D. A. Matthews, and P. G. Szalay. CFOUR, Coupled-Cluster techniques for Computational Chemistry, a quantum-chemical program package. With contributions from A.A. Auer, A. Asthana, R.J. Bartlett, U. Benedikt, C. Berger, D.E. Bernholdt, S. Blaschke, Y. J. Bomble, S. Burger, O. Christiansen, D. Datta, F. Engel, R. Faber, J. Greiner, M. Heckert, O. Heun, M. Hilgenberg, C. Huber, T.-C. Jagau, D. Jonsson, J. Jusélius, T. Kirsch, K. Klein, G.M. KopperW.J. Lauderdale, F. Lipparini, J. Liu, T. Metzroth, L.A. Mück, D.P. O'Neill, T. Nottoli, D.R. Price, E. Prochnow, C. Puzzarini, K. Ruud, F. Schiffmann, W. Schwalbach, C. Simmons, S. Stopkowicz, A. Tajti, J. Vázquez, F. Wang, J.D. Watts and the integral packages MOLECULE (J. Almlöf and P.R. Taylor), PROPS (P.R. Taylor), ABACUS (T. Helgaker, H.J. Aa. Jensen, P. Jørgensen, and J. Olsen), and ECP routines by A. V. Mitin and C. van Wüllen. For the current version, see http://www.cfour.de.

H. Suzuki, S. Yamamoto, M. Ohishi, N. Kaifu, S.-I. Ishikawa, Y. Hirahara, and S. Takano. A Survey of CCS, HC_3N, HC_5N, and NH_3 toward Dark Cloud Cores and Their Production Chemistry. *The Astrophysical Journal*, 392:551–570, 1992.

F. Tamassia, L. Bizzocchi, M. Melosso, M.-A. Martin-Drumel, O. Pirali, A. P. Charmet, E. Canè, L. Dore, I. E. Gordon, J.-C. Guillemin, et al. Synchrotron-based far-infrared spectroscopy of HC_3N: Extended ro-vibrational analysis and new line list up to 3360 cm-1. *Journal of Quantitative Spectroscopy and Radiative Transfer*, 279:108044, 2022.

E. Tenenbaum, N. Woolf, and L. M. Ziurys. Identification of phosphorus monoxide (X 2Πr) in VY Canis Majoris: detection of the First PO Bond in Space. *The Astrophysical Journal*, 666:L29, 2007.

J. Tennyson, P. F. Bernath, A. Campargue, A. G. Császár, L. Daumont, R. R. Gamache, J. T. Hodges, D. Lisak, O. V. Naumenko, L. S. Rothman, et al. Recommended isolated-line profile for representing high-resolution spectroscopic transitions (IUPAC Technical Report). *Pure and Applied Chemistry*, 86:1931–1943, 2014.

F. Tercero, J. López-Pérez, J. Gallego, F. Beltrán, O. García, M. Patino-Esteban, I. López-Fernández, G. Gómez-Molina, M. Diez, P. García-Carreño, et al. Yebes 40 m radio telescope and the broad band Nanocosmos receivers at 7 mm and 3 mm for line surveys. *Astronomy & Astrophysics*, 645:A37, 2021.

A. E. Thelen, C. Nixon, N. Chanover, E. Molter, M. Cordiner, R. Achterberg, J. Serigano, P. Irwin, N. Teanby, and S. Charnley. Spatial variations in Titan's atmospheric temperature: ALMA and Cassini comparisons from 2012 to 2015. *Icarus*, 307:380–390, 2018.

A. E. Thelen, C. Nixon, N. Chanover, M. Cordiner, E. Molter, N. Teanby, P. Irwin,

J. Serigano, and S. Charnley. Abundance measurements of Titan's stratospheric HCN, HC_3N, C_3H_4, and CH_3CN from ALMA observations. *Icarus*, 319:417–432, 2019.

S. Thorwirth, H. Müller, F. Lewen, S. Brünken, V. Ahrens, and G. Winnewisser. A concise new look at the l-type spectrum of $H_{12}C_{14}N$. *The Astrophysical Journal*, 585:L163, 2003.

F. Tonolo, J. Lupi, C. Puzzarini, and V. Barone. The quest for a plausible formation route of formyl cyanide in the interstellar medium: a state-of-the-art quantum-chemical and kinetic approach. *The Astrophysical Journal*, 900:85, 2020.

F. Tonolo, L. Bizzocchi, M. Melosso, F. Lique, L. Dore, V. Barone, and C. Puzzarini. An improved study of HCO^+ and He system: Interaction potential, collisional relaxation, and pressure broadening. *The Journal of Chemical Physics*, 155, 2021.

F. Tonolo, F. Lique, M. Melosso, C. Puzzarini, and L. Bizzocchi. Hyperfine resolved rate coefficients of $HC^{17}O^+$ with H_2 ($j = 0$). *Monthly Notices of the Royal Astronomical Society*, 516:2653–2661, 2022.

F. Tonolo, L. Bizzocchi, V. Rivilla, F. Lique, M. Melosso, and C. Puzzarini. Collisional excitation of PO+ by para-H2: potential energy surface, scattering calculations, and astrophysical applications. *Monthly Notices of the Royal Astronomical Society*, 527:2279–2287, 2024.

C. Townes. 16. Microwave and radio-frequency resonance lines of interest to radio astronomy. In *Symposium-International Astronomical Union*, volume 4, pages 92–103. Cambridge University Press, 1957.

C. Townes and A. Cheung. A pumping mechanism for anomalous microwave absorption in formaldehyde in interstellar space. *The Astrophysical Journal*, 157: L103, 1969.

C. H. Townes and A. L. Schawlow. *Microwave Spectroscopy*. Courier Corporation, 1975.

H. Tran, J.-M. Hartmann, F. Chaussard, and M. Gupta. An isolated line-shape model based on the Keilson–Storer function for velocity changes. II. Molecular dynamics simulations and the $Q(1)$ lines for pure H_2. *The Journal of Chemical Physics*, 131:154303, 2009.

D. G. Truhlar and J. T. Muckerman. Reactive scattering cross sections III: Quasi-classical and semiclassical methods. In *Atom-Molecule Collision Theory: A Guide for the Experimentalist*, pages 505–566. Springer, 1979.

R. J. Trumpler. Absorption of light in the galactic system. *Publications of the Astronomical Society of the Pacific*, 42:214–227, 1930.

B. Turner. Detection of interstellar SO^+-A diagnostic of dissociative shock chemistry. *The Astrophysical Journal*, 396:L107–L110, 1992.

B. Turner and J. Bally. Detection of interstellar PN-The first identified phosphorus compound in the interstellar medium. *The Astrophysical Journal*, 321:L75–L79, 1987.

G. Tyler, V. Eshleman, J. Anderson, G. Levy, G. Lindal, G. Wood, and T. Croft. Radio science investigations of the Saturn system with Voyager 1: Preliminary results. *Science*, 212:201–206, 1981.

F. van der Tak, J. H. Black, F. Schöier, D. Jansen, and E. F. van Dishoeck. A computer program for fast non-LTE analysis of interstellar line spectra-With diagnostic plots to interpret observed line intensity ratios. *Astronomy & Astrophysics*, 468:627–635, 2007.

F. F. van der Tak, F. Lique, A. Faure, J. H. Black, and E. F. van Dishoeck. The Leiden atomic and molecular database (LAMDA): Current status, recent updates, and future plans. *Atoms*, 8:15, 2020.

E. F. van Dishoeck. *Molecules in astrophysics: probes and processes*. Springer Science & Business Media, 1997.

J. H. van Vleck and V. F. Weisskopf. On the shape of collision-broadened lines. *Reviews of Modern Physics*, 17:227, 1945.

F. Vazart, C. Latouche, D. Skouteris, N. Balucani, and V. Barone. Cyanomethanimine isomers in cold interstellar clouds: insights from electronic structure and kinetic calculations. *The Astrophysical Journal*, 810:111, 2015.

F. Vazart, D. Calderini, C. Puzzarini, D. Skouteris, and V. Barone. State-of-the-art thermochemical and kinetic computations for astrochemical complex organic molecules: formamide formation in cold interstellar clouds as a case study. *Journal of Chemical Theory and Computation*, 12:5385–5397, 2016.

R. B. Viana, P. S. Pereira, L. G. Macedo, and A. S. Pimentel. A quantum chemical study on the formation of phosphorus mononitride. *Chemical Physics*, 363:49–58, 2009.

V. Vuitton, O. Dutuit, M. Smith, and N. Balucani. Chemistry of Titan's atmosphere. *Titan: Interior, Surface, Atmosphere, and Space Environment*, page 224, 2014.

K. M. Walker, F. Lique, F. Dumouchel, and R. Dawes. Inelastic rate coefficients for collisions of C_6H^- with H_2 and He. *Monthly Notices of the Royal Astronomical Society*, 466:831–837, 2017.

J. Ward, J. Cooper, and E. W. Smith. Correlation effects in the theory of combined Doppler and pressure broadening—I. Classical theory. *Journal of Quantitative Spectroscopy and Radiative Transfer*, 14:555–590, 1974.

J. K. Watson. Aspects of quartic and sextic centrifugal effects on rotational energy levels. *Vibrational spectra and structure*, 6:1–89, 1977.

J. D. Watts, J. Gauss, and R. J. Bartlett. Coupled-cluster methods with noniterative

triple excitations for restricted open-shell Hartree–Fock and other general single determinant reference functions. Energies and analytical gradients. *The Journal of Chemical Physics*, 98:8718–8733, 1993.

W. Welch, M. Wright, R. Plambeck, J. Bieging, and B. Baud. Millimeter-wavelength aperture synthesis of molecular lines toward Orion KL. *The Astrophysical Journal*, 245:L87–L90, 1981.

H.-J. Werner and P. J. Knowles. A second order multiconfiguration SCF procedure with optimum convergence. *The Journal of Chemical Physics*, 82:5053–5063, 1985.

M. Wernli, P. Valiron, A. Faure, L. Wiesenfeld, P. Jankowski, and K. Szalewicz. Improved low-temperature rate constants for rotational excitation of CO by H. *Astronomy & Astrophysics*, 446:367–372, 2006.

M. Wernli, L. Wiesenfeld, A. Faure, and P. Valiron. Rotational excitation of HC_3N by H_2 and He at low temperatures. *Astronomy & Astrophysics*, 464:1147–1154, 2007.

E. White, F. Ghigo, R. Prestage, D. Frayer, R. Maddalena, P. Wallace, J. Brandt, D. Egan, J. Nelson, and J. Ray. Green Bank Telescope: Overview and analysis of metrology systems and pointing performance. *Astronomy & Astrophysics*, 659: A113, 2022.

J. Whitten and M. Hackmeyer. Configuration interaction studies of ground and excited states of polyatomic molecules. I. The CI formulation and studies of formaldehyde. *The Journal of Chemical Physics*, 51:5584–5596, 1969.

L. Wiesenfeld, E. Scifoni, A. Faure, and E. Roueff. Collisional excitation of doubly deuterated ammonia ND_2H by para-H_2. *Monthly Notices of the Royal Astronomical Society*, 413:509–513, 2011.

R. C. Woods, T. A. Dixon, R. J. Saykally, and P. G. Szanto. Laboratory Microwave Spectrum of HCO^+. *Physical Review Letters*, 35:1269, 1975.

D. E. Woon. The Astrochymist: An Internet Resource for Astrochemists and Interested Bystanders. 2004. URL `www.astrochymist.org`.

D. E. Woon and T. H. Dunning Jr. Gaussian basis sets for use in correlated molecular calculations. III. The atoms aluminum through argon. *The Journal of Chemical Physics*, 98:1358–1371, 1993.

A. Wootten and A. R. Thompson. The Atacama large millimeter/submillimeter array. *Proceedings of the IEEE*, 97:1463–1471, 2009.

A. Wootten, R. Snell, and A. Glassgold. The determination of electron abundances in interstellar clouds. *The Astrophysical Journal*, 234:876–880, 1979.

S. Yamamoto. *Introduction to Astrochemistry*. Springer, 2017.

C. Yang, J. Buldyreva, I. E. Gordon, F. Rohart, A. Cuisset, G. Mouret, R. Bocquet, and F. Hindle. Oxygen, nitrogen and air broadening of HCN spectral lines at ter-

ahertz frequencies. *Journal of Quantitative Spectroscopy and Radiative Transfer*, 109:2857–2868, 2008.

C.-H. Yang, G. Sarma, J. Ter Meulen, D. Parker, G. C. McBane, L. Wiesenfeld, A. Faure, Y. Scribano, and N. Feautrier. Communication: Mapping water collisions for interstellar space conditions. *The Journal of Chemical Physics*, 133, 2010.

C.-H. Yang, G. Sarma, D. Parker, J. Ter Meulen, and L. Wiesenfeld. State-to-state differential and relative integral cross sections for rotationally inelastic scattering of H_2O by hydrogen. *The Journal of Chemical Physics*, 134:204308, 2011.

O. Yazidi, D. Ben Abdallah, and F. Lique. Revised study of the collisional excitation of HCO^+ by H_2 ($j = 0$). *Monthly Notices of the Royal Astronomical Society*, 441: 664–670, 2014.

R. V. Yelle. Non-LTE models of Titan's upper atmosphere. *The Astrophysical Journal*, 383:380–400, 1991.

Q. Yu and J. M. Bowman. Vibrational second-order perturbation theory (VPT2) using local monomer normal modes. *Molecular Physics*, 113:3964–3971, 2015.

R. N. Zare and W. G. Harter. Angular Momentum: Understanding Spatial Aspects in Chemistry and Physics. *New York*, 120, 1988.

S. Zeng, I. Jiménez-Serra, V. Rivilla, S. Martín, J. Martín-Pintado, M. Requena-Torres, J. Armijos-Abendaño, D. Riquelme, and R. Aladro. Complex organic molecules in the Galactic Centre: the N-bearing family. *Monthly Notices of the Royal Astronomical Society*, 478:2962–2975, 2018.

S. Zeng, Q. Zhang, I. Jiménez-Serra, B. Tercero, X. Lu, J. Martín-Pintado, P. De Vicente, V. Rivilla, and S. Li. Cloud–cloud collision as drivers of the chemical complexity in Galactic Centre molecular clouds. *Monthly Notices of the Royal Astronomical Society*, 497:4896–4909, 2020.

L. M. Ziurys. Detection of interstellar PN-the first phosphorus-bearing species observed in molecular clouds. *The Astrophysical Journal*, 321:L81–L85, 1987.